Journal of Geophysics Zeitschrift für Geophysik

Volume 49 1981

Springer International

Journal of Geophysics – Zeitschrift für Geophysik

This journal was founded by the Deutsche Geophysikalische Gesellschaft on the initiative of L. Mintrop in 1924 as the Zeitschrift für Geophysik and edited by G. Angenheister from Vol. 1–18 (1944). It reappeared in 1954 edited by B. Brockamp from Vol. 19–26 (1960), and edited by W. Dieminger from Vol. 27–33 (1961), and from Vol. 34 (1968) edited by W. Dieminger and J. Untiedt. After Vol. 40 (1970) the title was changed to Journal of Geophysics – Zeitschrift für Geophysik.

Published: Vols. 19–39 by Physica-Verlag, Würzburg, from Vol. 40 by Springer Berlin, Heidelberg, New York.

Springer-Verlag Berlin Heidelberg New York

Printed in Germany by Universitätsdruckerei H. Stürtz AG Würzburg

Author Index

Subject Index

Journal of Geophysics Zeitschrift für Geophysik

Volume 49 Number 1 1981

Springer International

J. Geophys. — ISSN 0340-062X — JGEOD4 49(1) 1–88 (1981) — January 1981

Journal of Geophysics – Zeitschrift für Geophysik

Edited for the **Deutsche Geophysikalische Gesellschaft** by **W. Dieminger and J. Untiedt**

This journal was founded by the Deutsche Geophysikalische Gesellschaft on the initiative of L. Mintrop in 1924 as the Zeitschrift für Geophysik and edited by G. Angenheister from Vol. 1–18 (1944). It reappeared in 1954 edited by B. Brockamp from Vol. 19–26 (1960), and edited by W. Dieminger and J. Untiedt from Vol. 27 (1961). After Vol. 40 (1970) the title was changed to Journal of Geophysics – Zeitschrift für Geophysik.

Published: Vols. 19–39 by Physica-Verlag, Würzburg, from Vol. 40 by Springer Berlin, Heidelberg, New York.

Manuscripts may be addressed to any of the Editors. For addresses see last cover page. Manuscripts should conform with the journal's accepted practice as described in the Instructions to Authors.

The Journal accepts

- Review Articles (invited by the Editors)
- Original Papers
- Short Communications
- Letters to the Editors
- Book Reviews

in the field of Geophysics and Space Physics.

Subscription Information

Volumes 49+50 (3 issues each) will appear in 1981. The price of a volume is DM 158,00 or $93.00. Prices for backvolumes are available on request. In addition, we also offer microform editions in 16 mm and 35 mm microfilm and microfiche. Correspondence concerning subscriptions should be addressed to the publisher.

Changes of Address: Allow six weeks for all changes to become effective. All communications should include both old and new addresses (with Zip Codes) and should be accompanied by a mailing label from a recent issue.

Members. Members of the Deutsche Geophysikalische Gesellschaft are entitled to purchase the Journal for their own use at a privilege price of DM 98,00 payable with the Membership dues. Orders should be sent to the Society's office at the following address: Postfach 230, D-3392 Clausthal-Zellerfeld.

North America. Subscription rate: $195.00, including postage and handling. Subscriptions are entered with prepayment only. Orders should be addressed to: Springer-Verlag New York Inc., Journal Sales Department Secaucus, 44 Hartz-Way, Secaucus, NJ 07094, USA, Tel. (201) 348-4033, Telex 0023-125994.

Japan: Subscription rate: DM 352,00 including postage (surface airmail lifted) and handling. Orders can either be placed with your bookdealer or sent directly to: Springer-Verlag KG, Heidelberger Platz 3, D-1000 Berlin 33, Tel. (030) 8207-1, Telex 01-83319.

All Other Countries. Subscription rate: DM 316,00, plus postage and handling. Orders can either be placed with your bookdealer or sent directly to: Springer-Verlag KG, Heidelberger Platz 3, D-1000 Berlin 33, Tel. (030) 8207-1, Telex 01-83319.

Offices

Springer-Verlag KG, Heidelberger Platz 3, D-1000 Berlin 33, Tel. (030) 8207-1, Telex 01-83319.

Springer-Verlag KG, Journal Production Department II, Postfach 105280, D-6900 Heidelberg 1, Tel. (06221) 487-1, Telex 04-61690.

Springer-Verlag New York Inc., 175 Fifth Avenue, New York, N.Y. 10010, USA, Tel. (212) 477-8200, Telex 0023-23223.

Responsible for Advertisements

G. Sternberg, Kurfürstendamm 237, D-1000 Berlin 15, Tel. (030) 8821031, Telex 01-85411.

Printed in Germany by Universitätsdruckerei H. Stürtz AG, Würzburg

Das Heft enthält eine Beilage des Springer-Verlages Berlin Heidelberg New York

Springer International

J. Geophys. 49, 1–10 (1981)

Journal of Geophysics

Palaeomagnetism of a Jurassic Ophiolite Series in East Elba (Italy)

H. Soffel

Institut für Allgemeine und Angewandte Geophysik, Universität München, Theresienstraße 41, D-8000 München 2, Federal Republic of Germany

Abstract. Thirty-nine sites from the East Elba (10.3° E, 42.8° N) ophiolite series, of Upper Jurassic age, with gabbro, diabase, pillow lava and radiolarite have been studied with regard to their rock magnetic and palaeomagnetic properties. After tectonic corrections yielding a positive fold test at the 99% level, 25 sites (23 reversed, 2 normal) had the following mean remanence direction: $N=25$, $R=23.7429$, $D=199.3°$, $I=-38.0°$, $k=19.0909$, $\alpha_{95}=6.4°$. There was no significant difference at the 95% level between the mean directions of the radiolarites and the magmatic rocks. Rock magnetic studies as well as a comparison of the observed predominance of reversed polarities with the Post Jurassic polarity time scale suggest a post genetic age of the most stable remanence component (Lower to Middle Cretaceous, around 120 m.y.). This conclusion is supported by the agreement of the observed inclination with inclinations predicted for East Elba from Lower to Middle Cretaceous (120 m.y.) pole positions from Africa and the Umbrian sequence on the Italian mainland. The pole position for the East Elba ophiolites is at 147.3° E, 63.2° N. The pole position for Africa is at 267° E, 48° N for an age of 120 m.y., for the Umbrian sequence it is at 281° E, 35° N, while for Eurasia it is at 153° E, 70° N. The predicted palaeodeclinations for East Elba indicate a Post Middle Cretaceous clockwise rotation of the East Elba ophiolites of 64° with respect to Africa and 82° with respect to Umbria, while the rotational movement with respect to Eurasia is not significant. As the East Elba ophiolites are a small allochthonous unit of rather limited lateral extent, no deductions concerning the rotation of autochthonous Elba or autochthonous Italy can be made. The Koenigsberger ratio of the rocks investigated was in general smaller than unity resulting in a predominance of the induced magnetization. This information, in combination with the post genetic origin of remanence, seems to be of importance for the interpretation of Mesozoic marine magnetic anomalies in the Mediterranean.

Key words: Palaeomagnetium – Ophiolites – Elba.

1. Introduction

Palaeomagnetic measurements indicate that there have been rotational movements in the Mediterranean region since the Upper Cretaceous (Van der Voo and Zijderveld 1969; De Jong et al. 1973; Van den Berg et al. 1975; Soffel 1978). These rotations are related to the collison and subsequent relative displacement of the African and European plates. The angle of counterclockwise rotation varies between 30° and 60°. The data from the Italian peninsula South of the Po Basin have mostly been obtained from allochthonous or parautochthonous pelagic sediments (limestones) from the Apennines. Nevertheless they seem to be indicative of the rotational movement of the Italian peninsula since Upper Mesozoic. Pre-Tertiary magmatic rocks are exposed in the Tuscany region in the form of an Upper Jurassic ophiolite sequence with serpentinites, gabbros, diabases, pillow lavas and radiolarites. A well exposed sequence outcrops in the Eastern part of Elba. An attempt was made to investigate the rock magnetic and palaeomagnetic properties and to compare the results with those obtained from the adjacent plates (Africa, Eurasia, Adria) and to get information about the origin of remanence of rocks formed on the bottom of an ocean.

2. Geology and Sampling

The geology of West Elba is dominated by the large granitic intrusion of Monte Capanne, with an age of 6 m.y. (Ferrara et al. 1961; Borsi et al. 1967). Smaller granitic bodies occur in the Central and Eastern parts of the island, where a larger subsurface granitic intrusion of the same age as the Monte Capanne granite has been confirmed by drilling (Bonadonna, private communication 1978). The geology of East Elba is more complicated. Autochthonous gneisses (complex I, after Trevisan 1953) above the granitic intrusion are overlain by allochthonous series of Upper Carboniferous to Lower Jurassic age showing various degrees of metamorphism (complexes II and III). On top of complex III is the allochthonous ophiolite series of East Elba (complex IV), striking NS and dipping between 30° and 50° west. The legend on the geological map of Elba (Trevisan and Marinelli 1967) indicates that the age of the ophiolite complex is Malm (Upper Jurassic). Middle to Upper Jurassic ages (165 ± 23 m.y.) have been confirmed by radiometric dating of ophiolites from the Northern Apennines, including samples from East Elba (Bigazzi et al. 1972; Bigazzi et al. 1973). The ophiolite complex is overlain by complex V consisting of non-metamorphic Upper Cretaceous to Lower Tertiary flysch sediments.

The ophiolite series is composed (from the bottom to the top) of serpentinite, gabbro, mostly spilitized diabase, pillow lava, chert and radiolarite. The contact of the pillow lavas with the overlying radiolarites is undisturbed in many places, allowing tectonic corrections to be made. However, in some places the tectonic situation was uncertain due to local structures leading to the exclusion of several otherwise suitable palaeomagnetic sampling localities.

The East Elba ophiolites seem to be closely related if not identical to those in Liguria studied by Decandia and Elter (1972).

0340-062X/81/0049/0001/$02.00

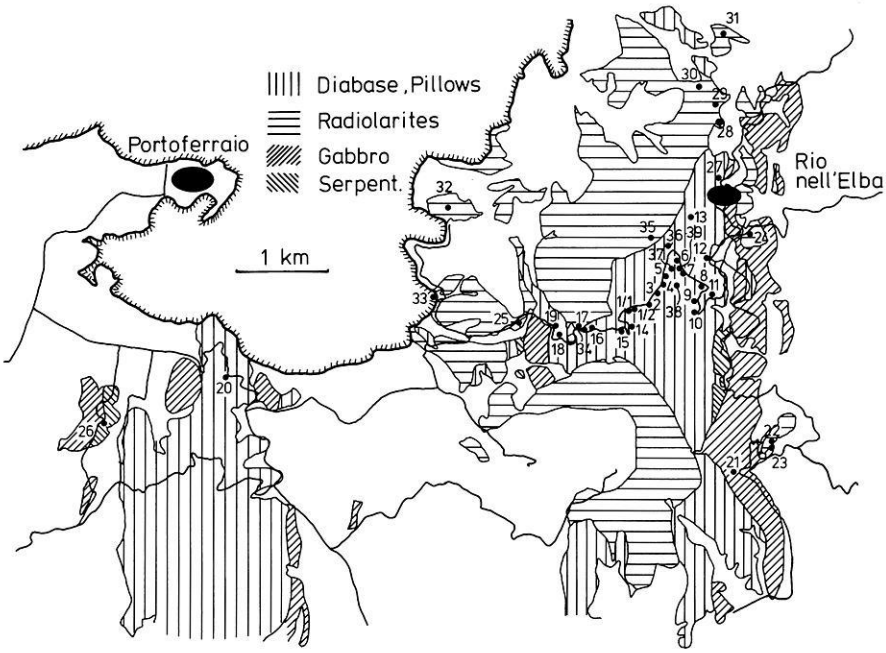

Fig. 1. Sketch map of the geology of NE Elba showing the sampling sites. Numbers refer to those in Table 1

The Ligurian ophiolites at least underwent in situ metamorphism (Cortesogno et al. 1975). Such an in situ metamorphism will also be discussed later in Sect. 4 of this paper. A review on the Ligurian ophiolites has recently been published by Cortesogno et al. (1978). Similar studies on East Elba ophiolites have been made by Horner (1974).

A sketch map of the sampling sites is shown in Fig. 1 (redrawn from Trevisan and Marinelli 1967). Thirty-nine localities with exposures of gabbro, diabase, pillow lava, chert and radiolarite were sampled. For details see Table 1. Most samples were taken with a portable drilling machine; however, from part of the very hard and brittle radiolarites oriented hand samples were taken.

3. Palaeomagnetic and Rock Magnetic Studies

3.1. Natural Remanent Magnetization (NRM)

The site mean directions of NRM are extremely scattered (see Fig. 2 and Table 1). However, there is some indication of a somewhat scattered, great circle distribution between the present geomagnetic field direction in the sampling area (star in Fig. 2) and a reversed direction in the third quadrant at approximately $D = 200°$, $I = -60°$. This direction is close to the mean directions (before tectonic correction) of all sites found after the application of various cleaning techniques (see Fig. 7). The mean intensities of NRM are variable within the different petrographic units, averaging around 50×10^{-6} G. The radiolarites had about the same intensity of NRM as the underlying pillow lavas, which was quite surprising. The Koenigsberger ratios are in general less than unity. Some of the extremely high values of NRM of several diabase cliffs are presumably due to lightning-strikes. For some sites (Nos. 1/1, 1/2, 3, 34, see Table 1) the NRM was so scattered that a mean direction was computed only for a few well grouped samples.

3.2. Demagnetization Experiments and Rock Magnetic Studies

From each sampling site at least one specimen was demagnetized with alternating fields up to 2,000 Oe. Several specimens from each petrographic unit were also thermally demagnetized up to 650° C. Examples of the variation of remanence during alternating field (AF) and thermal demagnetization treatment of radiolarites and magmatic rocks are shown in Fig. 3. As already indicated by the more or less well developed great circle distribution of Fig. 2, the NRM was only in a few cases a single component remanence. In the As-Zijderveld plots of Fig. 3a–d the dots are data points in the horizontal plane while the triangles are those in a vertical North-South directed plane with W being its Northern end.

Figure 3a shows a typical variation of NRM of the pillow lavas (here a specimen from site 1/1) during AF demagnetization up to 2,000 Oe. While the NRM direction remains practically unchanged during demagnetization, the intensity varies considerably. Firstly there is an increase by a factor of about two between NRM and 50 Oe, and a decrease to about two thirds of the initial NRM intensity between 50 and 75 Oe; this is followed by another increase by a factor of three between 75 and 1,500 Oe. Finally there is a drop of about 20% between 1,500 and 2,000 Oe. The intensity after 2,000 Oe is about 50% larger than the NRM. Four approximately antiparallel remanence components seem to be present: (1) an extremely stable reversed component with coercive forces larger than 2,000 Oe; (2) a less stable normal component with a maximum coercive force of 1,500 Oe; (3) a reversed unstable component with a narrow coercivity range between 50 and 75 Oe (this component was often not observed) and (4) a still softer normal component (approximately in the direction of the present geomagnetic field) with a maximum coercive force of 50 Oe.

An example for a thermal demagnetization of a specimen from site 1/2 (pillow lava, close to site 1/1) is presented in Fig. 3b. By stepwise heating and cooling (in zero magnetic field) the NRM intensity increases and reaches a maximum of about twice the NRM intensity after thermal demagnetization at 250°–300° C. At higher temperatures there is a steady decay of remanence without major directional change. From the aspect of the blocking temperatures the following remanence components seem to be present: (1) a reversed component with blocking temperatures higher than 580° C (Curie temperature of magnetite); (2) a likewise reversed component with blocking temperatures mainly between 400° and

Table 1. Palaeomagnetic data

1	2	3	4	5	6	7	8	9	10	11	12	13	14	15	16
1/1	Pillow	210/50 W	4	242.2	−36.6	7.8	25.1	500	7	239.5	−45.7	14.1	14.1	181.7	−46.3
1/2	Pillow	210/50 W	6	225.4	−29.5	6.7	22.1	750–1,000	7	224.6	−31.1	10.3	16.5	192.7	−29.7
2	Pillow	210/50 W	7	287.7	40.0	7.8	18.9	No consistent direction							
3	Pillow	Dubious	9	350.9	75.0	27.8	8.9	2,000	10	142.0	−48.4	9.0	14.8		
4	Pillow	210/50 W	13	318.3	69.9	5.9	16.0	No consistent direction							
5	Pillow	210/50 W	8	275.4	−75.6	9.2	16.3	No consistent direction							
6	Pillow	210/35 W	10	321.2	39.8	8.7	15.0	500–1,500	6	220.4	−23.7	8.9	19.2	204.0	−25.1
7	Pillow	210/35 W	9	237.9	53.4	8.8	15.7	500–750	5	210.0	−31.0	29.6	11.5	191.0	−25.0
8	Pillow	210/40 W	7	46.4	29.1	10.4	16.4	No consistent direction							
9	Pillow	210/35 W	10	272.5	−10.9	21.4	9.6	1,000–1,500	8	231.4	−36.9	11.0	14.9	201.9	−41.2
10	Pillow	Dubious	10	260.6	−45.5	6.3	17.6	500–1,000	10	293.5	−67.9	8.8	14.9		
11	Pillow	Dubious	7	351.1	−18.6	5.9	21.8	2,000	7	58.6	−73.1	3.9	26.9		
12	Pillow	210/35 W	10	203.8	−26.3	6.6	17.2	500–750	10	220.3	−42.1	18.1	10.4	189.3	−38.7
13	Pillow	Dubious	11	122.8	59.2	7.9	15.0	500–750	11	359.2	−80.7	18.6	9.8		
14	Pillow	Dubious	13	2.3	69.7	46.0	5.7	1,250	5	139.8	−56.4	18.1	14.7		
15	Pillow	240/55 W	8	274.0	58.3	5.7	20.7	500–2,000	8	262.7	−42.2	10.8	15.1	210.5	−38.3
16	Pillow	240/55 W	10	347.6	5.8	7.5	16.2	500–1,500	8	291.8	−47.5	13.4	13.5	204.4	−59.1
17	Pillow	240/55 W	11	285.4	− 0.4	3.0	24.4	1,500	11	255.9	−40.8	6.3	16.8	210.2	−33.0
18	Pillow	240/55 W	10	36.4	68.7	4.3	21.4	No consistent direction							
19	Gabbro	Dubious	11	109.0	−87.5	4.9	19.1	200–750	9	78.0	−76.4	11.4	13.8		
20	Diabase	Dubious	7	353.7	53.1	13.8	14.2	1,500	5	305.7	−41.3	13.1	17.3		
21	Gabbro	Dubious	10	358.1	51.3	30.5	8.0	No consistent direction							
23	Chert	240/35 W	9	198.4	−57.1	42.8	7.1	300	9	204.3	−48.6	27.5	8.9	185.7	−23.1
25	Diabase	180/50 W	12	33.6	1.1	6.8	15.5	1,500	12	29.3	−12.6	28.3	7.6	29.1	13.0
26	Gabbro	180/50 W	8	8.0	46.4	7.9	17.6	1,500–2,000	8	46.7	−12.7	33.1	8.6	43.0	23.7
27	Diabase	210/40 W	7	335.2	42.2	15.5	13.4	300	4	234.9	−51.8	8.2	24.4	181.4	−50.3
28	Radiol.	210/35 W	10	186.5	−49.5	20.6	9.8	400	10	199.1	−48.0	75.4	5.1	171.1	−32.4
29	Radiol.	250/30 W	11	191.3	−48.3	177.2	3.2	400	11	195.7	−48.8	145.5	3.5	184.6	−22.6
30	Radiol.	280/20 W	15	Scattered				400	15	248.8	−56.0	41.7	5.6	230.7	−42.8
31	Radiol.	280/20 W	10	240.7	−52.9	51.2	6.2	400	10	248.6	−64.3	151.2	3.6	225.4	−50.3
32	Radiol.	10/20 E	5	202.0	−53.4	6.2	25.1	400	4	190.8	−44.4	10.2	21.9	209.2	−40.8
33/1	Pillow	250/30 W	8	192.2	−65.1	8.2	17.3	200	8	260.2	−66.4	4.0	24.8	204.8	−56.0
33/2	Pillow	250/30 W	10	238.2	−47.6	46.1	6.5	1,000	10	238.7	−52.7	85.1	4.8	209.9	−39.0
34	Radiol.	240/55 W	9	236.7	−62.9	39.3	7.4	400	10	231.7	−68.0	62.5	5.6	175.1	−29.2
35	Radiol.	240/50 W	15	232.8	−55.7	20.0	8.1	400	15	214.8	−60.4	36.3	6.0	179.2	−23.4
36	Diabase	240/50 W	11	Scattered				500	11	238.8	−50.2	11.6	12.4	197.0	−28.9
37	Diabase	Dubious	9	Scattered				1,000–1,500	9	201.1	26.0	21.8	10.0		
38	Diabase	240/50 W	8	Scattered				2,000	8	284.1	−30.1	9.2	16.3	240.3	−51.6
39	Diabase	210/50 W	6	Scattered				750–1,000	6	254.2	−42.1	13.1	15.8	191.2	−55.8

1 Site number (see Fig. 1); 2: rock type; 3: strike/dip; 4–8: NRM data. 4: Number of samples used for calculation of the site mean direction; 5: declination in °E; 6: inclination; 7: precision parameter k; 8: α_{95}, semiangle of 95% cone of confidence; 9: peak alternating field; 10–14: RM data after partial demagnetization. 10: Number of samples; 11 declination in °E; 12: inclination; 13: precision parameter k; 14: α_{95} semiangle of 95% cone of confidence; 15 and 16: declination and inclination respectively, after tectonic correction

580° C; (3) a normal (approximately parallel to the present geomagnetic field) component with maximum blocking temperatures below 300° C.

Figures 4a and b show polished sections of a pillow lava from sites 12 and 1/2. The characteristic ore composition of this rock type is: (1) highly oxidized titanomagnetites (see Fig. 4a) with an oxidation class VI, after Ade-Hall et al. (1968) and (2) an occasionally large abundance of hematite needles (see Fig. 4b) in the silicates. The oxidized titanomagnetites consist of a cubic magnetic mineral (magnetite) and exsolution lamellae of an anisotropic phase (ilmenite). There is also some evidence for a low temperature oxidation in the form of secondary hematite along the margins and cracks. The hematite needles are about 10 μm long and 1 μm wide. Sometimes they are clustered together forming a sort of network in the reddish silicates.

Saturation magnetization versus temperature curves (J_s/T) are presented in Fig. 5. Figure 5a shows the heating and cooling curve of a pillow lava from site 4. Typical for this rock type is an initial increase of the saturation magnetization (measured at 5,000 Oe in air) between room temperature and about 160° C, then a decay with a slight kink in the gradient of the curve at about 450° C. The main Curie temperature of the heating curve is at 590° C. Some amount of saturation magnetization is still present and remains unchanged (no hyperbolic decay!) up to temperatures above 600° C (highest temperature possible for the apparatus). Similar J_s/T curves with a kink at temperatures below 200° C have been found by Ade-Hall et al. (1971) on highly altered basalts from Iceland. The cooling curve shows a Curie temperature at 580° C, which is 10° lower than that of the heating curve. This effect is not due to a temperature hysteresis of the instrument because it does not appear when pure magnetite is measured. It has often been observed by the author on exsolved titanomagne-

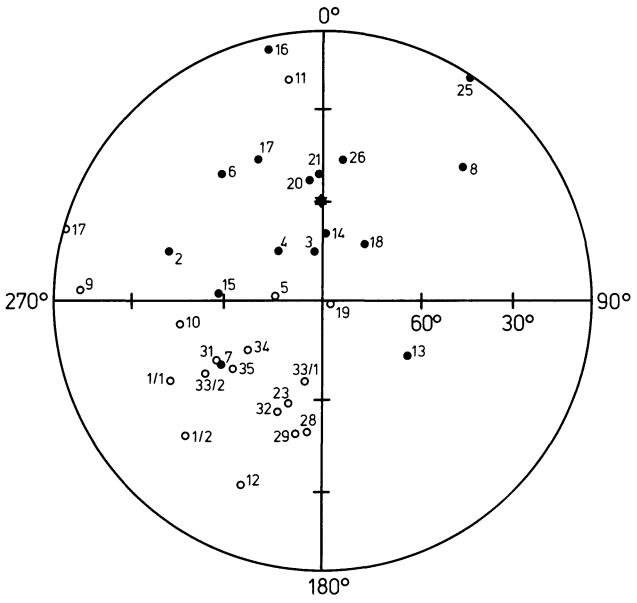

Fig. 2. Site mean directions of NRM in equal area projection. *Closed and open symbols*. positive and negative inclination respectively. *Star:* present geomagnetic field direction in the sampling area. *Numbers* refer to site numbers (Fig. 1, Table 1)

tites and is believed to be caused by diffusion of titanium from the titanium rich phase forming the exsolution lamellae (ilmenite?) back into the magnetite of the groundmass. None of the kinks at 160° and 450° C are seen on the cooling curve, which lies about 25% below the heating curve.

A further set of experiments is shown in Fig. 6, where the isothermal remanence (IRM) is plotted versus the exciting field in Oe. The data (normalized for the highest IRM intensity obtained) of pillow lavas and diabases are plotted in Fig. 6a and will be discussed below.

The observation of the demagnetization experiments (AF and thermal), the polished section studies, the J_s/T curves and IRM/H data are interpreted as follows. The main carrier of saturation magnetization of the magmatic rocks are titanomagnetites which have been almost entirely altered to magnetite plus another titanium rich phase (possibly ilmenite) by high temperature oxidation. This high temperature oxidation also affected the silicates (red colour). From the polished section studies it remains uncertain whether the exsolution of the titanomagnetites and the formation of hematite needles occurred simultaneously. Nevertheless the hematite does not contribute much to the saturation magnetization. Needle shaped hematite is not present in the diabases underlying the pillow lavas. Hematite (if present) is always found here along cracks and margins as a product of low temperature oxidation. The irreversible kink at around 160° C (see Fig. 5a) seems to be due to remnants of the primary titanium rich titanomagnetite (about TM 65, according to Bleil 1973). By heating above 600° C this phase is destroyed and probably also converted into magnetite plus ilmenite. The J_s/T curve shows a negative magnetostatic coupling between the (probably primary) TM 65 and the magnetite. The irreversible kink at 400°–450° C (which is much more pronounced in the diabases than in the pillow lavas) indicates the collapse of a minor amount of metastable titanomaghemite phases.

The dominance of magnetite in the diabases and in part also in the pillow lavas is also demonstrated in the IRM/H plots of Fig. 6a. Samples from sites 38 and 39 are diabases with altered (exsolved and/or low temperature oxidized) titanomagnetites without visible hematite needles and only minor amounts of secondary hematite along cracks and margins. They saturate as expected at fields below 3,000 Oe. Most of the pillow lavas containing hematite needles have IRM/H-curves similar to those of samples from sites 27 and 33.2 in Fig. 6a. After an initial saturation at a few thousand Oe (indicative of magnetite) the final saturation is obtained between 8,000 and 10,000 Oe (indicative of hematite). The sample from site 37 obviously has only a little magnetite besides hematite. The NRM at this site was extremely scattered and a stable endpoint could not be obtained with AF demagnetization (see Table 1).

From the above discussion it can be concluded that the magmatic rocks have essentially three major remanence components: (1) a normal component (with approximately the present geomagnetic field direction) with blocking temperatures below 300° C and maximum coercive forces below 1,500 Oe. There is evidence from the J_s/T curves, IRM/H data and polished section studies that this remanence resides in the magnetite. It is interpreted as a viscous component acquired in the local geomagnetic field. (2) A reversed component with maximum blocking temperature of 580° and a maximum coercive force of 1,500 Oe, eventually a little higher. The experiments indicate that this component is also located in the magnetite. It carries information about a reversed geomagnetic field at the time when most of this mineral was formed by an oxidation process. Section 4 of this paper discusses whether this oxidation process was syngenetic or a later event. (3) The third and likewise reversed component is not so clearly evident from the AF demagnetization experiments. It resides in a phase with coercive forces well above 2,000 Oe and blocking temperatures of at least 650° C. The experiments (J_s/T, IRM/H) point to hematite as the carrier of this remanence component. This component is strongest in the pillow lavas containing the hematite needles and less pronounced (or even absent) in the diabases, where the rarely occurring hematite is a product of low temperature oxidation. The coincidence of the remanence directions of the two reversed components indicate that formation of the hematite needles and the high temperature oxidation of the titanomagnetites occured at the same time.

The analysis of the rock magnetic and palaeomagnetic properties of the radiolarites is no less complicated. Figure 3c shows the results of the AF demagnetization of a typical specimen (site 30). All radiolarites (except many specimens from site 30 which had large superimposed viscous components) already had a quite well grouped reversed NRM direction (see Table 1). With a small directional change, the test specimen (Fig. 3c) shows a large drop of intensity between NRM and 200 Oe. At higher demagnetizing fields the intensity is only slightly reduced and the direction remains constant. Three main remanence components are present (1) a normal component (roughly parallel to the present geomagnetic field) with a maximum coercive force of about 200 Oe. (2) A reversed component with a maximum coercive force of about 500 Oe and (3) another reversed component of the same direction with coercive forces larger than 2,000 Oe. A sharp drop of NRM intensity could also be observed during thermal demagnetization (Fig. 3d, also a specimen from site 30). The strong component, which is removed between room temperature and 150° C, differs considerably in direction from the remaining component. For most sites this soft component was weak and roughly aligned along the present geomagnetic field, but for site 30 alone it was strong and almost randomly scattered. After 150° C the remanence decays steadily without systematic changes in direction towards zero. (The kinks in the plot may be due to secondary components originating

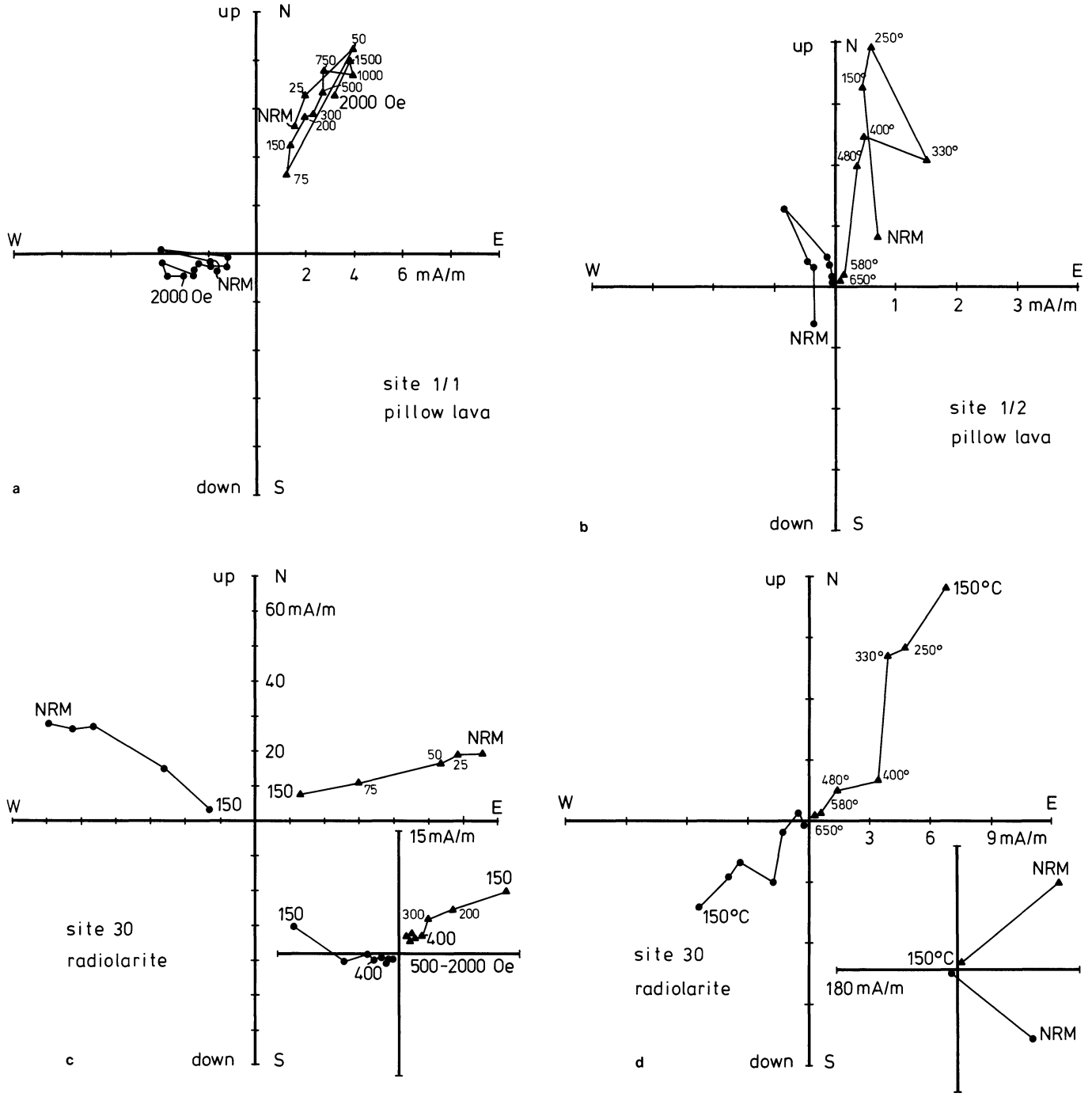

Fig. 3a–d. As-Zijderveld diagrams showing the variation of the remanence vector during progressive AF and thermal demagnetization. *Dots*. data points in the horizontal plane. *Triangles*. data points in a vertical North-South directed plane with W being its Northern end. **a** AF demagnetization of a pillow lava specimen from site 1/1. **b** Thermal demagnetization of a pillow lava specimen from site 1/2. **c** AF demagnetization of a radiolarite specimen from site 30. **d** Thermal demagnetization of a radiolarite specimen from site 30

from imperfections of the thermal demagnetizing equipment and uncontrolled field variations in the laboratory). At 580° C (Curie temperature of magnetite) there is still some remanence left which is further reduced at 650° C. Two remanence components seem to be present: (1) a soft component either parallel to the present geomagnetic field or randomly scattered with blocking temperatures below 150° C. (2) A reversed component with blocking temperatures higher than 650° C.

Figure 4c shows a polished section of a radiolarite from site 30 containing fragments of exsolved titanomagnetite grains, isolated hematite needles as well as fragments of silicates with hematite needles inside. The ores are similar to those found in the underlying pillow lavas and diabases. It can therefore be concluded that the remanence of the radiolarites is located mainly in detritus of the magmatic rocks underneath.

Figure 5b represents the heating and cooling J_s/T curve of

Fig. 4a–c. Polished sections. The long side of the figures corresponds to 270 μm.
a Pillow lava from site 12. Highly oxidized titanomagnetite grain with exsolved magnetite and ilmenite
b Pillow lava from site 1/2. Hematite needles in the silicates
c Radiolarite from site 30. Detrital magnetite grain and hematite needles

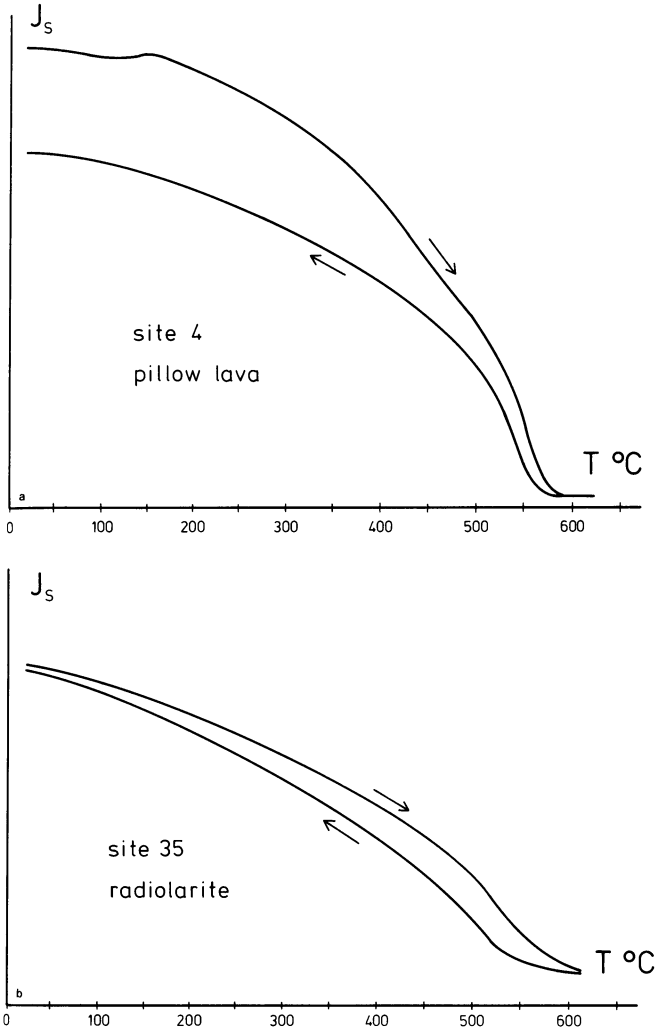

Fig. 5a and b. Saturation magnetization (in arbitrary units) versus temperature. **a** Powder of a pillow lava from site 4. **b** Separated magnetic material from a radiolarite specimen of site 35

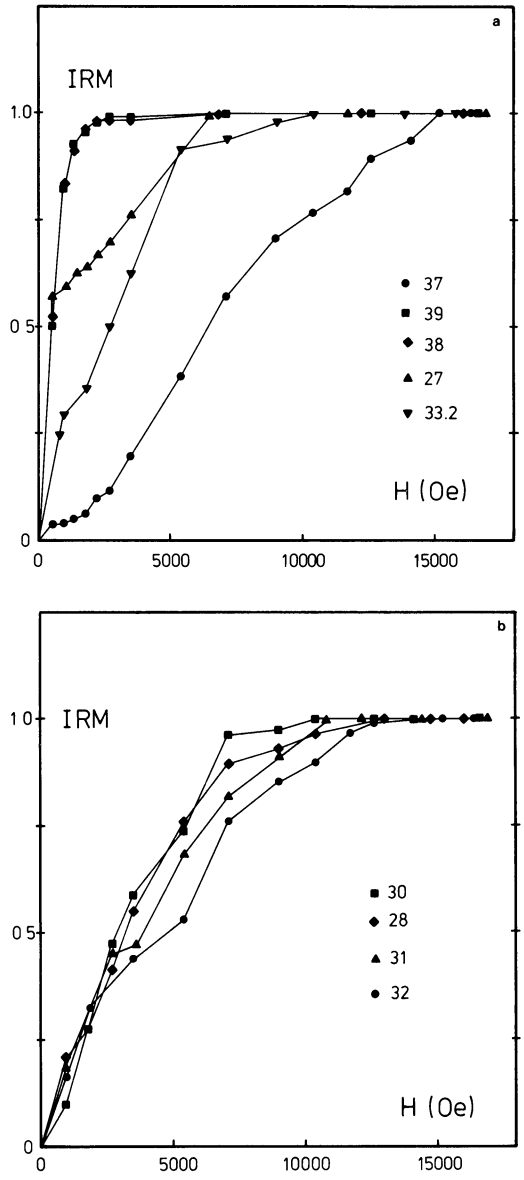

Fig. 6a and b. Isothermal remanence (IRM) as a function of the generating field H, normalized to the maximum value of IRM. Numbers refer to site numbers. For details see text. **a** Specimens of magmatic rocks. **b** Radiolarite specimens

a magnetic concentrate of radiolarites from site 35. The major phase has a Curie temperature of 550° C (close to magnetite). Above 600° C some hematite component may be responsible for the remaining intensity of J_s. The IRM/H plots (Fig. 6b) of radiolarites from several sites are more or less identical. Saturation is achieved in fields between 10,000 and 13,000 Oe. Magnetite, though the dominant phase in the J_s/T curves, does not contribute much to the IRM. This may, to a large extent, be due to the imperfect separation of the entire ore content by the hand magnet technique. The saturation field (10,000–13,000 Oe) points to coarse grained hematite as the main carrier of IRM. Goethite seems to be absent. Otherwise a saturation of IRM could not have been obtained below 15,000 Oe.

The experiments indicate that magnetite and hematite, probably both derived as detritus from the underlying magmatic rocks are the carrier of the remanence in the radiolarites. Geothite as a secondary mineral seems to be absent. Both magnetite and hematite carry a stable reversed remanence direction. This is demonstrated by the thermal demagnetization experiments. The question of the origin of the quite homogeneous reversed magnetization of the radiolarites (no normal polarities have been found so far in the whole sequence) are discussed in Sect. 4.

3.3. Palaeomagnetic Results

For some sites, a consistent mean direction could not be found for a statistically sufficient number of individual samples or specimens. Except for these cases the isolated most stable directions before tectonic correction are listed in Table 1 and plotted in Fig. 7. For nine sites (3, 9, 11, 14, 20, 23, 27, 29, 33/1) the scatter of NRM was smaller than that of the isolated most stable remanence component (see precision parameter in Table 1). In most cases (sites 3, 9, 11, 14, 20, 27) this was due to the presence of a large secondary component by which all vectors grouped along the present geomagnetic field in the sampling area irrespective of the scatter of a small stable (reversed) component. After the removal of the softer (normal) component the intensity of the stable reversed component was often smaller than 10^{-6} G

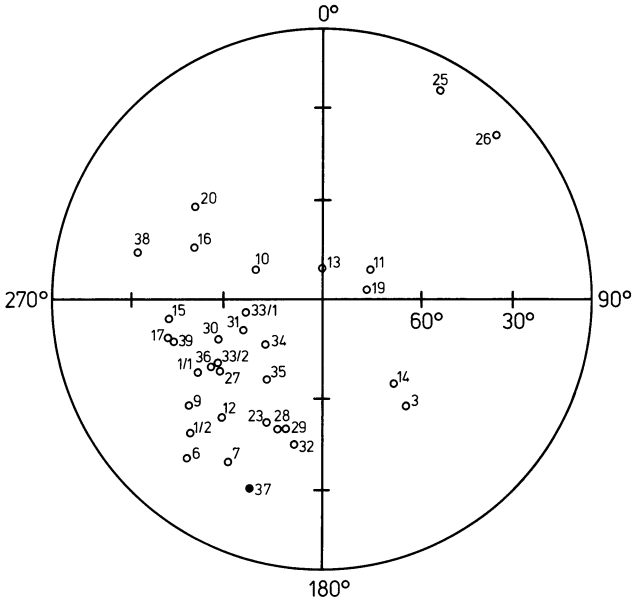

Fig. 7. Site mean directions after AF demagnetization without tectonic corrections. For symbols see legend of Fig. 2

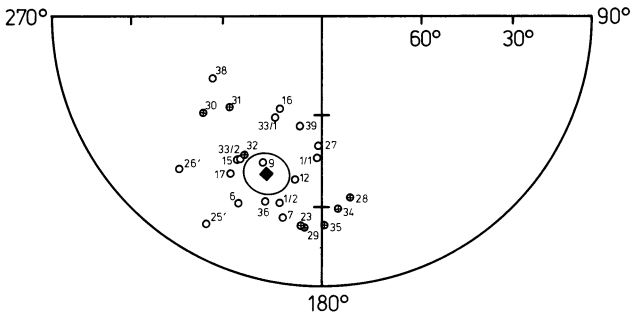

Fig. 8. Site mean directions after AF demagnetization with tectonic corrections. The directions of sites 25 and 26 have been reversed, all sites with dubious tectonic position have been omitted. *Square:* mean of all 25 directions together with cone of confidence. For symbols see legend of Fig. 2. Radiolarite sites are marked by a central cross

so that the noise level of the spinner magnetometer (Digico) was approached.

The mean remanence direction of the 25 palaeomagnetically suitable sites before tectonic correction is: $N=25$; $R=22.4117$; $D=232.2°$; $I=-45.4°$; $k=9.2724$; $\alpha_{95}=9.2°$ Application of structural corrections, omitting all sites with uncertain tectonic position (see Table 1), reduced the scatter of the stable directions considerably (Fig. 8). The mean direction of all 25 sites after tectonic correction is: $N=25$; $R=23.7429$; $D=199.3°$; $I=-38.0°$; $k=19.0909$; $\alpha_{95}=6.4°$. The ratio of the precision parameters after and before tectonic correction is 19.0909:9.2724, or 2.0589. The critical limit for $N=25$ to provide a positive fold test (McElhinny 1964) is 1.62 for the 95% level and 2.0 for the 99% level. So the fold test is positive even on the 99% level. It should be emphasized here that among the 17 suitable sites for magmatic rocks only two have normal polarity. All 8 radiolite sites have reversed polarity. There is no significant difference between the mean remanence direction of the radiolarites ($N=8$; $R=7.5270$; $D=192.5°$; $I=-34.8°$; $k=14.8$; $\alpha_{95}=12.9°$) and the underlying magmatic rocks ($N=17$; $R=16.2819$; $D=202.6°$; $I=-39.3°$; $k=22.3$; $\alpha_{95}=7.2°$). The critical value for both groups is 1.27, while a value of 2.5 would be required for a statistically significant difference of the remanence directions at the 95% level after Watson (1956). The coincidence of the remanence of the radiolarites and the magmatic rocks will be discussed again in Sect. 4.

With mean geographical latitude and longitude $\lambda=10.3°$ E, $\varphi=42.8°$ N, the pole position for the tectonically corrected remanence direction of all 25 sites ($D=199.3°$, $I=-38.0°$) is at $\lambda'=147.3°$ E, $\varphi'=63.2°$ N. It is plotted in Figure 9 together with a part of the Eurasian and African apparent polar wander paths after Irving (1977). Figure 9 also includes Cretaceous pole positions from the Italian peninsula (after Channell and Tarling 1975; Lowrie and Alvarez 1975) as well as Cretaceous pole positions from Northern Africa (after Hussain et al. 1980). Details will be discussed in Sect. 4.

4. Discussion and Conclusions

One major problem of this investigation is the age of the isolated most stable remanence component, for which the following characteristics have been found: large coercive forces (median destructive fields of 1,000 Oe and more); no significant difference in the mean remanence directions of the radiolarites and the pillow lavas lying immediately beneath, all being reversely magnetized; the occurrence of only two sites of normal polarity, both orginating in the lower parts of the ophiolite complex; positive fold test at the 99% level; lastly, a Fisherian distribution of directions with a normal degree of scattering ($k=19.3$).

Several possible age intervals for the acquisition of the stable remanence component can be discussed. (i) A Pliocene age, with remanence due to a magnetic overpring following the reheating by the 6 m.y. old granite intrusion beneath East Elba (during the reversed Gilbert polarity epoch 5.3–3.4 m.y.). This age of remanence is not likely, because only the lowermost complex I in East Elba (for definition see Sect. 2) has been seriously affected, and complexes II and III to a lesser degree. In the ophiolite complex IV only moderately increased temperatures (less than 300° C) are considered possible for the lowermost parts (serpentinites) according to Berner (1980, private communication). The radiolarites have probably not been reheated at all. It is therefore unlikely that a total magnetic overprint of the magmatic rocks and the overlying radiolarites took place in Uppermost Miocene/Lower Pliocene. The inclination which has been measured for the ophiolite complex ($-38.0°$) is also too low for a Tertiary age of remanence. An inclination of about 60° would be expected. (ii) The high temperature oxidation leading to an exsolution of the primary titanomagnetites and the formation of the hematite needles in the silicates (see Sect. 3.2) is, in general, indicative of a syngenetic age for remanence (in this case a Middle-Upper Jurassic age). Bigazzi et al. (1973) determined a radiometric age of 163 ± 23 m.y. for the ophiolites of Tuscany, including also samples from East Elba. During that time the geomagnetic field had constant normal polarity over a long interval, lasting from about 170 m.y. to 150 m.y. This is illustrated in Fig. 10. Following the compilation of McElhinny (1978) the polarity ratios, with a sliding window of 5 m.y., have been determined between 170 m.y. and 50 m.y. . From the predominance of the observed polarities of the East Elba ophiolites (see Sect. 3.3 and Table 1) it must be concluded that this remanence is not strictly syngenetic but younger, although the exsolution of the titanomagnetites in the pillow lavas may have occurred syngenetically. (iii) The coincidence of polarity and remanence direction of the pillow lavas

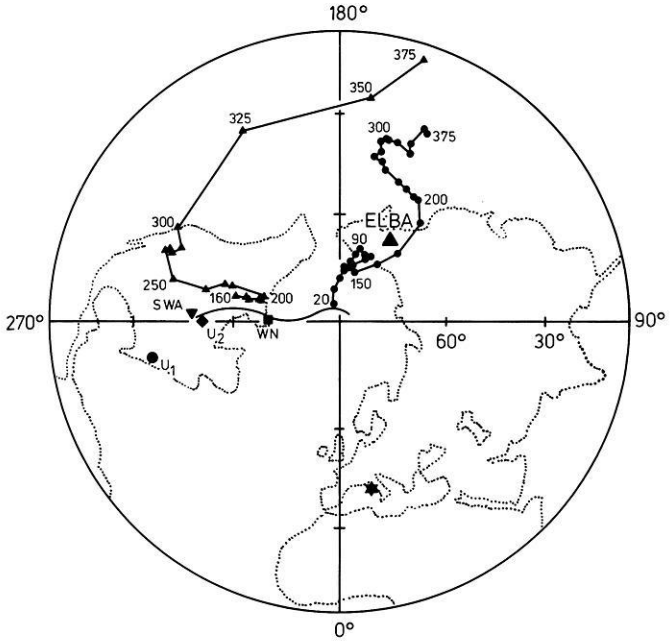

Fig. 9. Pole positions. Apparent polar wander paths of Eurasia *(small dots)* and Gondwanaland *(small triangles)* after Irving (1977). Large upward pointing triangle: pole position of the East Elba ophiolite sequence. WN: pole position of the 70 m.y. to 100 m.y. old rocks from Wadi Natash, Egypt (Hussain et al. 1980). SWA: Southwest African pole position of 110 m.y. to 128 m.y. old magmatic rocks after Gidskehaut et al. (1975). U_1: Umbrian sequence (Aptian age) after Channell and Tarling (1975). U_2: Umbrian sequence (Upper Cretaceous) after Lowrie and Alvarez (1975). The sinuous line is an apparent polar wander path for Afria between Middle Cretaceous and Lower Tertiary compiled by Hussain et al. (1980). *Star:* sampling locality

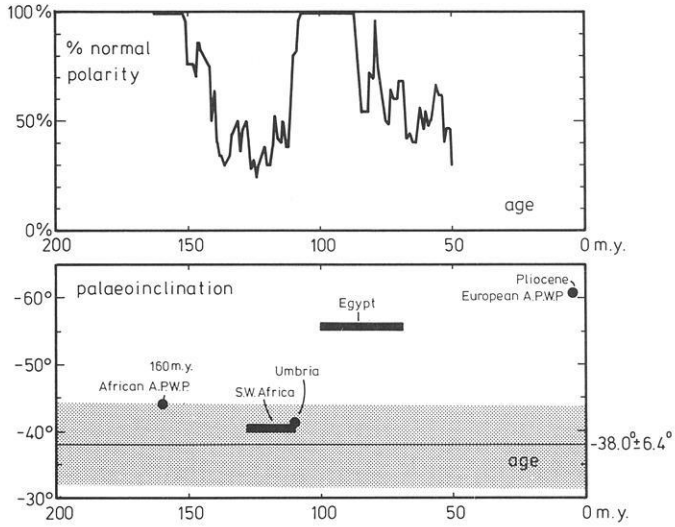

Fig. 10. Polarity ratio between 170 m.y. and 50 m.y. with a 5 m.y. window based on a compilation of polarity time scales by McElhinny (1978). The measured palaeoinclination of the East Elba ophiolite sequence ($-38.0° \pm 6.4°$) is indicated by a *horizontal line* and a *shaded area*. The palaeoinclination values which can be predicted for East Elba from other pole positions are also plotted. For details see text. The observed polarity ratio and the coincidence of the palaeoinclinations point to 120 m.y. as most probably age of remanence of the East Elby ophiolites

and the overlying radiolarites suggests a postgenetic origin of remanence during time intervals of predominantly reversed polarity. Several intervals can be considered in the Upper Mesozoic as well as during the Tertiary, with long periods of predominantly reversed polarity. Using McElhinny's (1978) compilation (see Fig. 10), there is an interval between 140 m.y. and 110 m.y. (Lower to Middle Cretaceous) with many polarity changes but a dominance of reversed polarities. The time interval 110 m.y.–85 m.y. can be excluded as a possible age for remanence, because this is the Cretaceous quiet zone of exclusively, or at least predominant, normal polarity. Since Uppermost Cretaceous there has been a tendency for a roughly even balance between normal and reversed polarity, none of them lasting longer than about 3 m.y. . So, any time interval with a reversed polarity long enough to allow a total magnetic overprint should be regarded as a possible age for the stable remanence of the East Elba ophiolites.

Channell et al. (1979) advocate that the foreland of Adria has moved in coordination with Africa since the Early Mesozoic. From the Gondwanaland (African) apparent polar wander path (Irving 1977) a pole position of 256° E, 60° N can be expected for an age of 160 m.y. . For the present geographic coordinates of East Elba (10.3° E, 42.8° N) a (reversed) remanence direction of $D=149.4°$, $I=-44.2°$ can be predicted. The inclination value is plotted in Fig. 10. The difference between the predicted inclination and that actually measured ($-38.0°$) is 6.2° and not significant ($\alpha_{95}=6.4°$) at the 95% level. However, it is unlikely that the age of remanence is younger than 80 m.y. . Otherwise an inclination of at least 55.6° should be observed (see Fig. 10). This value has been computed from the pole position (269° E, 70° N) of the volcanics and sandstones of Wadi Natash (Egypt) with an age of 70 m.y.–100 m.y. (Hussain et al. 1980). The best agreement with the observed inclination is obtained using the pole position at 267° E, 48° N determined by Gidskehaug et al. (1975) from age dated lavas (110 m.y.–128 m.y.) from SW Africa. The predicted (reversed) remanence direction for East Elba is: $D=134.9°$, $I=-40.4°$. A similar value for the inclination is obtained by using a Lower to Middle Cretaceous pole position determined by Channell and Tarling (1975) from 6 sites of Aptian age from the Umbrian sequence in the Apennines (all normal polarity). This pole is at 281.4° E, 35.2° N and yields a predicted remanence direction for East Elba of $D=116.7°$, $I=-41.4°$. This data point is also plotted in Fig. 10 (setting it at an age of 120 m.y.).

From the comparison of the inclination data and the predominance of the reversed polarity it is concluded that the ophiolite complex in East Elba has been remagnetized during the Lower Cretaceous at around 120 m.y. in a period of predominantly reversed polarity of the geomagnetic field.

For this time interval, a pole position at 267° E, 48° N has been determined for Africa by Gidskehaug et al. (1975). The corresponding Eurasian pole position for 120 m.y. is at 153° E, 70° N according to Irving (1977). The predicted remanence directions for East Elba are: $D=134.9°$, $I=-40.4°$ from the African, $D=193.3°$, $I=-44.3°$ from the Eurasian and $D=116.7°$, $I=-41.4°$ from the Aptian pole position of the Umbrian sequence. The palaeodeclination data suggest a Post Lower Cretaceous clockwise rotation of the East Elba ophiolites with respect to the African plate of about $199°-135°=64°$. The likewise clockwise rotation with respect to Italy is $199°-117°=82°$, while the rotational movement with respect to Eurasia is not significant ($199°-193°=6°$, which is the radius of the 95% circle of confidence).

It should be emphasized here that the ophiolite complex in East Elba is an allochthonous unit of rather restricted lateral

extent which rests on a pre-Triassic basement. The time of emplacement is not exactly known. It may be related to the closing of a Mesozoic ocean since Late Cretaceous. Part of the observed rotational movements with respect to Africa and the Umbrian sequence may have occurred during this emplacement. In the Pliocene the whole ophiolite complex was uplifted and tilted towards the Northwest by the granite intrusion. Additional (but smaller) rotational movements may have been caused by this event as well. So, no deductions concerning the rotation of autochthonous Elba or autochthonous Italy can be made from the East Elba ophiolite data.

Another aspect of this paper is the evidence for a post genetic origin for the remanence of ocean floor basaltic magma and radiolarites. The Koenigsberger ratio of the investigated rocks was in general smaller than unity which means a predominance of induced magnetization. The effect of a magnetic overpring on ocean floor basalts should therefore be considered seriously in the interpretation of the magnetic quiet zones of the marine magnetic anomalies.

Acknowledgements. The members of the palaeomagnetism group in Munich (Professor Dr. G. Angenheister, Dr. N. Petersen, Dr. A. Schult, Dr. P. Pohl) are kindly acknowledged for many helpful discussions. Thanks are due to Dr. B. Lammerer of the Geological Institute for his advice during sampling and the evaluation of the tectonic corrections. F. Dorner and W. Lüders helped to collect the samples, M. Testarmata and Dr. R. Veitch kindly read the manuscript. The author is also indepted to Professor W. Lowrie and Dr. R. Kligfield (Zürich) for their constructive comments with regard to the presentation and interpretation of the data.

References

Ade-Hall, J.M., Khan, M.A., Dagley, P., Wilson, R.L.: A detailed opaque petrological and magnetic investigation of a single Tertiary lava flow from Skye, Scotland. Geophys. J. R. Astron. Soc. **16**, 375–399, 1968

Ade-Hall, J.M., Palmer, H.C., Hubbard, T.R.: The magnetic and opaque petrological response of basalts to regional hydrothermal alteration. Geophys. J. **24**, 137–174, 1971

Bigazzi, G., Bonadonna, F.P., Ferrara, G., Innocenti, F.: Fission track ages of zircons and apatites from Northern Apennine ophiolites. Fortschr. Mineral. Beih. 3, **50**, 51–53, 1973

Bigazzi, G., Ferrara, G., Innocento, F.: Fission track ages of gabbros from Northern Apennines ophiolites. Earth Planet. Sci. Lett. **14**, 242–244, 1972

Bleil, U.: Synthese von Mischkristallen der Titanomagnetit-Reihe und Untersuchung ihrer für Probleme des Gesteins- und Paläomagnetismus wichtigen Kenngrößen. Dissertation, Fac. Earth Sciences, Univers. Munich, pp 109–113, 1973

Borsi, S., Ferrara, G., Tongiorgi, E.: Determinazione con il metodo del K/Ar della età delle rocce magmatiche della Toscana. Boll. Soc. Geol. Ital. **86**, 403–410, 1967

Channell, J.E.T., D'Argenio, B., Horváth, F.: Adria, the African Promontory, in Mesozoic Mediterranean Paleogeography. Earth Sci. Rev. **15**, 213–292, 1979

Channell, J.E.T., Tarling, D.H.: Palaeomagnetism and the Rotation of Italy. Earth Planet. Sci. Lett. **25**, 177–188, 1975

Cortesogno, L.G., Galbiati, B., Principi, G., Venturelli, G.: Le Brecce ofiolitiche della Liguria orientale: nuovi dati e discussione sui modelli paleogeografici. Boll. del gruppo di lavoro sule ofioliti mediterranee. Vol. **3**, "Ofioliti", No. 2/3, 99–160, 1978

Cortesogno, L.G., Gianelli, G., Piccardo, G.: Preorogenetic metamorphic and tectonic evolution of the ophiolite mafic rocks (Northern Apennine and Tuscany). Boll. Soc. Geol. Ital. **94**, 291–321, 1975

Decandia, F.A., Elter, P.: La zona ofiolitifera del Bracco nel settore compreso fra Levanto e la val Graveglia (Appennino Ligure). Mem. Soc. Geol. Ital. **11**, 503–530, 1972

De Jong, K.A., Manzoni, M., Stavenga, T., Dijk, F. Van, Voo, R. Van der, Zijderveld, J.D.A. Palaeomagnetic evidence for rotation of Sardinia during Early Miocene. Nature **243**, 281–283, 1973

Ferrara, G., Hirt, B., Marinelli, G., Tongiorgi, E.: Primi risultati sulla determinazione con il metodo del rubidio-stronzio dell' età di alcuni minerali dell' Isola d' Elba. Boll. Soc. Geol. Ital. **80**, 145–150, 1961

Gidskehaug, A., Creer, K.M., Mitchell, J.G.: Palaeomagnetism and K-Ar ages of the Southwest African basalts and their bearing on the time of initial rifting of the South Atlantic Ocean. Geophys. J. **42**, 1–20, 1975

Horner, C.: Hydrothermale Umwandlungen an basischen submarinen Laven der Ophiolitserie in Elba (Italien). Dissertation, University of Mainz, pp 1–109, 1974

Hussain, A.G., Schult, A., Soffel, H.: Preliminary polar wander path of Egypt between Cretaceous and Quaternary. Berliner Geowiss. Abh. Reihe A: **19**, 93–94, 1980

Irving, E.: Drift of the major continental blocks since the Devonian. Nature **270**, 304–309, 1977

Lowrie, W., Alvarez, W. Paleomagnetic evidence for the rotation of the Italian peninsula. J. Geophys. Res. **80**, 1579–1592, 1975

McElhinny, W.M.: Statistical significance of the fold test in palaeomagnetism. Geophys. J. **8**, 338–340, 1964

McElhinny, W.M.: The magnetic polarity time scale: prospects and possibilities in magnetostratigraphy. In: The geologic time scale. Am. Assoc Petrol. Geol. 57–65, 1978

Soffel, H.: Review of palaeomagnetic data from Italy and adjacent areas. Alps, Apennines, Hellenides, Closs, Roeder, Schmidt, eds.: Stuttgart E. Schweizerbart, pp 23–29, 1978

Trevisan, L.: La 55. riunione estiva della Società Geologica Italiana, Isola d' Elba, 18–23 septembre 1951. Boll. Soc. Geol. Ital. **70**, 435–470, 1953

Trevisan, L., Marinelli, G.: Carta Geologica dell' Isola d' Elba, Foglia Orientale, Scala 1:25000, 1967

Berg, J. Van den, Klootwijk, C.T., Wonders, T : Implications for the rotational movement of Italy from current palaeomagnetic research in the umbrian sequence, Northern Apennines. Progress in Geodynamics. pp. 165–175. Sciences, Amsterdam: Roy. Netherl. Acad. of Arts and Science, 1975

Voo, R. Van der, Zijderveld J.D.A.: Paleomagnetism in the Western Mediterranean Area. Verh. Kon. Ned. Geol. Mijnbouwkd. Gen. **26**, 121–138, 1969

Watson, G.S.: Analysis of dispersion on a sphere. Mon. Not. Astron. Soc. Geophys. Suppl. **7**, 153–159, 1956

Received August 1, 1979; Revised Version June 30, 1980
Accepted July 2, 1980

J. Geophys. 49, 11–19 (1981)

Journal of Geophysics

Paleomagnetic Evidence from Mesozoic Carbonate Rocks for the Rotation of Sardinia*

F. Horner and W Lowrie
Institut für Geophysik, ETH-Hönggerberg, CH-8093 Zürich, Switzerland

Abstract. The remanent magnetizations have been analysed in Cretaceous and Jurassic limestones, and Triassic dolomites, from Eastern and Central Sardinia. Ore microscopy and rock magnetic studies, including the acquisition of *isothermal remanent magnetization* (IRM) and the behavior of IRM during high temperature treatment, indicated that magnetite and goethite determine the paleomagnetic properties of these carbonate rocks. At all Cretaceous sites the remanences were either too weak or too unstable to be used for a paleomagnetic study. AF and thermal demagnetization were used to isolate the *characteristic remanent magnetization* (ChRM) in the Jurassic and Triassic samples. Rejection criteria were used to eliminate about one third of these samples because of directional instability, or because only very stable secondary magnetizations associated with goethite were present. For the remaining samples the ChRM direction associated with primary magnetite was extracted with the aid of vector diagrams or vector difference calculations. The ChRM directions are rotated by 70°–90° counterclockwise relative to European directions and by 35°–45° counterclockwise relative to African directions. Part of this results from the 30° microplate rotation of Sardinia in the Miocene. The remainder is due to an earlier phase of microplate rotation which took place in post-Late Jurassic time.

Key words: Rotation of Sardinia – Mesozoic limestones – paleomagnetism – rock magnetism.

Introduction

Sardinia plays a key role in Western Mediterranean tectonic history. Argand (1924) suggested a paleogeographical reconstruction in which the Corso-Sardinian block lies adjacent to Southern France. Several forms of geological evidence support this paleogeography.

Chabrier and Mascle (1975) presented facies evidence and other geological arguments in favour of a similar geological history in Sardinia and Provence. The geographic distribution of the Barremian foraminiferal *Valserina* association supports an Early Cretaceous position for Sardinia close to the south-east coast of France (Cherchi and Schroeder 1973). Micropaleontological research on Cretaceous elements in south-west Sardinia reveal microfaunal assemblages of Iberian provenance (Cherchi and Schroeder 1976).

Geometric fitting of the Corso-Sardinian block to the coast of Provence has been attempted by matching bathymetric contours qualitatively (Alvarez 1972) and with a computer (Westphal et al. 1973). Hercynian structural trends in Corsica, Sardinia and southern France are compatible with this initial paleogeography (Arthaud and Matte 1977).

Paleozoic paleomagnetic directions from Corsica (Nairn and Westphal 1968) and Sardinia (Zijderveld et al. 1970) suggested different amounts of rotation of the two islands relative to the European mainland. Differential rotation allowed also a better match of the Corso-Sardinian block against S. France and could have resulted in the opening of the gulf of Bonifacio (Alvarez 1973). However, Paleozoic tectonic structures show the same alignments on both sides of the straits, suggesting that the Corso-Sardinian block has remained as a unit since the Permian (Arthaud and Matte 1976). The paleomagnetic evidence for the Corsican rotation (Nairn and Westphal 1968) has also been questioned on the grounds that the rocks investigated are heavily altered and no longer possess primary magnetizations (Storetvedt and Petersen 1976).

Abundant paleomagnetic data from Sardinia indicate that the island has undergone at least two phases of counterclockwise rotation since the Late Paleozoic. Many studies of Tertiary volcanics have revealed north-westerly magnetic declinations from which about 30° of rotation relative to Europe may be inferred (see the summaries by Manzoni 1974; Manzoni and Ferriani 1976; Edel and Lörtscher 1977; Edel 1979). An age of 15–17 Myr has been determined radiometrically for this Tertiary rotation (Bellon et al. 1977).

Larger tectonic rotations of Sardinia have been deduced from paleomagnetic investigations in older rocks. Data from Permian ignimbrites from the Gallura region in northern Sardinia (Zijderveld et al. 1970; Westphal et al. 1976; Storetvedt and Markhus 1978) indicate rotation of about 45°–60°, while directions from Permian red sandstones from north-western Sardinia (Zijderveld et al. 1970) are rotated by 90° counter-clockwise relative to stable Europe. From these results it may be inferred that Sardinia underwent an earlier rotation of about 30°–60° relative to Europe between the Permian and Late Tertiary.

Only a meagre amount of rock magnetic data has been published for Sardinian volcanic rocks. In the Permian volcanics more than a single, potentially remanence-carrying magnetic mineral was often present; low temperature oxidation had altered the original magnetic mineralogy (Storedvedt and Markhus 1978).

There is a lack of paleomagnetic information from Sardinia for the period from Permo-Triassic to Tertiary, which is represented only by weakly magnetized sedimentary rocks. It has only recently become feasible to measure these with satisfactory accuracy. In this paper we present the results of a paleomagnetic investi-

* Institut für Geophysik contribution No. 307

0340-062X/81/0049/0011/$01.80

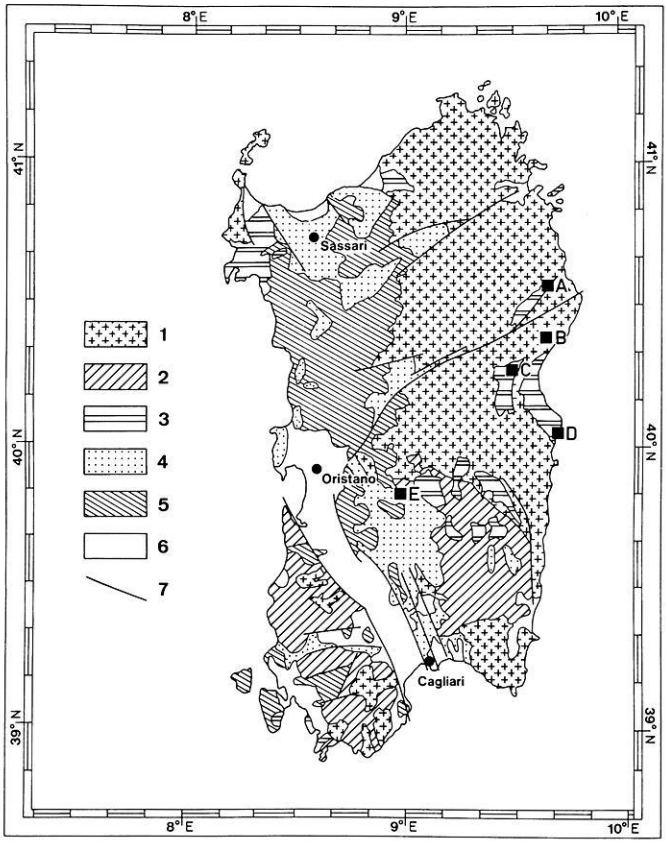

Fig. 1. Simplified geological-structural map of Sardinia (after Cocozza et al. 1974). Key: (1) granitoids, gneisses and micaschists of Variscan age or older, (2) Paleozoic sedimentary rocks, Variscan age or older, (3) post-Variscan Paleozoic rocks and Mesozoic sediments, (4) Tertiary sediments, (5) Tertiary and Quaternary volcanic rocks, (6) Quaternary sediments, (7) faults. Site locations: *A* Jurassic sites FH01, FH02, *B* Cretaceous sites FH04–FH06, *C* Cretaceous site FH03, *D* Jurassic sites FH07–FH09, *E* Triassic sites FH10–FH12

gation on limestones of Triassic, Jurassic and Cretaceous age from central and eastern Sardinia.

Geological Setting and Paleomagnetic Sampling

During the Mesozoic Sardinia was a part of a relatively stable platform which, since the end of the last Hercynian phase of folding, had been disturbed only by movements accompanying isostatic compensation, and otherwise exhibited many characteristics of a cratonic province (Cocozza and Jacobacci 1975). The Mesozoic sedimentary cover was deposited discordantly on the Variscan basement over much of Sardinia (Fig. 1). The sediments are mainly neritic, but pelagic sediments also occur in a few places. The Mesozoic facies pattern in western Sardinia is analogous to that in Provence (Chabrier and Mascle 1975), but somewhat different from that found in eastern Sardinia.

Except for the most westerly part of Sardinia (Nurra region), the Mesozoic cover has not undergone Alpine compressive deformation. It has remained subhorizontal, having been locally affected by post-Mesozoic normal faulting.

Fine-grained Cretaceous limestones were sampled at four sites; 73 cores (110 samples) were obtained. A single site (C, Fig. 1) of Turonian age (I. Dieni, personal communication 1978) was located in the Valle Lanaitto, west of Dorgali (Chabrier 1969), and three sites of Valangian to Albian age (B, Fig. 1) were located in a valley of Monte Tuttavista, called "Badde Funtana Morte", west of Orosei (Dieni and Massari 1966).

Two Jurassic sites (A, Fig. 1) were drilled in gently dipping beds of Callovian age (I. Dieni., personal communication 1978) in the autochthonous part of Monte Albo (Dieni and Massari 1970). Three additional Jurassic sites (D, Fig. 1) were placed in gently dipping beds of the Kimmeridgian, pelagic fine-grained "lithographic limestone" (so named because it was once favoured for preparing printing blocks) near to the village of Baunei (Amadesi et al. 1960). These two groups of sites are separated by NE-SW trending faults bounding the southeastern edge of the Monte Albo block (Fig. 1). Alvarez and Cocozza (1974) reconstructed the tectonic history of this part of Central Eastern Sardinia. Although the major faults were active as vertical faults during the Alpine orogeny, they may have been re-activated with a sinistral strike-slip component during the Neogene. As will later be seen, these faulting episodes did not result in major relative rotation: paleomagnetic directions on both sides of the fault zone are equivalent. A total of 139 Jurassic cores (158 samples) were obtained.

Samples of Triassic Muschelkalk were taken in flat-lying beds at three sites (E, Fig. 1) close to one another in quarries at the base of Monte Maiore in the central part of Sardinia (Damiani and Gandin 1974). These carbonate rocks consist of limey dolomites and contain very few fossils; 54 Triassic cores (83 samples) were taken.

Analysis of Remanent Magnetizations

The remanent magnetizations of the weakly magnetized limestones were measured with a three-axis cryogenic magnetometer. Replicate measurements were made of each remanence, and the accuracy of repeatability was used as a rejection criterion at each stage of demagnetization (Lowrie et al. 1980).

The *natural remanent magnetizations* (NRM) of the Cretaceous samples were exceptionally weak averaging only 2×10^{-8} G (Fig. 2). Many of these samples were too weak to be measured with reliability; at early stages of *alternating field* (AF) and thermal demagnetization the signal soon fell to unmeasurable levels. In those samples which were sufficiently magnetic to be AF or thermally demagnetized no stable vector could be isolated. The remanences of the Cretaceous collection were judged to be too weak or too unstable to be paleomagnetically useful, and all were rejected from further analysis.

Although the Triassic Muschelkalk samples and the Jurassic samples were also very weak, averaging 7×10^{-8} G and 5×10^{-7} G, respectively, the remanences of most samples were adequate to give reliable measurements. They were demagnetized progressively in order to separate individual magnetization components. Wherever possible, twin samples from the same core were subjected to AF or thermal demagnetization respectively. The component analysis was facilitated by the use of vector diagrams and vector difference computations. The categories of demagnetization behaviour observed corresponded to different magnetic mineral compositions of the limestones.

Samples with Remanences Dominated by Magnetite

In these samples the AF demagnetization behaviour (Fig. 3a) shows a slight initial increase of intensity and a large change in direction in fields up to 100 Oe accompanying removal of a low-coercivity component of normal polarity. The magnetization vector then decays more or less uniformly towards the origin,

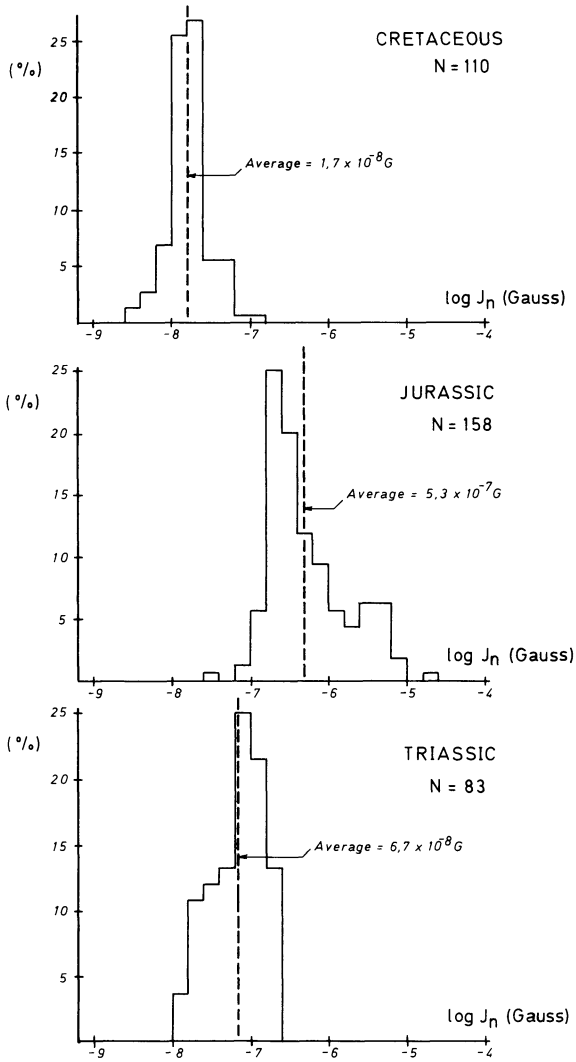

Fig. 2. Histograms of NRM intensities of the Cretaceous, Jurassic and Triassic limestone collections. (*N* number of samples)

which is not quite reached by 500 Oe. A small, high-coercivity component persists in alternating fields up to at least 1 kOe. The remanence component in the region 100–500 Oe is easily determined, and in the example shown has reversed polarity.

Progressive thermal demagnetization of the twin sample from this core showed similar behaviour (Fig. 3b). A component of normal polarity was removed below 200° C, and at higher temperatures a single component of remanence existed. Its direction was identical to that of the component removed by AF demagnetization between 100–500 Oe, and its maximum unblocking temperature was around 550° C.

On the basis of its coercivity and unblocking temperature spectra, we associate this component of remanence with magnetite and identify it as the primary or characteristic remanent magnetization (ChRM) of the sample.

Samples with Remanences Dominated by Goethite

In a large number of samples, the remanent magnetizations were extremely resistant to AF demagnetization. In fields up to 1 kOe no significant change of direction (Fig. 4a) or intensity (Fig. 4b) took place, although both behaved irregularly.

The total coercivity spectrum of the unheated sample was investigated by giving an isothermal remanent magnetization (IRM) in progressively increasing magnetic fields (Fig. 4c). Acquisition of IRM was uniform and continuous throughout the experiment indicating a very broad coercivity spectrum, and saturation IRM was not reached even in a field of 45 kOe produced by a cryogenic magnet.

The strong-field IRM was demagnetized thermally using a high-temperature vector magnetometer which permits quasi-continuous monitoring of all three remanence components (Heiniger and Heller 1976). An immediate, drastic decrease in intensity was observed below 100° C (Fig. 4d); above this temperature only a small erratic component remained.

During thermal demagnetization of the natural remanence of the twin sample from this core the direction changed erratically (Fig. 4e) after removal of a large initial component with very low blocking temperature (Fig. 4f).

The combination of very high coercivity with extremely low unblocking temperature (and Curie point, by inference) in the IRM and NRM indicates that each remanence is controlled by ferromagnetic goethite (Hedley 1971; Heller 1978) whose Curie point is below 110° C. Erratic behaviour of remanence carried by goethite can occur at room temperature (Fig. 4a, b), which corresponds to the blocking temperature of some of the grains.

Polished sections were examined with a reflecting ore-microscope. The observations were difficult because of the sparseness of any opaque minerals. However, goethite was clearly identified by its dull grey reflectance, with yellowish to reddish brown internal reflections, especially under oil-immersion. The goethite occurred both as accretions of minute grains and as a pseudomorph after pyrite, and may be presumed to have formed by alteration of pre-existing pyrite in the latter case. The accretionary form may have a similar origin, or it may be precipitated from iron solutions within the sediment (Berner 1969). In either case the goethite is secondary, and may originate long after deposition. Remanence components carried by goethite post-date the Late Tertiary folding of Jurassic limestones in the Swiss Jura mountains (Van der Voo and Lowrie 1979), and goethite magnetizations of opposing polarities were found in different samples from the same core in the Frankenjura limestones of southern Germany (Heller 1977).

Samples which contained a dominant fraction of goethite as magnetic mineral were therefore rejected from further paleomagnetic analysis, on the grounds that they did not possess a primary remanence component. The remanence directions carried by goethite showed no systematic grouping, before or after tectonic correction.

Summary

In most samples magnetite and goethite were present in comparable proportions. The AF and thermal demagnetization of NRM showed intermediate characteristics between those in Figs. 3 and 4. During IRM acquisition (Fig. 5a) there was an initial sharp increase in magnetization below 1 kOe. The saturation of the magnetite component was followed in higher fields by an increasingly steep acquisition curve which does not saturate in 45 kOe, typical for the goethite component. Continuous thermal demagnetization of the IRM (Fig. 5b) shows an initial sharp drop below 100° C due to the goethite component. This is followed by a more or

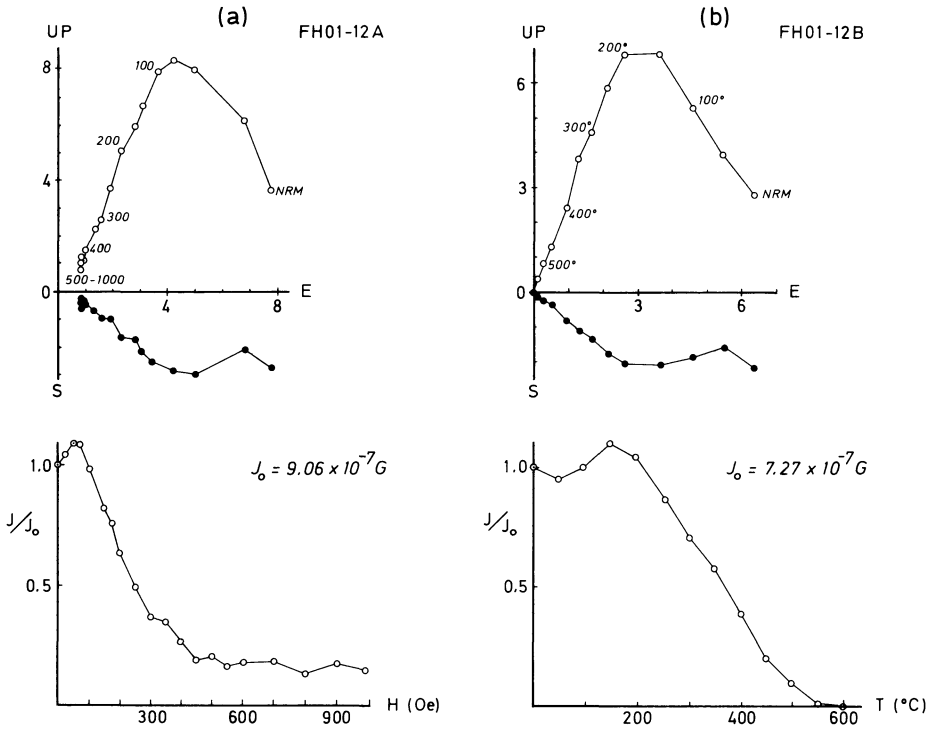

Fig. 3a and b. Comparison of (**a**) AF demagnetization and (**b**) thermal demagnetization of twin samples from the same (reversely magnetized) core FH01–12. *Open* and *solid dots* indicate components in the vertical EW and horizontal planes, respectively. *Numbers* on each diagram refer to the peak AF demagnetizing field in oersteds, or temperature in °C.

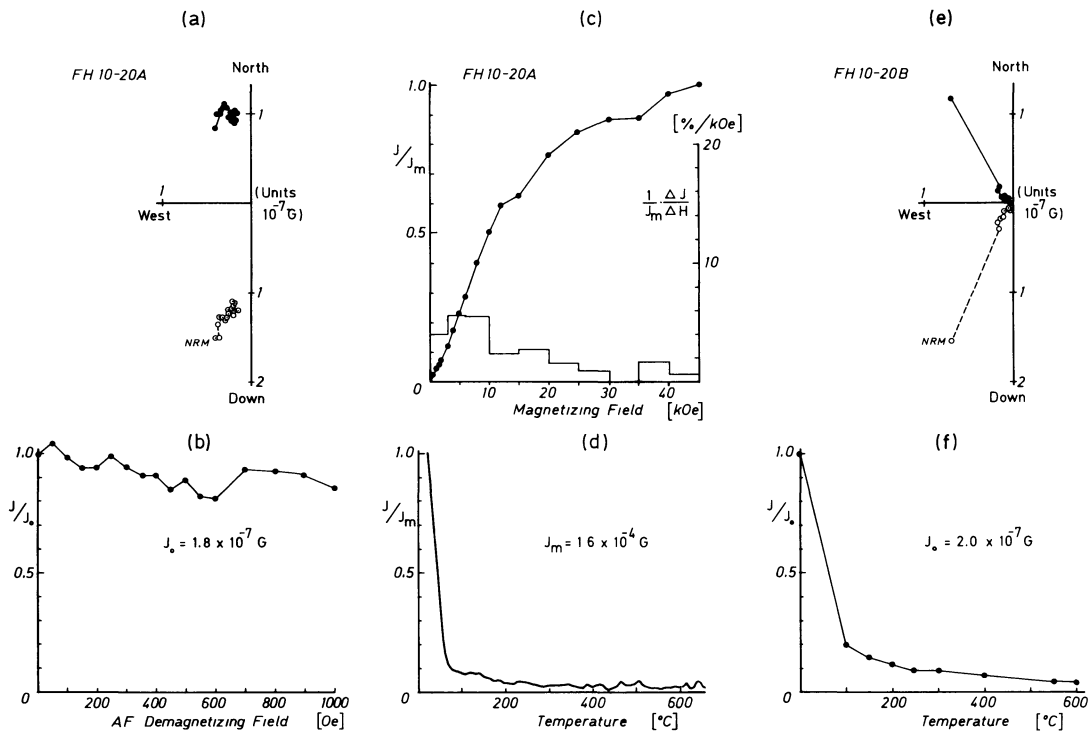

Fig. 4a–f. Magnetic characteristics of samples whose magnetization is dominanted by goethite. (**a**) The vector diagram shows stable directions, and (**b**) the intensity changes little during AF demagnetization. (**c**) Acquisition of IRM does not reach saturation even in 45 kOe, but (**d**) this IRM is almost entirely destroyed by heating to 100° C. Thermal demagnetization of the twin sample demonstrates the thermal instability of (**e**) direction and (**f**) intensity of the NRM associated with goethite

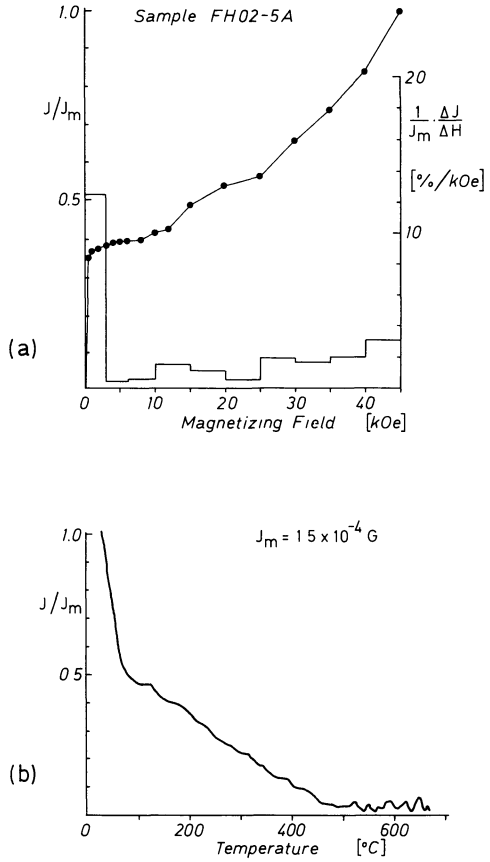

Fig. 5a and b. Magnetic characteristics of a sample whose magnetization contains comparable magnetite and goethite components. **a** Saturation IRM is not reached in 45 kOe but the histogram of coercivities reveals a strong fraction below 3 kOe. **b** On heating the IRM the goethite component disappears by about 100° C and the magnetite component unblocks uniformly until 500° C

less regular unblocking of the magnetite component until 500° C, above which the signal is mostly instrumental noise.

Demagnetization treatment was therefore specifically oriented towards extracting the direction of the magnetite component, by AF demagnetization in the range 100–500 Oe or by thermal demagnetization between 100° C and 500° C. A satisfactory general treatment consisted of thermal demagnetization to 150° C (to eliminate the goethite component) followed by AF demagnetization to define the direction of the magnetite component.

Characteristic Remanent Magnetizations

Each sample was AF or thermally demagnetized in several steps. The ChRM was derived with the aid of vector diagrams and vector difference computations. Data were rejected (a) if the magnetization was too weak to measure accurately, (b) if the remanence was too unstable to be of use, (c) if the only remanence component resided in goethite, and (d) if the intermediate (magnetite) component was too small or too weakly defined to be determined with acceptable precision. All Cretaceous samples, 34 Jurassic and 27 Triassic samples were rejected on the first two grounds, a further 30 Jurassic samples were rejected for the last two reasons.

In general the differently demagnetized (one AF, the other thermal) twin samples from the same core gave similar ChRM directions, which were therefore averaged. The ChRM sample directions for each of the 5 Jurassic and 3 Triassic sites are shown in Fig. 6 and 7 respectively. All Triassic samples were normally polarised, and the directions were closely grouped. A few reversely polarised samples were measured at one of the Jurassic sites (compare Fig. 3); the Jurassic directions were somewhat more dispersed than the Triassic directions.

At site FH08 the ChRM directions are smeared out, and some appear to lie near a great circle connecting the normal and reversed polarity groups. This is an indication that the ChRM directions

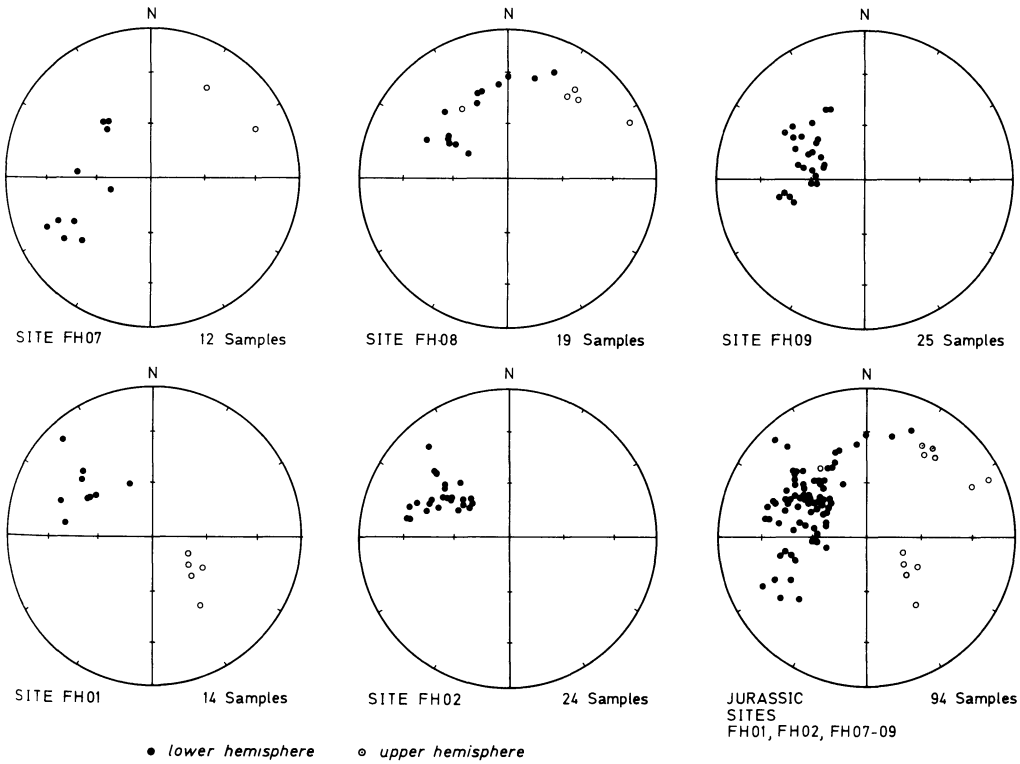

Fig. 6. Stereograms of ChRM directions at the 5 Jurassic sites, individually and collectively

Table 1. Fisher statistical analysis of sample directions

Sampling description			Mean Directions									
			Before bedding corrections					After bedding corrections				
Age	Site	$N(n)$	R	D	I	α	K	R	D	I	α	K
Jurassic	FH01	13(14)	12.49	304	31	8.7	23.59	12.42	307	47	9.3	20.66
	FH02	14(24)	13.49	288	40	8.0	25.47	13.64	303	46	6.8	35.68
	FH07	10(12)	8.72	251	28	19.6	7.03	8.71	260	49	19.7	6.95
	FH08	8(9)	7.74	308	63	10.8	27.35	7.74	318	47	10.8	27.30
	FH09	18(25)	17.32	282	36	7.1	24.98	17.38	290	55	6.7	27.59
All cores		63	57.06	285	39	5.8	10.44	58.66	296	51	4.9	14.29
								Jurassic Pole Position 292E 40N			5.8	10.63
Triassic	FH10	17(31)	16.75	296	33	4.5	62.82	16.74	294	43	4.6	60.69
	FH11	13(19)	12.73	290	43	6.3	44.78	12.72	295	41	6.4	42.61
	FH12	4(6)	3.96	286	42	10.7	74.39	3.96	290	41	10.8	74.03
All cores		34	33.26	293	38	3.7	44.63	33.41	294	42	3.3	55.91
								Triassic Pole Position: 285E 33N			3.1	62.26

$N(n)$ = number of cores (samples), D/I = declination/inclination of mean direction, α = 95% confidence circle radius, K = precision parameter (Fisher 1953)

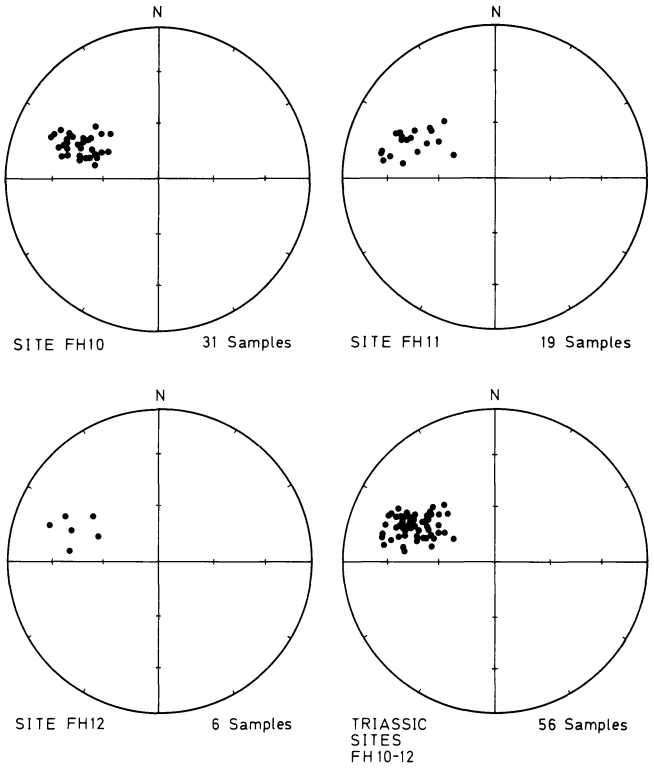

Fig. 7. Stereograms of ChRM directions at the 3 Triassic sites, individually and collectively

of these samples are not the primary directions. However, inspection of the AF demagnetization vector diagrams of these samples revealed well-defined trajectories to the origin. We have no satisfactory explanation for these deviant directions. The suspect samples came from a common region of a small roadside quarry in which the limestone was rather karstic in varying degrees. These ChRM directions were excluded from further paleomagnetic analysis.

The statistical analysis (Fisher 1953) of the core directions is given for each site and age in Table 1. Tectonic corrections within each site did not have much effect on the directional dispersion because within-site bedding attitudes did not vary much. Between-site corrections slightly improved the directional scatter of each age group.

Discussion

Although Permian and Carboniferous paleomagnetic pole positions are well defined for Europe, only a single African pole of acceptable quality exists for each of these geological epochs. The Mesozoic portions of African and European *apparent polar paths* (APW) are weakly defined. To overcome these difficulties Van der Voo and French (1974) reconstructed the ancient positions of the Atlantic-bordering continents and combined for each epoch paleomagnetic data which they considered to be of acceptable quality. Subsequently, Irbing et al. (1976a–b, c) compiled summaries of all paleomagnetic data up to 1975, including the latest Russian results. Irving (1977) adopted more liberal acceptability criteria for these data than Van der Voo and French had applied. He combined the data in fairly broad moving windows (20–40 Myr interval width) and produced smoothed APW paths for Eurasia, North America and Gondwana (in which the continental reconstruction of Smith and Hallam 1970, was assumed). These paths are in fact swathes of variable width (Fig. 8) corresponding to the different radii of 95% confidence along the trajectory.

A pseudo-African APW path (VandenBerg 1979) can be constructed by rotating the North American APW path about the appropriate rotation poles for the opening of the north Atlantic ocean (Sclater et al. 1977). This path (Fig. 8) lies quite far from the Gondwana APW path of Irving (1977). In order to bring North America and Africa into their positions for the Bullard et al. (1965) reconstruction a large dextral transcurrent displacement of about 3,500 km, ending by the Late Triassic, must be invoked (Irving 1977). The discrepancy between Laurasian and Gondwanan paleomagnetic data was noticed earlier by Van der

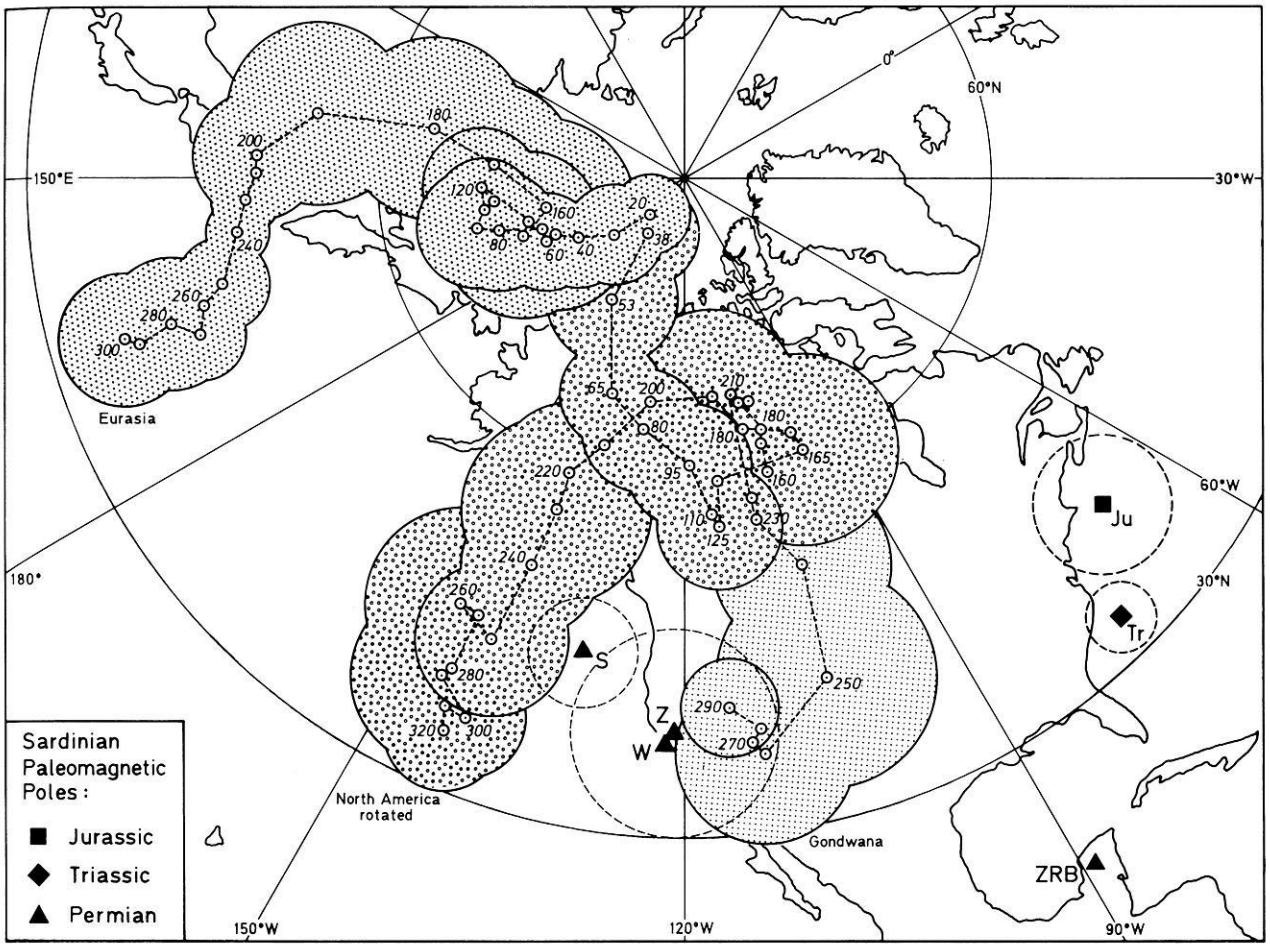

Fig. 8. Jurassic and Triassic paleomagnetic pole positions (with 95% confidence circles) from this study of limestones and Permian poles from studies of ignimbrites. *S* Storetvedt and Markhus (1978), *W* Westphal et al. (1976), *Z* Zijderveld et al. (1970). *ZRB* is the Permian pole from redbeds (Zijderveld et al., 1970). For comparison are shown (with their 95% confidence widths) the APW paths for Eurasia and Gondwana (Irving 1977) and the North American path rotated around the poles of opening of the Atlantic derived by Sclater et al. (1977)

Table 2. Comparison of palaeomagnetic directions measured in Sardinia (40.3° N, 9.7° E) in Mesozoic limestones with those expected from the Eurasian and African (Gondwanan) APW paths of Irving (1977)

	Middle and Late Jurassic		Triassic	
	D	*I*	*D*	*I*
Observed mean direction	296	51	294	42
Expected directions				
African	330	42	338	47
European	7	46	25	12
Inferred CCW rotation				
Sardinia relative to				
Africa	34°		44°	
Europe	73°		91°	

Voo and French (1974) who also proposed a dextral shear between the supercontinents, of smaller magnitude than that proposed by Irving (1977).

As reference APW path for Africa in this study we take the portion of the rotated North American APW path from the present to 160 Myr B.P. and the Gondwana APW path for ages older than 160 Myr. The Jurassic and Triassic pole positions for Sardinian limestones lie far from the Eurasian and 'African' APW paths (Fig. 8). By implication the island has undergone counterclockwise rotations relative to both Europe and Africa.

The Jurassic and Triassic directions expected in Sardinia from the appropriate segments of the Eurasian and 'African' APW paths were computed, and compared to the observed paleomagnetic directions in Sardinia for the purpose of determining the amounts of rotation involved (Table 2).

The total counterclockwise rotation of Sardinia relative to Europe has been estimated at 45° (Storetvedt and Markhus 1978) to 60° (Westphal et al. 1976; Zijderveld et al. 1970) from Permian porphyries, and up to 90° in Permian redbeds (Zijderveld et al. 1970). In a current study of Permo-Triassic rocks very large directional rotations of 50°–100° have been observed (J.-B. Edel personal communication 1979).

The 70°–90° counterclockwise rotation inferred from Sardinian Mesozoic limestones is in accord with the larger amounts of rotation in older rocks. It is greater than previous estimates (60°) based upon paleomagnetic data and on matching the Corso-Sardinian and Provencal coastlines.

The declinations of the mean Jurassic and Triassic directions measured in Sardinian Mesozoic limestones are practically identical. The total difference in direction of 9° is mainly due to the difference in inclinations. In this respect the Sardinian directions resemble African directions which have been rotated by 34°–44° counterclockwise (Table 2). The similarity of Sardinian Permian directions to African Permian directions was pointed out by Zijderveld et al. (1970).

Recently VandenBerg (1979) has associated Sardinia with Adria, a promontory of the African plate (Channell and Horvath 1976; Channell et al. 1979). VandenBerg proposed that Adria (with Sardinia) was decoupled from the African plate and underwent a 25°–30° counterclockwise rotation relative to Africa in the Late Tertiary. This rotation would be equivalent to the well-documented 30° rotation about 15–17 Myr B.P (Bellon et al. 1977). The earlier rotational history of Sardinia would represent the rotation of the African plate relative to the European plate.

Although our paleomagnetic observations follow the general sense of VandenBerg's interpretation, the total amount of observed rotation is appreciably greater than that required by his model. About 10°–15° of counterclockwise rotation of Sardinia relative to Africa is unaccounted for.

Sardinian paleomagnetic data support a paleohistory in which Sardinia rotated relative to both Africa and Europe, presumably as an independent microplate. The new Mesozoic data imply that the earlier rotational phase occurred since the Late Jurassic.

Conclusions

Paleomagnetic data from Mesozoic limestones in Sardinia were of variable quality. All Cretaceous samples were rejected because of instability or weakness of the remanent magnetization. The magnetizations of Jurassic and Triassic samples were carried by primary magnetite and secondary goethite. The direction of a stable ChRM component carried by magnetite was extracted in as many samples as possible.

The new Mesozoic data, interpreted in conjunction with Tertiary and Paleozoic data, support the concept that Sardinia has undergone two phases of counterclockwise rotation relative to both Europe and Africa. The more recent rotation as an independent microplate occurred in the Early Miocene. The earlier rotation was also at least partly a microplate rotation relative to both neighbouring plates. It occurred in the Paleogene or Cretaceous, since our Late Jurassic data also show its effects. In could not be timed more exactly in the present study because of the unsuitability of our Cretaceous samples for paleomagnetic analysis

Acknowledgements. During this project invaluable advice and suggestions were received from Drs. F. Heller and J.E.T Channell, who also critically reviewed the manuscript. The location and description of suitable sites for this study was facilitated in the field by the generous cooperation of A. Gandin, I. Dieni, and F. Massari. We are grateful to J.-B. Edel for a preprint of his study of Permo-Triassic rocks in Sardinia, to the Research Laboratory of Brown Boveri Company (Dällikon, Switzerland) for allowing us to use their cryogenic magnet and to M.S. Lowrie for kindly typing the manuscript.

References

Alvarez, W.. Rotation of the Corsica-Sardinia microplate. Nature Phys. Sci. **235**, 103–105, 1972

Alvarez, W.: The application of plate tectonics to the Mediterranean region. In: Implications of continental drift to the earth sciences, Vol. 2, pp. 893–908. London: Academic Press 1973

Alvarez, W., Cocozza, T . The tectonics of central eastern Sardinia and the possible continuation of the alpine chain to the south of Corsica. In: Paleogeografia del Terziario sardo nell'ambito del Mediterraneo occidentale. Suppl. ai Rend. Fac. Sci. Univ. Cagliari **43**, 5–34, 1974

Amadesi, E., Cantelli, C., Carloni, G., Rabbi, E.: Ricerche geologiche sui terreni sedimentari del foglio 208-Dorgali. G. Geol. **28**, 58–87, 1960

Argand, E.: La tectonique de l'Asie. 13th International Geological Congress (Brussels) pp. 171–372, 1924

Arthaud , F., Matte, P.: Arguments géologiques en faveur de l'absence de mouvements relatifs de la Corse par rapport à la Sardaigne depuis l'orogenèse hercynienne. C. R. Acad. Sci. Paris **283**, 1011–1014, 1976

Arthaud, F., Matte, P.: Détermination de la position initiale de la Corse et de la Sardaigne à la fin de l'orogenèse hercynienne grâce aux marqueurs géologiques anté-mésozoïques. Bull. Soc. Geol. Fr. **19**, 833–840, 1977

Bellon, H., Coulon, C., Edel, J.B.. Le déplacement de la Sardaigne. Synthèse des données géochronologiques, magmatiques et paléomagnétiques. Bull. Soc. Géol. Fr. **19**, 825–832, 1977

Berner, R.A.: Goethite stability and the origin of red-beds. Geochim. Cosmochim. Acta **33**, 267–273, 1969

Bullard, E.C., Everett, J.E., Smith, G.A.: The fit of the continents around the Atlantic. In: A symposium on Continental Drift. Philos. Trans. R. Soc. London Ser. A.: **258**, 41–51, 1965

Chabrier, G.: Sur la stratigraphie et la structure des monts d'Oliena (Sardaigne orientale). C. R. Somm. Seances Soc. Géol. Fr. **6**, 218–220, 1969

Chabrier, G., Mascle, G.: Comparaison des évolutions géologiques de la Provence et de la Sardaigne (à partir d'exemples de la région Toulonnaise et de la Nurra Sarde). Rev. Geogr. Phys. Geol. Dyn. **17**, 121–136, 1975

Channell, J.E.T., D'Argenio, B., Horvath, F.: Adria, the African promontory in Mesozoic Mediterranean palaeogeography. Earth Sci. Rev. **15**, 213–292, 1979

Channell, J.E.T., Horvath, F.: The African/Adriatic promontory as a palaeogeographical premise for Alpine orogeny and plate movements in the Carpatho-Balkan region. Tectonophysics **35**, 71–101, 1976

Cherchi, A., Schroeder, R.· Sur la biogéographie de l'association *Valserina* du Barrémien et la rotation de la Sardaigne. C. R. Acad. Sci. Paris **277**, 829–832, 1973

Cherchi, A., Schroeder, R.· Présence de galets du Vraconien supérieur-Cénomanien basal de provenance ibérique dans le Paléogène continental du Sud-Ouest de la Sardaigne. Bull. Soc. Geol. Fr. **18**, 1217–1219, 1976

Cocozza, T., Jacobacci, A.: Geological outline of Sardinia. In: Geology of Italy, C. Squyres, ed.· pp. 49–81. Tripoli: Earth Sci. Soc. Lybian Arab Republic 1975

Cocozza, T., Jacobacci, A., Nardi, R., Salvadori, I.: Schema stratigrafico-strutturale del Massiccio Sardo-Corso e minerogenesi della Sardegna. Mem. Soc. Geol. Ital. **13**, 85–186, 1974

Damiani, A.V., Gandin, A.: Geologia e ambiente di sedimentazione della successione triassica di Monte Maiore (Sardegna centrale). Note II. Boll. Soc. Geol. Ital. [Suppl.] **92**, 41–83, 1974

Dieni, I., Massari, F.: I foraminiferi del Valanginiano superiore di Orosei (Sardegna). Paleontol. Ital. **61**, 75–186, 1966

Dieni, I., Massari, F.: Tettogenesi gravitativa di età oligocenica nella Sardegna centro-orientale. Boll. Soc. Geol. Ital. **89**, 57–64, 1970

Edel, J.-B.: Palaeomagnetic study of the Tertiary volcanics of Sardinia. J. Geophys. **45**, 259–280, 1979

Edel, J.-B., Lörtscher, A.: Paléomagnétisme du volcanisme tertiaire de Sardaigne. Nouveaux résultats et synthèse. Bull. Soc. Geol. Fr. **19**, 815–824, 1977

Fisher, R.A.: Dispersion on a sphere. Proc. R. Soc. London, Ser. A: **217**, 295–305, 1953

Hedley, I.: The weak ferromagnetism of goethite (α-FeOOH). J. Geophys. **37**, 409–420, 1971

Heiniger, C., Heller, F.: A high temperature vector magnetometer. Geophys. J. R. Astron. Soc. **44**, 281–288, 1976

Heller, F.: Palaeomagnetism of Upper Jurassic limestones from Southern Germany. J. Geophys. **42**, 475–488, 1977

Heller, F.: Rock magnetic studies of Upper Jurassic limestones from Southern Germany. J. Geophys. **44**, 525–543, 1978

Irving, E.: Drift of the major continental blocks since the Devonian. Nature **270**, 304–309, 1977

Irving, E., Tanczyk, E., Hastie, J.: Catalogue of paleomagnetic directions and poles. Third issue. Paleozoic results 1949–1975. Energy, Mines and Resources, Canada, Geomagnetic Series, Nr. **5**, Ottawa, 1976a

Irving, E., Tanczyk, E., Hastie, J.: Catalogue of paleomagnetic directions and poles. Fourth issue. Mesozoic results 1954–1975 and results from seamounts. Energy, Mines and Resources, Canada, Geomagnetic Series No. **6**, Ottawa, 1976b

Irving, E., Tanczyk, E., Hastie, J.: Catalogue of paleomagnetic directions and poles. Fifth issue. Cenozoic results 1927–1975. Energy, Mines and Resources, Canada, Geomagnetic Series Nr. **10**, Ottawa, 1976c

Lowrie, W., Channell, J.E.T., Heller, F.: On the credibility of remanent magnetization measurements. Geophys. J. R. Astron. Soc. **60**, 493–496, 1980

Manzoni, M.: Un interpretazione dei dati paleomagnetici del Terziario dell Sardegna ed alcuni nuovi resultati. In: Paleogeografia del Terziario sardo nell'ambito del Mediterraneo occidentale. Suppl. ai Rendiconti del Seminario della Facultà di Scienze dell'Università di Cagliari, 283–295, 1974

Manzoni, M., Ferriani, A.: Trattamento statistico e validita dei dati paleomagnetici delle vulcaniti Terziarie della Sardegna. Boll. Soc. Geol. Ital. **95**, 1263–1281, 1976

Nairn, A.E.M., Westphal, M.: Possible implications of the palaeomagnetic study of late Palaeozoic igneous rocks of northwestern Corsica. Palaeogeogr. Palaeoclimatol. Palaeoecol. **5**, 179–204, 1968

Sclater, J.G., Hellinger, S., Tapscott, C.: The paleobathymetry of the Atlantic ocean from the Jurassic to the present. J. Geol. **85**, 509–552, 1977

Smith, A.G., Hallam, A.: The fit of the southern continents. Nature **225**, 139–144, 1970

Storetvedt, K.M., Markhus, L.A.: Multivectorial magnetization in late Palaeozoic volcanics from North Sardinia; partial remagnetization and rotation. Geophys. J. R. Astron. Soc. **53**, 245–258, 1978

Storetvedt, K.M., Petersen, N.: Postulated rotation of Corsica not confirmed by new palaeomagnetic data. J. Geophys. **42**, 59–71, 1976

VandenBerg, J.: Paleomagnetism and the changing configuration of the Western Mediterranean area in the Mesozoic and Early Cenozoic eras. Geol. Ultriectina **20**, 178 pp., 1979

Van der Voo, R., French, R.B.: Apparent polar wandering for the Atlantic-bordering continents: Late Carboniferous to Eocene. Earth Sci. Rev. **10**, 99–119, 1974

Van der Voo, R., Lowrie, W.: A preliminary magnetic study of Jurassic limestones from the Swiss Jura mountains and adjacent areas (abstract). EoS, Trans. AGU **60**, 569, 1979

Westphal, M., Bardon, C., Bossert, A., Hamzeh, R.: A computer fit of Corsica and Sardinia against southern France. Earth Planet. Sci. Lett. **18**, 137–140, 1973

Westphal, M., Orsini, J., Vallutini, P.: Le microcontinent corso-sarde, sa position initiale: données paléomagnétiques et raccords géologiques. Tectonophysics **30**, 141–157, 1976

Zijderveld, J.D.A., De Jong, K.A., Van der Voo, R.: Rotation of Sardinia: Paleomagnetic evidence from Permian rocks. Nature **226**, 933–934, 1970

Received May 2, 1980; Revised Version July 21, 1980
Accepted August 7, 1980

J. Geophys. 49, 20–25 (1981)

Journal of Geophysics

A Geotectonic Paradox: Has the Earth Expanded?

P.W. Schmidt and B.J.J. Embleton
CSIRO Division of Mineral Physics, P.O. Box 136, North Ryde, NSW 2113, Australia

Abstract. From the recognition of *common apparent polar-wander* (CAPW) paths for Africa, Australia, Greenland, and North America in the early Proterozoic, we have deduced that these continents today occupy approximately the same relative locations on the globe as they did in the early Proterozoic. However, there is abundant geochemical, geological, geochronological and tectonic evidence for landmasses having been much less dispersed in the Precambrian than they are now. It is shown in this paper that an Earth of about half the present radius accomodates the present continents in such a manner that this paradox can be satisfactorily resolved, and we propose that between about 1,600 Myr and 1,000 Myr ago, the Earth expanded to approximately its present dimensions. A change from Proterozoic to Phanerozoic tectonic styles is supported.

Key words: Tectonics – Earth expansion – Palaeomagnetism.

Introduction

Two types of model have been proposed to characterize the development of foldbelts (mobile belts) during the Proterozoic: those based on horizontal motions (plate tectonics), and those relying more on vertical motions (ensialic orogeny). The applicability of plate tectonic processes has been questioned, on the basis of the geological relationships between the mobile belts and their adjacent Archaean cratons (Clifford 1968; Anheusser et al. 1969; Shackleton 1969; Sutton and Watson 1974). In addition, Briden (1973) gives palaeomagnetic evidence from African cratons which 'flatly eliminates the possibility that hemisphere-sized oceans have been destroyed between these cratons'. Similar palaeomagnetic analyses of data from Africa (Piper et al. 1973), Australia (McElhinny and Embleton 1976; McElhinny and McWilliams 1977) and North America (Irving and Park 1972; Irving and McGlynn 1976; Roy and Lapointe 1976; Irving and McGlynn 1979; Irving 1979) indicate that Proterozoic mobile belts are not a consequence of large-scale horizontal motion, although it has always been accepted that small-scale motion would not be detectable. If small-scale motions were such that ocean basins closed, leaving the juxtaposed landmasses exactly as they were before opening, then obviously the motions would not affect *apparent polar-wander paths* (APWP). However, it has been stressed that this style of tectonics should only be expected under very special circumstances (McElhinny and McWilliams 1977) and, as Briden (1973) emphasizes, instantaneous Euler poles for young ocean basins move substantially, reducing the probability of reversibility.

In the face of the above, Burke et al. (1976) and Cavanough and Seyfert (1977) still propose large-scale horizontal motions and consequent collisions between cratons as the cause of Proterozoic mobile belts on the grounds of uniformitarianism, and have constructed sophisticated APWP for the North American Proterozoic in support of their proposals. However, this approach has been widely criticized by palaeomagnetists (McElhinny and McWilliams 1977; Roy et al. 1978; Irving 1979) because the APWP is needlessly corrupted. While large-scale horizontal motions have been shown to have occurred in recent geological time, it remains conjecture to extrapolate these recent tectonic styles to ancient geological situations. Until two decades ago, the uniformitarian doctrine was that the continents had never moved with respect to each other but, in the light of Palaeozoic and Mesozoic palaeomagnetic data (first obtained by Runcorn 1956; Creer et al. 1957; Graham and Hales 1957; Irving and Green 1958), this view had to be abandoned. Thus uniformitarian arguments can be completely misleading and, in fact, the over-riding opinion among authors is that tectonic styles have changed through geological time.

Comparisons of Proterozoic Apparent Polar-Wander Paths (APWP)

Analyses of Phanerozoic palaeomagnetic, palaeogeographic, biographical and climatological data (Smith et al. 1973; Irving 1977; Morel and Irving 1978; Scotese et al. 1979) all reveal that the continents were clustered in two or three supercontinents, which apparently drifted independently prior to their union to form Pangaea in the middle to late Phanerozoic.

Proterozoic reconstructions of continents are a more speculative topic. Piper et al. (1973) present palaeomagnetic evidence that Africa and South America, which comprise a major part of Gondwanaland, existed as a single continent from as early as 2,200 Myr until 500 Myr ago (i.e., from the beginning of the Proterozoic until its breakup in the late Phanerozoic). They suggest furthermore that North America might have been a part of this supercontinent, at least until 1,000 Myr ago. Subsequently, Piper (1974, 1976) concluded that most of the continental crust formed a Pangaea (in the broad sense) during the Proterozoic. However, Irving and McGlynn (1979) contend that the palaeomagnetic and geochronological evidence is insufficient to argue convincingly for or against the hypothesis of a single supercontinent.

Our approach (Embleton and Schmidt 1979) has been to compare APWP for the few intervals of time for which path sections are fairly well established for more than one continent. These are: (i) 2,300 Myr to 1,900 Myr ago, for which APWP have been constructed for North America (Irving and McGlynn 1976; Roy and Lapointe 1976; Irving and McGlynn 1979; Irving 1979) and

0340-062X/81/0049/0020/$01.20

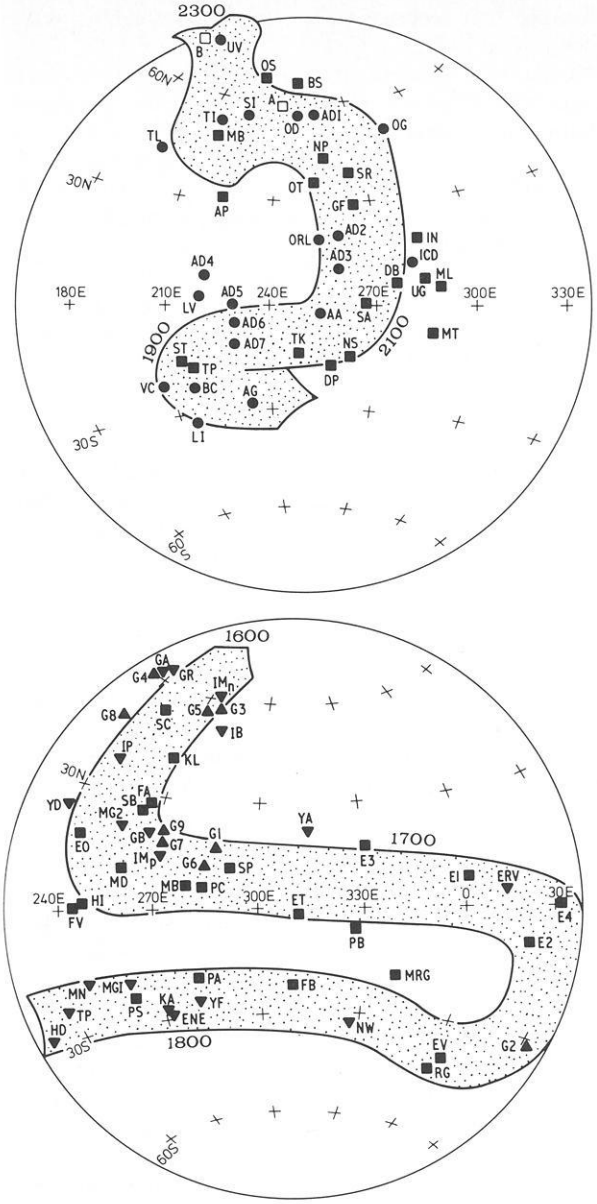

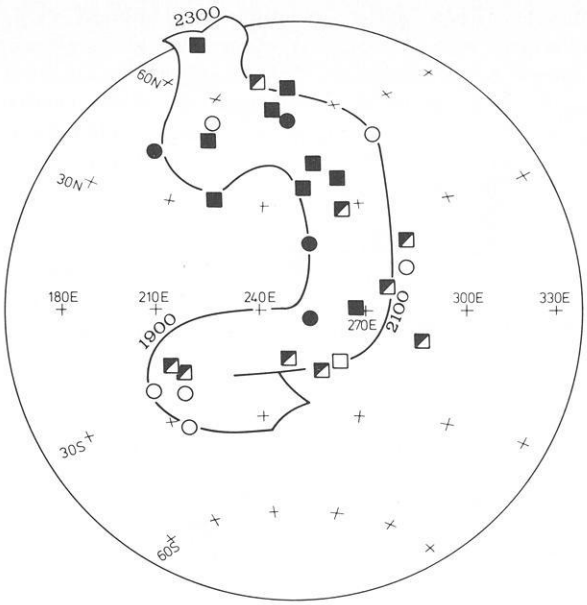

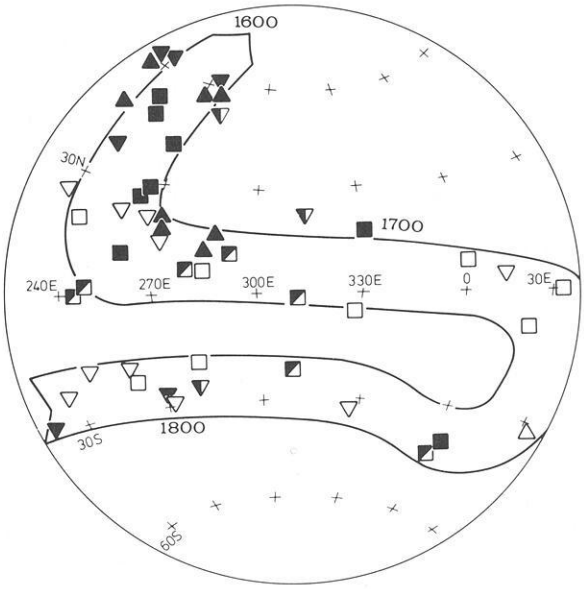

Fig. 1. Common apparent polar-wandering (CAPW) path from 2,300 Myr to 1,600 Myr ago. *Circles* are poles from Africa, *inverted triangles* from Australia, *upright triangles* from Greenland and *squares* from North America (after Embleton and Schmidt 1979). *Open symbols* refer to the obscured hemisphere. No reconstructions have been used

Fig. 2. Polarity patterns for the data plotted in Fig. 1. The polarities of magnetization of rock units have been determined, assuming the paths are north polar tracks. *Closed symbols* represent normal polarities, *open symbols* represent reversed polarities, and *other symbols* represent mixed polarities

for Africa (Piper et al. 1973; Briden 1973); and (ii) 1,800 Myr to less than 1,600 Myr ago, for which APWP have been defined for Australia (McElhinny and Embleton 1976; McElhinny and McWilliams 1977) and for Greenland (Piper and Stearn 1976), and through which the North American data cited above extend.

The agreement between the APWP from the different continents plotted on the present-day globe is striking (Fig. 1) and we find it very surprising that these Proterozoic pole positions should lie along the same path. On the other hand, it would not have been surprising to find this had we first constructed a supercontinent such as Pangaea, which existed in the early and middle Phanerozoic. Common apparent polar wandering (CAPW) would appear to have occurred relative to these three continents in their present-day positions.

Implications for the Arrangement of Precambrian Continents

From a fixed disposition, Africa, Australia, Greenland and North America, in much the same form as we now know them, apparently began to drift with respect to each other sometime after 1,600 m.y. ago. The continents coalesced to form Laurasia and Gondwanaland, which in turn formed Pangaea before the Mesozoic disintegration, returning them to their primaeval locations. This aspect of the data raises some important considerations regarding the early history of the continents. While the possibility of true polar wandering having occurred is interesting in itself, it is the relationships between the various continents, rather than the relationships of the continents and the pole, which are of prime concern here

The simplest interpretation of the data plotted in Fig. 1 is that, in the Proterozoic, the continents were arranged in a similar manner to their present-day configuration. Another possibility is that one (or more) of the pole paths has been assigned the wrong polarity, resulting in a 180° error in plotting the data, which would result in a 180° error in reconstruction of those continents from which the data had been obtained.

We believe we can eliminate this latter possibility on the grounds of the polarities of pole positions plotted in Fig. 2. If the pole paths shown in Fig. 1 are assumed to be north polar paths, then the polarities of rock units can be defined to be normal if greater than 90% of the samples studied have positive magnetic inclinations and the collection sites are closer than 90° to the pole position, or if the inclinations are negative and the sites are greater than 90° from the pole. Reversed polarities are defined if the converse of the above is true, and mixed polarities are defined on the basis of the ratio of polarities falling between 10% and 90%. Some directional data, particularly for African pole positions, are unavailable and consequently it is not yet possible to assign polarities to these poles (Piper et al. 1973). If the pole paths are actually south pole paths, then obviously the opposite of these definitions holds, but this does not affect the following argument.

While necessarily crude, the basic polarity biases revealed in Fig. 2 are fairly clear. Normal polarities predominate from 2,300 Myr to about 2,100 Myr ago, when reversed polarities become more common. Around 1,650 Myr ago normal polarities again prevail. If we had inadvertently assigned the opposite polarity to one of the pole paths, then it is doubtful that any pattern at all would have emerged, rather the paths should appear to be uniformly mixed. Thus we feel confident that the polarity convention assigned is the same for all pole paths – whether the real polarities are normal or reversed is immaterial at this stage.

A Tectonic Paradox

If continents have returned to relative locations similar to those that they occupied during a large part of Proterozoic time, then some fundamental tectonic mechanism must surely be implicated, which should be capable of explaining (i) why continents that were widely separated were not in relative motion and (ii) what became of the intervening crust when the continents eventually drifted to form supercontinents. On the basis of the distribution of Proterozoic foldbelts and their associated cratons, Hurley and Rand (1969), Engel and Kelm (1972), Hargraves (1976), Glikson (1976) and Moorbath (1977) believe that these ancient regions are now much more dispersed on the globe than when they were formed.

The tectonic argument as discussed by Engel and Kelm (1972) and Hargraves (1976) reveals a symmetrical alignment of major Archaean tectonic patterns over 3,000 Myr old within the framework of pre-drift continental clusters. From an analysis of the best preserved of these terrains in North America, Africa, Australia and India, it is apparent that the 'global tectonics between 2.5 and 0.7 b.y. did not involve the large-scale rifting, dispersion, reorientation and reagglomeration of the continental clusters that is typical of the post-Permian' (Engel and Kelm 1972). Evidence based on basement ages complements the tectonic argument and indicates that shield areas, when considered to be clustered in coherent groups, are surrounded by progressively younger continental crust. Such an ordered 'concentric arrangement and the limited degree of scattering of the ancient continental cratons make it difficult to conceive of a series of drift motions prior to the breakup that occurred within the last 200 million years' (Hurley and Rand 1969).

The notion of a coherent sialic regime was clearly favoured by Glikson (1979). However, in response to an explanation regarding the nature of the remaining three-quarters of the Earth's crust, Glikson concluded that 'a tectonically inert simatic regime is difficult to reconcile with the intense tectonic and thermal activity in contemporaneous mobile belts' An alternative model, comprising 'dispersed sial and sima plates', was discounted on geochemical grounds, unless evidence for a Proterozoic simatic regime has been removed (e.g., by subduction) without leaving a geological and geochemical trace. However, it is precisely this configuration of continental dispersion that is clearly favoured from our analysis of the palaeomagnetic data.

There are therefore two contradictory lines of argument. isotope geochemistry, geochronology and tectonics, favouring the in situ growth of mega-continents; and palaeomagnetism, apparently indicating dispersion of continents during the early Proterozoic. We believe that the evidence for both interpretations is cogent enough to warrant an attempt to reconcile this paradox.

A Possible Solution

The simplest interpretation of the palaeomagnetic data alone is to maintain the present Earth dimensions and invoke a modified, non-random form of plate tectonics. In the light of the geological and geochronological evidence for the existence of super-continents in the Precambrian, such an approach would appear to be naive. All aspects must be considered if the paradox is to be resolved.

We have noted previously (Embleton and Schmidt 1979) that the Lower Proterozoic and present locations of the continents are consistent with Carey's (1976) model of radial Earth expansion. However, we are not refuting the palaeomagnetic evidence against expansion according to Carey (Cox and Doell 1961; Ward 1963, 1966; McElhinny et al. 1978), but rather we are drawing attention to the fact that if the Earth expanded such that the continents moved radially apart, then the gross effect on the palaeomagnetic data would be very similar to that actually recorded (Fig. 1). Palaeomagnetic pole positions are invariant under radial expansion. This point has been elaborated recently (Schmidt and Clark 1980) and shown to indicate that an insignificant amount of Earth expansion has occurred since the Palaeozoic. Thus we are in full agreement with McElhinny et al. (1978), who applied Ward's (1963, 1966) method and concluded that Earth expansion is limited to 0.8% in the last 400 Myr. The intriguing point is that Proterozoic expansion of the Earth resolves the above paradox. The effect of expansion on the pole paths is shown in Fig. 3. By comparison with Fig. 1, it is clear that the general form of the pole paths remains the same for an Earth of almost half the present radius as it does for the present-sized Earth.

The method employed to recalculate the pole positions plotted in Fig. 3 is an adaptation of Ward's method (1963, 1966). First the mean palaeomagnetic site geographic coordinates are calculated for each separate continent and these points used as the zero-stress points in Ward's model. The method is not very sensitive to the choice of zero-stress point (Van Hilten 1968) unless it is greater than 90° away from the palaeomagnetic sites, in which case Ward's model fails (Schmidt and Clark 1980). This situation does not arise in the present analysis.

Each palaeomagnetic site and pole subtends the same geocentric angle for different Earth radii, so the effect of reducing the

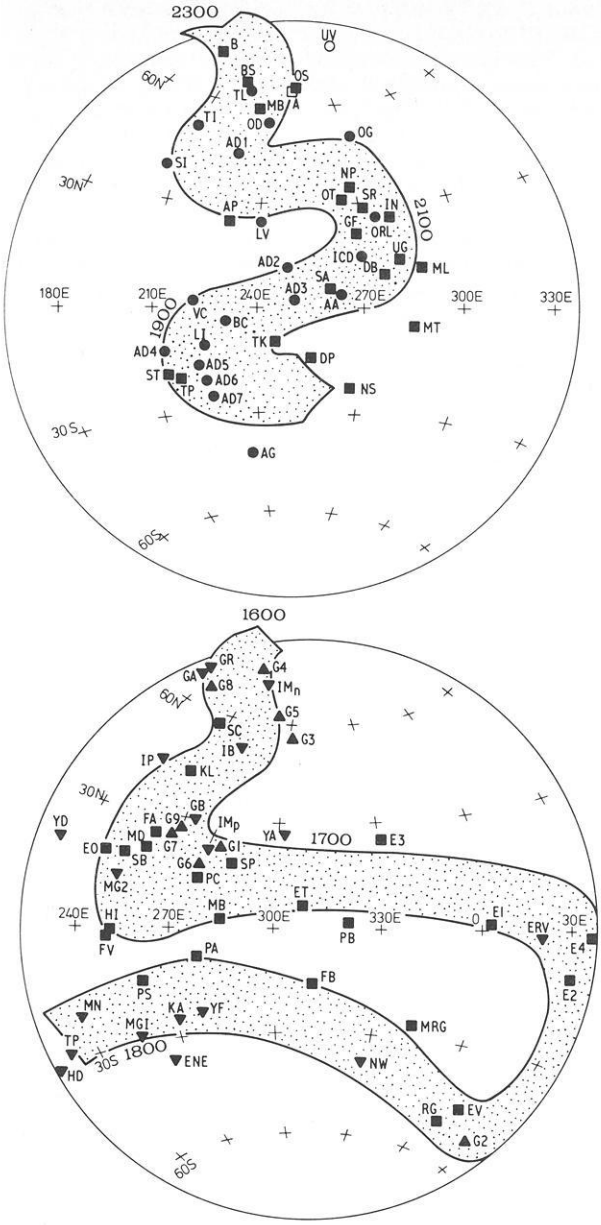

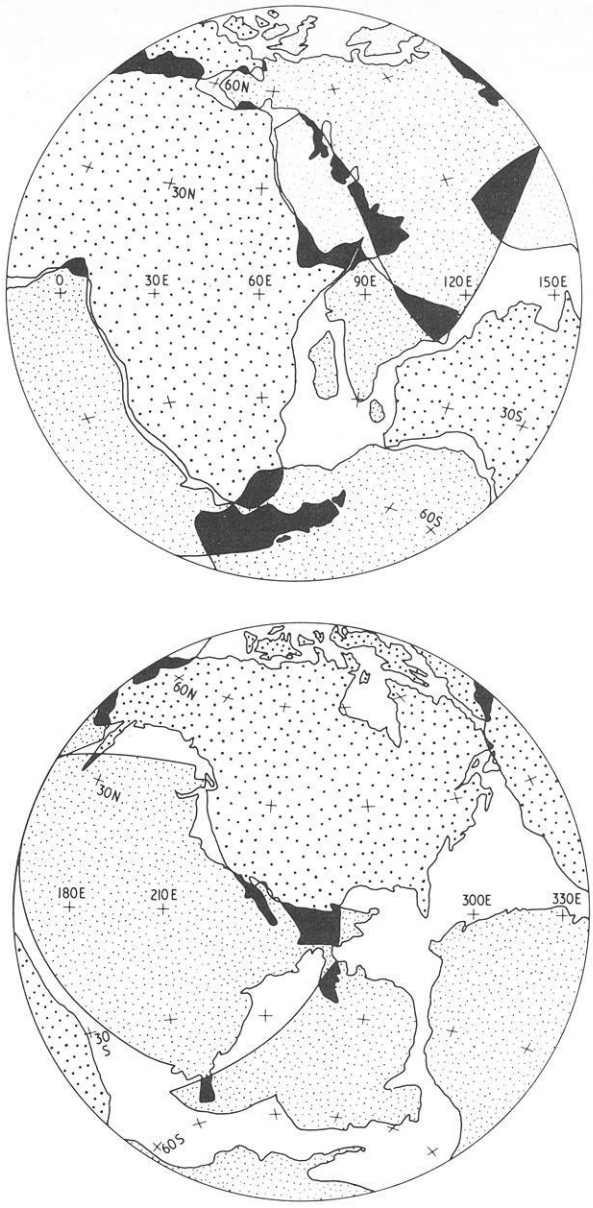

Fig. 3. The pole positions plotted in Fig. 1 have been recalculated following Ward (1963), for a small Earth of a radius equal to 0.55 of the present radius. This demonstrates the general invariance of APWP for different radii

Fig. 4. The continental outlines have been recalculated and fitted for a small Earth of 0.55 present radius by using an adaptation of Ward's (1963) method

radius and recalculating site and pole coordinates is to redistribute the poles, because the geocentric angle between sites and the zero-stress point will increase. This is the basis of Ward's method as applied to Phanerozoic data, and the radius that corresponds to the best grouping of poles (highest k, see Fisher 1953) is assumed to be the most likely radius. This radius estimate is probably biased upwards slightly, due to distortion inherent in the transformation (Schmidt and Clark 1980).

Precambrian palaeomagnetic data are not yet amenable to such treatment because they are relatively scarce and their age estimates are too imprecise. Interestingly enough, though, there appears to be a tendency for poles to group more closely at about 2,100 Myr and 1,900 Myr (and perhaps 2,200 Myr) ago on the small Earth model than they do on the present-sized Earth. It is not possible at this stage to ascertain the significance of this, because there is a possibility of real age differences between some of these poles. Nevertheless, the analogous application of Ward's method to Precambrian data would be to search for the radius that yields the most refined (narrowest and probably least complex) APWP. From this point of view, the small Earth model is seen to have some merit.

The choice of a globe with a radius equal to 0.55 of the present Earth radius stems from the demonstration (Creer 1965) that the present continents can be fitted to it without leaving serious underlap or overlap. The fit 'appears too good to be due to coincidence and hence requires explaining' (Creer 1965). While Creer used perspex shells for model continents, which proved far superior to earlier attempts at sketching continents on small globes, we

have digitized the continental outlines (roughly every 10°) and used Ward's method to recalculate the outlines for an Earth model of 0.55 present radius.

The main continents, with the exception of Eurasia, have been treated as individual and indivisible crustal units, in keeping with their supposed primaeval integrity (see above). Smaller islands, isthmuses and peninsulas (many of recent origin) have been dispensed with to simplify the analysis. The continental elements comprising Eurasia existed as a number of distinct regions during much of the Phanerozoic (Morel and Irving 1978; Scotese et al. 1979), and Eurasia has been subdivided accordingly into Baltica, Siberia, India and China (after Scotese et al. 1979).

There is little point in attempting a more rigorous treatment of Eurasia, which has undergone so much post-Proterozoic deformation. Indeed all continental areas have been deformed to some extent relatively recently, and there is obviously a difficulty in recognizing ancient outlines, particularly in the Pacific region. Thus it is unreasonable to expect that an analysis such as this should lead to the perfect fitting of present continents on a smaller globe. For Africa, Australia, Greenland, and North America, the same zero-stress point as that used for the palaeomagnetic analysis was used in calculating the continent outlines on the small globe. For other continental fragments, a point near the centre of each was chosen.

Once continental outlines were transformed to the small globe, Africa, Australia, Greenland, and North America were held fixed, because the pole positions plotted in Fig. 3 were calculated from these locations. South America was reconstructed to its pre-drift location by using an Euler pole equivalent to that defined by Smith and Hallam (1970), and Antarctica and Arabia were likewise reconstructed to Australia and Africa respectively. Siberia was fitted against the west coast of North America according to Sears and Price (1978), then India and China were fitted by inspection. Because of the slight, though unavoidable, distortion of the continental outlines on the small globe, it is not possible to calculate exactly equivalent Euler poles to those used on the present-sized Earth. However, taken in the context of this analysis, the problem is insignificant.

The resulting reconstruction (Fig. 4) reveals considerably more underlap than overlap, probably due to the omission of some small landmasses. Overall, though, the continents appear to interlock remarkably well. By implication, the proto-hydrosphere is present in the form of epicontinental seas. Most areas of overlap are related to Cenozoic or Mesozoic deformation, although those in North Africa and Greenland, and South Africa and Antarctica, appear to be related to Palaeozoic foldbelts. Thus for an Earth of 0.55 present radius, Proterozoic geological, geochronological and palaeomagnetic information can be simultaneously resolved.

While the Earth-expansion hypothesis is at present a controversial topic, it is perhaps appropriate to draw an analogy with the development of the plate tectonic theory. It is barely two decades ago that many eminent geophysicists denounced any suggestion that continents would drift. Now only an insigificant few doubt it. As Creer (1965) concluded, 'It may be fundamentally wrong to attempt to extrapolate the laws of physics as we know them today to times of the order of the age of the Earth and of the Universe'.

References

Anheusser, C.R., Mason, R., Viljoen, M.J., Vilgoen, R.P.: A reappraisal of some aspects of Precambrian shield geology. Geol. Soc. Am. Bull. **80**, 2175–2200, 1969

Briden, J.C.: Applicability of plate tectonics to pre-Mesozoic time. Nature **244**, 400–405, 1973

Burke, K., Dewey, J.F., Kidd, W.S.F.: Precambrian palaeomagnetic results compatible with contemporary operation of the Wilson Cycle. Tectonophysics **33**, 287–299, 1976

Carey, S.W.. The expanding earth. Amsterdam: Elsevier 1976

Cavanough, M.D., Seyfert, C.K.: Apparent polar wander paths and the joining of the Superior and Slave provinces during Proterozoic time. Geology **5**, 207–211, 1977

Clifford, T.M.: Radiometric dating and the pre-Silurian geology of Africa. In: Radiometric dating for geologists, E.I. Hamilton and R.M. Farquhar, eds.: pp. 299–416. New York: Interscience 1968

Cox, A., Doell, A.R.: Palaeomagnetic evidence relevant to a change in the earth's radius. Nature **189**, 45–47, 1961

Creer, K.M.: An expanding earth? Nature **205**, 539–544, 1965

Creer, K.M., Irving, E., Runcorn, S.K.: Geophysical interpretation of palaeomagnetic directions from Greater Britain. Philos. Trans. R. Soc. London, Ser. A:**250**, 144–156, 1957

Embleton, B.J.J., Schmidt, P.W.: Recognition of common Precambrian polar wandering: a conflict with plate tectonics. Nature **282**, 705–707, 1979

Engel, A.E.J., Kelm, D.L.: Pre-Permian global tectonics: A tectonic test. Geol. Soc. Am. Bull. **83**, 2325–2340, 1972

Fisher, R.A.: Dispersion on a sphere. Proc. R. Soc. London, Ser. A:**217**, 295–305, 1953

Glikson, A.Y.: Archaen to early Proterozoic shield elements: relevance of plate tectonics. Geol. Assoc. Can., Spec. Pap. **14**, 489–516, 1976

Glikson, A.Y.: The missing Precambrian crust. Geology **7**, 449–454, 1979

Graham, K.W.T., Hales, A.L.: Palaeomagnetic measurements on Karroo Dolerites. Philos. Mag. [Suppl., Adv. Phys.] **6**, 149–161, 1957

Hargraves, R.B.: Precambrian geologic history. Science **193**, 363–371, 1976

Hilten, D. Van: Global expansion and palaeomagnetic data. Tectonophysics **5**, 191–210, 1968

Hurley, R.M., Rand, J.R.: Pre-drift continental nuclei. Science **164**, 1229–1242, 1969

Irving, E.: Drift of the major continental blocks since the Devonian. Nature **270**, 304–309, 1977

Irving, E.: Paleopoles and paleolatitudes of North America and speculations about displaced terrains. Can. J. Earth Sci. **16**, 669–694, 1979

Irving, E., Green R.: Polar wandering relative to Australia. Geophys. J.R. Astron. Soc. **1**, 64–72, 1958

Irving, E., McGlynn, J.C.: Proterozoic magnetostratigraphy and the tectonic evolution of the Laurentia. Philos. Trans. R. Soc. London, Ser. A:**280**, 243–265, 1976

Irving, E., McGlynn, J.G.: Palaeomagnetism in the Coronation Geosyncline and arrangement of the continents in the middle Proterozoic. Geophys. J.R. Astron. Soc. **58**, 309–336, 1979

Irving, E., Park, J.K.: Hairpins and superintervals. Can. J. Earth Sci. **9**, 1318–1324, 1972

McElhinny, M.W., Embleton, B.J.J.: Precambrian and early Palaeozoic palaeomagnetism in Australia. Philos. Trans. R. Soc. London, Ser. A:**280**, 417–431, 1976

McElhinny, M.W., McWilliams, M.O.: Precambrian geodynamics – a palaeomagnetic view. Tectonophysics **40**, 137–159, 1977

McElhinny, M.W., Taylor, S.R., Stevenson, D.J.: Limits to the expansion of Earth, Moon, Mars and Mercury and to changes in the gravitational constant. Nature **271**, 316–321, 1978

Moorbath, S.: The oldest rocks and the growth of continents. Sci. Am. **236**, 92–104, 1977

Morel, P., Irving, E.: Tentative palaeo-continental maps for the early Phanerozoic and Proterozoic. J. Geol. **86**, 535–561, 1978

Piper, J.D.A.: Proterozoic crustal distribution, mobile belts, and apparent polar movements. Nature **251**, 381–384, 1974

Piper, J.D.A.: Palaeomagnetic evidence for a Proterozoic supercontinent. Philos. Trans. R. Soc. London, Ser. A:**280**, 469–490, 1976

Piper, J.D.A., Briden, J.C., Lomax, K.: Precambrian Africa and South America as a single continent. Nature **245**, 244–248, 1973

Piper, J.D.A., Stearn, J.E.F.: Palaeomagnetism of Ketilidian meta-

morphic rocks of S.W. Greenland, 1850–1600 m.y. apparent polar movements. Phys. Earth Planet. Inter. **13**, 143–156, 1976

Roy, J.L., Lapointe, P.L.: The palaeomagnetism of Huronian red beds and Nipissing diabase; Post-Huronian Igneous Events and apparent polar path for the interval −2,300 to −1,500 Ma for Laurentia. Can. J. Earth Sci. **13**, 749–773, 1976

Roy, J.L., Morris, W.A., Lapointe, P.L., Irving, E., Park, J.K., Schmidt, P.W.: Apparent polar wander paths and the joining of the Superior and Slave provinces during early Proterozoic times: Comment. Geology **6**, 132–133, 1978

Runcorn, S.K.: Palaeomagnetic comparisons between Europe and North America. Proc. Geol. Assoc. Can. **8**, 77–85, 1956

Schmidt, P.W., Clark, D.A.: The response of palaeomagnetic data to Earth expansion. Geophys. J.R. Astron. Soc. **61**, 95–100, 1980

Scotese, C.R., Bambach, R.K., Barton, C., Vander Voo, R., Ziegler, A.M.: Paleozoic base maps. J. Geol. **87**, 217–277, 1979

Sears, J.W., Price, R.A.: The Siberian connection: a case for Precambrian separation of the North American and Siberian craton. Geology **6**, 267–270, 1978

Shackleton, R.M.: Displacement within continents. In: Time and place in orogeny. Geol. Soc. London, Spec. Publ. **3**, 1–7, 1969

Smith, A.G., Briden, J.C., Drewry, G.E.: Phanerozoic world maps. In: Organisms and continents through time. Spec. Pap. Palaeontol. **12**, 1–42, 1973

Smith, A.G., Hallam, A.: The fit of the southern continents. Nature **225**, 139–144, 1970

Sutton, J., Watson, J.V.: Tectonic evolution of continents in early Proterozoic times. Nature **247**, 433–435, 1974

Ward, M.A.. On detecting changes in the Earth's radius. Geophys. J.R. Astron. Soc. **8**, 217–225, 1963

Ward, M.A.: Comments on detecting changes in the Earth's radius. Geophys. J.R. Astron. Soc. **10**, 445–447, 1966

Received February 19, 1980; Revised Version July 22, 1980
Accepted August 15, 1980

J. Geophys. 49, 26–34 (1981)

Journal of Geophysics

Application of Magnetotelluric and DC Electrical Resistivity Methods in the Neapolitan Geothermal Area

U. Hunsche[1]*, A. Rapolla[2], G. Musmann[1], and L. Alfano[2]

[1] Institut für Geophysik und Meteorologie der Technischen Universität Braunschweig, Mendelssohnstraße 1 A, D-3300 Braunschweig, Federal Republic of Germany

[2] Istituto di Geologia e Geofisica dell' Universita degli Studi di Napoli, Largo S. Marcellino 10, I-80138 Napoli, Italy

Abstract. In 1977 a number of electrical dipole-dipole deep soundings, magnetotelluric and geoelectrical Schlumberger soundings were carried out in the Neapolitan volcanic region in order to test the application of these electrical techniques in a geothermal area.

The geothermal anomalies in this area, which are bordered by faults and magnetic intrusions, are correlated with a decrease of the electrical resistivity of the carbonate basement and a broadening of one of the upper layers, which has a low resistivity.

The limestone basement morphology deduced from magnetotellurics agrees with that obtained from gravity interpretation. The methods applied, especially the magnetotelluric method, can evidently be very valuable in a geothermal area.

Key words: Magnetotellurics – Geoelectric dipole-dipole soundings – Geothermal areas.

Introduction

The Neapolitan volcanic area, in common with most of the areas affected by active or recent volcanic activity, is a very promising area for geothermal exploitation. The geothermal potential of this area has been recognized since 1940 and several bore holes have been drilled at Phlegraean Fields and Ischia.

The geological and tectonic situation of the area has been caused by continuing geodynamic processes, which have built up the Apennine chain on one side and the Thyrrenian bathyal plane on the other.

Four main volcanic systems are present in this area: Somma-Vesuvio, the Phlegraean Fields, Ischia and Roccamonfina (Fig. 1). Besides these main centers, several other volcanic displays or tracks of aborted volcanism have been identified.

Radiometric ages of the Campanian volcanic products show that activity started here between 1 and 2 m.y. ago.

In particular the Phlegraean Fields volcanism is very recent, its oldest outcrop being the Campanian ignimbrite about 30,000 years old. Activity has continued up to present, the last eruption being that of 1538 (Monte Nuovo).

A number of geological, geophysical and vulcanological studies have been carried out in recent years, aimed at the reconstruction of the main structural trends and the relationship between volcanic and tectonic activity, the evaluation of the vertical and the horizontal temperature distribution and the study of the tectonic state of the area (Barberi et al. 1977). The aim of such research was both the correct planning of the local volcanic surveillance and the evaluation of the geothermal potential of the area.

One of the main targets in both cases is the detection and physical characterization of hot magmatic bodies which are, in some way, intruded into the crust. Such bodies may stay at shallow or moderate depths and heat the host rock to create a thermal reservoir.

During 1977 a geophysical survey was carried out in this area as part of the European Community research program for geothermal energy development. Financial support was also granted by the German Ministry for Research and Technology and the Italian National Research Council, Special Energy Program. This research was planned and carried out jointly by research teams of the Institute of Geology and Geophysics of Naples, the Institute of Geophysics and Meteorology of the University of Braunschweig and the Vesuvian Observatory. Magnetotelluric and Schlumberger geoelectrical soundings were made with the aim of testing these methods in a geothermal area of sufficiently well known general structure. A number of dipole-dipole electrical deep soundings were carried out to compare this technique with others that could be used in an area of this type.

In this paper the conclusions of previous geological and geophysical research are reported briefly together with the results of the present geoelectrical and magnetotelluric campaign.

The aim of this paper is to define a general model of the area which takes into account all the available geophysical results and may represent a working model for the small scale detailed surveys which will be carried out in the area for geothermal exploration.

Structural Setting

Seismic refraction data together with long wavelength gravity anomalies show that, in the Neapolitan region, the Moho discontinuity is at a depth of about 30 km, with a dip toward the Apennine chain, and that the top of the crystalline layer is at about 9–10 km (Corrado et al. 1974).

Magnetic data show that the crust in the Italian western side is characterised by a low susceptibility indicating a continental crust. Magnetic anomaly maps indicate, in the Neapolitan area, the presence of conspicuous igneous masses within the crust and the sedimentary layers (Corrado et al. 1977).

* *Present address:* Bundesanstalt für Geowissenschaften und Rohstoffe, Stilleweg 2, D-3000 Hannover 51, Federal Republic of Germany

0340-062X/81/0049/0026/$01.80

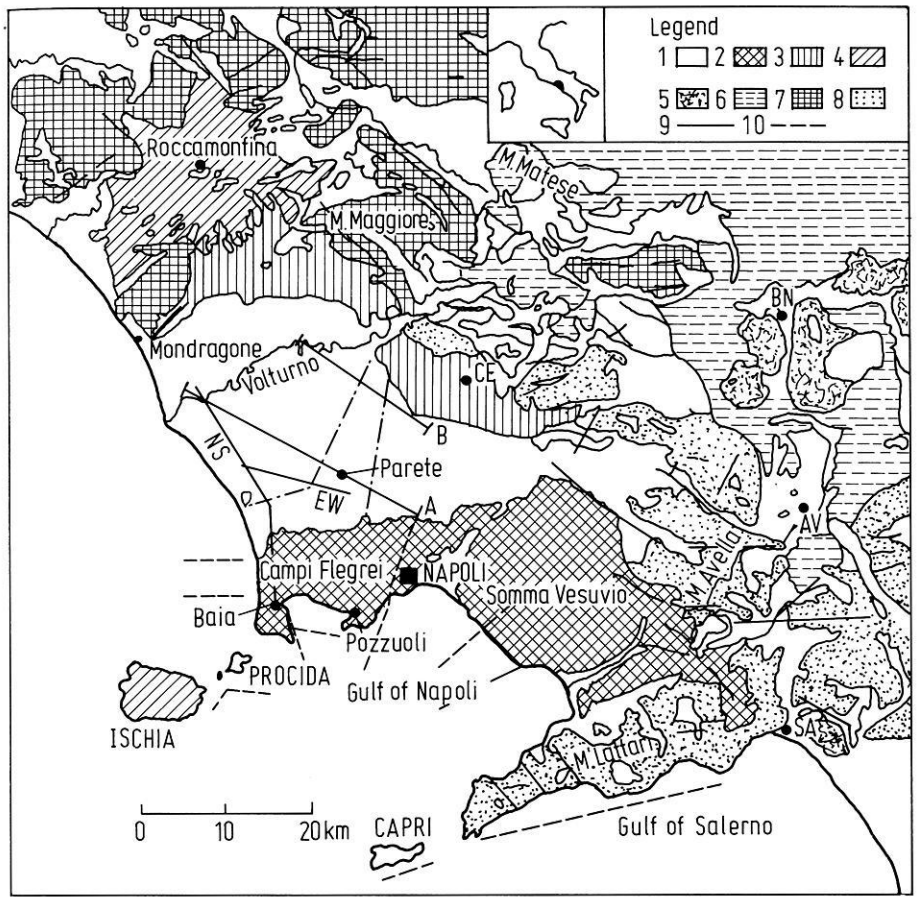

Fig. 1. Geological and structural sketch map of the Campanian volcanic area. *1* Alluvium deposits; *2* volcanics of Somma-Vesuvio and Phlegraean fields; *3* Campanian ignimbrite; *4* volcanics of Roccamonfina, Ischia and Procida; *5* Ariano units; *6* Irpine unit, Sicilid units; *7* Matese-M. Maggiore units; *8* Alburno-Cervati units; *9, 10* faults. *A, B:* gravimetric and magnetic profiles of Fig. 2. NS, EW: profiles shown in Fig. 6. –·–·– boundaries of structural high in Fig. 2

A detailed gravity survey carried out in the Neapolitan volcanic area, along profiles crossing the main gravity trends normally, allows a detailed reconstruction of the morphology of the carbonate Mesozoic basement (Carrara et al. 1973). It is interpreted as showing that the basement is divided by several normal faults into two structural lows. In the middle there is a structural high which approaches to within 1.5 km of the surface. The depth to the basement is about 4 km north and south of the central high (Fig. 2).

A detailed seismic reflection survey was carried out in the bays of Naples and Pozzuoli and the seismic data confirm the above interpretation (Finetti and Morelli 1974).

Intense magnetic short wavelength anomalies were recognized along the same profiles, often located where the gravity data indicate a fault. Figure 2 shows an example for this good correlation on the two parallel profiles, A and B. The boundaries of the structural high are shown in Fig. 1. As indicated in this figure, the northern boundary can be extended westward, to where Carrara et al. (1974) inferred another magnetic intrusion from a magnetic anomomaly near Lago Patria, which is shown in Fig. 12. This is an important result as it demonstrates first, that considerable magmatic activity is present in the whole Campanian region and in areas where no volcanic surface activity is recognized and second, that a close relationship exists between tectonic and magmatic activity, where the main faults are the preferential feeding channels of the local magmatism.

Taking into account the ages of both the neotectonic dilatant activity and of the volcanic products, it may be concluded that magmatic activity in this area depends strictly, in both space and time, on the Quaternary dilatant tectonic activity (Carrara et al. 1973).

Stratigraphy

The main units of the rock sequence constituting the sedimentary series of the Campanian area are the following (see Fig. 3):

Carbonaceous Mesozoic series (basement): made up of dolomitic rocks under limestone rocks with an overall thickness, inferred geologically, of about 6 km. Both the dolomite and the limestone have a high permeability due to the presence of a large number of fissures, as evident in outcrops and wells in the Apennine area. Impermeable marls and clay horizons are also present in the series, but they do not modify the general high permeability of the sequence.

Tertiary flysch complex: of variable thickness, generally some several hundred meters, with marls and clay horizons with variable, but generally low, permeability. This represents the main impermeable layer of the Campanian area.

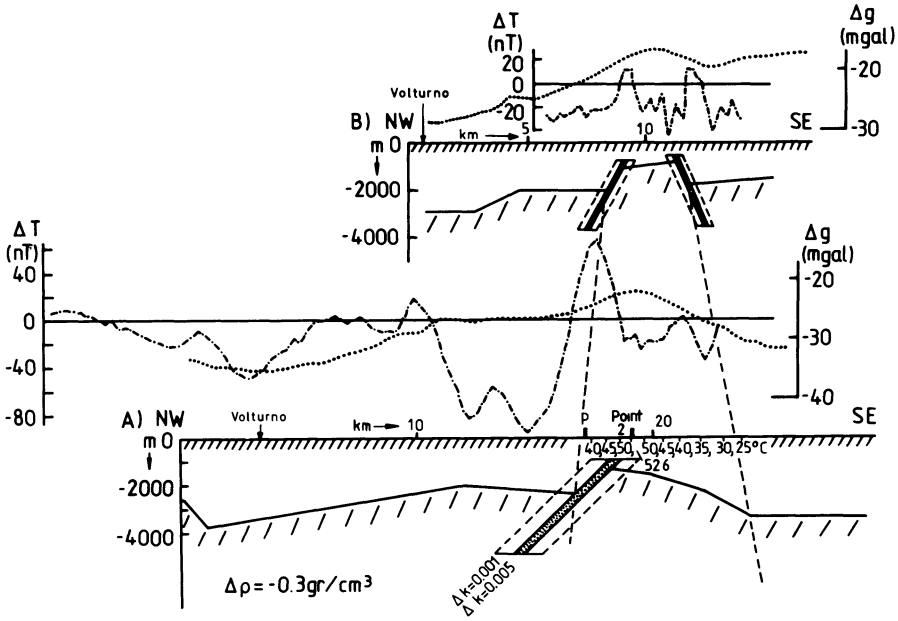

Fig. 2. Magnetic and gravimetric profiles in the geothermal area of Parete-Naples. In the figure the ΔT and Δg anomalies along profile **A** and **B** of Fig. 1 and the resulting models are shown. Carbonate basement deduced from gravity interpretation; igneous intrusions deduced from magnetic interpretation (Carrara et al. 1973, 1974). Temperature data from 5 different drillings are taken at a depth of 250 m (Baldi et al. 1976). *Point 2* has the highest thermal gradient. *Point P* is a deep well near Parete (1,800 m depth)

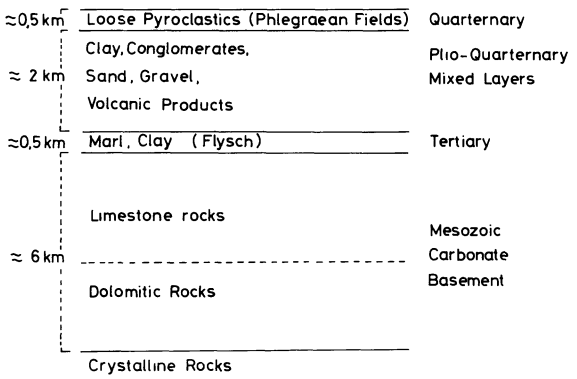

Fig. 3. Rough sketch of the sedimentary series of the Campanian area

Plio-Quaternary detritic complex. with impermeable (clays) and permeable (conglomerates, sand and gravel) horizons. Recent volcanic rocks are included in this complex. The main volcanic products are: ignimbrite and tuffs (Campanian grey tuff, Ischia green tuff, Phlegraean yellow tuff), incoherent pyroclastics, often altered by hydrothermal processes, scoriae and lava flows. The ignimbrite, tuffs and the other pyroclastic rocks show a high porosity and a low permeability.

In particular, the Phlegraean Fields area is covered mostly by loose pyroclastics; welded tuffs with variable porosity constitute the skeleton of the Phlegraean Fields and outcrops in the older volcanic centers. A few lava flows of limited extent are present at the surface. All these rocks often show chemical alteration due to the high temperature of the geothermal fluids.

Seismic Activity and Soil Deformation

The seismic activity is restricted mainly to the very center of the Phlegraean Fields area. Since 1970 attention has focussed on this area due to the exceptional ground uplift, reaching a maximum of 1.5 m in 1972. Results of the studies by Corrado et al. (1976–1977) also give valuable data for the evaluation of geothermal modelling of this area. Several epicenters are concentrated around the town of Pozzuoli and several others seem to be aligned parallel to the Baia coast (see Fig. 1). The focal depth data show that the great majority of quakes originated at depths less than 5 km, in most cases less than 3 km.

Several simple deformation source models were computed to fit experimental horizontal and vertical deformation trends. The best fit was obtained for a 75° inclined dike, having its top at the depth of about 3 km where most of the focal depths are located.

Seismic and deformation data are therefore compatible with the hypothesis of a dike-shaped magmatic mass intruded at shallow depth during that time interval.

Temperature Data

The anomalous thermal state of the area can be deduced from a number of high temperature fumaroles and hot springs. Moreover, several temperature measurements have been carried out in drill holes located in the Neapolitan area and particularly in the Phlegraean Fields and Ischia (Penta 1949; Penta and Conforto 1951a, b; Minucci 1964).

Data from the Phlegraean Fields (Penta 1949) area have been re-analyzed and the isotherm distribution based on data from the 8 most significant holes is reported in Fig. 4 (Rapolla 1977). It shows a drastic uplift of the isotherms in the center of the Phlegraean Fields.

On the basis of the isotherm pattern and assuming that the rocks at depth have similar thermal and hydrological properties, it can be hypothesized that temperatures higher than 300° C can be found at depths of about 2 km. It should be pointed out that a temperature higher than 300° C was measured at the bottom (1,842 m) of the Agnano well (CF23), which is located on the periphery of the geothermal system shown in Fig. 4.

Recently five test holes and a deep well (P in Fig. 2) were drilled north of the Phlegraean Fields. Gradients of geothermal

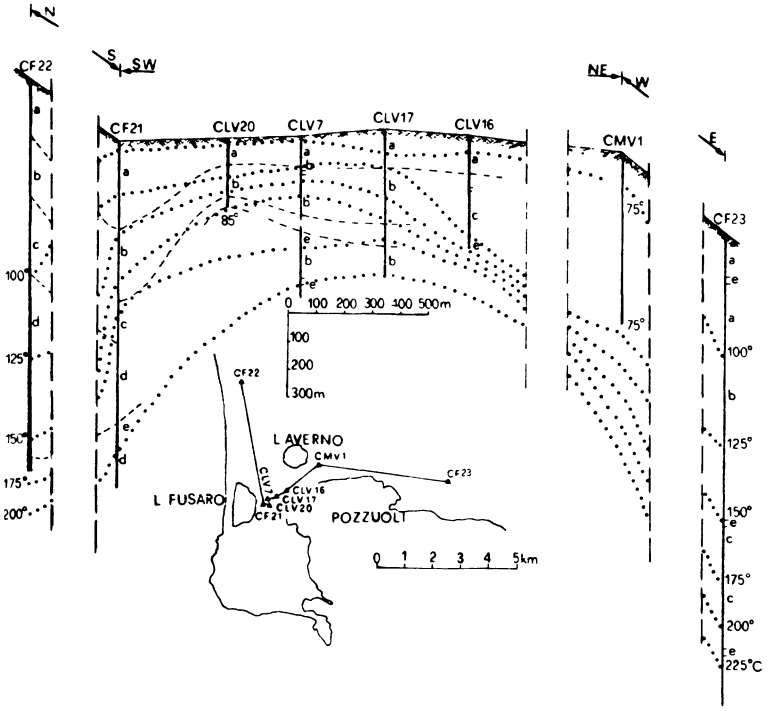

Fig. 4. Isotherm pattern in the Phlegraean Fields (after Rapolla 1977). **a, b, c, d, e** are different layers of volcanic products. ··· isotherms

interest were found only in an exploratory drilling (see Fig. 2) just south of Parete (≈150° C/km, point 2). West and east of this area temperature values decrease rapidly to normal. The deep well was located at about 2 km north-west of point 2 and a temperature of only 70° C was measured at the well bottom (1,800 m), confirming the normal gradient in this area.

DC Electrical Soundings

Shallow and deep Schlumberger vertical soundings were made in the Phlegraean Fields and surrounding areas. The results of these soundings reveal that the resistivity of the local volcanics is extremely variable. The electrical resistivity of the local pyroclastics is in the range 50–500 Ωm, and is reduced to less than 20 Ωm when the rocks are thermally altered or filled with saline water. Outcropping lava flows and compact ignimbrites show a resistivity as high as 3,000 Ωm (Carrara and Rapolla 1972).

About 25 deep Schlumberger soundings were carried out north of Phlegraean Fields by Baldi et al. (1976). Low resistivity areas were found between Parete and Giugliano (about 5 km south-east of Parete) with an electrode separation of about 1,000 m. The tendency toward high resistivity values at the longest electrode distances (AB/2 = 3,000 m and more) was interpreted by these authors as due to the resistive carbonaceous Mesozoic basement.

During the present survey nine DC electrical soundings were made using a polar dipole-dipole configuration (Alfano 1974). The distance between the two dipoles reached a maximum of 18 km (No. 2). The locations and directions of receiving dipoles are indicated in Fig. 6. The ground was energized by a current commutated at a period of 60 s, which was sufficiently low to avoid skin effects. The signal at the potential dipole was recorded digitally. The final evaluation of the potential differences was made subsequently by an autocorrelation computer analysis.

Dipole-dipole data were transformed into half Schlumberger data, as shown in Fig. 5, for interpretation. As both the dipole-

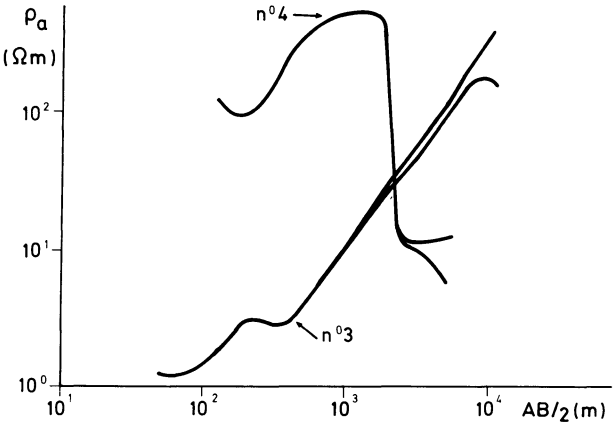

Fig. 5. Half-Schlumberger transformed dipole-dipole soundings nos. 3 and 4, Phlegraean Fields area (see Fig. 6 for location)

dipole and the half Schlumberger configuration are asymmetrical, the soundings should be referred not to the receiving dipole centre, but to a zone located towards the source dipole. But obviously, as the layering may not be horizontal, this criterion does not always hold. In spite of the limitations such as lack of geoelectrical stations and lateral control, a preliminary interpretation was attempted.

The interpretation of the field data shows that highly conductive layers (<20 Ωm), clearly correlated with the presence of sea water, are found in most cases at shallow depth in the area investigated. An example is curve No. 3 in Fig. 5. The thickness of the low resistivity layer is variable, from a few hundred meters to 1.5 km. At this depth a high clay content layer is generally found. Underneath this layer the resistivity increases. It seems probable that the geological sequence corresponding to the first part of the geoelectrical curve is the post-Mesozoic sedimentary

sequence in Fig. 3, whereas the highly resistive layer corresponds to the Mesozoic carbonate basement. The Tertiary flysch layer cannot be identified. Because of the very low resistivity of the surface layers, it was impossible to discriminate the increasingly resistive layers.

The whole resistive sequence reaches a depth of at least 5 km, which is the maximum depth explored. A different picture was found near the Cuma crater (sounding No. 4) where a clear lateral discontinuity occurs, indicated by the steep decrease of the ρ_a-curve at an AB/2 of 2 km. In this case it is not clear whether the low resistivity layer is covered by a high resistivity layer or whether this is an effect of the lateral discontinuity. Nevertheless the low resistivity layer seems to reach a much greater depth of at least 4 km. Because of a lack of data, we have been unable to interpret the soundings fully.

In conclusion, the results of these deep geoelectrical soundings can be considered only as preliminary. Although several technical and interpretative problems arise in the application of this configuration, it has proved to be the most convenient DC geoelectrical method for investigations down to several kilometers depth.

Magnetotelluric Soundings

In order to probe the structure of the crustal sections of the area down to about 10 km, 17 magnetotelluric measurements were carried out along two profiles as shown in Fig. 6 (Musmann et al. 1977; Hunsche and Duske 1978). The well-known geothermal anomaly of the Phlegraean Fields is located on the NS profile from point MT9 southward and the supposed geothermal anomaly of Lago Patria is located between points MT4 and MT6. The EW profile starts from this anomaly (MT5). The well-known thermal anomaly of Parete has its center at point MT 2/1, which corresponds within 100 m to point 2 of Baldi et al. (1976) and which has the highest gradient in this anomaly (see Fig. 2). The measurements were carried out with 3 MT stations, all measuring two orthogonal components of the electric field and the three components of the magnetic field by induction coils. Two stations (IFN0 and IGM1) worked completely automatically and were powered by batteries. The third (BGR) was equipped with a computer and was able to evaluate the complete ρ_a and phase curves in the field, which is very important for control of the quality of the results and for optimisation of measuring times. The stations operated in a frequency range 0.2–1,000 s (BGR), or 2–1,000 s (IFN0 and IGM1). The data were evaluated by statistical frequency analysis. The computed impedance tensors were rotated into the principal directions and the ρ_a and phase curves for the two orthogonal directions were calculated for each point. These were the basis for the model calculations, which were a combination of direct model calculations and an inversion method based on the Marquard algorithm, for which both, ρ_a and phase curves were used.

The derived ρ_a and phase curves are of high quality. Examples are shown in Fig. 7a and b. In most cases the ρ_a values have a standard deviation of less than 3% and the phases of less than 5° The ρ_a and phase curves for the two orthogonal measuring directions at one point, have very small differences in most cases. In addition, the corresponding skewness coefficients are very small (<0.1). These parameters indicate that the subsurface is essentially one-dimensional. In order to get an idea of the influence of the coast effect, two-dimensional model calculations with 3 different frequencies were carried out (Steveling, Göttingen, private communication). The results are not shown here, but they show that

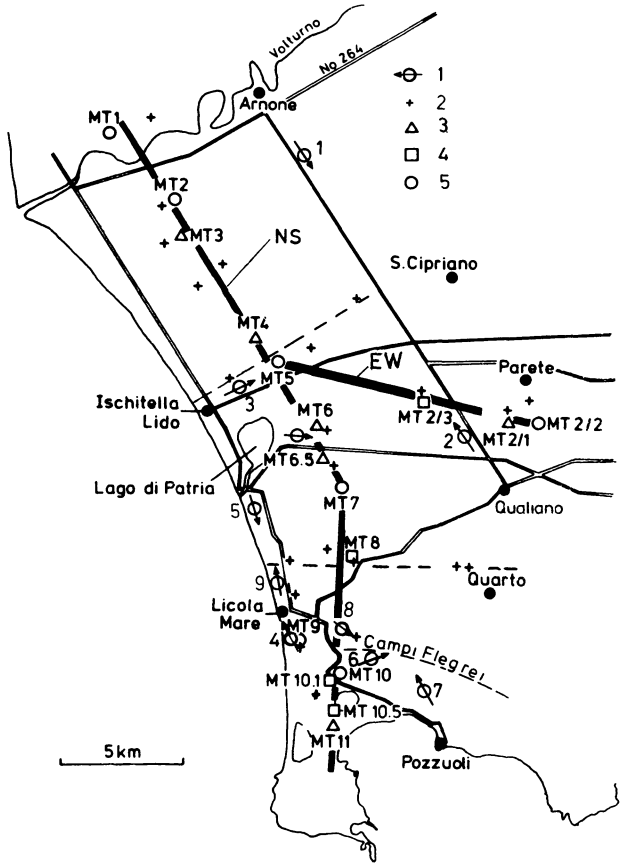

Fig. 6. Location of measuring points, magnetotelluric and geoelectric deep soundings in the area of Volturno-Campi Flegrei, 1977. *1* dipole-dipole soundings, location and direction of receiving depole; *2* Schlumberger soundings; *3, 4, 5* MT soundings (IFN0, IGM1, BGR); NS, EW · profiles of Figs. 8–13

the coast effect has an influence on the ρ_a curves of 20% in the worst case. For these reasons one-dimensional model calculations are suitable.

To get a first overview of the results, pseudo-cross-sections of both orthogonal ρ_a and both orthogonal phases are drawn for each profile. Because of the small differences, the results for only one direction are shown in Figs. 8a, b, 9a, and 9b. The magnetotelluric method is based on the electromagnetic skin-effect: the period T is a distorted depth scale and the ρ_a pseudo-sections are rough and distorted cross-sections of the subsoil. The phase cross-sections are more difficult to understand, but they show nearly the same information.

The most striking characteristics in Figs. 8a and 9a are the local minima of ρ_a at MT 5 (1.8 Ωm), MT 9 and MT 10 (1 Ωm) and MT 2/2 (4.8 Ωm). The minimum at MT 2/2 coincides quite well with the thermal anomaly at Parete which is centered on MT 2/1 and with the structural high, together with the dike shaped magnetic intrusion (see Fig. 2 and Fig. 13). The minimum at MT 9 and MT 10 correlates with the geothermal anomaly of the Phlegraean Fields and the minimum at MT 5 coincides with the magnetic anomaly and the inferred magnetic dike, shown in Fig. 12. These are promising results which have to be verified by exact model calculations.

In order to find out the resistivity of the upper 300 m, which are not covered by magnetotellurics, 23 Schlumberger soundings

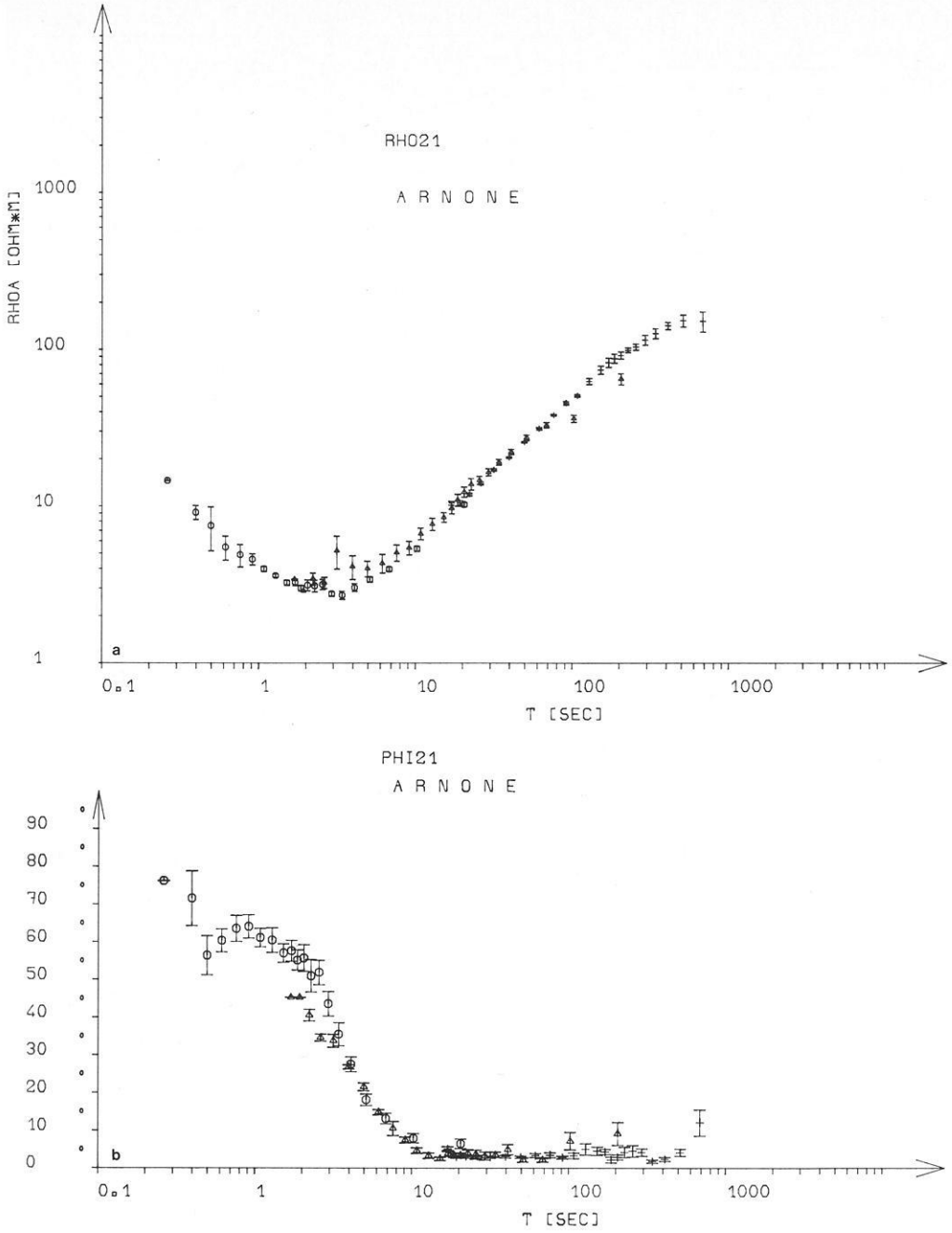

Fig. 7. **a** ρ_a curve for magnetotelluric sounding MT2. **b** Phase curve for magnetotelluric sounding MT2

with electrode separations up to 1.8 km were carried out. The results are described by Musmann et al. (1977). The measuring locations are shown in Fig. 6.

The final result of the one-dimensional magnetotelluric and DC-Schlumberger interpretation for the NS profile is shown in Fig. 10. Five layers were detected in the area; it was not possible to interpret the data by a consistent model with fewer layers.

1. The top layer is derived mainly from geoelectric soundings. It has a thickness varying between 30 m and 270 m and represents the freshwater layer. The resistivity and thickness is dependant on the distance from sea.

2. The second layer is a sedimentary and volcanic layer filled with saline or brackish water; its resistivity ranges between 4 and 20 Ωm. This layer reaches a maximum depth of about 1,600 m. It covers the most part of layers 1 and 2 in Fig. 3 and was also found by the DC dipole-dipole measurements.

3. The third layer has very low resistivities between 0.9 and 3 Ωm and a thickness up to 900 m. It is highly probable that it consists of clay deposits which are found in several wells. The thickness and the resistivity of this layer can be evaluated in nearly all cases within an accuracy of about 20%. Normally the parameters for low resistivity layers can be determined very well using magnetotellurics. It seems not to represent the Tertiary flysch layer which lies deeper, on top of the carbonate basement (see Fig. 3).

4. The fourth layer seems to be filled again with saline or brackish water, like layer two. In both layers (2 and 4) it is not

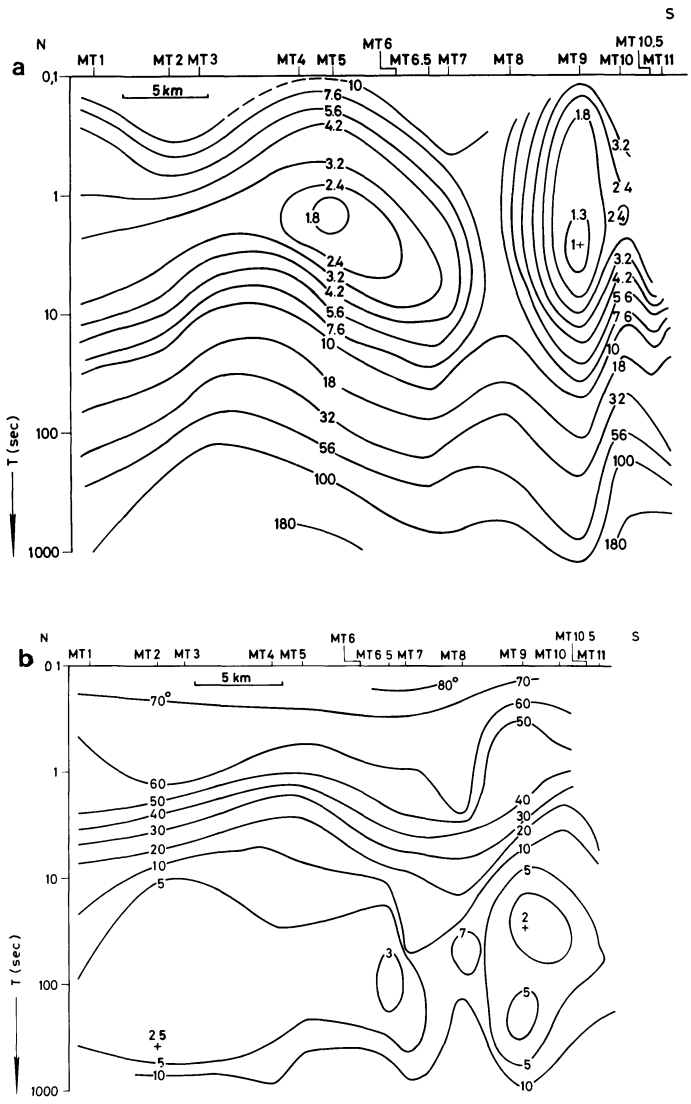

Fig. 8. **a** Magnetotelluric pseudo-cross-section of ρ_{a21} for the NS profile. The isolines of ρ_a in Ωm are shown as a function of period T. **b** Magnetotelluric pseudo-cross-section of phases φ_{21} for the NS profile. The isolines of φ in ° are shown as a function of period T

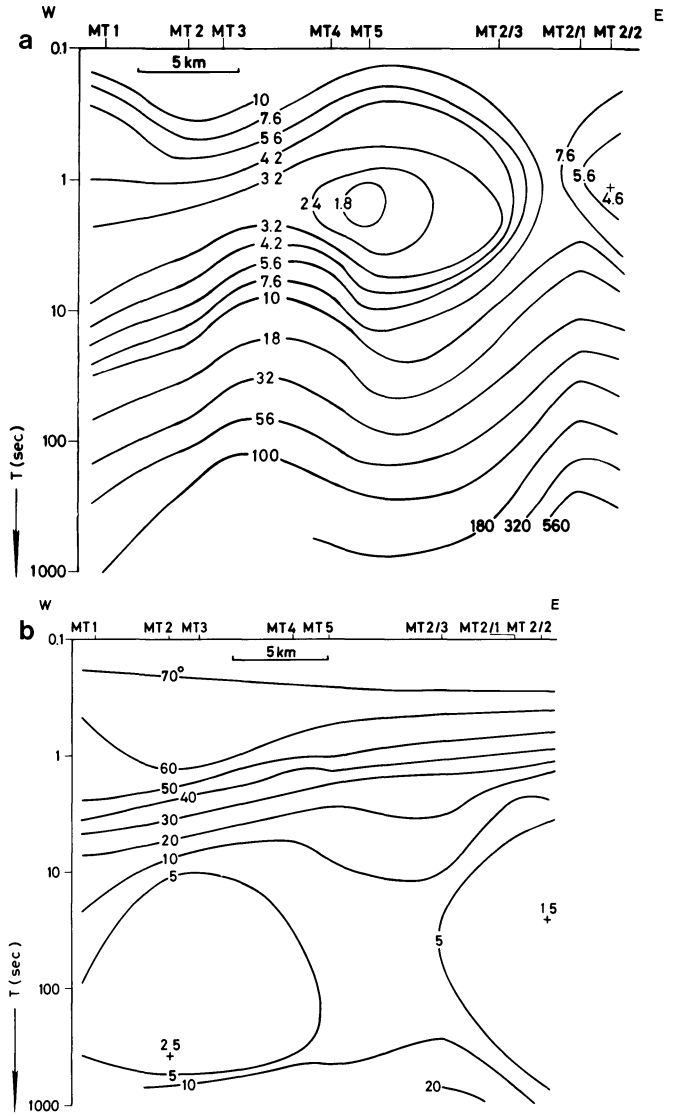

Fig. 9. **a** Magnetotelluric pseudo-cross-section of ρ_{a21} for the EW profile. The isolines of ρ_a in Ωm are shown as a function of period T **b** Magnetotelluric pseudo-cross-section of φ_{21} for the EW profile. The isolines of φ in ° are shown as a function of period T

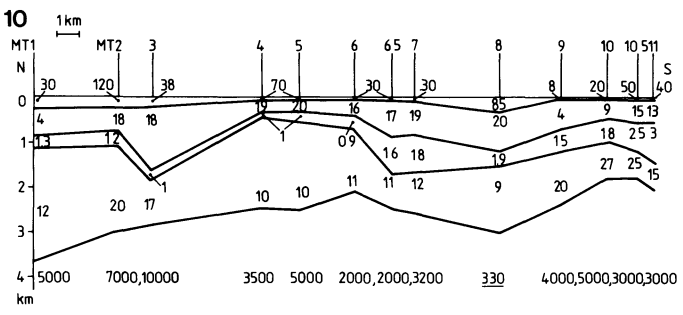

Fig. 10. Results of model calculations for the NS profile derived from Schlumberger soundings and magnetotelluric deep soundings. ρ values in Ωm

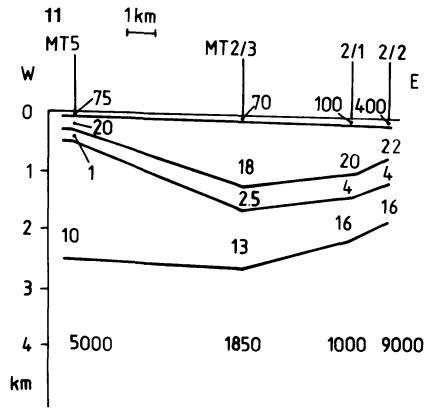

Fig. 11. Results of model calculations for the EW profile derived from Schlumberger soundings and magnetotelluric deep soundings. ρ values in Ωm

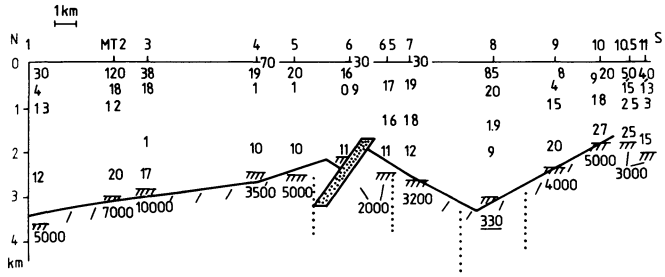

Fig. 12. Crustal section along NS profile (see Figs. 1 and 6 for location). Numbers: ρ in Ωm. ////// top of carbonate basement from magnetotellurics; ——— top of carbonate basement from gravity; /// magnetic intrusion. Low resistivity zones in the carbonate basement are also indicated

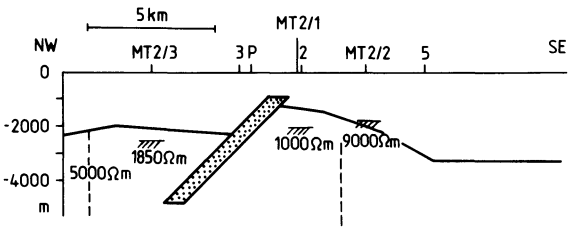

Fig. 13. Crustal section along EW profile (see Figs. 1 and 6 for location). ////// top of carbonate basement from magnetotellurics; ——— top of carbonate basement from gravity; /// magnetic intrusion. A low resistivity zone in the carbonate basement is also indicated

possible to find the further subdivisions suggested by drilling. Its resistivity ranges between 9 and 27 Ωm and its thickness reaches 2.5 km. This layer consists of the lower part of layer 2 and of layer 3 in Fig. 3. The layer could not be differentiated by the DC dipole-dipole measurements.

5. The highly resistive basement (generally 3,000 Ωm and more) represents the limestone and crystalline sequence which cannot be differentiated. The high resistivities of the carbonate and dolomitic rocks have been confirmed by two additional magnetotelluric measurements in the Appenine mountains, where the basement, as deduced from magnetotellurics, outcrops. The depth to the top of the carbonate basement varies between 3.7 and 1.8 km. The depth can be determined with an accuracy of ± 400 m taking into account the high quality of data and the assumption that the lateral differences of the resistivities in layers 2 and 4 in Fig. 10 have to be small. This fifth layer was also found by DC dipole-dipole measurements.

It can be seen clearly in Fig. 10 that the supposed limestone basement is closer to the surface toward the Phlegrean Fields area and shows special highs at the anomalies of Lago Patria and the Phlegraean Fields. This can also be said of the low resistivity layer 3. Moreover in the southern part the resistivity of layer 3 is higher by a factor of 2 or 3 and the layer is also much thicker. These results are not changing due to the principle of equivalence, and could not be found by the DC dipole-dipole measurements. The EW profile (Fig. 11) shows a very similar situation approaching the Parete anomaly. At first glance it is surprising that the striking ρ_a-minima in Figs. 8a and 9a do not appear so clearly in Figs. 10 and 11, but they can, in fact, be explained mainly by a rise in the level of layers 3 and 5 and a broadening of layer 3. As a final result Fig. 12 shows a crystal section of the NS profile obtained by magnetotelluric, gravity and magnetic data. It can be seen that there is good agreement between the gravity and magnetotelluric depths to the top of the carbonate basement. Moreover it is remarkable that lower resistivities result in the basement in the vicinity of the magnetic dike, which is situated on a tectonic fault. Another deep, low resistivity zone is at point MT 8, which lies on the north-western boundary of the Phlegraean Fields and may be due to a fault.

Figure 13 shows an equivalent crustal section for the EW profile. The agreement between the two top depths of the carbonate basement is a bit worse than for the NS profile. But again a low resistivity zone results in the vicinity of the magnetic dike just on the boundary of the above mentioned structural high. Moreover this is the area of the geothermal anomaly of Parete.

Conclusions

One of the results of this survey is the delineation of the local limestone basement morphology by magnetotelluric soundings. The picture obtained agrees fairly well with that deduced by gravity interpretation. The agreement between two independent geophysical methods makes the final picture very reliable. It should be stressed that magnetotellurics obtain deep results in a geological setting where the DC dipole-dipole sounding method seems to fail.

The resistivity of the Mesozoic basement is generally between 3,000 Ωm and 10,000 Ωm. Low values are found in the Lago Patria area (2,000 Ωm), on the western side of the Parete structural high (1,000 Ωm, 1,850 Ωm) and on the northwestern side of the Phlegraean Fields (330 Ωm). These values may be related to a local increase of the water content due to a higher amount of fissures in the vicinity of tectonic faults together with a possible increase of temperature and salinity.

Comparing the results obtained on the structure in the Phlegraean Fields and Parete areas and the available temperature distribution, a number of conclusions can be proposed:

1. In both geothermal areas there is a connection between the structural high and the welling up of the isotherms.

2. At least at Parete and most probably in the Phlegraean Fields area, the presumed heat sources are magmatic masses intruded in the faults which border this structural high.

3. Related with these faults there is a decrease of the basement electrical resistivity.

4. A hot magmatic body could not be detected as was hoped in the beginning of the investigation. Probably no magmatic body exists but there the problem of discriminating between the effects caused by water and by high temperature remains.

5. It should be mentioned moreover that the low resistivity layer 3, detected by the magnetotelluric survey, broadens in the Phlegraean Fields and Parete areas. This may be due to the alteration of the sediments as found by drillings in the Phlegraean Fields area. If this hypothesis holds the broadening of this layer at points MT 6.5 and MT 7 just south of Lago Patria can be explained in the same way.

6. The Lago Patria and Parete areas are characterized by magnetic anomalies. The anomalies centered between points MT 6.5 and MT 6 as well as between MT 2/3 and MT 2/1 were interpreted as caused by dike shaped intrusions into the limestone. Note that no thermal anomaly has yet been detected at Lago Patria. Although the tectonic situation is similar to the two other areas,

no magnetic anomaly seems to be present at the northern border of the Phlegraean Fields where the volcanic activity is much more recent and the thermal anomaly bigger.

7. As shown, the electrical methods applied, especially the magnetotelluric method, can be valuable tools for the exploration of areas of geothermal interest, if combined with other methods.

Acknowledgements. We are grateful to Dr. W. Losecke and his colleague M. Zeibig of the Bundesanstalt für Geowissenschaften und Rohstoffe, Hannover, for their support, advice and help during MT measurements in Italy. Moreover we thank the unknown referees for their valuable remarks.

References

Alfano, L.: A modified geoelectrical procedure using polar-dipole arrays – and examples of application to deep exploration. Geophys. Prospect. **22**, 510–525, 1974

Baldi, P., Cameli, G.M., D'Argenio, B., Oliveri del Castillo, A., Pescatore, T., Rossi, A., Puxeddu, M., Toro, B.. Geothermal research in western Campania (Southern Italy). A revised interpretation of the Qualiano-Parete structure. Proc. Int. Congr. Thermal Waters, Geothermal Energy and Vulcanism of the Mediterranean Area **1**, 56–70, Athens 1976

Barberi, F., Innocenti, F., Luongo, G., Nunziata, C., Rapolla, A.: Shallow magmatic reservoirs as heat source of geothermal systems: preliminary interpretation of data available for the Neapolitan active volcanic areas. Semin. Geothermal Energy, EUR 5920, Vol. 1, 19–37, Brussels 1977

Carrara, E., Iacobucci, F., Pinna, E., Rapolla, A.: Gravity and magnetic survey of the Campanian volcanic area, S. Italy. Boll. Geofis. Teor. Appl. **15**, 39–51, 1973

Carrara, E., Iacobucci, F., Pinna, E., Rapolla, A.: Interpretation of gravity and magnetic anomalies near Naples, Italy, using computer techniques. Bull. Volcanol. **38**, 1–10, 1974

Carrara, E., Rapolla, A.. Shallow DC resistivity of the Phlegraean Fields volcanic area, Naples, Italy. Boll. Geofis. Teor. Appl. **14**, 34–40, 1972

Corrado, G., Iacobucci, F., Pinna, E., Rapolla, A.: Anomalie gravimetriche e magnetiche e strutture crostali nell' Italia centro-meridionale. Boll. Geofis. Teor. Appl. **16**, 271–291, 1974

Corrado, G., Guerra, I., Lo Bascio, A., Luongo, G., Rampoldi, R.: Inflations and microearthquake activity of Phlegraean Fields, Italy. Bull. Volcanol. **40**, 169–188, 1976–1977

Corrado, G., Pinna, E., Rapolla, A.: The magnetic field of Italy: description and analysis of the new T, Z, and H maps between 40°N and 44°N. Boll. Geofis. Teor. Appl. **19**, 140–156, 1977

Finetti, I., Morelli, C.: Esplorazione sismica a riflessione dei Golfi di Napoli e Pozzuoli. Boll. Geofis. Teor. Appl. **16**, 175–222, 1974

Hunsche, U., Duske, J.: Magnetotellurische und geoelektrische Messungen zur geothermischen Exploration in den Phlegräischen Feldern, Italien. Auswertung und Modellrechnungen. Kolloquium: Erdmagnetische Tiefensondierung, 141–146, Neustadt/Weinstraße 1978

Minucci, G.: Rotary drilling for geothermal energy: proceedings of the U. N. conference on new sources of energy, pp. 234–244. New York: United Nations 1964

Musmann, G., Hunsche, U., Duske, J., Kertz, W.. Magnetotelluric and geoelectric measurements for geothermal exploration in the Phlegraean Fields (preliminary results). Semin. Geothermal Energy, EUR 5920, Vol. 1, 217–239, Brussels 1977

Penta, F.: Temperature nel sottosuolo della regione Flegrea. Ann. Geofis. **2**, 328–346, 1949

Penta, F., Conforto, B.: Risultati di sondaggi e di ricerche geominerarie nei "Campi Flegrei" per vapore, acque termali e "forze endogene" in generale. Ann. Geofis. **4**, 369–385, 1951 a

Penta, F., Conforto, B.: Sulle misure di temperatura del sottosuolo nei fori trivellati in presenza di acqua e sui relativi rilievi freatimetrici in regioni idrotermali. Ann. Geofis. **4**, 43–93, 1951 b

Rapolla, A.: Ricerca di fonti di energia geotermica: le masse magmatiche superficiali nelle aree di vulcanismo attivo. Paper presented at the meeting "Geotermia e Regioni", held in Chianciano, Tuscany, April 1977; edited by Regione Toscana, Firenze 1977

Received November 30, 1979; Revised Version May 20, 1980
Accepted May 28, 1980

J. Geophys. 49, 35–42 (1981)

Journal of Geophysics

Velocity Variations in Systems of Anisotropic Symmetry

S. Crampin [1] and S.C. Kirkwood [2]

[1] Institute of Geological Sciences, Murchison House, West Mains Road, Edinburgh EH9-3LA, Scotland
[2] Department of Geophysics, University of Edinburgh, James Clerk Maxwell Building, Edinburgh EH9-3JZ, Scotland

Abstract. Angular variations of seismic velocities have been observed in the Earth and attributed to some form of anisotropy caused by aligned crystals, orientated cracks and inclusions, and laminated strata. The exact analytical expressions for the velocities in each particular symmetry-system, derived from the Kelvin-Christoffel equations, are complicated functions of the elastic constants and cannot be easily manipulated. This paper examines the form of the velocity variations for the several systems of elastic symmetry; five of these seven symmetry-systems have been suggested for possible Earth structures. We shall demonstrate that the approximate equations of Backus (1965) and Crampin (1977a) are good estimates for the velocity variations in symmetry planes of all symmetry systems, but not in general for off-symmetry planes. These equations are linear in the elastic constants, and provide a convenient link between velocity variations and elastic constants, if used judiciously. The behaviour of shear waves in off-symmetry directions is complicated by pinches, caused by the proximity of shear-wave singularities, where the two shear-waves exchange polarizations. Despite the restrictions to their use, the equations are the fundamental relationship for a number of modelling studies.

Key words: Anisotropic symmetry – Velocity variations – Approximate anisotropic velocities – Shear-wave singularities: Kisses, Intersections and Point singularities.

Introduction

Azimuthal velocity variations of *Pn* waves have now been observed in a variety of tectonic regimes: in lithosphere formed at oceanic ridges (Hess 1964; Raitt et al. 1969; and many others); beneath the Rhinegraben (Bamford 1977); and beneath the Western USA (Bamford et al. 1979). Upper-mantle velocity-anisotropy beneath much of Eurasia is also implied by the polarization of higher-mode surface-waves (Crampin and King 1977), and beneath much of the Pacific Ocean by the polarization of fundamental-mode surface-waves (Kirkwood and Crampin in press 1980b). Azimuthal anisotropy throughout the whole of the oceanic lithosphere beneath the NAZCA plate is suggested by the velocity variations of fundamental-mode surface-waves (Forsyth 1975). Most of these observations are equivalent to measuring the velocity variations in a single plane-section of the anisotropic material, and place little constraint on the choice of symmetry-system or the three dimensional nature of the velocity variations in the upper mantle. This system is usually taken to be some orthorhombic orientation, since crystalline olivine, the supposed major anisotropic constituent, has orthorhombic symmetry.

In the crust, exploration seismologists have long recognised that regular sequences of thin sedimentary beds may simulate a homogeneous transversely-isotropic material, and hence have hexagonal symmetry (Postma 1955; Backus 1962; Levin 1978). However, it appears that very little direct evidence for transverse isotropy has yet been found. Crack anisotropy (Crampin 1978) also suggests a number of potential sources of anisotropy in the crust, with a variety of possible symmetry-systems, although only one has yet been observed (monoclinic symmetry. Crampin et al. 1980).

We see that anisotropy in the Earth is still in a largely descriptive stage of investigation, although the theoretical and numerical development is now quite advanced. Clearly, inversion of in situ anisotropy is important for the information it may contain on material composition, lithology, three-dimensional velocity-structure, and tectonics (by identifying the stress field) (Crampin 1977b; Crampin and Bamford 1977; Crampin et al. 1980; Kirkwood and Crampin in press 1980a and b). However, the larger number of elastic constants to be specified make it more difficult to invert anisotropic than isotropic structures (Crampin 1976; Crampin 1977a; Kirkwood 1978).

One further complication in anisotropic media is that the direction of the ray-, wave-, or group-velocity vector deviates from the phase-propagation vector for both body and surface waves. It is the phase-velocity which appears explicitly in most analytical expressions, whereas it is the group-velocity arrival which is usually observed on seismograms.

The phase-velocities of the three orthogonally-polarized body-waves that propagate in anisotropic media (a quasi *P*-wave, *qP*, and two quasi shear-waves, *qS1* and *qS2*, or *qSH* and *qSV* where appropriate) are solutions of the Kelvin-Christoffel equations (Musgrave 1970; Auld 1973). These solutions are rational functions of the elastic constants and direction cosines, depend on the particular symmetry-system, and are sufficiently complicated to make it difficult to estimate the constants from observations of velocity, even when the particular symmetry-system can be identified. Consequently, we make use of the approximate equations of Backus (1965) and Crampin (1977a), which are much easier to manipulate.

There are many references to anisotropic symmetry in crystallographic literature (Nye 1957; Musgrave 1970; Auld 1973). Perhaps the major reference in geophysics is Backus (1970), which gives a strictly mathematical background to symmetry-systems. The numerical techniques used in the present paper are applicable generally and do not depend on the particular symmetry-system. The

0340-062X/81/0049/0035/$01.60

paper discusses the velocity variations in six of the seven systems of anisotropic symmetry, five of which are possible configurations within the Earth (Table 1), and focuses attention on several aspects of particular importance to seismologists, which are not adequately treated elsewhere:

1. The relevance of the approximate equations of Backus (1965) and Crampin (1977a) to particular symmetry-systems,

2. the importance of the 2θ and 4θ variations with direction for understanding the behaviour of body-waves,

3. the significance of the singularities of shear-wave slowness-sheets for the propagation and polarization of shear-waves (see also Crampin and Yedlin 1980).

Approximate Equations for Variation of Phase-Velocity

Backus (1965) determined approximate equations for the variations of qP velocity over a plane in a weakly anisotropic solid in terms of linear combinations of the elastic constants, and cosines and sines of the angle of azimuth. We shall demonstrate in subsequent sections that these equations are strictly applicable only to velocity variations in planes of mirror symmetry, and, although they may be good approximations in some off-symmetry planes, they are not good in all such planes. Crampin (1977a) derived similar expressions for shear-waves propagating in symmetry planes. These equations of Backus and Crampin provide a simple direct link between the velocities and the elastic constants, and have proved very convenient for estimating anisotropic elastic constants from velocity variations (Crampin and Bamford 1977; Crampin 1978; Crampin et al. 1980).

The azimuthal variations in the velocities of body-waves propagating in the $x_3=0$ plane of mirror symmetry of a weakly anisotropic material can be written (Backus 1965; Crampin 1977a):

$$\begin{aligned}
&\rho V_{qP}^2 = A + B_c\cos 2\theta + B_s\sin 2\theta + C_c\cos 4\theta + C_s\sin 4\theta,\\
&\rho V_{qSH}^2 = D + E_c\cos 4\theta + E_s\sin 4\theta, \text{ and}\\
&\rho V_{qSV}^2 = F + G_c\cos 2\theta + G_s\sin 2\theta,
\end{aligned} \tag{1}$$

where
$$\begin{aligned}
A &= \{3(c_{1111}+c_{2222}) + 2\,(c_{1122}+2c_{1212})\}/8,\\
B_c &= (c_{1111}-c_{2222})/2,\\
B_s &= (c_{2111}+c_{1222}),\\
C_c &= \{c_{1111}+c_{2222}-2\,(c_{1122}+2c_{1212})\}/8,\\
C_s &= (c_{2111}-c_{1222})/2,\\
D &= \{c_{1111}+c_{2222}-2\,(c_{1122}-2c_{1212})\}/8\\
E_c &= -C_c,\\
E_s &= -C_s,\\
F &= (c_{1313}+c_{2323})/2,\\
G_c &= (c_{1313}-c_{2323})/2,\\
G_s &= c_{2313},
\end{aligned}$$

ρ is the density, V_{qP} is the velocity of the qP wave, V_{qSH} and V_{qSV} are the velocities of the quasi shear-waves with polarizations parallel (qSH), and perpendicular (qSV) to the plane of variation, c_{jkmn} are the moduli of the elastic tensor rotated so that the x_3-axis is normal to the plane of variation, and θ is the azimuth of propagation measured from the x_1-axis. The x_1, x_2, and x_3 axes are not necessarily principal axes. If θ is measured from a direction of sagittal symmetry ($x_2=0$, a plane of mirror symmetry), the coefficients of the sine terms are identically zero in Eq. (1) leaving the *reduced equations* in $\cos 2\theta$ and $\cos 4\theta$.

The shear-waves have polarizations strictly parallel and perpendicular to the plane of variation only if the plane possesses mirror symmetry (this restriction, although obvious, has not been stated explicitly in previous publications). The polarizations of the shear-waves ($qS1$ and $qS2$) are not parallel or perpendicular to generally orientated planes of variation, and the coefficients of the expansions in these cases are not simple combinations of elastic constants. The expansion for $qS1$ and $qS2$, even in solids with weak anisotropy, cannot generally be expressed in terms of trigonometric functions of 2θ and 4θ, but also require 6θ and higher terms for their description. The approximations are the first five terms of the Fourier Series expansion of the velocity variations – the complete expansions for general orientations contain an infinite number of terms. We find that the various restrictions on the application of these approximations to modelling studies present few problems in practice, because most symmetry-systems have sufficient symmetry planes for the equations to be easily applied.

Equations (1) are correct, with the restrictions given above, to the first order of the differences between anisotropic and isotropic elastic constants; the following figures demonstrate that the equations are good approximations even for strong anisotropy. It should be noted that the goodness of fit of the equations to any anisotropic velocity variation depends on the particular symmetries and the particular elastic constants and cannot be generalized in terms of, say, the fit being good to a certain percentage of velocity anisotropy.

Velocity Surfaces, Wave Surfaces, and Shear-Wave Singularities

We display the variations of phase-velocity with direction in various structures for the several systems of anisotropic symmetry. These curves are sections of what is sometimes called the velocity surface. However, this velocity surface is not what is usually observed in field or laboratory experiments. In anisotropic media, energy propagates with a component (usually small) parallel to the wave front. Thus the energy travels along a ray at an angle to the propagation vector and propagates with the group-velocity. The surface traced by this energy radiating along rays from a point source in a given time is known as the wave surface, or ray surface (Postma 1955; Musgrave 1970). This surface is the envelope of the wave fronts (Synge 1957). Sections of the wave surface cut by symmetry planes take a particularly simple form: the wave or group-velocity is

$$\begin{aligned}
&V_w = (V^2 + (dV/d\theta)^2)^{1/2},\\
&\text{in a direction}\\
&\phi = \tan^{-1}\,[(V\sin\theta + (dV/d\theta)\cos\theta)/(V\cos\theta - (dV/d\theta)\sin\theta)],
\end{aligned} \tag{2}$$

where $V(\theta)$ is the velocity in a direction θ in a symmetry plane (Postma 1955, first applied these equations to transversely-isotropic symmetry, but they are applicable generally, to symmetry planes in any system of anisotropic symmetry). The wave surface is very close to the velocity surface when the anisotropy is weak, and near symmetry directions in stronger anisotropy. In geophysics, where anisotropy is likely to weak (observed to be less than 8% in the upper-mantle although possibly stronger in some crustal rocks), velocity surfaces will generally be good approximations to wave surfaces.

Sections of the wave surfaces and velocity surfaces for structures with hexagonal symmetry are compared in Fig. 3 below.

These hexagonal examples have much weaker velocity-anisotropies (a maximum of 10% for qSH in zinc oxide, and 20% for qP in the cracked structure) than those in the remaining figures, and the wave surfaces and velocity surfaces are very close together. The structures with large anisotropies in the other figures have wave surfaces (not shown) which are substantially different from the velocity surfaces and frequently display cusps. However, we are using the structures to demonstrate the form of the velocity variations and the fit of the approximate equations for particular symmetry conditions, and these forms will be retained in weaker concentrations, where the wave and velocity surfaces do not differ significantly.

Crampin and Yedlin (1980) draw attention to the singularities of shear-wave velocities, where there are coincident roots. These are most easily considered in the slowness surfaces; there are three types of singularity; kiss singularities, where the two sheets touch tangentially, either convexly or concavely, but do not intersect; intersection singularities, where the two sheets intersect each other (possible only with hexagonal symmetry); and point singularities, where the two sheets have a common point at the vertex of two cones on their surfaces. Intersections are comparatively straightforward and do not cause any particular complications in either propagation or interpretation. Point singularities are places where the inner and outer surfaces exchange polarizations at a point. For variations in planes which pass near, but not through, such a point the waves exchange polarities at a pinch without coming into contact. When the pinch is tight, the approximations (1) for shear-waves are particular inappropriate. Pinches may cause considerable complications in some types of shear-wave propagation Crampin and Yedlin (1980).

Velocity Variations in Symmetry-Systems

The classes of elastic symmetry are usually divided into the seven named symmetry-systems listed in Table 1, which are described by the fourth-rank elastic-tensors of Fig. 1 (Nye 1957, noting the errors in Nye's specification for trigonal symmetry). These named systems encompass the full range of symmetry structures possible in homogeneous anisotropic elastic solids, and possible applications in the Earth are listed for five of the seven systems in Table 1. The triclinic system is omitted from the discussion: its description requires 21 independent elastic constants (Nye 1957), and the velocity variations are too general to be usefully summarized (conveniently, triclinic symmetry has not yet been suggested for any Earth structures).

The following figures show the velocity variations in symmetry planes and the orthogonal corner $x=0$, $y=0$, and $z=0$ (which we specify as x-cut, y-cut, and z-cut) for a range of anisotropic symmetry-structures. Since the amplitude and sign of each variation depends on the sum and difference of various combinations of elastic constants, these amplitudes and signs can vary widely from material to material even within the same symmetry system. The materials illustrated were chosen to display particular variations; further examples of crack systems relevant to the Earth can be found in Crampin (1978). The figures should be examined in relation to the other parameters of symmetry systems given in Tables 1 and 2, and in Fig. 1.

The velocity variations show a variety of different forms. The only general constraint is the near equality, but opposite sign, of the amplitudes of the 4θ variations of the squared qP and qSH velocities in symmetry planes, as expected from (1).

Table 1. Symmetry systems (referred to principal axes)

Symmetry system	Number of independent elastic constants	Number and specification of symmetry planes	Possible symmetry structures in the Earth
Cubic	3	9 { 3 identical: x-, y-, and z-cuts (Fig. 2a); 6 identical: planes joining opposite sides of cube (diagonal-cuts) (Fig. 2b) }	Orthogonal triplanar-systems of cracks with equal crack-densities (Fig. 5, Crampin 1978)
Hexagonal[a]	5	{ z-cut (Figs. 3b, and 3d); All planes through axis of cylindrical symmetry: z-axis (Figs. 3a and c) }	Lithologic alignments (Oil shale, Kaarsberg 1968); thin sedimentary sequences (Postma 1955; Backus 1962; Levin 1978); orientations of olivine in upper mantle (Francis 1969)
Trigonal	6(7)[b]	3 { 3 identical: sides of triangular prism; x-, $((1, \sqrt{3},0))$-, and $((1, \sqrt{3},0))$-cuts (Fig. 4a) }	None known
Tetragonal	6(7)[b]	5 { 2 identical: sides of square prism; x-, and y-cuts (Fig. 5a); z-cut (Fig. 5b); 2 identical: planes joining edges of prism; $((1, 1, 0))$-, and $((1, \bar{1}, 0))$-cuts (Fig. 5c) }	Orthogonal biplanar systems of cracks with equal crack-densities (Fig. 4, Crampin 1978)
Orthorhombic	9	3 { x-cut (Fig. 6a); y-cut (Fig. 6b); z-cut (Fig. 6c) }	Aligned olivine-crystals in the upper mantle (Hess 1964; Avé Lallemant and Carter 1970; Crampin and Bamford 1977)
Monoclinic	13	1 { z-cut (Fig. 7c) }	Biplanar cracks with unequal crack-densities (Crampin et al. 1980)
Triclinic	21	None	None known

[a] Systems with hexagonal symmetry are transversely isotropic when the symmetry axis is vertical

[b] The name of the system refers to two possible configurations of constants. The identification of symmetry planes and possible Earth structures refer to the configuration with fewer constants

ISOTROPIC

```
a c c . . .
c a c . . .
c c a . . .
. . . x . .
. . . . x .
. . . . . x
```

where

x = (a - c)/2

CUBIC

```
a c c . . .
c a c . . .
c c a . . .
. . . e . .
. . . . e .
. . . . . e
```

HEXAGONAL

```
a c d . . .
c a d . . .
d d b . . .
. . . e . .
. . . . e .
. . . . . x
```

where

x = (a - c)/2

TRIGONAL (1)

```
a c d f . .
c a d -f . .
d d b . . .
f -f . e . .
. . . . e y
. . . . y x
```

where

x = (a - c)/2,

and y = f

TRIGONAL (2)*

```
a c d f g .
c a d -f -g .
d d b . . .
f -f . e . z
g -g . . e y
. . . z y x
```

where

x = (a - c)/2,

y = f, and z = -g

TETRAGONAL (1)

```
a c d . . .
c a d . . .
d d b . . .
. . . e . .
. . . . e .
. . . . . f
```

TETRAGONAL (2)*

```
a c d . . g
c a d . . -g
d d b . . .
. . . e . .
. . . . e .
g -g . . . f
```

ORTHORHOMBIC

```
a d e . . .
d b f . . .
e f c . . .
. . . g . .
. . . . h .
. . . . . i
```

MONOCLINIC

```
a d e . j .
d b f . k .
e f c . l .
. . . g . m
j k l . h .
. . . m . i
```

Fig. 1. The form of the elastic tensors for the various systems of elastic symmetry, with the conventional choice of axes. The letters *a–m* represent independent quantities in each tensor, unless otherwise specified. The tensor for the triclinic system is not shown. The starred tensors are more complicated varieties of the unstarred tensors and will not be discussed in this paper

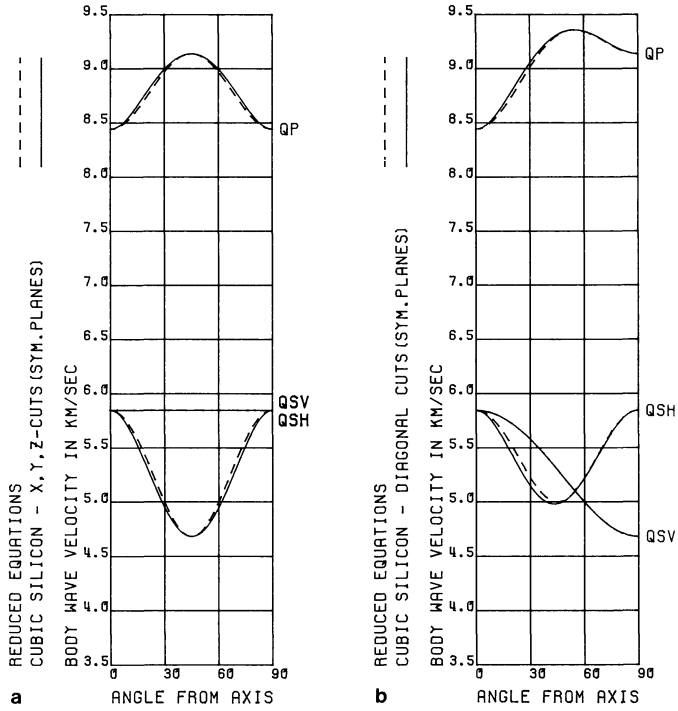

Fig. 2a and b. *Cubic symmetry.* Comparison of velocity variations of the approximate equations with the exact phase-velocities of silicon (elastic constants from McSkimin 1953), as a function of angle from a coordinate axis, in the symmetry planes: **a** *x*-, *y*-, and *z*-cuts; and **b** the diagonal cuts. In this and all following figures, the *solid lines* are the exact velocity variations, and the *dashed lines* are from the approximate Eq. (1)

Table 2. Singularities of the shear-wave slowness-sheets. The figures in brackets represent alternative but less-common configurations. The figures with asterisks represent point singularities on axes where symmetry planes intersect (Crampin and Yedlin 1980)

Symmetry system	Kiss singularities	Intersection singularities	Point singularities
Cubic	6	0	8
Hexagonal	2	2, (0)	0
Trigonal	0	0	2*+6, (2*+18), etc.
Tetragonal	2	0	8
Orthorhombic	0	0	4, (12, as in Fig. 6), etc.
Monoclinic	0	0	8, etc.

In order to make the results more easily intelligible to those unfamiliar with crystallographic notation, we specifiy, where necessary, the direction of wave propagation and orientation of planes, not in terms of Miller indices, but in terms of the direction cosines of the normal referred to the conventional Cartesian coordinate system of the elastic tensor. Thus, the plane specified, within double parentheses, as the ((*a, b, c*))-cut is the plane normal to the line with direction cosines proportional to *a, b,* and *c.*

The velocity variations are drawn in rectangular rather than polar coordinates, which would have preserved the direction of propagation, because rectangular coordinates show details of the variations more clearly. The solid lines in the figures are the exact velocities calculated by the eigenvalue techniques of Crampin (1977a), and the dashed lines are the approximate velocity variations obtained by substituting the appropriate elastic constants into (1).

Cubic

The velocity variations in the two types of symmetry plane of cubic silicon, shown in Fig. 2, are typical of cubic structures. The velocity variations in the symmetry planes are very simple and the approximations (1) are very close. The simplicity is deceptive. The shear-wave slowness-sheets have more singularities than most other symmetry-systems (Table 2: there are six kisses, two on each of the principal axes, and eight point singularities, one in each solid quadrant at the intersection of the three diagonal symmetry-planes. The shear-wave approximate equations (1) are not good for off-symmetry directions, when there are so many point singularities. The equations for *P*-waves are also not good approximations in many off-symmetry directions: the ((1, 1, 1))-cut has small 6θ variations which clearly cannot be modelled by the 2θ and 4θ variations of (1).

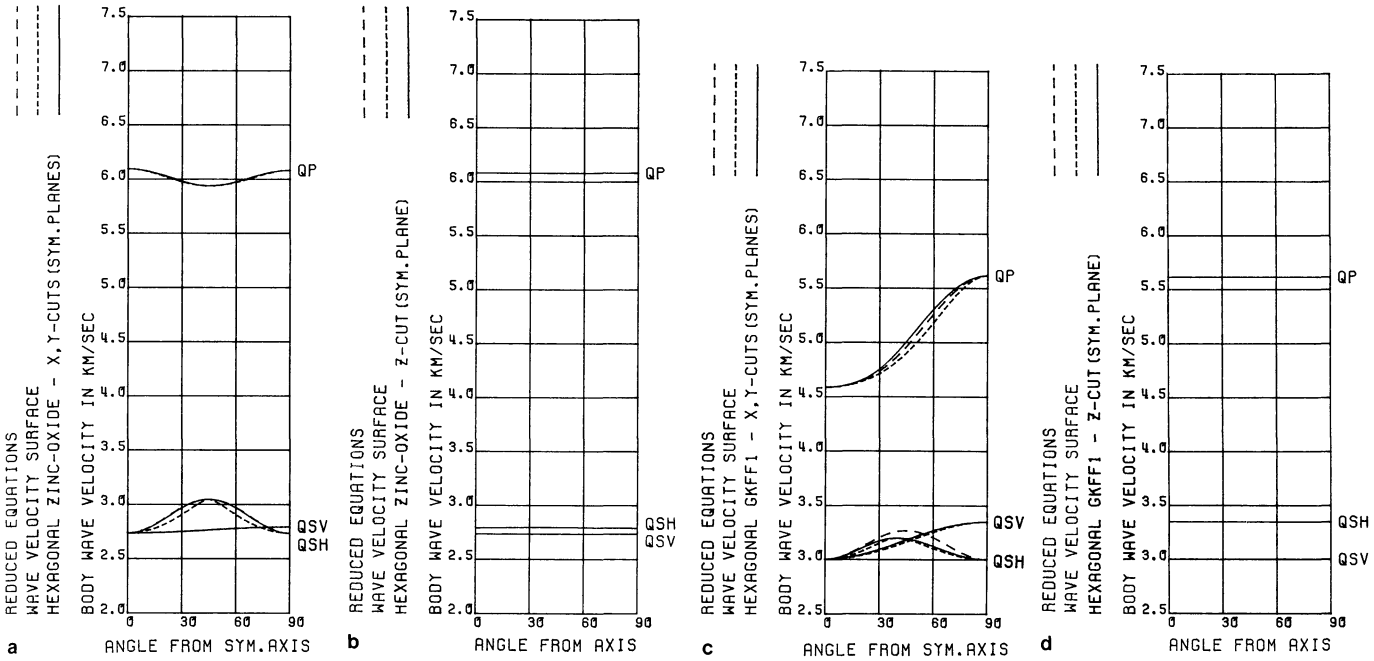

Fig. 3a–d. *Hexagonal symmetry.* Comparison of approximate velocities, with phase and wave velocities of zinc oxide (Bateman 1962), in the symmetry planes: **a** through the axis of symmetry; and **b** perpendicular to the axis of symmetry. Velocity variations of a structure GKFF1 with small dry parallel-cracks (Crampin 1978), in the symmetry planes: **c** through the axis of symmetry (the normal to the cracks); and **d** perpendicular to the axis of symmetry. The *fine-dashed lines* are sections of the wave velocity-surface calculated by Postma's (1955) equations

Hexagonal

Figure 3 shows the velocity variations in crystalline zinc-oxide, where the *P*-wave variation has a largely 4θ variation, and in dry parallel cracks (GKFF1, Crampin 1978), where the *P*-wave has a largely 2θ variation. Most hexagonal structures have shear-wave slowness-sheets intersecting as they do in both structures in Fig. 3. However, this is not always the case; randomly oriented cracks with co-planar normals may have shear-wave slowness-sheets with only two kiss singularities.

The reduced equations are good approximations to the phase-velocities, and the variations of qP and qSV in any plane through the axis determine all five elastic constants. Figure 3 also compares the wave-and velocity-surfaces. As discussed previously, there is very little difference between the two velocities for these comparatively weak anisotropies.

Earth structures in which the velocities of body-waves are invarient in horizontal directions are called transversely isotropic by seismologists. Structures with hexagonal symmetry are transversely isotropic perpendicular to the symmetry axis, and the term "transverse isotropy" is sometimes used as if it were synonymous with hexagonal symmetry. Strictly speaking, however, transverse isotropic refers only to cylindrical symmetry, and structures will possess hexagonal symmetry only if the average properties are constant over depth intervals greater than a seismic wavelength. Postma (1955) and Backus (1962) present techniques for deriving the hexagonal elastic constants of structures made up of regular laminations of thin isotropic beds.

Trigonal

Apart from the constraints on the 4θ variations of qP and qSH in the symmetry planes, wide variations of sign and amplitude are possible for different trigonal structures.

The approximate Eq. (1) model the velocity variations of alpha-quartz reasonably well in the symmetry planes (Fig. 4a), although they cannot model the rapid changes in direction of qP and qSH at some 75° from the z axis. The y- and z-cuts are not planes of symmetry, and the shear-waves display pinches due to the proximity of point intersections on the planes of symmetry. Consequently, the shear-wave Eq. (1) are poor approximations in these and other off-symmetry planes. The z-cut demonstrates the lack of generality of the Backus (1965) *P*-wave approximations.

Tetragonal

The approximate Eq. (1) follow the main trends of the velocity variations in the three types of symmetry plane of tetragonal rutile (Fig. 5) but are not particularly close estimates, because rutile has large velocity-anisotropy (50% for qSH wave in the z-cut) with a marked 8θ contribution. Apart from the constraints on the 4θ variations, the signs and amplitudes of the variations may vary widely between different tetragonal structures. The shear-wave equations are often poor approximations in the off-symmetry directions due to the proximity of point singularities.

Orthorhombic

A comparison of the approximate velocities and the phase-velocities in the three symmetry planes of orthopyroxene-bronzite are shown in Fig. 6. Except for the constraints on the 4θ variations of qP and qSH, all combinations of sign and amplitude variation are possible for structures with orthorhombic symmetry. The reduced equations are good approximations in all three symmetry planes. A variety of possible configurations of shear-wave singular-

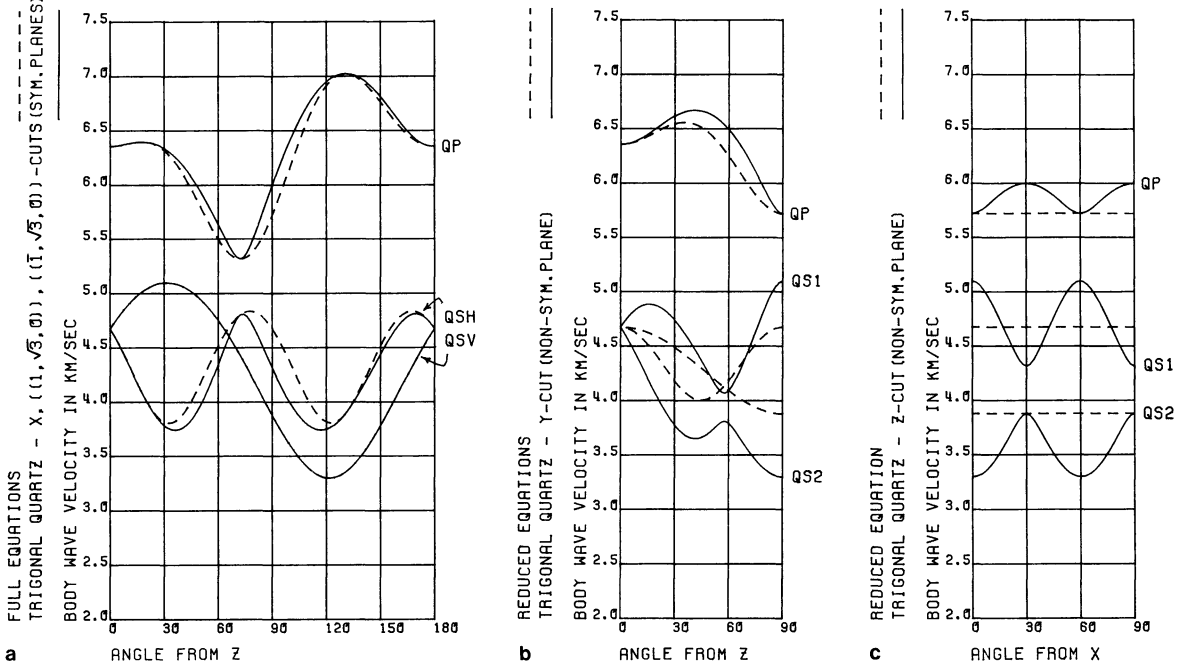

Fig. 4a–c. *Trigonal symmetry.* Comparison of approximate velocities with phase velocities of alpha-quartz (Bechman 1958), in the planes: **a** *x*-, ((1, $\sqrt{3}$,0))-, and ((1̄, $\sqrt{3}$,0))-cut symmetry planes; **b** *y*-cut, not a symmetry plane; and **c** *z*-cut, not a symmetry plane

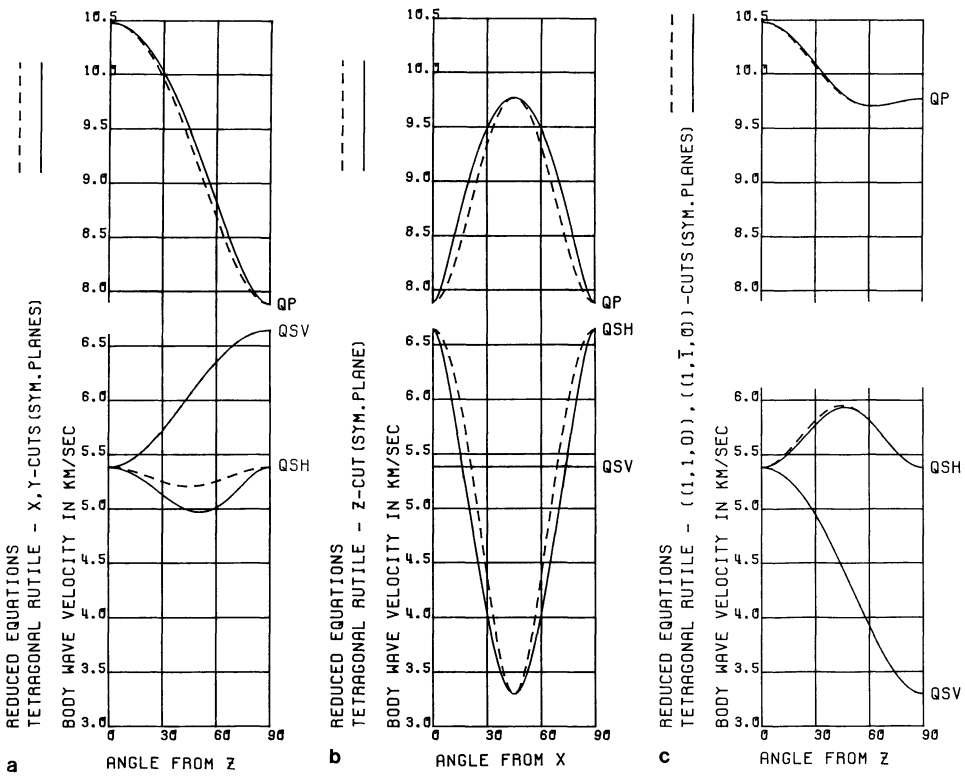

Fig. 5a–c. *Tetragonal symmetry.* Comparison of approximate velocities with phase velocities of rutile (National Lead 1967), in the symmetry planes: **a** *x*-, and *y*-cuts; **b** *z*-cut; and **c** ((1, 1, 0))-, and ((1, 1̄, 0))-cuts

ities in other orthorhombic materials make the equations poor approximations in many off-symmetry planes.

Olivine and many of the possible upper-mantle pyroxenes take orthorhombic symmetry with comparatively minor differences of sign and amplitude of the velocity variations. We note here that the sign of the 4θ variation of the *P*-wave in *z*-cut olivine is positive (Crampin 1976), whereas the corresponding sign in orthopyroxene is negative in Fig. 6c. Crampin and Bamford (1977) suggested that the sign and amplitude of the 4θ variations in observed *qP* velocity-anisotropy may be important as a structural discriminant. Crampin and Bamford could fit observed oceanic velocity-anisotropy very well with mixtures of olivine and isotropic media, whereas the velocity-anisotropy beneath the continental Rhinegraben displayed negative 4θ variations, and could not be directly fitted by olivine mixtures. It is possible that the negative sign of the observed velocity-anisotropy may be due to a higher pyrox-

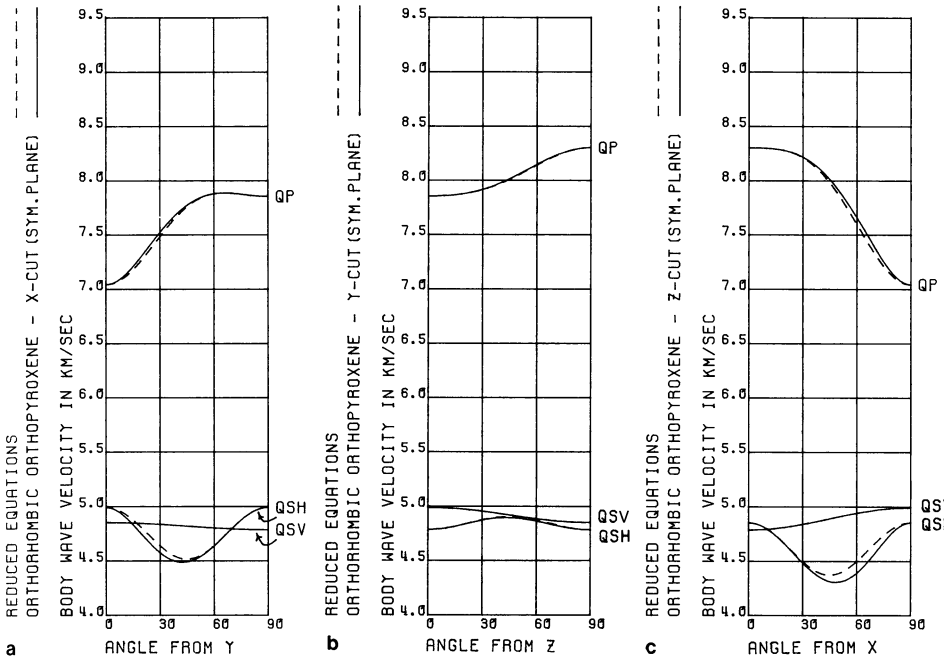

Fig. 6a–c. *Orthorhombic symmetry.* Comparison of approximate velicities with phase velocities of orthopyroxene–bronzite (Kumazawa 1969), in the symmetry planes: **a** *x*-cut; **b** *y*-cut; and **c** *z*-cut

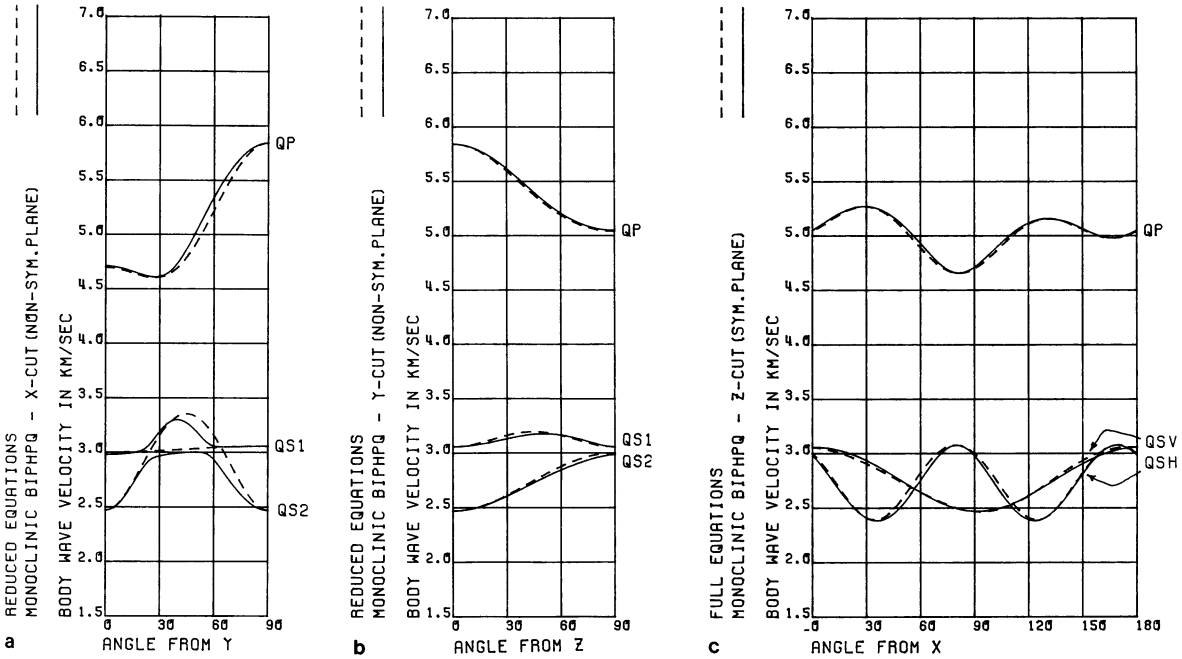

Fig. 7a–c. *Monoclinic symmetry.* Comparison of approximate velocities with phase velocities of BIPHQP, a structure with a biplanar system of cracks (Crampin et al. 1980), in the planes: **a** *x*-cut, not a symmetry plane; **b** *y*-cut, not a symmetry plane; and **c** *z*-cut symmetry plane

ene content in the upper-mantle beneath continents, although, as the velocities of pyroxene are generally lower than the usual sub-Moho velocities, the pyroxene would have to be mixed with higher-velocity isotropic media to produce typical upper-mantle velocities.

Monoclinic

The approximate velocities and phase-velocities for the monoclinic structure BIPHPQ observed by Crampin et al. (1980) are shown in Figure 7. The shear-waves in off-symmetry planes do not in general have polarizations parallel or perpendicular to the planes, however, by chance, the shear wave polarizations in the *y*-cut for this particular system are nearly parallel and perpendicular to the plane. Except for the constraints on the 4θ variations of *qP* and *qSH* in the symmetry plane, there are wide variations of velocity and shear-wave singularity configurations possible in monoclinic structures. The approximate equations are very good approximations in the symmetry plane (*z*-cut) and the *y*-cut in Fig. 7, but not in the *x*-cut, which demonstrates shear-wave pinching: the *qS1* wave has nearly *SV* polarization, except between the pinches at 20° and 60°, where the polarization is nearly *SH*; similarly, *qS2* has *SH* motion except for *SV* polarization between 20° and 60°.

BIPHPQ is derived from an observed *P*-wave velocity an-

isotropy in Carboniferous limestone (Bamford and Nunn 1979) due to a biplanar system of joints and fractures. The assumption of cracks enables the *P*-wave anisotropy to be inverted to give the full parameters of the cracks and the equivalent anisotropic structure BIPHQP (Crampin et al. 1980).

Conclusions

The velocities in Figs. 2–7 display wide variations in amplitude and phase for different symmetry-systems. Wide variations are possible for different materials within the same symmetry-system, particularly in the behaviour of shear-waves for variations in off-symmetry planes, where the two shear-waves may pinch together and exchange polarization characteristics due to the proximity of singularities in nearby planes.

The approximate expressions of Backus (1965) for *P*-waves, and Crampin (1977a) for shear-waves, are good estimates for the velocity variations in symmetry planes, and provide a direct link between velocities and constants in these planes. In off-symmetry planes, the approximate equations may be very poor estimates of both *P* and shear-wave velocities. However, despite these limitations to the use of approximate equations, they are very valuable in practice for transforming from velocities to constants (Crampin 1978; Crampin and Bamford 1977; Crampin et al. 1980). Systems of symmetry have a number of symmetry planes (Table 1), and the equations may be used by judicious choice of origin and plane of variation.

It is interesting to note that it is difficult to place the systems of anisotropic symmetry in any sequential order. It seems that any particular parameter used for ordering – number of elastic constants, number of planes of symmetry, number of shear-wave singularities – leads to a different order. Each symmetry system is unique and has unique features.

Anisotropic velocity variations take a number of significantly different forms, which are difficult to classify in any simple way. The percentage of velocity variation $((V_{max}-V_{min})/V_{max})$, usually of the *P*-wave, in any given plane is sometimes called the coefficient of anisotropy. It is clearly a very uninformative description: it contains no information about the symmetry, the velocities of the other body-waves in the given plane, or the velocities of any waves in other planes, and we suggest it is not used in future.

Acknowledgements. We are grateful to Russ Evans for his comments on the manuscript. The work of S.C. was supported by the Natural Environment Research Council, and is published with the approval of the Director of the Institute of Geological Sciences.

References

Auld, B.A.: Acoustic fields and waves in solids. New York: John Wiley and Sons Inc. 1973

Avé Lallemant, H.G., Carter, N.L.: Syntectonic recrystallization of olivine and modes of flow in the upper mantle. Geol. Soc. Am. Bull. **81**, 2203–2220, 1970

Backus, G.E.: Long-wave elastic anisotropy produced by horizontal layering. J. Geophys. Res. **67**, 4427–4440, 1962

Backus, G.E.: Possible forms of seismic anisotropy in the uppermost mantle under oceans. J. Geophys. Res. **70**, 3429–3439, 1965

Backus, G.: A geometrical picture of anisotropic elastic tensors. Rev. Geophys. Space Phys. **8**, 633–671, 1970

Bamford, D.: Pn velocity anisotropy in a continental upper mantle. Geophys. J.R. Astron. Soc. **49**, 29–48, 1977

Bamford, D., Jentsch, M., Prodehl, C.: Pn anisotropy studies in Northern Britain, and the Eastern and Western United States. Geophys. J.R. Astron. Soc. **57**, 397–429, 1979

Bamford, D., Nunn, K.R.: In situ seismic measurements of crack anisotropy in the Carboniferous limestone of Northwest England. Geophys. Prospect. **27**, 322–338, 1979

Bateman, T.B.: Elastic moduli of single-crystal zinc oxide. J. Appl. Phys. **33**, 3309–3312, 1962

Bechman, R.: Elastic and piezoelectric constants of alpha-quartz. Phys. Rev. **110**, 1060–1061, 1958

Crampin, S.: A comment on 'The early structural evolution and anisotropy of the oceanic upper-mantle' Geophys. J. Astron. Soc. **46**, 193–197, 1976

Crampin, S.: A review of the effects of anisotropic layering on the propagation of seismic waves. Geophys. J.R. Astron. Soc. **49**, 9–27, 1977a

Crampin, S.: Palaeoanisotropy in the upper mantle. Nature **270**, 162–163, 1977b

Crampin, S.: Seismic-wave propagation through a cracked solid: polarization as a possible dilatancy diagnostic. Geophys. J.R. Astron. Soc. **53**, 467–496, 1978

Crampin, S., Bamford, D.: Inversion of *P*-wave velocity anisotropy. Geophys. J.R. Astron. Soc. **49**, 123–132, 1977

Crampin, S., King, D.W.: Evidence for anisotropy in the upper-mantle beneath Eurasia from the polarization of higher-mode seismic surface-waves. Geophys. J.R. Astron. Soc. **49**, 59–85, 1977

Crampin, S., McGonigle, R., Bamford, D.: Estimating crack parameters from observations of *P*-wave velocity-anisotropy. Geophysics **45**, 345–360, 1980

Crampin, S., Yedlin, M.: Shear-wave singularities in wave propagation in anisotropic media. J. Geophys. **49**, 43–46 1981

Forsyth, D.W. The early structural evolution and anisotropy of the oceanic upper-mantle. Geophys. J.R. Astron. Soc. **43**, 103–162, 1975

Francis, T.J.G.: Generation of seismic anisotropy in the upper mantle along the mid-oceanic ridges. Nature **221**, 162–165, 1969

Hess, H.: Seismic anisotropy of the uppermost mantle under oceans. Nature **203**, 629–631, 1964

Kaarsberg, E.A.: Elasticity studies of isotropic and anisotropic rock samples. Trans. Soc. Min. Eng. **241**, 470–475, 1968

Kirkwood, S.C.: The significance of isotropic inversion of anisotropic surface-wave dispersion. Geophys. J.R. Astron. Soc. **55**, 131–142, 1978

Kirkwood, S.C., Crampin, S.: Surface-wave propagation in an ocean basin with an anisotropic upper-mantle: numerical modelling. Geophys. J.R. Astron. Soc. in press 1980a

Kirkwood, S.C., Crampin, S.: Surface-wave propagation in an ocean basin with an anisotropic upper mantle: observations of polarization anomalies. Geophys. J.R. Astron. Soc in press 1980b

Kumazawa, M.: The elastic constants of single-crystal orthopyroxene. J. Geophys. Res. **74**, 5973–5980, 1969

Levin, F.K.: The reflection, refraction, and diffraction of waves in media with an elliptical velocity dependence. Geophysics **43**, 528–537, 1978

McSkimin, H.J.: Measurement of elastic constants at low temperature by means of ultrasonic waves – data for silicon and germanium single crystals, and for fused silica. J. Appl. Phys. **24**, 988–997, 1953

Musgrave, J.J.P.: Crystal acoustic. San Francisco: Holden-Day 1970

National Lead Company: Physical Properties of Stoichiometric Rutile (TiO_2), Titanium Div. Res. Lab., South Amboy, New Jersey, 1967

Nye, J.F.: Physical properties of crystals. London: Oxford University Press 1957

Postma, G.W.: Wave propagation in a stratified medium. Geophysics **20**, 780–806, 1955

Raitt, R.W., Shor, G.G., Francis, T.J.G., Morris, G.B.: Anisotropy of the Pacific upper-mantle. J. Geophys. Res. **74**, 3095–3109, 1969

Synge, J.L.: Elastic waves in anisotropic media. J. Math. Phys. **35**, 323–334, 1957

Received June 18, 1979; Revised Version July 25, 1980
Accepted August 8, 1980

J. Geophys. 49, 43–46 (1981)

Journal of Geophysics

Shear-Wave Singularities of Wave Propagation in Anisotropic Media

S. Crampin [1], and M. Yedlin [2]

[1] Institute of Geological Sciences, Murchison House, West Mains Road, Edinburgh EH9–3LA, Scotland
[2] Department of Physics, University of Alberta, Edmonton, Canada

Abstract. Shear-wave singularities in systems of anisotropic symmetry are comparatively well known, but it has not been generally realised that they may cause anomalies in shear-wave propagation for neighbouring directions due to the behaviour of the polarizations. Singularities are places where the two shear-wave slowness-surfaces are continuous with each other through common points. The most frequent type, a point singularity, is a place where the two surfaces are continuous with each other through the vertices of cone-shaped projections from the surfaces. For directions of propagation in a plane, which cuts the slowness surfaces near a singularity, the velocities of the two shear-waves approach each other in a pinch and at the pinch exchange polarizations and velocity gradients. These singularities do not cause anomalies in plane waves propagating in a uniform medium, but may cause mode conversion and pulse-shape modification to waves with spherical wave-fronts, and to rays of shear-waves, in varying anisotropic media.

Key words: Shear-wave singularities – Point-, kiss-, and intersection-singularities – Pinches – Anisotropic shear-waves – Shear-wave polarizations.

Introduction

There are three orthogonally-polarized body-waves propagating in every direction in anisotropic elastic solids (Crampin 1977); a quasi *P*-wave, *qP*, and two quasi shear-waves, *qS1* and *qS2*, or *qSH* and *qSV* if appropriate. The velocities of these waves vary with the direction, and are roots of an equation, which can either be written as a third-order polynomial in V^2 (Synge 1957), or a third-order eigen-value problem in V^2 (Crampin 1977).

The three body-waves in each direction are generally distinct and their velocities vary independently with direction. However, the two shear-wave slowness-surfaces are analytically continuous, which, in some directions, may introduce complications into the shear-wave propagation. The easiest way to observe this continuity is to trace the intersections of the shear-wave slowness-sheets with the three orthogonal symmetry-planes round an orthogonal corner of an orthorhombic material. It can be demonstrated that polarizations of the two shear waves, propagating parallel to a symmetry plane, are parallel and perpendicular, respectively, to the symmetry plane (Crampin and Kirkwood 1980, henceforth called Paper 1). Hence, following the polarizations of one of the slowness sheets, the inner sheet say, round the orthogonal corner, the symmetry-plane polarizations indicate that the intersections must cross each other an odd number of times. The shear waves of orthorhombic orthopyroxene (Fig. 6, Paper 1), for example, cross three times, so that on completion of the corner we are now on the outer sheet. The places where the waves cross are singularities of the shear-wave surfaces.

Singularities in shear-wave slowness-sheets have been recognised for many years (Duff 1960). Indeed, singularities of various kinds are very common for shear waves in anisotropic media. Symmetry considerations indicate that the two shear-wave slowness-sheets of orthopyroxene have 12 singularities as just described, and the two sheets of a cubic solid, which one might have thought was a comparatively simple structure, have 14 singularities of various kinds (Paper 1). What has not been recognised, however, is the behaviour of shear-wave polarizations near such singularities and the disturbance this may cause to propagating shear-waves in neighbouring directions. This paper investigates the properties of singularities and the behaviour of shear waves at the various types of singularity. It is meant to be read in parallel with Paper 1, which lists the singularities and other properties of the various systems of anisotropic symmetry.

It is appropriate to publish this work in the geophysical literature, because anisotropy may be important for mapping structures in the crust (Crampin et al. 1980b). In particular, investigating shear-wave polarization-anomalies appears to be an important technique for estimating upper-mantle anisotropy (Crampin 1977; Ando et al. 1980), and for monitoring the progress of earthquake dilatancy (Crampin 1978; Crampin et al. 1980a).

Types of Singularity and Their Effect on Shear-Wave Polarization

Duff (1960) demonstrated that the inner, *qP*, slowness sheet is convex and wholely interior to the shear-wave slowness-sheets. The two shear-wave sheets, however, come into contact at least twice in anisotropic symmetry systems, and usually much more frequently (Paper 1). The directions where the sheets are in contact are singularities of the shear-wave propagation. In these directions, the shear waves have coincident phase-velocities, possible group-velocities form a cone about the phase-velocity direction, and polarizations are any two vectors mapping out the plane perpendicular to the *qP* polarization.

There are three main types of singularity. The first two types, point- and kiss-singularities, mark discontinuities in the shear-wave polarizations, where the polarizations on both sheets vary rapidly with direction about the singularity. These singularities

0340-062X/81/0049/0043/$01.00

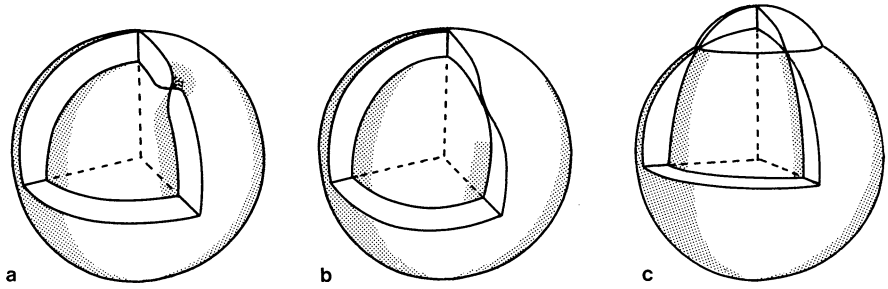

Fig. 1a–c. Diagrams of the two shear-wave slowness-surfaces showing the topology near the various types of singularity:
a Point singularity,
b kiss singularity (class i), and
c intersection singularity

may cause complications to shear-wave propagation in neighbouring directions. The third type, an intersection singularity, is a formal singularity only, and causes no particular complication in shear-wave propagation.

Point Singularities

The velocity variations in the symmetry planes of the various anisotropic symmetry systems frequently show the two shear-waves crossing each other (Paper 1). In hexagonal symmetry systems, the crossing marks the simple intersection of the two shear-wave slowness-sheets (see below). In all other symmetry systems, the crossing marks a *point singularity*, where the two slowness-sheets are continuous through the vertices of cone-shaped projections from the surfaces. The topological configuration is shown in Fig. 1 a.

Point singularities are observed to lie in at least one symmetry plane. The velocity variations of each of the two orthogonally-polarized shear-waves in such symmetry planes behave no differently in the direction of the singularity from other directions in the plane. In particular, the polarizations of the two shear-waves, parallel and perpendicular, respectively, to the symmetry plane, appear continuous across the singularity. However, in neighbouring planes, which-pass near but avoid the singularity, the velocity variations of the shear waves approach each other in a *pinch*, and at the pinch, the waves on the inner and outer slowness-sheets exchange polarizations, and velocity gradients. Figure 2a shows the behaviour of the shear-wave velocities and polarizations in one of the diagonal symmetry-planes of cubic silicon (see also Fig. 2, Paper 1), and in some neighbouring planes. The pinches may be extremely sharp for variations in planes passing very near to point singularities, and the exchange of polarizations take place within a very narrow range of directions.

Similar exchanges occur between modes in Generalized surface-wave propagation in anisotropic layered media. The polarizations and gradients of the velocity variations may be exchanged as the dispersion curves of the two modes approach each other in a pinch (Crampin and Taylor 1971). This happens in layered anisotropic structures, where the dispersion curves of Rayleigh and Love modes cross each other in equivalent isotropic structures.

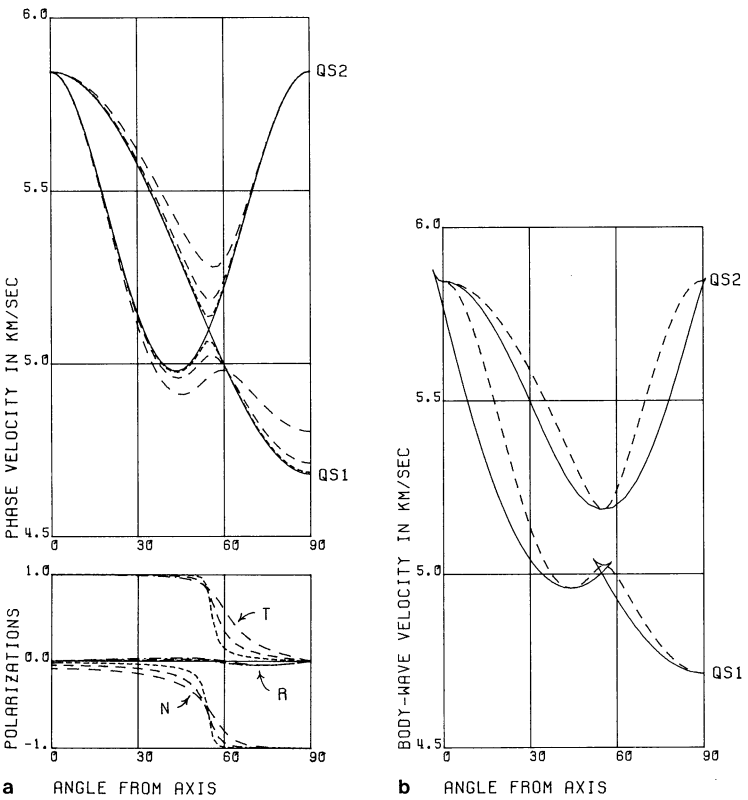

Fig. 2a and b. Variations in cubic silicon near a point singularity in a diagonal symmetry plane (see Paper 1).
a *Upper figure*: Phase-velocity variations: *solid line* – diagonal symmetry plane, showing a point singularity; *dotted line* – plane 2° off symmetry-plane, showing tight pinch; *dashed line* – plane 5° off symmetry-plane, showing pinch; and *broad dash* – plane 10° off symmetry-plane. *Lower figure:* Direction cosines of the polarization of the slower shear-wave in the off-symmetry planes, relative to normal (N), radial (R), and transverse (T) directions to the plane of the phase-velocity variations.
b Phase and group velocity in the plane 5° off symmetry-plane: *dashed line* – phase velocity, as dashed line in (**a**) above; and *solid line* – group velocity showing cups.
Note: the *solid line* is the projection of the non-planar group-velocity on the plane of the phase-velocity variation

The physical effects of a point singularity on wave propagation will depend on the behaviour of the group or wave velocity, rather than the phase velocity. Since both the gradient and the velocity are exchanged at a pinch, the group velocity will also be exchanged. Pinches will have no effect on plane waves propagating in uniform structures, but may have large effects on spherical wavefronts and rays of shear waves through varying anisotropic structures. As the direction of propagation of a ray sweeps through a pinch, energy will tend to jump to the body wave which continues with the same polarization, and there will be an increase or decrease of velocity.

The exact effects of this phenomenon will very much depend on the particular configuration of the pinch and the speed that the ray sweeps the pinch. In some configurations, the behaviour may be similar to that illustrated in Fig. 14b of Crampin (1978), where the energy of a shear wave with one polarization is largely transferred (by mode conversion), to the shear wave with the orthogonal polarization, on propagating through a homogeneous anisotropic medium. In other circumstances, the pulse shape of shear waves will be broadened as continuous constructive and destructive interference takes place. This type of behaviour at pinches may lead to modification and attenuation of the primary shear-wave pulse.

The rapid variation of the phase velocity near a pinch may introduce cusps into the group-velocity surface (usually called the wave surface). Figure 2b shows a section of the wave surface for one of the phase-velocity variations in Fig. 2a. Strictly, the group velocity associated with the planar phase-velocity variation is not co-planar, but the deviations are usually small, as in this case, and we show the projection on the phase-velocity plane. In Fig. 2b there are cusps on the slower shear-wave sheet (*qS1*) at the pinch and at the axis, and on the faster sheet (*qS2*) at 90° from the axis. The behaviour at cusps, caused both by overall velocity variations and by variations at pinches, produces rapid variations in the ray. The direction of a ray through a varying structure depends on two phenomena. The behaviour of the phase velocity is determined by applying Snell's Law to the phase-velocity directions, and the relationship of the ray direction to the phase direction is determined by the anisotropic structure of the media. Since a cusp is a place where there are rapid changes in group-velocity direction for slower variations in phase-velocity, a cusp can produce rapid changes in the direction of a ray.

It is interesting to note that Fig. 2b provides an example of the sensitivity of cusps to the curvature of the phase-velocity sheets (strictly, the curvature at inflexions in the phase-slowness sheets). In order of increasing curvature, there is no cusp on the *qS2* sheet at the axis (0°), a small cusp at 90°, and a distinct cusp on the *qS1* sheet at 0°.

Kiss Singularities

A *kiss singularity* is a point where the two shear-wave slowness-surfaces touch tangentially, with any combination of convex or concave curvature, but do not intersect. Three classes of kiss can be distinguished:

(i) Figure 1b illustrates the simplest topological configuration of a kiss: the place where the two slowness-sheets of a hexagonal medium touch in the direction of the symmetry axis (Paper 1). The polarizations of the shear waves on these two slowness-sheets are parallel and perpendicular, respectively, to planes through the symmetry axis. The polarizations have cylindrical symmetry about the symmetry axis.

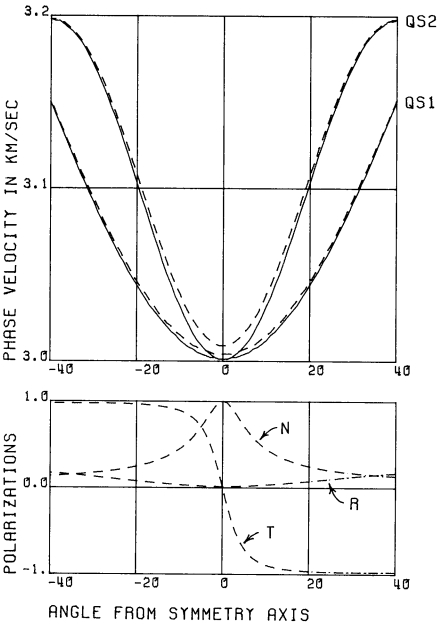

Fig. 3. Variations in hexagonal GKFF1 (Paper 1) near a kiss singularity. *Upper figure:* Phase-velocity variations. *Solid line* – variations in a plane through the symmetry axis showing a kiss singularity; and *dashed line* – variations in a plane 5° off symmetry-axis, showing a broad pinch. *Lower figure:* Direction cosines of the polarization of the faster shear-wave in the off-symmetry plane. Notation as in Fig. 2a

(ii) Kiss singularities may also occur in directions parallel to the axis of intersection of several symmetry-planes, as in cubic and tetragonal symmetry systems (Paper 1). Figure 2a shows the behaviour at this class of kiss, where the shear waves meet the axis. The polarizations do not have cylindrical symmetry, but do have reflection symmetry in the axis.

(iii) Kiss singularities may also occur in non-symmetry directions in symmetry planes, as at about 55° from the z-axis in y-cut orthorhombic orthopyroxene (Fig. 6b, Paper 1). Note that kisses of this class are not, in any sense, centres of symmetry.

Similarly to the behaviour of velocity variations near point singularities, velocity variations in planes which pass near, but not through, the first two types of kiss singularity (i and ii, above) approach each other in a broad pinch. Near this pinch the polarizations show rapid but temporary deviations. Figure 3 shows the velocities and polarizations near a kiss singularity in the hexagonal medium GKFF1 (Paper 1). Both these types of kiss singularity may cause disturbances to shear-wave propagation, as discussed in the preceding section. The third type of kiss (iii) is believed to cause no disturbance to wave propagation.

Intersection Singularities

Intersection singularities are the intersection of two shear-wave slowness-surfaces in the usual sense of two surfaces intersecting. Such singularities only occur in hexagonal symmetry-systems, where the two sheets may intersect in a circle about the symmetry axis. Figure 1c shows the topology of such an intersection. The polarizations of the shear waves on the two sheets are parallel and perpendicular to planes through the symmetry axis. There are no disturbances to wave propagation.

The two shear-wave slowness sheets, in anisotropic systems with symmetry very close to hexagonal, may separate at the position of the hexagonal intersection, and the two sheets pinch together in a nearly circular ring. The polarizations and velocity gradients of the two shear-wave sheets are interchanged at the *ring pinch,* and the phenomenon may cause disturbances to shear-wave propagation.

Discussion

Shear-wave singularities are very common in anisotropic symmetry-systems (Paper 1). Plane waves will not be disturbed by the proximity of a singularity even when propagating directly at the singularity. However, spherical wavefronts or rays of shear waves may be considerably disturbed, when the direction of propagation passes near to a point singularity or near to the first two classes of kiss singularity. Depending on the particular wave-path geometry, the wave form may be modified and attenuated by mode conversion, and constructive and destructive interference caused by cusps in the group-velocity variations and by rapid changes in the fixed polarizations.

Acknowledgements. The work of S.C. was supported by the Natural Environment Research Council, and is published with the approval of the Director of the Institute of Geological Sciences.

References

Ando, M., Ishikawa, Y., Wada, H.: *S*-wave anisotropy in the upper mantle under a volcanic arc. Nature **286**, 43–46, 1980

Crampin, S.: A review of the effects of anisotropic layering on the propagation of seismic waves. Geophys. J. R. Astron. Soc. **49**, 9–27, 1977

Crampin, S.: Seismic-wave propagation through a cracked solid: polarization as a possible dilatancy diagnostic. Geophys. J. R. Astron. Soc. **53**, 467–496, 1978

Crampin, S., Evans, J.R., Üçer, B., Doyle, M., Davis, J.P., Yegorkina, G.V., Miller, A.: Observations of dilatancy-induced polarization-anomalies and earthquake prediction. Nature **286**, 874–877 1980a

Crampin, S., Kirkwood, S.C.: Velocity variations in systems of anisotropic symmetry. J. Geophys. **49**, 35–42, 1981

Crampin, S., McGonigle, R., Bamford, D.: Estimating crack parameters from observations of *P*-wave velocity-anisotropy. Geophysics **45**, 345–360, 1980b

Crampin, S., Taylor, D.B.: The propagation of surface waves in anisotropic media. Geophys. J. R. Astron. Soc. **25**, 71–87, 1971

Duff, G.F.D.: The Cauchy problem for elastic waves in an anisotropic medium. Philos. Trans. R. Soc. Ser. A: **252**, 249–273, 1960

Synge, J.L.: Elastic waves in anisotropic media. J. Math. Phys. **35**, 323–334, 1957

Received March 26, 1980; Revised Version July 25, 1980
Accepted August 8, 1980

J. Geophys. 49, 47–56 (1981)

Journal of Geophysics

Temperature Derivatives of Compressional and Shear Wave Velocities in Crustal and Mantle Rocks at 6 kbar Confining Pressure

H. Kern and A. Richter

Mineralogisch-Petrographisches Institut der Universität Kiel, Olshausenstr. 40–60, D-2300 Kiel, Federal Republic of Germany

Abstract. Measurements of compressional and shear wave velocities, V_P and V_S, were made in a cubic anvil apparatus up to 700° C at 6 kbar in igneous and metamorphic rocks typical of the crust and mantle. Samples range in composition from acidic to ultramafic, with bulk density of 2.67–3.46 g/cm^3 at 6 kbar. Mean atomic weights of the rocks vary between 20.37 and 23.03. A rough dependence of wave velocity on bulk density is apparent. However, there is considerable scatter, and the velocities do not generally follow lines of constant mean atomic weight. Both V_P and V_S increase with increasing amphibole, garnet, pyroxene and olivine content. High quartz content produces relatively low *P*-wave and high *S*-wave velocities, giving significantly low Poisson's ratios. In contrast, a high feldspar content is related to relatively high *P*-wave and low *S*-wave velocities and consequent high Poisson's ratios. The calculated temperature derivatives of V_P and V_S for the range 20–500° C at 6 kbar confining pressure, using best-fit solutions, cover the range -1.60 to -4.94×10^{-4} km/s° C and -1.39 to -3.93×10^{-4} km/s° C, respectively. The results compare fairly well with the few data published so far. For the dunite and peridotite rocks the $(dV_P/dT)_p$-values are in excellent agreement with published Voigt-Reuss-Hill values calculated from single crystal data.

Using the experimental results, *P*-velocity profiles were calculated along a geotherm of a cold Precambrian shield crust and a warm continental crust. The temperature gradients for the latter cause velocity inversion in numerous rocks, rich in olivine or quartz.

Key words: High-temperature wave-velocities – Rock-sample wave-velocities – Velocity anisotropy.

Introduction

In recent years rapid progress has been made in the experimental determination of temperature derivatives of elastic wave velocities for natural rocks at pressures between 1 and 10 kbar and temperatures up to 750° C (Fielitz 1971; Kern and Fakhimi 1975; Stewart and Peselnick 1977, 1978; Ramananatoandro and Manghnani 1978; Christensen 1979; Kern 1978, 1979; Kern and Richter 1979). However, compared with the wealth of data about the pressure dependence of ultrasonic waves in rocks (Birch 1960, 1961; Simmons 1964; Christensen 1965, 1966, 1974), the literature about the influence of temperature at high confining pressure is scarce. There is a need for further investigations of the temperature dependence of compressional and shear wave velocities in crustal and mantle rocks. Elastic wave propagation through dry natural crystalline rocks are known to be sensitive to the state of microcracking of the material, in addition to its mineralogical composition. Therefore, only those measurements obtained at high confining pressure are valid for study of the influence of temperature.

We report here measurements compressional and shear wave velocities and the elastic constants of magmatic and metamorphic rocks typical of the crust and mantle. The metamorphic rocks chosen are representative of amphibolite and granulite facies conditions. The measurements were carried out at up to 700° C under a hydrostatic pressure of 6 kbar. Special attention is drawn to the relationship between mean velocities and the major mineral composition of the rocks.

Rock Samples

Fifteen samples which show a wide range of mineralogical and chemical composition (acidic to ultramafic) were selected for this study. Most of the metamorphic rocks were recovered from the metamorphic basement of Norwegian and Finnish Lappland. Sample number and locality, along with modal analyses are given in Table 1, where the samples are arranged in order of increasing density. Bulk densities were calculated using the weights and dimensions of the sample cubes. Chemical analyses of major oxides and the resultant mean atomic weights are presented in Table 2.

Experimental Technique

The seismic velocities have been measured by the ultrasonic transmission method in a cubic anvil apparatus designed for velocity measurements at high temperature T and high pressure p. Compressional and shear waves were generated by means of 2 MHz barium titanate transducers. Particulars of the device can be found in Kern and Fakhimi (1975).

A state of near hydrostatic stress is arrived at by advancing six pyramidal pistons in three mutually orthogonal directions onto cube shaped specimens. One end of each piston next to the specimen is surrounded by a furnace and heat is transmitted from the pistons to the specimens. Thus, a very homogenous temperature distribution is obtained within the large-volumed specimens. Temperature was measured using thermocouples placed in a cavity at the end of each piston, very close (about 1 mm) to the specimen. The temperature drop between the thermocouples and the center of the specimens is not more than 5° C at 700° C. Transducers are placed on the low temperature side of the pistons. The travel

0340-062X/81/0049/0047/$02.00

Table 1. Modal analyses (Percentages by volume)

Sample, No, locality	qu	mi	plg	or	hbl	gar	px	ep (zo)	ol	Others
Quartzite, 1452 Lam, Bayr. Wald, Germany	80	15	–	–	–	1	–	–	–	2 ctd 1 st
Bi-opx-plg-gneiss, 1400 Karasjok, Finnmark, Norway	15	3	66	–	–	–	13	–	–	2 ore 1 ap
Plg-amph-gneiss, 268 Karasjokka, Finnmark, Norway	33	–	40	–	24	1	–	–	–	1 ore 1 mi, cpx
Norite, 84 Radautal, Harz, Germany	1	1	57	–	8	–	28	–	–	5 sauss.
Px-plag-gar-gneiss, 1398 Karasjokka, Finnmark, Norway	33	–	40	–	3	16	5	–	–	2 ore
Amphibolite, 1387 S.-Alta, Finnmark, Norway	–	3	43	–	45	–	–	–	–	3 ore, 5 tit
Amphibolite, 1396 Karasjok, Finnmark, Norway	3	–	24	–	72	1	–	–	–	
Sill-gar-gneiss, 1403 Karasjok, Finnmark, Norway	24	–	6	25	–	27	–	–	–	14 sill, 1 rt
Plg-qu-amph-gneiss, 298 Karasjok, Finnmark, Norway	27	–	18	–	48	–	–	4	–	2 ore 1 tit
Ep-amphibolite, 1454 Hoher Bogen, Bayr. Wald, Germany	–	–	12	–	72	–	–	10	–	4 ser, 2 tit
Dunite, 1675 Aarheim, Norway	–	–	–	–	–	–	6	–	92	2 chl
Eclogite, 11 Münchberg, Fichtelgebirge, Germany	7	1	–	–	6	35	44	–	–	4 sympl. 2 rt
Ecoligte, 886c Saualpe, Austria	2	–	–	–	4	29	45	(10)	–	9 sympl 1 rt
Peridotite 475 Finero/Ivrea, Italy	–	–	–	–	–	–	15	–	80	3 serp 2 ore

Abbreviations: ap = apatite, bi = biotite, chl = chlorite, ctd = chloritoid, ep = epidote, gar = garnet, hbl = hornblende, mi = mica, ol = olivine, or = orthoclase, plg = plagioclase, px = pyroxene, qu = quartz, rt = rutile, sauss = saussurite, ser = sericite, serp = serpentinite, sill = sillimanite, st = staurolite, sympl = symplecitite, tit = titanite, zo = zoisite

Table 2. Major oxide analyses (wt.%) and mean atomic weights ($\bar{m}$). Analyst: P.K. Hörmann

	1452	1400	268	84	1398	1387	1396	1403	298	1454	1675	11	886
SiO_2	89.46	63.01	66.91	50.40	64.82	51.87	47.40	56.30	49.73	47.60	41.14	50.24	48.54
Al_2O_3	6.36	16.70	14.55	18.14	14.89	13.80	13.71	23.95	14.83	14.84	2.20	13.60	15.05
TiO_2	0.12	0.67	0.35	0.24	0.47	1.84	1.13	0.92	1.23	0.97	0.004	2.04	1.12
Fe_2O_3	0.92	1.87	2.32	0.56	1.84	6.19	3.00	1.13	5.31	3.70	1.10	4.72	2.65
FeO	1.21	3.37	3.96	4.64	6.18	7.17	9.43	8.55	8.45	6.07	5.34	9.05	5.82
MnO	0.026	0.079	0.120	0.129	0.182	0.139	0.201	0.088	0.237	0.021	0.088	0.249	0.145
MgO	0.08	3.15	1.93	8.69	1.95	4.19	9.35	3.90	4.78	7.83	48.03	6.46	8.82
CaO	0.02	5.34	6.12	13.06	7.06	7.45	11.10	0.72	10.77	13.82	0.09	9.67	13.67
Na_2O	0.03	3.35	3.15	1.77	2.11	4.84	2.71	0.90	2.66	2.69	0.06	3.11	3.04
K_2O	0.93	1.85	0.63	0.17	0.25	1.00	0.46	2.65	0.43	0.23	0.02	0.13	0.03
P_2O_5	0.051	0.242	0.089	0.010	0.172	0.126	0.123	0.048	0.084	0.081	0.002	0.249	0.072
H_2O^+	0.80	0.57	0.19	1.20	0.42	0.96	1.68	0.47	1.16	1.97	0.89	0.74	0.49
H_2O^-	0.07	0.14	0.08	0.39	0.10	0.06	0.08	0.13	0.08	0.15	0.11	0.11	0.07
CO_2	0.04	0.16	0.02	0.09	0.04	0.05	0.28	0.16	0.10	0.06	0.07	0.05	0.01
$\Sigma =$	100.12	100.50	100.42	99.49	100.48	99.69	100.65	99.92	99.85	100.03	99.14	100.42	99.53
$\bar{m} =$	20.37	21.55	21.65	21.67	21.97	22.63	22.88	21.94	22.90	20.26	20.78	23.03	22.37

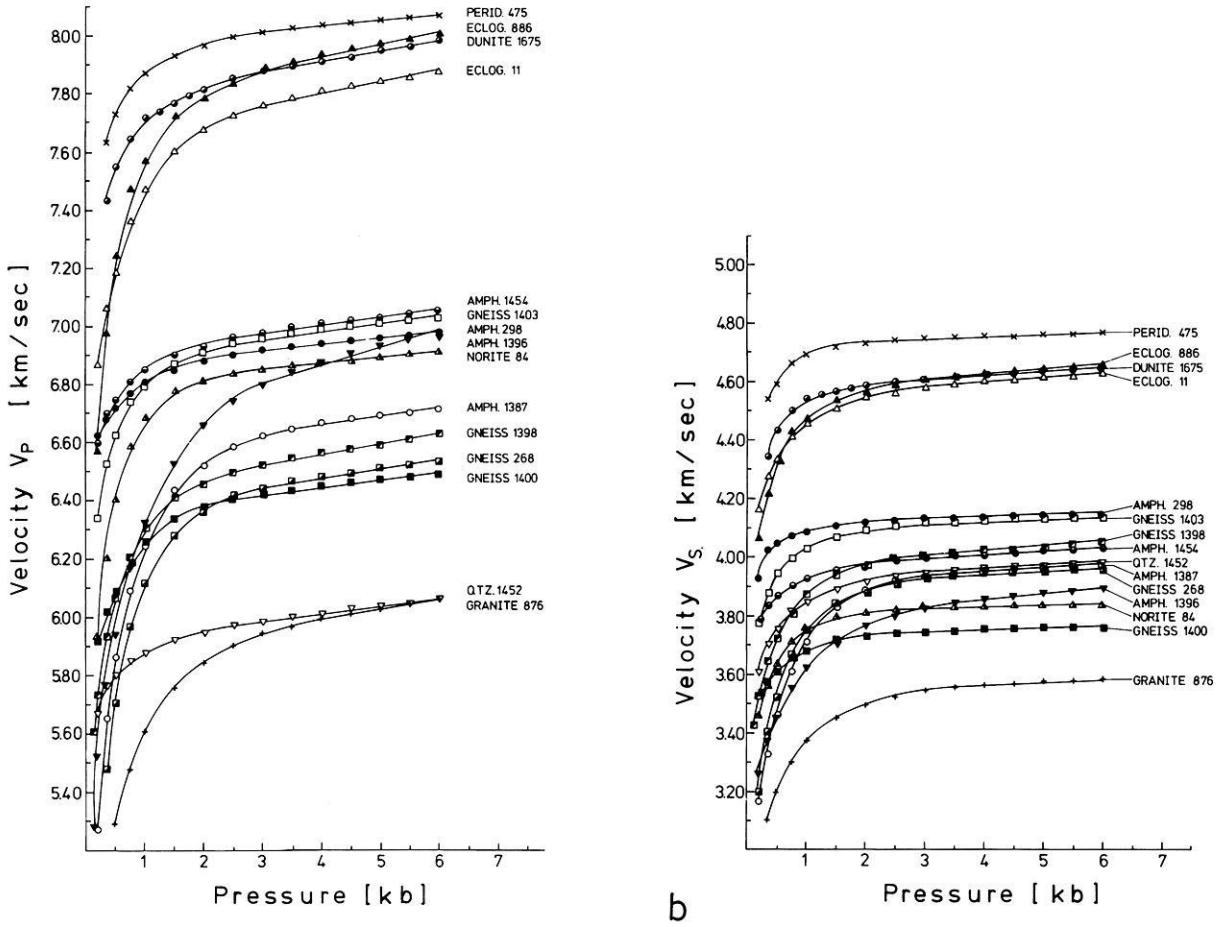

Fig. 1a and b. Velocities of (**a**) compressional waves and (**b**) shear wave as a function of pressure at room temperature. V_P is the mean of the velocities measured in the three orthogonal directions (x,y,z) of the sample cubes, V_S is the velocity in the x direction

time of the pulses through the specimens is obtained by subtracting the calibrated time needed for the pulse to travel to and from the specimen through the pistons from the total time measured by the transducers.

The experiments were carried out on rock cubes (43 mm on edge) cut from larger blocks, free of macroscopic fractures and secondary alteration. Edges of the sample cubes were parallel to visible macroscopic fabric directions (foliation, banding). The compressional wave velocity was measured simultaneously in the three orthogonal directions (x, y, z) of the cubes to obtain information on the directional dependence of the wave velocities. In one direction (x) the velocities of compressional and shear waves were measured at the same time. In general the x direction was normal to foliation or banding. The travel time was determined with a digital counter by comparing the output and input impulses on a dual-trace oscilloscope. The precision of timing measurements is ± 5 ns, and the timing accuracy is believed to better than $\pm$ 0.5%.

Wave velocities were measured at about 0.5 kbar intervals during the pressure increase to 6 kbar. Maintaining the hydrostatic pressure of 6 kbar, the temperature was increased in steps of about 50°–80° C over 30-min periods. To ensure that the samples had reached pressure and temperature equilibrium, successive readings were taken at time intervals of at least 40 min.

Results and Discussion

All the measurements described above were obtained from runs on fresh cubes of rocks. In general, the data presented were obtained from specimens compressed and heated for the first time. To check reversibility, velocities for two specimens were measured during heating as well as during cooling. A correction for the change of length of the specimens with pressure and temperature, was applied to the calculation of velocity.

The pressure and temperature dependence of wave velocities and the respective dynamic elastic parameters of polycrystalline rocks depend on two factors: (1) the pressure and temperature sensitivity of the elastic parameters of the constituent minerals and (2) on the state of microfracturing of the material.

Relations Between Velocity, Density, Chemistry, and Mineralogy at Room Temperature

The pressure dependence of V_P and V_S at room temperature is shown in Fig. 1. The velocity curves were obtained from measurements made while raising pressure to the 6 kbar confining pressure being applied for the velocity measurements at high temperatures. The general velocity increase with pressure may be attributed to

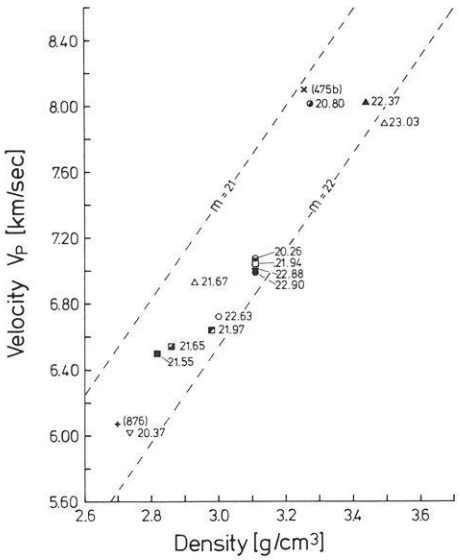

Fig. 2. Compressional wave velocities versus density at 6 kbar confining pressure. The numbers attached to *symbols* are mean atomic weights (Table 2). *Dashed lines* represent lines of constant mean atomic weight, according to Birch (1961)

compaction of pore space, in particular the closing of microcracks. Above about 2 kbar the velocity-pressure relations tend to become linear, indicating the intrinsic effect of pressure on wave velocities.

In Fig. 2 mean values of V_P are plotted against density. The numbers attached to the symbols represent mean atomic weights (Table 1). Also shown are the mean atomic weight lines, $m=21$ and $m=22$, as determined for compressional wave velocities by Birch (1961). The mean atomic weights of the rocks investigated vary between 20.37 (acidic) and 23.03 (mafic). As already shown by Birch (1961), differences in mean atomic weights of rocks are primarily related to iron and titanium content – the higher their content, the higher is the mean atomic weight (see also Table 1).

A rough dependence of wave velocities on bulk density is apparent. However, there is considerable scatter and the velocities in general do not follow lines of constant mean atomic weight. This partially irregular behavior can be explained by the mineralogical complexities. In Fig. 3 comparison is made between the percentages of major minerals and the compressional and shear wave velocities at 6 kbar confining pressure. From this it is evident that velocities are closely related to the percentages of major minerals in rocks and the respective single crystal velocities. In general, high contents of olivine, garnet, pyroxene and amphibole produce high compressional and shear wave velocities. Increasing quartz

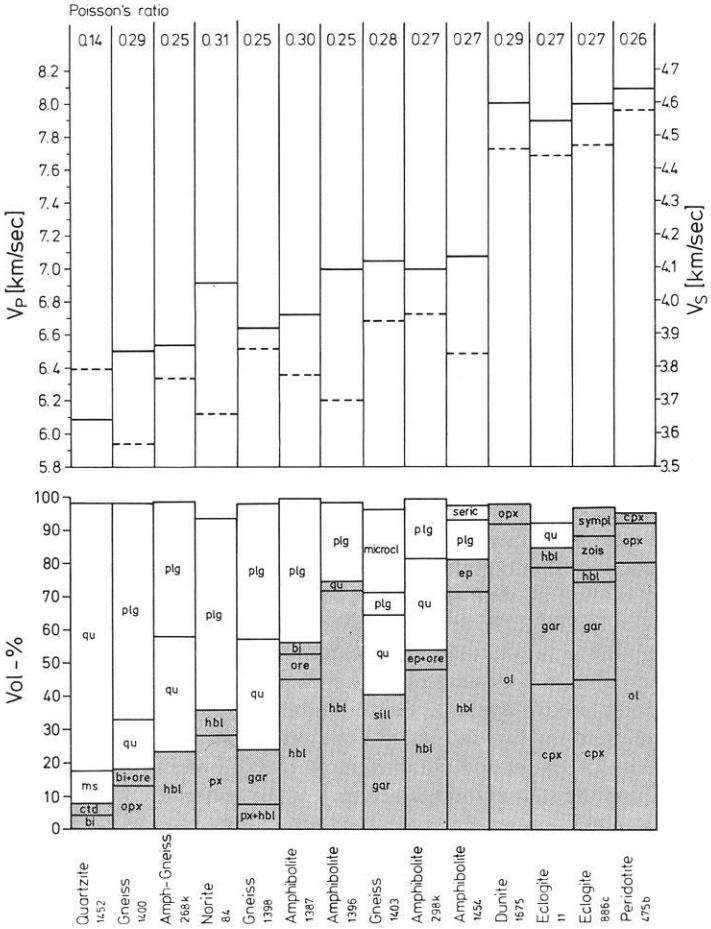

Fig. 3. Comparison between the percentages of major minerals and compressional wave velocities, shear wave velocities, and Poisson's ratio at 6 kbar confining pressure. For abbreviations see Table 3. The samples are arranged in order of increasing density (except 475). The *dark shaded areas* represent the dark minerals with generally high single crystal velocities. *Solid bars* (upper diagram) refer to V_P, *dashed* to V_S

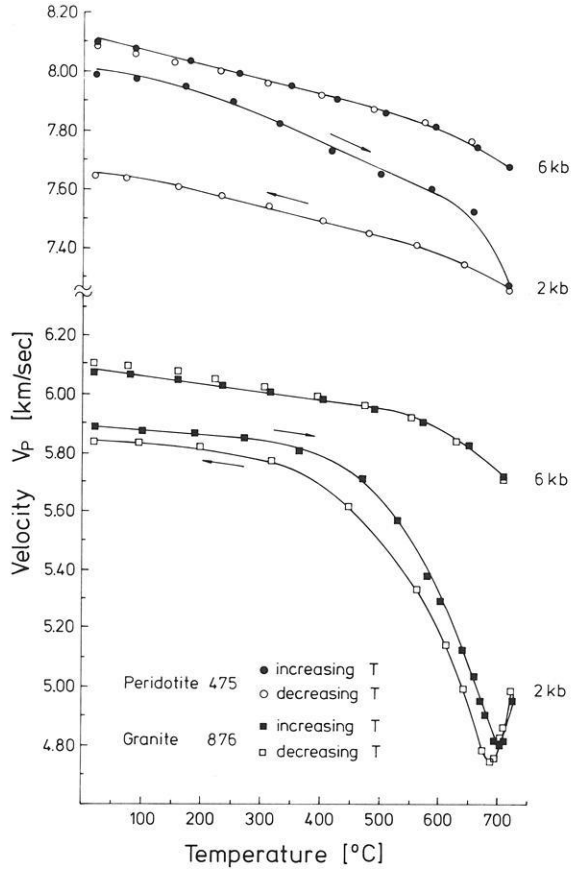

Fig. 4. Compressional wave velocities for peridotite 475 and granite 876 as a function of temperature at 2 kbar and 6 kbar confining pressure. *Solid symbols* indicate measurements with increasing temperature; *open symbols* indicate measurements with decreasing temperature. The velocity inversion in granite at 2 kbar is caused by the high-low transition in the constituent quartz minerals

content (samples No. 1398, 268 1452) results in a decrease of V_P and an accompanying increase in V_S, thereby significantly lowering Poission's ratio (Table 4). Compared to most major rock-forming silicates, quartz has an extremely low Poisson's ratio (Christensen and Fountain 1975; Kern 1979). On the other hand, high feldspar contents produce relatively low shear velocities and high Poisson's ratio (samples No. 84 and 1400).

Velocity-Temperature Relations at 6 kbar Confining Pressure

At a given pressure differential thermal expansion of the constituent minerals of rocks may cause grain boundary cracks to widen and new cracks to open. However, the microfracturing induced by the rapid thermal change of volume of the mineral phases will be more and more suppressed with increasing confining pressure and microfracturing should have little effect at pressures of a few kilobars. As was shown earlier (Kern 1978), the minimum pressure needed to prevent damage seems to be about 1 kbar per 100° C. The arguments borne out by that paper are substantiated by the observations on two cycled samples of granite and periodotite (Fig. 4). At 2 kbar confining pressure non-linear slope and significant hysteresis is observed on the velocity-temperature curves, indicating microfracturing. At 6 kbar confining pressure, however, the slope is near linear and reversibility is obtained on both plots. Thus, the values obtained under these conditions are considered to be the most nearly correct intrinsic properties of the compact aggregates. Therefore, in order to determine the temperature derivatives of velocities, the measurements of V_P and V_S were carried out under confining pressure conditions of 6 kbar.

V_P and V_S as a function of temperature at 6 kbar are presented in Fig. 5a–b. The data show that the decrease of *P*-and *S*- wave velocities is almost linear as temperature is increased from room value up to about 500° C. However, there is a significant decrease in the slope beyond this temperature, and the velocity-temperature curves become highly non-linear, indicating the onset of thermal cracking.

It should be noted, that a velocity minimum due to the high-low quartz transition (compare Fig. 4) is not observed on the velocity curves of the quartz-bearing rocks at 6 kbar. The pressure dependence and the shift of the α–β quartz transition temperature in polycrystalline aggregates (Kern 1978, 1979) places the transition temperature outside the temperature range investigated.

The best-fit solutions of the velocity-pressure and velocity-temperature data using the equations

$$V_P(p,T) = V_{P0} + (dV_P/dp)_T \cdot p + (dV_P/dT)_p \cdot T$$

and

$$V_S(p,T) = V_{S0} + (dV_S/dp)_T \cdot p + (dV_S/dT)_p \cdot T$$

are given in Table 3.

The pressure derivatives refer to 2–6 kbar at room temperature and the temperature derivatives to 20° C–500° C at 6 kbar confin-

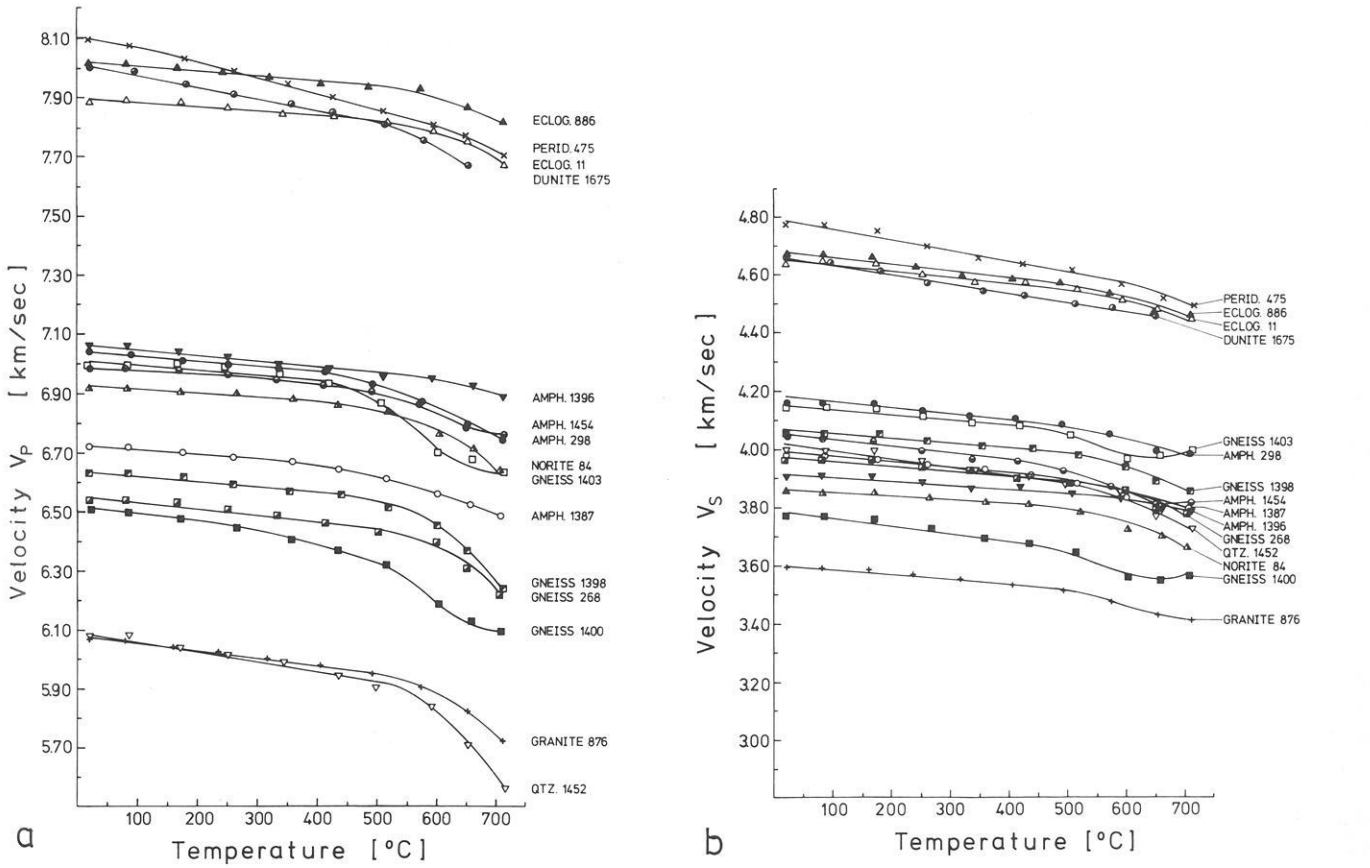

Fig. 5a and b. Velocities of (**a**) compressional waves and (**b**) shear waves for the different rock types as a function of temperature at 6 kbar confining pressure. V_P is the mean of the velocities measured in three orthogonal directions of the sample cubes, V_S is the velocity in one direction

Table 3. Pressure and temperature derivatives of *P*- and *S*-waves velocities of various rocks
V_P is the mean of the velocites measured in the three orthogonal directions of the sample cubes, V_S is the velocity in one direction
The reference state $V = V_0$ is 0 kbar and 0° C

Rock type/ Sample No.		V_{P_0} V_{S_0} (km × s^{-1})	$dV_P/dp \times 10^2$ $dV_S/dp \times 10^2$ (km × s^{-1} kbar^{-1})	$-dV_P/dT \times 10^4$ $-V_S/dT \times 10^4$ (km × s^{-1}°C^{-1})
Quartzite	V_P	5.905 ± 0.004	2.94 ± 0.1	4.01 ± 0.3
1452	V_S	3.910 ± 0.004	1.46 ± 0.08	2.85 ± 0.3
Bio-cpx-plg-gneiss	V_P	6.360 ± 0.006	2.42 ± 0.1	4.78 ± 0.3
1400	V_S	3.727 ± 0.003	0.84 ± 0.08	2.85 ± 0.2
Cpx-plg-gar-gneiss	V_P	6.420 ± 0.007	3.67 ± 0.2	2.46 ± 0.2
1398	V_S	3.964 ± 0.004	1.60 ± 0.09	1.70 ± 0.2
Amph-plg-gar-gneiss	V_P	6.339 ± 0.01	3.56 ± 0.3	2.51 ± 0.2
268	V_S	3.884 ± 0.006	1.49 ± 0.1	2.01 ± 0.2
Sill-gar-gneiss	V_P	6.871 ± 0.01	3.03 ± 0.2	3.61 ± 0.3
1403	V_S	4.091 ± 0.003	1.01 ± 0.07	2.22 ± 0.2
Amphibolite	V_P	6.516 ± 0.01	3.63 ± 0.3	2.37 ± 0.2
1387	V_S	3.885 ± 0.006	1.68 ± 0.1	2.08 ± 0.2
Amphibolite	V_P	6.610 ± 0.02	6.59 ± 0.50	0.72 ± 0.2
1936	V_S	3.746 ± 0.01	2.79 ± 0.2	1.39 ± 0.2
Ep-amphibolite	V_P	6.905 ± 0.005	2.80 ± 0.1	2.99 ± 0.2
1454	V_S	3.965 ± 0.003	1.27 ± 0,06	2.65 ± 0.2
Amphibolite	V_P	6.857 ± 0.005	2.28 ± 0.1	2.02 ± 0.2
298	V_S	4.109 ± 0.003	0.92 ± 0.06	1.81 ± 0.2
Eclogite	V_P	7.641 ± 0.01	4.17 ± 0.2	1.60 ± 0.2
11	V_S	4.535 ± 0.006	1.73 ± 0.1	2.11 ± 0.3
Eclogite	V_P	7.740 ± 0.01	4.75 ± 0.3	1.86 ± 0.1
886c	V_S	4.548 ± 0.006	2.09 ± 0.1	2.48 ± 0.2
Norite	V_P	6.770 ± 0.005	2.58 ± 0.1	1.73 ± 0.2
84	V_S	3.803 ± 0.003	0.94 ± 0.07	1.49 ± 0.1
Dunite	V_P	7.772 ± 0.004	3.73 ± 0.1	4.12 ± 0.1
1675	V_S	4.566 ± 0.004	1.59 ± 0.09	3.54 ± 0.2
Granite	V_P	5.818 ± 0.01	4.37 ± 0.3	2.69 ± 0.1
876	V_S	3.496 ± 0.008	1.79 ± 0.1	2.08 ± 0.1
Peridotite	V_P	7.949 ± 0.007	2.36 ± 0.2	4.94 ± 0.2
475	V_S	4.721 ± 0.002	0.946 ± 0.07	3.93 ± 0.3

ing pressure. The computed coefficients cover the range 2.28–6.59×10^{-2} km/s kbar for compressional wave velocities and 0.84–2.79×10^{-2} km/s kbar for shear wave velocities. The temperature derivatives range from -1.6 to -4.94×10^{-4} km/s °C for compressional wave velocities and from -1.39 to -3.93×10^{-4} km/s °C for shear wave velocities. The resulting temperature coefficients of V_P and V_S are in general largest in quartz-bearing and olivine-bearing rocks.

Because experimental work on temperature derivatives for crustal and mantle rocks under conditions of high confining pressure is still scarce, only limited camparisons can be made with published data. Comprehensive temperature data for V_P for a wide variety of igneous and metamorphic rocks (Christensen 1979) came to the attention of these authors as this manuscript was being submitted. Christensen estimated temperature coefficients at 2 kbar confining pressure up to 500° C. Because of the relatively low confining pressure, the velocity is an approximately linear function below 300° C only, thus indicating intrinsic behavior only within this temperature range. The T derivatives of V_P at higher temperatures are believed to be influenced by grain boundary openings. In general, Christensen's values are a little larger than our own for rocks of comparable composition.

For dunite we obtained a $(dV_P/_P/dT)_p$-value of -4.12×10^{-4} km/s °C. Christensen estimated -5.6×10^{-4} km/s °C, while Ramananantoandro and Manghnani (1978) measured a mean of -6.1×10^{-4} km/s °C for an anisotropic dunite at 10 kbar, for the range 25°–500° C. Peselnick and Nicolas (1978) measured T derivatives of V_P in a harzburgite and Iherzolite rock for the range 20°–250° C at 8 kbar confining pressure. The results for the two rocks are approximately the same (-6×10^{-4} to -7×10^{-4} km/s °C) and are again a little larger than our value for a peridotite rock (-4.94×10^{-4} km/s °C).

Our experimental data for dunite and peridotite (80% olivine by volume), however, compare fairly well with T derivatives of V_P calculated from single crystal data using the Voigt-Reuss-Hill assumption. Kumazawa and Anderson (1969) calculated -4.95×10^{-4} km/s °C for an isotropic aggregate of olivine and Ramananantoandro and Manghnani (1978) calculated -4.4×10^{-4} to -4.6×10^{-4} km/s °C for three anisotropic dunite cores.

For eclogites we measured significantly smaller temperature coefficients of V_P(-1.6×10^{-4} to -1.86×10^{-4} km/s °C) than Christensen ($-5.3 \cdot 10^{-4}$ km/s °C). Better agreement was obtained in quartz-bearing rocks. For granite, granulitegneiss and quartzite we obtained temperature derivatives of V_P between -2.69×10^{-4} and -4.1×10^{-4} km/s °C. Christensen obtained temperature coefficients ranging from -3.9×10^{-4} to -5.4×10^{-4} km/s °C for the

Table 4. V_{P_x}, V_{S_x} and elastic constants for selected temperatures at 6 kbar (for explanation of symbols see text)

Rocktype Sample No.	T (°C)	ρ (g/cm^3)	V_{P_x} (km/s)	V_{S_x} (km/s)	V_{P_x}/V_{S_x}	σ	ϕ (km^2/s^2)	K (Mbar)	β (Mbar^{-1})	G (Mbar)	E (Mbar)	λ (Mbar)
Granite	20	2.701	5.989[a]	3.397	1.763	0.262	20.48	0.553	1.807	0.311	0.787	0.345
876	160	2.695	5.955	3.383	1.760	0.261	20.20	0.544	1.836	0.308	0.778	0.338
$A=2.0\%$	315	2.693	5.911	3.346	1.766	0.264	20.01	0.538	1.855	0.301	0.762	0.337
	490	2.690	5.872	3.304	1.777	0.268	19.92	0.535	1.865	0.293	0.744	0.340
	710	2.667	5.648	3.201	1.764	0.263	18.23	0.486	2.055	0.273	0.690	0.304
Quartzite	20	2.735	5.883[b]	3.800	1.548	0.142	15.35	0.419	2.380	0.394	0.902	0.156
1452	170	2.733	5.849	3.796	1.540	0.136	14.99	0.409	2.439	0.393	0.894	0.147
$A=6.0\%$	340	2.726	5.763	3.723	1.547	0.141	14.73	0.401	2.490	0.377	0.862	0.149
	500	2.711	5.680	3.674	1.545	0.140	14.26	0.386	2.585	0.365	0.834	0.142
	710	2.680	5.337	3.520	1.516	0.115	11.96	0.320	3.119	0.332	0.740	0.099
Gneiss	20	2.816	6.578[c]	3.574	1.840	0.290	26.23	0.738	1.353	0.359	0.928	0.499
1400	170	2.817	6.532	3.556	1.836	0.289	25.80	0.726	1.375	0.356	0.918	0.489
$A=2.4\%$	360	2.815	6.442	3.489	1.846	0.292	25.26	0.711	1.405	0.342	0.885	0.482
	515	2.810	6.340	3.436	1.845	0.292	24.45	0.687	1.455	0.331	0.857	0.465
	710	2.801	6.103	3.362	1.815	0.282	22.17	0.621	1.609	0.316	0.811	0.410
Amphibole	20	2.857	6.499[a]	3.769	1.724	0.246	23.29	0.665	1.502	0.405	1.011	0.395
Gneiss	170	2.860	6.481	3.769	1.719	0.244	23.06	0.659	1.516	0.406	1.011	0.388
268	335	2.860	6.423	3.726	1.723	0.246	22.74	0.650	1.537	0.397	0.989	0.385
$A=1.5\%$	505	2.854	6.371	3.679	1.731	0.249	22.54	0.643	1.554	0.386	0.965	0.385
	710	2.832	6.136	3.572	1.717	0.243	20.63	0.584	1.710	0.361	0.898	0.343
Norite	20	2.930	6.976[c]	3.658	1.907	0.310	30.82	0.903	1.107	0.392	1.027	0.641
84	170	2.934	6.958	3.648	1.907	0.310	30.66	0.899	1.111	0.390	1.023	0.639
$A=1.6\%$	360	2.935	6.926	3.611	1.918	0.313	30.58	0.897	1.114	0.382	1.005	0.642
	520	2.929	6.870	3.580	1.918	0.313	30.10	0.881	1.133	0.375	0.986	0.631
	700	2.918	6.678	3.454	1.933	0.317	28.68	0.837	1.194	0.348	0.917	0.605
Gneiss	20	2.976	6.644[a]	3.858	1.722	0.245	24.29	0.723	1.382	0.442	1.103	0.427
1398	180	2.980	6.625	3.856	1.718	0.243	24.06	0.717	1.394	0.443	1.102	0.421
$A=0.8\%$	350	2.978	6.571	3.810	1.724	0.246	23.82	0.709	1.409	0.432	1.077	0.421
	520	2.967	6.520	3.777	1.726	0.247	23.48	0.696	1.434	0.423	1.056	0.414
	710	2.946	6.256	3.649	1.714	0.242	21.38	0.629	1.587	0.392	0.974	0.368
Amphibolite	20	2.999	7.041[c]	3.778	1.863	0.297	30.54	0.916	1.091	0.428	1.111	0.630
1387	175	2.999	7.026[a]	3.761	1.868	0.299	30.50	0.914	1.093	0.424	1.102	0.632
$A=8.0\%$	360	3.001	6.991	3.724	1.877	0.301	30.38	0.911	1.096	0.416	1.083	0.634
	515	2.995	6.935	3.673	1.888	0.305	30.10	0.901	1.109	0.404	1.054	0.632
	710	2.976	6.809	3.586	1.898	0.308	29.21	0.869	1.150	0.382	1.001	0.614
Amphibolite	20	3.106	6.471[a]	3,711	1.743	0.254	23.51	0.730	1.369	0.427	1.073	0.445
1396	170	3.111	6.455	3.709	1.740	0.253	23.32	0.725	1.378	0.427	1.072	0.440
$A=11.0\%$	335	3.114	6.406	3.666	1.747	0.256	23.11	0.719	1.389	0.418	1.051	0.440
	510	3.109	6.355	3.646	1.743	0.254	22.66	0.704	1.419	0.413	1.037	0.429
	710	3.087	6.270	3.580	1.751	0.258	22.22	0.686	1.457	0.395	0.995	0.422
Gneiss	20	3.107	7.155[c]	3.949	1.811	0.280	30.40	0.944	1.058	0.484	1.241	0.621
1403	175	3.108	7.121	3.938	1.808	0.279	30.03	0.933	1.071	0.481	1.233	0.612
$A=3.3\%$	340	3.106	7.054	3.888	1.814	0.281	29.60	0.919	1.087	0.469	1.203	0.606
	505	3.099	6.957	3.844	1.809	0.280	28.69	0.889	1.124	0.457	1.172	0.584
	710	3.081	6.741	3.798	1.774	0.267	26.20	0.807	1.238	0.444	1.126	0.511
Amphibolite	20	3.107	7.077[b]	3.961	1.786	0.271	29.16	0.906	1.103	0.487	1.240	0.581
298	170	3.109	7.065	3.958	1.784	0.271	29.02	0.902	1.108	0.487	1.238	0.577
$A=4.8\%$	330	3.107	7.019	3.910	1.795	0.275	28.88	0.897	1.114	0.475	1.211	0.580
	490	3.102	6.970	3.882	1.795	0.275	28.48	0.883	1.131	0.467	1.192	0.572
	710	3.082	6.793	3.777	1.798	0.276	27.12	0.835	1.196	0.439	1.122	0.542
Amphibolite	20	3.109	6.885[a]	3.842	1.792	0.273	27.72	0.861	1.160	0.458	1.169	0.555
1454	170	3.107	6.853	3.822	1.793	0.274	27.48	0.854	1.170	0.453	1.156	0.551
$A=6.0\%$	335	3.109	6.781	3.759	1.803	0.278	27.14	0.843	1.185	0.439	1.123	0.550
	490	3.102	6.712	3.718	1.805	0.278	26.61	0.825	1.211	0.428	1.096	0.539
	710	3.084	6.515	3.614	1.802	0.277	25.03	0.771	1.295	0.402	1.029	0.503
Dunite	20	3.278	8.227[c]	4.462	1.843	0.291	41.13	1.348	0.741	0.652	1.685	0.913
1675	180	3.280	8.163	4.408	1.851	0.294	40.72	1.335	0.748	0.637	1.649	0.910
$A=4.8\%$	355	3.271	8.072	4.337	1.861	0.297	40.07	1.310	0.762	0.615	1.596	0.900
	510	3.261	8.022	4.292	1.869	0.299	39.79	1.297	0.770	0.600	1.561	0.897
	710	3.271	7.925	4.291	1.846	0.292	38.25	1.251	0.799	0.602	1.557	0.849

Continuation on p. 54

Table 4 (continued)

Rocktype Sample No.	T (°C)	ρ (g/cm^3)	V_{P_x} (km/s)	V_{S_x} (km/s)	V_{P_x}/V_{S_x}	σ	ϕ (km^2/s^2)	K (Mbar)	β (Mbar^{-1})	G (Mbar)	E (Mbar)	λ (Mbar)
Eclogite	20	3.495	7.886[b]	4.438	1.776	0.268	35.92	1.255	0.796	0.688	1.746	0.796
11	175	3.499	7.880	4.436	1.776	0.268	35.85	1.254	0.797	0.688	1.746	0.795
$A=0.3\%$	340	3.496	7.822	4.372	1.789	0.272	35.69	1.247	0.801	0.668	1.701	0.802
	515	3.488	7.783	4.346	1.790	0.273	35.39	1.234	0.810	0.658	1.677	0.795
	710	3.463	7.622	4.242	1.796	0.275	34.10	1.180	0.846	0.623	1.589	0.765
Ecologite	20	3.442	7.975[c]	4.470	1.784	0.270	36.95	1.272	0.786	0.687	1.748	0.813
886	170	3.443	7.954	4.457	1.784	0.271	36.77	1.266	0.789	0.683	1.738	0.810
$A=0.8\%$	320	3.437	7.893	4.395	1.795	0.275	36.54	1.256	0.796	0.663	1.693	0.813
	485	3.435	7.863	4.365	1.801	0.277	36.42	1.251	0.799	0.654	1.671	0.814
	710	3.409	7.730	4.256	1.816	0.282	35.60	1.213	0.823	0.617	1.583	0.801
Peridotite	20	3.290	8.010[b]	4.575	1.750	0.257	36.25	1.192	0.838	0.688	1.732	0.733
475	180	3.288	7.955	4.543	1.751	0.258	35.76	1.175	0.850	0.678	1.707	0.723
$A=4.7\%$	350	3.282	7.842	4.448	1.763	0.262	35.11	1.152	0.867	0.649	1.640	0.719
	510	3.272	7.733	4.404	1.755	0.259	33.93	1.110	0.900	0.634	1.599	0.687
	715	3.259	7.474	4.280	1.746	0.256	31.43	1.024	0.976	0.596	1.499	0.626

V_{P_x} and V_{S_x} are velocities in the x direction of the sample coordinates

[a] Lowest velocity in the anisotropic aggregates

[b] Intermediate

[c] Highest

[d] In this run the x direction of the sample coordinates is parallel to the foliation

same rocks. Our results for quartz-bearing granite and gneiss rocks are almost within the range of values reported by Spencer and Nur (1976) for Westerly granite (-1×10^{-4} to -5×10^{-4} km/s °C) heated to 400° C at 5 kbar confining pressure.

To our knowledge, temperature coefficients of V_S have not yet been published, so that no comparison is possible.

In general, the temperature derivatives of V_S are smaller than those of V_P except for eclogites and amphibolites (Table 3). In both eclogite samples V_S decreases significantly more than V_P with increasing temperature. In amphibolites the temperature coefficients of V_S equal, more or less, those of V_P or are a little larger.

Velocity Anisotropy

Significant velocity anisotropies

$$A=\frac{V_{\max}-V_{\min}}{V_{\max}}\times 100\%$$

were measured in peridotite, dunite, amphibolite and quartzite rocks. The directional dependence of elastic wave velocities is at least a result of both (1) preferred lattice orientation of minerals and (2) microcracks which are preferrently orientated parallel to grain boundaries. As was shown by Kern (1978) the part of the velocity anisotropy that may be attributed to oriented cracks is eliminated at higher confining pressure. Therefore, the velocity anisotropies for 6 kbar confining pressure listed in Table 4 must be due to preferred lattice orientation of constituent minerals. Petrofabric analyses with the X-ray goniometer (amphibolite) and the universal stage (dunite, peridotite, quarzite) show significant preferred lattice orientation of dominant minerals (i.e., hornblende, olivine, quartz, mica) in these rocks, and this part of the elastic anisotropy is unavvected by temperature even at 700° C.

Dynamic Elastic Parameters at High Pressure and Temperature

Compressional and shear wave velocities measured simultaneously in one sample direction at 6 kbar confining pressure are given in Table 4 for various temperatures, together with the values of the compressional to shear velocity ratio (V_P/V_S), Poisson's ratio (σ), the seismic parameter (ϕ), the bulk moduls (K), the compressibility (β), the shear moduls (G), Young's modulus (E), and the Lamé's constant (λ) as calculated from measured densities and velocities. The dynamic elastic parameters for significantly anisotropic samples must be treated with caution because the elastic constants were calculated by use of the formulas proposed by Birch (1960) for isotropic bodies.

In general, the values of K, G, E, and ϕ at high confining pressure show a decrease with temperature. It should be noted that in quartz-bearing rocks the bulk moduls decreases much more than the shear moduls.

Application to Geology and Geophysics

The quasi-linearity of the velocity-pressure relations between 2 and 6 kbar at room temperature and of the velocity-temperature relations at 6 kbar in the range 20°–500° C for the rocks investigated (Fig. 5) suggest that calculated pressure and temperature derivatives approach those of pore-free aggregates. It should be noted, however, that our measurements were carried out on dry samples and it is well established that pore fluids may affect compressional

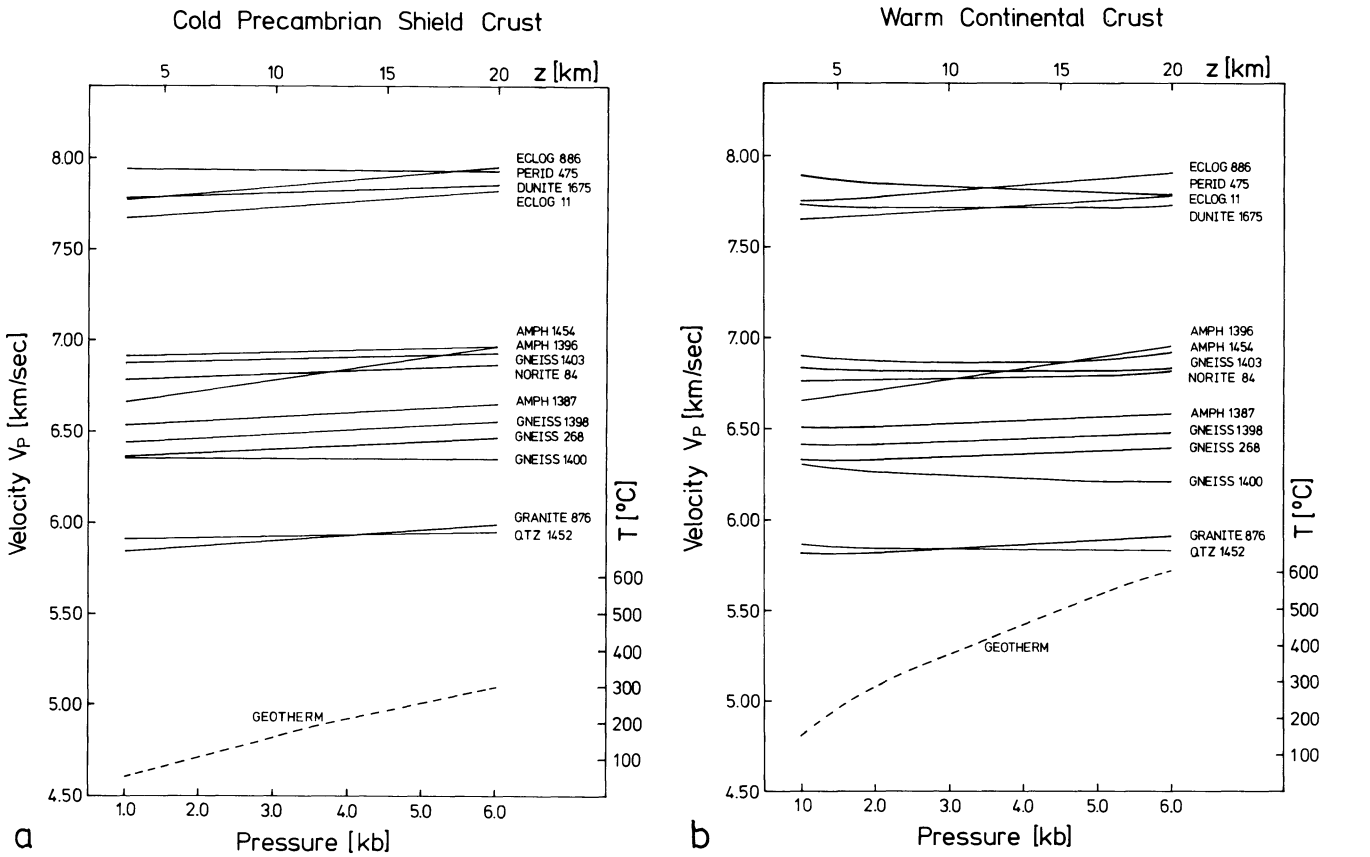

Fig. 6a and b. Compressional wave velocities for different rock types under pressure and temperature conditions of **a** a cold Precambrian shield and **b** a warm continental crust geotherm. The assumed geotherms (after Theilen and Meissner, 1979) are shown by the *bottom curve*

wave velocities (Nur and Simmons 1969; Spencer and Nur 1976). Crustal and mantle igneous and high-grade metamorphic rocks, however, are in general water-depleted. Therefore, at deeper crustal levels, pore fluid pressure may be very small and the effective pressure nearly identical to the lithostatic pressure.

On the basis of this assumption we used our experimentally determined pressure and temperature derivatives of the mean values of V_P to calculate velocity-depth profiles. In Fig. 6 we have plotted *P*-velocities of different rocks for a cold Precambrian shield crust (a) and for a warm continental crust (b). The computation is based on geotherms (bottom curve) reported by Theilen and Meissner (1979).

Along the geotherm of a Precambrian shield crust (a) the velocity function increases with depth for all rocks investigated (except for the peridotite rock), but the rate of velocity increase may be different from rock type to rock type. The temperature gradients valid for a warm continental crust (b), however, cause a velocity inversion in numerous rocks. As is evident from Fig. 6b the velocity-depth relations show small negative velocity gradients for olivine-bearing rocks and less significantly for quartz-bearing rocks (gneiss, quartzite), due to the temperature sensitivity of wave velocity in olivine and quartz single crystals.

This observation is compatible with results from deep seismic sounding, which indicate that large velocity reversals are not found in the crust of the Russian shield (Meissner 1976) but are quite abundant in young orogenic areas like the Alps (Giese 1968, 1970). On the other hand, large parts of mesozoic continental crust with average geotherms seem to have a rather constant velocity over many kilometers in the middle crust.

The pronounced velocity anisotropy in the amphibolite and peridotite rocks measured at high confining pressure and high temperatures, i.e., at conditions of great depth, may account for significant velocity anisotropy reported from deep seismic sounding. Bamford (1977) and Fuchs (1979) measured velocity anisotropy of 7–8% in the continental subcrustal litosphere. Seismic measurements reported by Hess (1964), Francis (1969), and Keen and Barett (1971) indicate anisotropy of the upper mantle under the Pacific Ocean. Velocities averaging 8.3 km/s. perpendicular to mid-ocean ridges contrast with velocities of about 8.0 km/s. parallel to the ridges, corresponding to anisotropy values of about 3.6%. Raitt et al. (1969) observed a large velocity anisotropy of about 7% in the region between California and Hawaii. These seismic anisotropies may be best explained by preferred latice orientation of the constituent minerals in the mantle material (see also Kern and Fakhimi 1975). As shown in this paper and by Kern (1978), elastic anisotropy induced by preferred lattice orientation is unaffected by high pressures and temperatures up to 700° C.

Acknowledgements. We wish to thank R. Meissner (Kiel), H.R. Wenk (Berkeley) and J. Zschau (Kiel) for helpful discussions and critical reading of the manuscript. We are grateful to P.K. Hörmann for oxide analyses and to M. Schroetel for assistance in performing the experiments. Financial support by the Deutsche Forschungsgemeinschaft, Bonn – Bad Godesberg, is gratefully acknowledged.

References

Bamford, D.: *P* velocity anisotropy in a continental upper mantle. Geophys. J. **49**, 29–48, 1977

Birch, F.: The velocity of compressional waves in rocks to 10 kbar, Part 1 J. Geophys. Res. **65**, 1083–1102, 1960

Birch, F.: The velocity of compressional waves in rocks to 10 kbar, Part 2. J. Geophys. Res. **66**, 2199–2224, 1961

Christensen, N.I.: Compressional wave velocities in metamorphic rocks at pressures to 10 kbar. J. Geophys. Res. **70**, 6147–6164. 1965

Christensen, N.I.. Shear-wave velocities in metamorphic rocks at pressures to 10 kbar. J. Geophys. Res. **71**, 3549–3556, 1966

Christensen, N.I.: Compressional wave velocities in possible mantle rocks to pressures of 30 kbar. J. Geophys. Res. **79**, 407–412, 1974

Christensen, N.I.: Compressional wave velocity in rocks at high temperatures and pressures. Critical thermal gradients, and crustal low-velocity zones. J. Geophys. Res. **84**, 6849–6857, 1979

Christensen, N.I., Fountain, D.M.: Constitution of the lower continental crust based on experimental studies of seismic velocities in granulite. Geol. Soc. Am.Bull. **86**, 227–236, 1975

Fielitz, K.. Untersuchungen von Kompressions- und Scherwellengeschwindigkeiten in Gesteinen unter erhöhtem Druck. Geophys. **37**, 943–956, 1971

Francis, T.J.G.: Generation of seismic anisotropy in the upper mantle along the mid-oceanic ridges. Nature **221**, 162–165, 1969

Fuchs, K.: The subcrustal lithosphere – mechanical properties, differentiation and dynamical processes. Tectonophysics **56**, 1–15, 1979

Giese, P.: Die Struktur der Erdkruste im Bereich der Ivrea-Zone. Schweiz. Mineral. Petrogr. Mitt. **48**, 261–284, 1968

Giese, P.: The structure of the earth's crust in central Europe. Proc. 10th Gen. Ass. Europ. Seismol. Comm. (Leningrad 1968), 387–403. Moscow: Acad. Sci. USSR 1970

Hess, H.H.. Seismic anisotropy of the uppermost mantle under oceans. Nature **204**, 629–631, 1964

Keen, C.E., Barett, D.L.: A measurement of seismic anisotropy in the North-East Pacific. Can. J. Earth Sci. **8**, 1056–1064, 1971

Kern, H.. The effect of high temperature and high confining pressure on compressional wave velocities in quartz-bearing and quartz-free igneous and metamorphic rocks. Tectonophysics **44**, 185–203, 1978

Kern, H.. Effect of high-low quartz transition on compressional and shear wave velocities in rocks under high pressure. Phys. Chem. Minerals **4**, 161–167, 1979

Kern, H., Fakhimi, M.: Effect of fabric anisotropy on compressional wave propagation in various metamorphic rocks for the range 20°–700° C at 2 kbars. Tectonophysics **28**, 227–244, 1975

Kern, H., Richter, A.: Compressional and shear wave velocities at high temperature and high confining pressure in basalts from the Faeroe islands. Tectonophysics **54**, 231–252, 1979

Kumazawa, M., Anderson, O.L.: Elastic moduli, pressure derivatives, and temperature derivatives of single-crystal olivine and single-crystal forsterite. J. Geophys. Res. **74**, 5961–5972, 1969

Meissner, R.: Comparison of wide-angle measurements in the USSR and the Federal Republic of Germany. In: Explosion seismology in central europe, P. Giese, C. Prodehl, A. Stein, eds.: pp 380–384. Berlin, Heidelberg, New York: Springer 1976

Nur, A., Simmons, G.: The effect of saturation on velocity in low porosity rocks. Earth Planet. Sci. Lett. **7**, 183–193, 1969

Peselnick, L., Nicolas, A.: Seismic anisotropy in an ophiolite peridotite: application to oceanic upper mantle. J. Geophys. Res. **83**, 1227–1235, 1978

Raitt, R.W., Shor, G.G., Francis, T.J.G., Morris, G.B.. Anisotropy of the Pacific upper mantle. J. Geophys. Res. **74**, 3095–3109, 1969

Ramananantoandro, R., Manghnani, M.H.: Temperature dependence of the compressional wave velocity in an anisotropic dunite: Measurements to 500° C at 10 kbar. Tectonophysics **47**, 73–84, 1978

Simmons, G.: Velocity of shear waves in rocks to 10 kbar. J. Geophys. Res. **69**, 1123, 1964

Spencer, J.W., Jr., Nur, A.M.: The effect of pressure, temperature and pore water on velocities in Westerly granite. J. Geophys. Res. **81**, 899–904, 1976

Stewart, R., Peselnick, L.: Velocity of compressional waves in dry Franciscan rocks to 8 kbar and 300° C. J. Geophys. Res. **82**, 2027–2039, 1977

Stewart, R., Peselnick, L.: Systematic behavior of compressional velocity in Franciscan rocks at high pressure and temperature. J. Geophys. Res. **83**, 831–839, 1978

Theilen, F., Meissner, R.. A comparison of crustal and upper mantle features in Fennoscandia and the Rhenish shield, two areas of recent uplift. Tectonophysics **61**, 227–242, 1979

Received February 21, 1980; Revised Version July 1, 1980
Accepted August 7, 1980

J. Geophys. 49, 57–65 (1981)

Journal of Geophysics

A Crustal Gravity Model of the Mare Serenitatis – Mare Crisium Area of the Moon

P. Janle

Institut für Geophysik der Universität, Bundesstr. 55, D-2000 Hamburg 13, Federal Republic of Germany and
Institut für Geophysik der Universität, D-2300 Kiel, Federal Republic of Germany

Abstract. Several published mass configurations of mascon models have been used to calculate and compare gravity models for Mare Crisium. The calculations are based on line-of-sight (LOS) gravity data from the Apollo missions. A new model consisting of mare basalts, a crust-mantle mix, and a mantle plug is presented. Additionally, an isostatic model has been developed. A detailed regional model from southern Imbrium over Mare Serenitatis to Mare Crisium has been calculated, based upon the new model. Crustal thickenings have been introduced in order to fit the gravity lows bordering the mare basins.

A discussion of the stability of the mascons, presented in this paper, leads to the following conclusions: (1) the average postmare upper mantle viscosity must be greater or equal to 10^{27} poise; (2) high temperature models seem to be inappropriate considering this high viscosity and the mascon shear stresses of 65 bar at a depth of 200 km. The second statement could be revised in the light of investigations of a totally dry rheology.

Key words: Crustal gravity models – Lunar mascons – Lunar upper mantle rheology.

Introduction

Since lunar line-of-sight (LOS) gravity data derived from spacecraft Doppler tracking signals have been available, several methods of gravity modelling have been developed. Conventional geophysical computation of the vertical gravity component of a given mass model is not possible (1) because of the line-of-sight nature of the data and (2) because of the least squares procedure of orbit determination which introduces an amplitude compression of 25%–30%. The methods and problems of data acquisition and reduction are described by Gottlieb (1970) and Sjogren et al. (1976).

There are three methods for computing LOS gravity of given mass configurations: (1) direct dynamic modelling of a gravity anomaly with a complex orbit determination program (Michael and Blackshear 1972), (2) dynamic estimation of the acceleration vectors and a subsequent static gravity modelling of the vectors (Bowin et al. 1975), and (3) a quasi-dynamic modelling with a simplified orbit simulation program. Method 3 and a comparison of all three methods are described by Phillips et al. (1978). Methods 1 and 2 require large computational times, while method 3, the one used in this paper, is comparatively fast.

The first Doppler gravity profiles of the moon received revealed large positive gravity anomalies associated with most circular maria (Muller and Sjogren 1968). These gravity maxima were explained by mass concentrations (mascons) soon after their discovery. Several models have been developed to describe the mascon anomalies. Most are based on mass excesses, but there are also some mass configurations which are in isostatic equilibrium.

The purpose of this paper is

(1) to compare old models of mass surpluses with each other and to develop a new model,

(2) to present an isostatic model,

(3) to develop a complete crustal model extending from the Apennines area over Mare Serenitatis to Mare Crisium, based on LOS gravity data from orbits of different heights.

Gravity Data and Boundary Conditions

The observational data for model fitting are low and high altitude LOS gravity data from the Apollo 15 Command and Service Modules (CSM), revolutions 5 and 15. The spacecraft altitudes are about 12–20 km for revolution 5 and 100–110 km for revolution 15. Gravity data for two different altitude levels permit a refined model fitting of possible model configurations. The profile location is shown in Fig. 1.

In addition to the LOS gravity data, there are several boundary conditions which influence the model parameterization

- topography of the mare basins,
- mean crustal thickness,
- density-depth distribution,
- thickness of mare basalts,
- initial depth of the impact basins.

These conditions will now be discussed in detail.

The gravity effects of the mare basin topography have a large influence on quantitative mass modelling. The basins of Serenitatis and Crisium contribute −89 mgal and −140 mgal to the measured gravity for revolution 5 in the central areas. This increases the gravity anomaly which has to be fitted by 40%–70% (Fig. 2). Several older published models ignore these topographic effects.

The mean altitude levels of the surroundings of the Serenitatis and Crisium areas and of the basins themselves have been determined from modern Lunar Topographic Orthophotomaps (LTO, Schimerman 1973). The values of the altitude levels are given as distance from the center of mass of the moon:

surroundings:	1,736.0 km,
Crisium basin:	1,733.7 km,
Serenitatis basin:	1,734.35 km.

0340-062X/81/0049/0057/$01.80

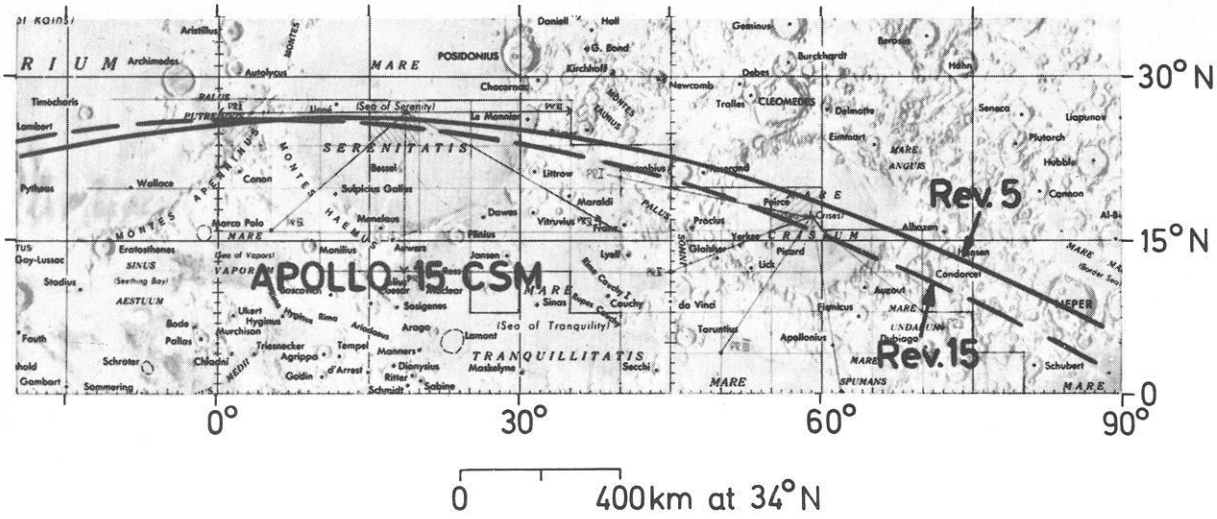

Fig. 1. Profile location, Apollo 15 Command and Service Modules (CSM), *Rev. 5 and 15.* Spacecraft altitudes: *Rev. 5:* 12–20 km; *Rev. 15:* 100–110 km

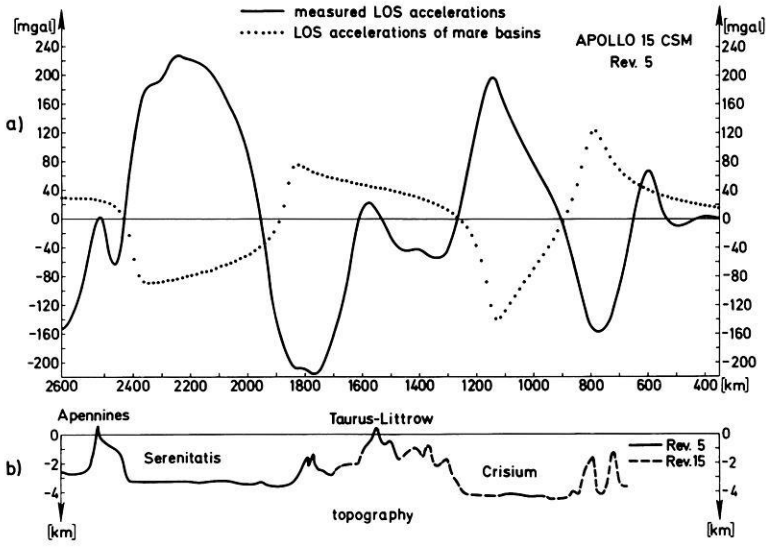

Fig. 2a and b. Line of sight (*LOS*) gravity effect of mare basin topography, *Appollo 15 CSM, Rev. 5.*
a Measured LOS accelerations and calculated LOS accelerations of mare basin topography
b topography from Lunar Topographic Orthophotomaps (LTO); zero level of elevation scale is related to a mean lunar radius of 1,738 km

The zero level of all elevation and depth scales in the figures is related to a mean lunar radius of 1,738 km.

A mean crustal thickness of 60 km has been assumed for the nearside of the moon. This value has been derived from seismic investigations (Toksöz et al. 1974).

The mean density-depth distribution of the crust and upper mantle is based upon petrologic models, seismic models, and rocks returned to Earth (Cooper et al. 1974; Solomon 1974). Following these investigations a density of 2.7 g/cm^3 has been assumed for the upper crust with density increasing to 3.0 g/cm^3 for the lower crust. A value of 3.3 g/cm^3 has been adopted for the mare basalts. A decrease of the mean density to 2.4 g/cm^3 has been assumed for the uppermost layers to a depth of 3–4 km presumed due to the loosening by impacts in agreement with measurements of Talwani et al. (1973) on returned samples. According to Solomon (1974), the upper mantle density should be rather high and is assumed here to be 3.5 g/cm^3. A boundary condition for the thickness of the mare basalts has been adopted from investigations by De Hon and Waskom (1976). They found a maximum thickness of 1–2 km in the shelf areas of the mare basins from rim height estimations for impact craters partially buried by mare basalts. A further confirmation of this result is given by Andre et al. (1979) from orbital X-ray data. According to Hörz (1978) the mare basalt thicknesses found by De Hon and Waskom (1976) should be reduced by a factor of 2. Thus the maximum thickness of the mare basalts should be much less than 10 km. A maximum value of 7 km is used in this paper.

Each mascon model proposed must be in accordance with a reasonable model history, which depends on the initial depth of the impact basin. Estimations of this depth differ over a very large range: Head et al. (1975) estimate for Imbrium a value of 8–27 km, while Dence (1977) assumes, for the same basin, 160 km. Thus this boundary condition cannot provide much constraint in model construction.

Values of the boundary conditions are summarized in Table 1.

Non-Isostatic Mascon Models

In this section some basic non-isostatic mascon model solutions from the literature are presented and a further development of these models is described for the mascons of Mare Crisium and

Table 1

Topography (mare basin depth)	2.3 km 1.65 km	Crisium Serenitatis
Mean crustal thickness	60 km	
Density-depth distribution	2.4 g/cm^3 2.7 g/cm^3 2.9–3.0 g/cm^3 3.3 g/cm^3 3.5 g/cm^3	uppermost crust upper crust lower crust mare basalts upper mantle
Thickness of mare basalts	$\leqq$ 1–2 km $\leqq$ 7 km	shelf areas central areas
Initial depth d of the impact basins	10 km $< d <$ 160 km	

Mare Serenitatis. A similar investigation has been presented by Sjogren and Smith (1976) for the Orientale basin.

All models have been fitted to the gravity maxima of both Crisium and Serenitatis in order to take into account the long distance effects of gravity. As a first step, the mass models have been fitted to the high altitude orbit Apollo 15 CSM, revolution 15. Different model solutions for Crisium are given in Fig. 3.

Nearly all models (except the "mixed crust model" of Fig. 3d) originate from a medium depth of the initial impact basin of several tens of kilometers.

Figure 3a represents the near surface solution (Conel and Holstrom 1968). The mare basalt thickness of 26.5 km is considerable and not compatible with the boundary condition of thin mare basalts.

The mantle plug solution of Wise and Yates (1970) is presented in Fig. 3b. It is assumed in this model that the mare basalts have no excess density or are negligibly thin. Relative large vertical movements of the crust-mantle boundary are necessary in order to explain a mantle plug of 40 km. Two processes could be responsible for a Moho rise: (1) rebound immediately after the impact and (2) later isostatic adjustment.

Figure 3c shows the two-body mare basalts and mantle plug model previously suggested by Bowin et al. (1975). In order to observe the boundary condition of 7 km mare basalt thickness, a mantle plug of 25 km is required.

In Fig. 3d a mixed crust consisting of crustal and intruded mantle material is introduced in addition to a thin mare basalt layer. Intrusions of mantle material into the crust underlying the basin are favoured (1) by the hydrostatic pressure deficit of the basin and (2) by the disturbed crust consisting of fallback breccia in the upper part and a ruptured zone in the lower part, down to the mantle and, perhaps, reaching into the upper mantle. A relative density increase with regard to the undisturbed crust, of from 0.2 at the uppermost crust to 0.4 g/cm^3 at the Moho, is introduced for the crust-mantle mix. This two-body model requires an initial basin depth of only a few kilometers, in agreement with the estimation of Head et al. (1975) due to its thin mare basalt layer of 3.5 km.

All previous model types are combined in the three-body model suggested last (Fig. 3e): (1) a mare basalt thickness of 6 km, in agreement with the boundary condition of a thin mare basalt layer, (2) a mixed crust with a density increase of 0.2 g/cm^3, and (3) a moderately sized mantle plug of 12 km. Based on this model, an example of a complete model for Serenitatis and Crisium, together with measured and computed gravity anomalies, is presented in Fig. 4.

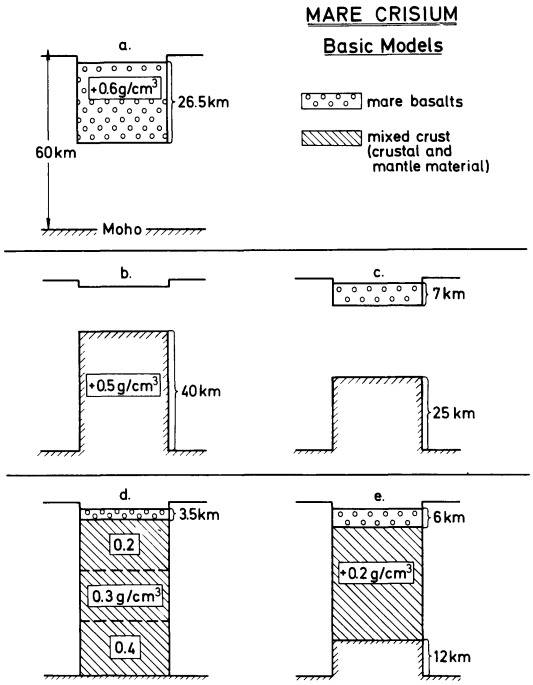

Fig. 3a–e. Basic gravity model solutions of Crisium (all calculated models include a mass model of Serenitatis), Apollo 15 CSM, Rev. 15. **a** Mare basalts (Conel and Holstrom 1968); **b** mantle plug (Wise and Yates 1970); **c** mare basalts and mantle plug (Bowin et al. 1975); **d** mare basalts and mixed crust (consisting of crustal and mantle material); **e** mare basalts, mixed crust, and mantle plug. (**a**, **b**: one-body models; **c**, **d**: two-body models; **e**: three-body model)

An Isostatic Model Solution

Non-isostatic mascon models cause considerable stress differences in the crust and mantle (Figs. 9 and 10). That is, the mass surpluses should have sunk into the mantle since their formation about 3×10^9 years ago, if the viscosity of the upper mantle is low. This may be the case for some high temperature models which have near-solidus temperatures at a depth of 200 km (Kuckes 1974; Sonett and Duba 1975). Isostatic modesl circumvent this problem provided that the depth of compensation lies far enough above the zone of near-solidus temperatures. Thus, the schematic solution pursued here aimed to find a minimum level of compansation.

Isostatic mascon models have already been proposed in earlier papers (Hulme 1972; Kunze 1974). They require that $\int_0^{z_0} g(z)\,\Delta\rho(z)\,dz$ where $\Delta\rho(z)$ = lateral density contrast, $g(z)$ = gravity, and z = depth, vanishes at the depth of isostatic compensation z_0. In order to account for the positive gravity anomaly of the mascons, the following restrictions on $\Delta\rho(z)$ are imposed: there must be compensating (1) surplus masses near to the surface producing larger gravity anomalies than observed, (2) there must be compensating mass deficits at depth, whose negative gravity anomalies at the altitude of observation are small compared to the positive anomaly due to the distance effect. The mass deficit due to the topographic depression of the mare surface leads to a further increase of the necessary mass surplus and depth of the mass deficit, respectively.

Kunze (1974) proposed a partial melt of the upper mantle below the basins due to pressure relief after basin excavation. Some melts rise up into the basins leaving a residuum of lower density which represents the compensating deficit mass. The depth

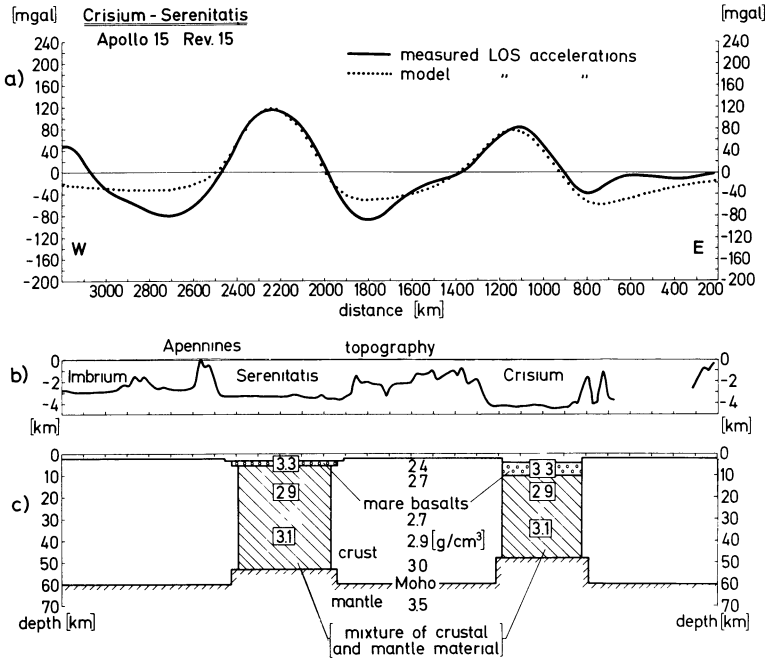

Fig. 4a–c. Model of mare basalts, mixed crust, and mantle plug for Serenitatis and Crisium, Apollo 15 CSM, Rev. 15; zero level of elevation and depth scales is related to a mean lunar radius of 1,738 km.
a Measured and model LOS accelerations;
b topography;
c density model

of compensation in this model lies at 450 km, which is not in agreement with the high temperature models mentioned above. Nevertheless, the possible existance of a compensating body lying higher is not in contradiction to the model history of Kunze.

Hulme (1972) proposed a model which was based mainly on gravitational sinking due to basin loading with heavy mare basalts. Thus, light crustal material is bent down into the higher density mantle causing a compensating body of negative density difference. The depth of compensation in this model lies at 150 km (with the assumption of a mean crustal thickness of 100 km), which is considerably above the zone of near solidus temperatures of the high temperature models.

In this paper, ignoring first the conception of a model history, a minimum depth solution for Crisium has been investigated. For this purpose, the upper limit of 7 km thickness for the mare basalts has been suspended. The mass surpluses of the mare basalts are compensated by an underlying body with negative density contrast to the surroundings of -0.5 g/cm^3

Every attempt failed to achieve isostatic compensation above the depth of the crust-mantle boundary. The final model led to a rather extreme solution with a mare basalt thickness of 60 km with an underlying zone of decreased density down to a depth of 116 km.

The following model history is proposed (compare Fig. 5): An initial basin depth of 100 to 150 km is assumed, consistent with the estimation of Dence (1977). About half the basin was filled with brecciated crustal and mantle material immediately after basin excavation, partly by fallback and partly by basin collapse. The remaining basin was subsequently flooded by mare basalts. Before basin flooding the density of the brecciated zone was 2.5 g/cm^3 or less (Talwani et al. 1973; Cooper et al. 1974). Intrusions of mantle material and later the pressure of the excess masses of the superimposed mare basalts caused a density increase in this zone, up to 3.0 g/cm^3, i.e., the density difference between these compensation masses and the undisturbed upper mantle is -0.5 g/cm^3

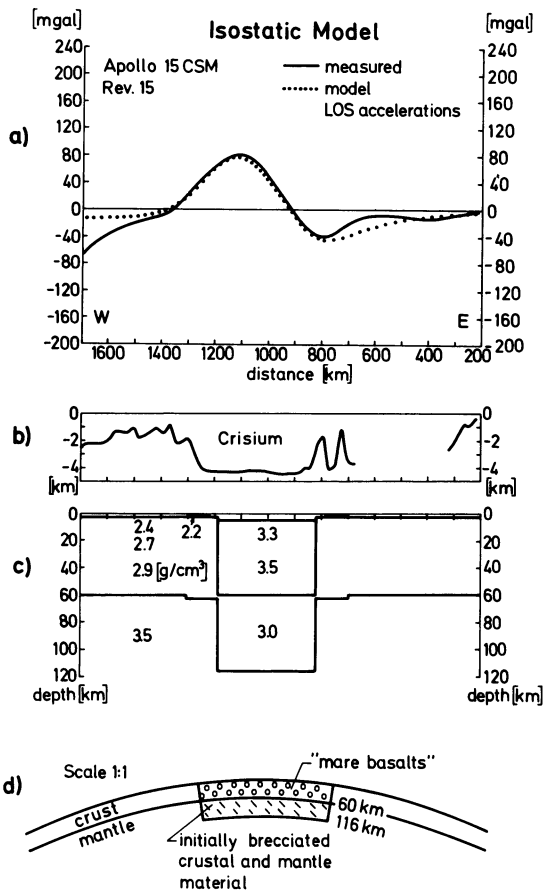

Fig. 5a–d. Isostatic model solution for Crisium, Apollo 15 CSM, Rev. 15. **a** Measured and model accelerations; **b** topography; **c** density model; **d** density model scaled 1:1

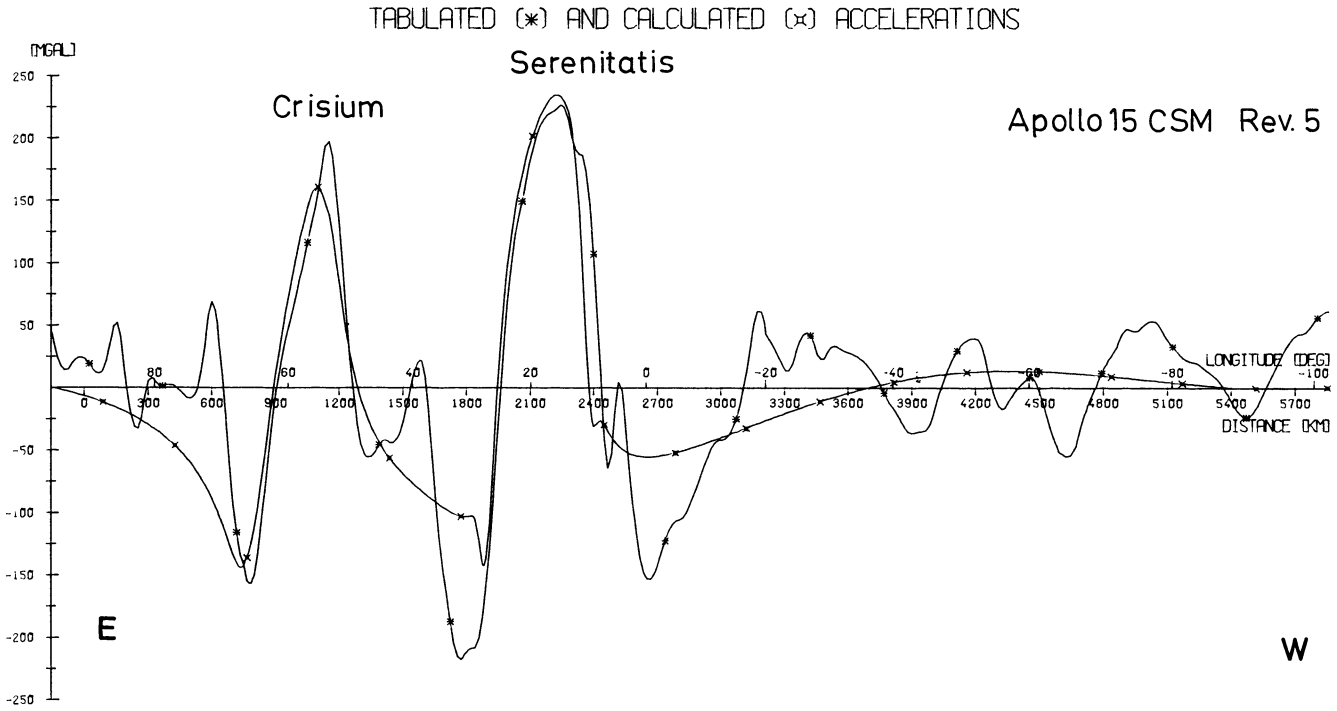

Fig. 6. Calculated gravity of the three-body model of Fig. 3e for Crisium and Serenitatis relating to the orbit of *Apollo 15 CSM, Rev. 5;* no additional fit to gravity of Rev. 5 (tabulated = measured, calculated = model LOS accelerations)

The isostatic model proposed here is very similar to the isostatic solution of Hulme (1972), however, the model histories are partly different.

Model Calculations for the Low Altitude Orbit and Model Discrimination

A strong restriction on the model solutions is given by the boundary condition of thin mare basalts, which rules out the pure basalt model (Fig. 3a) and the isostatic model (Fig. 5).

The model fits described above for revolution 15 have shown that many mass configurations satisfy the measured gravity data. This reflects the ambiguity of the gravity inverse problem. In order to achieve a further discrimination of different model solutions and to select a type for a final complete profile, the LOS gravity of all models presented above has also been computed for the low altitude orbit of Apollo 15 CSM, revolution 5. An example of these calculations is given in Fig. 6. The differences between computed and measured gravity maxima of Crisium and Serenitatis are listed in Table 2.

The model calculations show that the large gravity minima bordering the maria Imbrium, Serenitatis, and Crisium are only partly caused by negative boundary effects of the mascons (Figs. 4 and 6). This problem will be treated in the next section, in connection with a final model solution.

Table 2 shows that model fitting at two different altitudes does not constrain model discrimination significantly. There are still enough free parameters (density differences, height of mantle plug, horizontal extent of mass anomalies) which can be varied in order to fit the gravity anomalies in both orbital altitudes (Compare also differences of measured and calculated gravity of Fig. 6). Thus, the most stringent boundary condition is the upper limit for mare basalt thicknesses of 7 km. As mentioned above, the consideration of the topographic basin also greatly influences the model structure because it considerably increases the gravity anomalies which have to be fitted (Fig. 2).

Table 2. Apollo 15 CSM, Rev. 5. Differences between measured and model gravity maxima, mass distributions of Fig. 3, no additional fit to gravity of Rev. 5

Model type	Serenitatis (max. = 227 mgal)	Crisium (max. = 197 mgal)
Fig. 3		
(a) Mare basalts	38	15
(b) Mantle plug	37	26
(c) Mare basalts + mantle plug	7	50
(d) Mare basalts + mixed crust	−39	45
(e) Mare basalts + mantle plug + mixed crust	− 5	44
Isostatic model (only fit for Crisium, Fig. 5)	–	1

The isostatic model calculated for Crisium only can be excluded because of the extreme mare basalt thickness of 60 km, although it provides an excellent fit to the low altitude gravity data (Table 2).

Considering now the non-isostatic models, both one-body models can be excluded. In one case the mare basalt model (Fig. 3a) with a basalt thickness of 26.5 km is in contradiction to the boundary condition of a thin mare basalt layer. In the other case the mantle plug model (Fig. 3b) is in contradiction to the observed existence of high density basalts with a thickness of at least two kilometers. Another objection to this model is the requirement of an extremely high mantle plug of 40 km, i.e.,

$^2/_3$ of crustal thickness. Both two-body models (Figs. 3c, d) and the three-body model (Fig. 3e) agree with the boundary condition of thin mare basalt thicknesses.

The two-body model, combining a mixed crust and mare basalts (Fig. 3d), differs only slightly from the three-body model. The lower part of the mixed crust with a density difference of 0.4 g/cm^3 can also be interpreted as a mantle plug with minor crustal constituents. Thus, a discrimination between these two models is no longer necessary.

A discrimination between the two-body mare basalt/mantle plug model and the three-body model will now be suggested in relation to basin evolution processes. The mantle plug of 25 km in the two-body model seems to be rather large, but it cannot be excluded in view of rebound processes. The introduction of a zone of crust-mantle mix seems to be reasonable considering the following two processes during basin evolution. (1) in the case of an initial cavity deeper than crustal thickness (Dence 1977) a material mixing results in a crust-mantle mix below the basin, (2) during the mare basalt period, mantle material has intruded into the fractured region below the basins and finally flowed out into the basins; these mantle intrusions result in a density increase below the basins. The introduction of a zone of a crust-mantle mix leads, consequently, to a decrease of the mantle plug, comparing the two-body and the three-body models (Fig. 3c, e).

Summarizing the arguments above leads to the conclusion that the three-body model agrees best with the boundary conditions and the processes of basin building and mascon evolution. This model solution will be developed to a complex model in the next section.

A Complete Crustal Model from Southern Imbrium Over Serenitatis to Crisium

The main problems for a complete model fit of the measured gravity data extending from southern Imbrium over Serenitatis to Crisium are the large regional minima bordering the mascon anomalies (Figs. 4 and 6). They are caused partly by negative boundary effects from the mascons. Ferrari et al. (1978) proposed a crustal thickening between Imbrium and Serenitatis due to rebound processes after the impacts. This model is confirmed by a terrestrial experimental high-explosive crater (Snowball Crater, Roddy 1976, Fig. 15). The idea of crustal thickening has been adopted here. It has been modelled by several discs with a negative density contrast of -0.5 g/cm^3 The maximum thickening necessary is 20 km. In order to include the negative boundary effects of Imbrium on the western shores of Serenitatis, this mascon had also to be considered in the model configuration. The entire model was fitted to both the high and low altitude orbits (Figs. 7 and 8).

The final crustal model presented here gives a solution satisfying the gravity data of high and low altitude profiles for a rather large area with an extent of 3,000 km, i.e., long distance effects of the mascons of Imbrium, Serenitatis and Crisium and of the crustal thickenings are considered. The introduction of a mixed crust has the advantage of avoiding extremely thick mare basalts and large mantle plugs.

Conclusions

Considering the problem of isostasy of the complex model presented here, the central mascon area with its high positive lithostat-

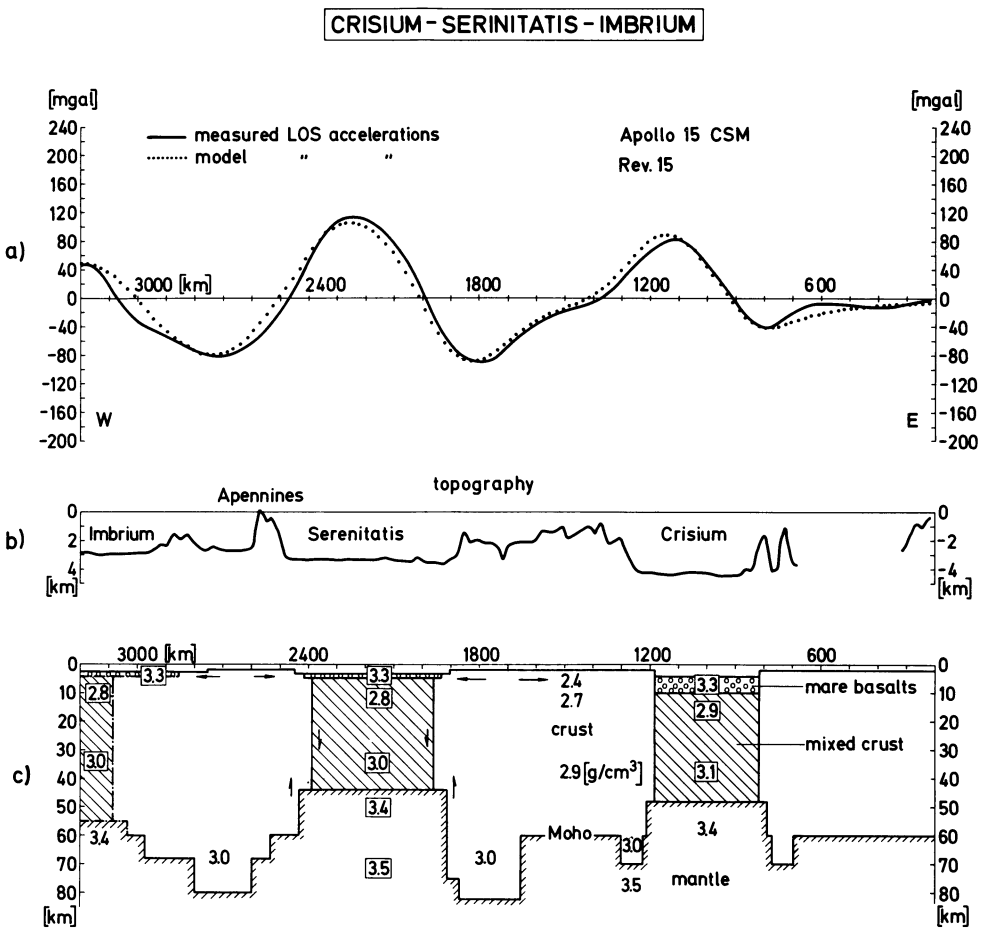

Fig. 7a–c. Complete crustal model from southern Imbrium over Serenitatis to Crisium, *Apollo 15 CSM, Rev. 15.*
a Measured and model accelerations;
b topography;
c density model (*half arrows* indicate tendencies of crustal uplift and sinking, *full arrows* indicate areas of extensional surface stresses)

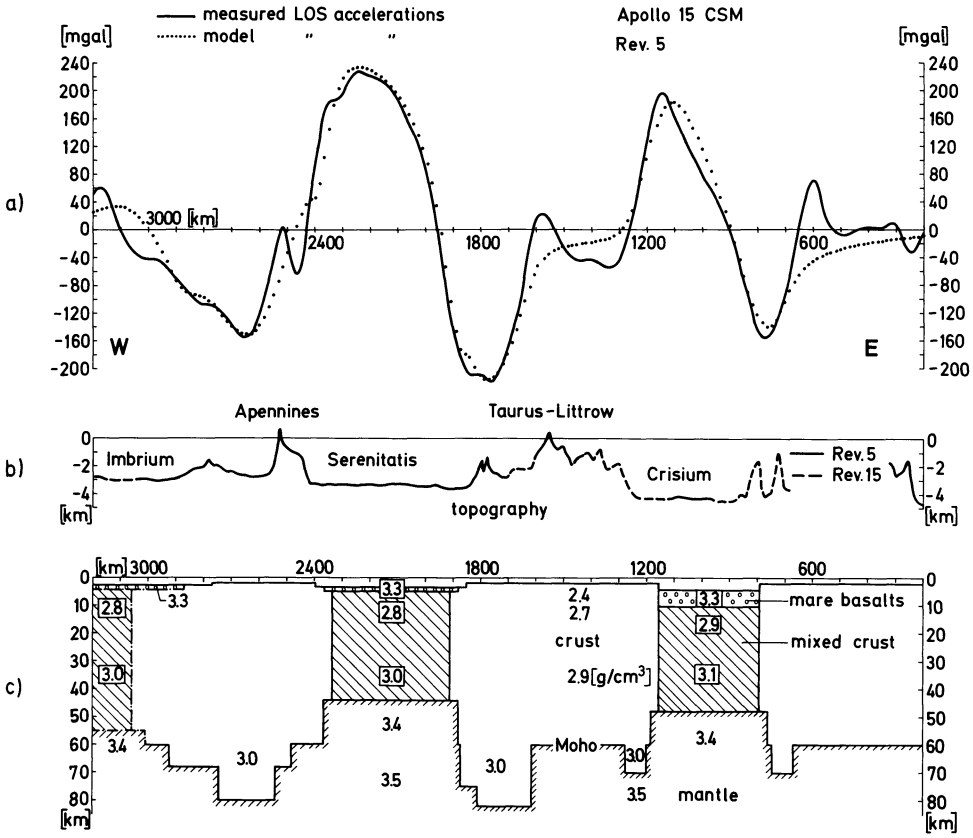

Fig. 8a–c. Complete crustal model from southern Imbrium over Serenitatis to Crisium, *Apollo 15 CSM, Rev. 5.*
a Measured and model accelerations;
b topography;
c density model

ic stresses of 150–180 bar (Fig. 9) should have a tendency to crustal sinking (mass surpluses are associated in this paper with positive lithostatic stresses, mass deficits with negative stresses).

Compensation of the mass deficits of the 20 km crustal thickenings should result in a surrounding mountain range with an elevation of 4.2 km. From the elevation profiles of Figs. 7 and 8, there is no indication, in the areas of crustal thickening, of such large mountain ranges; i.e., the mass deficits are more or less uncompensated. Assuming a density difference of -0.5 g/cm^3 leads to negative lithostatic stresses of -161 bars with an uplift tendency. This is the same order of magnitude as the positive stresses of the central mascon areas. Thus the contact zones of the areas of crustal sinking and uplift should be favoured for progressive tectonic failure zones.

These conclusions are in accordance with two morphologic structures: (1) the basin edges are favoured for the origin of the youngest lava flows (Boyce 1976); (2) the tendency to crustal sinking in the mascon area combined with the tendency to crustal uplift in the bordering zones results in an extensional stress field in the bordering zones, which may be the cause for the surrounding rilles of many maria (Fig. 7). Extensional stresses for the bordering zones of Serenitatis have been calculated by Solomon and Head (1979) based on a one-body mare basalt model. The crustal thickenings proposed in the model of this paper lead to a strengthening of the surrounding extensional stress field.

In the following the question of stability of non-isostatic mascon models is discussed.

Age determinations of mare basalts showed that the main phases of basin filling are terminated at about 3×10^9 years B.P., although many younger flows exist, up to 2.5×10^9 years B.P. (Boyce and Johnson 1978; Boyce 1976). This means that the lunar crust/mantle system must have been able to sustain lithostatic stresses of 160 to 180 bars (Fig. 9) for 3×10^9 years.

The lithostatic stresses acting on the mantle can be used (1) to estimate the upper mantle viscosity η and (2) to calculate the maximum shear stresses applied to the upper mantle.

(1) Considering the lunar mantle as a half space with the rheologic properties of a Maxwell body, the elastic and viscous parts can be decoupled for long loading times (Cathles 1975, pp. 59–60). Assuming a cylindrical load, the vertical elastic displacement u and the vertical viscous displacement velocity v for the center of the load are given by Nadai (1963), pp. 241–246):

$$u = \frac{(1-\sigma)\, P_z\, a}{k}$$

$$v = \frac{\Delta z}{\Delta t} = \frac{P_z\, a}{2} \qquad \eta = \frac{P_z\, a\, \Delta t}{2\, \Delta z}$$

where

P_z = load (lithostatic stress, Fig. 9)
a = radius of the load
σ = Poisson ratio
k = modulus of shear
Δz = vertical displacement of the load
Δt = loading time

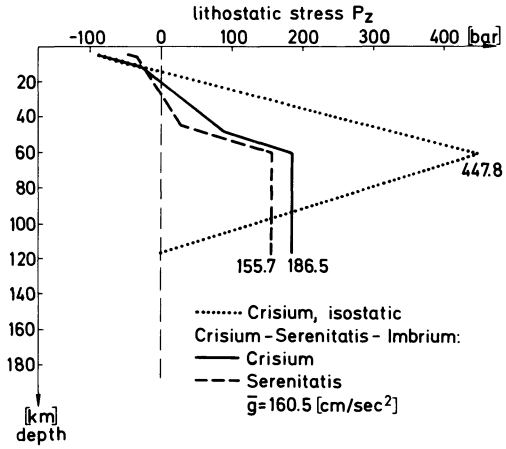

Fig. 9. Lithostatic stresses P_z of Serenitatis and Crisium (relating to mass distributions of Figs. 5 and 7). $\left(P_z=\bar{g}\sum_{i=1}^{n}\Delta\rho_i\Delta z_i;\ \bar{g}=\text{mean acceleration},\ n=\text{number of layers with density } \Delta\rho_i \text{ and thickness } \Delta z_i\right)$

A Poisson ratio of 0.25 is adopted from Nakamura et al. (1976). A shear modulus k of 7.7×10^{11} dyne/cm^2 is found using $k=\rho V_s^2$, with an upper mantle density ρ of 3.5 g/cm^3 used in this paper and an upper mantle shear wave velocity V_s of 4.7 km/s (Nakamura et al. 1976).

The vertical displacement Δz of the load results from elevation statistics of Runcorn (1974), who found a systematically lower level of 1 to 1.5 km of the circular maria relative to the irregular maria which are older and do not have excess masses.

All parameters used in displacement and viscosity calculations are summarized in Table 3.

The elastic displacement u is about 35 m for Crisium and Serenitatis. This value may be neglected in relation to 1 km of total sinking. An effective upper mantle viscosity of 10^{27} poise assumed constant for the whole time period of 3×10^9 years, is obtained. This value is in agreement with investigations of Arkani-Hamed (1973) for postmare viscosity and Meissner (1975).

In reality there should be a gradual increase of viscosity with time due to cooling; however the sparse data included in the estimations in this investigation do not justify evaluation of more detailed viscosity models.

(2) Maximum shear stresses (τ_{max}) applied to the upper mantle half space can be calculated from lithostatic stresses of Crisium and Serenitatis with the assumption of cylindrical loading (Fig. 9; Nadai 1963, p. 245):

$$\tau_{max}=(^1/_4)P_z(-1+2\sigma-2(1+\sigma)z(a^2+z^2)^{-1/2}+3z^3(a^2+z^2)^{-3/2}$$

z = depth

The resulting maximum shear stresses in the upper mantle are shown in Fig. 10.

These results have an important bearing on the lunar thermal history. The high average effective upper mantle viscosity of 10^{27} poise and the shear stresses of 65 bar at a depth of 200 km are not compatible with some temperature models (Kuckes 1974; Sonnett and Duba 1975) which are not more than about 200° K below the solidus at this depth. Considering a mantle solidus of about 1,600° K (T_m) at a depth of 200 km (Hodges and Kushiro 1974) a mantle temperature of 1,300° K (T) yields a relation

Table 3

Load P_z	Crisium	186.5 bar
	Serenitatis	155.7 bar
Radius a	Crisium	182 km
	Serenitatis	243 km
Poisson ratio		0.25
Shear modulus K		7.7×10^{11} dyne/cm^2
Loading time Δt		3×10^9 years
Vertical displacement Δz of the load		1 km

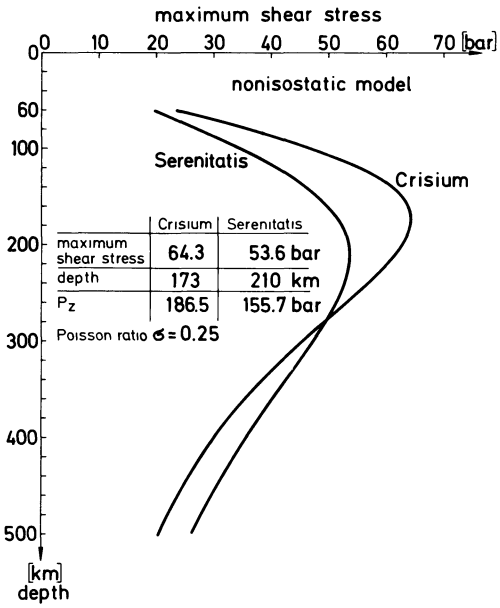

Fig. 10. Maximum shear stresses below Serenitatis and Crisium (relating to mass distributions of Fig. 7)

$T/T_m=0.8$. A conversion of T/T_m into viscosity, according to the method of Meissner and Lange (1977), gives a value of less than 10^{20} poise which is unreasonably low.

Turcotte (1979) developed a stress relaxation temperature T_e depending on an olivine deformation law:

$$T_e=\frac{6.16\times10^4}{\ln(2.62\times10^9\,\sigma_0^2\,t_r)}$$

(σ_0 = initial stress in bars, t_r = relaxation time in s, T_e in °K).

Assuming for the lunar case $\sigma_0=100$ bar and $t_r=10^9$ years gives in $T_e=900$° K. This result shows that high temperature models are not compatible with significant mascon stresses. Recent calculations of upper mantle temperatures by Keihm and Langseth (1977), which vary from 300° K to 600° K below the solidus at a depth of 200 km, are more appropriate to a high upper mantle viscosity and the existence of significant shear stresses. Considering the estimation of the stress relaxation temperature above, the cooler values should be preferred.

The discussion above did not consider the effect of the absence of volatiles, especially water, in lunar materials. Laboratory investigations by Mitzutanni et al. (1977) and theoretical calculations by Kirby (1977) and Meissner (in press 1980), in the case of

the Earth, show an increase of strength with decreasing water content of the materials. Since it seems impossible to extrapolate from terrestrial conditions to the moon, a repetition of these experimental and theoretical investigations under lunar conditions, especially under totally dry conditions, is necessary.

Acknowledgements. This study was sponsored by the Deutsche Forschungsgemeinschaft (German Research Society). I thank Dr. W.L. Sjogren, Jet Propulsion Laboratory in Pasadena, California, for leaving the program ORBISIM which made the model calculations possible. The gravity data from the Apollo missions were made available by World Data Center A in Greenbelt, Maryland. I want to thank Professor Dr. R. Meissner, Dr. A. Binder, and Dr. J. Voss, Kiel, for reading the manuscript and for helpful discussions. I am further indebted to J. Ropers, Hamburg, for computational support.

References

Andre, C.G., Wolfe, R.W., Adler, K., Clark, P.E.: Mare basalt depth from orbital X-ray data. Lunar Planet. Sci. **10**, 38–40, 1979

Arkani-Hamed, J.: Viscosity of the Moon I. The Moon **6**, 100–111, 1973

Boyce, I.M.: Ages of flow units in the lunar nearside maria based on Lunar Orbiter IV photographs. Proc. Lunar Sci. Conf. 7th, 2717–2728, 1976

Boyce, I.M., Johnson, D.A.: Ages of flow units in the eastern maria and Mare Humorum based on crater density. Lunar Planet. Sci. **9**, 117–119, 1978

Bowin, C., Simon, B., Wollenhaupt, W.R.: Mascons: A two-body solution. J. Geophys. Res. **80**, 4947–4955, 1975

Cathles, L.M., III: The viscosity of the earth's mantle. Princeton, New Jersey: Princeton University Press 1975

Conel, J.E., and Holstrom, G.B.: Lunar mascons: A near-surface interpretation. Science **162**, 1403–1405, 1968

Cooper, M.R., Kovach, R.L., Watkins, J.S.: Lunar near-surface structure. Rev. Geophys. and Space Phys. **12**, 291–308, 1974

De Hon, R.A., Waskom, J.D.: Geologic structure of the eastern mare basins. Proc. Lunar Sci. Conf. 7th, 2729–2746, 1976

Dence, M.R.: Meteoritic bombardment of the moon. Philos. Trans. R. Soc. London A. **285**, 259–265, 1977

Ferrari, A.J., Nelson, D.L., Sjogren, W.L., Phillips, R.J.: The isostatic state of the lunar Apennines and regional surroundings. J. Geophys. Res. **83**, 2863–2871, 1978

Gottlieb, P.: Estimation of local gravity features. Radio Sci. **5**, 303–312, 1970

Head, J.W., Settle, M., Stein, R.S.: Volume of material ejected from major lunar basins and implications for the depth of excavation of lunar samples. Proc. Lunar Sci. Conf. 6th, 2805–2829, 1975

Hodges, F.N., Kushiro, I.: Apollo 17 petrology and experimental determination of differentiation sequences in model moon composition. Proc. Lunar Sci. Conf. 5th, 505–520, 1974

Hörz, F.: How thick are lunar mare basalts? Proc. Lunar Sci. Conf. 9th, 3311–3331, 1978

Hulme, G.: Mascons and isostasy. Nature **238**, 448–450, 1972

Keihm, S.J., Langseth, M.G.: Lunar thermal regime to 300 km. Proc. Lunar Sci. Conf. 8th, 499–514, 1977

Kirby, S.H.: State of stress in the lithosphere: inferences from the flow laws of olivine. Pure Appl. Geophys. **115**, 245–258, 1977

Kuckes, A.F.: Lunar magnetometry and mantle convection. Nature **252**, 670–672, 1974

Kunze, A.W.G.: Lunar mascons: another model and its implications. The Moon **11**, 9–17, 1974

Meissner, R.: Lunar viscosity as obtained from the selenotherms. The Moon **12**, 179–191, 1975

Meissner, R.: Limits on stresses in continental crusts. J. Geophys. Res. in press, 1980

Meissner, R., Lange, M.: An approach for calculating temperatures and viscosities in terrestrial planets. Proc. Lunar Sci. Conf. 8th, 551–562, 1977

Michael, W.H., Blackshear, W.T : Recent results on the mass, gravitational field and moments of inertia of the moon. The Moon **3**, 388–402, 1972

Mizutanni, H., Spetzler, H., Getting, I., Martin, R.J., III, Soga, N.: The effect of outgassing upon the closure of cracks and the strength of lunar analogues. Proc. Lunar Sci. Conf. 8th, 1238–1248, 1977

Muller, P.M., Sjogren, W.L.: Mascons: Lunar mass concentrations. Science **161**, 680–684, 1968

Nadai, A.: Theory of flow and fracture of solids, vol. 2. New York, Toronto, London: McGraw-Hill 1963

Nakamura, Y., Latham, G.V., Dorman, H.J., Duennebier, F.K. Seismic structure of the moon: a summary of current status. Proc. Lunar Sci. Conf. 7th, 3113–3121, 1976

Phillips, R.J., Sjogren, W.L., Abbott, E.A.: Simulation gravity modelling to spacecraft-tracking data: analysis and application. J. Geophys. Res. **83**, 5455–5464, 1978

Roddy, D.J.: High-explosive cratering analogs for bowl-shaped, central uplift and multiring impact craters, Proc. Lunar Sci. Conf. 7th, 3027–3056, 1976

Runcorn, S.K.: On the origin of mascons and moonquakes. Proc. Lunar Sci. Conf. 5th, 3115–3126, 1974

Schimerman, L.A. (ed.): NASA lunar cartographic dossier, vol. 1. St. Louis: Defense Mapping Agency, Aerospace Center 1973

Sjogren, W.L., Anderson, J.D., Phillips, R.J., Trask, D.W.: Gravity fields. IEE transactions on Geoscience electronics, **GE-14**, 1972–183, 1976

Sjogren, W.L., Smith, J.C.: Quantitative mass distribution models for Mare Orientale. Proc. Lunar Sci. Conf. 7th, 2639–2648, 1976

Solomon, S.C.: Density within the moon and implications for lunar composition. The Moon **9**, 147–166, 1974

Solomon, S.C., Head, J.W.: Vertical movement in mare basins: relation to mare emplacement, basin tectonics, and lunar thermal history. J. Geophys. Res. **84**, 1664–1682, 1979

Sonnett, C.P., Duba, A.: Lunar temperature and global heat flux from laboratory electrical conductivity and lunar magnetometer data. Nature **258**, 118–121, 1975

Talwani, M., Thompson, G., Dent, B., Kahle, H.-G., Buck, S.: Traverse gravimeter experiment. In: Apollo 17, Preliminary Science Report. NASA SP-330, 13-1-13-13, 1973

Toksöz, M.N., Press, F., Dainty, A.M., Anderson, K.R.: Lunar velocity structure and compositional and thermal inferences. The Moon **9**, 31–42, 1974

Turcotte, D.L.: Flexure. Adv. Geophys. **21**, 51–86, 1979

Wise, D.U., Yates, M.T : Mascons as structural relief on a lunar "Moho" J. Geophys. Res. **75**, 261–268, 1970

Received September 18, 1979; Revised Version March 13, 1980
Accepted July 2, 1980

J. Geophys. 49, 66–68 (1981)

Journal of Geophysics

On the Origin of the Annual Wave in Hemispheric Geomagnetic Activity

J. Meyer [1] and D. Damaske [2]

[1] Institut für Geophysik, Universität Göttingen, Herzberger Landstraße 180, D-3400 Göttingen, Federal Republic of Germany
[2] Institut für Geophysikalische Wissenschaften, Freie Universität Berlin, Rheinbabenallee 49, D-1000 Berlin 33

Abstract. The modulation of hemispheric magnetic activity (as measured by *Kn* and *Ks*) displays a specific modification compared to planetary activity (*Km* indices), in terms of both the diurnal UT variation and the appearance of an additional annual wave. To allow for the observational results Damaske (1976, 1977) suggests a modification of the planetary modulation function $\sin^2\beta$ (where β is the angle between the solar wind flow and the earth's dipole axis) through an additional constant angle β_0. In a quite different interpretation Mayaud (1977, 1978), while retaining the modulation function unchanged, attributes the observed modifications to the combined action of various sources: the main component involving certain LT features in connection with DP2 fluctuations, and a second component related to a universal modulation of the LT variation. The present paper demonstrates that the latter interpretation fails quantitatively in explaining sufficiently all of the observed hemispheric effects.

Key words: Geomagnetic activity – Annual wave – Hemispheric activity indices.

Introduction

Despite the well-known 6-month wave in geomagnetic acitivty, the search for a persistent 12-month wave has long met with failure, as long as the analysis has been based on monthly means of daily values. Only during the past decade, with a refinement of the methods and a new type of data, has the existence of *two* different annual waves definitely been revealed, the two being distinguishable in respect of both their morphological structure and origin.

The first of these two annual waves has been established by Meyer (1972, 1973) through a harmonic sequence analysis of daily values at intervals of 27 days, i.e., one solar rotation. Its amplitude is large (almost 3 times that of the semiannual wave) for years before and including sunspot minima, whereas the wave is almost vanishingly small in years around sunspot maxima. Its phase changes arbitrarily with a wave maximum close to either one of the two equinoxes. Hence the wave is partially averaged out when utilizing monthly means and thus could not be detected by ordinary harmonic analysis of monthly values. Meyer (1972, 1973) has interpreted this kind of annual wave as a temporary north-south asymmetry of the large-scale solar wind structure within single solar sectors in connection with the same magnetospherical modulation mechanism responsible for the semiannual wave. The results of Berthelier (1975; Fig. 1a, b) indicate that the polarity of the interplanetary field with its quasi-persistent sector structure may also be essential for producing the observed effect.

The second kind of annual wave was disclosed by Damaske (1976, 1977, 1978) from 27-day means of *hemispheric* activity indices, again through a harmonic sequence analysis. In the case of the quasi-logarithmic indices (*Kn, Ks*), the amplitude of this hemispheric annual wave is also larger than that of the semiannual wave and appears to be independent of the solar cycle (with a slightly, but not significantly, larger magnitude for the southern hemisphere). Its phase, however, is nearly opposite in each hemisphere, corresponding to a wave maximum close to the respective meteorological summer solstice. Hence, this wave is again averaged out when utilizing planetary, i.e., worldwide indices and thus could not be detected in *Km* or *Kp*. Damaske (1976, 1977) reduces this annual wave, as an additional hemispheric effect, to a modification of the modulation function $\sin^2\beta$ describing the modulation of *planetary* magnetic activity (where β is the angle between the direction of the solar wind flow and the earth's dipole axis). Physically, this modification implies a modified modulation mechanism without involving additional excitation.

In effect, the hemispheric annual wave corresponds to the observed winter-summer difference in geomagnetic activity (Wulf 1971), as well as to the annual wave noticed in ratios (Mayaud 1972) or differences (Berthelier 1975; Fig. 1c) between the magnetic activity in each hemisphere. However, the qualitative methods applied have in no case led to an accurate determination of the amplitude and phase of the observed periodicity. Recently Mayaud (1977) has investigated further the annual wave in hemispheric activity indices, again by various superposed epoch analyses. His analyses also include separate studies for the eight (i.e., five northern and three southern) longitude sectors from which the hemispheric indices are derived. He suggests that the annual wave is due mainly to two additional and independent sources whose effects are then superimposed on the general planetary modulation through $\sin^2\beta$: the one consisting of additional activity around local afternoon, predominantly during summer, in connection with the DP2 fluctuations; the other being related to a multiplicative modulation of the local time (LT) variation of activity, again by the function $\sin^2\beta$ (see also Mayaud, 1979). The purpose of the present paper is to examine quantitatively to what extent the two components of this source model can actually contribute to the observed hemispheric annual wave and whether this model may possibly provide an equally valid or still better representation of the observational results than does the modified modulation function.

0340-062X/81/0049/0066/$01.00

The Modified Modulation Function

The classical method of investigating a given periodicity in geophysics is the statistical harmonic analysis developed by Bartels (1932, 1935; see also Chapman and Bartels 1940) and, for many years, applied successfully by Bartels and his co-workers. The strength of this method is that, through combination with a variance test, it yields at the same time quantitative statements on the significance of the results. The harmonic sequence analysis introduced by Meyer (1972, 1973) is a modified version especially suited to the study of annual variations in solar-terrestrial relationships.

With regard to planetary activity indices (such as the 3-hourly *Km* and daily *C9*), a complete harmonic analysis of daily and annual variations has yielded harmonic constituents which are in full accordance (within the limits of statistical error) with the ones obtained by a Fourier expansion of the modulation function $\sin^2\beta$, in terms of both phase and amplitude ratio (Damaske 1976, 1977). All significant periodicities (diurnal, semidiurnal waves including their annual amplitude modulation, and the semiannual wave) and *only* these are represented by the expanded planetary modulation function. Accordingly, $\sin^2\beta$ provides a complete representation of planetary activity modulation.

Likewise, a comprehensive harmonic analysis of quasi-logarithmic *hemispheric* indices (3-hourly *Kn, Ks* and daily *C9n,s*) has revealed, as specific features, a modification of the diurnal UT wave and an additional (hemispheric) annual wave (Damaske 1976, 1977). Apart from merely statistical scattering it appears that the seasonal average vectors in the harmonic dial for the diurnal wave are systematically shifted towards the mean vector direction during meteorological winter. The same finding is readily apparent in a corresponding shift of the annual amplitude modulation curve for the diurnal wave in either hemisphere. It is equivalent to an additional diurnal wave in both hemispheres, with *constant amplitude and phase* throughout the year. Its maximum occurs near the hour of planetary wave maximum in local winter, i.e., at 04.30 hours UT in the southern hemisphere and 16.30 hours UT in the northern. Thus the total diurnal wave appears enhanced in local winter and diminished during local summer. Damaske (1976, 1977) accounts for the observed hemispheric modification of the diurnal wave by a modification of the modulation function $\sin^2\beta$ through an additional constant angle β_0 (with $\beta_0 = \pm 11°$, as computed from the amplitude ratio of the planetary diurnal wave to the additional wave). Subsequently, by another Fourier expansion, he was able to deduce, from the modified modulation function $\sin^2(\beta+\beta_0)$, the particulars of all significant (and *only* the significant) periodicities in *Kn* and *Ks* including the hemispheric annual wave, within the limits of statistical error. Hence, the modified modulation function provides again a complete representation of hemispheric magnetic activity modulation.

The numerical value of $\pm 11°$ for β_0 ($+11.9°$ and $-10.6°$ for the northern and southern hemispheres, respectively) may well appear somewhat high. But it must again be emphasized that it is the result of a strictly quantitative harmonic analysis which corresponds to a statistical least-square method. As such, the calculated value is of course subject to statistical error. (In fact this is the reason why we are using an integer average of 11°). Hence, any deviation of observational results from that predicted with a certain value of β_0 has to be judged not by its relative amount as Mayaud (1979) does but, instead, relative to the respective probable error circle. In the case of the observed annual wave in the hemispheric *Kn* and *Ks*, the deviation of the result clearly lies within the range of one standard deviation (which is 1.20 times the probable error) from the predicted annual wave (see Damaske 1976, Fig. 32; or Damaske 1977, Fig. 19). From the sample group of years investigated, the value calculated comes out as an amount necessary to allow for the observed modification of geomagnetic acitivity modulation, once a modification of the modulation function $\sin^2\beta$ through an additional constant angle β_0 has been allowed.

Since β refers to the internal dipole of the main geomagnetic field, β_0 can be described formally by an additional tilt of an "effective dipole axis" which is equivalent to an additional external dipole for either hemisphere possibly due to the large-scale magnetospheric current systems in connection with the asymmetric polar oval (Damaske 1976, 1977; Meyer and Damaske 1978). Any physical interpretation of this formal result may, admittedly, be regarded as only tentative. Clearly there has to be made a distinction between definite results of a quantitative analysis of experimental data and their physical explanation.

The DP2 Annual Wave Source

Mayaud (1977, 1979) suggests, as an alternative to the modified modulation function, two main source components, the first consisting of additional magnetic activity especially in the horizontal component around 15.00 hours LT, which Mayaud relates to the DP2 fluctuations. He finds that in either hemisphere the effect is much larger during local summer and almost vanishing in local winter. In the way Mayaud understands and describes the phenomenon, its amplitude variation with longitude would induce an additional UT component in the hemispheric *Kn, Ks* (or *an, as*) which should then account for the observed modification of the diurnal UT variation during local summer. Besides the fact that such a local time effect would create an annual variation in hemispheric indices only if the daily average is also affected (see Damaske and Meyer 1980), the suggested source model fails absolutely in providing a possible explanation for the additional diurnal UT wave in local *winter,* which occurs with the same amplitude and phase as in local summer (see above). Moreover, any additional UT component that is confined to local summer (or any other meteorological season) would be retained instead of being eliminated when averaged over both hemispheres. But such an elimination of the specific hemispheric effects is required for correspondence with the observed *planetary* activity modulation following the $\sin^2\beta$ law. (In particular, since *am* is the average of *an* and *as,* it is quite clear that the activity modulation bearing on *am* has to display exactly the average of the modulation curves for *an* and *as*).

Hence, although the reality of the peculiar LT effect Mayaud discusses is not disputed, it turns out that this phenomenon does not explain sufficiently the observed modification of hemispheric magnetic activity modulation as far as the diurnal UT variation and the annual wave are concerned. It remains to be examined whether the second component of Mayaud's source model might allow for all the deficiencies discovered.

Modulation of the Diurnal LT Variation

The second component of Mayaud's (1977, 1979) annual wave source model is based on the assumption that the daily LT variation at every station undergoes a multiplicative modulation by the planetary modulation function $\sin^2\beta$ (without including the additional angle β_0). As any LT variation can be written formally as a UT variation with longitude dependent phase, such a modulat-

ed sinusoidal LT variation can be expressed (in relative units) by

$$\sin^2\beta \times \cos(t-\lambda+\lambda_0)$$
$$= \sin^2\beta \times \{\cos t \cos(\lambda-\lambda_0) + \sin t \sin(\lambda-\lambda_0)\}, \quad (1)$$

where t is the hour angle of universal time (15° per hour), λ being the (eastward) longitude of the station, and λ_0 a constant phase angle corresponding to the daily maximum of the LT variation. (If the formulation is applied to the southern hemisphere, another phase angle of 180° has to be added to account for the reverse sign of the daily variation at an antipodal station). Replacing $\sin^2\beta$ by its Fourier expansion (Damaske 1976, 1977) and forming daily averages (to determine the annual variation) yields:

$$\frac{1}{2\pi}\int_0^{2\pi} \sin^2\beta \times \cos(t-\lambda+\lambda_0)\,dt$$
$$= \tfrac{1}{2}(0.146\cos\alpha - 0.003\cos 3\alpha)\cos(\lambda-\lambda_0), \quad (2)$$

where α describes the seasonal variation, i.e., increasing by 360° per year with $\alpha=0$ at the beginning of the (northern) summer solstitial day (22 June). All other terms in Eq. (1) have vanished on account of the orthogonality conditions for trigonometric functions.

From Eq. (2) it is immediately apparent that for any longitude λ (or longitude sector) an additional annual wave indeed occurs with constant phase and a longitude dependent amplitude including change of sign, namely: $0.073\cos(\lambda-\lambda_0)\cos\alpha$. (The other harmonic constituent in Eq. (2), of 4 month period, is negligibly small). But this annual wave is completely cancelled out when averaged over all values of λ, i.e., over a full hemisphere. Thus, even when considering the non-homogeneous net of stations, it cannot give a noticeable contribution to the annual wave observed in hemispheric indices *Kn, Ks* or *an, as*.

When averaging Eq. (1) directly over all values of λ (hemispheric averages), for a certain time t (or a certain 3-hour interval), all terms vanish identically because $\sin^2\beta$ is independent of λ. This means that a modulated LT variation also cannot contribute to the UT variation in hemispheric indices. The observed modification of the diurnal UT wave in *Kn* and *Ks* relative to the one in *Km* can in no part be attributed to a universal modulation of the LT variation in the way Mayaud suggests. Such an effect can definitely be excluded from any explanation of the characteristic features of hemispheric activity modulation.

The assumption of a purely sinusoidal LT variation implies no loss of generality. As can easily be shown by Fourier expansion of a non-sinusoidal LT variation, the inferences concerning the annual wave remain unchanged. Additionally, there is a small but persistent (sinusoidal) activity variation with longitude. But again all constituents vanish when averaged over the whole hemisphere, with respect to daily values as well as a particular 3-hour interval.

Conclusions

To summarize, quantitative examination of the two alternative annual wave interpretations has ascertained that the modified modulation function provides at least a complete description of hemispheric activity modulation, as far as magnetic activity is measured by *Kn* and *Ks*. Against this, Mayaud's concept of two additional sources does not explain satisfactorily the observed *hemispheric* effects. Nevertheless, his suggestion of a modulated LT variation may well contribute to an understanding of any superimposed amplitude variation of the annual wave in *sectorial* indices which cannot quite be excluded from the present material (Damaske 1978). It would be highly desirable to investigate this effect further with respect to a higher statistical significance.

References

Bartels, J.: Terrestrial-magnetic activity and its relations to solar phenomena. Terr. Magn. Atmos. Electr. **37**, 1–52, 1932 (reprinted by Carnegie Institution of Washington, 1959a)

Bartels, J.: Random fluctuations, persistence, and quasi-persistence in geophysical and cosmical periodicities. Terr. Magn. Atmos. Electr. **40**, 1–60, 1935 (reprinted by Carnegie Institution of Washington, 1959b)

Berthelier, A.: Influence de la polarité du champ magnétique interplanétaire sur la variation annuelle et sur la variation diurne de l'activité magnétique. C.R. Acad. Sci. Paris, Sér. B: **280**, 195–198, 1975

Chapman, S., Bartels, J.: Geomagnetism, vol. 2. Oxford: Clarendon Press 1940

Damaske, D.: Der Weltzeitgang der erdmagnetischen Aktivität als magnetosphärischer Modulationseffekt. Geophys. Abh., Inst. Geophys., Freie Universität Berlin, Heft 5, Berlin: Reimer 1976

Damaske, D.: Magnetospheric modulation of geomagnetic activity, I. Harmonic analysis of quasi-logarithmic indices *Km, Kn,* and *Ks*. Ann. Géophys. **33**, 461–478, 1977

Damaske, D.: On the annual wave of hemispheric geomagnetic activity. J. Geophys. **45**, 81–90, 1978

Damaske, D., Meyer, J.: Comment on "On the sources of the 12-month wave in the *an* and *as* geomagnetic activity indices" by P.N. Mayaud. J. Geophys. **48**, 54–55, 1980

Mayaud, P.N.: The *aa* indices: A 100-year series characterizing the magnetic activity. J. Geophys. Res. **77**, 6870–6874, 1972

Mayaud, P.N.: Analyse d'une série centenaire d'indices d'activité magnétique, IV Les diverses composantes de l'onde annuelle aux latitudes subaurorales. Ann. Géophys. **33**, 479–501, 1977

Mayaud, P.N.: Morphology of the transient irregular variations of the terrestrial magnetic field, and their main statistical laws. Ann. Géophys. **34**, 243–276, 1978

Mayaud, P.N.: On the sources of the 12-month wave in the *an* and *as* geomagnetic activity indices. J. Geophys. **46**, 261–271, 1979

Meyer, J.: A 12-month wave in geomagnetic activity. J. Geophys. Res. **77**, 3566–3574, 1972

Meyer, J.: Zur Modulation der erdmagnetischen Aktivität. Geophys. Abh., Inst. Geophys., Freie Universität Berlin, Heft 3, Berlin: Reimer 1973

Meyer, J., Damaske, D.: Geomagnetic evidence for large-scale magnetotail current systems. J. Geomagn. Geoelectr. **30**, 207, 1978

Wulf, O.R.: Winter-summer difference in geomagnetic activity. J. Geophys. Res. **76**, 1837–1840, 1971

Received November 28, 1979; Revised Version June 2, 1980
Accepted July 2, 1980

J. Geophys. 49, 69–73 (1981)

Journal of Geophysics

On the Relation Between Magnetic Field-Aligned Electrostatic Electron Acceleration and the Resulting Auroral Energy Flux

K. Wilhelm

Max-Planck-Institut für Aeronomie, D-3411 Katlenburg-Lindau 3, Federal Republic of Germany

Abstract. Supra-thermal electron fluxes measured above auroral arcs aboard two Porcupine sounding rocket payloads in 1977 and 1979 were used to study the relation between the acceleration potential difference as deduced from the position of the peak in the energy spectrum and the resulting electron energy flux. It was found, contrary to the findings of other authors, that the dependence of the energy flux on the acceleration voltage could be described by a linear relationship to a good approximation, above discrete auroral arcs. A stronger dependence of the energy flux on the acceleration voltage was however observed near the edges of auroral forms. Supported by model calculations, the suggestion is put forward that different distribution functions of the source electron populations might be responsible for the change of the relationship.

Key words: Auroral electron flux – Field-aligned electrostatic acceleration.

Introduction

The acceleration or post-acceleration of electrons by electrostatic fields along magnetic lines of force above discrete auroral forms appears to be the only physical concept available for explaining a variety of distinct features of auroral electron distribution functions, such as spectral peaks and field-aligned pitch angle distributions (Whalen and McDiarmid 1972; Evans 1974; Arnoldy et al. 1974; Kaufmann et al. 1976; Mizera and Fennell 1977; Croley at al. 1978; Sharp et al. 1979; Wilhelm 1979). On the other hand, our present knowledge is not sufficient to allow us to understand the acceleration process and the subsequent interactions of the electron beam with the magnetospheric plasma in any detail, as was recently pointed out by Whalen and Daly (1979). Further clarification can be expected to result mainly from observational programmes. Lyons et al. (1979) studied auroral electron fluxes on board several sounding rocket payloads and found a relationship between the net electron energy flux ε into the ionosphere and the acceleration potential difference V_0 of the form $\varepsilon = KV_0^2$ with values of the constant K between 0.1 and 0.96 erg cm^{-2} s^{-1} kV^{-2}, for various auroral conditions. The authors interpret their findings to mean that a direct physical connection exists between the acceleration voltage and the field-aligned current carried by energetic electrons, as derived from the electron energy flux.

In an attempt to verify these observations, the electron flux observations made during the Porcupine sounding rocket flights F-2 and F-4 were studied whenever a well developed peak in the electron energy spectrum could be detected. The results obtained seem to be consistent with the observations by Lyons and co-workers near the edges of auroral forms, but show characteristic differences above discrete auroral arcs.

Observations

Electron spectrometers (denoted KL 7) operating in the suprathermal energy range, from 0.1–25 keV, were flown aboard the Porcupine payloads F-2 and F-4 launched from ESRANGE, Kiruna, on 20 March 1977 at 19:22 UT and on 31 March 1979 at 22:29 UT, respectively. Both flights encountered auroral electron precipitation over discrete auroral forms with maximum energy fluxes in the range 0.1–25 keV of 12 erg cm^{-2} s^{-1} on F-2 and 28 erg cm^{-2} s^{-1} on F-4. No electron fluxes with strongly field-aligned pitch angle distributions could be found during the time intervals showing peaked electron spectra. It was thus possible to simplify the data analysis by selecting an instrument channel (A2) essentially sensitive to downgoing electrons. The measurements of upgoing electrons were limited to a pitch angle range just above 90° thus precluding a determination of the net electron fluxes. However, it has been established in other investigations (Evans et al. 1977; Wilhelm 1979) that a reduction of 15% – 25% of the downcoming energy flux leads to a good estimate of the net flux.

The spectral information obtained during flight F-4 has been compiled in a three-dimensional co-ordinate system in Fig. 1. The payload flew into and over a bright auroral form on its upward flight path and left the intense aurora shortly after 300 s from launch. Within the region of auroral activity, a distinct electron energy peak was developed at an energy of 9 keV at the beginning of the flight, decreasing to less than 1 keV near the nothern edge of the arc. North of this region irregular spectral features prevailed until a knee distribution with low-intensity and a change in slope at 2 keV energy formed for the remaining portion of the flight. In addition to the peak at high energies, a secondary maximum at approximately 2 keV can be noticed before 200 s elapsed time. Details of the spectral features during the time period with peaked energy spectra can be seen in Fig. 2, as well as the continuation to higher energies (Stüdemann, personal communication).

Using the data displayed in Fig. 1, the electron number and energy fluxes were computed and are presented in Fig. 3 together with the values of the peak energies when such a determination was possible. In a similar fashion, the data of flight

0340-062X/81/0049/0069/$01.00

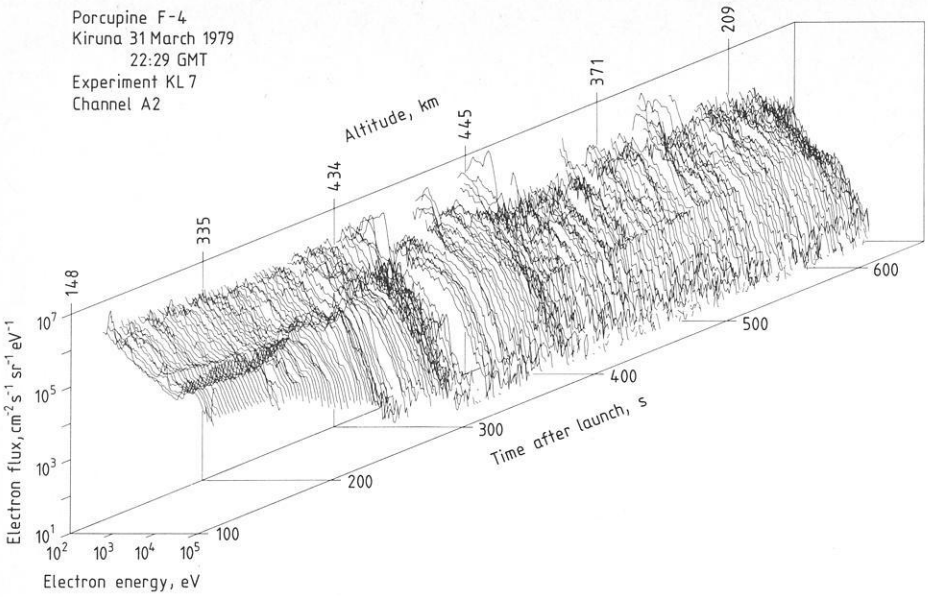

Fig. 1. Electron energy spectra observed during Porcupine flight F-4. The lower energy limits of all spectra were at 0.1 keV and the upper cutoffs at 25 keV. A well developed peak was present during the first part of the flight. Several high-intensity low-energy bursts superimposed on a knee distribution were observed after about 400 s elapsed time

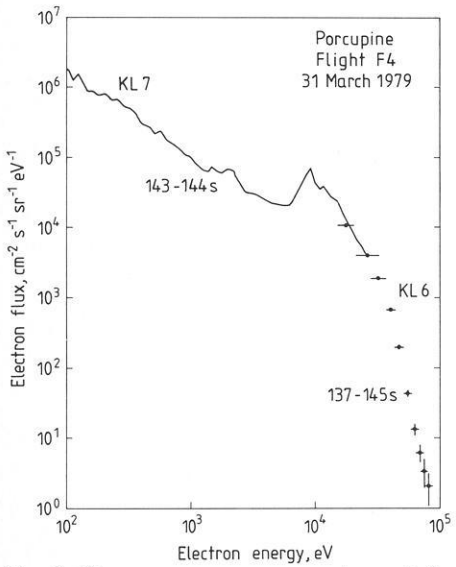

Fig. 2. Electron energy spectrum observed during an interval with a pronounced peak near 9 keV. The measurements have been obtained by two different instruments KL7 in the energy range 0.1–25 keV and KL6, 15–100 keV

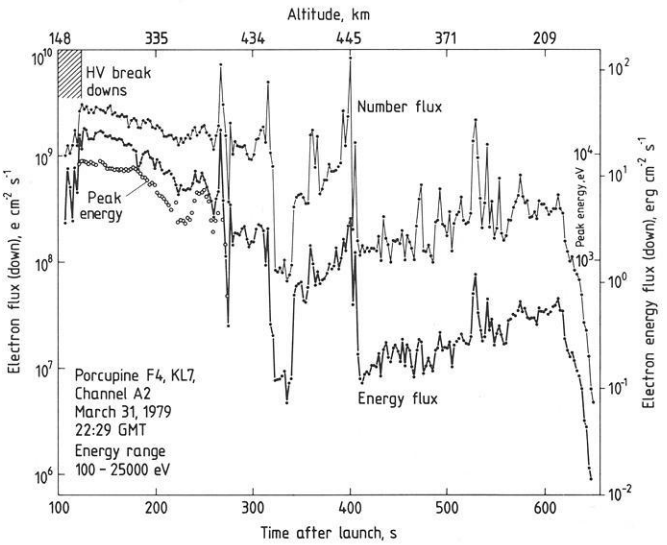

Fig. 3. Electron number and energy fluxes for flight F-4 calculated by using the data of Fig. 1 have been plotted together with the peak energy at the beginning of the observations. The first 20 s of the measurements were influenced by high voltage breakdown within the instrument caused by artificial plasma releases

F-2 have been summarized in Fig. 4. The geophysical conditions during this flight were characterized by several homogeneous auroral arcs. The spectral features allowed a determination of the peak energy for most of the flight time.

Discussion

The measurements made during both flights suggest that a linear relationship exists between the value of the peak energy and the electron energy flux at times of intense electron precipitation. A stronger dependence of the energy flux on the peak energy could be detected near the edges of the auroral forms, in particular near 200 and 330 s elapsed time of flight F-2 and 270 s of F-4. The energy flux was, however, nearly independent of the peak energy during the time interval 470 to 530 s of flight F-2 in Fig. 3. These observations imply that the functional form $\varepsilon = KV_0^2$ derived by Lyons et al. (1979) may not be representative for all auroral conditions. For periods when a linear approximation of the form $\varepsilon = K^* V_0$ was appropriate, the factor K^* was calculated to be equal to 3.2 and 3.0 erg $cm^{-2}\,s^{-1}\,kV^{-1}$ for F-2 and F-4, respectively. The degree of linearity can be seen in Fig. 5 where the electron energy fluxes observed during the first portion of flight F-4 have been plotted as a function of the peak energy, together with the corresponding linear regression. A reduction of the K^* value by 20%, thereby accounting for reflected electrons, gives about 2.5 erg $cm^{-2}\,s^{-1}\,kV^{-1}$. Assuming $\varepsilon = KV_0^2$ to be valid between 200 and 250 s elapsed time of F-2, the value of K has to be chosen to be 0.8 erg $cm^{-2}\,s^{-1}\,kV^{-2}$ in reasonable agreement with the figures obtained by Lyons

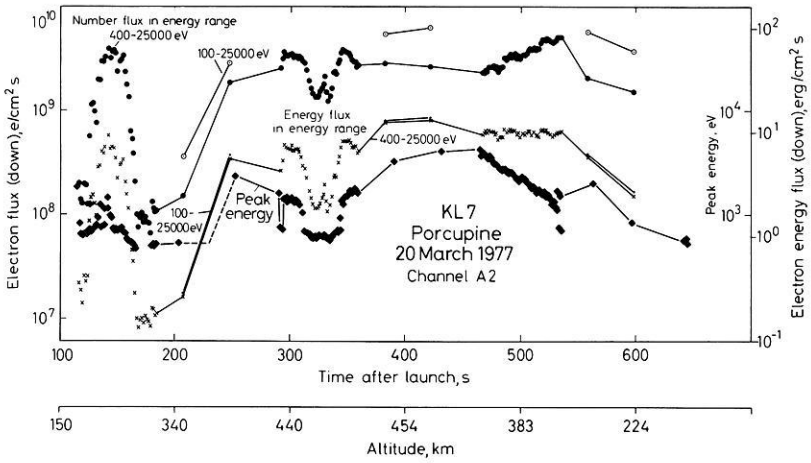

Fig. 4. Electron number and energy fluxes for flight F-2 are shown in the upper graphs. The instrument automatically switched between different modes during this flight leading to varying time resolutions and energy ranges. A peaked spectrum could be observed for most of the flight time with peak energies given in the lower graph

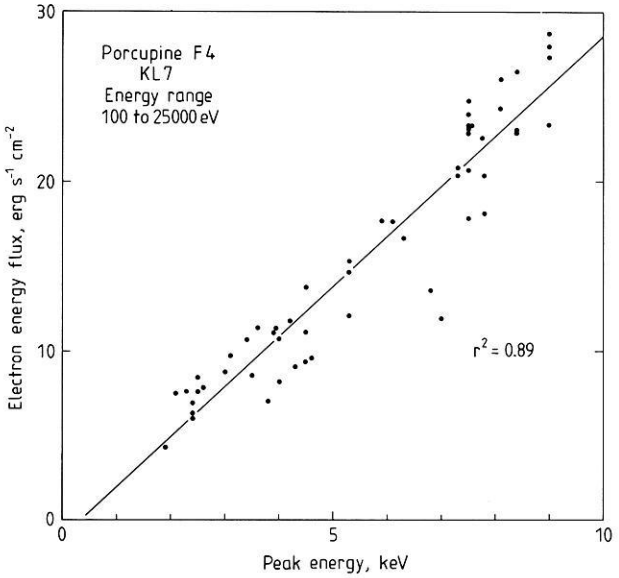

Fig. 5. Electron energy flux in the energy range 0.1–25 keV as a function of the peak energy observed during Porcupine flight F-4. The line of regression and the coefficient of determination are also given

et al. (1979). Both approximations give the same energy flux of 7.8 erg cm $^{-2}$ s $^{-1}$ for a peak energy of 3.1 keV. Whether this crossing point has any physical significance could not be determined from the available data. However, the conclusion seems to be justified that changes of the functional form have occurred near the edges of auroral arcs.

Taking for granted the concept of electrostatic field acceleration as the cause of the peaked energy spectra, an interpretation of the observations might be obtained by the following consideration:

The velocity distribution function of the unaccelerated electron population

$$f_e(\mathbf{v}) = (m_e^2/2W)\, j_e(W, \alpha) \tag{1}$$

where $\mathbf{v}$ is the electron velocity, m_e the electron mass, W the electron energy, α the pitch angle and j_e the directional electron flux, should have a special form defined by

$$j_e(W) = A W^{-\gamma} \tag{2}$$

with $A = 8 \times 10^{11}$ cm^{-2} s^{-1} sr^{-1} eV^{-1}, W measured in eV and $\gamma = 2.5$. No dependence of the downgoing flux on pitch angle was assumed as the observations did not show such a dependence even after the acceleration process. Justification for this rather arbitrary selection may be found in the fact that the high-energy portion of the spectra at 500 s elapsed time given in Fig. 1 could be approximated by such a function and that these spectra do not indicate any post-acceleration effects.

Applying Liouville's theorem to the distribution function above and below the accelerating potential difference, along the dynamical path of the particles, provides the electron flux of the accelerated electron population

$$j_e^*(W^*) = \begin{cases} A \dfrac{W^*}{W^* - \Delta W} (W^* - \Delta W)^{-\gamma} & \text{for } W^* > \Delta W \text{ and } \alpha^* \leqq \alpha_0 \\ 0 & \text{otherwise} \end{cases} \tag{3}$$

with

$$\alpha_0 = \sin^{-1} \left\{ \frac{B^*}{B_0} \frac{W^* - \Delta W}{W^*} \right\}^{1/2}.$$

ΔW is the electron energy gained in the acceleration process and B_0 and B^* are the magnetic field values at the positions considered. Provided the lowest initial energy before the acceleration was $W_0 > 0$, it follows that $W^* \geqq W_0 + \Delta W$. The pitch angle cone $\alpha^* \leqq \alpha_0$ opens up to $\alpha_0 = 90°$ when

$$\frac{B^*}{B_0} \frac{W^* - \Delta W}{W^*} \geqq 1. \tag{4}$$

The observational evidence that no significant dependence of the downgoing electron flux on pitch angle was present during the intervals under discussion suggests that condition (4) was fulfilled for all directly precipitated electrons. Assuming a vertical magnetic field direction and $B \propto R^{-3}$, an electron source distribution at $1 R_E$ (Earth's radius) would thus lead to

$$8(W^* - \Delta W) \geqq W^* \tag{5}$$

showing that the energy W^* after the acceleration could not be greater than 8 times the initial energy of a particular electron.

Alternative explanations involving isotropization by pitch angle scattering that might be appropriate for interpreting the data will not be considered here mainly because of lack of quantitative information on such processes.

Without a dependence upon α^* the electron energy flux

$$\varepsilon = 2\pi \int_0^{\frac{\pi}{2}} \int_0^{\infty} W^* j_e^*(W^*) \sin\alpha^* \cos\alpha^* \, dW^* d\alpha^* \tag{6}$$

can, in a certain energy range, be determined analytically by solving

$$\varepsilon'(W_2, W_1) = \pi \int_{W_1}^{W_2} W^* j_e^*(W^*) \, dW^*. \tag{7}$$

As $j_e^*(W) = 0$ for $W^* < W_0 + \Delta W$, the integral reduces to

$$\varepsilon'(W_2, W_0, \Delta W) = \pi A \int_{W_0+\Delta W}^{W_2} \frac{W^*}{W^* - \Delta W} (W^* - \Delta W)^{-\gamma} \, dW^*. \tag{8}$$

The upper limit will, for all practical purposes, be determined by the restricted energy range of the instrument employed. Here a value of $W_2 = 25$ keV has been used throughout the calculations. However, electrons with higher energies were measured aboard the payload F-4 (Stüdemann, personal communication) and it was therefore possible to evaluate the contribution of electron fluxes with energies above W_2. At 143 s after launch, for instance, when the energy peak was located near 9 keV (Fig. 2), the contribution was 5 erg $cm^{-2} s^{-1}$ as compared to 27 erg $cm^{-2} s^{-1}$ carried by low-energy electrons. The bulk of the energy flux was, therefore, contained in the restricted energy range under the conditions prevailing during the flight.

Equation (8) can be integrated to give the energy flux up to 25 keV

$$\varepsilon'(W_0, \Delta W) = \pi A F(W^*)\Big|_{W_0+\Delta W}^{25\,\mathrm{keV}} \tag{9}$$

with

$$F(W^*) = \frac{(W^* - \Delta W)^{2-\gamma}}{\gamma} \left\{ \frac{2}{1-\gamma} \frac{W^*}{W^* - \Delta W} - \frac{W^{*2}}{(W^* - \Delta W)^2} - \frac{2}{(1-\gamma)(2-\gamma)} \right\}.$$

The energy flux ε' thus becomes a function of W_0 and ΔW. It can easily be shown that ε' can be approximated by a quadratic form of $W_0 + \Delta W$ for values W_0 much smaller than ΔW. This can also be seen from Fig. 6, where examples with $W_0 = 0.05$, 0.1 and 0.2 keV are given. Condition (5) would require that, in this case, field-aligned fluxes should be observable unless the acceleration occurred much higher than $1 R_E$. For higher initial energy cutoffs, e.g., 1, 2 and 4 keV, the dependence of ε' on $W_0 + \Delta W$ becomes weaker and can be described reasonably well by a linear function, at least for certain energy ranges, as demonstrated for the three examples. The sum $W_0 + \Delta W$ was chosen as the independent variable, because this value should be related to the peak energy and thus be conveniently observable.

By comparing the absolute energy flux values in Figs. 5 and 6, it can be concluded that a cutoff energy W_0 of approximately 1.2 keV was required to generate the observed energy flux. Considering again condition (5), this cutoff would be consistent with the observed lack of field-aligned precipitation up to energies of 9 keV.

Before any conclusions can be drawn from this model calculation, the physical significance and a method of observation of ε has to be considered. Lyons and his co-workers argued and demonstrated that, in contrast to the electron number flux, the energy flux was not significantly dependent upon the lower limit

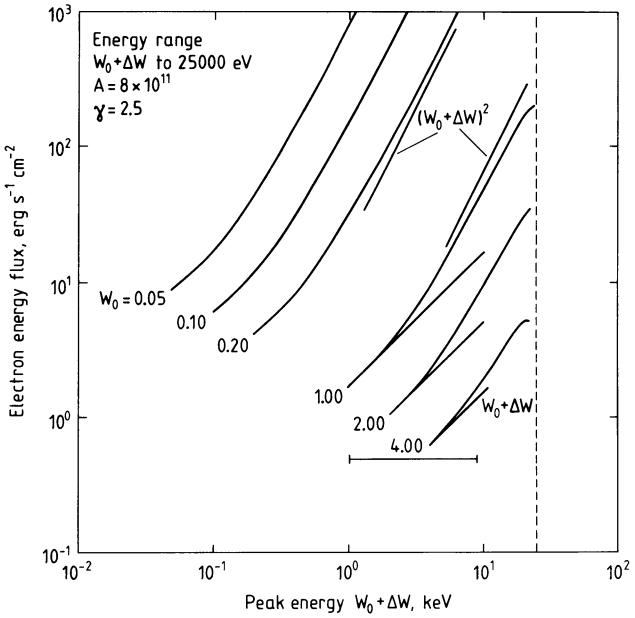

Fig. 6. Model calculations for the dependence of the energy flux upon the peak energy for some electron source distributions of the form $j_e(W) = AW^{-2.5}$ with $W > W_0$. Some segments of linear and quadratic functions of the peak energy $W_0 + \Delta W$ have been added for comparison. The bar in the lower portion of the diagram indicates the energy range in which peaked energy spectra and a linear relation have been observed during the flights F-2 and F-4

of the instrumental energy range. This fact is also borne out by the data presented in Fig. 4, where electron number and energy fluxes were evaluated for two different lower cutoff values during some portions of the flight time. Although the contribution of electrons in the energy range from 0.1 to 0.4 keV to the number flux was significant, the energy flux did not depend upon the low-energy limit used for the integration, even at times when the peak energy approached the 0.4 keV limit. It thus appears as if the energy flux ε' calculated above can be compared with the observed electron energy flux in the energy range from 0.1 to 25 keV. In this sense, the linear relationship between the peak energy value and the energy flux above bright auroral arcs might be indicative of an energetic electron population above the acceleration region, whereas electrons with less energy constitute the source population near the edges of the arc, resulting in a quadratic dependence.

Acknowledgements. The contributions of C. Becker and R. Schmidt to the development and calibration of the electron spectrometer are greatly appreciated. The efforts of G. Haerendel and B. Häusler as project scientist and experiment co-ordinator were essential for the success of the Porcupine programme. This work was supported by the German Bundesministerium für Forschung und Technologie through the DFVLR grant No. 01 OM 015-B21 WRK 274:3 (KL7). I should also like to thank D.S. Evans for his criticism and comments on the first version of this paper. W. Stüdemann kindly provided unpublished data covering the high-energy continuation of the observations considered here.

References

Arnoldy, R.L., Lewis, P.B., Isaacson, P.O.: Field-aligned auroral electron fluxes. J. Geophys. Res. **79**, 4208-4221, 1974

Croley, D.R., Mizera, P.F., Fennell, J.F.: Signature of a parallel electric field in ion and electron distribution in velocity space. J. Geophys. Res. **83**, 2701–2705, 1978

Evans, D.S.: Precipitating electron fluxes formed by a magnetic field aligned potential difference. J. Geophys. Res. **79**, 2853–2858, 1974

Evans, D.S., Maynard, N.C., Tröim, J., Jacobsen, T., Egeland, A.: Auroral vector electric field and particle comparisons. 2. Electrodynamics of an arc. J. Geophys. Res. **82**, 2235–2249, 1977

Kaufmann, R.L., Walker, D.N., Arnoldy, R.L.: Acceleration of auroral electrons in parallel electric fields. J. Geophys. Res. **81**, 1673–1682, 1976, 1976

Lyons, L.R., Evans, D.S., Lundin, R.: An observed relation between magnetic field aligned electric fields and downward electron energy fluxes in the vicinity of auroral forms. J. Geophys. Res. **84**, 457–461, 1979

Mizera, P.F., Fennell, J.F.: Signatures of electric fields from high and low altitude particles distribution. Geophys. Res. Lett. **4**, 311–314, 1977

Sharp, R.D., Johnson, R.G., Shelley, E.G.: Energetic particle measurements from within ionospheric structures responsible for auroral acceleration processes. J. Geophys. Res. **84**, 480–488, 1979

Whalen, B.A., Daly, P.W.: Do field-aligned auroral particle distributions imply acceleration by quasi-static parallel electric fields? J. Geophys. Res. **84**, 4175–4182, 1979

Whalen, B.A., McDiarmid, I.B.: Observations of magnetic-field-aligned auroral electron precipitation. J. Geophys. Res. **77**, 191–202, 1972

Wilhelm, K.: Auroral particle fluxes in the ionosphere. J. Geophys. **46**, 151–169, 1979

Received May 5, 1980; Revised Version June 30, 1980
Accepted August 8, 1980

J. Geophysik 49, 74–81 (1981)

Journal of Geophysics

Application of Different Methods for the Determination of Ionospheric Conductivities from Sounding Rocket Observations

K. Brüning [1], W. Baumjohann [1], K. Wilhelm [2], W Stüdemann [2], A. Urban [3], W Ott [4], K. Spenner [4], G.L. Schmidtke [5], and H.M. Fischer [5]

[1] Institut für Geophysik der Universität Münster, Gievenbecker Weg 61, D-4400 Münster, Federal Republic of Germany
[2] Max-Planck-Institut für Aeronomie, D-3411 Katlenburg-Lindau 3, Federal Republic of Germany
[3] Institut für Weltraumforschung der Österreichischen Akademie der Wissenschaften, A-8010 Graz, Austria
[4] Fraunhofer Institut für Physikalische Meßtechnik, D-7800 Freiburg, Federal Republic of Germany
[5] Institut für Reine und Angewandte Kernphysik der Universität Kiel, D-2300 Kiel, Federal Republic of Germany

Abstract. On 2 November 1977, at 2015 UT, the sounding rocket payload F1B of the 'Substorm Phenomena' campaign was launched from Andenes (Norway). The rocket flew approximately northwards and traversed first an area of weak and diffuse auroral forms in the Harang discontinuity region and then an auroral arc in the region of the westward electrojet. From the particle measurements obtained during the flight ionospheric conductivities are calculated using two different methods. When the classical method is used, i.e., height-integrated conductivities are calculated from the measured thermal electron densities and temperatures, only two values can be determined which are temporally and spatially averaged over the upleg and downleg part of the trajectory, respectively. The calculation of height-integrated conductivities from the measured energetic electron spectra, on the other hand, yields instantaneous values for every location where a spectrum has been sampled. Since there were substantial fluxes of energetic protons during the flight F1B, we also take those into account. The height-integrated conductivities calculated with the two different methods for closely neighbouring regions and the same geophysical situation are nearly identical. A comparison between the contributions of energetic electrons and protons shows that, above 130 km altitude, the ionization rates of the incident protons were higher than those of the electrons while below this altitude the ionization caused by the incident electrons prevailed. Hence, most of the ionospheric conductivity above 130 km was created by energetic protons while below 130 km altitude the energetic electron contribution was dominant.

Key words: Auroral zone – Ionization – Electron density – Conductivities – Energetic electrons – Energetic protons.

Introduction

Ionospheric conductivities play an important role in the electrodynamics of the auroral oval. While the meridional and even two-dimensional distributions of other important parameters like magnetic and electric fields are already rather well known (Baumjohann et al. 1980, and references therein), the spatial and temporal variations of the ionospheric Hall and Pedersen conductivities are still relatively unexplored. They may be calculated for a particular location and moment of time if the instantaneous vertical (along a magnetic flux tube) altitude profile of the electron density (N_e) between 90 and about 200 km is known.

In general, there are two different methods for the determination of N_e altitude profiles in the auroral zone. The first is based on relatively direct measurements of the thermal electrons by incoherent scatter and rocket borne plasma analyzers. Vertical and nearly instantaneous N_e altitude profiles have been measured with the Chatanika incoherent scatter radar (e.g. Brekke et al. 1974; Banks and Doupnik 1975), but the measurements were restricted to only a few locations in the auroral ionosphere. Altitude profiles of N_e have also been measured during rocket flights (e.g. Primdahl et al. 1979) but the profiles were neither vertical nor instantaneous. Hence, the authors could give only two values for the height-integrated conductivity, one for the upleg and one for the downleg part of the rocket trajectory. These values were only approximate values, since the height-integration of the conductivities was not made along flux tubes of homogeneous energy deposition but along the rocket trajectory and was thus dependent on the temporal and spatial variability of the energy deposition along the trajectory.

The second method is based on measurements of the energy spectra of precipitating energetic particles. Here, the ionization caused by the incident energetic electrons and protons is computed using the methods given by Rees (1963) and Eather and Burrows (1966), respectively. By assuming reasonable values for the recombination coefficients, vertical and instantaneous altitude profiles of N_e may be calculated for every flux tube where a spectrum has been sampled. Hence, height-integrated conductivities may be calculated nearly everywhere along the whole rocket trajectory, provided that electron and proton spectra cover a sufficiently broad energy range and have been sampled high enough above the absorbing layers of the ionosphere.

The second method has already been used by several authors (Sharp et al. 1975; Rees et al. 1976; Evans et al. 1977; Behm et al. 1979). In all these studies the ionization caused by incident energetic electrons alone was considered, since the incident proton fluxes were either weak or not measured. However, by comparing the ionization efficiencies of energetic electrons given by Rees (1963; his Fig. 2) with those of energetic protons given by Eather and Burrows (1966; their Fig. 5a) one may note that the ionization caused by incident energetic protons is not negligible if the proton fluxes are of the same order or slightly lower than the electron fluxes.

In the present study we shall calculate height-integrated conductivities using data from a sounding rocket payload which included a thermal plasma analyzer and several energetic electron

0340-062X/81/0049/0074/$01.60

Table 1. Experiments flown aboard the payload 'Substorm Phenomena F1B' and used in this study

Experiment	Technique	Measurements	Institution
Plasma experiment TF 4	Retarding potential analyser	Electron temperature, ion density, ion wind, vehicle potential electron flux 0–30 eV	IPM, Freiburg
Particle spectrometer Electrons TL 7 Protons TZ 1	Hemispherical electrostatic analyser and open electron multipliers	Electron and proton fluxes $0.1(1) \leqq E_e(E_p) \leqq 25(40)$keV	MPAE, Lindau INW, Graz
Particle spectrometer TL 6	Magnetic particle analyser and solid-state detectors	Electron and proton fluxes $20(40) \leqq E_e(E_p) \leqq 200(300)$keV	MPAE, Lindau
Particle spectrometer TK 1	Solid-state detector telescope	Proton fluxes $0.07 \leqq E_p \leqq 2$ MeV	IFKKI, Kiel

and proton detectors. This extensive data suite enables us to apply both methods and, for the first time, to include the energetic proton contribution when using the second method. Where possible, we shall compare the values given by the two different methods and in particular, we shall discuss the relevance of energetic proton fluxes in creating ionospheric conductivities.

Instrumentation

The payload F1B was integrated as part of a larger sounding rocket programme named 'Substorm Phenomena'. The experiment complements were selected to provide a set of plasma, particle and field observations during various phases of magnetospheric substorm events. Details of the experiments used in this study are compiled in Table 1, which also indicates the various institutions responsible for the particular instrument developments.

The payloads were launched by Skylark 12 motors from the Andøya rocket range, Norway, and flight F1B, which was launched on 2 November 1977 at 2015 UT, lasted for about 12 min and reached a peak altitude of 542.4 km. The payload was controlled in attitude so as to point $20° \pm 10°$ off the negative geomagnetic field direction and had a spin period of 350 ms. The trace of the rocket trajectory is shown in Fig. 1, at a height of 100 km (projected down along magnetic field lines).

Geophysical Situation During Flight

In order to establish the configuration of the electrojet and the optical aurora during the rocket flight, data from the Scandinavian Magnetometer Array (SMA; Küppers et al. 1979; Maurer and Theile 1978) and from the all-sky camera at Abisko (Sweden) have been analysed.

In Fig. 1 the equivalent current arrows on the Earth's surface and the location of an auroral arc are displayed for 2020 UT, the most relevant interval. The coordinate system indicated in Fig. 1 has been introduced by Küppers et al. (1979) and named the Kiruna system. It is a Cartesian system obtained by a projection of the globe onto a tangential plane centered at Kiruna, Sweden (67.8°N, 20.4°E). The y_{KI} axis of the system has been chosen as the tangent to the projection of the ϕ_c (KIR) = 64.8° line with ϕ_c being the revised corrected geomagnetic latitude as given by Gustafsson (1970). The x_{KI} axis is perpendicular to the y_{KI} axis and is directed approximately 12° west of geographic north at Kiruna, where the system has its origin ($x_{KI} = y_{KI} = 0$).

The SMA observations (Fig. 1) indicate that between 2000 and 2030 UT (i.e., 1 h before magnetic midnight) Scandinavia was

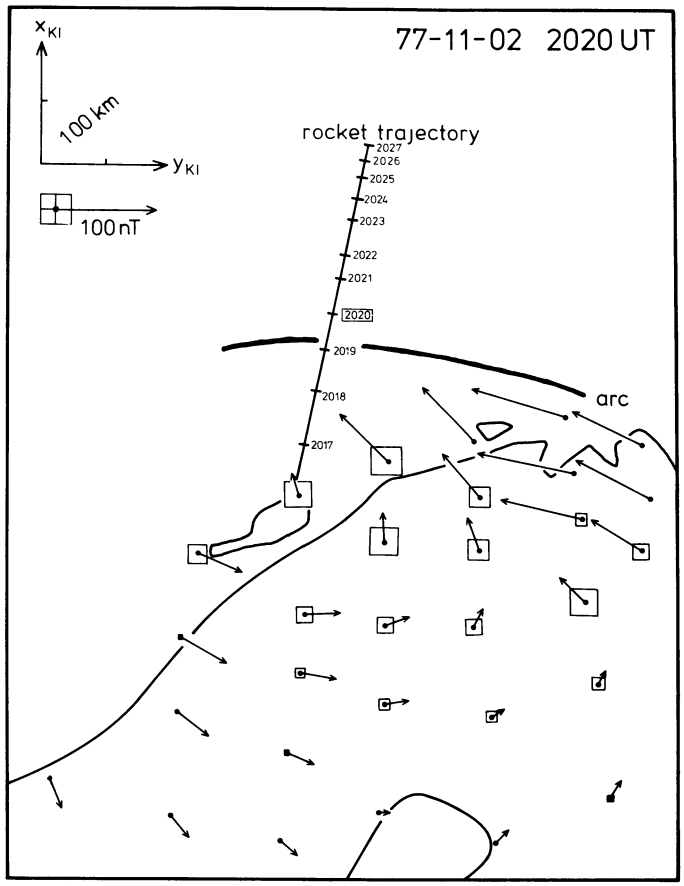

Fig. 1. Equivalent current arrows on the Earth's surface. The *current arrows* have their origin at the station, where the corresponding magnetic disturbances have been observed. The *squares* denote negative Z components. The position of the auroral arc and the rocket trajectory have been added

situated under the Harang discontinuity region (Harang 1946; Heppner 1972; see Baumjohann et al. 1980, for SMA signatures of the Harang discontinuity) and both SMA and all-sky camera data show the signatures of substorm activity. After the passage of a westward travelling surge around 2000 UT the aurora intensified again and after 2010 UT formed a large spiral which broke up at 2013 UT. Later, the aurora became weaker and more diffuse in the south. At the northern boundary of auroral activity a single arc formed which was located north of the Norwegian coast at 2020 UT (see Fig. 1). This arc intensified again at 2026 UT leading

to another breakup at 2028 UT. Each of the auroral intensifications was accompanied by a strong enhancement of the westward electrojet. A compilation of additional observations relevant to this event has been given elsewhere (Wilhelm 1980).

In summary, the payload F1B traversed an area of diffuse auroral forms near the Harang discontinuity shortly after the launch. Between 235 and 275 s after launch it traversed an auroral arc located in the westward electrojet region.

Calculation of Ionospheric Conductivities from Measured Electron Density and Temperature Profiles

Using suitable models for the neutral atmospheric densities, it is possible to compute ionospheric electrical conductivities from measured electron density (N_e) and temperature (T_e) profiles. The altitude dependent Hall (σ_H) and Pedersen (σ_P) conductivities are defined by the well-known expressions (neglecting ion-electron collisions):

$$\sigma_H = \frac{N_e e}{B}\left(\frac{\omega_e^2}{\omega_e^2+\nu_e^2}-\frac{\omega_i^2}{\omega_i^2+\nu_i^2}\right)$$
$$\sigma_P = \frac{N_e e}{B}\left(\frac{\omega_e \nu_e}{\omega_e^2+\nu_e^2}+\frac{\omega_i \nu_i}{\omega_i^2+\nu_i^2}\right) \quad (1)$$

where e is the electron charge, B is the magnetic field magnitude, $\omega_{i,e}=eB/m_{i,e}$ is the ion (or electron) gyrofrequency, $m_{i,e}$ is the ion (or electron) mass and $\nu_{i,e}$ is the ion (or electron) neutral collision frequency. The collision frequencies may be calculated as follows (note that only T_e was measured and thus a T_i-independent expression for ν_i has to be used):

$$\nu_e = 1.5\times 10^{-17}\, M\, T_e$$
$$\nu_i = 4.2\times 10^{-16}\, M \quad (2)$$

where M is the number of neutrals (Boström 1973; Jones and Rees 1973).

The N_e and T_e profiles which have been measured by a retarding potential analyzer (plasma experiment TF4; see Table 1) during the flight F1B are displayed in Figs. 2 and 3. In both figures a pronounced difference between the upleg and downleg profiles can be noted. These differences can be explained by the fact that the payload entered regions with different auroral activity and probably left the auroral oval at about 660 s after launch (2026 UT). At this moment, the electron fluxes observed by the spectrometer TL7 (see Table 1) fell below the instrument threshold, supporting the assumption of polar cap conditions after 2026 UT, since in the polar cap only electrons below 1 keV precipitate (polar rain, Winningham et al. 1975; Heelis et al. in press 1980). Such electrons do not reach altitudes below 150 km (Rees 1963), a fact that may explain the extremely low electron densities after 2026 UT and below 200 km altitude.

The minima and maxima in the upleg T_e profile are related to strong spatial and partially also to temporal variations of the ionospheric conditions. A comparison with the all-sky camera photographs reveals that the rocket traversed a diffuse auroral patch near 2016 UT and was located between this patch and an auroral arc after 2017 UT. Hence, the T_e maximum between 75 and 100 s after launch is probably related to the auroral patch, while the high electron temperatures around 250 s after launch (2019–2929 UT) coincide with the auroral arc crossing (Fig. 1). Also plotted in Fig. 3 is a model T_e profile as given by Jones and

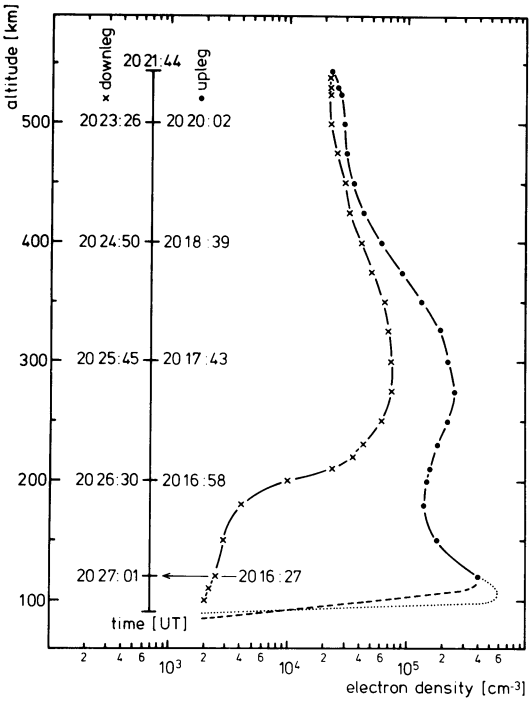

Fig. 2. Altitude profiles of electron density measured during the upleg and downleg part of flight F1B. *Dotted* and *dashed lines* give possible extrapolations of the upleg curve (for details see text)

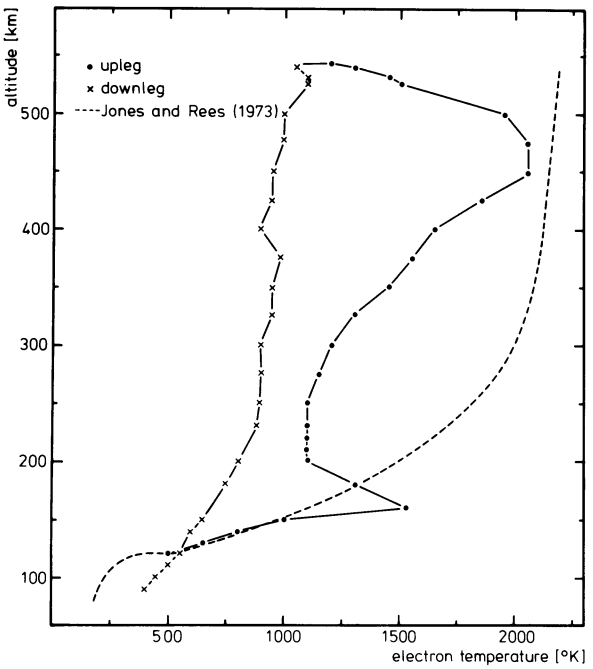

Fig. 3. Altitude profiles of electron temperature measured during the upleg and downleg part of flight F1B. For comparison the model curve of Jones and Rees (1973) has been added

Rees (1973) for the night-time auroral zone. The significant difference between this profile and the measured ones indicates that one has to be careful in using model T_e profiles for estimating ν_e in Eq. (2). Model T_e values must nevertheless be used in this study for the upleg profile below 120 km, since no T_e measurements

were possible during this part of the flight (before the third stage burned out).

Similarly the electron density could not be measured below 120 km on the upleg profile. Hence, we had to assume N_e values between 90 and 120 km. Two possibilities are indicated in Fig. 2. The dashed curve was drawn with the assumption that the measured electron density at 120 km is the maximum value (a) while the dotted line represents an increase of N_e below 120 km to a maximum of 6×10^5 electrons/cm^3 at 105 km altitude (b). Justification for the latter extrapolation (b) may be found in the fact that similar values have been measured by the Chatanika incoherent scatter radar for disturbed times (Baron 1972) and in the N_e values calculated by the second method for a neighbouring region (Fig. 7).

The height-integrated (90–400 km) Hall and Pedersen conductivities calculated from the profiles in Figs. 2 and 3 are as follows:

upleg:

(a) $\Sigma_H = 23$ mho, $\Sigma_P = 15$ mho, $\frac{\Sigma_H}{\Sigma_P} = 1.5$

(b) $\Sigma_H = 46$ mho, $\Sigma_P = 17$ mho, $\frac{\Sigma_H}{\Sigma_P} = 2.7$

downleg:

$\Sigma_H = 0.2$ mho, $\Sigma_P = 0.2$ mho, $\frac{\Sigma_H}{\Sigma_P} = 1.0$

The height-integrated conductivities and their ratio during the upleg part of the trajectory are within the range of values given by other authors for similar auroral conditions (Brekke et al. 1974; Wedde et al. 1977; Horwitz et al. 1978a, b). Since Σ_H depends strongly on the electron densities between 90 and 120 km, where the plasma parameters could not be measured, the calculated values give only an order of magnitude. The calculated value for Σ_P is more reliable since σ_P has its maximum at higher altitudes and only 15% of the total contribution to Σ_P is influenced by the uncertainty in N_e between 90 and 120 km. Of course, additional errors could be introduced by temporal and spatial fluctuations. However, about 70% of the total height-integrated Pedersen conductivity stems from contributions of σ_P between 120 and 150 km. The rocket flew through this altitude range within 15 s covering a horizontal distance of 15 km. Accordingly $\Sigma_P = 16 \pm 8$ mho seems to be a representative value for the time 2016:30 UT and the location $x_{KI} \approx 250$ km.

The Hall and Pedersen conductivities calculated from the downleg N_e and T_e profiles are extremely small. This is mainly caused by the very low electron density measured in the *E*-layer. In line with the above arguments, the height-integrated conductivities given are probably representative for the polar cap region.

Since the payload traversed regions with quite different ionospheric conditions, the height-integrated conductivities along the trajectory are by no means constant and the method described yields useful information only in areas where the payload was within or close to the *E*-layer. For a more exact calculation of the height-integrated conductivities along the trajectory, we need, at least, instantaneous N_e profiles for a number of locations. These may be calculated by the method given in the next section.

Calculation of Ionospheric Conductivities from Measured Energetic Particle Spectra

Instantaneous N_e altitude profiles for numerous locations along the rocket trajectory may be calculated from the measured energetic particle spectra. This is done by computing altitude profiles of the ionization rate $q(h)$ due to the measured precipitating energetic particles with the methods given by Rees (1963), Eather and Burrows (1966), and Eather (1970). Below 200 km the N_e profile is then given by (Rishbeth and Garriott 1969)

$$N_e(h) = \sqrt{\frac{q(h)}{\alpha(h)}} \tag{3}$$

where $\alpha(h)$ is the altitude dependent recombination coefficient (we use the values given by Evans et al. 1977). When substituting these instantaneous N_e profiles into Eq. (1) instantaneous and vertical σ_H and σ_P altitude profiles can be obtained.

As already indicated, our study goes further than earlier ones in that we incorporate the contribution of energetic protons to

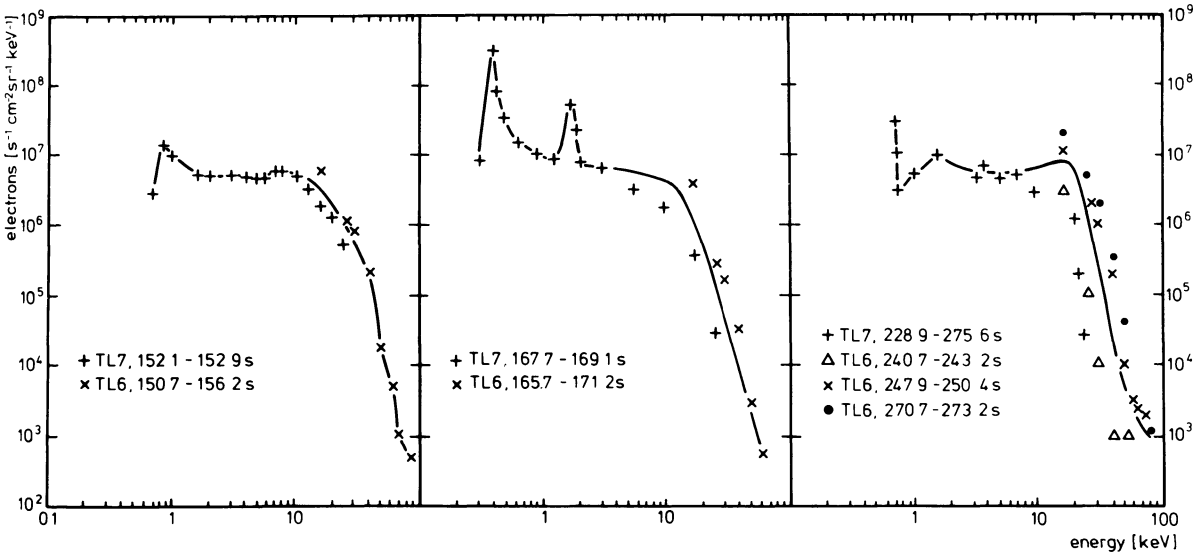

Fig. 4. Representative electron spectra constructed from measurements of the experiments TL6 and TL7. The *left* and *middle spectra* have been measured when the rocket traversed diffuse auroral forms near the Harang discontinuity. The *right spectrum* was measured when the rocket crossed an auroral arc

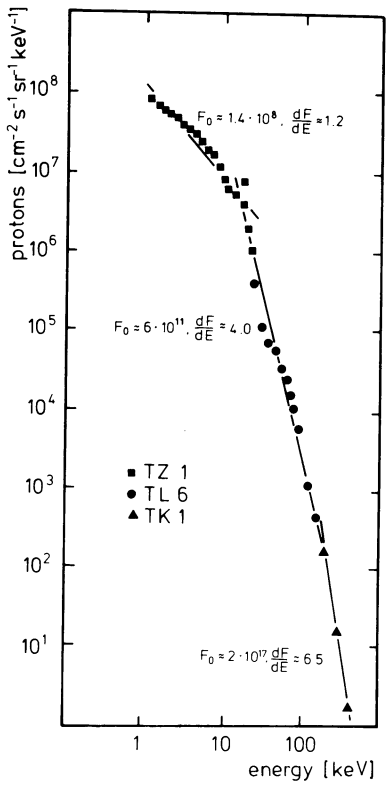

Fig. 5. Representative proton spectrum constructed from measurements of the experiments *TZ*1, *TL*6, and *TK*1 made around 125 s after launch

the ionization rates. We have also gone further than earlier studies by combining spectra measured by particle spectrometers covering adjacent energy ranges (TL7 and TL6 for electrons; TZ1, TL6, and TK1 for protons; see Table 1) in order to determine the contributions from particles in a wider energy range (0.4–100 keV for electrons and 1–400 keV for protons as compared to the maximum 16 keV used by Evans et al. 1977). This is important since high-energy particles penetrate deeper into the ionosphere (especially into the lower *E*-layer) and ionize more neutral particles. Their small number densities compared to particles with energies below, say, 20 keV can thus be partially balanced by their greater efficiency in creating ionization.

Experiment TL7 measured electron spectra at 152–215 s and 357–442 s after launch with a short sweep time of 1.4 s while at 229–352 s the scan time was 46.7 s. Experiment TL6 measured electron spectra every 0.6 s at 106–280 s after launch, which were integrated over times of 2.5 and 5.5 s. For those times shown in Fig. 4 spectra of both experiments are combined. The pitch angle distributions (not shown here) were also determined and helped to decide whether isotropic ($<80°$) or cosine-dependent particle distributions had to be used in Rees' algorithm.

The proton spectra are combined from the data obtained by the experiments TZ1, TL6, and TK1 for the interval 100–340 s. Each of the spectra can be represented by power law functions in the energy ranges 1–20, 20–200, and 200–400 keV. An example is given in Fig. 5 for a time of 125 s after launch. For intervals in which the spectral indices and parameters are rather similar, we use average spectra. Although the observed proton fluxes were anisotropic (field-aligned), we decided to employ the ionization rates given by Eather and Burrows (1966) for isotropic distributions only. The proton flux measured at 20° pitch angle was taken to be representative in the interval 0°–60°.

In the following we shall use (average) spectra sampled at 150–300 s after launch. During this interval the payload flew at altitudes above 400 km. Hence, we can assume that the fraction of energy already deposited by the incident energetic particles is negligible and that there are hardly any neutral hydrogen atoms to cause spreading of the proton beam (Eather 1967).

In order to show that the number of precipitating energetic protons is indeed high enough to ionize a significant number of neutrals, we compare the integral particle fluxes for energetic electrons and protons (in the energy range 1–100 keV) in Fig. 6. It is apparent that during the flight F1B the integral proton flux was unusually strong and always higher than the electron flux. This is especially significant immediately south of the auroral arc where the electron fluxes were even below the instrument threshold. Only when the payload traversed the auroral arc around 250 s after launch and at about $x_{KI}=450$ km, were the flux levels of electrons and protons nearly identical (about 10^9 particles/cm^2 s). Hence, one may conclude that to omit to consider the proton

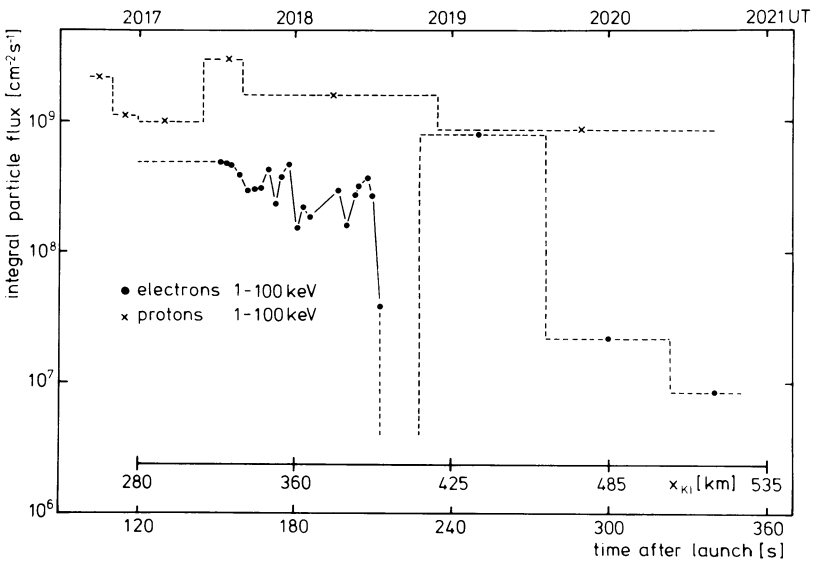

Fig. 6. Comparison of integral electron and proton fluxes (1–100 keV). The *dashed lines* represent averages while the *solid lines* connect values computed from high time-resolution spectra

contribution would lead to a serious underestimation of the ionization rates as well as the electron densities and thus the ionospheric conductivities.

For a more detailed analysis of the influence of electrons and protons on the altitude profiles of ionization rate, electron density and Hall and Pedersen conductivities, we calculate those values from the electron and proton spectra measured near 152 s after launch (the electron spectrum is shown in the left panel of Fig. 4 while the proton spectrum was similar to that displayed in Fig. 5). The results are displayed in Figs. 7 and 8. It can easily be seen that the ionization rate and the electron density below 110 km are dominated by the energetic electron contribution, while above this altitude the energetic proton contribution prevails. The different altitude dependence can be explained by the fact that the mean free path for energetic protons is smaller than that of electrons having the same energy and hence, on the average, the protons do not penetrate so deeply into the lower ionosphere. The altitude dependence is also reflected in the Hall and Pedersen conductivity profiles: the Pedersen conductivity with its maximum at 130 km is caused mainly by incident energetic protons while the Hall conductivity which has its maximum at 100 km height, is dominated by the energetic electron contribution.

The same tendency can also be seen in Fig. 9 where we display the height-integrated Hall and Pedersen conductivities and their ratio along the rocket trajectory and compare the values calculated from $q_e(h)$ only (left diagram) and from $q(h)=q_e(h)+q_p(h)$ (right diagram). This comparison shows that for flight F1B the ionization by energetic protons cannot be neglected. In particular, both to the south (215–230 s after launch) and north (> 280 s) of the auroral arc the height-integrated conductivities are caused mainly by energetic proton fluxes, which were about 100 times more intense than the electron fluxes at these locations (Fig. 6). In these areas,

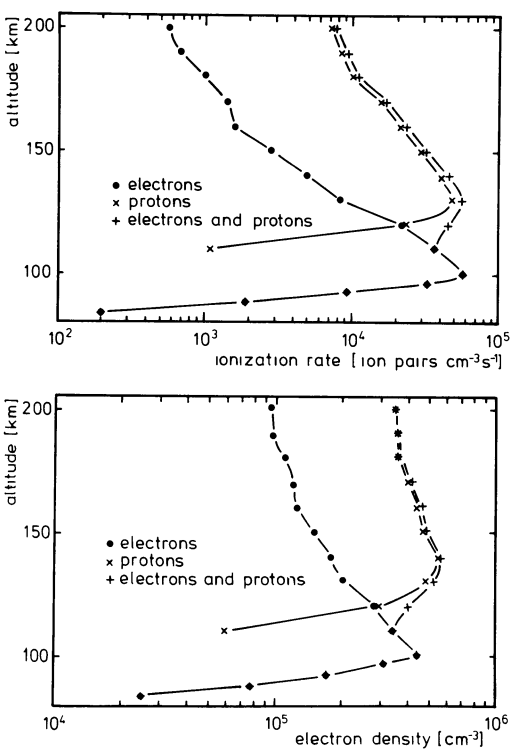

Fig. 7. Altitude profiles of total ionization rates (*upper panel*) and electron densities (*lower panel*) around 152 s after launch. Also given are curves representing the contributions of electrons and protons separately

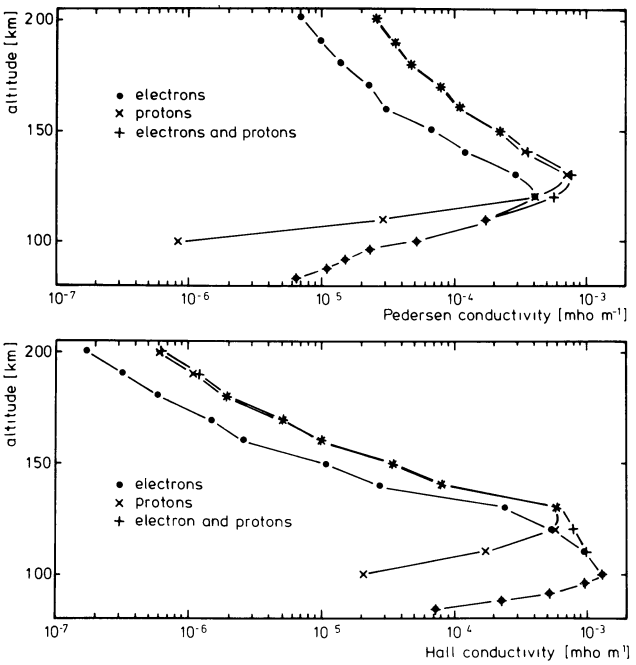

Fig. 8. Altitude profiles of Pedersen (*upper panel*) and Hall (*lower panel*) conductivities calculated from the electron density profiles given in Fig. 7

the height-integrated Hall conductivity is also mainly due to protons, while otherwise the energetic protons contribute mainly to the height-integrated Pedersen conductivity, as already shown in Fig. 8. The fact that about one half of the height-integrated Pedersen conductivity, but only about 20% of the height-integrated Hall conductivity, is caused by protons is also reflected in the Σ_H/Σ_P ratios (lower panels in Fig. 9). They range between 1 and 3 when considering precipitating electrons only and between 1 and 2 when the additional effects of precipitating protons are taken into account.

When considering the height-integrated conductivities and their ratio in relation to the optical aurora and the electrojets (see above) it seems noteworthy that in the Harang discontinuity, where diffuse auroral forms have been observed, the calculated values ($\Sigma_H=40$ mho, $\Sigma_P=20$ mho) are slightly higher than those given by Horwitz et al. (1978a). The values calculated for times when the rocket traversed the auroral arc within the westward electrojet ($\Sigma_H=48$ mho, $\Sigma_P=22$ mho) are comparable to those given by Evans et al. (1977) and Horwitz et al. (1978a). Finally, it seems interesting that the Σ_H/Σ_P ratio is always close to 2 in regions where aurora has been observed and close to 1 outside these regions (south and north of the arc).

Summary and Conclusions

In Table 2 we summarize the calculated height-integrated conductivities and their ratio in different latitudinal regions of the high-latitude ionosphere. The values in the first and last row are calculated from the measured N_e and T_e profiles (method 1 above) while the other four are calculated from the energetic particle spectra (method 2 above). It is apparent that there are strong variations of the height-integrated conductivities along the rocket trajectory which can only be resolved when using the second method. Since additional atmospheric model parameters (e.g., recombination

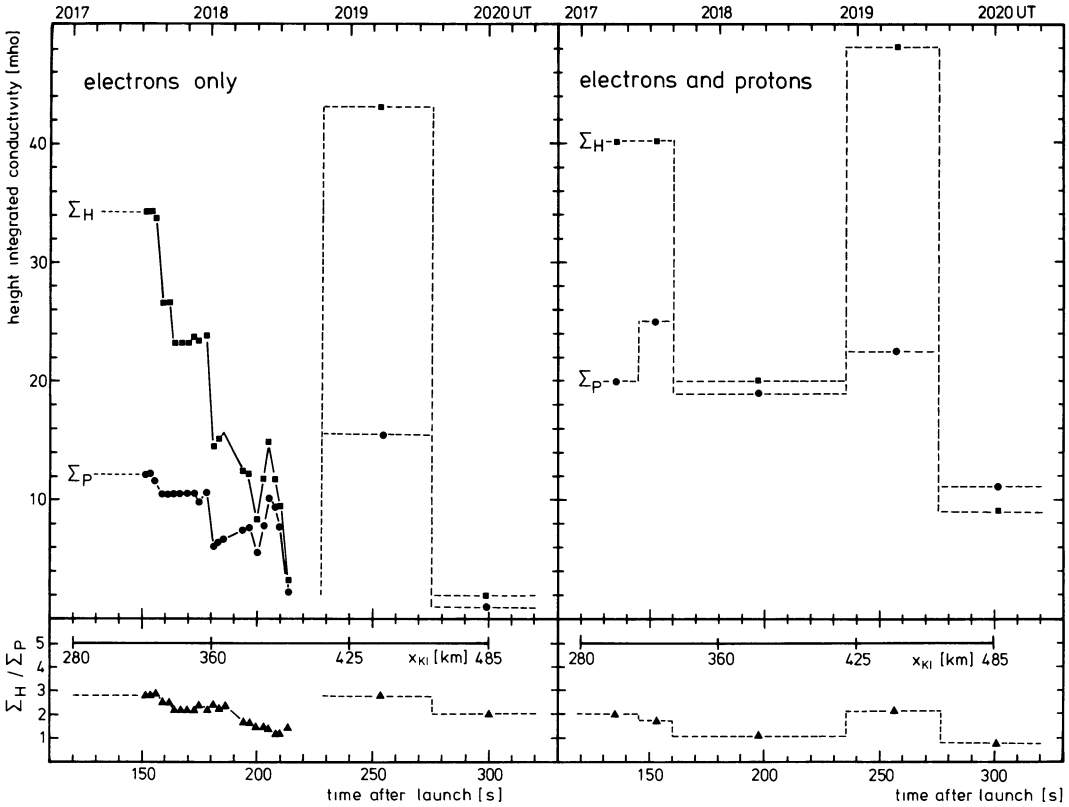

Fig. 9. Height-integrated conductivities and Σ_H/Σ_P ratio along a part of the rocket trajectory. The values in the left diagram are calculated from the electron spectra only, while in the right diagram electron and proton contributions are taken into account

Table 2. Average conductivities for the different regions traversed by the rocket

x_{KI} [km]	Aurora	Electrojet	Σ_H [mho]	Σ_P [mho]	Σ_H/Σ_P	Method used
~250	Diffuse auroral forms	Harang discontinuity	~35	16	~2	1
280–330	Diffuse auroral forms	Harang discontinuity	40	22	1.8	2
330–420	No aurora	Westward electrojet	20	19	1.1	2
420–460	Auroral arc	Westward electrojet	48	22	2.2	2
460–500	No aurora	Westward electrojet?	9	11	0.8	2
~700	No aurora	Polar cap?	0.2	0.2	1.0	1

coefficients) have to be used for the electron density calculations in method 2, it is probably less accurate than method 1. However, a comparison of the values given in the first two rows of Table 2, which are representative of closely neighbouring regions and the same geophysical conditions but are calculated by the two different methods, shows that both methods yield nearly the same results. A comparison of these values with the corresponding ones in the left diagram of Fig. 9 shows that a neglect of the energetic proton contribution in method 2 results in an under-estimation of the conductivities and the height-integrated Pedersen conductivity in particular, at least for conditions with high proton fluxes.

Acknowledgements. Many individuals at various institutions contributed to this sounding rocket programme. In particular, we should like to mention J. Hörle as project manager of DFVLR-PT. We also want to thank the integration team of Dornier System, the DFVLR launch team and the personnel of the Andøya Rocket Range for their support of the project. The work was supported financially by the German Bundesministerium für Forschung und Technologie and by the Österreichische Akademie der Wissenschaften. The SMA observations were made in cooperation with various institutions (Küppers et al. 1979) and supported financially by the Deutsche Forschungsgemeinschaft. We are indebted to M.H. Rees and R.H. Eather for useful comments on an earlier version of the manuscript. Finally, we would like to thank H. Lauche for putting the all-sky camera pictures at our disposal and H. Maurer for the data from the Braunschweig magnetometer chain.

References

Banks, P.M., Doupnik, J.R.: A review of auroral zone electrodynamics deduced from incoherent scatter radar observations. J. Atmos. Terr. Phys. **37**, 951–972, 1975

Baron, M.J.: DNA Project 617 radar, final report: Auroral ionospheric measurements. Menlo Park, California: Stanford Res. Inst. 1972

Baumjohann, W., Untiedt, J., Greenwald, R.A.: Joint two-dimensional observations of ground magnetic and ionospheric electric fields associated with auroral zone currents. 1. Three-dimensional current

flows associated with a substorm-intensified eastward electrojet. J. Geophys. Res. **85**, 1963–1978, 1980

Behm, D.A., Primdahl, F., Zanetti, L.J. Jr., Arnold, R.L., Cahill, L.J.Jr.: Ionospheric electrical currents in the late evening plasma flow reversal. J. Geophys. Res. **84**, 5339–5343, 1979

Boström, R.: Electrodynamics of the ionosphere. In: Cosmical geophysics, A. Egeland et al., eds.: pp. 181–192. Oslo: Universitetsforlaget 1973

Brekke, A., Doupnik, J.R., Banks, P.M.: Incoherent scatter measurements of *E* region conductivities and currents in the auroral zone. J. Geophys. Res. **79**, 3773–3790, 1974

Eather, R.H.: Auroral proton precipitation and hydrogen emissions. Rev. Geophys. **5**, 207–285, 1967

Eather, R.H.: Ionization produced by auroral proton precipitation. Ann. Géophys. **26**, 609–613, 1970

Eather, R.H., Burrows, K.M.: Excitation and ionization by auroral protons. Aust. J. Phys. **19**, 309–322, 1966

Evans, D.S., Maynard, N.C., Trøim, J., Jacobsen, T., Egeland, A.: Auroral vector electric field and particle comparisons. 2. Electrodynamics of an arc. J. Geophys. Res. **82**, 2235–2249, 1977

Gustafsson, G.: A revised corrected geomagnetic coordinate system. Ark. Geofys. **5**, 595–617, 1970

Harang, L.: The mean field of disturbance of polar geomagnetic storms. Terr. Magn. Atmos. Electr. **51**, 353–380, 1946

Heelis, R.A., Winningham, J.D., Hanson, W.B., Burch, J.L.: The relationships between high latitude convection reversals and the energetic particle morphology observed by Atmosphere Explorer. J. Geophys. Res. in press 1980

Heppner, J.P.: The Harang discontinuity in auroral belt ionospheric currents. Geofys. Publ. **29**, 105–120, 1972

Horwitz, J.L., Doupnik, J.R., Banks, P.M.: Chatanika radar observations of the latitudinal distributions of auroral zone electric fields, conductivities, and currents. J. Geophys. Res. **83**, 1463–1481, 1978a

Horwitz, J.L., Doupnik, J.R., Banks, P.M., Kamide, Y., Akasofu, S.-I.: The latitudinal distributions of auroral zone electric fields and ground magnetic perturbations and their response to variations in the interplanetary magnetic field. J. Geophys. Res. **83**, 2071–2084, 1978b

Jones, R.A., Rees, M.H.: Time dependent studies of the aurora – I. Ion density and composition. Planet. Space Sci. **21**, 537–557, 1973

Küppers, F., Untiedt, J., Baumjohann, W., Lange, K., Jones, A.G.: A two-dimensional magnetometer array for ground-based observations of auroral zone electric currents during the International Magnetospheric Study (IMS). J. Geophys. **46**, 429–450, 1979

Maurer, H., Theile, B.: Parameters of the auroral electrojet from magnetic variations along a meridian. J. Geophys. **44**, 415–426, 1978

Primdahl, F., Walker, J.K., Spangslev, F., Olesen, J.K., Fahleson, U., Ungstrup, E.: Sunlit cleft and polar cap ionospheric currents determined from rocket-borne magnetic field, plasma, and electric field observations. J. Geophys. Res. **84**, 6458–6470, 1979

Rees, M.H.: Auroral ionization and excitation by incident energetic electrons. Planet. Space Sci. **11**, 1209–1218, 1963

Rees, M.H., Romick, G.J., Anderson, H.R., Casserly, R.T.: Calculation of auroral emissions from measured electron precipitation: Comparison with observations. J. Geophys. Res. **81**, 5091–5096, 1976

Rishbeth, H., Garriott, O.K.: Introduction to ionospheric physics. New York, London: Academic Press 1969

Sharp, R.D., Shelley, E.G., Rostoker, G.: A relationship between synchronous altitude electron fluxes and the auroral electrojet. J. Geophys. Res. **80**, 2319–2324, 1975

Wedde, T., Doupnik, J.R., Banks, P.M.: Chatanika observations of the latitudinal structure of electric fields and particle precipitation on November 21, 1975, J. Geophys. Res. **82**, 2743–2751, 1977

Wilhelm, K.: Study of magnetospheric substorm events. In: The Fifth ESA Symp. on European Rocket and Balloon Programmes and on Related Research, Bournemouth, 14–18 April 1980, ESA Special Publication, 1980

Winningham, J.D., Yasuhara, F., Akasofu, S.-I., Heikkila, W.J.: The latitudinal morphology of 10 eV to 10 keV electron fluxes during magnetically quiet and disturbed times in the 2100–0300 MLT sector. J. Geophys. Res. **80**, 3148–3171, 1975

Received June 27, 1980; Revised Version August 6, 1980
Accepted August 7, 1980

J. Geophys. 49, 82–84 (1981)

Journal of Geophysics

Short Communication

Numerical Experiments on Convection in a Chemically Layered Mantle

U. Christensen*

Institut für Geophysik und Meteorologie der Technischen Universität, Mendelssohnstraße 1A, D-3300 Braunschweig, Federal Republic of Germany

Key words: Mantle convection – Finite element model – Chemical heterogeneity – Boundary layer – Mantle temperatures.

Introduction

It is still an unresolved question whether the convection cells connected with lithospheric plate motion are restricted to the upper mantle or involve the whole mantle. In the last few years a number of papers have appeared which favor whole mantle convection because: the viscosity of the lower mantle seems to be only low or moderate (Davies 1977); it can explain large-scale heterogeneities in the lower mantle (O'Connell 1977); it can explain the D″-layer as a thermal boundary layer of whole mantle convection (Elsasser et al. 1979); it ensures reasonably high temperatures in the upper mantle (Kopitzke 1979).

The opponents of whole mantle convection argue that the temperature would be too low at the core-mantle boundary (Jeanloz and Richter 1979) or they deal with the stress distribution and seismic energy release in descending plates above the seismic cutoff at 720 km depth (Richter 1979). Formerly it was often assumed that high rigidity of the lower mantle or the hindering action of phase transitions would inhibit whole mantle convection. Now the idea of a chemically heterogenous mantle is preferred. Some authors consider the 650-km discontinuity to be a pure chemical change (Liu 1979), or possibly a phase boundary with a superimposed increase of iron content (Anderson and Jordan 1970), while others exclude any chemical differences (Watt and O'Connell 1978). Geochemical arguments may also support different chemical reservoirs in the mantle (O'Nions et al. 1979). Sammis (1976) found by marginal stability analysis that convection in separated layers is the prefered mode, if the density difference is more than 0.1%. However, since mantle convection is vigorous and far from the marginal stability case, it is likely that the limit must be higher. Because the viscosity of the lower mantle can hardly be assumed to be extremely high, two separate layers of convection in the upper and lower mantle must develop if there is a substantial chemical boundary.

In order to investigate the dynamics and temperature distribution of two-layer mantle convection, such a boundary is introduced into a dynamical finite element model of convection.

* Former name: U. Kopitzke

Model Design

A detailed description of the model is given elsewhere (Kopitzke 1979, hereafter cited as paper 1; Christensen 1980, paper 2). Bicubic and biquadratic spline functions with Ritz-Rayleigh and upwind finite element techniques are used to evaluate the steady state flow and temperature field. Position-dependent viscosity, thermal diffusivity and expansivity, as well as inner heat production, bottom heat flux, frictional heating and adiabatic gradient are included. An advantage of this model is the realistic simulation of the upper thermal boundary layer which behaves mechanically and thermally like a nearly rigid lithospheric plate. The depth of the (plane) model is restricted to 1,750 km, in order to adjust the volume of the cell to the volume of a spherical sector of same surface area and 2,900 km depth extent. By slight variations of the Rayleigh-number (which is in the order of 10^7), the overturn time of the model lithosphere is made to equal the mean overturn time in the earth's plate system. This ensures realistic simulation of the heat balance in the mantle.

The chosen viscosity distribution exhibits a maximum of $>10^{25}$P on top of the lithosphere, a minimum of 10^{21}P at 200 km, rises again with increasing depth, reaching 10^{23}P at 500 km, and remains fairly constant (about $4\cdot10^{23}$P) in the lower mantle. Weak zones at the active margins of the lithosphere ensure its plate-like behavior (paper 1). The chemical boundary at $\simeq$650 km depth is represented by a point-chain, as in a previous investigation, where a phase boundary was modelled (paper 2). However, its depth is not controlled by temperature as in the case of phase transition, but it is shifted up or down by material flow perpendicular to the boundary. There is a negative feed-back on the flow because of the buoyancy forces associated with boundary distortion, and usually steady state with zero flux through the dividing line is achieved (for a detailed description of buoyancy calculation in the finite element scheme see paper 2).

Results

In the first model the whole density increase at the 650-km discontinuity ($\Delta\rho/\rho=10\%$) is assumed to be due to chemical change, according to the petrological model of Liu (1979) with pure perovskite in the lower mantle. The initial temperature distribution was chosen in order to establish two cells with opposite circulation in the upper and lower mantle. Steady state was attained easily by iteration; the results are demonstrated in Figs. 1 and 2. The upper cell looks very similar to a previous model with upper mantle convection only and a no-slip lower boundary (paper 1),

0340-062X/81/0049/0082/$01.00

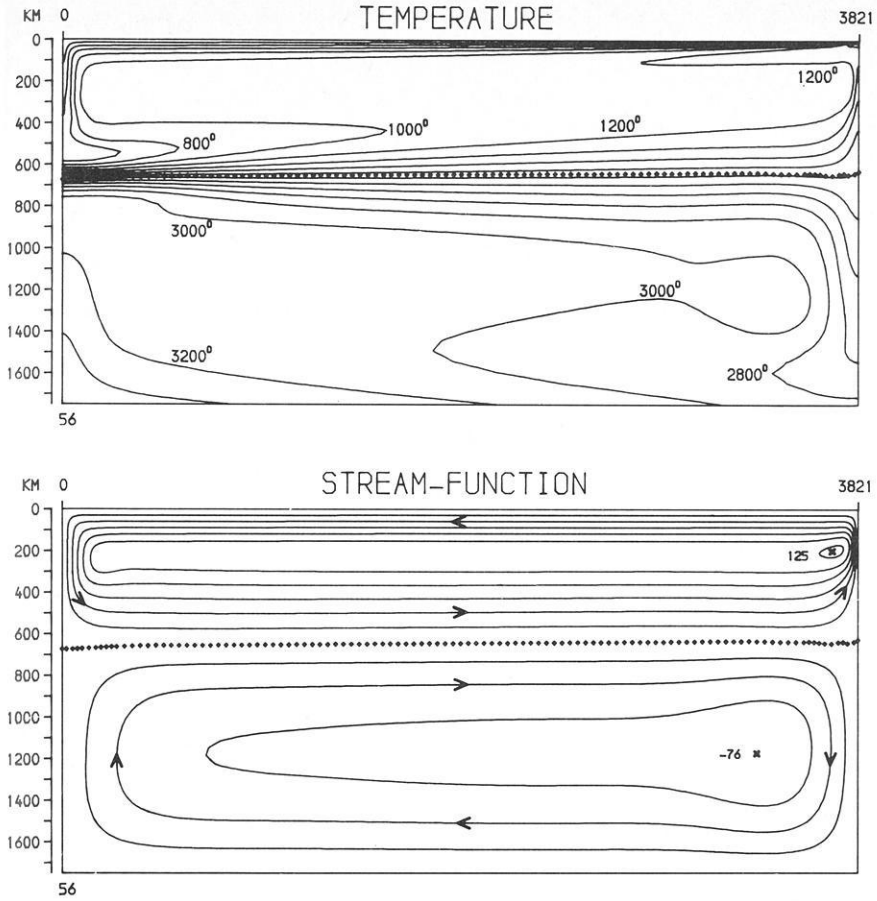

Fig. 1. Two layer convection, $\Delta\rho/\rho = 10\%$, temperature (contour interval 200°) and stream function (contour interval 20 dimensionless units). The chemical boundary is marked by dotted line. The spreading center is on the right, the subduction zone on the left

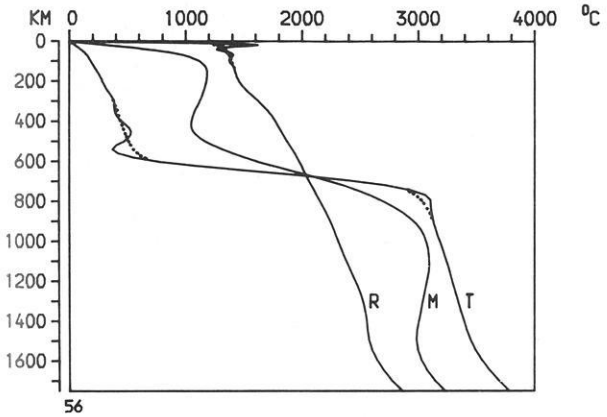

Fig. 2. Geotherms beneath the ridge (*R*), in the middle of the cells (*M*), and at the trench (*T*). Numerical over-swing effects are smoothed by *dotted lines*. The middle geotherm is representative for most of the length of the cell except narrow marginal regions

in terms of the flow as well as the temperature distribution. In the lower cell the flow is slower than in the upper one – 1 cm/a maximum velocity compared to 2.2 cm/a plate velocity and up to 10 cm/a in the ascending current beneath the spreading center. The temperature distribution in the lithosphere is in accordance with current estimates (about 1,100° C at its bottom), however, below the plate discrepancies occur. The mean temperature at the depth of the olivine-spinel transition (370 km) is 1,060° C – too far below the temperature estimates of 1400° C deduced from the properties of the phase transition (Graham 1970; Akimoto et al 1976). The chemical boundary is shifted down beneath the subduction zone and elevated beneath the spreading center by some tens of kilometers. At the dividing line a huge thermal boundary layer has developed – a result of the fact that 75% of the total surface heat flux must pass this boundary by thermal conduction. The mean temperature difference over the depth range from 500 to 800 km depth is 1,600°. Accordingly, temperatures are much higher in the lower mantle (Mean value 3,000° C, 3,200° C at the bottom7).

Another model, with a chemical density difference of only 3% (e.g., due to increased iron content of the lower mantle) failed to reach steady state. Wavy oscillations of the boundary established themselves in the region of diverging flow beneath the spreading center. Slight traces of these waves can also be seen in the first model (Fig. 1). It seems possible that smaller lumps (< 10 km) of the heavy material can be torn off and transported to the surface by the fast rising flow in the spreading axis, provided that the chemical density difference is only a few percent.

In a third experiment the chemical boundary was suddenly removed from the first model after steady state had been established. Immediately the descending plate penetrated the lower mantle and soon the separate lower cell was completely superceded by whole mantle convection. Thus the two-layer mode of convection seems extremely inferior without chemical heterogeneity.

Lastly, the experiment was carried out in reverse: a chemical boundary ($\Delta\rho/\rho = 10\%$) was introduced into a steady state whole mantle convection cell. Two separate layers of convection devel-

oped, the direction of plate motion was the same as before, however, the circulation in the lower cell was anticlockwise at the beginning, just as in the upper cell – in the opposite sense to the first model in Fig. 1. During this stage, the distortion of the chemical boundary was rather high – its depth varied by up to 180 km over the length of the cell. Yet the lower cell was not stable, a third 'embryo cell' with clockwise rotation appeared in the lower mantle and gradually superseded the other one. Finally everthing became the same as in Fig. 1.

Conclusions

1. Provided the viscosity in the lower mantle is not much higher than 10^{24} P (which is unlikely), a chemical boundary seems necessary for two-layer convection.

2. Two-layer convection can easily produce temperatures at its lowermost boundary, which are in the range of current estimates of the temperature at the core-mantle boundary (Stacey 1977), whereas the whole mantle model displays considerably lower ones. However, as discussed in paper 1, the latter is very probably due to several model idealizations.

3. It seems difficult for two-layer convection (as well as for upper mantle convection alone) to yield reasonable high temperatures in the upper mantle, while the whole mantle model was successful (paper 1). However, it is possible that special model assumptions or idealizations are responsible.

4. The very vigorous thermal boundary layer between the two cells would have a striking influence on a number of physical properties: seismic velocities (only moderate influence) and Q-factor, electrical conductivity, viscosity. For example: if Sammis et al. (1977) are right, and the activity energy for creep does not increase by more than 10 kcal/mol at the seismic discontinuities in the mantle, the viscosity would decrease by 8 orders of magnitude from the top to the bottom of the boundary layer. Temperatures as high as 2,800° C at 800 km depth would probably cause extensive partial or total melting. However, the temperature difference through the layer may be smaller than in the model, due to a smaller amount of heat sources in the lower mantle and core or due to higher velocity in the boundary layer. Furthermore the temperature effect on these properties may by obscured by the superimposed chemical effect. Nevertheless, if any boundary layer exists, it is not easy to understand why it has not yet been detected by its influence on seismic velocity or by the drop in Q, η, or σ.

5. If the coincidence between this model and the real mantle is not too weak (due to model idealizations or incorrect assumptions about model parameters such as viscosity or heat sources), a slight preference for whole mantle convection can be deduced.

Acknowledgements. I am indebted to the 'Deutsche Forschungsgemeinschaft' for financial support.

References

Akimoto, S., Akaogi, M., Kawada, K., Nishizana, O.: Mineralogical distribution of iron in the upper half of the transition zone in the earth's mantle. In: The geophysics of the pacific ocean basin and its margins. G.H. Sutton et al., eds.: pp. 399–406. Washington: AGU, 1976

Anderson, D.L., Jordan, T.: The composition of the lower mantle. Phys. Earth Planet. Inter **3**, 23–35, 1970

Christensen, U.: Phase boundaries in finite amplitude mantle convection. Geophys. J.R. Astron. Soc. in press 1980

Davies, G.F.: Whole mantle convection and plate tectonics. Geophys. J.R. Astron. Soc **49**, 459–486, 1977

Elsasser, W.M., Olson, P., Marsh, B.D.: The depth of mantle convection. J. Geophys. Res. **84**, 147–155, 1979

Graham, E.K.: Elasticity and composition of the upper mantle. Geophys. J.R. Astron. Soc. **20**, 285–302, 1970

Jeanloz, R., Richter, F.M.: Convection, composition, and the thermal state of the lower mantle. J. Geophys. Res. **84**, 5497–5504, 1979

Kopitzke, U.: Finite element convection models: comparison of shallow and deep mantle convection, and temperatures in the mantle. J. Geophys. **46**, 97–121, 1979

Liu, L.: On the 650 km seismic discontinuity. Earth Planet. Sci. Lett. **42**, 202–208, 1979

O'Connell, R.J.: On the scale of mantle convection. Tectonophysics **38**, 119–138, 1977

O'Nions, R.K., Evensen, N.M., Hamilton, P.J.: Geochemical modelling of mantle differentiation and crustal growth. J. Geophys. Res. **84**, 6091–6101, 1979

Richter, F.M.. Focal mechanism and seismic energy release of deep and intermediate earthquakes in the Tonga-Kermadec region and its bearing on the depth extent of mantle flow. J. Geophys. Res. **84**, 6783–6795, 1979

Sammis, C.G.: The effect of polymorphic phase boundaries on vertical and horizontal motions in the earth's mantle. Tectonophysics **35**, 169–182, 1976

Sammis, C.G., Smith, J.C., Schubert, G., Yuen, D.A.: Viscosity-depth profile of the earth's mantle: effects of polymorphic phase transitions. J. Geophys. Res. **82**, 3747–3761, 1977

Stacey, F.D.. A thermal model of the earth. Phys. Earth Planet. Inter **15**, 341–348, 1977

Watt, J.P., O'Connell, R.J.. Mixed oxide and perovskite structure model mantles from 700–1200 km. Geophys. J. R. Astron. Soc. **54**, 601–630, 1978

Received May 20, 1980; Revised Version June 19, 1980
Accepted June 27, 1980

J. Geophys. 49, 85–86 (1981)

Journal of Geophysics

Book Reviews

H. Stiller und M.-P. Volarovich, editors. Physical Properties of Rocks and Minerals Under Extreme *P,T*-Conditions. Akademie-Verlag: Berlin, 1979, pp. 233, 146 figures, DDR-M 38,–.

This book contains a selection of papers summarising results obtained by working group 1.11 of the commission of the Academies of Sciences of Socialist Countries on the complex problem "Planetary Geophysical Studies". As is emphasised in many of the papers, knowledge of the behaviour of rocks and minerals with increasing pressure and temperature is essential to our understanding of many geophysical and geological processes. However, the title of this book is very misleading: the thermodynamic conditions described are in general $P \lesssim 25$ kb (or more often $\lesssim 15$ kb) and $T \lesssim 500$ °C. In view of the current capabilities of quasi-hydrostatic compression apparatus with internal heating ($P \sim 150$ kb, $T \sim 1{,}200$ °C) and diamond anvil cells ($P \sim 1$ Mb, or $P \sim 260$ kb, $T \sim 2{,}000$ °C with laser heating) these values can hardly be considered extreme. The scope of this book is thus limited to properties relevant to crustal and uppermost mantle processes, and does not include discussions of mantle phase changes, the nature of the low velocity zone and its relation to magma generation, or the lithosphere-asthenosphere boundary. There are also no references to shock was studies, which are certainly relevant to extreme *P,T* behaviour, nor is there any discussion of anelastic behaviour such as attenuation, although some determinations of effective viscosity are included.

The book is divided into six chapters, as follows:

1. Elastic Properties

Six papers, including two describing the apparatus used, covering determinations of ultrasonic velocities and elastic moduli in various rocks and minerals at pressures up to 15 kb and temperatures to 400 °C. The sixth paper summarises the results of a number of studies and applies them to determining lithological models for the crust in the Ukralnian shield. There is no discussion of the problems associated with ultrasonic velocity determinations, especially in small samples, nor is there any reference to Brillouin scattering techniques.

2. Deformational Studies

This section includes a theoretical analysis of systems of cracks in a stress field, a study of residual strain in granites under differential stress, and measurements of physical properties including strength, velocity and viscosity of various rocks which are then compared with seismic data for the crust in Armenia.

3. Electrical Properties

The first paper contains much useful information on the resistivity of upper mantle rocks and minerals ($P \lesssim 20$ kb, $T \lesssim 650$ °C). The next two describe electrical spectroscopy of second order phase transitions, and the surface conductivity and polarisation of rocks at high pressures. Unfortunately there is no detailed discussion of the relationship between high conductivity layers and partial melting in the light of the experimental results. The final paper, on the electrical conductivity of MSS structures in the Fe-Ni-S system, is of relevance to the structure of the earth's core, but the range of pressure (< 57 kb) and temperature (< 300 °C) makes large extrapolations necessary, and there is no reference to other determinations of the Fe-Ni-S phase diagram to 100 kb or to the implications of recent shock wave measurements on iron and iron sulphides.

4. Magnetic and Thermal Properties

Three papers covering the magnetic properties of iron cherts, the Hopkinson effect in magnetite and titanomagnetite, and the application of pulse measuring techniques to determination of thermal conductivities.

5. Physical Properties of Lunar Rocks

A single paper covering resistivity, thermal expansion, Young's modulus and compressibility of several types of rock.

6. Geophysical Consequences and Applications

The first paper contains a formulation describing the effect of porosity and pressure on wave velocity and its bearing on earthquake prediction. The authors address the difficult problem of the interaction between crack systems, but make no comparison between their results and those of other theories, and omit a discussion of the effects of varying crack aspect ratios. The statement that liquid movements are unimportant at pressures over 100 MPa is open to dispute; if true then the dilatancy-diffusion theory used to explain many precursory effects would not be valid for depths $\gtrsim 3$ km. The remaining papers discuss the use of laboratory measurements in the interpretation of DSS profiles, the connection between high pressure and planetary physics (including accretion) and a mathematical model for the occurrence of sudden stepwise phase transformations as an explanation of deep earthquake activity.

The scope of the work described here is extremely broad: unfortunately the individual papers are often too detailed to provide a clear overview or too general, perhaps because of length restrictions, to satisfy the specialist. It will mainly be of interest to those already working in the field of high pressure geophysics, for whom it provides a useful review of Soviet and eastern European literature (references to recent work in America and Japan are sparse) and those involved in the interpretation of deep electrical or seismic sounding data. Unfortunately the appeal of the book is lessened by the large number of printing errors, the poor reproduction of photomicrographs and the quality of the English which is frequently bad enough to obscure the meaning completely.

S.A. Raikes, Karlsruhe

W.L. Pilant: Elastic Waves in the Earth. Elsevier, Amsterdam 1979.

Bereits beim ersten, oberflächlichen Durchblättern des Buches bemerkt man, daß der Schwerpunkt dieser Abhandlung über elastische Wellen bei der theoretischen Formulierung und Erarbeitung der Seismologie liegt. Das bedeutet jedoch nicht, daß das Buch vorwiegend nur für die Hand des theoretisch arbeitenden Seismikers zu empfehlen wäre; vielmehr wird hier ein konsequentes theoretisches Fundament aufgebaut, mit dem dann auch kompliziertere Probleme der Seismologie verstanden werden können. Dies theoretische Konzept der Seismologie wird streng und didaktisch hervorragend entwickelt, sodaß auch der mehr praktisch orientierte Geophysiker ohne Schwierigkeiten den theoretischen Rahmen der Seismologie überschauen kann. Der Autor versteht es, niemals beim Leser das Gefühl eines Verlustes des Bezugs zur Praxis aufkommen zu lassen; insbesondere im zweiten Teil des Buches finden sich zu den Theoretischen Ableitungen passend ausgewählte Anwendungsbeispiele. Besonders geeignet ist das Buch auch zur Verwendung im Rahmen von Vorlesungen über seismische Wellen für Studenten der Physik bzw. Geophysik; schließlich ist es ja aus der Vorlesungsreihe des Autors an der University of Pittsburgh entstanden. Erfreulich auch die Angabe der wichtigsten Originalveröffentlichungen zu den einzelnen Kapiteln, sodaß der Leser leicht den Faden aufnehmen kann, wenn er in das eine oder andere Teilgebiet tiefer eindringen möchte.

Der fachliche Rahmen des Buches beginnt mit der Theorie der elastischen Wellen, hergeleitet aus der Elastizitätstheorie. Es folgen Kapitel über das Verhalten von Wellen an Grenzflächen und an der freien Oberfläche, Strahlentheorie der Seismik (ray tracing), Mode-theorie, Oberflächenwellen, elastische Wellen in einer inhomogenen Erde, das Problem der Seismizität, Eigenschwingungen des Erdkörpers, Dämpfung seismischer Wellen, Herdmechanismen, Seismic Noise und abschließend Seismometertheorie.

Insgesamt liegt nun hier ein Buch vor, welches für den Studenten, den akademischen Lehrer und den in der Praxis arbeitenden Seismiker gleichermaßen nützliches Hilfsmittel sein sollte.

L. Engelhard

H. Walter: Vegetation of the Earth and Ecological Systems of the Geobiosphere. (Translated from the 3rd rev., German edition by J. Wieser, Heidelberg Science Library, 2nd edition 1979)
124 Figures XX, 274 pages. Soft cover DM 28,– ; approximately US $ 15.40, Springer, Berlin Heidelberg New York, ISBN 3-540-90404-2

The author is well known as editor and writer of textbooks on general botany, systematics, and ecology in a strict sense. The title *"Vegetation of the Earth"* first appeared for a large work of two volumes (1964 and 1968) which together reached more than 1,700 pages in the later editions. It has an immense number of tables, graphs, and photographs, and it gives many details especially to the geobotanist. To find a synthesis from all of this in such an excellent way as in the present book called for someone who overlooks his discipline of science like H. Walter. He had wone his experience in plant ecology during research journeys in each climate zone, and floral realm of the earth. This version of the book invites every kind of geoscientist to read it from beginning to end. Therefore he gets an excellent idea of the principles in which ways vegetation plays its role in the different ecological systems. Under this respect the division of the books content resembles strictly the division of the continents into large ecological units (zonobiomes, pedobiomes, and orobiomes). The text is well illustrated by pictures.

H. Pape, Clausthal-Tellerfeld

Finn Ronne: Antarctica, My Destiny. 278 Seiten, Hastings House, Publishers, Inc. New York, 1979, US $ 12.95

Finn Ronne ist Amerikaner norwegischer Herkunft. Neunmal besuchte er den antarktischen Kontinent. Er betrachtet seine Beziehung zum ewigen Eis der Antarktis als schicksalshaft. Das ist nur allzu verständlich. Schon sein Vater Martin Ronne nahm an zwei Antarktis-Expeditionen teil. Das Zelt, welches Amundsen im Dezember 1911 am Südpol hinterließ, war von jenem Martin Ronne gebaut worden und trug in einem eingenähten Etikett die Namen seiner sieben Kinder, darunter auch den Namen Finn Ronne. Während Martin Ronne bei der ersten Expedition an Bord des Versorgungsschiffes blieb, hielt er sich bei der zweiten Expedition unter der Leitung des Admiral Byrd mehrere Monate in der Antarktisstation Little America auf. Finn Ronne war zu jener Zeit als Elektro-Ingenieur in den Vereinigten Staaten tätig. Kurz vor Beginn einer neuen Antarktis-Expedition unter der Leitung von Byrd verstarb Martin Ronne unerwartet. Byrd bot daraufhin Finn Ronne die Mitreise an. Dieser sagte zu und verschrieb sich damit für den Rest seines Lebens der antarktischen Forschung.

Beginnend mit einem historischen Abriß der Antarktisforschung kommt Ronne auf seine eigenen Antarktis-Expeditionen zu sprechen. Einen breiten Raum nimmt dabei die Expedition während des Internationalen Geophysikalischen Jahres (1956–1958) ein. Während dieser Zeit war Ronne Kommandant der amerikanischen Ellsworth-Station.

Ronne versteht es, Erlebnisse und Tatsachen in einer gut gelungenen Mischung auf spannende Weise darzustellen. Bei seiner ersten Expedition benutzte Ronne als Transportmittel Hundeschlitten und Skier. Geheizt wurde mit einem kleinen Kerosinofen. Später hat Ronne dann die Zeit erlebt, in der in festen Behausungen gewohnt wurde und der Transport weitgehend mit Traktoren und Flugzeugen durchgeführt wurde. Ronne schildert die technischen Probleme, die vom Hundeschlitten bis zum Flugzeug auftreten können, in fast lehrbuchhafter Weise. Ebenso werden die menschlichen Probleme, die bei einem engen Zusammenleben der meist sehr individuell veranlagten Expeditionsteilnehmer in der Isolation der Antarktis auftreten, lebensnah geschildert. Manchmal fast störend – ziehen sich zwei Themen wie ein roter Faden durch das ganze Buch. Das erste ist eine Kontroverse mit Byrd. Immer wieder taucht eine heftige Kritik an Byrd, sowohl als Mensch als auch als Expeditionsleiter, auf. So behauptet Ronne unter anderem, daß Byrd den Nordpol nie überflogen habe und führt dafür auch Beweise an. Das zweite Thema ist das Herausstellen der eigenen Verdienste um die Antarktis-Forschung. Diese stark persönlich geprägten Motive brauchten nicht so deutlich in dem sonst sehr sachlich geschriebenen Buch hervorgehoben zu werden.

Zusammenfassend ist das Buch sehr zu empfehlen. Zahlreiche schwarzweiß Fotografien illustrieren den Text. Ein Sach- und Namenregister erleichtert das Aufsuchen von Textstellen. Wer dieses Buch gelesen hat, kann viele geographische Namen der Antarktis mit Personen und deren Leben verbinden. Besonders geeignet dürfte das Buch für denjenigen sein, der ohne eigene Erfahrung in hohen Breiten etwas über die besonderen Probleme arktischer bzw. antarktischer Forschungsarbeit lernen möchte.

Burkhard Theile

Alfred-Wegener-Stiftung

Das geowissenschaftliche Weltbild hat in den letzten 10 Jahren eine kopernikanische Wende durchlaufen. Die Ausbreitung der Ozeanböden und die Plattentektonik haben in eindrucksvoller Weise die Kontinentalverschiebungstheorie von ALFRED WEGENER bestätigt. Die damit vor den Geowissenschaften liegenden neuen Aufgaben erfordern sowohl neue Formen interdisziplinärer Kooperation als auch die Entwicklung neuer Wissenschaftsstrukturen.

Deshalb gründen die deutschen geowissenschaftlichen Gesellschaften zum 100. Geburtstag ALFRED WEGENERS die:

Alfred-Wegener-Stiftung

zur Förderung interdisziplinärer Zusammenarbeit auf dem Gebiet der Erdwissenschaften.

Alle Freunde und Förderer der Geowissenschaften sind aufgerufen, die ALFRED-WEGENER-STIFTUNG zu unterstützen. Beim Stifterverband für die Deutsche Wissenschaft ist das folgende Konto eingerichtet worden:

Konto-Nr. 253770212
BLZ: 36070050
Deutsche Bank AG, Essen
„Stifterverband für die Deutsche Wissenschaft"
(Kennwort: Alfred-Wegener-Stiftung).

Eine Steuerbescheinigung wird zugesandt.

J Geophys (1981) 49:89–92

Journal of Geophysics

Steady State Creep of Fine Grain Granite at Partial Melting

F Auer[1]*, H. Berckhemer[1], and G. Oehlschlegel[2]

[1] Institut für Meteorologie und Geophysik, Universität Frankfurt, Frankfurt, Federal Republic of Germany
[2] Institut für Mineralogie, Ruhr Universität, Bochum, Federal Republic of Germany

Abstract. Steady state creep under constant stress has been measured in a fine grain granite (aplite) from Schauinsland, Germany for the temperature range of partial melting 860°–1,060° C, under a hydrostatic pressure of 4.2 kbar, and at low shear stresses of 5–50 bar. The apparatus used is described briefly. Rheological measurements are complemented by microscopic investigations. With a melt fraction of up to about 20%, creep can be described by a power law with a stress exponent of 3–4 and an activation energy of 80 kcal/mole, typical for creep in solids. Above 1,010° C or 20% melt, the activation energy increases rapidly to a value of 200 kcal/mole simultaneously with a rapid increase of the melt fraction and a decrease of feldspar content. From the grain structure and from etching tests it is concluded that quartz contributes little to the plastic deformation which is governed mainly by the stress and temperature induced recrystallization of feldspar. The large temperature dependence of the creep rate above 1,010° C may be caused by the decreasing area of grain contacts and consequent rise in local stress. These results support those of Arzi (1974) and Roscoe (1952).

Key words: Steady state creep – Partial melting – High pressure research

Introduction

The creep behaviour of earth materials in the mantle governs all deep reaching tectonic processes. Almost no creep measurements have yet been performed on rocks under high hydrostatic pressure and at the low shear stresses ($\sigma < 100$ bar) typical of most parts of the upper mantle.

Controversial opinions are held and few data are available on the rheological behaviour of partially molten rocks, in particular. There is one central question: up to what melt fraction does the material creep like a solid and when does it begin to behave like a viscous liquid. Press (1959), Ringwood (1969) and Ritsema (1972) expressed the opinion that a small percentage of melt is sufficient to reduce drastically the 'strength' of the upper mantle. The experimental results of Roscoe (1952), Arzi (1974), and of this study do not support this theory. Roscoe studied suspensions of solid particles in viscous fluids and found the transition from solid to fluid behaviour in the range 20%–40% melt. Arzi found, in three successful runs, that the creep behaviour of a granite did not deviate significantly from the subsolidus behaviour for up to 10% melt. However, his samples were water saturated and showed prescribed fault lines.

In this study an air-dried, fine grain granite (aplite) from Schauinsland, Black Forest, Germany, is investigated. It is composed of approximately 50% sericitized plagioclase and orthoclase, 40% quartz and 10% coarse mica, mainly muscovite and chloritized biotite. The grain size ranges from 0.5 to 1 mm. Granite has been chosen for this study for two reasons: First, because melting begins at relatively low temperature, and second, the melt does not recrystallize so that the quenched melt can easily be identified, in the form of glass, under the microscope.

Experimental Procedure

Figure 1 shows a schematic section through the pressure vessel: the sample (1) is exposed simultaneously to a hydrostatic gas pressure p of up to 10 kbars and an axial stress of 1–200 bars. Argon gas is used as pressure medium. All experiments in this study were carried out at $p = 4.2$ kbar. Constant axial stress is produced by a helical spring (2) which is loaded from outside the vessel by a male screw (7).

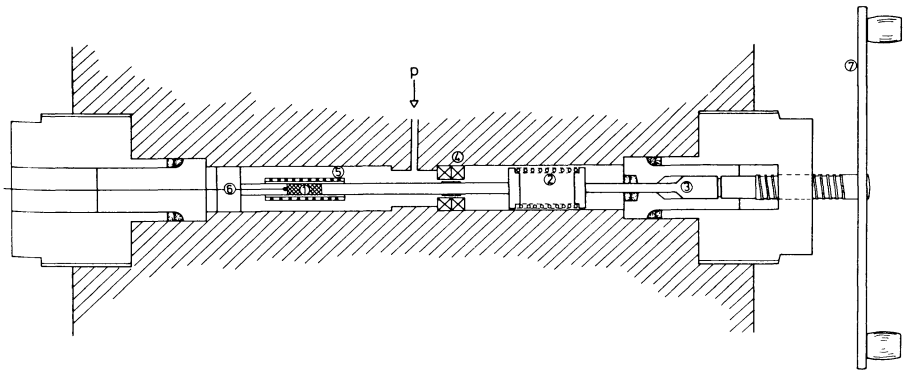

Fig. 1. Schematic cross-section of the 10 kbar pressure vessel. For description of numbered components see text

* *Present affiliation*. Battelle Institut, Frankfurt, FRG

0340-062X/81/0049/0089/$01.00

The cylindrical specimen, 20 mm long and 9 mm in diameter, is jacketed with dispersion-strengthened platinum of 0.1 mm wall thickness. Both ends are closed with platinum caps and welded pressure-tight. Axial deformation of the specimen is measured with high resolution by a differential transformer (4) mounted inside the pressure vessel. A system free of any mechanical friction is required if measurements are made under small deviatoric stress. The sample is heated in an internal Pt-Rh furnace (5). The sample temperature is measured and controlled by a thermocouple (6). The temperature in the sample varies from the center to the end by only about 5° C.

The actual measurements begin after the sample has shortened under pressure, temperature, and moderate axial stress by about 2% in plastic creep. This secures perfect adjustment of the end faces of piston and sample and reduces drastically the influence of primary creep on the measurements. The major experimental problem is that during deformation the platinum jacket frequently fails. Each sample is carefully checked after the experiment in this respect.

Results

Creep Experiments

An empirical equation of the form

$$\dot{\varepsilon} = A \ \sigma^n \ \exp(-E/RT) \qquad p = \text{const}$$

where $\dot{\varepsilon}$ = creep rate
σ = deviatoric stress (bar)
E = activation energy (kcal/mole)
T = temperature (Kelvin)
A = a parameter only weakly temperature dependent
R = gas constant
n = stress exponent
p = hydrostatic pressure

is suitable to describe the steady state creep behaviour of many materials (Weertman and Weertman 1975). From this equation it follows:

$$n = \frac{\log \dot{\varepsilon}}{\log \sigma}, \qquad T = \text{const}$$

$$E = -2.3 \ R \ \frac{d \log \dot{\varepsilon}}{d 1/T}, \qquad \sigma = \text{const}.$$

On a $\dot{\varepsilon}$ (σ) plot with double logarithmic scale the stress exponent n appears as the slope of the experimental curve. Similarly, the activation energy E can be derived from a semilogarithmic plot of $\dot{\varepsilon}$ ($1/T$), frequently called an Arrhenius plot.

Figure 2 shows the strain rate $\dot{\varepsilon}$ as a function of the stress σ at two different temperatures. After raising or lowering the stress in small steps, constant strain rate was generally reached ($\dot{\varepsilon} \approx 10^{-6}$–$10^{-7}$ s^{-1}) after 5–15 min. The duration of individual measurements was typically about one hour but varied between half a day and several minutes, depending on strain rate. Measurements were carried out up to a final strain of the sample of about 10%. The question of stationarity of creep is a very fundamental one and does not refer only to the present measurements (Paterson 1979). Stationarity requires equilibrium in the microscopic stress field and the distribution of lattice defects. It also requires chemical and structural equilibrium (with respect to grain size) corresponding to given p, T conditions. It is evident that in this broad sense a steady state is never reached under laboratory conditions. In the usual restricted sense, however, which excludes

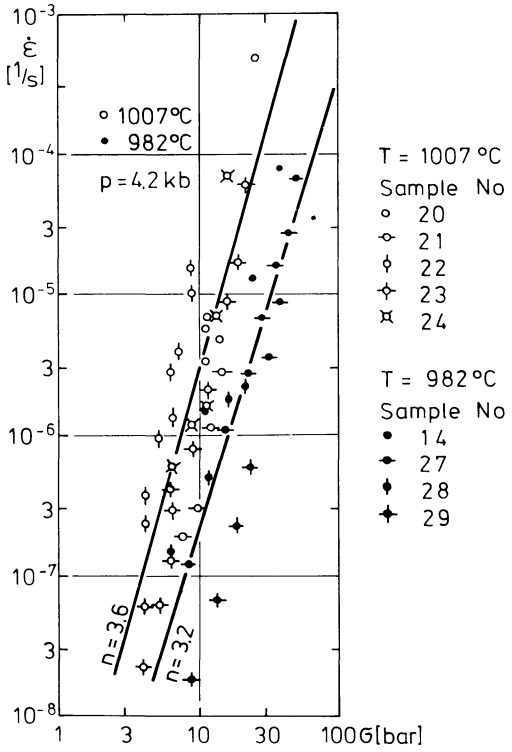

Fig. 2. Stress vs strain-rate plot for aplite. Data from the same sample are marked by identical symbols

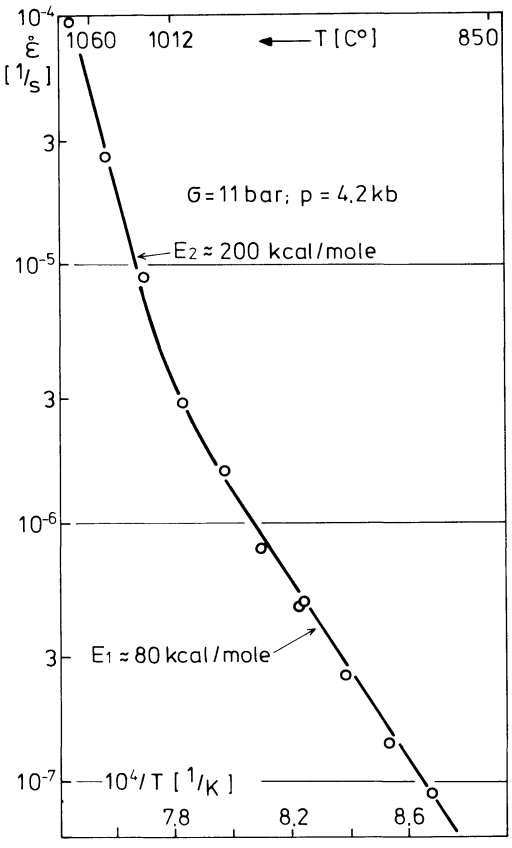

Fig. 3. Arrhenius plot for aplite at partial melting

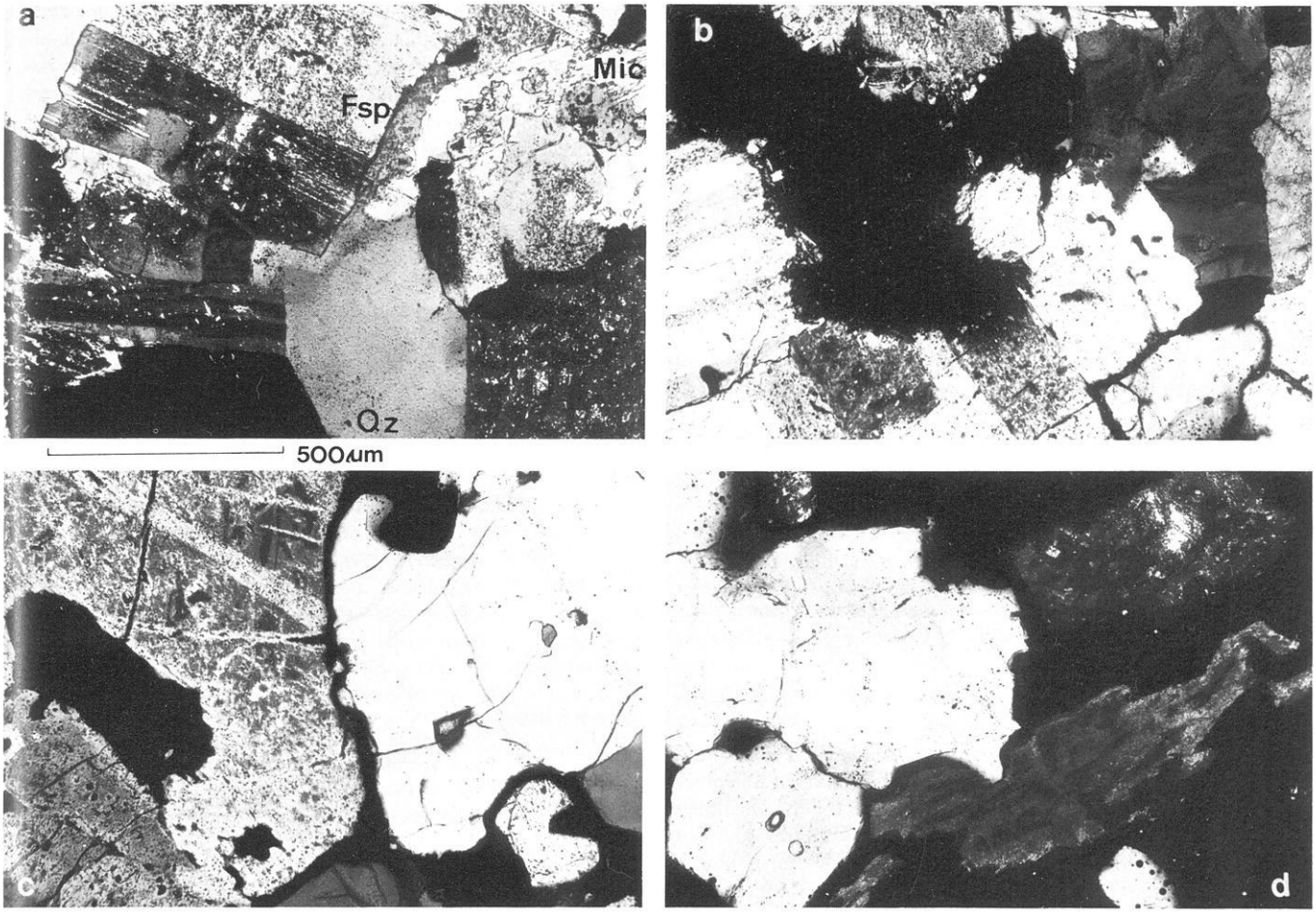

Fig. 4a–d. Thin sections of aplite in polarized light. **a** Original aplite; **b** $T=968°$ C, 13% melt; **c** $T=1009°$ C, 18% melt; **d** $T=1040°$ C, 37% melt. Q_z = quartz, F_{sp} = feldspar (plagioclase and orthoclase), Mic = muscovite and chloritized biotite, opaque areas are alteration products of mica, the melt is isotropic under crossed polarizers

long term transient phenomena, our data can be considered steady state and are compatible with each other. As an average over the stress range 5–50 bar a value of n between 3 and 4 is obtained. This value is common for creep in minerals below $\sigma \approx 1$ kbar. The rather large scatter of data is due to the fact that at $T=982°$ C four different samples, and at $T=1{,}007°$ C five samples were used. Although they have all been taken from the same piece of rock, at equal stress and temperature the strain rate may vary by an order of magnitude due to mineralogical and mechanical inhomogeneities. Measurements from the same sample are marked by identical symbols.

The strain rates shown in Fig. 3 were obtained at a constant stress of $\sigma=11$ bar while the temperature varied from 860°–1,060° C. Two different activation energies can be distinguished which take over near 1,010° C. The lower branch corresponds to $E_1 \approx 80$ kcal/mole, the upper branch to $E_2 \approx 200$ kcal/mole. This means, in simple terms, that the temperature dependence of the creep rate increases strongly above 1,010° C.

Microscopic Structure

In order to find the cause of the rapid increase of activation energy at 1,010° C, the process of partial melting has been investigated microscopically. Five samples were exposed for three hours each to a hydrostatic pressure of $p=4.2$ kbar and temperatures of 929° C, 968° C, 1,007° C, 1,040° C, and 1,046° C, respectively, at a deviatoric stress $\sigma=0$ bar. From thin sections (Fig. 4a–d) the following qualitative statements can be made: At the lowest temperature minerals containing water (muscovite, biotite, chlorite) begin to disintegrate into a glassy melt and opaque relicts. A seam of optically isotropic melt develops which broadens with increasing temperature at the quartz/feldspar grain boundaries. The quartz/quartz boundary remains unwetted by the melt until higher temperatures are reached. At the highest temperature, it is mainly quartz which remains unmelted. Locally, more than 50% melt occurs with opaque decomposition products of mica (mainly haematite, some iron-rich opaque melt and iron-silicates) floating in the melt. The melt is chemically extremely inhomogeneous.

Figure 5 shows the result of a quantitative evaluation. The cross section of each rock sample was divided into 1,800 points and each point classified as melt, quartz, feldspar, coarse mica and its opaque disintegration products. The melt curve can be extrapolated to the beginning of partial melting at a temperature of about 870° C. The proportion of melt increases steadily to about 18% at 1,010° C, where it begins to grow more rapidly at the expense of feldspar. With further increase of temperature feldspar ultimately disappears. The quartz fraction remains essentially constant.

In an attempt to gain some information on the microscopic mechanisms of plastic deformation at partial melt three samples which were exposed to a temperature of 1,000° C and $\sigma=0, 8, 25$ bar

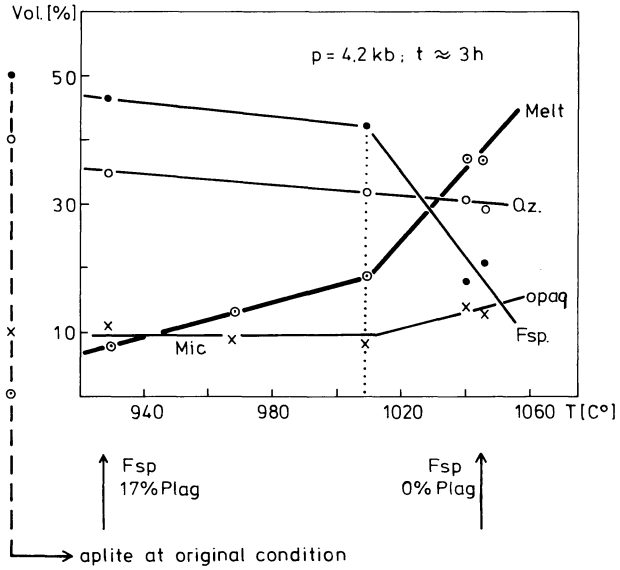

Fig. 5. Mineral composition of aplite at partial melting. Q_z = quartz, Mic, opaq = mica and its opaque alteration products, F_{sp} = feldspar (plagioclase (plag) and orthoclase), t = duration of measurement

were examined microscopically after being etched with HF. Quartz crystals showed a considerable dislocation density (approximately $1\text{-}3 \cdot 10^4$ etching pits/mm^2) these had apparently been introduced beforehand by Variscan tectonics. There is no significant difference between the dislocation density in the quartz in the three samples and in that of the starting material. Apparently quartz does not contribute much to the plastic deformation but shows rather rigid or brittle behaviour. In contrast, the feldspar does not fracture. The sericitic alteration products of the feldspars decompose to yield clear recrystallized feldspar grains with occasional inclusions of opaque minerals like haematite. In the course of this process, the lamellar twinning in feldspars remains unchanged.

Discussion and Conclusions

From Figs. 2 and 5 we conclude that even in the presence of about 20% melt the creep deformation of the granite under investigation follows a power law, characteristic of creep in solids. If we assume that the intergranular melt has a comparatively low viscosity, the creep resistance at low to moderate melt fractions is apparently still controlled by the deformation within grains and at grain boundaries. This conclusion is also supported by the value of the activation energy $E_1 \approx 80$ kcal/mole which is close to that for creep of several dry, polycrystalline minerals such as quartzite or enstatolite (Carter 1976).

From microscopic inspection and etching tests, it appears that in our experiments the quartz grains remain rather brittle and contribute little to the plastic deformation. Although no relevant experimental data exist, it might be expected from general experience that recrystallization from partial melt and polygonization of original sericitized feldspar is compatible with power law creep (Carter 1976). The step in activation energy at 1,010° C coincides with the rapid increase of melt and the corresponding reduction of crystalline feldspar which is supposed to govern the creep process. An increase in the proportion of melt and the corresponding decrease of grain size in the remaining solid matrix reduces the area of the effective solid grain contacts and, consequently, raises the local stress which results in a higher creep rate. The increase of E may, therefore, be mainly an apparent one reflecting the change of the solid matrix contact area rather than a new creep mechanism. Within the range of our experiments, our data support the result obtained by Arzi (1974) and Roscoe (1952) that somewhere in the range of 10–30% melt, the 'rheological critical melt percentage' (Arzi 1978), a drastical lowering of the effective rock viscosity occurs. Our experimental set up was not suitable for measurements in the regime in which creep is fully governed by the relatively low viscosity of the melt and in which a Newtonian type of creep has to be expected.

It should be pointed out that a much smaller fraction of melt or even subsolidus grain boundary relaxation may suffice to influence drastically the elasticity and the anelastic absorption, and to produce a low velocity, low Q zone in the mantle (Berckhemer et al. 1979).

Addenda

After completion of this paper a publication on the experimental deformation of partially melted granite by van der Molen and Paterson (1979) appeared. A major conclusion of their extensive investigations, carried out at higher shear stresses, is that the critical melt fraction separating granular-framework-controlled flow behaviour from suspension-like behaviour is deduced to be approximately 30–35 vol.%.

Acknowledgements. Thanks are expressed to Professor Flörke, Bochum, and Dr. S. Schmid, Zürich for stimulating discussions. Engineers E. Aulbach and M. Bruns operated the high pressure apparatus. This research was supported by the German Research Society as part of the priority program 'Geophysical high pressure research'.

References

Arzi, A: Partial melting in rocks: rheology, kinetics, water diffusion. Ph.D. Thesis, Harvard University 1974

Arzi, A: Critical phenomena in the rheology of partially melted rocks. Tectonophysics **44**, 173–184, 1978

Berckhemer, H., Auer, F., Drisler, J: High temperature anelasticity and elasticity of mantle peridotite. Phys. Earth Planet. Inter. **20**, 48–59, 1979

Carter, N: Steady state flow of rocks. Rev. Geophys. Space Phys. **14**, 301–360, 1976

Goetze, C: A brief summary of our present day understanding of the effect of volatiles and partial melt on the mechanical properties of the upper mantle. In: High pressure research, M.H. Manghnani, S.I. Akimoto, eds: pp. 3–24. New York: Academic Press 1977

Molen, I. Van der, Paterson, M.S: Experimental deformation of partially melted granite. Contrib. Mineral. Petrol. **70**, 299–318, 1979

Paterson, M.S: The mechanical behaviour of rock under crustal and mantle conditions. In: The earth, its origin, structure and evolution, M.W.Mc Elhinny, ed. New York: Academic Press 1979

Press, F: Some implications of mantle and crustal structure from G waves and Love waves. J. Geophys. Res. **64**, 565–568, 1959

Ringwood, A.E: Composition and evolution of the upper mantle. In: The Earth's Crust and Upper Mantle, P.J. Hart, ed.: Geophys. Monogr. **13**, 1–17 Wash. D.C.: Am. Geophys. Union 1969

Ritsema, A.R: Synopsis of some comments on Sir Herold Jeffrey's paper on creep in the earth and planets. Tectonophysics **13**, 579–580, 1972

Roscoe, R: The viscosity of suspension of rigid spheres. Br. J. Appl. Phys. **3**, 267–269, 1952

Weertman, I., Weertman, I.R: High temperature creep of rock and mantle viscosity. Annu. Rev. Earth Planet. Sci. **3**, 293, 1975

Received February 15, 1980; Revised Version August 4, 1980
Accepted September 5, 1980

J Geophys (1981) 49:93–100

Journal of Geophysics

Laboratory Synthesis of Aluminium-Substituted Titanomaghemites and Their Characteristic Properties

Ö. Özdemir* and W. O'Reilly
Department of Geophysics and Planetary Physics, School of Physics, University of Newcastle upon Tyne, NE1 7RU, Great Britain

Abstract. Sintered polycrystalline specimens of titanomagnetite containing aluminium, of composition $Fe_{2.6-\delta}\ Ti_{0.4}\ Al_\delta\ O_4$ and $Fe_{2.4-\delta}\ Ti_{0.6}\ Al_\delta$ ($\delta=0$, 0.1, and 0.2) were prepared by the method of partial self buffering. X-ray and magnetic analysis confirm that the synthesized materials are single phase spinels. The synthesized material was ball-milled in a high purity methanol slurry to produce submicron particle sizes and the fine grain material oxidized in air at temperatures below about 350° C. The titanomaghemites so produced are single phase spinels over almost the entire oxidation range. Characteristic properties of the samples such as Curie temperature and unit cell edge were determined as an aid in the identification of titanomaghemites in basalts.

Key words: Titanomaghemites – Oxidation – Gravimetry – Curie temperatures – Mineral identification – Deep sea basalts

Introduction

A large part of the established picture of the history of the Earth's crust has come from the information stored in the magnetic minerals of the crust. The continuing evolution of the crust has been traced out in the latest phase of such investigations, the *Deep Sea Drilling Project* (DSDP). The fine grain magnetic minerals produced in quenched submarine basalts should carry a faithful record of the geomagnetic field. However, submarine weathering appears to rapidly alter the magnetic minerals and the consequent modification in their magnetic properties may obscure the palaeomagnetic record.

The remanence carriers in almost all igneous rocks are the titanomagnetites ($Fe_{3-x}\ Ti_x\ O_4$, $0<x<1$) and their derivatives. Naturally occurring titanomagnetites often contain 'impurity' cations. According to the electron microprobe analysis of titanomagnetites from subaerial basalts, typical impurities are aluminium and magnesium up to 4% by weight (Creer and Ibbetson 1970). Other cation species such as manganese, chromium, nickel and zinc are also often present. Analysis of titanomagnetites in pillow basalts from the FAMOUS Rift Valley indicates that the weight percentage of the aluminium is about 1.5% and that this is the most abundant minor cation species (Lecaille and Prevot, in press 1980).

The single phase spinel oxidation products of titanomagnetites are known as titanomaghemites, $Fe_{(3-x)R}\ Ti_{xR}\square_{3(1-R)}\ O_4$, $R=8/\{8+z(1+x)\}$ and $z(0<z<1)$ is the degree of oxidation). R may be considered as simply a parameter of convenience or may be called the 'spinel stoichiometry parameter' It is equal to the ratio of the oxygen in the stoichiometric composition to that in the nonstoichiometric case. For oxidation $1<R<8/(9+x)$. In the compositional formula R shows the number of cations per spinel formula unit reducing as they are spread throughout the crystal, physically enlarged when oxidation takes place by addition of oxygen. The oxidation process, which is generally referred to as "maghemitization", appears to be especially favoured by the submarine environment.

The laboratory simulation of the maghemitization of titanomagnetites will provide us with a better understanding of the magnetic properties of naturally occurring material in the oceanic crust. Ozima and Sakamoto (1971), Readman and O'Reilly (1972), and O'Donovan and O'Reilly (1977) studied the magnetic properties of the cation-deficient products of titanomagnetites which were oxidized in air. Joshima (1975) presents a brief report of studies on the effect of aluminium contamination in titanomagnetites and titanomaghemites. More recently Ryall and Hall (1979) have heated submarine basalts in water in the laboratory in order to study the variation of magnetic properties with oxidation. In some studies only a limited range of oxidation maintaining the spinel structure could be achieved.

The purpose of the present study is to prepare synthetic analogues of naturally occurring titanomagnetite and titanomaghemites substituted by aluminium, this being the most abundant species of cation, other than iron or titanium, in oceanic rocks. The characteristic properties of the synthetic analogues, such as lattice parameter and Curie temperature, may then be used for identification of the magnetic minerals in submarine basalts. An understanding of the alteration process and its magnetic consequences are necessary for the interpretation of the palaeomagnetic record and of the anomalies in the geomagnetic field, observed over the ocean basins, due to the remanence of the basement rocks. Conversely, magnetic studies of the rocks may be used to trace out the thermal and chemical evolution of the basement material.

Experimental Method

The results of the previous investigations of maghemitization – the characteristic properties of the titanomaghemites produced and the range of non-stoichiometry attainable – are not in good agreement. The successful preparation of single phase well-characterized homogeneous materials is crucial to such investigations.

* *Present address*. Department of Geology and Geophysics, 108 Pillsbury Hall, 310 Pillsbury Drive SE, Minneapolis, Minnesota, 55455, USA

0340-062X/81/0049/0093/$01.60

The synthesis and characterization procedures adopted in the present investigation are therefore described in some detail.

Synthesis of Titanomagnetites

Polycrystalline specimens of six compositions in the systems $Fe_{2.4-\delta}Al_{\delta}Ti_{0.6}O_4$ ($x=0.6$, the ATM60 series) and $Fe_{2.6-\delta}Al_{\delta}Ti_{0.4}O_4$ ($x=0.4$ the ATM40 series) ($\delta=0$, 0.1 and 0.2 in both cases) were synthesized by the method of partial self buffering.

The starting materials Fe, TiO_2, Al_2O_3 and Fe_2O_3 were pre-treated before firing. The iron powder was heated in pure dry hydrogen at 350° C to remove any surface oxide layer The Fe_2O_3 was heated in a stream of dry oxygen at 625° C to oxidize any Fe^{2+} ions to Fe^{3+} Al_2O_3 and TiO_2 were heated in air for 23 h at 620° C and 30 h at 320° C, respectively, to remove adsorbed moisture. The stoichiometric mixtures of the powders were pressed into pellets and placed in a mullite tube which was evacuated and flushed with argon at a pressure of 200 torr. The tube was heated at 1,350° C for six hours then the pellets allowed to cool down to room temperature in 25 h in the furnace. Finally the material was re-crushed and pelleted and fired at 1,350° C in the mullite tube, this time containing a mixture of 90 vol.% argon and 10 vol.% CO_2–CO, in a proportion slightly reducing with respect to the mixture corresponding to stoichiometry at the firing temperature.

After each of the two firings the X-ray cell edges were determined from Debye-Scherrer powder photographs and the Curie temperatures found from the temperature dependence of initial volume-susceptibility (Özdemir and O'Reilly 1978). The cell-edges for the composition $\delta=0.10$ and 0.2, decreased by a considerable amount after the second firing. This may be because aluminium diffusion through the crystalline lattice was only completed after the second firing and the stoichiometry was improved. The synthesized materials were single phase spinels.

Curie temperature is very sensitive to the degree of high temperature non-stoichiometry and cell edge rather less sensitive. Increasing non-stoichiometry results in a higher Curie temperature and decreased cell edge. The method of partial self-buffering and two firings used in the present study produces more highly stoichiometric material than single firings or total self-buffering. This may account for differences between the present data and that of Readman and O'Reilly (1972) and Richards et al. (1973). The degree of non stoichiometry for the TM60 material can be estimated using the Hauptman (1974) formula. This gives $z=0.028$.

Preparation of Fine Grain Titanomagnetites

To prepare the fine particle titanomagnetites, the twice-fired materials were ground for 16 h in a high purity methanol slurry in a tungsten carbide ball mill. Then the slurry was gently dried under an infra-red lamp for half an hour The Curie temperature and cell-edge parameters were remeasured after ball-milling. The results are given in Table 1 The Curie temperatures of the finely ground samples were found to be slightly higher than the twice-fired coarse grain samples. This is a result of the oxidation which invariably takes place during the grinding process. This was confirmed by wet-chemical analysis. Values of the oxidation parameter, z, obtained from the chemical analysis are given in Table 1.

Electron Microscope Observations of Fine Grain Material

Grain size measurements were made using the transmission electron microscope. The particle size distribution was determined from separate grains on the high magnification electron micrographs. The low magnification micrographs showed that the particles tended to flocculate, due to magnetostatic interactions between grains, into agglomerates in the size range 0.1–0.4 μm. However the observations at higher magnification (Fig. 1) show the presence of separate grains which, together with the small agglomerates within which separate grains could be distinguished, allowed an attempt to determine the grain size distribution. Because of the tendency to flocculate, only 103 separated grains were measured from four micrographs, projected through a photographic enlarger. The grain size distribution is shown as a histogram in Fig 2a. The grain size was found to be about 300 ± 70 Å. However, this value can only be approximate when the small number of grains counted is taken into account. Readman and O'Reilly (1970) produced fine grain material by a similar technique and the mean crystal size from X-ray line broadening appeared to be about 400 Å.

The shape of grains was not equidimensional as expected. Apparently the ball milling produces irregular shapes although the particles are rounded. An attempt has been made to determine the ratio of the smallest (d_B) to the largest diameter (d_A) on the grains counted. The results are shown in the histogram of Fig. 2b. The mean value of the distribution was found to be 0.66 ∓ 0.11.

Table 1. Cell edge, Curie temperature and initial oxidation parameters for finely ground samples of the ATM40 and ATM60 series

	Composition	Chemical analysis			Curie[a] temperature T_c (°C)	Cell edge[b] a (Å)	X-ray densities (gm/cm^3)
		Fe^{2+}% (Stoichiometric, theoretical)	Fe^{2+}% (Experimental)	z			
$Fe_{2.6-\delta}Al_{\delta}Ti_{0.4}O_4$	0	34.48	29.49 ± 0.04	0.14 ± 0.03	363	8.459 ± 0.005	4.925
	0.10	34.92	28.75 ± 0.04	0.18 ± 0.03	325	8.448 ± 0.007	4.982
	0.20	35.38	30.06 ± 0.04	0.15 ± 0.03	270	8.435 ± 0.006	5.080
$Fe_{2.4-\delta}Al_{\delta}Ti_{0.6}O_4$	0	39.40	34.13 ± 0.04	0.13 ± 0.04	206	8.486 ± 0.006	4.839
	0.10	39.91	33.89 ± 0.04	0.15 ± 0.03	148	8.473 ± 0.006	4.908
	0.20	40.43	34.14 ± 0.08	0.16 ± 0.07	102	8.462 ± 0.006	4.981

[a] The samples were heated in sealed evacuated silica capsules for T_c measurements to prevent oxidation
[b] The cell parameters were derived from Guinier de Wolff powder pictures

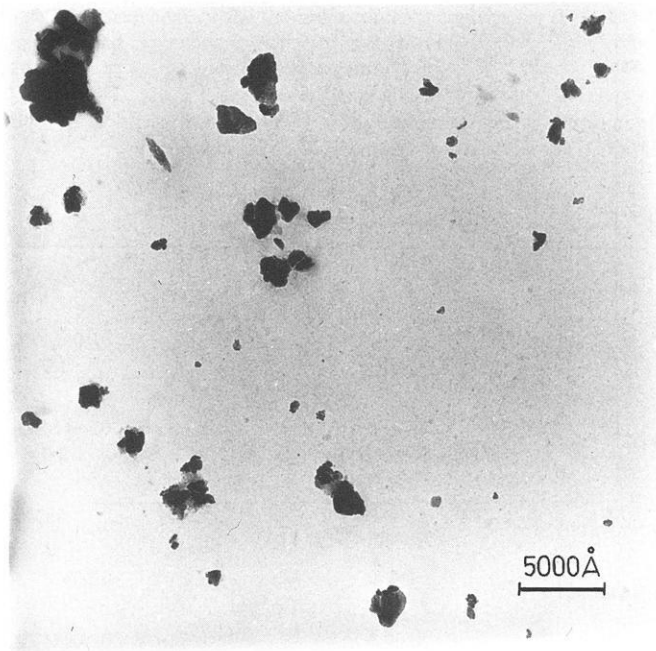

Fig. 1. Electron micrograph of a fine grain titanomagnetite sample showing isolated grains and small agglomerates

Preparation of Titanomaghemites

The same technique was used to prepare the titanomaghemites as described by Readman and O'Reilly (1970) for unsubstituted titanomaghemite and O'Donovan and O'Reilly (1977) for magnesium substituted compositions. Samples of the finely ground titanomagnetite were oxidized by heating in air in a Stanton Massflow thermobalance. The instrument consists of a precision air-damped analytical balance with electric weight loading. The standard tube furnace is counterbalanced by its own low voltage transformer and may be raised or lowered over the charge. A chart recorder provides simultaneous recording of weight change and temperature.

The oxidation experiments were carried out in two stages: (i) First, straight runs were made in which specimens (1 gm) were heated at a constant rate to about 900° C. The derivatives of such weight-temperature curves are DTG curves. The DTG curves for the ATM60 series are given Fig. 3. The curves of all samples show two peaks or can at least be fitted by two independent peaks. The lower temperature peak, which is centered at about 250° C, is the higher. The second, less definite, peak occurs at about 350° C. This has been attributed to the limited availability for oxidation of Fe^{2+} in the tetrahedral sites of the structure (O'Donovan and O'Reilly 1977). The various parameters (onset of weight gain, position and height of peaks, end of weight gain, relative areas under the inferred peaks) of the curves change systematically with composition within each of the two series. The parameters of the DTG curves are listed in Table 2.

X-ray powder pictures of the products of the straight DTG runs were made using a Guinier de Wolff camera for the ATM40 samples. The samples heated to high temperatures (say 900° C) show mixed phases, consisting of a rhombohedral (haematite) and a Ti-rich phase (pseudobrookite). The samples of ATM40 ($\delta=0.1$) heated between temperatures 100°–550° C show spinel and rhombohedral phases. The cell edge of the spinel phase is 8.348 ± 0.009 Å. Heating above 550° C results in a titanium-rich phase together with haematite.

(ii) Secondly, isothermal runs were made at temperatures below about 350° C to produce single-phase homogeneous titanomaghemites of the required composition.

Differential thermogravimetric analysis indicates that the oxidation of the fine grain titanomagnetite takes place readily between 100°–350° C. Heating above this temperature is expected to result in multiphase products.

A starting weight of 1 gm was used in each oxidation experiment. The titanomaghemite samples were prepared by heating at isotherms between 100° and 350° C in air in the thermobalance for times of the order of 10 h.

In some of the most highly oxidized compositions very faint lines due to non-spinel phases were just visible. Because of the sensitivity of the Guinier de Wolff system the concentration of the non-spinel phases is considered to be low enough (~a few percent) that the error in the estimated composition of the spinel phase is negligible and that the observed magnetic properties are those of the spinel phase only.

The oxidation parameter, z, is defined as the fraction of the Fe^{2+} ions in the stoichiometric composition oxidized to Fe^{3+}.

$$Fe^{2+}+\tfrac{1}{2}zO\rightarrow zFe^{3+}+(1-z)Fe^{2+}+\tfrac{1}{2}zO^{2-}.$$

When the desired weight increase was obtained, the sample was quenched to room temperature by raising the furnace. No weight increase was found to have taken place during the cooling period. Before quenching to room temperature the sample was allowed to come into 'equilibrium', i.e., the rate of weight increase became

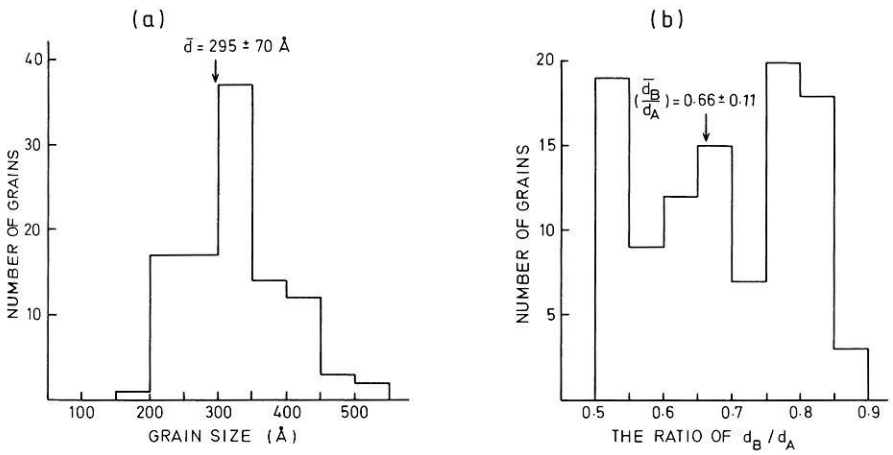

Fig. 2. Histograms of the grain size distribution and the ratio of the longest to smallest dimension (d_B/d_A) for the fine grain sample of $Fe_{2.2}\ Ti_{0.6}\ Al_{0.2}\ O_4$ determined from electron micrographs such as Fig. 1

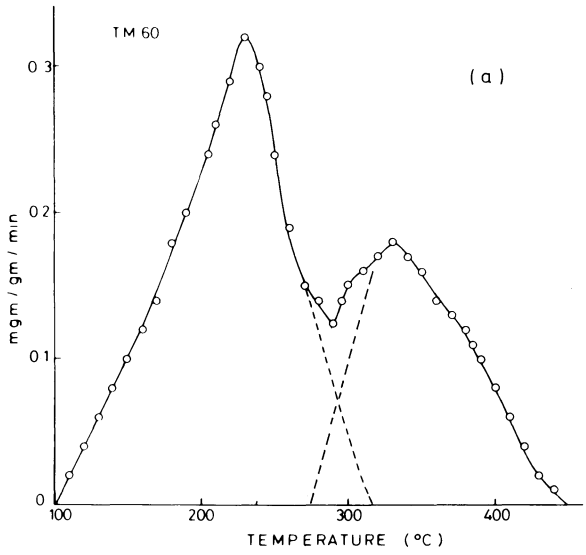

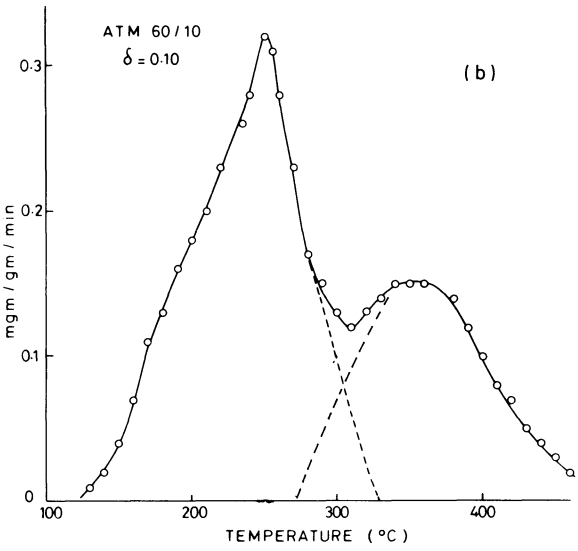

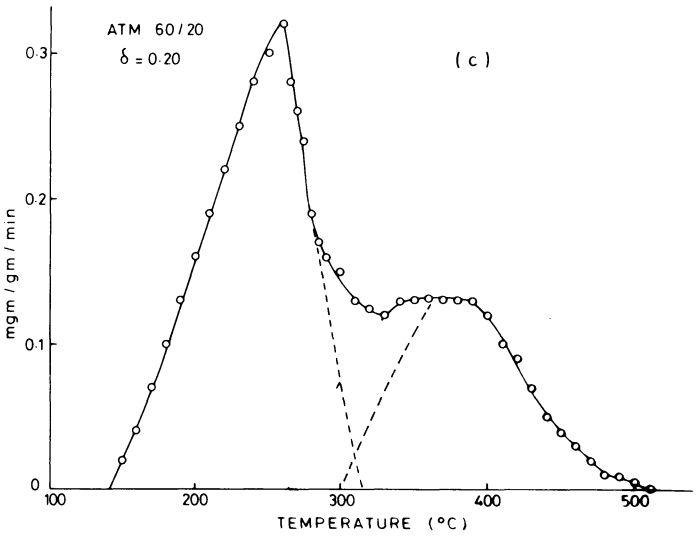

Fig. 3. Differential thermogravimetric analysis curves for the oxidation of the ATM60 series in air, showing rate of fractional weight increase as a function of ascending temperature. The two peaks may correspond, at least in part, to oxidation of Fe^2 from the octahedral and tetrahedral sites of the spinel lattice

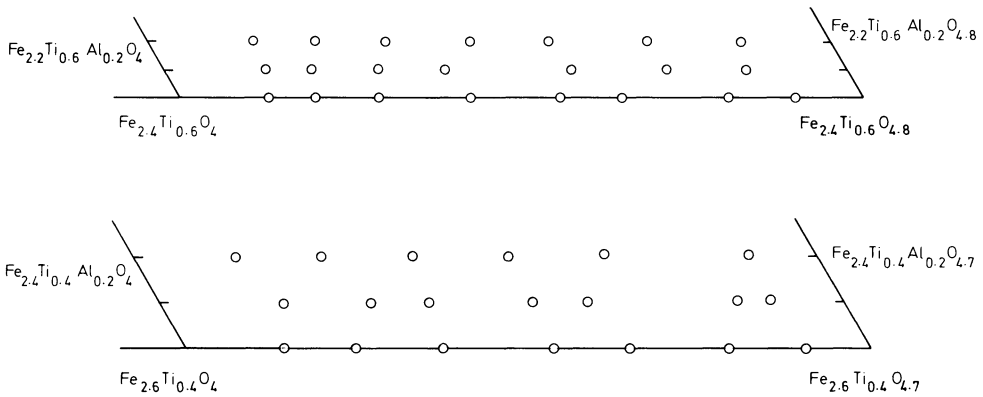

Fig. 4. Location of the synthesized titanomaghemites in the relevant quadrilaterals of the Al_2O_3–FeO–TiO_2–Fe_2O_3 quaternary tetrahedron

undetectably small. This gave a definite final weight and also promoted homogeneity in the specimen by annealing at the isotherm.

The oxidation parameter z was calculated from the observed weight increase during the oxidation by $z=(\Delta m \cdot M)/\{8 \cdot m(1+x)\}$ where Δm is the observed weight increase, m is the constant starting weight (taken after the adsorbed water or other volatiles were driven off), M and x are the molecular weight and composition parameter respectively.

The initial z parameter for the samples produced by ball-milling

Table 2. Parameters of the thermogravimetric analysis for the ATM40 and ATM60 series

Sample	Onset of weight gain			Positions of the peaks			
	weight loss (mgm)	constant weight (gm)	Position of the DTG curve	Low temperature		High temperature	
				Maximum weight change (mgm/gm/min)	Relative area	Maximum weight change (mgm/gm/min)	Relative area
TM40	2.2 (20°–120° C)	0.9981 (120°–125° C)	130°–430° C	0.32 at 250° C	0.68	0.12 at 350° C	0.23
ATM40/10 $\delta=0.1$	4.1 (20°–120° C)	0.9965 (120°–130° C)	130°–450° C	0.3 at 245° C	0.73	0.12 at 330° C	0.33
ATM40/20 $\delta=0.2$	3.5 (20°–120° C)	0.9967 (120°–130° C)	130°–460° C	0.32 at 250° C	0.75	0.14 at 340° C 0.08 at 400° C	0.33
TM60	2.8 (20°–95° C)	0.9982 (95°–105° C)	100°–450° C	0.32 at 230° C	0.65	0.18 at 330° C	0.37
ATM60/10 $\delta=0.1$	3.2 (20°–130° C)	0.997 (130° C)	120°–470° C	0.32 at 250° C	0.63	0.15 at 350° C	0.35
ATM60/20 $\delta=0.2$	3.8 (20°–130° C)	0.9964 (130° C)	140°–500° C	0.32 at 260° C	0.60	0.13 at 370° C	0.32

Table 3. X-ray cell edge and Curie and inversion temperatures of the oxidized ATM60 series. An asterisk indicates faint haematite lines in the X-ray powder picture estimated at a few percent

	z Oxidation degree	Cell edge (Å) G-de-W camera	T_c (°C) (Titano-maghemite)	T_I (°C) (Inversion temperature)	T_c (heating) (°C) (First stage inversion product)	T_c (cooling) (°C) (Second stage inversion product)
$\delta=0$	0.13	8.486	206	–	–	–
	0.20	8.472	299	323	567	463
	0.29	8.464	320	333	560	513
	0.43	8.452	360	370	554	531
	0.56	8.436	367	377	568	562
	0.65	8.408	375	381	582	561
	0.8	8.380*	423	437	598	578
	0.9	8.351*	438	458	595	580
$\delta=0.1$	0.15	8.473	147	–	–	–
	0.22	8.476	236	290	520	393
	0.32	8.465	271	293	539	463
	0.41	8.459	304	325	571	464
	0.59	8.417	317	360	555	536
	0.74	8.376*	368	434	573	558
	0.85	8.356*	384	464	562	544
$\delta=0.2$	0.16	8.462	102	–	–	–
	0.25	8.459	198	253	532	397
	0.35	8.455	242	268	573	459
	0.47	8.446	261	299	557	467
	0.59	8.394	275	360	570	521
	0.73	8.352*	326	442	580	512
	0.87	8.330*	373	367	464	521

was determined by wet-chemical analysis. The wet chemically determined initial values are adopted and gravimetry used to monitor changes in degree of oxidation. Therefore the quoted z values of Tables 3 and 4 are determined by a combination of thermogravimetric and wet-chemical analysis.

The location of the fine grain aluminium-substituted titanomaghemites (oxidized ATM40 and ATM60 series) in the relevant quadrilaterals of the Al_2O_3–FeO–TiO_2–Fe_2O_3 quaternary tetrahedron are shown in Fig. 4.

Thermomagnetic Properties – Curie Temperatures and Inversion

The metastable non-stoichiometric titanomaghemites 'invert' without change in bulk chemical composition when heated above

Table 4. X-ray cell edge and Curie and inversion temperatures of the oxidized ATM40 series. An asterisk indicates faint haematite lines in the X-ray powder picture estimated at a few percent

	z Oxidation degree	Cell edge (Å) G-de-W camera	T_c (°C) Titano-maghemite	T_I (°C) (Inversion temperature)	T_c (cooling) (Final inversion product)	M_F/M_I
	0.14	8.459	363	–	–	–
	0.25	8.437	410	250	410	1.08
	0.37	8.413	440	250	424	1.11
$\delta=0$	0.54	8.385	450	290	435	1.28
	0.65	8.376	470	300	453	1.43
	0.79	8.362*	475	300	455	1.58
	0.90	8.339*	–	–	–	–
	0.18	8.448	325	–	–	–
	0.31	8.418	402	250	400	1.16
	0.39	8.409	404	280	392	1.12
$\delta=0.1$	0.054	8.389	420	260	410	1.36
	0.62	8.382	424	290	402	1.77
	0.84	8.349*	440	280	420	1.82
	0.89	8.339*	460	260	450	2.11
	0.15	8.435	270	–	–	–
	0.28	8.418	359	300	348	1.45
$\delta=0.2$	0.41	8.412	380	300	326	1.19
	0.55	8.369	395	300	334	1.17
	0.67	8.345	420	300	350	1.67
	0.90	8.325*	430, 580	280, 320	308, 610	1.8

about 350° C (or at lower temperatures under increased pressure). The simplest case is the inversion of maghemite to haematite. The inversion products of titanomaghemites are generally multiphase, one phase being a near stoichiometric Fe^{2+}-containing spinel (except for $z=1$). The high-field thermomagnetic curve of a titanomaghemite therefore shows a rise in magnetization at temperatures of about 350° C. This may be obscured if the Curie point of the titanomaghemite lies above this temperature. Continuation of the thermomagnetic run to higher temperatures reveals the Curie temperature of the first-formed magnetic inversion product. Inversion seems to be a two-stage process, however, and the Curie point of the (final) inversion product found on the cooling run is often lower than that of the first formed magnetic phase. The saturation magnetization of the final assemblage is generally higher than that of the starting titanomaghemite.

In the present investigation the temperature dependence of magnetic properties was studied using three instruments – a susceptibility bridge, a magnetic balance and a *vibrating sample magnetometer* (VSM). The first instrument measures initial susceptibility. This property is not necessarily easily related to the concentration of a magnetic phase but usually shows a sharp peak just below the Curie temperature. Difficulties also arise if inversion starts before the Curie temperature of the titanomaghemite is reached. The second instrument measures high field magnetization. This property is simply related to the concentration of a magnetic phase. The transition at the Curie point is less sharply defined in this case and a convention has to be adopted for defining the Curie point. However, a 'virtual' Curie point, lying above or near the inversion temperature can be estimated by extrapolation. The inversion is also unambiguously revealed by the rise (or fall in the case of small x and high z values) in magnetization. The third instrument (VSM) can also be used to measure high field magnetization usually during the process of recording hysteresis loops as a function of temperature. A high temperature VSM run would therefore normally require a much slower rate of temperature increase than runs on a bridge or a balance, and the sample would spend a longer time at each temperature.

The Curie temperatures of the ATM60 series, being generally below about 400° C, could be determined from runs on the susceptibility bridge. The Curie temperatures, so determined, of the ATM60 series are listed in Table 3 together with the Curie temperatures of the first-formed and final inversion products and the inversion temperatures. However these latter are believed to be overestimated perhaps because the susceptibility is not a good indicator of inversion.

The susceptibility bridge is unsuitable for metastable samples with Curie points above about 350° C, such as the ATM40 series, and these were run on the magnetic balance. The Curie temperatures, inversion temperatures and Curie temperatures of the final inversion product are given in Table 4. Also given in the table are the ratios (M_F/M_I) of the magnetization of the inverted material after completing the run to that of the starting titanomaghemite.

Some of the ATM60 samples were run on the high temperature VSM. The titanomaghemite Curie temperatures obtained in this way are similar to those from the susceptibility bridge. The inversion temperatures were however lower, in the range 300°–350° C

Identification of Naturally Occurring Titanomaghemites

It is a tradition to plot the Curie temperature, unit cell edge and saturation magnetization as contours on the FeO–Fe_2O_3–TiO_2 ternary diagram since the pioneering work of Akimoto et al. (1957). Ozima and Sakamoto (1971), Readman and O'Reilly (1972), and O'Donovan and O'Reilly (1977) have presented characteristic properties for cation-deficient spinels in the titanomaghemite quadrilateral or subsystems containing magnesium. The cell edge and Curie temperature data for the aluminium-substituted

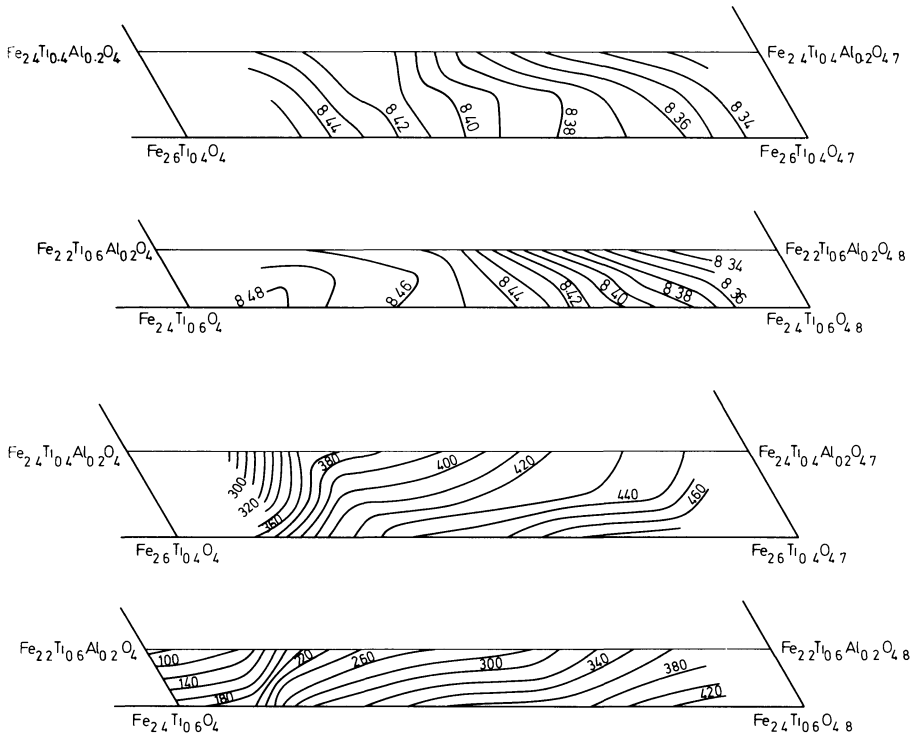

Fig. 5. Contours of constant unit cell edge (determined using a Guinier de Wolff camera) for the synthesized titanomaghemites

Fig. 6. Contours of constant Curie temperature for the synthesized titanomaghemites

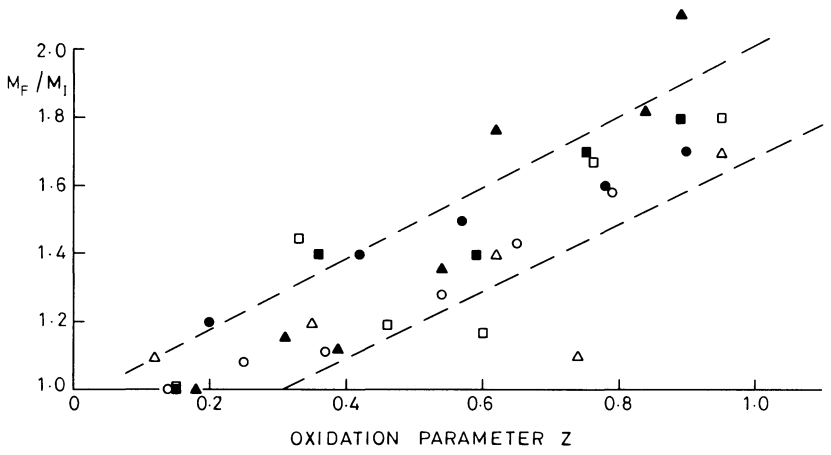

Fig. 7. The ratios (M_F/M_I) of the magnetization of inverted titanomaghemites (of different x values and substituted cations) after heating to about 700° C in a magnetic balance (in times of the order of 1 h) to the magnetization of the initial titanomaghemites, plotted against degree of maghemitization, z. The data are from Table 4 and from O'Donovan and O'Reilly (1977). (Composition parameters: *open circles, triangles,* and *squares* correspond to $x=0.4$; $x=0.6$, $\delta(\mathrm{Mg})=0.25$; $x=0.4$, $\delta(\mathrm{Al})=0.2$ respectively; *Solid circles, triangles,* and *squares* correspond to $x=0.6$, $\delta(\mathrm{Mg})=0.15$; $x=0.4$, $\delta(\mathrm{Al})=0.1$, $x=0.6$, $\delta(\mathrm{Mg})=0.05$ respectively)

synthetic titanomaghemites of the present investigation are shown in contour form in Figs. 5 and 6.

The use of any single technique (e.g., the measurement of Curie temperature) does not unambiguously identify a magnetic mineral. At least two methods are needed to narrow down the compositional field, within which a mineral may lie, to a useful range. The intersection of Curie temperature and cell edge contours serves this function but the latter property may be difficult to measure, requiring extraction of the magnetic phase. In the case of the fine grain titanomaghemites in DSDP basalts the prolonged pulverization needed to achieve an adequate degree of refinement may indeed lead to alteration in the minerals themselves. The inversion of titanomaghemites qualitatively indicates their presence and may also provide a quantitative measure of the degree of non-stoichiometry. A single thermomagnetic run may therefore contain enough information to provide at least a first approximation to the composition of a titanomaghemite. Such a run will provide (i) the Curie temperature of the univerted titanomaghemite, (ii) the Curie temperature of the inversion product, and (iii) the ratio (M_F/M_I) of the magnetization of the inversion product to that of titanomaghemite. All three are functions of the composition coordinates (x,z) of the titanomaghemite. However the inversion process would have to be better understood before it could be put to such a use. The M_F/M_I ratios of Table 4 and data from O'Donovan and O'Reilly (1977) who studied Mg substituted titanomaghemites are plotted against oxidation parameter, z, in Fig. 7. Although there is some scatter in the data the general trend is clear. The reason for the scatter may lie in the different heating rates which might be employed in runs on a magnetic balance, for example, although an hour might be a typical heating time. It may be that inversion proceeds in a different way or is incomplete depending on the time available. Indeed M_F/M_I ratios as high as about 5 were found for some samples of the TM60 series run in the high temperature VSM (for the order of a day). For this reason we have not combined the data of Table 4 with Fig. 4 to produce contours of M_F/M_I,

and the Curie temperature of the inversion product. A standard inversion procedure would have to be worked out before the inversion phenomenon could be used for quantitative determination of titanomaghemite composition.

Conclusions

The magnetic properties of basalts recovered from the submarine basement provide an important means of investigating both the history of the geomagnetic field and the evolution of the Earth's crust. The determination of the physical and chemical state of the remanence-carrying magnetic minerals is a necessity in either case. The present study provides characteristic data on synthetic analogues of the magnetic minerals believed to occur in submarine basalts. Such data should be useful in tracing out the petrological history of the basement rocks.

Acknowledgements. This work forms part of an NERC sponsored research programme "Thermoremanence in titanomagnetites". We thank Dr. Z. Hauptman, for his invaluable help in the preparation of materials, and Mr. E. Boult of the Electron Optical Unit, University of Newcastle upon Tyne. One of the authors (Ö.Ö.) has been in receipt of a studentship from the Turkish Ministry of National Education.

References

Akimoto, S., Katsura, T., Yoshida, M.: Magnetic properties of $TiFe_2O_4$–Fe_3O_4 system and their change with oxidation. J. Geomagn. Geoelectr. **9**, 165–178, 1957

Creer, K.M., Ibbetson J.D.: Electron microprobe analyses and magnetic properties of non-stoichiometric titanomagnetites in basaltic rocks. Geophys. J.R. Astron. Soc., **21**, 485–511, 1970

Hauptman, Z.: High temperature oxidation, range of non-stoichiometry and Curie point variation of cation deficient titanomagnetite, $Fe_{2.4}Ti_{0.6}O_{4+\delta}$. Geophys. J. R. Astron. Soc. **38**, 29–47, 1974

Joshima, M.: Titanomagnetite and titanomaghemite containing aluminium. Rock Magn. Paleogeophys. **3**, 5–9, 1975

Lecaille, A., Prevot, M.: Rock magnetism of FAMOUS Rift Valley pilow basalts and implications for maghemitization of oceanic crust., Geophys. J. R. Astron. Soc. in press 1980

O'Donovan, J.B., O'Reilly, W.: Range of non-stoichometry and characteristic properties of the products of laboratory maghemitization. Earth Planet. Sci. Lett. **34**, 241–299, 1977

Özdemir, Ö., O'Reilly, W.: Magnetic properties of monodomain aluminium-substituted titanomagnetite. Phys. Earth Planet. Inter. **16**, 190–195, 1978

Ozima, M., Sakamoto, N.: Magnetic properties of synthesized titanomaghemite. J. Geophys. Res. **76**, 7035–7046, 1971

Readman, P.W., O'Reilly, W.: The synthesis and inversion of non-stoichiometric titanomagnetites. Phys. Earth Planet. Inter. **4**, 121–128, 1970

Readman, P.W., O'Reilly, W.: Magnetic properties of oxidized (cation deficient) titanomaghemites $(Fe, Ti, \square)_3O_4$. J. Geomagn. Geoelectr. **24**, 69–90, 1972

Richards, J.C.W., O'Donovan, J.B., Hauptman, Z., O'Reilly, W., Creer, K.M.: A magnetic study of titanomagnetite substituted by magnesium and aluminium. Phys. Earth Planet. Inter. **7**, 437–444, 1973

Ryall, P.J.C., Hall, J.M.: Laboratory alteration of titanomagnetites in submarine pillow lavas. Can. J. Earth Sci. **16**, 496–504, 1979

Received June 19, 1980; Revised September 15, 1980
Accepted September 16, 1980

J Geophys (1981) 49:101–107

Journal of Geophysics

Densities and Magnetic Susceptibilities of Precambrian Rocks of Different Metamorphic Grade (Southern Indian Shield)

C. Subrahmanyam[1] and R.K. Verma[2]
[1] National Geophysical Research Institute, Uppal Road, Hyderabad-500007, India
[2] Indian School of Mines, Dhanbad, India

Abstract. Densities of 1294 Precambrian rocks from the Southern Indian Shield, confined to low-grade granite-greenstone (Karnataka) and high-grade granulite (Eastern Ghats Belt) terrains are presented and categorized into 16 metamorphic and igneous varieties. In Karnataka, densities of granites (2.65 g/cm^3), gneisses (2.68 g/cm^3) and granodiorites (2.73 g/cm^3) are considerably less than those of greenstone belts (2.84 g/cm^3) and dolerites (3.03 g/cm^3). An average density of 2.75 g/cm^3 is obtained for surface rocks from this terrain. Over the Eastern Ghats belt, densities of charnockites range from 2.71 g/cm^3 to 3.12 g/cm^3 as they vary from acidic to ultrabasic composition. An average density of 2.85 g/cm^3 is obtained for surface rocks from this belt. The contrast in the average densities of surface rocks from the low- and high-grade terrains may play a significant role in a proper assessment of the regional gravity fields over these terrains. The results compare well with the data from similar terrains in other shield regions. Magnetic susceptibilities for 482 of these samples are also presented. All the rock types include a wide range of susceptibilities, as is to be anticipated in metamorphic terrains. A plot of density versus magnetic susceptibility for thirteen of these rock types suggests a linear relationship.

Key words: Densities – Magnetic susceptibilities – Precambrian metamorphic terrains

Introduction

The two-fold classification of shield areas into low-grade greenstone-granite terrains and high-grade granulite terrains is by now widely known (Windley and Bridgwater 1971). Regional gravity investigations indicate that these diverse metamorphic terrains are usually characterized by gravity fields which are mutually distinguishable (Gibb and Thomas 1976; Subrahmanyam 1978). While the long-wavelength components of these gravity fields are often attributed to deep-seated crustal and upper mantle inhomogeneities, the local anomalies are generally accounted for by near surface lithologies and their surface distribution. Thus, the interpretation of local gravity anomalies in crystalline areas requires adequate knowledge of the densities of the various exposed metamorphic and igneous rocks over the terrains. This point has been stressed by Marshall and Narain (1954), Woollard (1962), Gibb (1968), and Smithson (1971), among others. Density data for various rock types from the crystalline terrain are important, not only for interpreting the gravity anomalies, but also for estimating the mean density and composition of the crust in different parts of the continents.

Precambrian rocks in the Southern Indian Shield occur in both the low- and high-grade metamorphic environments, confined to the provinces of Karnataka, Bastar and the surrounding Eastern Ghats Belt (Fig. 1). While Karnataka and Bastar constitute the low-grade terrains of the shield, the Eastern Ghats Belt belongs to granulite facies metamorphism. The present study is a compilation and presentation of the density and susceptibility data for various rocks from these terrains. The significance and implication of the density data for a proper assessment of gravity fields associated with the metamorphic terrains in shield areas will also be discussed.

The metamorphic rocks involved in the present study range from greenschist to granulite facies. Similarly, the igneous intrusive rocks range from acidic to ultrabasic. Major rock types include metasedimentary-metavolcanic sequences (Archaean schists), biotite and hornblende gneisses, granites, granodiorites, amphibolites, dolerites, migmatites of uncertain origin, anorthosites, granulite facies gneisses, acid to ultrabasic charnockites, khondalites and other minor varieties. While a reasonable amount of data is available for schists, gneisses, and granites from Karnataka (Qureshy et al. 1967), data for rocks from the high-grade Eastern Ghats Belt are very meagre.

During the course of gravity and magnetic surveys by one of the authors over these metamorphic terrains (Subrahmanyam 1978), about 655 fresh rock samples were collected. Their densities (and susceptibilities for 482 samples) were measured in the laboratory. These data are supplemented with density data already published for another 639 samples (Balakrishna and Ramana 1968; Balakrishna et al. 1968, 1971, Qureshy et al. 1967) and the results are presented here.

Sampling and Distribution

In general, rock samples were collected from outcrops situated near gravity and magnetic stations. Samples for which data were published earlier (639 samples) also cover all the important lithologic formations in the Southern Indian Shield. Special attention has been paid to charnockites and other granulite facies rocks from the high-grade Eastern Ghats Belt as little data have been available from this province uptill now.

Density Measurements

Laboratory density measurements were based on the formula

$$\rho = \frac{W_1}{W_1 - W_2},$$

0340-062X/81/0049/0101/$01.40

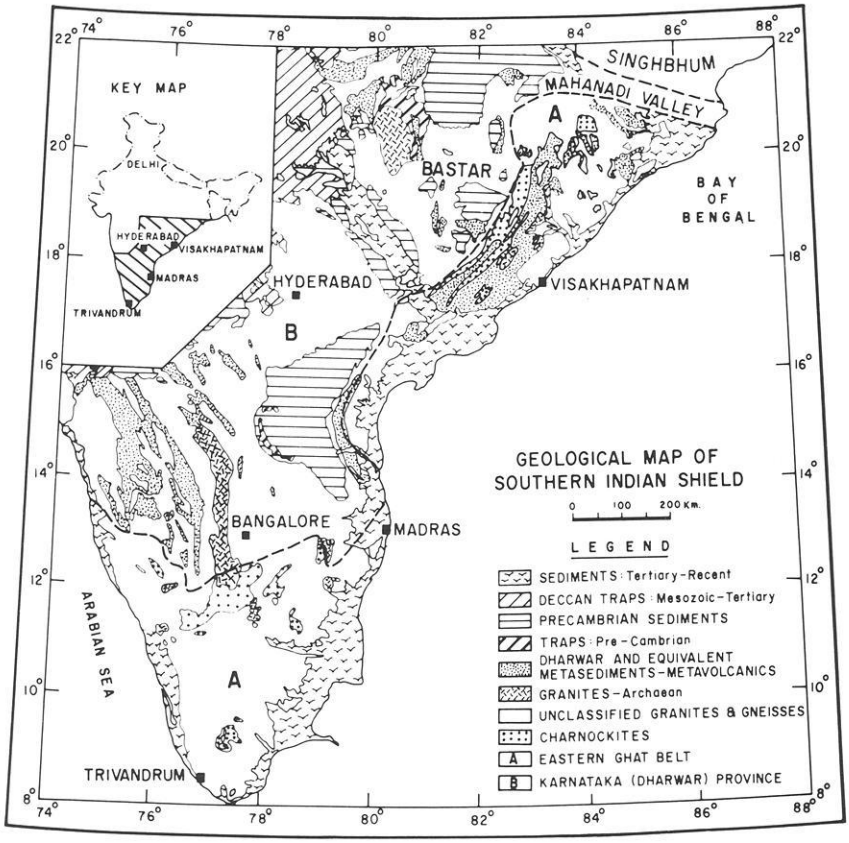

Fig. 1. Geological map of the Southern Indian Shield

where ρ is the density, W_1 is the weight of the sample in air, W_2 is weight of the sample in water. All the samples measured were either igneous or metamorphic rocks having little or no pore space so the density values obtained are very close to the actual grain density of the rock. The accuracy of the results is expected to be within ± 0.02 g/cm^3 or about 1%.

Results

The 1294 rock samples have been categorized into sixteen major metamorphic and igneous varieties; these varieties and the density values are summarised in Table 1. For rock types with sample numbers exceeding twenty, histograms were also prepared and are shown in Figs. 2–4. Descriptions of the rock types and the densities obtained are discussed below, for the low- and high-grade metamorphic terrains separately.

Rocks from Low-Grade Terrains

Granites. The data for granites are mostly from the published work of Qureshy et al. (1967) and Balakrishna et al. (1971). In Karnataka, these granites intrude both the gneisses and schists. A concentration at 2.60–2.70 g/cm^3 is clearly seen in the histogram (Fig. 2) with the average value being 2.65 g/cm^3. Like the biotite gneisses, these granites do not show a wide distribution on the histogram which probably indicates a uniform composition.

Table 1. Densities of igneous and metamorphic rocks from South India

Sl. No.	Rock Type	No. Samples	Mean (g/cm^3)	S.D. (g/cm^3)	Range (g/cm^3)
1.	Gneisses and granites (undivided)	544	2.67		2.54–3.24
	Low-grade terrain				
1.	Granites	371	2.65	0.02	2.54–2.83
2.	Biotite gneisses	135	2.68	0.05	2.55–2.80
3.	Granodiorites	11	2.73	0.03	2.70–2.78
4.	Archean schists	82	2.84	0.20	2.48–3.35
5.	Amphibolites	54	3.01	0.10	2.81–3.35
6.	Dolerites	82	3.03	0.07	2.74–3.19
	High-grade terrain				
7.	Syenites	4	2.66	0.04	2.59–2.70
8.	Anorthosites	64	2.85	0.13	2.58–3.28
9.	Gneisses	38	2.89	0.11	2.70–3.24
10.	Migmatites	21	2.89	0.10	2.70–3.14
11.	Khondalites	25	2.89	0.18	2.59–3.33
12.	Hornblendites	5	3.21	0.15	3.05–3.47
13.	Acid charnockites	140	2.71	0.07	2.57–2.89
14.	Intermediate charnockites	114	2.78	0.08	2.66–3.15
15.	Basic charnockites	124	2.99	0.15	2.67–3.41
16.	Ultrabasic charnockites	24	3.12	0.13	2.84–3.36
	Total	1294			

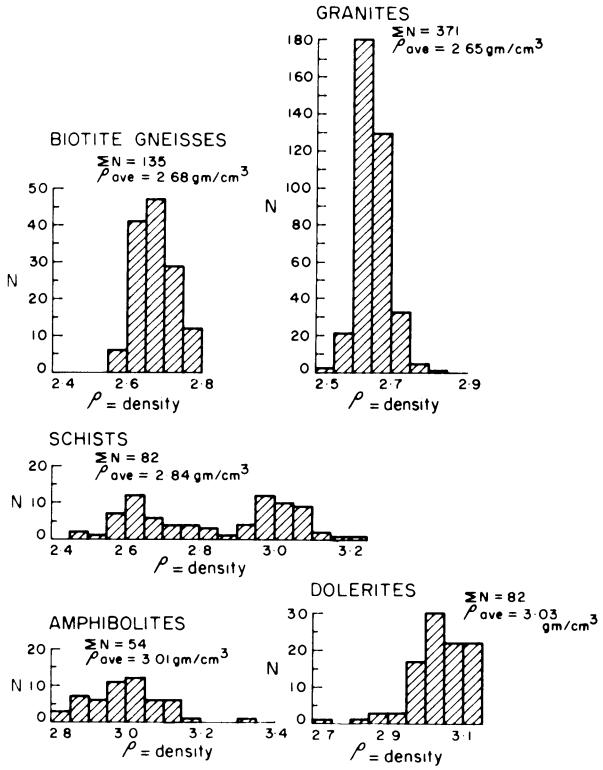

Fig. 2. Density histogram for rocks from Karnataka low-grade terrain

Biotite Gneisses. These are associated with schists, migmatites, granitic gneisses and amphibolites and are characterised by their monotonous occurrence and uniform appearance. This is reflected in the narrow density range of 2.55–2.80 g/cm^3. An average value of 2.68 g/cm^3 has been obtained for these rocks. The histogram (Fig. 2) shows a peak in the range 2.65–2.70 g/cm^3.

Granodiorites. Data for only 11 samples could be obtained for this variety despite their widespread occurrence. The density range is 2.70–2.78 g/cm^3, the mean value 2.73 g/cm^3.

Archaean Schists. These rocks are abundantly distributed over the low-grade greenstone-granite terrains and are intruded by younger K-rich granites. Both were engulfed by a vast gneissic complex known as the Peninsular Gneiss. The present data are for rocks from Karnataka province. A mean density of 2.84 g/cm^3 is obtained but with a wide range. In Fig. 2, the histogram shows two modes, one between 2.45 g/cm^3 and 2.70 g/cm^3 and the other between 2.90 and 3.10 g/cm^3. The two modes correspond approximately to the chlorite and hornblende varieties of schist. Some biotite schists may have been included in the latter variety. Usually crystalline rocks do not show densities less than 2.6 g/cm^3 and the lower densities of 2.48–2.60 g/cm^3 in the present data may be due to weathering of some of the measured samples.

Amphibolites. These occur as enclaves within the gneisses with width varying from a few centimetres to more than a metre. An average density of 3.10 g/cm^3 is obtained but with a range 2.81–3.35 g/cm^3, which is well illustrated by the histogram (Fig. 2). This may be due to contamination of the original basic rocks by later granitization processes.

Dolerites. Karnataka province is noted for widespread occurrence of dolerite dyke swarms of Precambrian age. An average value of 3.03 g/cm^3 is obtained with a range 2.74–3.19 g/cm^3 for these rocks. But the histogram (Fig. 2) shows a concentration towards the basic end (2.95–3.15 g/cm^3) with a tail towards the acidic end.

Rocks from High-Grade Terrains

These are mostly confined to the Eastern Ghats Belt with its regional granulite-facies metamorphic grade. It is believed that this belt may represent a deeper crustal domain (Subramaniam 1967) as it is characterized by the widespread distribution of the charnockite-khondalite suite of rocks, anorthosites, garnetiferous gneisses, migmatites and other minor varieties. In the present sampling, special attention has been paid to the charnockitic rocks. The categorisation of charnockites into four varieties, acidic to ultrabasic (Holland 1900) is retained here. In almost all the rocks, garnet occurs in variable amounts which to some extent makes the densities obtained dependent on this factor (Tanner 1969; Smithson and Brown 1977).

Anorthosites. The anorthosite occurrences are a common characteristic of all the high-grade shield terrains in the world. In the Eastern Ghats Belt these are reported to occur in nineteen localities (De 1969; Kanungo and Chetty 1978) but the present data are from only three of these outcrops. Densities ranging from 2.58–3.28 g/cm^3 with an average of 2.85 g/cm^3 have been obtained. The densities generally increase as the anorthosites tend to gabbroic composition. The histogram (Fig. 3) shows a tail towards the high density end but a peak near 2.80–2.85 g/cm^3 is also seen. In comparison with data for anorthosites from other continents, in particular Canada where they generally range from 2.70–2.78 g/cm^3 (Gibb 1968; Tanner 1969; Smithson 1971) the average of 2.85 g/cm^3 obtained in the present case appears to be slightly on the high side. Whether this is due to the inclusion of anorthosites which tend to be more gabbroic in composition and are thus necessarily of higher density, is at present not clear. Based on density data alone, these rocks could be classified as gabbroic anorthosites.

Granulite Facies Gneisses. These are associated in the field with the charnockite-khondalite suite of rocks, migmatites and other rock types. An average density of 2.89 g/cm^3 has been obtained with a range of 2.70–3.24 g/cm^3. However, the histogram in Fig. 3 shows a concentration between 2.80–3.00 g/cm^3.

Migmatites. As described by Smithson (1971), these are 'mixed rocks containing a granitic portion and a darker, more dense portion'. Variations in density are probably a result of the increase or decrease of either of these portions. About 21 samples (density range 2.70–3.14 g/cm^3), yield a mean value of 2.89 g/cm^3, which is well illustrated by the histogram (Fig. 3) with a tail towards the acidic end.

Khondalites. These are garnet-sillimanite gneisses and schists which, together with the pyroxene granulites, constitute the basement into which the magma responsible for generation of acid charnockites has intruded. Compositionally these are similar to the stronalites of Strona valley in Italy. Khondalites are highly susceptible to weathering and it is often difficult to obtain a fresh sample in the field. This factor and the garnet content in these rocks tend to alter their density values considerably which is reflected in their wide density range (2.59–3.33 g/cm^3) shown in

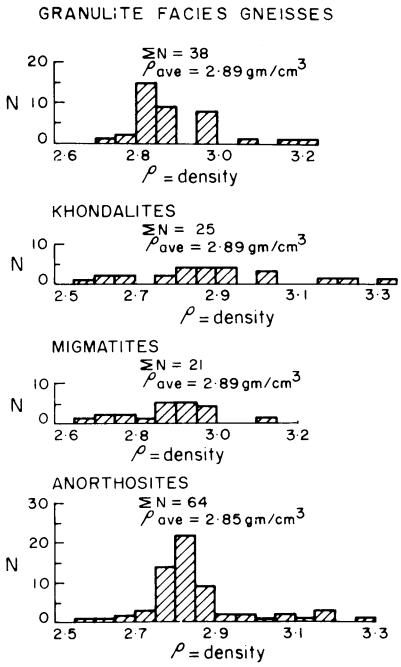

Fig. 3. Density histogram for rocks from Eastern Ghats high-grade belt

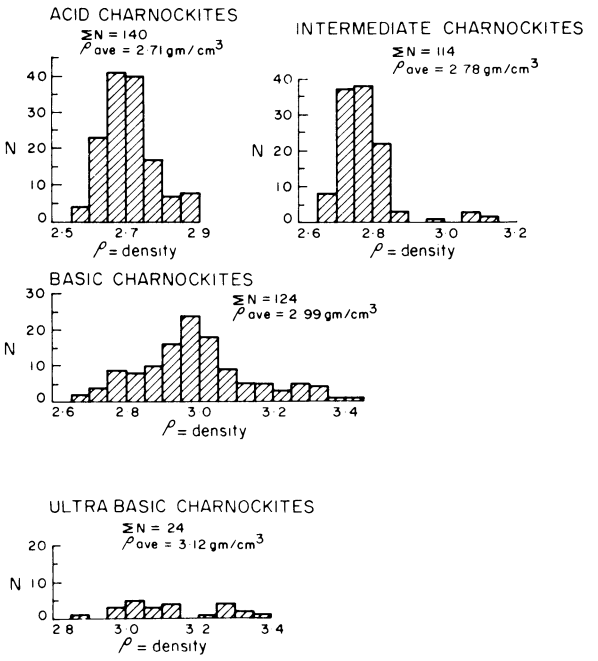

Fig. 4. Density histogram for charnockites from Eastern Ghats high-grade belt

the histogram (Fig. 3). For 25 samples, the average density is 2.89 g/cm^3.

Acid Charnockites. According to Holland (1900) these are hypersthene granites having a specific gravity of 2.67 g/cm^3, and 75% silica. Subramaniam (1959) redefined charnockite as a hypersthene quartz feldspar rock and included in this variety, enderbites, hypersthene syenites, alaskites and leptynites and suggested their magmatic origin. In the present analysis, an average density value of 2.71 g/cm^3 has been obtained, which is very near to that reported by Holland (1900) and well reflected in the histogram (Fig. 4) by the peaks in the range 2.65–2.75 g/cm^3.

From the histogram, it can be seen that for about 20 samples the densities are on the high side, between 2.80–2.99 g/cm^3. This may be due either to the presence of large amounts of garnet, known to occur in these rocks, or their intercalations with the higher density basement rocks (basic charnockites).

Intermediate Charnockites. These are hybrid rock types formed by interaction of the magma, which gave rise to the acid charnockites described above, with the basement rocks (Subramaniam 1959). Several hill ranges in South India are composed of these rocks. An average density of 2.78 g/cm^3 with a range of 2.65–3.15 g/cm^3 has been obtained. The histogram (Fig. 4) indicates a tail towards the basic end, while the majority of the samples lie in the range 2.70–2.85 g/cm^3, probably indicating a uniform composition.

Basic Charnockites. Pyroxene granulites and their variants constituting the basement are classified as basic charnockites (Subramaniam 1959). Data for 124 samples yield an average value of 2.99 g/cm^3 but the histogram (Fig. 4) indicates a wide range, 2.67–3.41 g/cm^3. Peaks are observed near 3.00 g/cm^3 and the average of 2.99 g/cm^3 may be a good representative value. For about 15 to 20 samples, the histogram (Fig. 4) shows lower values of 2.65–2.75 g/cm^3. This may be due to contamination of these basement rocks by acid charnockite magma intrusion.

Ultrabasic Charnockites. According to Subramaniam (1960) these are syntectonic lenses of norite with pyroxenite schleiren occurring in large masses of charnockite outcrops. A mean density of 3.12 g/cm^3 has been obtained for this variety. Fig. 4 shows the histogram.

In addition to the above rocks, 4 samples of syenites have yielded an average density of 2.66 g/cm^3, while 5 samples of hornblendites gave an average of 3.21 g/cm^3 (Table 1). A comparison of the present data from both the low- and high-grade metamorphic terrains in the Southern Indian Shield with those from similar terrains in other shield areas of the world is much in order as geologically and geochemically these are comparable. This comparison is presented in Table 2. It is quite obvious that the data obtained from the present study for various rock types are in fair agreement with those obtained from other shield areas of the world.

Density of the Upper Continental Crust

For a proper assessment of the gravity anomalies due to local geological variations in a given region, at least an approximate idea of the probable density of the exposed crystalline continental crust is necessary. Woollard (1962, 1969), arrived at a figure of 2.74 g/cm^3 for density of the upper crust instead of the 2.67 g/cm^3 which is normally used. On the other hand, Gibb (1968) suggested that the exposed metamorphic rocks in shield areas tend to possess an average granodioritic composition as against the tonalitic composition proposed by Woollard (1962). According to Gibb the value of 2.67 g/cm^3 is more representative of the average density of surface rocks in shield areas and hence more suitable for Bouguer reduction in continental areas. Smithson (1971) analysed density data from widely separated continental masses like the U.S.A., Antarctica and Europe. His data fall within the range 2.70–2.79 g/cm^3 and more or less confirm Woollard's (1962, 1969) average value of 2.74 g/cm^3. Smithson (1971) con-

Table 2. Mean densities of some metamorphic and igneous rocks

Rock type	Present study			Woollard (1962)			Gibb (1968)			Smithson (1971)		
	N	*R*	*M*	*N*	*R*	*M*	*N*	*R*	*M*	*N*	*R*	*M*
Gneisses and granites (Undifferentiated)	544	2.54–3.24	2.69	117	2.59–3.14	2.74	944	2.50–2.78	2.64	58	2.58–2.77	2.70
Schists (Undifferentiated)	82	2.60–3.35	2.84	51	2.62–3.14	2.84	25	2.55–2.96	2.73	128	2.59–3.11	2.75
Amphibolites	54	2.81–3.35	3.01	–	–	–	132	2.66–3.47	3.01	68	2.85–3.20	3.03
Granulite facies gneisses	38	2.70–3.24	2.89	–	–	–	–	–	–	13	2.63–3.20	2.86
Granodiorites[a]	11	2.70–2.78	2.73	–	–	–	–	–	–	–	–	–
Anorthosites	64	2.58–3.28	2.85	–	–	–	27	2.63–2.97	2.78	–	–	–

N: Number of samples; *R*: Range; *M*: Mean
[a] *M* given by Daly et al. (1966) is 2.72 ($N=11$)

tends that even the so-called granitic terrains do not have mean density as low as 2.67 g/cm^3 which disagrees with Gibb's (1968) conclusions. A high-grade granulite terrain (Jotunheim) in central Norway similar to the Eastern Ghats Belt of the present study, however, gives an average upper crustal density of 2.86 g/cm^3 which is considerably higher than that of the normal upper continental crust which is either 2.74 g/cm^3 or 2.67 g/cm^3.

The foregoing data from different continental regions of the world indicate that substantial variations in mean upper crustal densities resulting in gravity anomalies of considerable magnitude do occur. In view of this, a proper assessment of the density data for rocks from the Southern Indian Shield presented in this study, is very necessary. This may enable us to arrive at a suitable value for the mean upper crustal densities for both the low- and high-grade metamorphic terrains which would be very useful for better quantitative interpretation of gravity data.

Over the low-grade Karnataka province, the major rock types are, gneisses, granites, granodiorites, Archean schists, amphibolites and dolerites. A simple way of obtaining the average density of the upper crust in Karnataka is to average the densities of all these rocks. The average density of 735 samples, including all the varieties, is 2.75 g/cm^3. For rocks in Northern Manitoba in the Canadian Shield, Gibb (1968) however, has obtained the mean (2.67 g/cm^3) by weighing the densities of each rock type according to their surface distribution. Over Karnataka province, the more abundant rock types are the gneisses, schists and granites. The average for 588 samples of these rocks is 2.69 g/cm^3 which is close to that obtained by Gibb (1968). However, it should be noted from Table 1 that in this averaging, low-density granites predominate in number (371) over the high-density gneisses and schists (217) which suggests that the average value of 2.69 g/cm^3 is a low estimate. Until the areal distribution of surface rocks is accurately known, the only way to obtain the mean value is to average out the densities of all rock types which, as mentioned earlier, yields a value of 2.75 g/cm^3. This value is intermediate between the high-density schists (2.84 g/cm^3) and the low to medium density granites (2.65 g/cm^3) and the gneisses (2.69 g/cm^3), and could be used as the density for the crystalline basement in interpretion of gravity anomalies due to local geological variations over Karnataka province.

A similar analysis could be attempted to obtain the average upper crustal density of the Eastern Ghats Belt. Results from the other shield areas have already indicated that granulite terrains are made up of high-density rocks and so also possess higher upper crustal densities (Tanner 1969; Fairhead and Scovell 1976; Anfiloff and Shaw 1973; Smithson 1971; Subrahmanyam 1978). Tanner (1969) indicated that the increase in grade of metamorphism tends to increase the density by an amount somewhere in the range 0.05–0.20 g/cm^3. Acid to ultrabasic charnockites, khondalites, granulite facies gneisses, and anorthosites are the major rock types which constitute the upper crust in the high grade Eastern Ghats Belt and these may control its upper crustal density and composition to a large extent. About 550 samples of the rock types mentioned above give an average density of 2.85 g/cm^3. It is interesting to note that Smithson (1971) obtained nearly the same value (2.86 g/cm^3) for a granulite terrain in Central Norway. Within this high grade belt, acid charnockites, which are essentially hypersthene granites, and syenites, have the lowest values of 2.71 g/cm^3 and 2.66 g/cm^3 respectively and, as shown elsewhere (Subrahmanyam 1978), are probably the cause of some strong local negative anomalies over the southern parts of the Eastern Ghats Belt.

Thus, the densities of surface rocks from the Southern Indian Shield suggest a possible density and compositional contrast between the low- and high-grade metamorphic terrains. The available data suggest that the upper crustal density contrast may amount to 0.1 g/cm^3 to 0.16 g/cm^3, a result which will have a direct bearing on the quantitative interpretation of gravity anomalies over these metamorphic terrains.

Susceptibility Measurements

Magnetic susceptibilities (*K*-values) of various rock types were determined for 482 of the above samples, using Mooney's susceptibility bridge apparatus. The rock types included acidic to ultrabasic charnockites, schists, dolerites, amphibolites, low- and high-grade gneisses, granodiorites, granites, migmatites and khondalites. Table 3 presents these data, where the rock type, number of samples, mean and range are indicated. A notable feature is the decrease in susceptibility values of charnockites as they grade from ultrabasic to acidic varieties. The highest value obtained is 157079×10^{-6} SI for ultrabasic charnockites, but in general, all the rock types show a wide range of susceptibilities (see Table 3), as might be anticipated for metamorphic rocks. Geological processes like deformation,tectonism and metamorphism have strong effects on the magnetization of rocks (Heiland 1946) so that in metamorphic rocks, which have been subjected to the above pro-

Table 3. Magnetic susceptibilities for some metamorphic and igneous rocks from South India

Sl. No.	Rock Type	No. Samples	Mean $K \times 10^{-6}$ SI	Range $K \times 10^{-6}$ SI
1.	Khondalites	12	1,898	226– 7,401
2.	Biotite gneisses	24	3,720	138– 10,317
3.	Migmatites	20	7,904	138– 35,186
4.	Granites	47	11,020	226– 38,956
5.	Acid Charnockites	76	11,385	226– 53,407
6.	Granodiorites	10	11,523	226– 28,274
7.	Granulite facies gneisses	30	15,883	440– 13,823
8.	Amphibolites	44	18,610	666–103,672
9.	Intermediate charnockites	76	19,289	226– 85,451
10.	Basic charnockites	83	21,614	226–113,097
11.	Dolerites	28	27,696	892– 99,274
12.	Archean schists	25	31,239	226– 87,964
13.	Ultrabasic charnockites	6	33,640	452–157,079
Total		482		

cesses, the magnetic character or the orientation of the magnetizing minerals will be highly disturbed and non-uniform. This normally results in a large scatter of the observed susceptibilities.

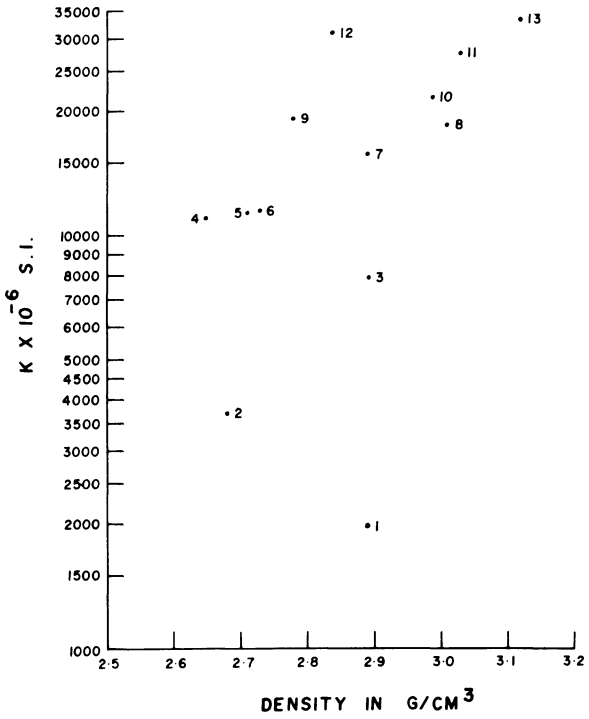

Fig. 5. Diagram showing density-magnetic susceptibility relationship for Precambrian rocks from the present study area. *Numbers* indicate the rock types listed in Table 3

Density-Susceptibility Relationship

The density of a rock is primarily dependent on its mineral and chemical compositions. Henkel (1976) suggested that in acid plutonic rocks the amount of mafic minerals present controls the density while in basic rocks it is controlled by the amount of plagioclase. Similarly, SiO_2 content also has a significant effect on the density: acidic rocks, high in SiO_2, have low densities while basic rocks are low in SiO_2 and have high densities.

The magnetic susceptibility of a rock is significantly controlled by the magnetite content of that rock (Aravamadhu 1974; Henkel 1976). Aravamadhu (1974) obtained a linear relationship for variation of susceptibility with percentage by weight of magnetite for samples of charnockites and khondalites in the present study area. Lidiak (1974) observed that the magnetic properties of a rock depend to a certain extent on their grade of metamorphism and the degree of oxidation and in general observed an increase in *K*- values as the rocks grade from greenschist to granulite facies.

Henkel (1976) studied the correlation between density and magnetic susceptibility for Precambrian rocks from northern Sweden and observed that these, together with the magnetite content in rocks provide a useful tool for classifying rocks and for investigating the geological processes behind their formation. For the present rocks from South India, the magnetite contents have not been determined but the covariation of susceptibility with density could at least be examined.

A plot of density versus susceptibility for thirteen rock types is shown in Fig. 5.

Excluding Archean schists, migmatites and khondalites, the remaining rock types exhibit a linear relationship as K-values increase with increase in densities. One interesting feature for charnockites is that the increase in density from acidic to ultrabasic varieties is also marked by an increase in their K-values. As mentioned earlier the SiO_2 content decreases from acidic to ultrabasic and as can be seen, this is marked by an increase in densities. Data on the magnetite content of these rocks are not however available so the effect of this on these relationships cannot be assessed.

Conclusions

The present density data have demonstrated a significant density contrast between the upper crusts underlying the low- and high-grade metamorphic terrains. An average density of 2.75 g/cm^3 is obtained for the upper crust in Karnataka geological province which appears to be nearer to the values suggested by Woollard (1962), Smithson (1971), and Ramberg (1976). In contrast to this, the average upper crustal density in the Eastern Ghats Belt is relatively high (2.85 g/cm^3), which is in agreement with data from some granulite terrains in other shield areas and, in particular, the granulite terrain in Central Norway (Smithson 1971).

A linear relationship between density and susceptibility has been observed for most of the rock types presented in this study. In general, the susceptibility increases with density. This dependence is more pronounced in charnockites and may be directly related to the magnetite content of these rocks.

The possibility of determining the average composition of the upper crust from the average surface densities can be examined. Gibb's (1968) estimate of 2.67 g/cm^3 closely corresponds with that of the granodiorite reported by him and he suggested that in northern Manitoba and Finland the average composition of surface rocks may be granodioritic rather than tonalitic. However, even for the small number of samples of granodiorites presented in this study and also those of Daly et al. (1966) the densities are relatively high at 2.73 g/cm^3 which is nearer to the value

of 2.75 g/cm^3 suggested for surface rocks in Karnataka. Incidentally, this value is also nearer to the value of 2.74 g/cm^3 suggested for surface rocks having tonalitic compositions (Woollard 1962). Thus, from estimates of average densities in the present study, it was not possible to determine whether the surface rocks have granodioritic or tonalitic composition. The problem may perhaps be resolved when more data on granodiorite samples become available.

Acknowledgements. This paper is published with the kind permission of the Director, National Geophysical Research Institute, Hyderabad.

References

Anfiloff, W., Shaw, R.D.: The gravity effects of three large uplifted granulite blocks in separate Australian shield areas. Proc. Symp. Earth's gravitational field and secular variations in position pp. 273–289, 1973

Aravamadhu, P.S.: Certain aspects of magnetic studies of charnockites at Waltair, India – Field investigations. Can. J. Earth Sci. V, **11**, 503–509, 1974

Balakrishna, S., Ramana, Y.V.: Elastic properties of some Indian rocks constituting the earth's crust. J. Phys. Earth **16**, 103–110, 1968

Balakrishna, S., Ramana, Y.V., Rao, M.V.M.S.: Shear wave velocities in Indian rocks. Bull. Nat. Geophys. Res. Inst. **6**, 1–16, 1968

Balakrishna, S., Venkatanarayana, B., Gogte, B.S.: Some studies on granites along Mysore-Hyderabad traverse. Bull. Nat. Geophys. Res. Inst. **9**, 67–87, 1971

Daly, R.A., Manger, G.E., Clark, Jr., S.P.: Density of rocks. Hand Book of Physical Constants. Geol. Soc. Am. Mem. **97**, 20–26, 1966

De, A.: Anorthosites of eastern ghats. In: Origin of anorthosites and related rocks. I.Y. Isachsen, ed. N.Y. State Mus. Sci. Serv. Mem. **18**, 425–434, 1969

Fairhead, J.D., Scovell, P.: Gravity study of the Limpopo belt, southern Africa. Annual Report, Res. Inst. Afr. Geol., Dept. Earth Sci., Univ. Leeds **20**, 31–35, 1976

Gibb, R.A.: The densities of Precambrian rocks from northern Manitoba. Can. J. Earth. Sci. **5**, 433–438, 1968

Gibb, R.A., Thomas, M.D.: Gravity signature of fossil plate boundaries in the Canadian shield. Nature **262**, 199–200, 1976

Heiland, C.A.: Geophysical exploration. New York: Prentice-Hall Inc. 1946

Henkel, H.: Studies of density and magnetic properties of rocks from northern Sweden. Pageoph, **114**, 235–249, 1976

Holland, T.H.: The charnockite series; a group of Archean hypersthenic rocks in Peninsular India. Mem. Geol. Surv. India, **28**, 87–90, 1900

Kanungo, D.N., Chetty, T.R.K.: Anorthosite body in the Nellore Mica-pegmatite belt of Eastern India. J. Geol. Soc. India **19**, 87–90, 1978

Lidiak, E.G.: Magnetic characteristics of some Precambrian basement rocks. J. Geophys. **40**, 549–564, 1974

Marshall, C.E., Narain, H.: Regional gravity investigations in the Eastern and Central Commonwealth. Dep. Geol. Geophys. Univ. Sydney, Mem. **1954/2**, 101 pp., 1954

Qureshy, M.N., Krishnabrahmam, N., Verma, R.K., Bhalla, M.S., Garde, S.C., Divakara Rao, V., Naqvi, S.M.: Geological, geochemical and geophysical studies along the 14th parallel in Mysore. Proc. Symp. Upper Mantle Project, Jan. 1967, Hyderabad, India pp. 211–225, 1967

Ramberg, I.B.: Gravity interpretation of the Oslo Graben and associated igneous rocks. Nor. Geol. Unders. **325**, 1–194, 1976

Smithson, S.B.: Densities of metamorphic rocks. Geophysics **36**, 690–694, 1971

Smithson, S.B., Brown S.K.: A model for lower continental crust. Earth Planet. Sci. Lett. **35**, 134–144, 1977

Subrahmanyam, C.: Relationship of gravity field to structural provinces in peninsular shield of South India. Doctoral Thesis Indian School of Mines, Dhanbad, India pp. 236, 1978

Subramaniam, A.P.: Charnockites of the type area near Madras-A reinterpretation. Am. J. Sci. **257**, 321–350, 1959

Subramaniam, A.P.: Petrology of charnockite suite of rocks around St. Thomas Mount and Pallavaram near Madras City, India. Rept. 21st Int. Geol. Congr. Sect **8**, 394–403, 1960

Subramaniam, A.P.: Charnockites and granulites of Southern India – A review. Medd. Fra. Dansk. Geol. Gorening **17**, 473–493, 1967

Tanner, J.G.: A geophysical study of structural boundaries in the eastern Canadian shield. Doctoral Thesis, Univ. Durham, England 1969

Windley, B.F., Bridgwater, D.: The evolution of Archean low and high-grade terrains. Geol. Soc. Aust. Spec. Publ. **3**, 33–46, 1971

Woollard, G.P.: The relationship of gravity anomalies to surface elevation, crustal structure and geology. Univ. Wisconsin, Geophys. Polar Res. Centre, Rept. **62–9**, 292 pp., 1962

Woollard, G.P.: Regional variations in gravity. In: The earth's crust and upper mantle. P.J. Hart, ed. Am. Geophys. Union, Monograph No. **13**, 320–341, 1969

Received July 26, 1979; Revised Version July 16, 1980
Accepted August 8, 1980

J Geophys (1981) 49:108–114

Journal of Geophysics

Lithospheric Structure and Teleseismic *P*-Wave Reflection Delays Under Fennoscandia and Siberia

Ian C.F. Stewart
Department of Physics, Memorial University, St. John's, Newfoundland, A1B 3X7, Canada

Abstract. Differential ($PP-P$) travel-time residuals from published teleseismic data are used to locate anomalous velocity structure near reflection points in Fennoscandia and Siberia. Reflections up to 2 s early correspond to shield areas, such as the Siberian platform, while later reflections (slower velocity structure), with positive residuals, tend to occur under less stable areas, such as the West Siberian lowlands. Exceptionally late reflections (about 2 s positive) in part of the latter region may be related to major lithosspheric sutures. The reflection delays are generally consistent with trends observed elsewhere for the residuals of *P*-waves.

Key words: *PP* reflections – Lithospheric structure – Seismic velocity – Travel-time residuals

Introduction

The travel-time delays or residuals of telseismic *P*-wave reflections (*PP* waves) may be used to locate regions of anomalous velocity structure in the crust and upper mantle near the reflection point, approximately half-way between the source and receiver. The effects of structure near the source and receiver can be minimised by taking differential ($PP-P$) residuals, where P is the direct (unreflected) compressional wave (Stewart 1976). Positive ($PP-P$) residuals correspond to later reflections than would be expected from the assumed Earth model used in theoretical travel-time calculations. Late reflections could be due to slower than normal velocity structure near the reflection point. For example, a delay of one second in the *PP* reflection time would be caused by an increase in crustal thickness of about 10–15 km compared to average values elsewhere. The minimum lateral dimension of anomalies which can be resolved by the *PP* residuals is of the order of 100 km, which is comparable to the size of the first Fresnel diffraction zone for reflections at teleseismic distances.

Published data have been used to correlate areas giving abnormal ($PP-P$) reflection delays with regional tectonic features for parts of the Arctic ocean and Greenland (Stewart in press 1980). The extension of the data set into northern Eurasia is considered here, and it is shown that trends in reflection residuals tend to be consistent with the known lithospheric structure and with *P*-wave residuals observed elsewhere.

Data Analysis

The *PP* and *P*-wave travel-time residuals are taken from the Bulletins of the International Seismological Centre (I.S.C.) from 1964 through 1976. Some of the problems associated with using this source of data and in analysing the reflection residuals have been discussed by Stewart (1976 in press 1980). Only phases identified by the I.S.C. as *PP* waves are used, to reduce the possibility of errors arising from incorrect identification of waves by the seismograph operators. The ($PP-P$) residuals used in this study are restricted to the range -8 to $+9$ s, in order to exclude values which are likely to be due to incorrect phase identifications or excessive errors in reading the seismograms. Since genuine reflection delays may approach these values (Stewart and Keen 1978), minimal restrictions are placed on the data range used in the analysis.

The data are given here for two areas, from the Urals westwards, and for Siberia. Most of the data are from earthquakes in the vicinity of the north-western margin of the Pacific Ocean, recorded at stations in Europe. For the area west of the Urals, the values of the ($PP-P$) residuals in seconds at the reflection points, averaged over regions 1/2° by 2/5° geocentric in area, are given in Fig. 1 Allowance is made for the focal depth in calculating the reflection points. In Fig. 1, letters correspond to negative residuals (early reflections), with A equivalent to -2–-1 s, and so on. The number of data used to give each value in Fig. 1 is shown in Fig. 2. The data in Fig. 1 and 2 comprise 971 reflections from 306 events. The data for Siberia are shown in Fig. 3, averaged as for Fig. 1, with the data density indicated in Fig. 4. The area of this data set partially overlaps that given in Fig. 1, and includes 4055 points from 656 events. Good data coverage is achieved around 90° E longitude, approximately half-way between most of the events along the north-west Pacific margin, and the European seismograph stations.

Although the data can be contoured to show the broad trends in values, this process tends to smooth out details of residual variations which may occur at tectonic boundaries. High-order contour surfaces can show such changes, but tend to be unstable in areas of lower data density, especially where the noise may be several seconds in amplitude. Following the procedure used by Stewart (in press 1980), the lateral variations are shown as averages along great circle profiles. Points within $2^1/_2$ degrees geocentric of a profile are projected perpendicularly on to the line, and a running mean within a window of length 3 geocentric degrees is then taken along the profile. Individual data points are used in this process, rather than the averaged values shown in Fig. 1 and 3.

The locations of the profiles across Fennoscandia and the Russian Platform are indicated in Fig. 5, which also shows the main tectonic and bathymetric features. The residual values along the profiles are given in Fig. 6. Values derived from averages of less

0340-062X/81/0049/0108/$01.40

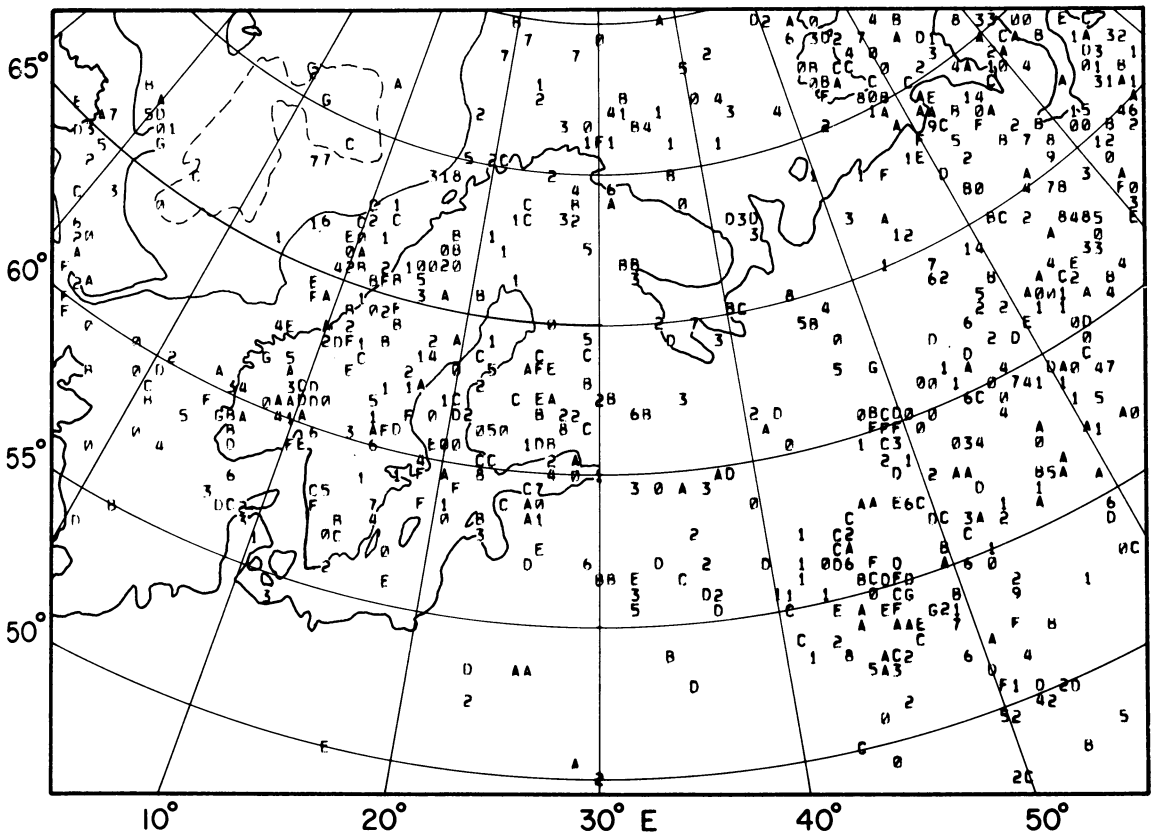

Fig. 1. ($PP-P$) travel-time residuals for reflection points in Fennoscandia and the Russian platform. The values in seconds are averages over areas 2/5° by 1/2° geocentric. Letters correspond to negative values, with A equivalent to $-2--1$ s, B $-3--2$ s, and so on

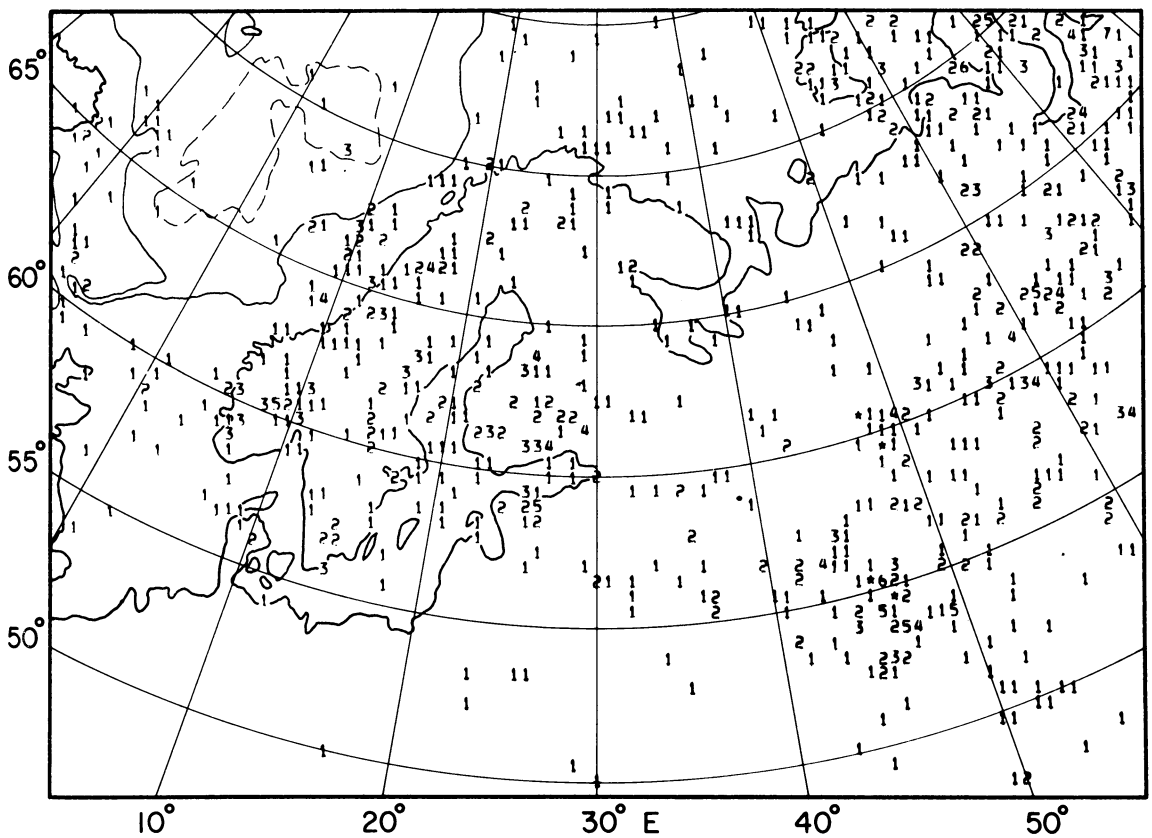

Fig. 2. The number of reflections averaged to give each data value in Fig. 1. Asterisks correspond to more than 9 points per unit area

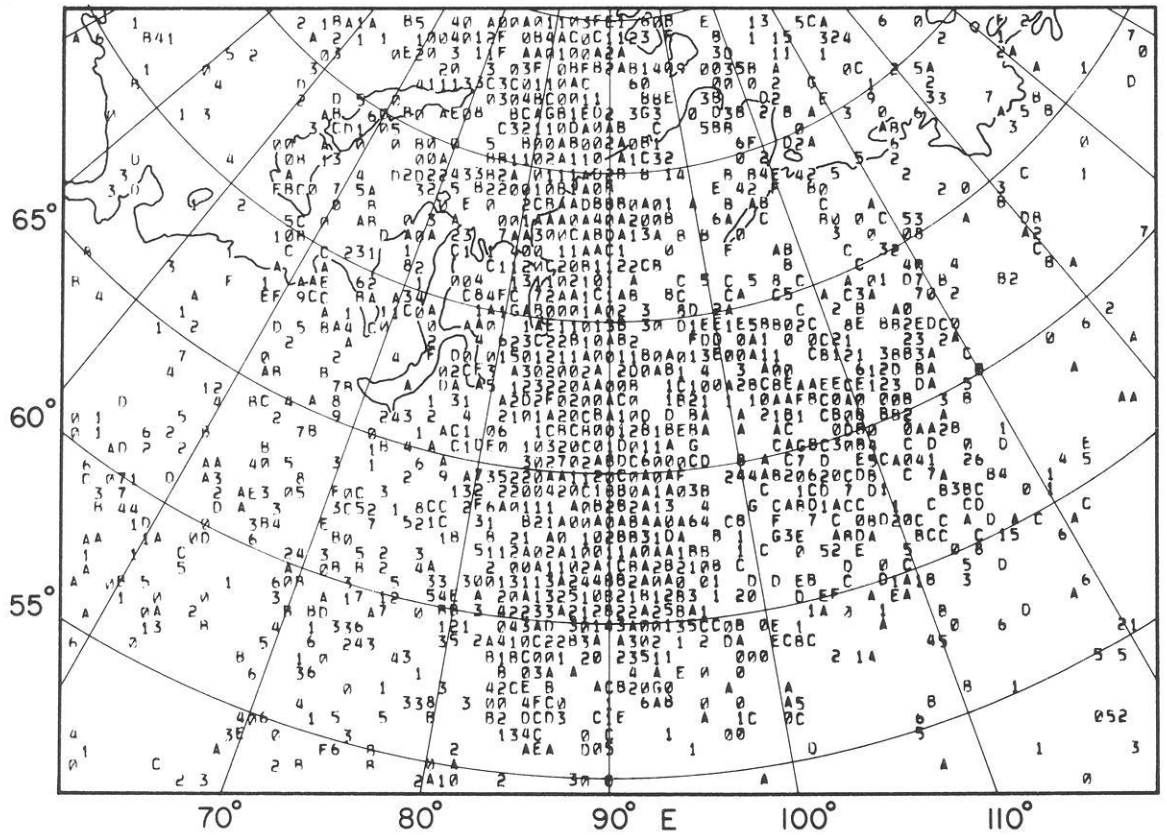

Fig. 3. Travel-time residuals in seconds for reflections under Siberia, plotted similarly to Fig. 1

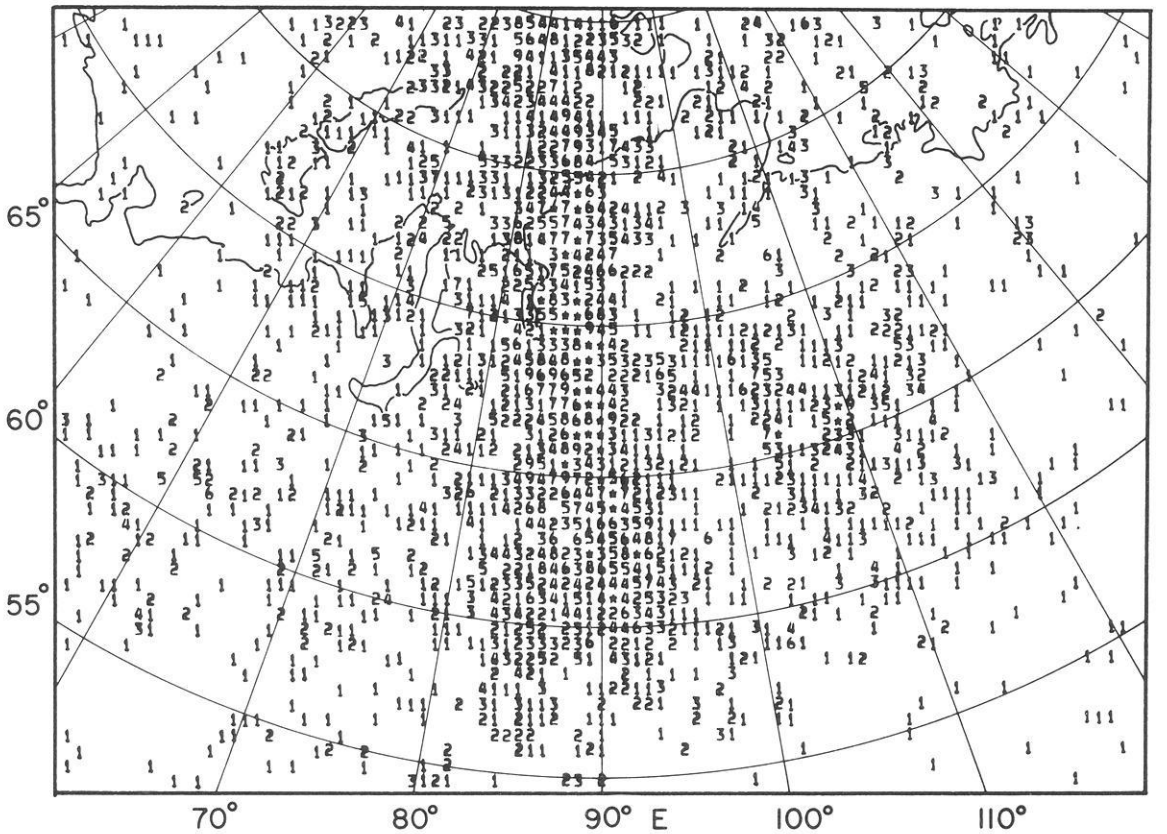

Fig. 4. The number of reflection residuals averaged to give each value in Fig. 3

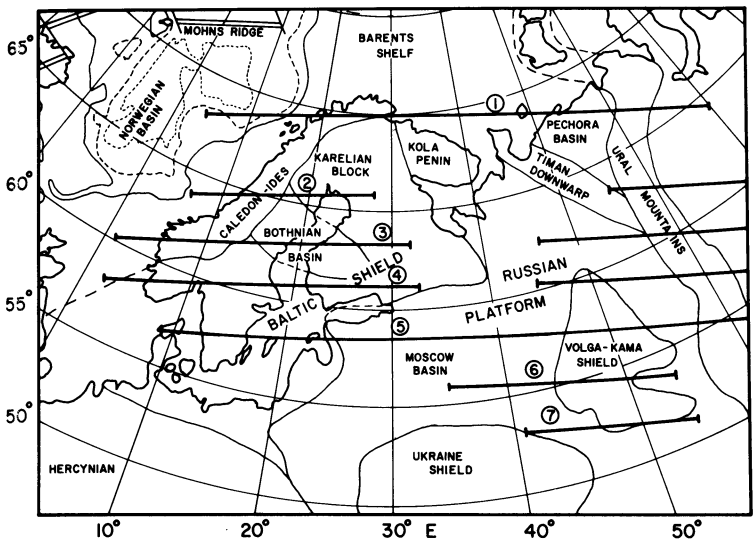

Fig. 5. The main tectonic features of the area covered by Fig. 1. The 1000, 2000, and 3000 m isobaths are also shown. The locations of the profiles along which reflection residuals are averaged in Fig. 6 are also indicated

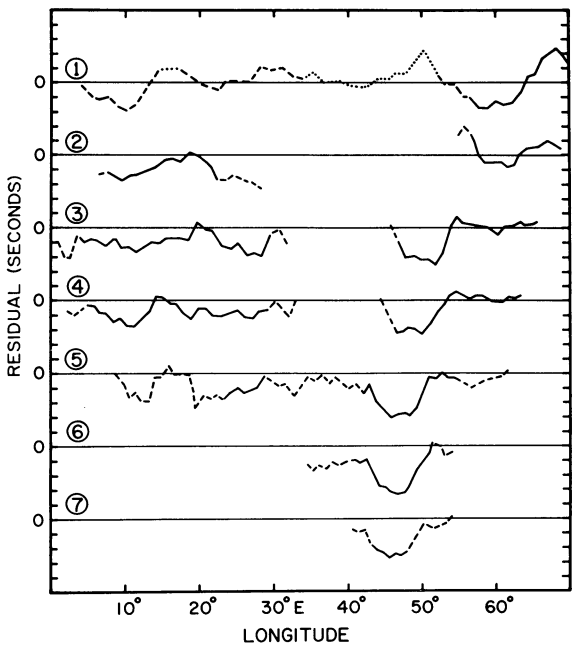

Fig. 6. Averages of $(PP-P)$ residuals along great circle profiles. Data within $2^1/_2°$ geocentric of a profile are averaged within a running window of length 3° along the line. Averages of less than 10 and 20 data points are shown dotted and dashed respectively. The *profile numbers* correspond to those given in Fig. 5

than 10 data points are shown dotted (which only occurs on Profile 1 in Fig. 5), and averages of less than 20 points are dashed. For the regions of better data coverage in Fig. 5, up to about 50 points are averaged to give each profiled value.

The profile locations for the Siberian data are shown in Fig. 7, and the profiles are given in Fig. 8. A greater density of data occurs for parts of Siberia compared to the Fennoscandian data, and hence some sections of the profiles in Fig. 8 represent averages of more than 400 points.

In the areas which are well covered by reflection points, the effects of random errors should be minimished by averaging along the profiles. A given area of reflections may include data from a range of source-receiver geometries. Hence it is unlikely also that trends in abnormal reflection delays observed in the areas of better coverage are due entirely to any source or receiver effects remaining after taking differential $(PP-P)$ residuals. However, the profiles should be treated with caution in the areas of fewer data.

The standard deviations of the profile values tend to be in the range 2–3 s. This is comparable to the standard deviations observed for residuals at single stations using data from restricted source regions of the order of 1°–2° across, and may be due largely to random errors in the data. The statistical significance of the variations along the profiles may be tested by using a two-tailed *t*-test to compare residual values in adjacent areas (Stewart in press 1980). The more prominent anomalies tend to be significant at least at the 95% confidence level. In the areas of better coverage, variations of only 1 s along the profiles are significant at better than the 99% level.

As discussed by Stewart (in press 1980), the features with shorter wavelengths (a few hundred kilometers) on the profiles are probably due to structure within the tectosphere. Variations in residuals with wavelengths of the order of 1,000 km or more are probably due largely to deeper lateral changes in velocity. Romanowicz (1979) suggests that about 70% of the variation in travel-time delays in North America is caused by lateral heterogeneity within 250 km of the surface, although lateral changes in velocity below Eurasia may be significant down to 700 km depth (England et al. 1977).

Profiles in Fennoscandia and the Russian Platform

Much of the Baltic Shield appears to give early reflections, with residuals up to about 2 s negative (Fig. 6). This is consistent with observations of direct *P*-wave arrivals, which tend to be up to 1 s early in shield areas (Herrin and Taggart 1968). The variations given here (of the order of 2 s) for reflection residuals in Fennoscandia are consistent with lateral changes of about 1 s in *P*-wave residuals given by Noponen (1977). Similar variations are also observed by Brown (1973) for *P*-wave residuals at distances less than 55°.

For the present data set, few reflections exist in the vicinity of any of the seismograph stations. Hence the *P*-wave delays at

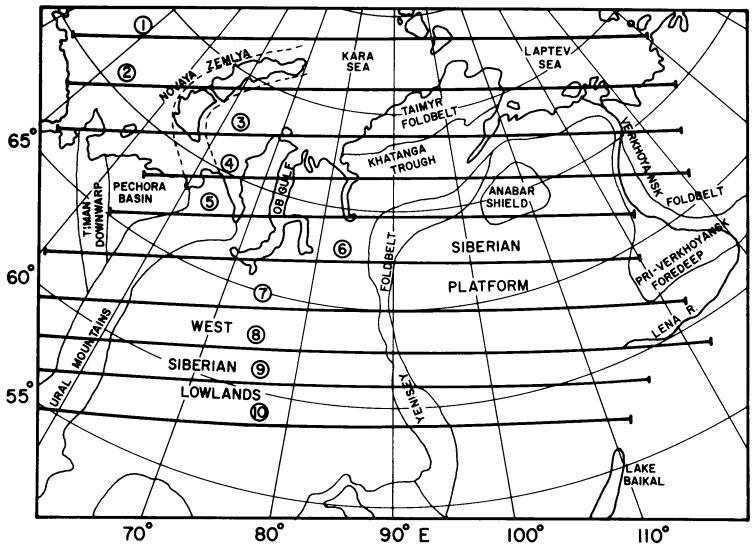

Fig. 7. The main tectonic features of Siberia and the locations of the profiles given in Fig. 8

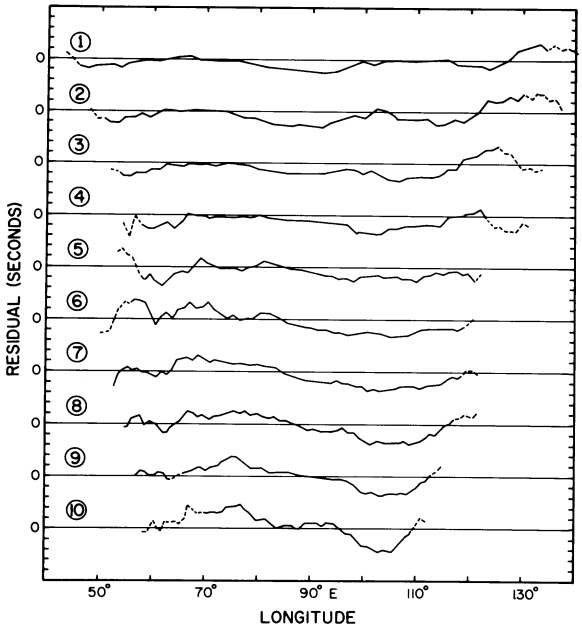

Fig. 8. Averages of $(PP-P)$ residuals along profiles across Siberia, obtained in a similar fashion to those in Fig. 6

individual stations cannot be compared readily with the $(PP-P)$ residuals, which are also subject to noise. It should also be noted that in general there is not good agreement between the various estimates of *P*-wave residuals at Scandinavian stations (Enayatollah 1972; Brown 1973; Noponen 1977; Poupinet 1979). Brown (1973) suggests that the *P*-wave residuals have large azimuthal components (up to several seconds in amplitude), which may be due to a large-scale dipping discontinuity in the mantle at about 600 km depth. The effects of a dipping interface should to some extent be cancelled out in the reflection residuals, if the boundary is traversed by both the upgoing and downgoing sections of the *PP* ray. The *PP* travel time may therefore yield the non-azimuthally dependent residual for the region.

The Bothnian basin tends to give reflection residuals later than in adjacent areas by about 1 s (Profiles 2 and 3 in Fig. 6). Local crustal thickening of the order of 5 km in the vicinity of the Gulf of Bothnia and central Sweden (Sellevoll 1973) would delay reflections by only about 0.2 s. However, in general the data density in Scandinavia is too low to permit a comparison of the reflection residuals with localised tectonic features. There appears to be no consistent correlation of trends in early reflections (high seismic velocities) with areas of low heat flow in Fennoscandia or the Russian platform (Čermák and Hurtig 1978).

The density of reflection data varies across the Russian platform, but values tend to be negative over much of the region. The seismograph stations in the U.S.S.R. for which *P*-wave residuals have been published (Herrin and Taggart 1968; Poupinet 1979) are not located in the areas of good $(PP-P)$ data coverage, and hence the residuals cannot be compared. Prominent negative reflection residuals (up to about 3 s early) coincide with part of the Volga-Kama shield. This may result from an abnormally thin low-velocity layer or a cooler than normal upper mantle, perhaps analogous to the possible "cold spot" in West Africa proposed by Chapman and Pollack (1974). Although the regional heat flow may not be exceptional (Kutas et al. 1978), it is possible that the upper mantle is relatively cool with a Curie isotherm depressed by up to 20 km in the region of the Volga-Kama shield (Belyaevsky et al. 1973). It is difficult to correlate the relatively few $(PP-P)$ residuals elsewhere in the Russian platform with major structures given by Nalivkin (1976) or with relief on the Moho discontinuity (Belyaevsky et al. 1973). Crustal thickness in the platform may vary by up to 20 km (Belyaevsky et al. 1973), which could contribute more than 1 s to the changes in residual values.

Siberian Profiles

Over much of its length, the Paleozoic geosyncline forming the Ural mountains is associated with reflection residuals which are of the order of 1 s negative towards the east, compared to values which are near zero or even positive towards the west (Fig. 8). While the Russian platform has an average crustal velocity of 6.5 km s^{-1} (Beliayevsky et al. 1968), velocities tend to be lower in the vinicinity of the Urals by up to 0.5 km s^{-1} for a given depth (Alekseev et al. 1973), and the crustal thickness is also increased by perhaps 5 km (Belyaevsky et al. 1973), Velocities of about 8.0 km s^{-1} below the Moho along the main axis of the Urals are about 0.2 km s^{-1} lower than in adjacent regions, and

Beliayevsky et al. (1968) indicate that velocities as low as 6.8 km s^{-1} occur under the area of greatest sedimentary thickness, which may reach 10 km. Thus the observed variations within the lithosphere could account for changes in reflection delays of the order of 2 s. Čermák and Hurtig (1978) also suggest that the temperature at the Moho under the Urals may be higher by 100°–200° C than in the platform regions to the west.

From seismic profiling, the boundary of the Urals to the east may continue under the West Siberian lowlands for up to 100 to 200 km (Beliayevsky et al. 1968), with velocities exceeding 7 km s^{-1} at depths of only a few kilometers. Relatively high velocity material, exceeding 6.4 km s^{-1}, comprises 80% of the crustal thickness of the eastern Urals (Belyaevskiy et al. 1971). The crustal variations may account for about 1 s in the negative residuals on the eastern margin of the Urals. The geology of the Urals has been interpreted in terms of a former subduction zone dipping to the east (Hamilton 1970). While high velocities can be observed in dipping slabs which have become inactive only in the past few million years (Solomon and Butler 1974), it is unlikely that any velocity contrast extending below the lithosphere would remain from the Urals subduction (Toksöz et al. 1971), especially if the lithosphere is decoupled from the upper mantle.

Much of the West Siberian lowlands appears to give late reflections (positive residuals), with localised anomalies up to about 2 s in magnitude (Profiles 6–10 in Fig. 8). If the profiles are obtained by averaging over smaller areas, then the larger anomalies can even exceed 3 s. The positive residuals generally coincide with relatively low crustal and upper mantle velocities. Average crustal velocities in the West Siberian lowlands are 5.8–6.0 km s^{-1}, which is about 0.5 km s^{-1} lower than in the adjacent platform areas, but velocities tend to increase towards the eastern margin of the lowlands (Belyaevskiy et al. 1971).

There appears to be no consistent correlation of the residuals with crustal thickness (Beliayevsky et al. 1968; Vashchilov 1971). Changes in crustal parameters alone are unlikely to account for the larger anomalies exceeding 1 s in Fig. 8. A velocity decrease of several percent would have to extend vertically over at least 100 km to give the observed late reflections. The later reflection anomalies are comparable in amplitude to those expected from observations of *P*-wave residuals in active rift zones, which are of the order of 1 s (Fairhead and Reeves 1977), where reduced upper mantle velocities and a thinner than normal lithosphere usually prevail. The later reflections around 70° E longitude may lie in the vicinity of a Triassic boundary underlying the lowlands, between the Siberian and Northern European lithospheric blocks (Burrett 1974). The zone of very late reflections is approximately bounded on the east by the major Paleozoic suture extending south from the Ob gulf, postulated by Burke et al. (1977). The region of the late reflections also underwent widespread volcanism related to the Urals subduction during the Paleozoic (Hamilton 1970).

The physical properties of the lithosphere appear to vary appreciably across the lowlands, in both the crustal and sub-crustal layering (Vashchilov 1971). To the south of the Ob gulf, the depth to the top of the asthenosphere may be reduced, which could imply that the isotherms are elevated in the area. In the region of the late reflections, a local maximum occurs in the heat flow, with values of 60–70 mW m^{-2} (Kutas et al. 1978). For the eastern part of the West Siberian lowlands, the heat flow values are typically less than 50 mW m^{-2} (Jessop et al. 1976). Pollack and Chapman (1977a, b) predict a local minimum in the mantle heat flow under the lowlands, with an abnormally great lithospheric thickness of about 300 km. However, in the region of the late reflections around 60° N, the temperature at the Moho may be elevated by perhaps 100°–200° C compared to adjacent areas (Fotiadi et al. 1969). Gravity observations are not available for the area for comparison with the reflection data.

Much of the Siberian platform is well covered by the present data set. The platform is separated from the West Siberian lowlands by the Yenisey foldbelt, which was formed by east-dipping subduction during the late Precambrian (Hamilton 1970). Early reflections tend to occur under this foldbelt, and the residuals become more negative towards the interior of the Siberian platform. This is consistent with observations of *P*-wave residuals in shield areas (Poupinet 1979). The residuals in the platform appear to have no correlation with the thickness of the sedimentary sequences, which may exceed 6 km in some parts, nor with the depth to the Moho, which only varies by a few kilometers over most of the region (Fotiadi et al. 1978).

Negative residuals occur at the western end of the Paleozoic Taimyr foldbelt, and become more positive towards the east, where the crust thickens by several kilometers (Fotiadi et al. 1978). These geosynclines continue offshore into the southern Kara sea (Hamilton 1970). Reflections along the Khatanga trough (North Siberian lowland) vary progressively from about zero in the west to around 2 s negative in the east (Profiles 3 and 4 in Fig. 8). This Mesozoic trough may have been caused by regional tension (Hamilton 1970), with more than 3 km of subsidence (Bazanov et al. 1976) and a crust which may be thinner than adjacent areas by more than 6 km (Fotiadi et al. 1978).

On the eastern continuation of the trough, approximately 20 late reflections occur, which may represent a significant local trend possibly several hundred kilometers in extent near the Lena river delta (Profiles 1, 2 and 3 in Fig. 8). If this is a real anomaly, then the residuals could indicate the location of former hot spot activity (Stewart and Keen 1978). The Arctic mid-ocean spreading center (Nansen or Gakkel Ridge) probably continues across the Laptev sea, through the region of these late reflections, and into a broad zone of seismicity which extends eastwards from the Verkhoyansk foldbelt (Chapman and Solomon 1976). The Khatanga trough may then be an aulacogen, with the Mesozoic Verkhoyansk foldbelt and the spreading center as other tectonic features radiating from a former hot spot. This would be analogous to triple junctions centered on hot spots in other locations (Burke and Dewey 1973).

Poupinet (1979) notes that *P*-wave residuals at Tiksi (71.6° N, 128.9° E), near the Lena delta, tend to be exceptionally early (−1.5 s). Unfortunately no *PP* data are plotted in Fig. 3 within at least 100 km of this seismograph station. The late reflections giving the positive trends on Profiles 1 to 3 in Fig. 8 tend to be to the north and west of Tiksi, while the few reflection values to the south tend to be negative. A hot spot centered possibly several hundred kilometers from Tiksi would not affect most of the *P*-wave residuals observed at that station. Hence the reflection data are not necessarily inconsistent with this single published *P*-wave residual for the region.

Conclusion

The broad variations in the ($PP-P$) travel-time residuals can be correlated with the major tectonic features in the areas of better data coverage, especially Siberia. As expected from directly-observed *P*-wave residuals, shield areas such as the Siberian platform tend to give reflections early by about 1–2 s compared to less stable regions, such as the West Siberian lowlands. The larger

residuals, which may be several seconds positive or negative (late or early), probably indicate changes in structure throughout the lithosphere, and possibly also in the thickness of the asthenosphere. An extensive area of late reflections occurs in the central sections of the West Siberian lowlands, and locally the anomalies become about 2 s positive. The region may have been the location of a major lithospheric suture. The variations observed across the Paleozoic Ural geosyncline, with residuals changing from positive in the west to about 1 s negative towards the east, are probably consistent with the known velocity structure of the lithosphere.

Where suitable source-receiver configurations exist, the reflection residuals enable large areas to be examined more readily than is possible with directly observed *P*-wave residuals, particularly in remote regions. While local anomalies of small extent (less than 100 km across) cannot be observed well by teleseismic *PP* waves, larger-scale lateral variations in whole lithospheric and upper mantle structure can be detected.

References

Alekseev, A.S., Belonosova, A.V., Burmakov, I.A., Krasnopevtseva, G.V., Matveeva, N.N., Nersessov, G.L., Pavlenkova, N.I., Romanov, V.G., Ryaboy, V.Z.: Seismic studies of low-velocity layers and horizontal inhomogeneities within the crust and upper mantle on the territory of the U.S.S.R. Tectonophysics **20**, 47–56, 1973

Bazanov, E.A., Pritula, Y.A., Zabaluev, V.V.: Development of main structures of the Siberian Platform: History and dynamics. Tectonophysics **36**, 289–300, 1976

Beliayevsky, N.A., Borisov, A.A., Volvovsky, I.S., Schukin, Y.K.: Transcontinental crustal sections of the U.S.S.R. and adjacent areas. Can. J. Earth Sci. **5**, 1067–1078, 1968

Belyaevskiy, N.A., Vol'vovskiy, I.S., Razinkova, M.I., Ryaboy, V.Z.: Average crustal velocities of longitudinal seismic waves in the U.S.S.R. Dokl. Akad. Nauk S.S.S.R. **198**, 164–167, 1971

Belyaevsky, N.A., Borisov, A.A., Fedynsky, V.V., Fotiadi, E.E., Subbotin, S.I., Volvovsky, I.S.: Structure of the Earth's crust on the territory of the U.S.S.R. Tectonophysics **20**, 35–45, 1973

Brown, R.J.: Azimuthally varying *P*-wave travel-time residuals in Fennoscandia and lateral inhomogeneity. Pure Appl. Geophys. **105**, 741–758, 1973

Burke, K., Dewey, J.F.: Plume-generated triple junctions: Key indicators in applying plate tectonics to old rocks. J. Geol. **81**, 406–433, 1973

Burke, K., Dewey, J.F., Kidd, W.S.F.: World distribution of sutures – the sites of former oceans. Tectonophysics **40**, 69–99, 1977

Burrett, C.F.: Plate tectonics and the fusion of Asia. Earth Planet. Sci. Lett. **21**, 181–189, 1974

Čermák, V., Hurtig, E.: The preliminary heat flow map of Europe and some of its tectonic and geophysical implications. Pure Appl. Geophys. **117**, 92–103, 1978

Chapman, D.S., Pollack, H.N.: Cold spot in West Africa: Anchoring the African plate. Nature **250**, 477–478, 1974

Chapman, M.E., Solomon, S.C.: North American-Eurasian plate boundary in northeast Asia. J. Geophys. Res. **81**, 921–930, 1976

Enayatollah, M.A.: Travel times of P waves for the Swedish-Finnish seismograph network. Pure Appl. Geophys. **94**, 101–123, 1972

England, P.C., Worthington, M.H., King, D.W.: Lateral variation in the structure of the upper mantle beneath Eurasia. Geophys. J. R. Astron. Soc. **48**, 71–79, 1977

Fairhead, J.D., Reeves, C.V.: Teleseismic delay times, Bouguer anomalies and inferred thickness of the African lithosphere. Earth Planet. Sci. Lett. **36**, 63–76, 1977

Fotiadi, E.E., Moiseyenko, U.I., Sokolova, L.S.: The heat field of the West Siberian Platform. Dokl. Akad. Nauk S.S.S.R. **189**, 385–388, 1969

Fotiadi, E.E., Surkov, V.S., Grishin, M.P., Zhero, O.G.: Regional geophysical investigations of the structure of the Earth's crust of Siberia. Sov. Geol. Geophys. **19**, 90–95, 1978

Hamilton, W.: The Uralides and the motion of the Russian and Siberian Platforms. Geol. Soc. Am. Bull. **81**, 2553–2576, 1970

Herrin, E., Taggart, J.: Regional variations in P travel times. Bull. Seismol. Soc. Am. **58**, 1325–1337, 1968

Jessop, A.M., Hobart, M.A., Sclater, J.G.: The World heat flow data collection – 1975. Energy, Mines and Resources Canada, Earth Phys. Branch, Geothermal Ser. **5**, 1976

Kutas, R.I., Lubimova, E.A., Smirnov, Y.B.: Heat flow map of the European part of the U.S.S.R. Pure Appl. Geophys. **117**, 104–107, 1978

Nalivkin, V.D.: Dynamics of the development of the Russian Platform structure. Tectonophysics **36**, 247–262, 1976

Noponen, I.: The Blue Road geotraverse: The relative residual of the teleseismic P-wave: Application to the study of deep structure in Fennoscandia. Geol. Foeren. Stockholm Foerh. **99**, 32–36, 1977

Pollack, H.N., Chapman, D.S.: Mantle heat flow. Earth Planet. Sci. Lett. **34**, 174–184, 1977a

Pollack, H.N., Chapman, D.S.: On the regional variation of heat flow, geotherms, and lithospheric thickness. Tectonophysics **38**, 279–296, 1977b

Poupinet, G.: On the relation between *P*-wave travel time residuals and the age of continental plates. Earth Planet. Sci. Lett. **43**, 149–161, 1979

Romanowicz, B.A.: Seismic structure of the upper mantle beneath the United States by three-dimensional inversion of body wave arrival times. Geophys. J. R. Astron. Soc. **57**, 479–506, 1979

Sellevoll, M.A.: Mohorovičić discontinuity beneath Fennoscandia and adjacent parts of the Norwegian Sea and the North Sea. Tectonophysics **20**, 359–366, 1973

Solomon, S.C., Butler, R.G.: Prospecting for dead slabs. Earth Planet. Sci. Lett. **21**, 421–430, 1974

Stewart, I.C.F.: Travel time residuals of *PP* waves reflected under Atlantic Canada. Bull. Seismol. Soc. Am. **66**, 1203–1219, 1976

Stewart, I.C.F.: Anomalous travel times of teleseismic *P*-waves reflected under Arctic marine areas. Mar. Geophys. Res. in press, 1980

Stewart, I.C.F., Keen, C.E.: Anomalous upper mantle structure beneath the Cretaceous Fogo seamounts indicated by *P*-wave reflection delays. Nature **274**, 788–791, 1978

Toksöz, M.N., Minear, J.W., Julian, B.R.: Temperature field and geophysical effects of a downgoing slab. J. Geophys. Res. **76**, 1113–1138, 1971

Vashchilov, Y.Y.: Structure of the upper mantle and crust of the Western Siberian Lowland. Izv. Akad. Nauk. S.S.S.R., Phys. Solid Earth **1**, 51–64, 1971

Received February 19, 1980; Revised Version May 20, 1980
Accepted August 8, 1980

J Geophys (1981) 49:115–122

Journal of Geophysics

Propagation of Surface Waves in Marine Sediments

H.-H. Essen, H. Janle, F. Schirmer, and J. Siebert
Institut für Geophysik, Universität Hamburg, Bundesstr. 55, D-2000 Hamburg 13, Federal Republic of Germany

Abstract. In 1977 seismic investigations were carried out on the shore belt of the North Sea in order to observe slow surface waves. The water depth was about 1 m. Most of the seismic sections show two wave groups with a mean frequency of 4 Hz and velocities of 100 and 230 ms^{-1}. The axial ratios of horizontal to vertical amplitude are 0.5 and 2.3, respectively. Some seismograms are analysed by multiple filter techniques. By means of least-squares fits the observed and theoretical group-velocity curves are compared. It turns out that a simple two-layer model of the sedimentary sea floor yields reasonable results with respect to group velocities but not with respect to the axial ratios of horizontal and vertical amplitudes. This discrepancy is overcome by introducing an additional near-surface layer of lower shear-wave velocity. The final model consists of a water layer (1 m) and three sedimentary layers (3 m, 15 m, ∞) with shear-wave velocities of 75 ms^{-1}, 150 ms^{-1}, and 250 ms^{-1}, respectively.

Key words: Shear-wave velocities – Marine sediments – Interface waves – Multiple-filter technique – Model computations

Introduction

Interest in sedimentary shear-wave velocities has increased considerably during recent years (Essen 1977; Hawker 1979) particularly with reference to underwater acoustics. Low-velocity shear waves may be responsible for energy losses in the acoustic waveguide, and the amount of loss depends strongly on the shear-wave velocity. Shear-wave velocities in marine sediments are also of importance in other geophysical problems but there is still a great lack of measured data. This is due mainly to experimental difficulties. A detailed discussion of this subject is given by Hamilton (1976) and will not be repeated here.

In seismology Rayleigh waves, which propagate along the free surface, are of great importance for determining the elastic parameters of the upper mantle. Similar methods may be applied for the measurement of shear-wave velocities in the upper layers of ocean sediments. Following Cagniard (1962) we call the surface waves existing at the boundary between a fluid and a solid Scholte waves, so as to distinguish from Stoneley waves which propagate along a solid-solid interface.

In the case of homogeneous halfspaces both Rayleigh and Scholte waves are nondispersive. In the presence of layers, however, the Rayleigh as well as the Scholte wave splits up into a finite number of dispersive modes. This effect is important for the interpretation of the experimental results presented in this paper.

Surface-wave measurements at the sea floor were carried out with the objective of determining the shear-wave velocities in the uppermost layers of marine sediments. In order to avoid underwater measurements, the shore belt was chosen as the experimental site. Explosives were detonated under low water cover on a shoal, geophones were mounted on land.

The experimental configuration and results are presented in the following two sections. It was not possible, using refraction seismic methods, to construct a clear model of the shear-wave velocities within the sea floor. It turns out that this difficulty results from the thinness of the uppermost sedimentary layer. On the other hand, the seismograms show the features of trapped surface modes. For this reason a dispersion analysis by means of multiple filter techniques was performed, and is described later. Following this, computations are presented which attempt to model the shear-wave velocity as a function of depth.

Experimental Configuration

The measurements were carried out in 1977 on the North Sea coast of the Federal Republic of Germany. Figure 1 shows the location of the area which was investigated.

Bore holes near the measured profile revealed that the holocene layer thickness is in the range 15–20 m (Barkhausen, Bundesanstalt für Geowissenschaften und Rohstoffe, Hannover, personal communication 1979). The essential constituents of the holocene are various sands and clays.

Figure 1 also shows the exact location of the record section and the positions of shot points and geophones. The shots were detonated on a shoal over a horizontal range of 1200 m with 100 m distance between adjacent points. In order to obtain maximum energy coupling the explosive charges were placed in flat holes during ebb-tide and detonated at flood-tide under a water cover of about 1 m. The size of the charges varied between 3 and 15 kg TNT. Six geophones were set up on the section line on land. The closest distance between a shot point and geophone was about 50 m. In the first part of the experiment the geo-

0340-062X/81/0049/0115/$01.60

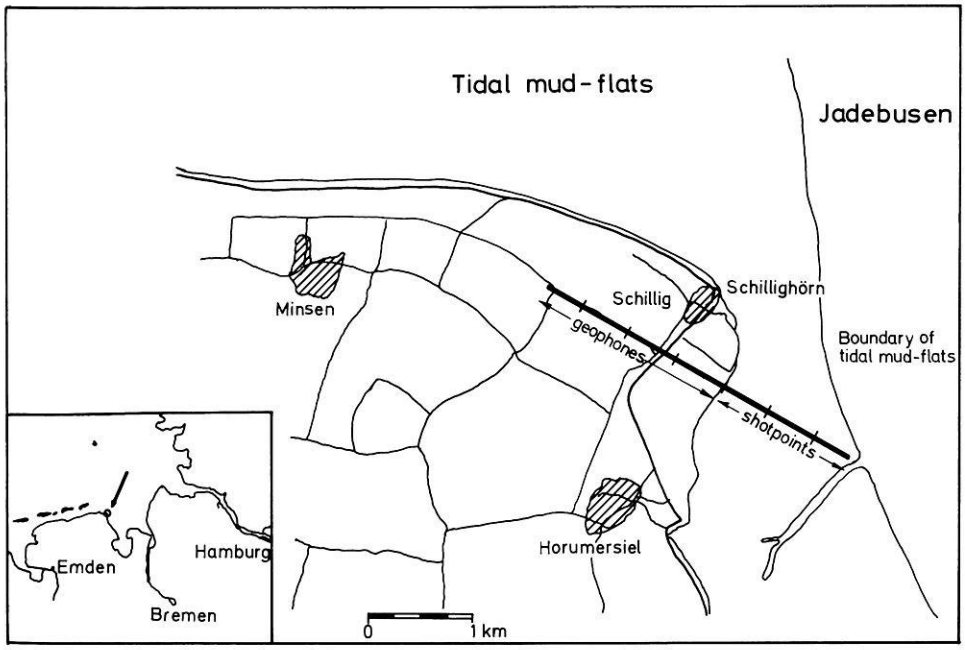

Fig. 1. Map of the experimental site

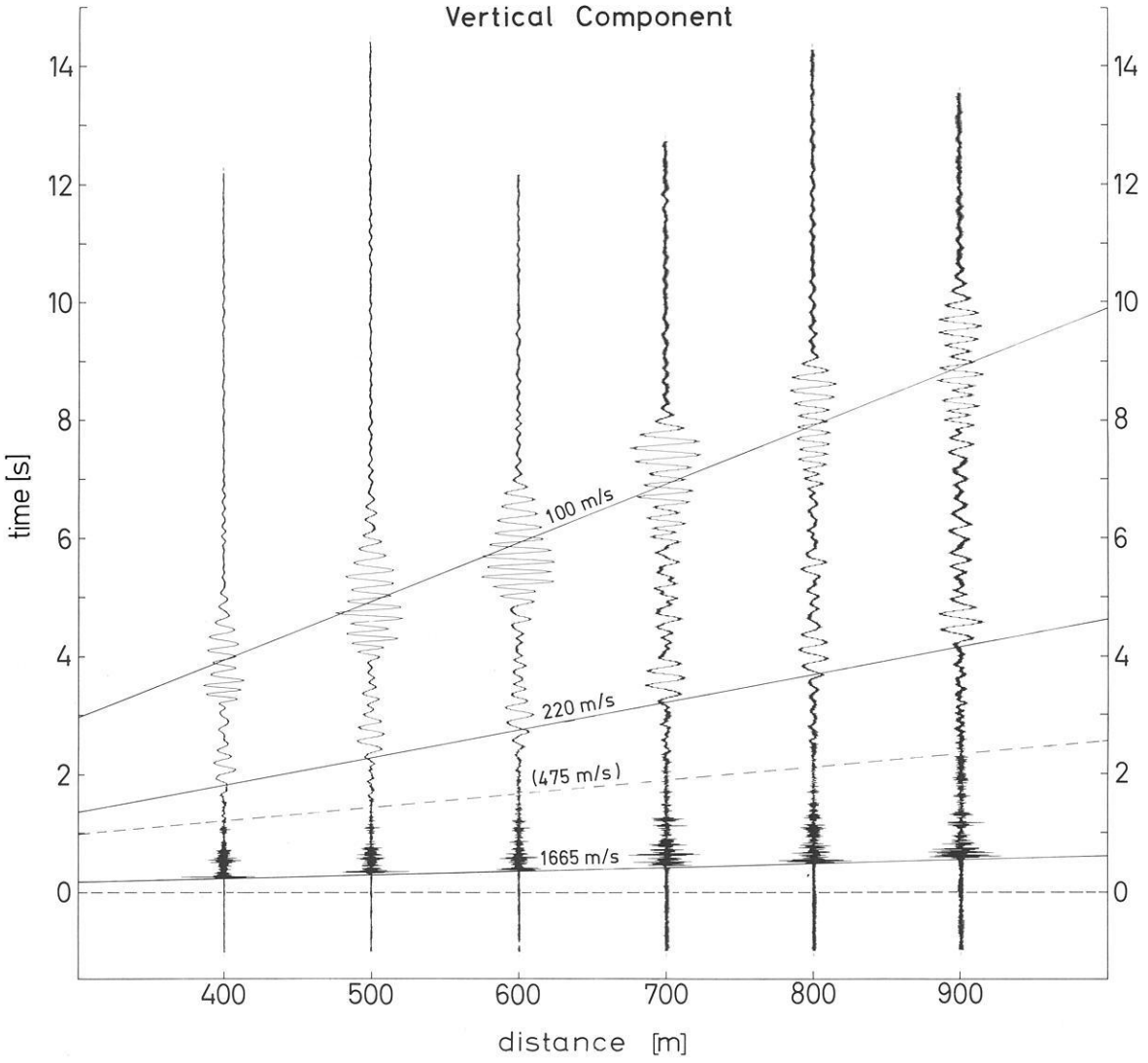

Fig. 2. Seismic section (shot points 12–17) for the fixed geophone G4, vertical component (*Z*)

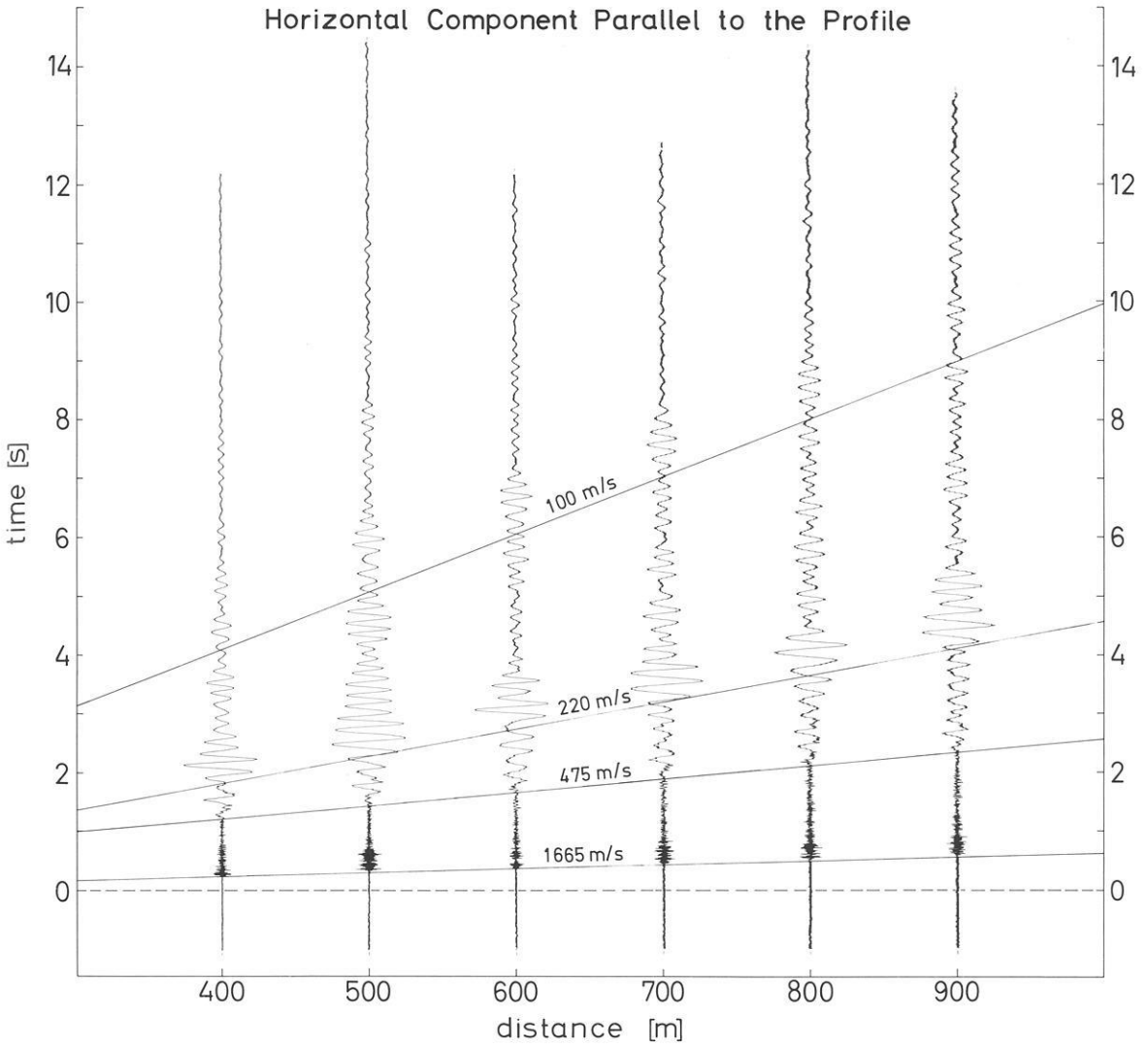

Fig. 3. Seismic section (shot points 12–17) for the fixed geophone G4, component in direction of profile (X)

phones were spread over 500 m on the profile line with a spacing of 100 m between adjacent geophones. In the second part the geophones were placed on a lengthened section line with a separation of 500 m, extending 1,500 m inland.

Geophones of the Geospace type with three components were used for the recordings. Their resonant frequency was 7.5 Hz. The data were recorded by FM equipment and telemetered by a UHF link to a central station.

Experimental Results

A total of 62 seismic sections were constructed. Thirty-two seismic sections were produced in such a way that the 6 geophones were combined with a fixed shotpoint for one section. For the remaining 30 sections seismograms from different shotpoints and a fixed geophone were combined. Comparisons of these types of representation showed that phase correlation between various shots for a fixed geophone delivered considerably better results. The coupling of the geophones with the soft and silty sand varied greatly. On the other hand, detonation occurred under relatively homogeneous conditions, since the charges were always set off near the surface under an approximately uniform water cover of about 1 m. The record sections were drawn separately for each component (Z: vertical, X: in the direction of profile, Y: perpendicular to profile). As an example we present the three sections in Figures 2–4 for shotpoints 12–17 and for the fixed geophone G4. The distance range extends from 0.4 km–0.9 km and the time range runs from 0 s (shot break) to 14 s.

A compressional wave velocity of $1{,}670 \pm 70\ \mathrm{ms}^{-1}$ was determined for most of the sections. As a result of several investigations we know that the compressional wave velocity for moist sand lies in the range of $1{,}600\ \mathrm{ms}^{-1}$ to $2{,}000\ \mathrm{ms}^{-1}$ (Schirmer et al. 1979).

The wave designated by $480\ \mathrm{ms}^{-1}$ is a refracted wave from a lower boundary layer. The portion comprising surface waves is well separated from these refraction events even for small offsets.

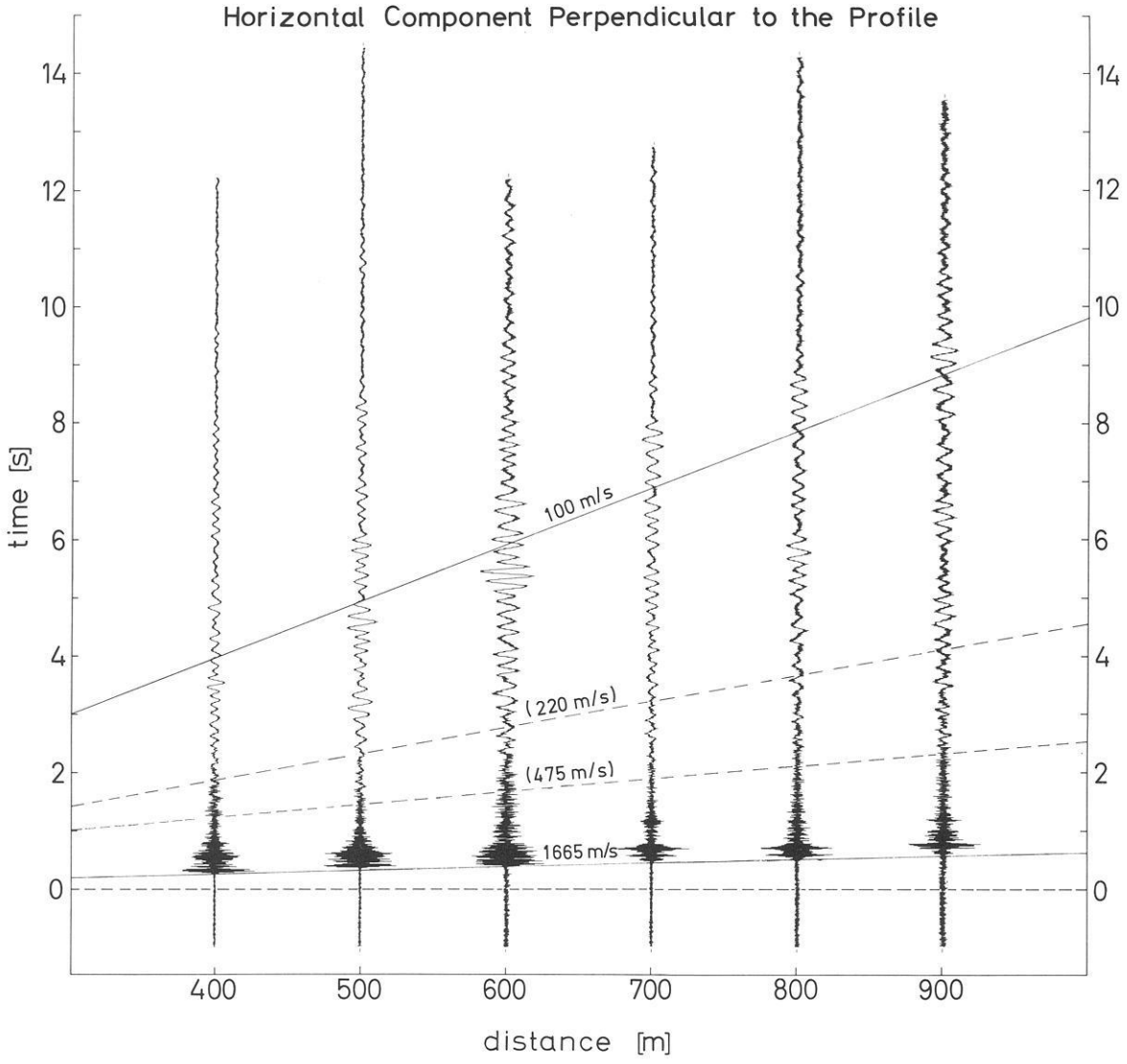

Fig. 4. Seismic section (shot points) 12–17) for the fixed geophone G4, component perpendicular to profile (Y)

Two velocities result from the many sections:

I: $100 \pm 10\ \mathrm{ms}^{-1}$

II: $230 \pm 20\ \mathrm{ms}^{-1}$.

Both are characteristic of the surface waves which were sought, i.e. the velocities of these surface waves are very low. Particle motions (hodographs) derived from the seismograms were computed. The following examples are shown:

I: for waves associated with a velocity of $100\ \mathrm{ms}^{-1}$ (Fig. 6)

II: for waves associated with a velocity of $230\ \mathrm{ms}^{-1}$ (Fig. 7),

each presented in the $X-Z$, $Y-Z$ and $X-Y$ planes. Figure 5 shows the respective seismograms. The particle motion is polarized in the $X-Z$ plane. The smoothness of the curve is attributed to the fact that the high-frequency portion of the spectrum is suppressed in the particle motion diagrams. By means of the hodographs, it was determined that both waves are of the Rayleigh type. The axial ratio amounted to:

I: $X/Z = 0.5 \pm 0.1$ (spread 0.33–0.65)
for waves associated with the velocity of $100\ \mathrm{ms}^{-1}$

II: $X/Z = 2.3 \pm 0.3$ (spread 1.7–2.6)
for waves associated with the velocity of $230\ \mathrm{ms}^{-1}$.

The first case (I) of surface waves involves an ellipse which is circumscribed clockwise, the second case (II) an ellipse which is circumscribed counter-clockwise.

Dispersion Analysis

The multiple filter technique is an efficient method of analyzing multi-mode dispersed signals. In this paper we follow the method of Dziewonski et al. (1969). The individual seismograms are filtered by a narrow bandpass at different center frequencies. This procedure is carried out by multiplying the Fourier-transformed time series with a Gaussian function. From the windowed spectrum the filtered in-phase and in-quadrature seismograms are obtained by inverse Fourier transformation. These

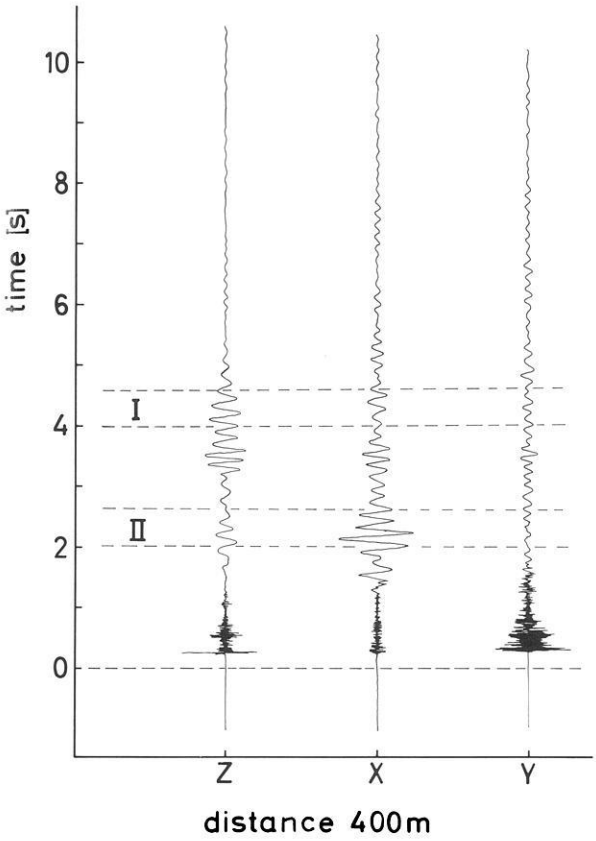

Fig. 5. Time series of seismograms in three components (Z vertical, X in direction of profile, Y perpendicular to profile) for a distance of 400 m between shot point and geophone. Particle motions were computed for sections I and II (Figs. 6 and 7)

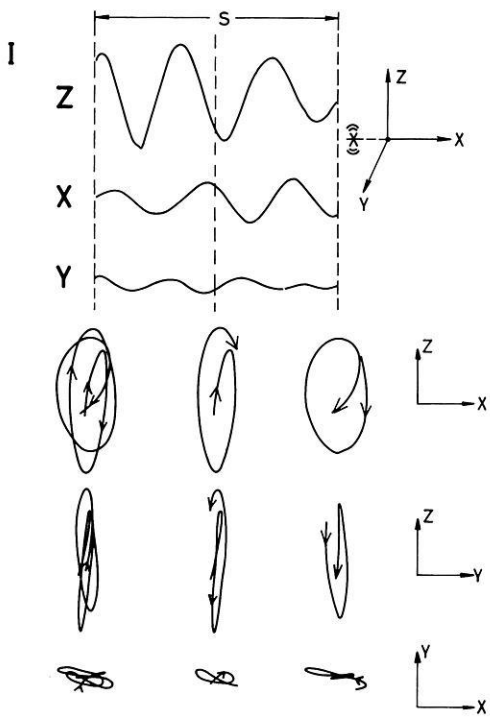

Fig. 6. Particle motion for the associated velocity of 100 ms^{-1} (Z vertical, X in direction of profile, Y perpendicular to profile, S section of seismogram in time domain, section I of Fig. 5)

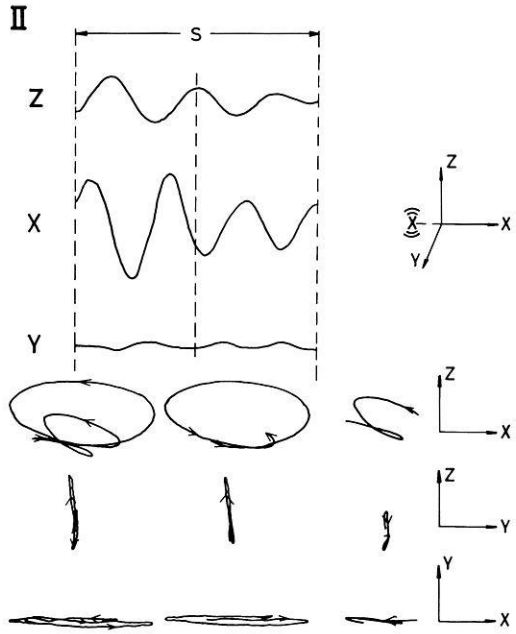

Fig. 7. Particle motion for the associated velocity of 230 ms^{-1} (Z vertical, X in direction of profile, Y perpendicular to profile, S section of seismogram in time domain, section II of Fig. 5)

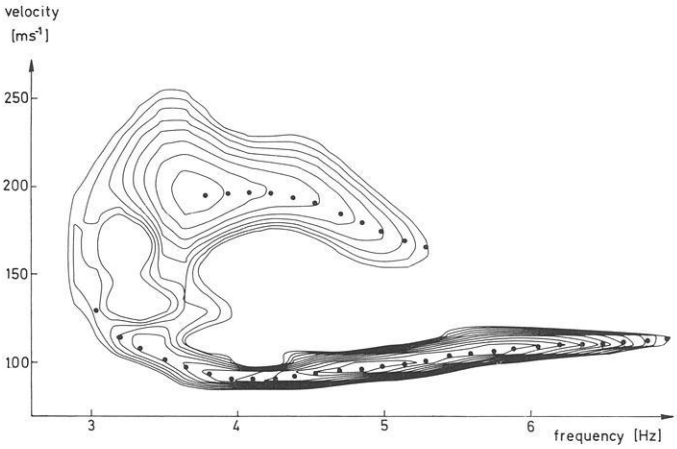

Fig. 8. Contours of the instaneous amplitude from the vertical component of particle velocity at 900 m distance, Fig. 2. The contours are drawn at 1 dB intervals, and the dots refer to the maxima of the amplitudes at the chosen center frequencies. Window function, (Dziewonski et al., 1969):

$$H(\omega,\omega_i)=\begin{cases}\exp\left(-100\left(\dfrac{\omega-\omega_i}{\omega_i}\right)^2\right) & \text{for } 0.8\cdot\omega_i\leqq\omega\leqq1.2\cdot\omega_i\\ 0 & \text{else}\end{cases}$$

time series yield the instantaneous amplitudes and phases as a function of time or propagation velocity. It may be shown that the maxima of the instantaneous amplitudes propagate approximately with the group velocity.

Figure 8 shows the contoured instantaneous amplitude as a function of frequency and group velocity from the vertical velocity component of geophone G4 at 900 m distance (Fig. 2).

Table 1. Axial ratios (ε) and phase differences ($\Delta\Phi$) of horizontal and vertical components of particle velocity, as derived from the filtered seismograms of Figs. 8 and 9

Center frequency {Hz}	1st mode		2nd mode	
	ε	$\Delta\Phi$	ε	$\Delta\Phi$
3.80	–	–	1.0	98°
3.95	–	–	1.3	105°
4.10	–	–	1.8	110°
4.25	–	–	2.1	113°
4.40	–	–	2.2	114°
4.55	0.35	−86°	2.3	113°
4.70	0.35	−89°	2.1	107°
4.85	0.35	−93°	2.1	100°
5.00	0.40	−95°	2.1	102°
5.15	–	–	2.1	110°

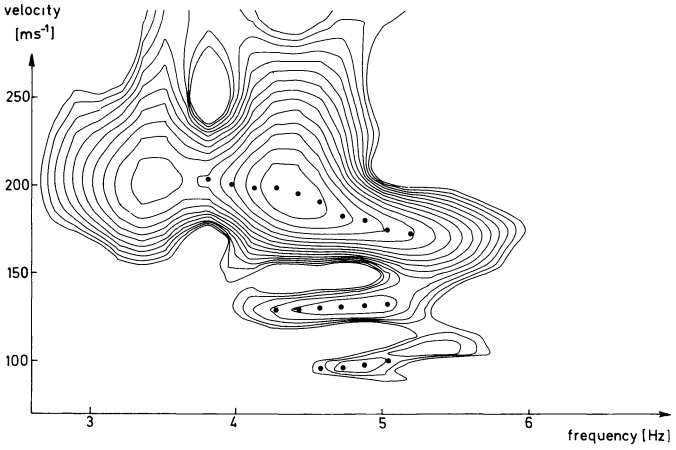

Fig. 9. Contours of the instantaneous amplitude from the in-line horizontal component of particle velocity at 900 m distance, Fig. 3. The contours are drawn at 1 dB intervals, and the dots refer to the maxima of the amplitudes at the chosen center frequencies. Window function: same as Fig. 8

The contours are drawn at 1 dB intervals, and the dots refer to the maxima of the filtered wave-group envelopes at the chosen center frequencies. As a result, it may be stated that there are at least two different modes of Rayleigh type. The analysis of further vertical velocity components at different distances and from other geophones yields similar contours. The resolution is not always as good, but the observed group velocities are the same, to within about 10%. This spread is the same as was obtained from the seismic sections (see previous section) and may be caused by the inhomogeneity of the sea floor.

The analysis of the velocity component parallel to the profile yields good agreement with respect to the (higher-velocity) 2nd mode, but the 1st mode can be observed only in the narrow frequency range 4.5–5.0 Hz (Fig. 9).

In Table 1 the axial ratios of horizontal and vertical amplitudes as well as the phase differences of the two components are presented for those frequencies where wave groups in both components are observed. A phase difference $\Delta\Phi$ of $-90°$ corresponds to clockwise and of 90° to counter-clockwise rotation (see next section). Thus, the results are in good agreement with the hodographs of the previous Chapter.

Figure 9 shows a third wave group which is found in the velocity component perpendicular to the profile. These waves may correspond to Love modes. Again, inhomogeneity of the sea floor might be responsible for Love-wave components parallel to the profile. A unique resolution of Love modes is not possible with our data. The main reason is the low energy of the velocity component perpendicular to the profile, which also seems to be influenced by the Rayleigh modes.

Model Calculations

The aim of this chapter is to find a model of shear-wave velocities in the sedimentary sea floor which allows the propagation of waves with the observed properties. These can be summarized as follows: the low-velocity part of the observed seismograms shows two different wave groups which propagate with velocities of about 100 and 230 ms^{-1} and which are both of Rayleigh type, and the group velocities as well as the axial ratios of the particle motion have been obtained by dispersion analysis for a number of frequencies within the range 3.2–6.8 Hz. Furthermore it is known from borings that the thickness of the holocene layer is between 15 and 20 m at the experimental site. Thus, a discontinuous change of sedimentary parameters may be expected at this depth which is small compared with the horizontal propagation ranges of 100 to 2,500 m. For this reason the observed wave groups may be interpreted as trapped modes within the uppermost sedimentary layer. This assumption is in accordance with the observed dispersion, i.e., the frequency dependence of group velocity.

Considering a fixed position of the geophone at the water-sediment interface the Rayleigh-type modes may be described by,

$$u = \int_0^{\infty} \sum_{n=1}^{N(\omega)} G_n(\omega)\,\varepsilon_n(\omega)\cos\left\{\omega t - \phi_n(\omega) + \frac{\pi}{2}\right\} d\omega$$
$$w = \int_0^{\infty} \sum_{n=1}^{N(\omega)} G_n(\omega)\cos\{\omega t - \phi_n(\omega)\}\, d\omega \qquad (1)$$

with,

(u, w) = particle velocity, in-line horizontal component and vertical component, respectively
$G_n(\omega)$ = mode amplitudes
$\phi_n(\omega)$ = mode phases
$\varepsilon_n(\omega)$ = axial ratios of horizontal to vertical mode amplitudes

In our description we assumed the z-axis pointing upwards, so that a negative ε_n corresponds to an ellipse which is circumscribed clockwise. For comparison with Table 1, a difference of $-\pi/2$ or $\pi/2$ between horizontal and vertical phase means clockwise or counter-clockwise rotation, respectively.

The experimental results presented show waves, as described by Eq. (1), propagating along the water-sediment interface. From theoretical investigations it is known that such waves exist only for a non-zero shear-wave velocity in the sedimentary sea floor. As consequence of the measurements it can be assumed that the shear-wave velocity is smaller than the sound velocity in water, i.e.,

$$0 < \beta_s < \alpha_w < \alpha_s \qquad (2)$$

with,

α_w = sound velocity in water
β_s = shear-wave velocity in the sedimentary sea floor
α_s = compressional-wave velocity in the sedimentary sea floor

Considering a sea-floor model of a certain number of homogeneous layers of constant depth the group velocity may be determined theoretically as function of frequency. The simplest model which allows the propagation of interface waves consists of a water layer of constant depth overlying a homogeneous sedimentary halfspace. In this case the dispersion relation in accordance with Eq. (2) becomes,

$$\rho_w c^4 \gamma_s \tanh\left(\frac{\omega}{c}\gamma_w h\right) = \rho_s \beta_s^4 \gamma_w (4\gamma_s \hat{\gamma}_s - (1-\hat{\gamma}_s^2)^2) \qquad (3)$$

with,

$$\gamma_{w,s} = \left(1 - \left(\frac{c}{\alpha_{w,s}}\right)^2\right)^{\frac{1}{2}}, \quad \hat{\gamma}_s = \left(1 - \left(\frac{c}{\beta_s}\right)^2\right)^{\frac{1}{2}}$$

and,

h = water depth
$\rho_{w,s}$ = density of water and sediment, respectively
$\frac{\omega}{2\pi}$ = frequency
c = phase velocity

In the two limiting cases,

$\tanh\left(\frac{\omega}{c}\gamma_w h\right) = 0$ (no water coverage, Rayleigh waves)

$\tanh\left(\frac{\omega}{c}\gamma_w h\right) = 1$ (high water coverage, Scholte waves),

there is no dispersion, i.e., the phase velocity does not depend on frequency. Between these cases, where wavelength and water depth are of the same order of magnitude, the phase velocity depends on frequency. But computations show that this dispersion is weak. It turns out that even for more complicated sea-floor models, the influence of the water layer is of less importance. In the case of phase velocities which are small compared to that of sound in water ($c \ll \alpha_w$) the phase velocity is nearly independent of α_w and α_s. This result also holds for more complicated models.

In disagreement with our experimental results, the simple 1-layer sea-floor model allows the propagation of one mode only. This problem can be overcome by assuming the shear-wave velocity to increase with depth. Considering a number of discrete layers the well-known Thomson-Haskell matrix formalism can be applied in order to compute the dispersion relation, as in Schwab and Knopoff (1972). It should be noted that the conditions of Eq. (1) are different from usual seismic conditions where shear-wave velocities (of rocks) exceed the sound velocity of water.

First computations were carried out with a 2-layer sea-floor model covered by an additional water layer. As already mentioned the depth of the water layer as well as the compressional velocities of water and sediment have little influence on the group velocities. The same applies to the densities, within the reasonable limits known from experience. Thus, there are only three free parameters in our model: depth of the first sedimentary layer (the second one is a halfspace), and the shear-wave velocities in the two layers.

A lower limit to the layer depth is determined by the cutoff frequency of the second mode which should not be higher than 3.8 Hz (Fig. 8). In order to find a good fit to the observed group-velocities as a function of frequency, the so-called Hedgehog method is applied. The three free parameters are varied within the following ranges:

layer depth (1st layer): 15 m–20 m
shear-wave velocity (1st layer): 80 ms^{-1}–150 ms^{-1}
shear-wave velocity (2nd layer): 240 ms^{-1}–280 ms^{-1}

The theoretical group velocities are compared with the observed ones by means of a least-squares fit, where the observed values are represented by the dots in Fig. 8,

$$\sum_{\omega_i} \left(\frac{v_T - v_E}{v_T}\right)^2 = \min \qquad (4)$$

with,

v_T = theoretical group velocities } at the frequencies ω_i
v_E = observed group velocities } as defined by Fig. 8.

In this sum the group velocities of both modes are included. Due to the consideration of relative errors, higher absolute deviations are allowed for the (faster) second mode as compared to the first mode. This is in accordance with our observations which yield approximately the same percentage spread for the two mode velocities.

It turns out that there is only one well-defined minimum within the parameter ranges considered. The resolution of our method is 0.5 m with respect to the layer depth and 5 ms^{-1} with respect to the shear-wave velocities. Figure 10 shows the result of this group-velocity fit and also the corresponding axial ratios of horizontal and vertical amplitude. The corresponding model parameters are given in Table 2. Positive ω are related to counter-clockwise rotation and negative ω to clockwise rotation

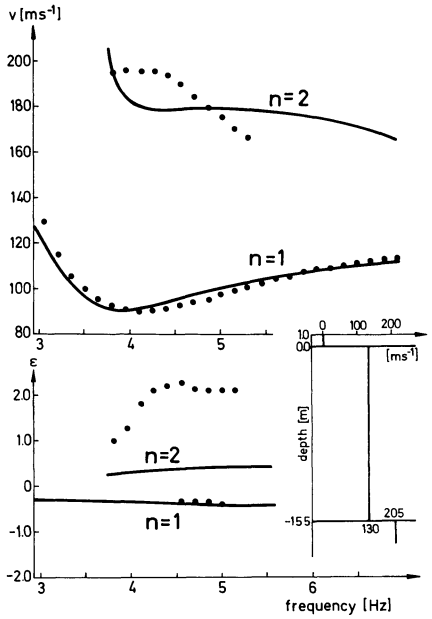

Fig. 10. Theoretical determination of group velocities (v) and axial ratios of horizontal and vertical amplitude (ε) for a two-layer sea-floor model. The dots refer to the observed values as presented in Fig. 8 and Table 1, respectively. Model parameters are given in Table 2

Table 2. Parameters of best-fit 2-layer model

Model parameters	h[m]	ρ[gcm^{-3}]	α[ms^{-1}]	β[ms^{-1}]
Covering water layer	1	1	1,500	0
1st sedimentary layer	15.5	1.8	1,700	130
2nd sedimentary layer	∞	1.9	1,800	205

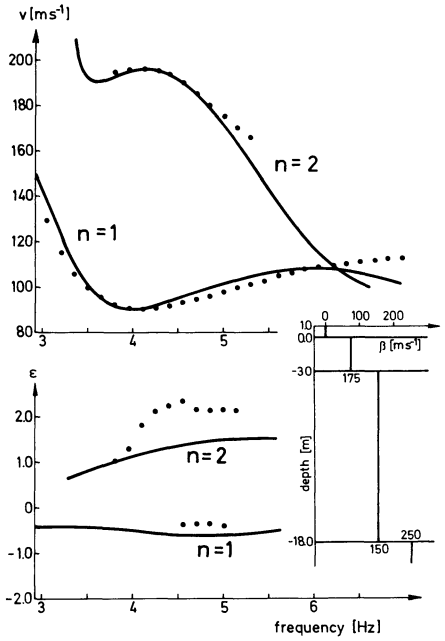

Fig. 11. Theoretical determination of group velocities (v) and axial ratios of horizontal and vertical amplitude (ε) for a 3-layer sea-floor model. The dots refer to the observed values as presented in Fig. 8 and Table 1, respectively. Model parameters are given in Table 3

Table 3. Parameters of best-fit 3-layer model

Model parameters	h[m]	ρ[gcm ^{3}]	α[ms^{-1}]	β[ms^{-1}]
Covering water layer	1	1	1,500	0
1st sedimentary layer	3	1.8	1,700	75
2nd sedimentary layer	15	1.8	1,700	150
3rd sedimentary layer	∞	1.9	1,800	250

(see Eq. (1)). The agreement of computed and observed group velocities is good for the first mode but not satisfactory for the second mode. The same applies to the particle motion where the direction of rotation as well as the axial ratios for the first mode are well-predicted by theory, but the axial ratios differ considerably for the second mode. Numerical tests show that this discrepancy cannot be overcome within the 2-layer sea-floor model. Thus it is necessary to modify the model.

One possibility is to introduce a gradient in the shear-wave velocity in the first layer, which requires only one more model parameter. But a number of numerical experiments did not yield satisfactory results. For this reason a 3-layer model is investigated, which requires two additional model parameters as compared to the 2-layer model.

Equation (4) is used for the 3-layer model also, in order to obtain an optimal fit to group velocities. It turns out that the discrepancy in second-mode axial ratios may be reduced by considering a near-surface layer of lower shear-wave velocity. In this model the agreement of first-mode group velocities may be maintained and improved for second-mode group velocities. Figure 11 and Table 3 show the best fitting model. Still the agreement of computed and observed axial ratios is not optimal, especially with respect to the second mode. But this deviation might be explained by the several shortcomings of the experiment, and it is not meaningful to investigate more sophisticated models. First of all the sea floor is not homogeneous, and while the group velocity is a mean value with respect to the whole propagation range the particle motion is influenced mainly by the local constitution of the sea floor. Furthermore variation in the quality of coupling for the different geophone components in the sediment may produce errors in the measured axial ratios.

Conclusions

Comparison of the experimental results with model calculations shows satisfactory agreement. By means of a relatively simple model, consisting of three homogeneous layers within the sea floor, we are able to interpret the propagation velocities and axial ratios of particle motion including the direction of circumscription of the ellipses. This is a surprising result because the upper layers of the sea floor are usually not at all homogeneous. Borings and sea floor probes in the North Sea show quite large variations of physical parameters such as compressional wave velocity and density. Also our seismic measurements yield different velocities at different ranges within the same area. For this reason the model presented describes only a vertically and horizontally averaged shear-wave velocity profile.

The values from 75 ms^{-1} to 250 ms^{-1} in the region of the uppermost 20 m yield ratios of compressional- to shear-wave velocity in the range from 21 to 6.5, which agree well with the measurements of Hamilton et al. (1970). Our model also compares well with the depth dependence of shear-wave velocities as reviewed by Hamilton (1976). Our result is of interest with respect to underwater acoustics as shear-wave velocities of 250 ms^{-1} may contribute considerably to low-frequency sound attenuation in shallow water (Essen, 1977).

Acknowledgements. The authors are indebted to the Erprobungsstelle E71 der Bundeswehr for their help during the measurements. We also thank Professor Behle for helpful discussions and Dr. Barkhausen who made the bore-hole data available to us. The work was supported by the Sonderforschungsbereich 94, the Bundesminister für Verteidigung and the Bundesminister für Forschung und Technologie.

References

Cagniard, L.: Reflection and refraction of progressive seismic waves, pp. 244–246. New York: McGraw-Hill 1962

Dziewonski, A., Bloch, S., Landisman, M.. A technique for the analysis of transient seismic signals, Bull. Seismol. Soc. Am. **59**, 427–444, 1969

Essen, H.-H.: Attenuation coefficients of acoustic normal modes in shallow water. J. Geophys. **43**, 569–580, 1977

Hamilton, E.L.: Shear-wave velocity versus depth in marine sediments: a review. Geophysics **41**, 985–996, 1976

Hamilton, E.L.: Bucker, H.P., Keir, D.L., Whitney, J.A.: Velocities of compressional and shear waves in marine sediments determined in situ from a research submersible. J. Geophys. Res. **75**, 4039–4049, 1970

Hawker, K.E.: The existence of Stoneley waves as a loss mechanism in plane wave reflection problems. J. Acoust. Soc. Am. **65**, 682–686, 1979

Schirmer, F., Schmalfeldt, B., Siebert, J.: Schallgeschwindigkeit und Impedanz des oberen Meeresbodens in Gebieten der Nordsee, des Skagerraks, des Kattegatts und der Ostsee. Dt. hydrogr. Z. **32**, 279–288, 1979

Schwab, F.A., Knopoff, L.: Fast surface wave and free mode computations, In: Methods of computational physics, **11**, 87–180. New York, London: Academic Press 1972

Received June 11, 1979; Revised Version August 19, 1980
Accepted September 10, 1980

J Geophys (1981) 49:123–127

Journal of Geophysics

Simultaneous Observation of an Intense 65 keV Field-Aligned Proton Beam and ULF-Waves During a Break-up Event

W. Stüdemann and C.K. Goertz

Max-Planck-Institut für Aeronomie, D-3411 Katlenburg-Lindau 3, Federal Republic of Germany

Abstract. Measurements of nearly mono-energetic 65 keV protons above active auroral forms were obtained on a rocket flight from Andenes (Norway) on 13 October 1977. Analysis of the pitch angle distribution of the >30 keV protons and the azimuthal anisotropy of the proton fluxes support a model of a proton beam of finite spatial extent. The particle observations occur simultaneously with ULF-waves in the frequency range 0.5–5 Hz. The particle distribution function is unstable and causes an amplification of obliquely propagating Alfvén waves. We argue that the waves are amplified by resonant interaction with the proton beam.

Key words: Particle acceleration – Monoenergetic ions – ULF waves – Wave-particle interaction – Break-up phase – Magnetospheric substorm

Introduction

The energization of plasmas occuring over auroral arcs is of great current interest and importance. This region is known to display the characteristic signatures of field-aligned acceleration of charged particles, which comprise an important part of the auroral current system. The mechanism of acceleration is still controversial simply because there are not enough measurements available to permit us to assess the role of any of the suggested mechanisms in a quantitative fashion. It is now believed that acceleration takes place at altitudes in the range ~1–3 earth radii (R_E), i.e., in regions not covered by rocket campaigns (Shawhan et al. 1978). Measurements made from rockets can detect (cheaply) the signatures of such acceleration mechanisms and thus provide crucial information for assessing the importance of particle energization.

In this note we report an especially spectacular case of ion acceleration which occured during a substorm on 13 October 1977 near auroral arcs. The case reported here is unusual in at least two ways. Firstly, the ions were found to be accelerated downwards along the magnetic field and secondly, the energy of the accelerated ions was of the order of 65 keV.

It has become customary to associate field aligned charged particle beams with acceleration by electrostatic fields parallel to the magnetic field. Such fields may exist along wirth others in double layers or regions of anomalous resistivity. However, the case reported here of field aligned 65 keV ions cannot be explained by electrostatic fields because electrons were not affected, quite apart from the rather extreme value of 65 kV for a field-aligned electrostatic potential. Neither can other mechanisms such as enhanced particle precicipation by pitch angle scattering, ion-cyclotron heating or betatron acceleration across field lines explain the observations.

In addition to its spectactular nature and rather puzzling features the event is characterised by a close temporal association of the ion beam with large amplitude ULF waves. The waves are most likely to be Alfvén waves confined to a narrow region in space. Such waves are in fact "kinetic Alfvén waves" (Hasegawa 1977) which can interact reasonantly with charged particles. We believe that our measurements are the first evidence from space for such a resonant interaction. Our understanding of this process is far from complete. Nevertheless, the process is significant and may play an important role in the magnetosphere-ionosphere coupling (Goertz and Boswell 1979).

Instrumentation

Basically, the instrument consists of a solid-state detector measuring electrons and a solid-state detector telescope for ions with charge $Z \geqq 1$, using a permanent magnetic field to separate the electrons and the ions. Details of the instrument and the calibration procedures are described elsewhere (Stüdemann and Winterhoff in press 1980). The energy ranges covered are 15–200 keV for electrons and 20–300 keV for protons. The energy resolution was set to 8 keV for the 7 lower energy channels and increased logarithmically above 80 keV. The system resolution of the detector-amplifier combination was 7 keV full width at half maximum. The geometric factors for isotropic particle fluxes are $2 \cdot 10^{-4}$ cm^2 sr for electrons and $5 \cdot 10^{-4}$ cm^2 sr for protons.

The data presented in this paper are taken from two identical sensor systems which measure at a pitch angle of about 20° and in the range 60°–100° due to built-in angles of 5° and 80° with respect to the rocket's spin axis and a nominal attitude of 20° between the spin axis and the geomagnetic field direction. The attitude was actively controlled by means of a gyro-based attitude control system and the actual pitch angle for each measurement was derived from the on-board magnetometer.

Observations

The payload F3A was launched on 13 October 1977 during a magnetospheric substorm which commenced at 20:22 UT and continued in several stages until 23:30 UT The substorm occurred during a period of low-level geomagnetic disturbance with Kp = 3−. During the substorm the disturbance in the X-com-

0340-062X/81/0049/0123/$01.00

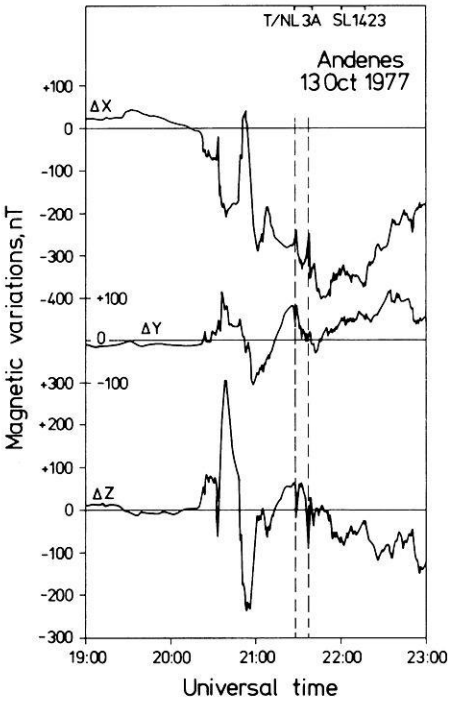

Fig. 1. Magnetometer recording at Andenes. The *dashed lines* mark the flight time of the payload F3A

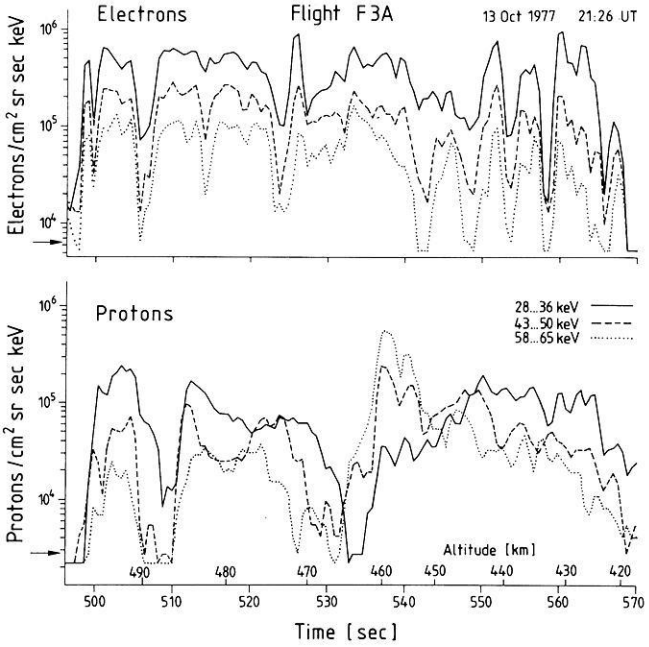

Fig. 2. Measurements of electron fluxes (*upper part*) and proton fluxes (*lower part*) at various energies for particles having pitch angles of about 20°. The *arrows* on the vertical axis mark the fluxes equivalent to one count per sampling interval. Energy passbands specified are the same for electrons and protons

ponent reached a maximum of 400 nT. Figure 1 is a magnetometer recording taken at the launch site in Andenes, Norway (McIllwain parameter $L=6.2$). Prior to the flight of F3A auroral activity was concentrated in a faint homogeneous arc with a sharp northern edge moving slowly to the south. The rocket was launched at 21:26 UT simultaneously with an intensification of the arc, a further decrease in the X-component and an increase in the micropulsation activity. During the first part of the flight the rocket crossed the bright arc with a maximum intensity of 50 kR in the 5,577 Å oxygen line approximately 120 s after launch. It reached the sharp northern edge at about 240 s flight time. At about 21:31 UT (300 s after launch) auroral break-up took place with rapid expansion of the aurora to the north.

The observations discussed in this paper were taken in the time interval 490–570 s flight time when the rocket was magnetically above a region of active discrete auroral luminosity of more than 20 kR for the 5,577 Å oxygen line. Figure 2 presents the measured electron and proton fluxes at different energies for this time interval. The data are taken from the sensor system which is directed nearly parallel to the rocket's spin axis and accepts particles having pitch angles around 20°. The arrows on the vertical axis mark a count rate of 1 count per sampling interval (0.1 s). The energy spectra of the protons normally follow a power law. Following the increase of the count-rates at about 534 s (altitude 460 km) the energy spectrum shows a well pronounced maximum near 65 keV energy. After 542 s the spectral curve starts to return to its original power law form. Figure 3 displays the peaked energy spectra for both sensors. The vertical bars represent the statistical uncertainties and the horizontal bars give the width of the energy passbands.

In Figure 4 the nature of the mono-energetic peak is investigated further by combining the measurements from two additional proton instruments on the same payload (courtesy of Schmidtke and Urban). The left-hand side of Fig. 4 is an exam-

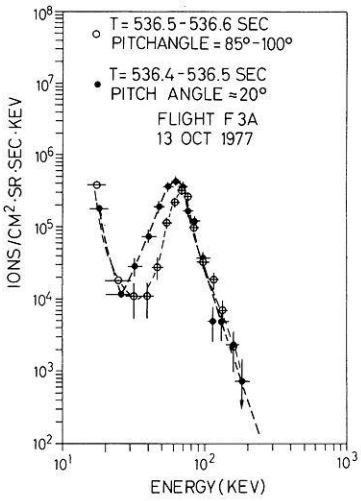

Fig. 3. Example out of a series of peaked ion energy spectra during flight F3A with data from two 100 ms sampling intervals. The energy axis of all ion measurements in this paper refers to the energy deposited in the sensitive volume of the solid state detector. In the case of protons a small correction term of a few keV must be added due to the energy loss in the dead layer of the solid state detector (>15 μg/cm², Al-contact)

ple of the normal power-law energy spectrum well before the observation of the mono-energetic peak. Nearly the same spectrum is again measured after the event at about 550 s. The measurements shown on the right-hand side of Fig. 4 are taken at the time when the peak was most pronounced. All measurements contained in Fig. 4 cover the pitch angle range 85°–100°. The figure demonstrates that all instruments agree very well where their energy ranges overlap giving high confidence to the

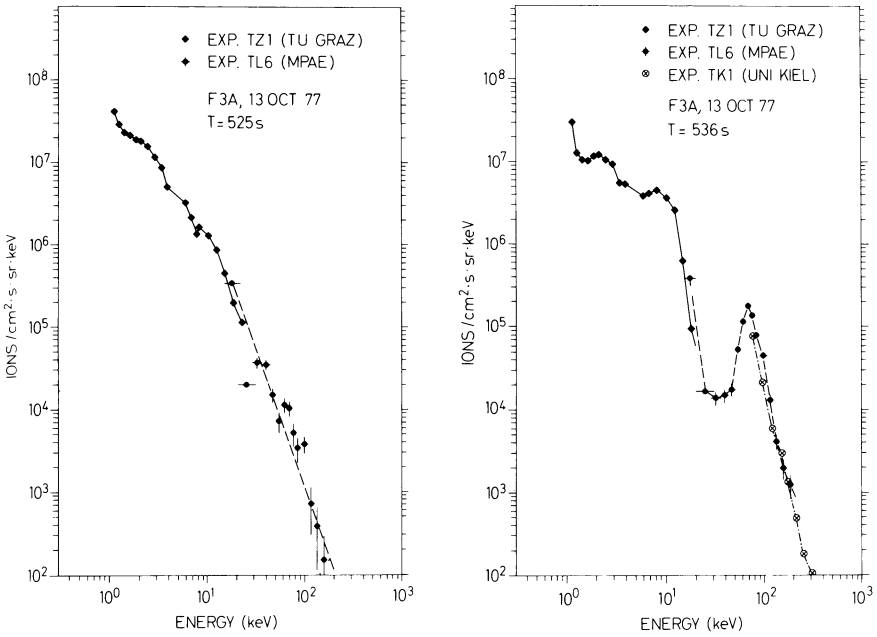

Fig. 4. Composition of energy spectra of all instruments sensitive to positive ions on the same rocket flight prior to the observation of the energy peak (*left side*) and during the event (*right side*). (Courtesy of Urban, University Graz, and Schmidtke, University Kiel)

observation of the mono-energetic proton peak. At the same time the pitch angle distributions measured for protons above 30 keV energy change from a normal distribution to a field-aligned pitch angle distribution. This transition can be seen in Fig. 5. Each panel contains data for half a spin rotation from both sensor systems. Fluxes at pitch angles above $\approx 70°$ stay nearly constant whereas the flux of precipitated protons increases.

Even at the highest time resolution of the spectral proton data we cannot detect any velocity dispersion in the data during the time interval 535–545 s. In contrast, such dispersion is clearly visible at the end of the previous burst (527–532 s, Fig. 2). We condude that the intensity variations following 532 s either originate from modulations in a region close to the point of observation or are the effect of spatial gradients in particle densitites. The first alternative seems unlikely because the electrons are not dramatically affected at this time, thus precluding any process involving static electric fields. The existence of a gradient in the proton density is supported by their azimuthal anisotropy. In Fig. 6 the upper curves represent the count-rates of the 80° sensor (60°–100° pitch angle) at times when the sensor is looking eastward (crosses) and westward (dots) at the same pitch angle of 80°. From these curves an anisotropy factor A is calculated defined as the ratio between the difference in fluxes seen from the east and the west and the sum of both (Fig. 6, upper middle part). This anisotropy could be caused either by $E \times B$-drift (E is electric field, B magnetic) or by density gradients. Using measured values for the perpendicular electric field of ~ 100 mV/m (Grabowsky, private communication) and the magnetic field of ~ 40.000 nT the $E \times B$ drift velocity is of the order of 1 km/s and far too small to account for the observed azimuthal anisotropy. Thus the anisotropy is interpreted as beeing due to a density gradient in the north-south direction (higher fluxes in the south, $A > 0$). The curves in the lower middle part of Fig. 6 show the flux of the precipitating proton beam with the highest time resolution obtainable for reference. During the steep increase at 536 s and, even more pronounced, during the decreases following 538 s and 541 s A becomes large. Our interpretation is as follows: The north-going rocket is overtaken

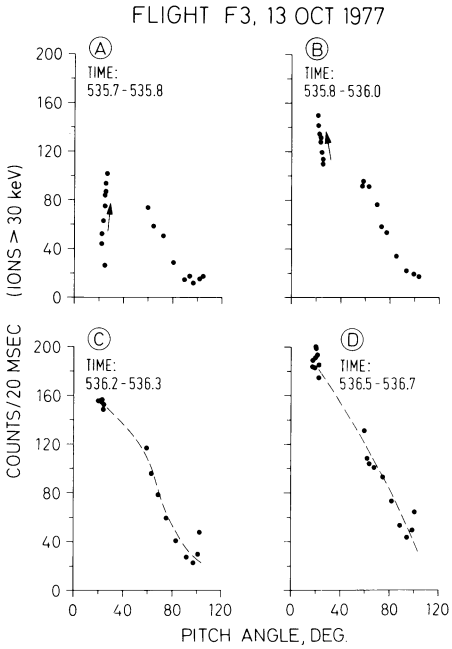

Fig. 5. Pitch angle distribution of protons above 30 keV showing the transition from a normal distribution prior to 535 s to a well pronounced field-aligned distribution. For further details see text

by a northwardly expanding region of higher proton precipitation at ≈ 536 s. As soon as its northern edge reaches the position of the rocket the anisotropy factor A drops to zero and becomes slightly negative. At this time the rocket is inside the region of enhanced proton precipitation with some indication that the tendency for A to become negative is caused by the approach to the southern edge of this narrow region. Thus the north-south extension, d, of the region is estimated to be of the order of 5 km. The northward movement slows down at 538 s and the rocket again leaves the region of high proton precipitation through its northern boundary (A positive again).

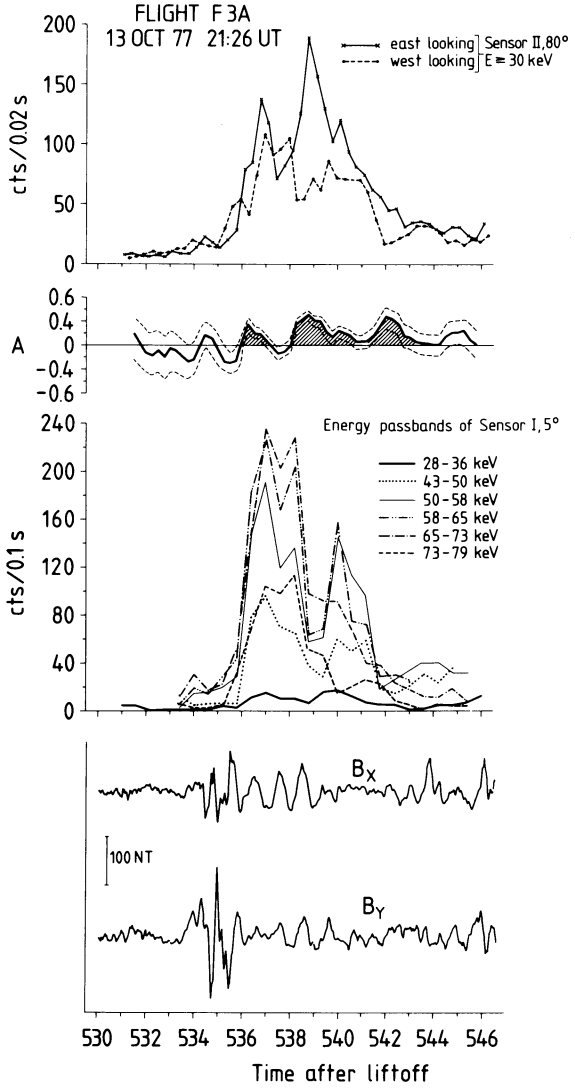

Fig. 6. Comparison between proton data with highest time resolution (0.02 s) available and measurements from the magnetometer (taken from Klöcker and Theile 1979, Fig. 2) for the time of observation of the peaked energy spectrum. Upper part: count-rates of the nearly perpendicular directed sensor in two azimuthal directions 180° apart for 80° pitch angle particles. *Upper middle part:* anisotropy factor A (defined in text) derived from the above curves. *Lower middle part:* count-rates of precipitated protons for different energies. *Lower part:* magnetic field variations (B_x = north, B_y = east components of the earth's magnetic field vector) after high pass filtering with a cut-off at 0.65 Hz

From these observations we deduce that the rocket enters, for a short time, a narrow region in which a mono-energetic proton beam of 65 keV with a field-aligned pitch angle distribution exists. The width of this region is estimated to be of the order of a few km. During the time when the rocket is close to or stays in this region the magnetometer detects ULF waves with a frequency of a few Hz and an amplitude of ≈ 100 nT (Klöcker and Theile 1979). For comparsion the B_x and B_y components of the magnetic field are reproduced in the lower part of Fig. 6.

Discussion

The remarkable temporal (and by implication spatial) association of the field aligned-ion beam and the ULF wave activity

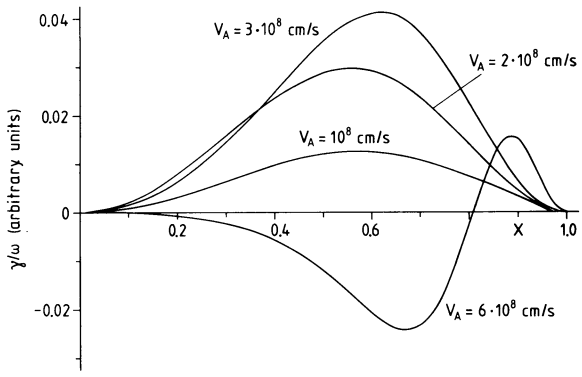

Fig. 7. Calculated growth rates, γ/ω, as a function of $x = (\omega/\omega_0) \cdot \tan\Theta$ for different values of the Alfvén velocity V_A according to the equation given in the text. The velocity V of the protons in the beam are taken to be equivalent to 65 keV, the thermal width V_0 of the beam is taken to be equivalent to 10 keV. For $V_A = 3 \cdot 10^8$ cm/s the Alfvén velocity is about equal to the particle velocity

suggests a physical connection between the two in the sense that either the waves produce the beam (by non-linear trapping) or that the beam produces the waves (by amplification). The energy flux in the beam $P_b = 8.2$ erg/cm$^2 \cdot$ s is about equal to the energy flux in the waves. P_w:

$$P_w = \frac{b^2}{8\pi} V_g \simeq \frac{b^2}{8\pi} V_A = 11.9 \text{ erg/cm}^2 \cdot \text{s}$$

b = perturbation of magn. field

where we have assumed that the group velocity of the ULF waves (V_g) is of the order of the Alfvén speed (V_A). Thus from an energetics point of view it is not clear which way the energy is flowing: from particles to waves or vice-versa. However, the ion-distribution function shows a well defined peak at 65 keV (not only the flux) and it is quite unlikely that such a distribution can be produced by particle trapping. On the other hand such a distribution is unstable and could give rise to a growth of obliquely propagating Alfvén waves (Fejer and Kan 1968). The resonant growth rate γ of a wave with frequency $f = \omega/2\pi$ and wave vector $\mathbf{k} = (k_\parallel, k_\perp)$ for an ion-beam of velocity $V = v V_A$ along the magnetic field and thermal width $V_0 = v_0 V_A$ is given by Fejer and Kan as

$$\gamma/\omega = -\pi^{1/2} \frac{m_e}{m_i} \frac{N_b}{N_o} X^2 (1 - X^2)((1 - X^2)^{1/2} - v) \exp\left| - \left(\frac{(1 - X^2)^{1/2} - v}{v_0}\right)\right|$$

where m_e and m_i are the electron and ion masses, $X = \omega \tan\Theta/\omega_0$, $\tan\Theta = k_\perp/k_\parallel$, N_b is the density of the beam and N_o is the background plasma density. $\omega_0 = (\Omega_i \Omega_e)^{1/2}$ is the lower hybrid frequency. This relation holds for a cold plasma (electron thermal velocity less than the Alfvén velocity). In Fig. 7 we show the calculated growth rates as a function of X for different values of V_A. We do not know the exact value of the Alfvén velocity because the average ion mass is not known. The measured plasma density at the rocket is 2×10^4 cm^{-3}. For a hydrogen plasma V_A is 6,800 km/s, and for an average ion mass of four atomic masses V_A is 3,400 km/s. We see that generally the maximum growth rate occurs at $X \approx 0.6$. Since locally $\omega_0 = 9 \cdot 10^4$ Hz a frequency of 2 Hz is only appreciably amplified for nearly perpendicular propagation ($\tan\Theta \gg 1$). Furthermore the path length for the wave-particle interaction must be long

enough because the growth rates are small due to a ratio $N_b/N_o \approx 10^{-4}$. However, the waves may have been amplified further up the field line where ω_0 is less and N_b/N_o is larger. Nevertheless, an infinitely extended beam (perpendicular to the magnetic field) will in general amplify higher frequencies than are observed.

Waves which do not propagate in the finite sized beam for long enough, i.e., waves not guided exactly along the field, will be amplified less along their ray-path even though the local amplification rate in the beam could be larger. As we have argued above, the beam has a finite width ($d \simeq 5$ km). This finite width is of great importance because the approximate effective half width of the spatial Fourier spectrum of waves generated in the beam is

$$k_x \simeq 1/2d$$

and only waves with frequencies below ω_c will be effectively guided along the field lines, where ω_c is given by Fejer and Lee (1967)

$$\omega_c = \Omega_i \frac{1}{2} \left(\frac{m_e}{m_i}\right)^{1/2} \frac{c}{\omega_{pi} d}$$

$$\omega_{pi}^2 = \frac{4\pi N_0 e^2}{m_i}$$

$$\Omega_i = \frac{eB}{m_i c},$$

e = elementary charge,
$m_{e,i}$ = electron, ion mass,
B = magn. flux density,
c = speed of light.

Higher frequency waves are not confined to the narrow ion beam and, although the local growth rate may be larger, the waves will not stay in the beam long enough to be amplified to detectable levels. Using appropriate values for $d \approx 5$ km, $N_0 \approx 2 \cdot 10^4$ cm^{-3}, $m_i \approx 4\, m_{\text{proton}}$ and $B = 0.44$ G, we find

$$\omega_c \approx 4 \text{ Hz}.$$

Thus inside the beam we expect the frequency spectrum to show a peak near ω_c. Waves above ω_c should be observed outside the beam presumably at a reduced intensity. Waves below ω_c are confined to the beam but are amplified less. This is in excellent agreement with the ULF observations reported by Klöcker and Theile (1979).

It is interesting to note that at the time of observation of the magnetic ULF waves the electric field instrument on board the rocket measured large fluctuations of the electric field perpendicular to the earth's magnetic field. The amplitude of these fluctuations was of the order of 100 mV/m (Grabowsky, private communication) and the amplitude of the magnetic fluctuations are in accordance with the existence of an Alfvén wave.

The question of the ultimate origin of the beam has not been answered. We can rule out a number of possibilities without being able to suggest a reasonable explanation. Since the electrons do not show a decrease of intensity simultaneously with the increase of ions, electrostatic fields parallel to the magnetic field cannot be responsible for the ion beam. Enhanced pitch angle scattering into the loss-cone by ion-cyclotron waves in the magnetosphere would not cause the highly field-aligned beam observed. Betatron acceleration or ion-cyclotron heating would increase the perpendicular energy and a field-aligned beam would not be expected. The only, albeit highly speculative, suggestion we can make involves kinetic Alfvén waves (Hasegawa and Chen 1976; Hasegawa 1977), which at large distances along the field lines may have accelerated the ions up to the Alfvén speed. Kinetic Alfvén waves can be produced by drift wave instabilities and by mode conversion of shear Alfvén waves at steep gradients of plasma density, say at the plasmapause (Hasegawa and Chen 1976). Such an acceleration would be the inverse process of the one we have discussed above.

Acknowledgements. The authors wish to acknowledge the assistance of H.P. Winterhoff in manufacturing and calibrating the energetic particle instrument. For many fruitful discussions one of us (W.S.) wishes to thank Dr. K. Wilhelm. Measurements from additional instruments of the same payload were kindly provided by Dr. R. Grabowsky, W. Ott, and H. Wolf, APW, Freiburg; G.L. Schmidtke, University of Kiel; A. Urban, TU Graz; N. Klöcker, TU Braunschweig.

The rocket programme "Substormphenomena" was funded by the "Bundesministerium für Forschung und Technologie" and managed by the DFVLR-BPT.

References

Fejer, J.A., Kan, J.R.: A guiding centre Vlasov equation and its application to Alfvén waves. J. Plasma Physics, **3**, 331–351, 1969

Fejer, J.A., Lee, K.F.: Guided propagation of Alfvén waves in the magnetosphere. J. Plasma Phys. **1**, 387–406, 1967

Goertz, C.K., Boswell, R.W.: Magnetosphere-ionosphere coupling. J. Geophys. Res. **84**, 7239, 1979

Hasegawa, A.: Kinetic properties of Alfvén waves. Proc. Indian Acad. Sci. **86**, 151, 1977

Hasegawa, A., Chen, L.: Kinetic processes in plasma heating by resonant mode conversion of Alfvén wave. Phys. Fluids **19**, 1924, 1976

Klöcker, N., Theile, B.: Magnetic ULF-waves in the vicinity of active auroral forms. J. Geophys. **46**, 229–236, 1979

Shawhan, S.D., Fälthammar, C.G., Block, L.P.: On the nature of large auroral zone electric fields at $1 - R_E$ altitude. J. Geophys. Res. **83**, 1049–1054, 1978

Stüdemann, W., Winterhoff, H.P.: Principle of operation, performance and first results of the energetic particle instruments onboard the Substorm- and Porcupine-payload. BMFT-Report, BMFT-FB-W., 1980 (in press)

Received May 16, 1980; Revised Version September 15, 1980
Accepted September 16, 1980

J Geophys (1981) 49:128–137

Journal of Geophysics

Observations of Field-Aligned Current Sheets Above Discrete Auroral Arcs

K. Wilhelm[1], N. Klöcker[2], B. Theile[2], W. Ott[3], K. Spenner[3], R. Grabowski[3], H. Wolf[3], W. Stüdemann[1], G. Dehmel[4], H.M. Fischer[5], G.L. Schmidtke[5], W. Baumjohann[6], W. Riedler[7], and A. Urban[8]

[1] Max-Planck-Institut für Aeronomie, D-3411 Katlenburg-Lindau 3, Federal Republic of Germany
[2] Institut für Geophysik und Meteorologie der Technischen Universität Braunschweig, D-3300 Braunschweig, Federal Republic of Germany
[3] Fraunhofer Institut für physikalische Meßtechnik, D-7800 Freiburg, Federal Republic of Germany
[4] Institut für Nachrichtentechnik der Technischen Universität Braunschweig, D-3300 Braunschweig, Federal Republic of Germany
[5] Institut für Reine und Angewandte Kernphysik der Universität Kiel, D-2300 Kiel, Federal Republic of Germany
[6] Institut für Geophysik der Universität Münster, D-4400 Münster/Westfalen, Federal Republic of Germany
[7] Institut für Nachrichtentechnik und Wellenausbreitung der Technischen Universität Graz, A-8010 Graz, Austria
[8] Institut für Weltraumforschung der Österreichischen Akademie der Wissenschaften, A-8010 Graz, Austria

Abstract. A high-altitude sounding rocket payload was launched into an auroral break-up event from the Andøya Rocket Range on 13 October 1977. The comprehensive experiment complement of the payload allowed particle and field observations over wide energy and frequency ranges. In addition, good coverage of the event was provided by ground-based instrumentation. The payload encountered at least two well-developed current sheets at the northern boundary of the auroral activity and westward electrojet region. In the upward-directed current regimes, with widths of approximately 10 km and current densities of up to 40 μA m $^{-2}$, the charge carriers were, predominantly, precipitating energetic electrons embedded in a low-density, high-temperature magnetospheric plasma. The downward-directed currents, on the other hand, were accompanied by a high-density, low-temperature plasma. Signatures of the current sheets could also be identified in the perpendicular electric field as abrupt intensity and direction variations as well as in spectral modifications of high-energy electron and proton fluxes.

Key words: Auroral arcs – Field-aligned current sheets

Introduction

The understanding of the complex physical processes leading to the generation of auroral displays was significantly advanced when it became clear that low-altitude acceleration of electrons played an important rôle in the energy and mass transfer above discrete auroral arcs (Evans 1974; Mende and Shelley 1976; Kaufmann et al. 1976; Mizera and Fennell 1977; Raitt and Sojka 1977, Bryant et al. 1977; Croley et al. 1978; Cattell et al. 1979, Wilhelm 1979). Both theoretical considerations and experimental evidence supported the conclusion that magnetically aligned electric fields were responsible for the acceleration and subsequent precipitation of magnetospheric electrons into the ionosphere (Swift 1978, 1979; Kan and Akasofu 1979). However, the subject is still very controversial, and evidence that a straightforward electrostatic acceleration of charged particles is inconsistent with many observations has recently been summarized by Whalen and Daly (1979).

The downward flow of energetic auroral electrons forms part of a large-scale system of Birkeland currents connecting the outer magnetosphere with the ionosphere (Anderson and Vondrak 1975). In the same region, upward-directed ion beams have been observed adding to the electric current density (Sharp et al. 1979). The identification of the charge carriers of the currents into the ionosphere has not been accomplished unambigiously, although the current flow has been clearly detected by magnetometer observations from satellites and sounding rockets (Zmuda et al. 1970; Theile and Praetorius 1973; Armstrong et al. 1975). Theile and Praetorius (1973) demonstrated that the field-aligned currents occurred above auroral arcs. In a recent paper, Cattell et al. (1979) discussed the consequences of different particle populations in regions with upward- or downward-directed currents. It was assumed that the plasma carrying downward currents would be populated by cold, high-density, ionospheric electrons and that upward current regions could be characterized by relatively low-density, hot, magnetospheric electron populations.

In this paper, we present a comprehensive set of measurements made by an experiment complement aboard a sounding rocket during an auroral break-up event. The observations demonstrate the above assumption directly and, moreover, relate the transitions between the different plasma regions to electrostatic field transitions. The high time-resolution available combined with the relatively low horizontal velocity of the payload provided a spatial resolution of less than 30 m, assuming the current structure to be at rest with respect to the earth's surface.

Instrumentation

The payload under discussion here was part of a sounding rocket programme, named "Substorm Phenomena" Identical experiment complements in four payloads were selected to provide a set of plasma, particle and field observations during various phases of magnetospheric substorm events. Details of the experiments are compiled in Table 1 which also indicates the various institutions responsible for the particular instrument developments.

The payloads were launched by Skylark 12 motors from the Andøya Rocket Range, Norway, and flight 3A, which we consider here, reached a peak altitude of 536.4 km. All experiments and

0340-062X/81/0049/0128/$02.00

Table 1. List of experiments flown aboard the payloads "Substorm phenomena"

Experiment	Technique	Measurements	Institution
Electric field experiment			
DCTF 3	2 boom-mounted double probe sensors	DC electric field resolution 0.1 1 mV/m	IPM, Freiburg
ACTN 1		AC electric field 50 Hz–20 kHz	ESTEC, Noordwijk
Förster' magnetometer TS 1	3-component fluxgate magnetometer	DC magnetic field 0–500 Hz, resolution 1 nT	TU, Braunschweig
AC magnetometer TS 2	1-component search coil	Magnetic component of wave fields 50 Hz–5 kHz	TU, Braunschweig
Plasma experiment TF 4	Retarding potential analyser	Electron temperature, ion density ion wind, vehicle potential electron flux 0–30 eV	IPM, Freiburg
Particle spectrometer Electrons TL 7 Protons TZ 1	Hemispherical electrostatic analyser and open electron multipliers	Electron and proton fluxes $0.1(1) \leqq E_e(E_p) \leqq 25(40)$ keV	MPAE, Lindau INW, Graz
Particle spectrometer TL 6	Magnetic particle analyser and solid-state detectors	Electron and proton fluxes $20(40) \leqq E_e(E_p) \leqq 200(300)$ keV	MPAE, Lindau
Particle spectrometer TK 1	Solid-state detector telescope	Proton fluxes $0.07 \leqq E_p \leqq 2$ MeV	IFKKI, Kiel

other subsystems worked perfectly thus providing a wealth of data, some of which will be discussed in this paper. The payload was controlled in attitude so as to point $20° \pm 10°$ off the negative geomagnetic field direction and had a spin period of 350 ms.

Geophysical Conditions During Launch

The payload flew on 13 October 1977 during a magnetospheric substorm starting at 20:22 UT and lasting until 23:30 UT Two auroral break-ups occurred during this substorm. The variations of the magnetic field components recorded at Andenes as displayed in Fig. 1 provide an overview of the situation which occurred during a period of moderate planetary geomagnetic disturbance levels with Kp=3− Except during the first 40 min of the substorm, both the positive and negative variations of the Z and Y components were less than 100 nT, while X reached a minimum of −400 nT Of particular interest is the time interval 20:48–20:55 UT, characterized by strong negative Z variation. The corresponding auroral forms showed a violent disruption of the east-west oriented band with, at times, nearly north-south directed curtains.

While the X-component attained large negative values, the auroral activity subsequently concentrated in a faint homogeneous arc with sharp northern boundary which moved slowly southwards. Based on the decreasing X-component, an intensification of the arc and a slight enhancement of the geomagnetic micropulsation activity at 21:22 UT, the rocket was fired at 21:26 UT Shortly after launch, the arc brightened to an intensity of more than 50 kR in the 557.7 nm oxygen line. The payload crossed the arc two minutes later and reached the northern boundary of the auroral activity at about 21.30 UT The measurements of the Andenes scanning photometer are displayed in a time-distance coordinate system in Fig. 2 for the 557.7 nm auroral line. It can be seen that at 21:31 UT an auroral break-up occurred with rapid expansion of the aurora to the north. Further information on the geophysical conditions during the flight has been compiled elsewhere (Wilhelm 1980). Without discussion it should be pointed out that a fading of the auroral brightness occurred before

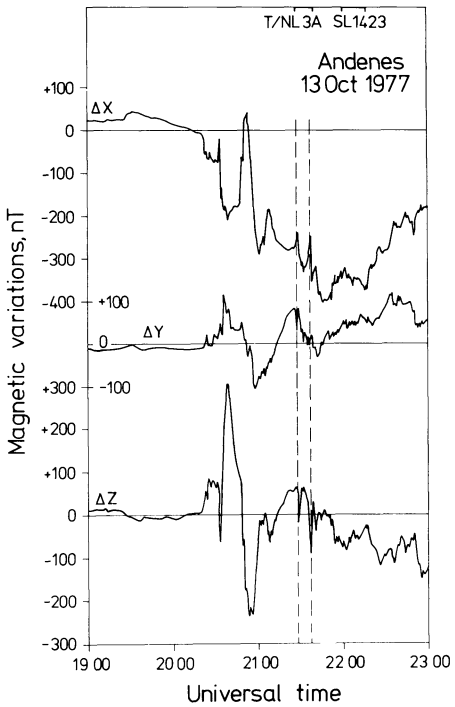

Fig. 1. Variations of the geomagnetic field at Andenes on 13 October 1977. The variations of the north, east and vertical components are denoted by ΔX, ΔY, and ΔZ, respectively. The flight times of the two sounding rocket payloads T/NL 3A and SL 1423 (the latter not discussed in this paper) have been indicated. Note the two impulsive changes of ΔX at 21:27 UT and 21 35 UT The pulse at 21:27 UT coincided with an auroral break-up

the break-up similar to the observations by Pellinen and Heikkila (1978). The sequence of events has been documented by all-sky photographs from Andenes shown in Fig. 3. The trajectory of the payload has been projected downwards along the magnetic field lines to an altitude of 120 km and has been overlaid on both the photometer and the all-sky camera data in order to

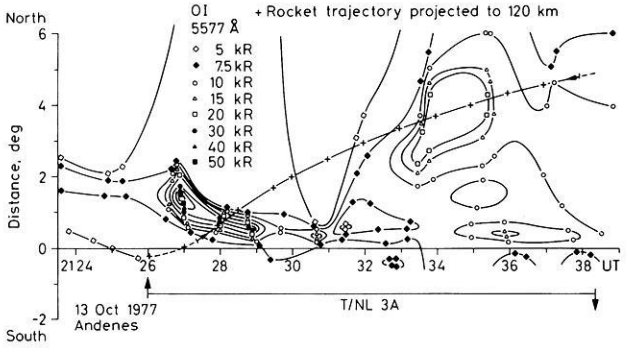

Fig. 2. Isophotes of the green oxygen line at 557.7 nm presented in a spatial-temporal co-ordinate system and derived from scanning photometer observations. The distance is measured from the launch site on an azimuth of 340° corresponding to the launch direction of the rocket. The rocket trajectory projected down along the local magnetic field direction to a height of 120 km is also shown

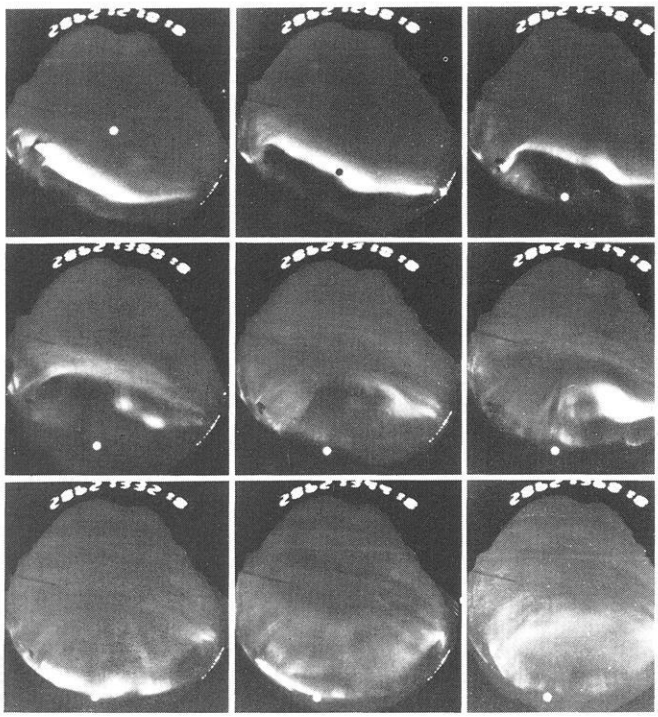

Fig. 3. All-sky camera photographs during the flight of payload T/NL 3A. The frames (from left to right) were taken at approximately 1 min intervals at 21:27:01, 28:01, 29:01, 30:01, 31:01, 31:41, 33:21, 34:41, and 36:01, respectively. The exposure time was 16 s. North is at the bottom of the frames and east to the right. The instantaneous position of the payload was projected down to an altitude of 120 km and marked by *dots* in the frames of this figure

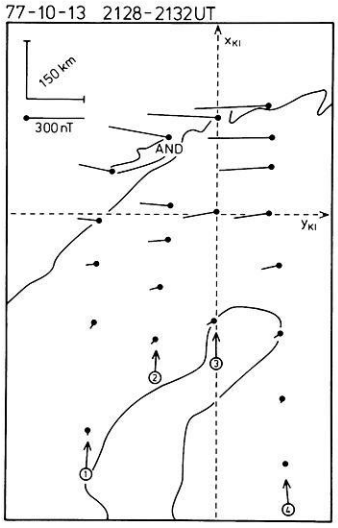

Fig. 4. Averaged equivalent current vectors on the earth's surface showing the direction of the current and the magnitude of the disturbance field. The current vectors have their origin at the station where the corresponding magnetic disturbances were observed (the station denoted by AND is located at the Andøya rocket range). The numbers in circles denote the different profiles. The co-ordinate system is explained in the text

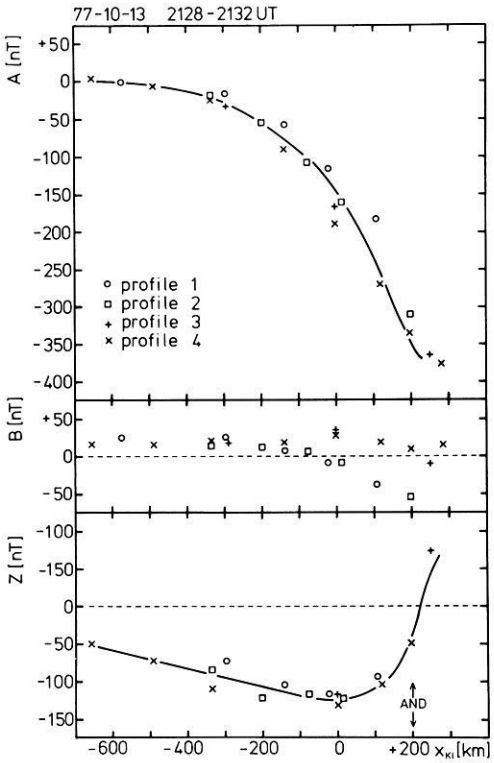

Fig. 5. Latitudinal distribution of 4 min averaged magnetic components observed on four different profiles (see Fig. 4). The *solid lines* denote A and Z components averaged over the profiles. Also indicated is the location of the Andøya rocket range (*AND*)

establish the spatial relationship of the auroral forms with respect to the payload. The riometer recording at Andenes on 27.6 MHz showed a relatively smooth absorption event of approximately 0.9 dB over the flight.

The observations and subsequent discussion pertain to small-scale phenomena observed by the instrumentation of the payload. The prevailing large scale electrojet configuration was observed by the Scandinavian Magnetometer Array (Küppers et al. 1979). Analysis has been carried out for the interval between 2128 and 2132 UT. Since the gross spatial configuration of the magnetic field did not change and an increase of only 10% in amplitude was observed during this interval, it should suffice to consider values averaged over 4 min in the following discussion.

In Fig. 4 the averaged equivalent currents, in terms of their magnetic field amplitude at the earth's surface, are displayed, whereas Fig. 5 shows the amplitudes, averaged in time, of the north, east and vertical magnetic components along the x_{KI} axis.

The coordinate system used in Fig. 4 is a Cartesian system obtained by a projection of the globe onto a tangential plane centred at Kiruna, Sweden. The y_{KI} axis of the system has been chosen as the tangent to the projection of the ϕ_c (KIR)=64.8° line with ϕ_c being the revised corrected geomagnetic latitude as given by Gustafsson (1970). The x_{KI} axis is perpendicular to the y_{KI} axis and is directed approximately 12° west of geographic north at Kiruna.

Both figures show that a westward electrojet was centred near x_{KI}=200–250 km decreasing slightly in strength in the westward direction. The southward-directed equivalent currents in sub-auroral latitudes and the distribution of the B components (parallel to y_{KI}) along the x_{KI} axis seem to indicate a divergence of the westward electrojet. Whether this divergence was balanced by upward-flowing field-aligned currents (Hughes and Rostoker 1977, 1979; Baumjohann 1979) remains to be determined.

As can be seen in Fig. 17, the large-scale ionospheric electric field is directed southwards. The westward electrojet could therefore be attributed to an ionospheric Hall current. In order to calculate the height-integrated ionospheric Hall current density we have applied the method of field separation and subsequent upward continuation (Mersmann et al. 1979; Baumjohann et al. 1979) to the averaged latitudinal profiles of the A and Z components displayed in Fig. 5. As no magnetic field data were available north of the Norwegian coast the assumption was made that the A and Z components were symmetric and anti-symmetric with respect to x_{KI}=200–250 km.

The resulting x_{KI} profile of the height-integrated westward Hall current density at 100 km height is shown in Fig. 6. It can be seen that the westward electrojet has its maximum height-integrated current density of about 8×10^5 μAm^{-1} slightly north of Andøya and close to the region of maximum auroral luminosity. The main part of the current was confined to a region of $\pm$300 km around this maximum. The northern boundary of the current flow was close to the boundary of the auroral activity as indicated by the rocket results, which supports our earlier assumption of a symmetric current flow.

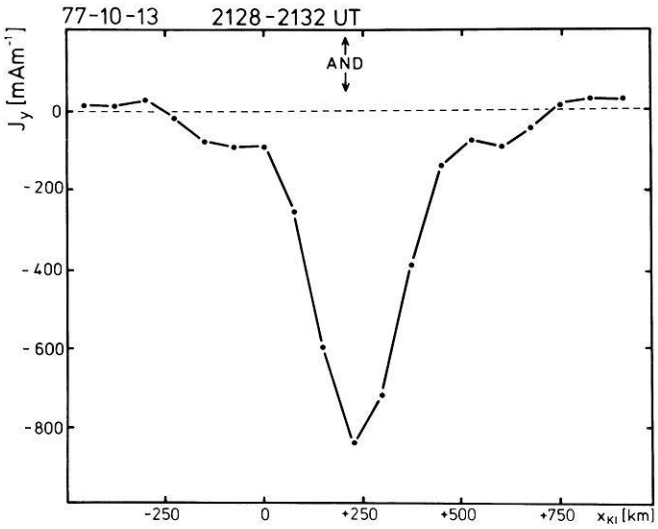

Fig. 6. Latitudinal distribution of the height-integrated Hall current density. Also indicated is the location of the Andøya rocket range (*AND*). The current density north of Andenes was calculated assuming symmetry

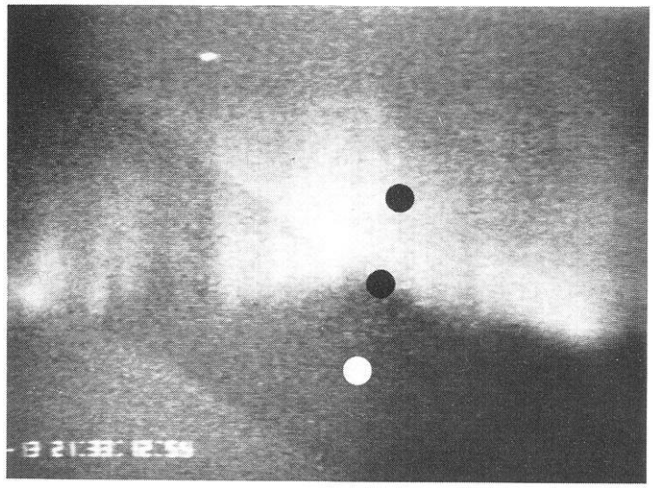

Fig. 7. Active auroral from overflown by the payload shortly before this TV observation was made at 21:33 UT (420 s after launch) (courtesy G.Webb). The *white dot* indicates the location of the payload projected along the magnetic field direction down to 110 km at that time. The *black dots* show the locations at 21:30 (240 s) and 21:31 UT (300 s), respectively. The *star in the upper left-hand area* is Alkaid

Observations

The observations pertaining to small-scale field-aligned current flow were made during the time interval 190–260 s after launch. As can be seen from Figs. 2 and 3, the payload was near the northern boundary of the auroral activity at this time. Visual and television observations in Fig. 7 show more clearly than Fig. 3 that the region in question was occupied by discrete auroral arcs with a pronounced ray structure. This is supported by the measurements of low-energy electron fluxes given in Fig. 8. As long as the instrument was in the appropriate mode, highly-structured, intense electron precipitation was detected followed by steep decreases in numbers as well as energy fluxes, shortly after 260 s elapsed time. North of this region the energy flux carried by low-energy electrons in the range 0.1–25 keV was smaller than 10^{-2} erg cm^{-2} s^{-1}, whereas inside the area with auroral activity the energy flux was nearly three orders of magnitude higher. A conspicuous spike between 210 and 220 s elapsed time is investigated in detail in Fig. 9. The lower curves of this figure and of Fig. 10 are the magnetic field variations derived from the fluxgate magnetometer measurements. The originally spin- and coning-modulated magnetometer data have been transformed into an earth-fixed coordinate system. B_x points towards magnetic north, B_y towards magnetic east, and B_z downwards parallel to the undisturbed geomagnetic field. A reference field was deduced from the transformed measurements to obtain the variations of the magnetic field vector. The data shown cover the times 190–226 s and 230–260 s after launch, respectively. Activation of the attitude control system affected the magnetic field measurement during the missing time section. No magnetic field variations were observed in B_z. B_x shows some variations at frequencies of a few Hz between 210 and 216 s. Short-period variations were observed in the same time interval in B_y. In addition, B_y increased between 190 and 211 s. A decrease in B_y is seen from 211 to 216 s. The short-period variations can be explained in terms of hydromagnetic waves (Klöcker and Theile 1979). The event in Fig. 10, occurring half a minute later, showed very similar signatures. The low-energy electron experiment had switched to another mode allowing high-time-resolution measurements at the expense of spectral information. The low-energy electron flux decreased by two orders of

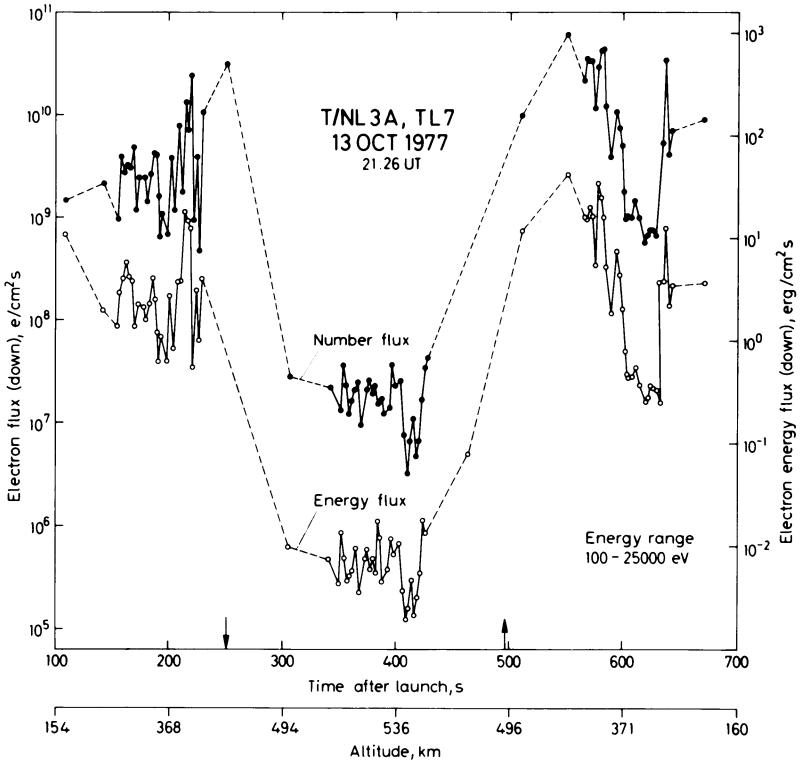

Fig. 8. Summary diagrams of the electron number flux and energy flux during flight 3A. The different time resolution apparent in this figure results from different operating modes of the instrument

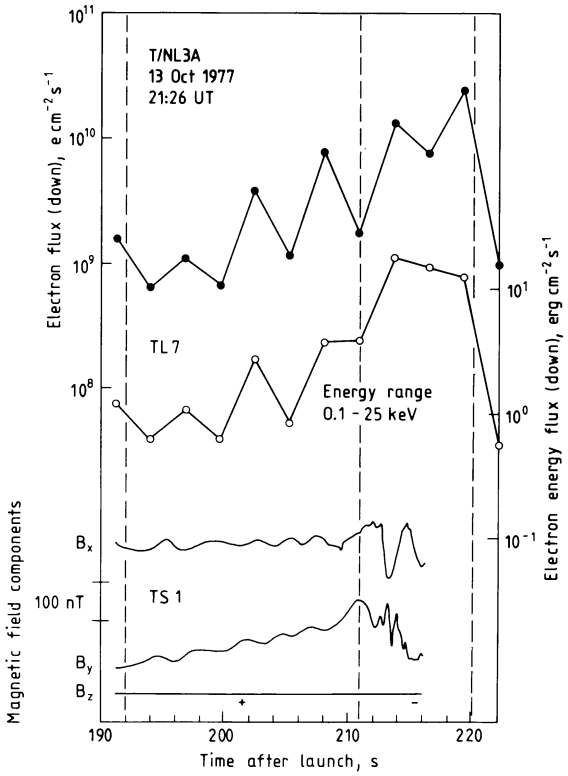

Fig. 9. Comparison between electron flux data and magnetic field observations made aboard payload T/NL 3A during the time interval 192–220 s elapsed time. The apparent, smooth wave forms occurring coherently in the B_x and B_y components result from residual spin contributions to the magnetic field variations measured aboard the moving payload. Regions marked + and − are characterized by downward- and upward-directed currents, respectively

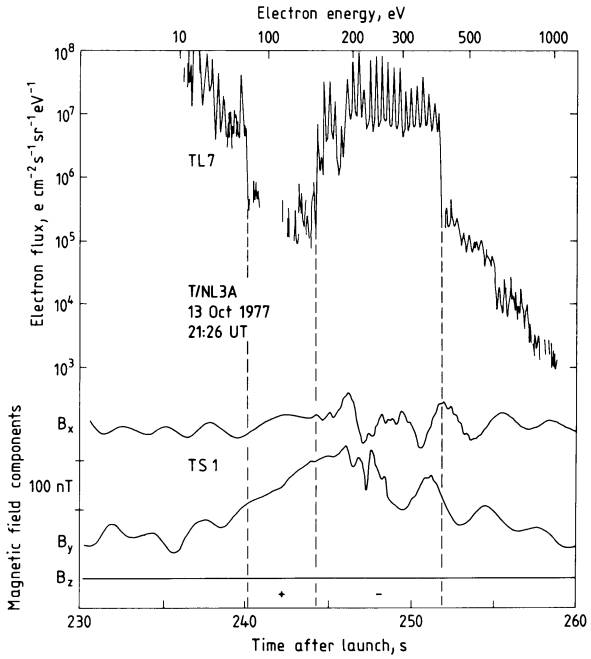

Fig. 10. High time-resolution electron flux measurements as compared to magnetic field observations made aboard payload 3A between 230 and 260 s elapsed time. The magnetic field observations have been given in the same format as in Fig. 9. The electron data were obtained in a slow energy scan mode with an energy increment every spin period. The spin modulation present near 250 s resulted from a field-aligned electron flux distribution. The lack of detailed correspondence between particle and field data is not surprising in view of the fact that the magnetometer observations represent an integrated response to an extended current distribution

magnitude between 240.1 and 243.9 s and after 251.6 s elapsed time. It is important to note that all three variations occurred within one spin period each, while the experiment was set on fixed energy levels. Consequently, they have to be considered as time-space variations rather than spectral features. The apparent modulation of the electron flux resulted from a pitch angle anisotropy with fluxes peaked along the magnetic field direction. A model pitch angle distribution of $F(\alpha) \sim 40 \cos^{12}\alpha + 1$ for $0 \leqq \alpha \leqq 90$ and $F(\alpha) \sim 1$ for $90 \leqq \alpha \leqq 120$ best fits the data in the energy range 200–370 eV.

In both cases, the magnetic data suggest that the payload encountered field-aligned electric current sheets with downward-directed currents at the southern boundary and upward-directed currents north of it. The low-energy electron flux observations support this interpretation as far as the upward-directed current is concerned by identifying intense electron fluxes flowing along the magnetic field lines into the ionosphere. On the other hand, very low fluxes were measured in the regions of downward currents.

These interesting events seem to merit extensive investigation making full use of the available data set provided by this payload. Energy spectra of the low-energy electrons were measured with high time-resolution during the first event and have been displayed in Fig. 11. Before and after the event the spectrum can be approximated by a single power law function $F(W) \sim W^{-\gamma}$, with exponent $\gamma = 2.3$. During the period with increased flux the spectrum changed considerably. This spectral variation was accompanied by a change in the directional distribution. In the energy range 0.1–0.6 keV, the pitch angle distribution peaked along the magnetic field direction with a best-fit model of approximately $F(\alpha) \sim 50 \cos^{15}\alpha + 1$ for angles of $0 \leqq \alpha \leqq 90$. At higher energies, near 2 keV, the distribution was also field-aligned as can be seen from Fig. 12 where, in addition, a model fit of $F(\alpha) \sim 10 \cos^{15}\alpha + 1$ is shown.

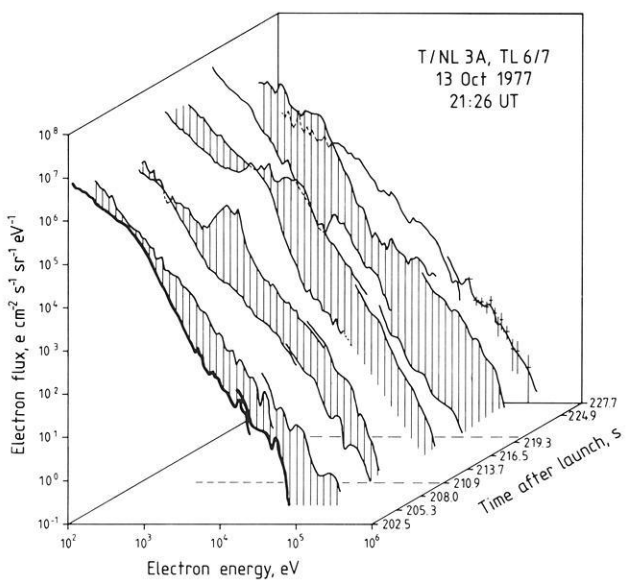

Fig. 11. Electron energy spectra as measured during the first of the events described. The observations were made by two instruments in different energy ranges with some overlap near 25 keV. A spectral peak developed between 210.9 and 216.5 s near 2 keV accompanied by an increase of the flux near 25 keV of more than an order of magnitude. Representative statistical errors have been indicated. At lower energies statistical errors are insignificant. The intervals of the first upward-directed current sheet has been marked by *broken lines*

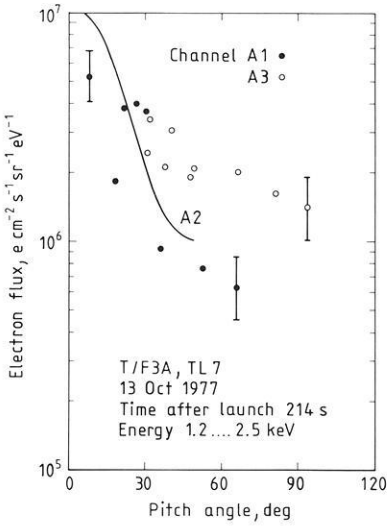

Fig. 12. Pitch angle distribution of 1.2–2.5 keV electrons at 214 s after launch measured by three different instrumental channels. Channels A1 and A3 provided directional observations. The field-aligned electron flux described by the model function $10 \cos^{15}\alpha + 1$ (*solid line*) was deduced from channel A2, with fan-shaped viewing cone covering 96°. Statistical errors are small. The absolute errors for the directional channels have been estimated to be approximately $\pm 20\%$ while channel A2 should be accurate to $\pm 10\%$

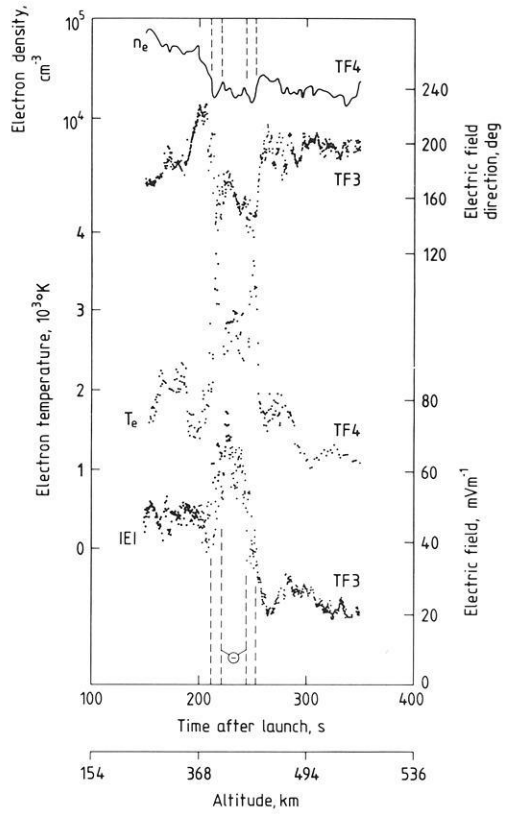

Fig. 13. Electron density, electric field direction, electron temperature and electric field intensity as functions of time after launch and altitude. The regions of upward-directed field-aligned currents have been marked by – and *broken lines*

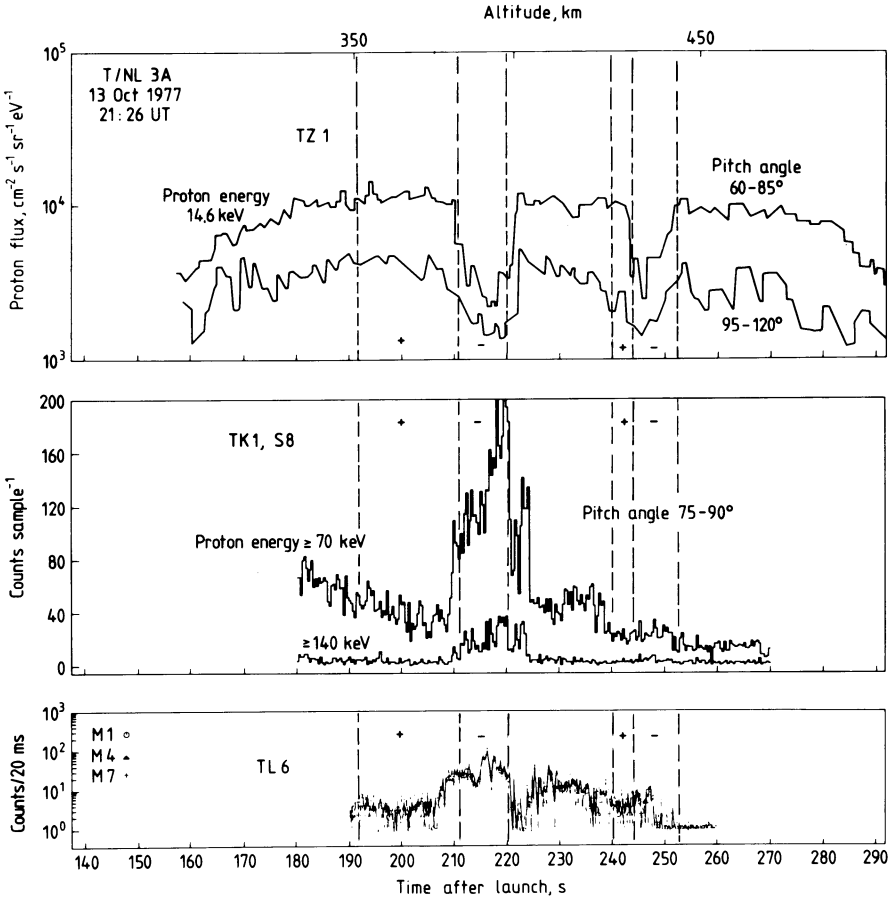

Fig. 14. Energetic proton and electron observations. Both current sheets affected the 14.6 keV proton flux significantly as shown in the *upper graphs*. The high-energy proton flux as well as the electron flux (*middle and lower part*) increased during the first current sheet encounter, but showed no significant effect during the second. Three electron channels $E >$ 15 keV have been plotted (M1: pitch angle $\approx$ 20°, M4: 5°–45° and M7: 30°–70°). The high energy proton data cover the pitch angle domain 75°–90° and were taken when the viewing cone was looking in westward directions. Regions of upward- and downward-directed current flow have been indicated

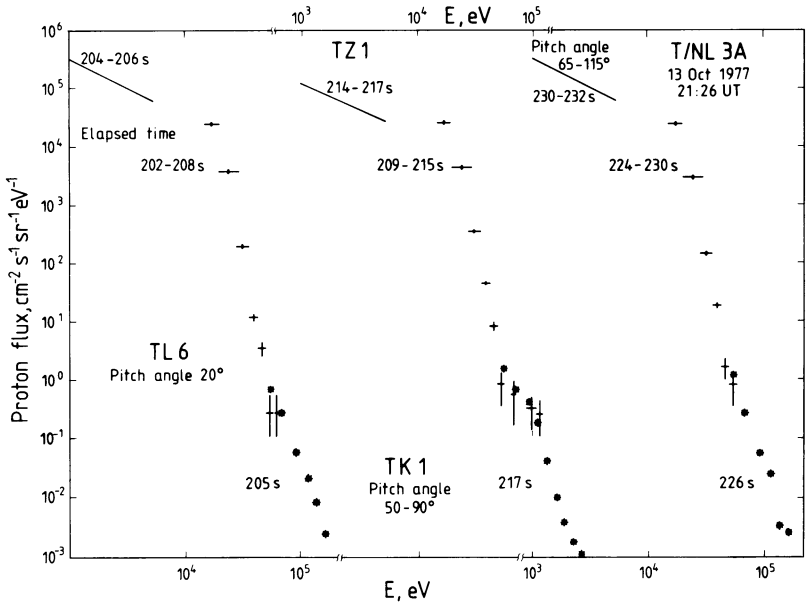

Fig. 15. Proton spectra observed before, during and after the first current sheet crossing by three different instruments. The low-energy depression and the high energy enhancement shown in Fig. 14 can be understood as spectral changes of the proton population

Physical effects related to the current sheets as seen by the low-energy electron and magnetometer experiments were also observed by the other instruments. First, we present plasma data from the retarding potential analyser and electric field experiments in Fig. 13. The density of the thermal electrons dropped by a factor of roughly two during the time intervals with upward-directed currents, whereas the electron temperatures increased from values near 1,500° to 3,500° K attaining their peak values exactly inside the regions with upward-directed currents. The data presented in Fig. 13 suggest, however, that both current sheets did not occur independently, but were generated by a common process. The electric field measurements presented in the lower portions of this figure show abrupt variations both in intensity and in direction. Specifically, the quasistatic electric field increased

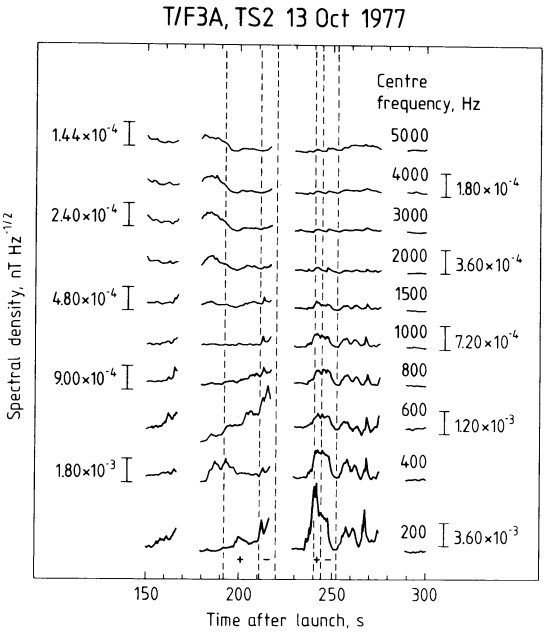

Fig. 16. Magnetic wave field observations in several frequency bands each having 100 Hz band width. The instrument suffered from interference when the attitude control system was activated and the data could not therefore be evaluated continuously. Enhancements of the magnetic fluctuations in the lower frequency bands seem to be related to the currents sheets, although a one-to-one correspondence can not be seen

from 40 to 80 mV/m during the first interval and decreased from approximately 60 to 20 mV/m in the course of the second event while the azimuth of the electric field direction varied between about 200 and 110° in both cases.

A summary of the energetic proton and electron observations has been compiled in Fig. 14. The important point to note is that the low-energy channel at 14.6 keV is clearly anticorrelated with the electron flux whereas the high-energy proton flux shows a positive correlation with the electrons during the periods of upward-directed electric currents. The proton spectra given in Fig. 15, for a time interval covering the first current-sheet encounter, demonstrate that the proton flux near 30 keV had been relatively constant. At energies below this level flux decreases were observed, whereas enhancements were present at higher energies. In particular, the high energy tail above 60 keV should be mentioned, as well as the fact that the high-energy proton flux was field-aligned in the electron precipitation region.

The observations of the perpendicular magnetic wave field given in Fig. 16 show increased activity in all frequency bands from 200–2,000 Hz in relation to the current layers, however, a clear one-to-one correspondence could not be detected. The spectral densities at different centre frequencies are given with a bandwidth of 100 Hz. The pulses of the attitude control system have been suppressed in this figure. There is some enhancement at 400 Hz between 185 and 200 s. A more pronounced noise level can be seen between 240 and 270 s. The maximum amplitude is at 200 Hz or below. This observation is consistent with results of Gurnett and Frank (1972), who found that inverted "V" events and ELF-noise very often occurred simultaneously. No satisfying physical explanation is yet available. Spectrograms of the AC electric field covering the whole of this flight exhibit a strong hiss signal with a cut off at the lower hybrid frequency near 7 kHz without any pronounced structures related to the current sheet encounters.

Discussion

The all-sky camera data, the low-energy electron fluxes, the electron temperature and the electric field characteristics all suggest that the payload reached the northern boundary of the auroral oval shortly after 251 s elapsed time. Whether the observed structures were of spatial or temporal type could not be determined unambiguously from the rocket data alone. Since the auroral activity regions and the large-scale electrojet were, however, stationary in latitude during this time interval, it can be concluded that the payload traversed spatial structures with a velocity of approximately 1,100 ms^{-1} normal to the magnetic field lines. The abrupt transitions from one plasma regime to the other, apparent in the electron data of Fig. 10, occurred over a distance of about 70 m. It also follows that the double sheet near 250 s had a total thickness of 13 km, of which 8 km were occupied by the upward-directed current. The corresponding figures as determined from the magnetometer measurements were 12 and 7 km, respectively. The width of the upward-directed current sheet centred near 215 s was 10 km and it was separated from the sheet at 250 s by approximately 38 km. Structures with a width of only several 100 m as quoted by Kan et al. (1979) could not be found although the resolution of the instruments would have been sufficient for an unambiguous detection. In addition to the good agreement as far as the width of the current sheets is concerned, the evaluation of the current densities in the upward-directed current regions led to reasonable agreement between the field and particle data. Assuming a current sheet of infinite extent and a payload motion perpendicular to it, the current density can be related to the magnetic field according to $j=(1/\mu_0)dB/dx$. The downward current cannot be determined from the electron precipitation data. The relevant parameters of the current sheets as far as they could be determined from the observations have been compiled in Table 2.

The current density values as derived from the electron flux data should, however, be qualified in two respects. Firstly, it should be noted that the upward-directed electron flux was only measured in the pitch angle range 90–120° and, secondly, observations were not available over the full energy range. The fact that in both cases the electron data yield higher current densities might indicate an under-estimation of the return flux of energetic electrons contained implicitly in the model pitch angle distributions. The current densities were several times larger than the threshold density of 2.5 μAm^{-2} for auroral arc spiral formation (Davis and Hallinan 1976; Hallinan 1976).

The plasma measurements demonstrate that the two different current regimes were populated by different electron distributions. A low-density, high-temperature electron gas was observed in the upward-directed current sheet and a high-density, low-temperature one in the adjacent region. As the events were observed by this payload at an altitude of approximately 400 km, the conclusion can be drawn that magnetospheric electron populations were carried down to at least that altidue. The strong field alignment of the energetic electron fluxes confirms the concept that low-altitude electric fields parallel to the magnetic lines of force exist above the auroral ionosphere. Judging from the positions of the peak and knee in the spectral electron distributions in Fig. 11, the maximum potential drop during the 210 s event was approximately 4 kV. The data discussed so far consistently describe current sheets connecting the outer magnetosphere with the ionosphere during the main phase of a magnetospheric substorm. We will now attempt to relate the additional information to these structures.

Table 2. Current sheet parameters

Event	192–211 s	211–220 s	240–244 s	244–252 s
Current direction	Downwards	Upwards	Downwards	Upwards
Width, km				
Magnetic data[a]	9	–	8	7
Electron data[b]	–	10	5	8
Current density, μAm^{-2}				
Magnetic data	13	25	18	17
Electron data	–	40	–	22

[a] Width deduced depends on details of current sheet structure in E-W direction. Values given refer to simple E-W extending sheets. Spirals as indicated in Fig. 3 would tend to broaden the width

[b] Width calculated assuming perpendicular traverses

The electric field measurements exhibit large variations in amplitude as well as in azimuth across the current sheet structures. It has already been noted that the electric field data clearly relate the observed current sheets to a single feature characterized by an increase in the electric field intensity and a distinct change in the direction. In an attempt to identify this structure, the electric field information provided by the STARE system (Greenwald et al. 1978) was compared with the sounding rocket data and the auroral observations in Fig. 17. A study by Cahill et al. (1978) showed good agreement between electric fields determined from STARE and sounding rocket data. The bright auroral arc denoted by *A* delineated a change in the direction of the electric field in all three intervals. In region *B* between the bright arc *A* and the northern edge of the auroral activity, southward directed fields prevailed. Neither an intensification nor a variation of the direction could be detected near the arc *C* at 71–72° latitude, as would have been expected from the rocket measurements during the current sheet encounters. Besides this difference, there was a general disagreement between the electric field magnitude observed by the rocket instrument and STARE. The radar beam covering the trajectory of the payload was however not operating satisfactorily thus precluding any detailed comparison. Nevertheless, it can be inferred from Fig. 17 that the current sheets were encountered at the northern boundary of a region with electric fields above the STARE threshold having a latitudinal extension of several hundred kilometres and a southward direction.

The electron flux observations have provided evidence that the field-aligned current sheets were accompanied by quasi-static electric potential differences along the magnetic field lines. Such a configuration, if directed so as to accelerate electrons downwards, should of course decelerate precipitating protons and indications of such an effect could indeed be found at the low-energy end of the observations presented in Figs. 14 and 15. The enhancement of both the energetic electron and proton fluxes accompanying the current sheet at 210–220 s point to another process related to the various phenomena. This is particularly true for the high-energy tail of the proton spectrum at 209–215 s.

The energetic particle fluxes during the second current-sheet encounter were considerably lower, in line with a general decrease of the mean energy of the low-energy electron population from approximately 6 keV near the bright auroral arc to 0.1 keV at the northern edge of the auroral activity, which can be determined using the data shown in Fig. 8.

In summary, the observations presented here demonstrate that field-aligned current sheets having current densities in excess of 10 μAm^{-2}, with opposite directions, occurred near the northern

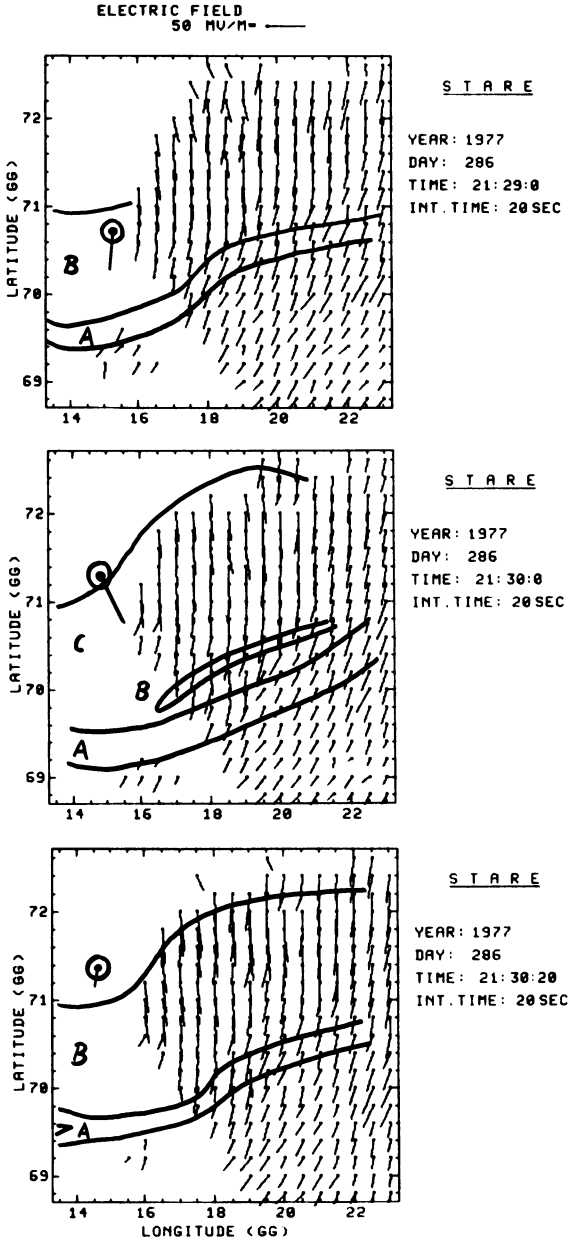

Fig. 17. Ionospheric electric fields as derived from STARE observations for three integration intervals during the first part of the sounding rocket flight 3A. Also shown are the positions of the bright auroral arcs (*lines*) as well as the electric field observed aboard the rocket and projected down to 100 km along the magnetic field direction (*circles*). The observations were made at 180, 240, and 260 s after launch with an integration time of 20 s

edge of an auroral break-up region. The sheets could be related to active discrete auroral forms. The sheet parameters, current density and latitudinal width, as determined by the on-board magnetometer and electron spectrometer instruments, were in reasonable agreement. In particular, it could be concluded that the upward current was carried predominantly by energetic electrons. The widths of the sheets ranged from 5–10 km. Although the instrumentation was capable of resolving narrower structures, such features were not observed. The edges of the different plasma regimes were extremely sharp accompanied by quasi-static electric field transitions as well as magnetic ULF and VLF wave field

activity. The plasma parameters could be characterized by decreases in the electron density and strong enhancements of the electron temperature. High-energy charged particle measurements indicated that very energetic processes were involved in the generation mechanisms of these structures, while low-energy electron and proton observations provided strong evidence of field-aligned acceleration and deceleration within the upward-directed current sheets. The lack of any detailed correspondence between both the magnetic and electric AC fields and the other current sheet parameters points to a propagation effect and thus to the fact that the interaction region was located away from (presumably above) the observation point.

Acknowledgements. Many individuals at the various institutions contributed to this sounding rocket programme. In particular, we should like to mention Dr. Hörle as project manager of DFVLR-PT. We also want to thank the integration team of Dornier System, the DFVLR launch team and the personnel of the Andøya Rocket Range for their support of the project. The work was supported financially by the German Bundesministerium für Forschung und Technologie and by the Austrian Akademie der Wissenschaften. Drs. R.A. Greenwald and E. Nielsen kindly provided the STARE data used in this study.

References

Anderson, H.R., Vondrak, R.R.: Observations of Birkeland currents at auroral latitudes. Rev. Geophys. Space Phys. **13**, 243–262, 1975

Armstrong, J.C., Akasofu, S.-I., Rostoker, G.: A comparison of satellite observations of Birkeland currents with ground observations of visible aurora and ionospheric currents. J. Geophys. Res. **80**, 575–586, 1975

Baumjohann, W.: Spatially inhomogeneous current configurations as seen by the Scandinavian Magnetometer Array. In: Proceedings of the International Workshop on Selected Topics of Magnetospheric Physics, Japanese IMS Committee, ed.: pp. 35–40. Tokyo 1979

Baumjohann, W., Sulzbacher, H., Potemra, T.A.: Joint magnetic observations of small-scale structures in a westward electrojet with Triad and the Scandinavian Magnetometer Array. In: Procedings of the International Workshop on Selected Topics of Magnetospheric Physics, Japanese IMS Committee, ed.: pp. 49–52. Tokyo 1979

Bryant, D.A., Hall, D.S., Lepine, D.R., Mason, R.W.N.: Electrons and positive ions in an auroral arc. Nature **266**, 148–149, 1977

Cahill, L.J., Jr., Greenwald, R.A., Nielsen, E.: Auroral radar and rocket double-probe observations of the electric field across the harang discontinuity. Geophys. Res. Lett. **5**, 687–690, 1978

Cattell, C., Lysak, R., Torbert, R.B., Mozer, F.S.: Observations of differences between regions of current flowing into and out of the ionosphere. Geophys. Res. Lett. **6**, 621–624, 1979

Croley, D.R., Mizera, P.F., Fennell, J.F.: Signature of a parallel electric field in ion and electron distribution in velocity space. J. Geophys. Res. **83**, 2701–2705, 1978

Davis, T.N. and Hallinan, T.J.: Auroral spirals. 1. Observations. J. Geophys. Res. **81**, 3953–3958, 1976

Evans, D.S.: Precipitating electron fluxes formed by a magnetic field aligned potential difference. J. Geophys. Res. **79**, 2853–2858, 1974

Greenwald, R.A., Weiss, W., Nielsen, E., Thomson, N.R.: STARE: A new radar auroral backscatter experiment in northern Scandinavia. Radio Sci. **13**, 1021–1039, 1978

Gurnett, D.A., Frank, L.A.: ELF noise bands associated with auroral electron precipitation. J. Geophys. Res. **77**, 3411–3417, 1972

Gustafsson, G.: A revised corrected geomagnetic coordinate system. Ark. Geofys. **5**, 595–617, 1970

Hallinan, T.J.: Auroral spirals, 2. Theory. J. Geophys. Res. **81**, 3959–3965, 1976

Hughes, T.J., Rostoker, G.: Current flow in the magntosphere and ionosphere during periods of moderate activity. J. Geophys. Res. **82**, 2271–2282, 1977

Hughes, T.J., Rostoker, G.: A comprehensive model current system for high-latitude magnetic activity – I. The steady state system. Geophys. J. R. Astron. Soc. **58**, 525–569, 1979

Kan, J.R., Akasofu, S.-I.: A model of the auroral electric field. J. Geophys. Res. **84**, 507–512, 1979

Kan, J.R., Lee, L.C., Akasofu, S.-I.: Two-dimensional potential double layers and discrete auroras. J. Geophys. Res. **84**, 4305–4315, 1979

Kaufmann, R.L., Walker, D.N., Arnoldy, R.L.: Acceleration of auroral electrons in parallel electric fields. J. Geophys. Res. **81**, 1673–1682, 1976

Klöcker, N., Theile, B.: Magnetic ULF-waves in the vicinity of active auroral forms. J. Geophys. **46**, 229–236, 1979

Küppers, F., Untiedt, J., Baumjohann, W., Lange, K., Jones, A.G.: A two-dimensional magnetometer array for ground-based observations of auroral zone electric currents during the International Magnetospheric Study (IMS). J. Geophys. **46**, 429–450, 1979

Mende, S.B., Shelley, E.G.: Coordinated ATS 5 electron flux and simultaneous auroral observations. J. Geophys. Res. **81**, 97–110, 1976

Mersmann, U., Baumjohann, W., Küppers, F., Lange, K.: Analysis of an eastward electrojet by means of upward continuation of ground-based magnetometer data. J. Geophys. **45**, 281–298, 1979

Mizera, P.F., Fennell, J.F.: Signatures of electric fields from high and low altidue particles distribution. Geophys. Res. Lett. **4**, 311–314, 1977

Pellinen, R.J., Heikkila, W.J.: Observations of auroral fading before breakup. J. Geophys. Res. **83**, 4207–4217, 1978

Raitt, W.J., Sojka, J.J.: Field-aligned suprathermal electron fluxes below 270 km in the auroral zone. Planet. Space Sci. **25**, 5–13, 1977

Sharp, R.D., Johnson, R.G., Shelley, E.G.: Energetic particle measurements from within ionospheric structures responsible for auroral acceleration processes. J. Geophys. Res. **84**, 480–488, 1979

Swift, D.W.: Mechanisms for the discrete aurora – a review. Space Sci. Rev. **22**, 35–75, 1978

Swift, D.W.: On the structure of auroral arcs: The results of numerical simulations. J. Geophys. Res. **84**, 469–479, 1979

Theile, B., Praetorius, H.M.: Field-aligned currents between 400 and 3000 km in auroral and polar latitudes, Planet. Space Sci. **21**, 179–187, 1973

Whalen, B.A., Daly, P.W.: Do field-aligned auroral particle distributions imply acceleration by quasi-static parallel electric fields? J. Geophys. Res. **84**, 4175–4182, 1979

Wilhelm, K.: Auroral particle fluxes in the ionosphere. J. Geophys. **46**, 151–169, 1979

Wilhelm, K.: Study of magnetospheric substorm events. Proceedings of the Vth ESA Symp. on European Rocket and Balloon Programmes and Related Research. ESA Special Publication **152**, 269–277, 1980

Zmuda, A.J., Armstrong, J.C., Heuring, F.T.: Characteristics of transverse magnetic disturbances observed at 1,100 km in the auroral oval. J. Geophys. Res. **75**, 4757–4762, 1970

Received July 1, 1980; Revised Version November 14, 1980
Accepted December 22, 1980

J Geophys (1981) 49:138–145

Journal of Geophysics

Multi-Method Observations and Modelling of the Three-Dimensional Currents Associated with a Very Strong Ps6 Event

G. Gustafsson [1], W. Baumjohann [2], and I. Iversen [3]

[1] Kiruna Geophysical Institute, S-981 27 Kiruna, Sweden
[2] Institut für Geophysik der Universität Münster, Gievenbecker Weg 61, D-4400 Münster, Federal Republic of Germany
[3] Danish Space Research Institute, DK-2800 Lyngby, Denmark

Abstract. A pulsation event has been studied which showed Ps6-type characteristics with a period of about 20 min. Data from a number of magnetometer and riometer measurements over a large area have been combined with balloon measurements of the electric field to obtain a detailed description of the ionospheric current system during the event. The pulsations reported here occured over an interval longer than 3 h and showed large magnetic variations, up to 700 nT A model of the three-dimensional current flow has been derived which agrees with the data. It is concluded that most of the magnetic disturbance measured on the ground is caused by Hall-currents.

Key words: Auroral zone – Magnetic fields – Electric fields – Riometer absorption – Ps6 pulsations – Omega bands – Three-dimensional current systems

Introduction

Long-period geomagnetic pulsations are common during substorms in the auroral zone, pulsations with periods greater than 150 s being called Pi3 type according to international classification. These irregular pulsations have been subdivided into two distinct groups namely PiP (Raspopov 1970) and Ps6 (Saito 1972). The groups are separated mainly by their occurrence in local time and by magnetic signature (Kiselev and Raspopov 1976). Ps6 pulsations are quasi-periodic with periods in the range 10–40 min and are strongest in the Y component of the magnetic field both on the ground and at high altitudes. They occur mainly in the morning hours and are closely correlated with auroral activity.

The magnetic variations reported here showed the characteristics of Ps6 pulsations, but were longer-lasting and stronger than those usually measured. They occurred over a local magnetic time period from 0430 to 0700. The peak to peak amplitudes in the Y and Z components were up to about 700 nT The maximum intensity was measured at a latitude between Kiruna and Tromsö which made this event particularly suitable for study due to the reasonably good coverage of groundbased measurements in that area. Furthermore electric field measurements were carried out from balloons during the same time interval as the magnetic pulsations and they showed a clear correlation. A map showing the location of the observing stations is shown in Fig. 1.

Due to the fact that groundbased magnetic measurements alone cannot distinguish between numerous possible two-or three-dimensional equivalent current systems in the ionosphere and magnetosphere (Fukushima 1976) it is necessary to support them with other measurements in order to get a more complete physical description. Here we have used electric field and cosmic noise absorption measurements to put constraints on the three-dimensional model for the current system.

The characteristics of the Ps6 pulsations have been studied in some detail by Saito (1974, 1978). He proposed a mechanism with field-aligned currents at the eastern and western ends of the substorm westward electrojet and attributed Ps6 to the meandering of the current system during the course of the substorm from the midnight region toward both east and west. Kawasaki and Rostoker (1979) have suggested a three-dimensional current model of narrow longitudinal extent in which antiparallel Birkeland current sheets are linked by equatorial flowing ionospheric current.

In this study the pulsation event of 8 July 1975, an unusually strong and long-lasting Ps6 event, has been studied in detail. The results are compared with earlier suggested mechanisms, and a model of the three-dimensional current flow which agrees with the data is presented.

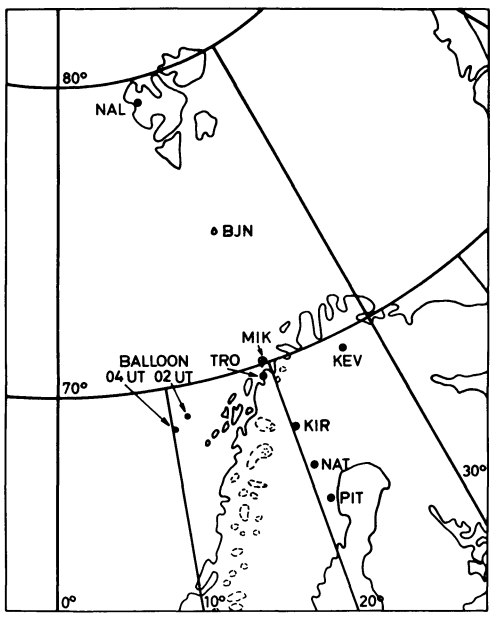

Fig. 1. Map showing the location of the observing stations and the balloon

0340-062X/81/0049/0138/$01.60

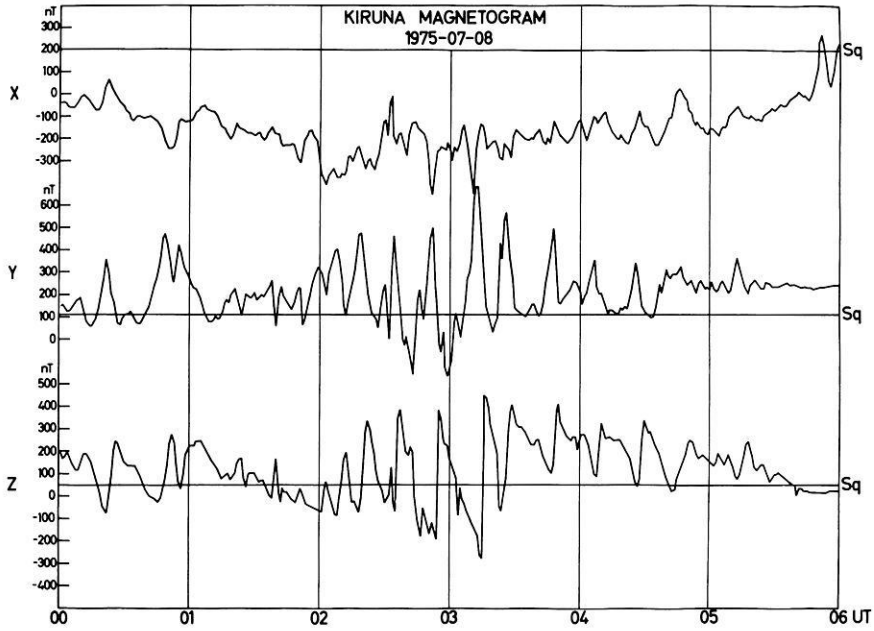

Fig. 2. Standard magnetogram, Kiruna

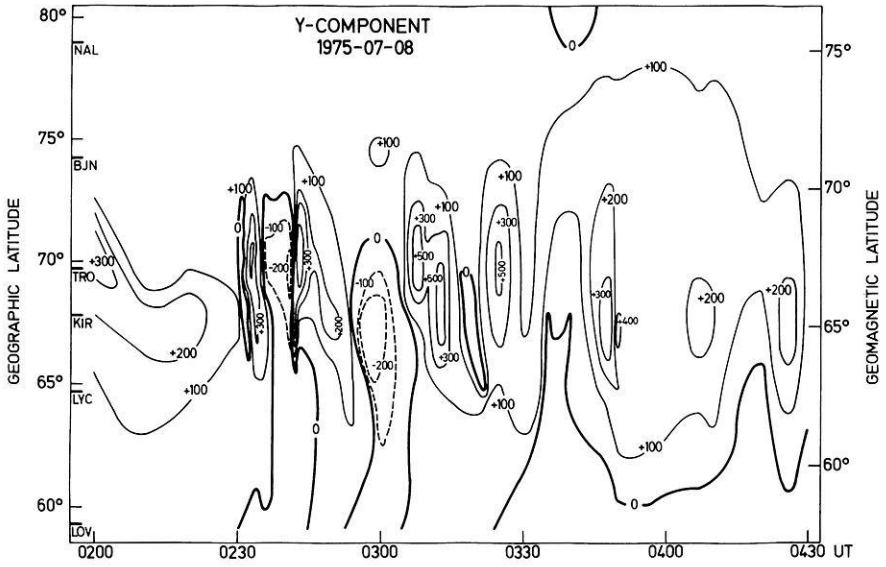

Fig. 3. Boström-Zaitsev diagram for the magnetic Y component

Description of Measurements

The magnetic event observed by ground based magnetometers in Northern Scandinavia, 8 July 1975 between 0200 and 0500 UT, corresponding to 0430–0730 MLT, showed regular periodic variations. Figure 2 shows the magnetogram from Kiruna where large Z component variations (up to 700 nT) were recorded throughout the 3-h period. The positive excursions have time constants of less than one minute while those for the negative excursions are of the order of 20 min. The Y component showed symmetrical changes of up to 600 nT with peaks coinciding with the rapid positive excursions in the X component. The X component showed that the periodic structure was superimposed on a westward electrojet of about 500 nT.

Comparison with 3 years of magnetic recordings at Kiruna showed that the unique features of this event were the very long duration (most events were less than one hour) and the large amplitudes. Data from a chain of standard magnetic stations from 59° to 78° latitude (Fig. 1) have been used to locate the disturbance in latitude. The center varied very little during the night and was generally located between Kiruna and Tromsö, the latitudinal extent being about 5° as shown in Fig. 3 for the Y component in the form of a Zaitsev-Boström diagram (Zaitsev and Boström 1971).

The University of Münster operated a meridian chain of closely spaced magnetometers with high time resolution (10 s) at Mikkelvik (MIK, 70°04′, 19°02′), Kiruna (KIR, 67°50′, 20°25′), Nattavaara (NAT, 66°45′, 21°00′) and Piteå (PIT, 65°15′, 21°35′). These stations constituted the first part of the Scandinavian Magnetometer Array which was built up during the years 1974–1976 (Küppers et al. 1979). The recordings from these stations are shown in Fig. 4. The A and B components are aligned along the x_{KI}, and y_{KI}, axes of the Kiruna system, respectively (cf. Küppers et al. 1979). Since those axes are perpendicular and parallel respectively to Φ_i (KIR) = 64.8° with Φ_i denoting the revised corrected geomagnetic latitude (Gustafsson 1970), A and B components may

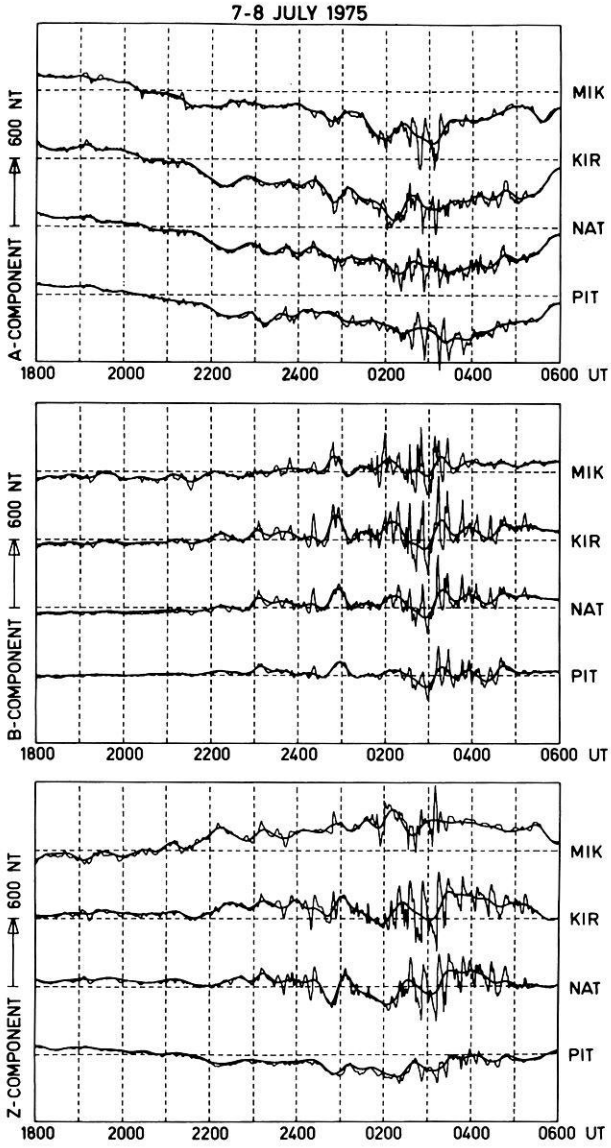

Fig. 4. Münster magnetograms, with low pass filtered ($T > 30$ min) data superimposed

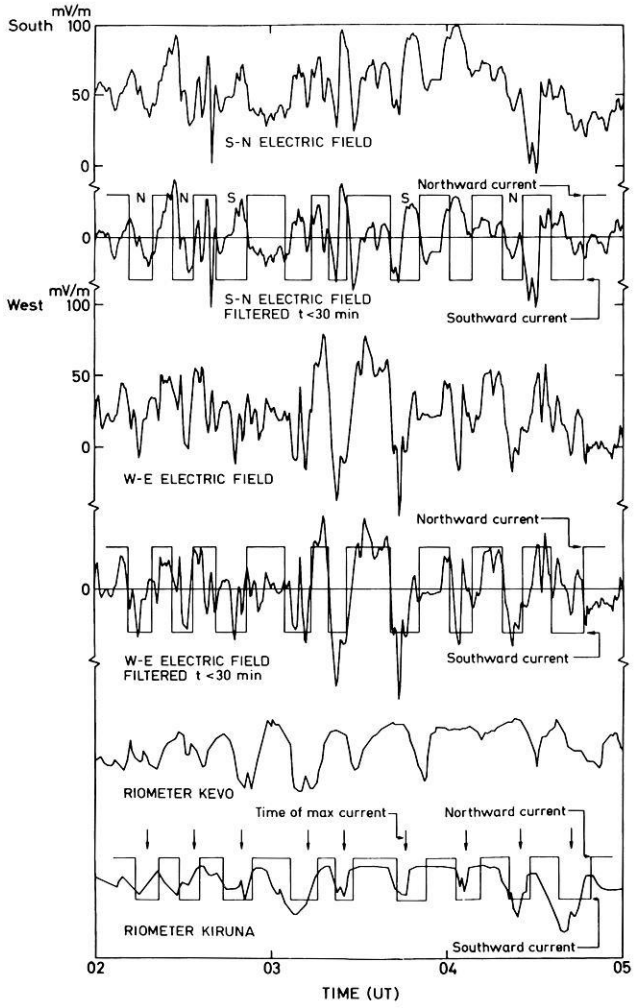

Fig. 5. Balloon electric field data and ground based riometer recordings. The periods of northward and southward magnetic equivalent current vectors, defined from the Münster magnetometers, have been drawn as a "square wave". The "square wave" has been shifted by 3 min when superimposed on the electric field recordings to compensate for the location of the balloon. The *arrows* indicate the time of due southward current

be regarded as corrected geomagnetic north and east components, respectively. In order to separate the 20-min variations from the more slowly varying contribution of the electrojet a filter (with the -6 dB cutoff point at a period of 30 min) has been used; the low frequency signal, i.e., the slowly varying electrojet contribution has also been included in Fig. 4. The disturbance vectors discussed in this paper are measured relative to this new reference line and thus represent the more rapid variations.

In order to derive information about the particle precipitation during the present event, recordings from the riometers at Kiruna and Kevo (69°45′, 27°01′, Fig. 1) have been used. From Fig. 5 it can be seen that the recordings at both stations look very similar but that the absorption recorded at Kevo is delayed relative to Kiruna by 3–5 min. Kevo is located about 350 km east of Kiruna which means that this time delay corresponds to an eastward motion of the maximum absorption region with a velocity of a few km/s.

The 20-min variation is very pronounced in the riometer data and shows good correlation with the magnetic variations of Figs. 2 and 4. Therefore, it may be concluded that the magnetic variations are closely related to precipitation of electrons of a few tens of keV.

The Danish Space Research Institute had a balloon equipped with electric field detectors a few hundred km west of Kiruna during the night discussed in this paper. The balloon was located as follows: at 0200 UT: 68°42′, 11°21′; at 0300 UT: 68°36′, 10°46′; at 0400 UT: 68°30′, 10°00′ (Fig. 1). The horizontal components of the electric field are shown in Fig. 5. These recordings show more structure than the absorption data but the 20-min variation can be identified easily particularly in the east-west component. Peak to peak amplitudes of more than 100 mV/m were recorded. It may also be seen from Fig. 5 that variations with periods greater than 30 min are very small in the east-west component and somewhat larger in the north-south component, although still smaller than the higher frequency components. It was mentioned earlier that a filter technique was used to separate the

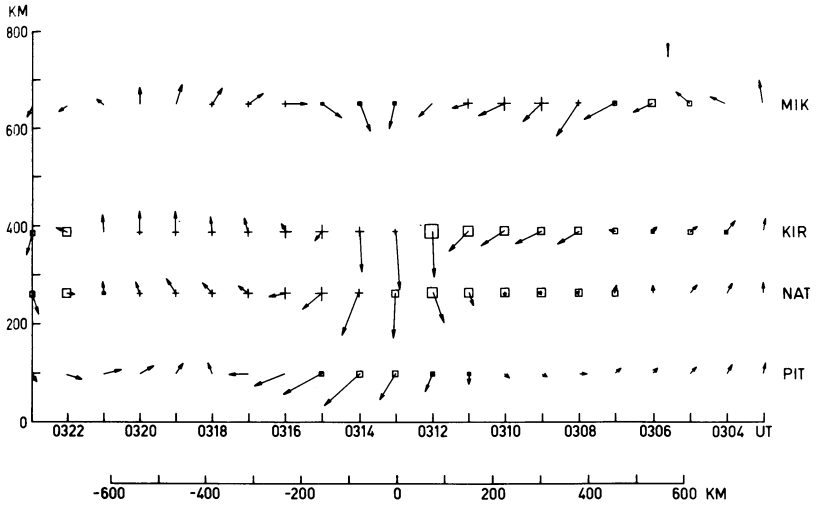

Fig. 6. Two-cell equivalent current structure. The time has been drawn from right to left to illustrate a possible stable structure drifting in the eastward direction over the north-south magnetometer chain. A velocity of 1.3 km/s has been assumed. The signs + and □ refer to positive and negative Z components, respectively

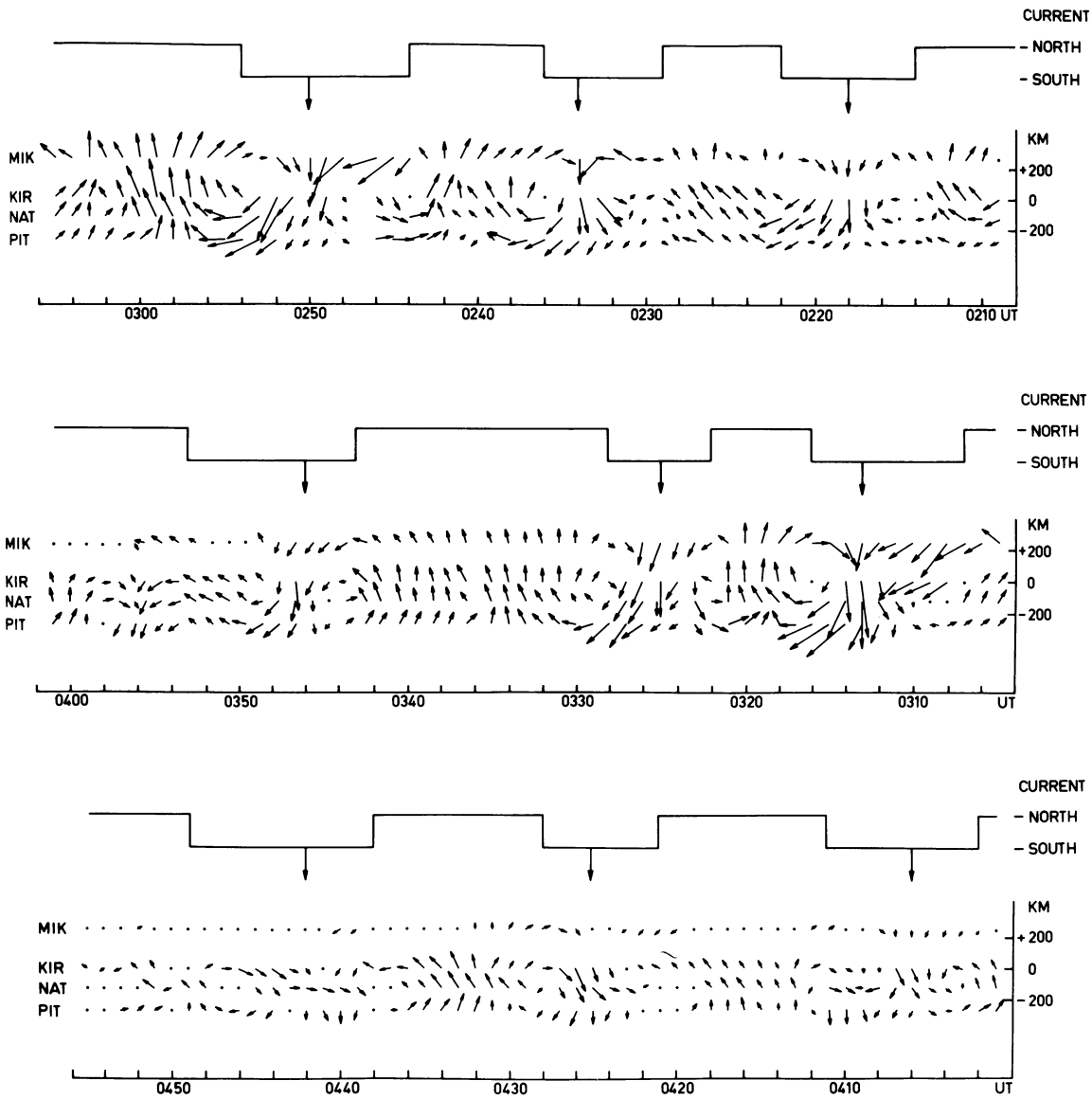

Fig. 7. Continuous current cell structures during the whole event similar to Fig. 6

current system due to the electrojet from the system that is attributable to variations with a period of about 20 min. Figure 4 shows that the northward A component was dominated by a rather steady electrojet during the interval of interest. On the other hand, the eastward B component was dominated by the 20-min variations. In the following a detailed description will be made of the magnetic data after it has been passed through the high pass filter.

In order to indicate the equivalent current pattern associated with the magnetic disturbance, the magnetic disturbance vectors at the four stations operated by the University of Münster have been rotated 90° clockwise. Figure 6 shows the equivalent current pattern for the time interval centered at 0313 UT, when a maximum in the eastward magnetic component corresponding to a southward current vector was observed. The time axis has been drawn from right to left to illustrate a possible stationary system moving in the eastward direction. The same horizontal and vertical distance scale is obtained in Fig. 6 if the assumption is made that the current pattern drifted with an eastward velocity of 1.3 km/s over the meridian-chain magnetic stations (as indicated by the riometer observations). The current pattern shows two cells with a southward current between them, where the largest current was also concentrated. Similar two cell patterns could be drawn for all maxima in the eastward magnetic component during the time interval 0200–0500 UT (see Fig. 7). The center of each current cell separates regions of current vectors with northward and southward components. The "square wave" in Fig. 6 corresponds to time intervals of a northward and southward component of the currents, and the arrows indicate the time of maximum southward current. The same square wave also been superimposed on the riometer recording from Kiruna in Fig. 5. A comparison between the magnetic and riometer data obtained at Kiruna as seen in Fig. 5 shows that the maximum in the absorption was closely correlated with the change from northward to southward directed equivalent currents but the time of maximum southward current was delayed relative to the maximum absorption. Therefore, maximum precipitation of electrons occurred inside the eastern counterclockwise current cell. At the balloon a similar time difference (2–3 min) between the maxima of the measured X-rays and eastward maxima of the electric field was observed (Iversen et al. 1977).

To illustrate the relation between the east-west electric field component and the equivalent current component the same square wave pattern was superimposed on the electric field measurements in Fig. 5, where the wave has been advanced 3 min relative to the balloon recording to compensate for the fact that the electric field measurements were made about 300 km west of Kiruna. The 3-min delay has been estimated from the measured difference between the riometer absorptions at Kiruna and Kevo, assuming the same velocity for the structures west of Kiruna. The observed time difference between the maximum eastward electric field at the balloon and southward current observed at Kiruna varied between 3 and 4 min. Although electric and magnetic measurements were not made at the same locations, there is good evidence that the eastward electric field corresponds to southward equivalent currents. The electric field measurements show considerable high frequency fluctuations and a rather steady bias but a good correspondence can be found between eastward and westward directed excursions of the electric field and southward and northward directed components of the equivalent currents, respectively.

The other component of the horizontal equivalent current (east-west direction) in the two cell pattern has the following behaviour: south of the latitudinal center line through the cells, the direction will change from eastward to westward at the time when the maximum southward current passes the meridian of the stations (see Fig. 6) and the opposite change occurs north of the center line. Therefore, the east-west component of the current vectors will show different temporal variations for recording stations north and south of the latitudinal center of the disturbance. The change from eastward to westward current has been indicated in Fig. 5 on the panel showing the north-sourth electric field component and marked N (also shifted by 3 min, see above). The change in the opposite sense has been marked S. It can be seen from Fig. 5 that the period of southward currents generally corresponds to large changes in the north-south component of the electric field. It may be noted that the electric field measurements of the north-south component showed short period variations, particularly in the time interval 0235–0245 UT, which can also be identified in the magnetic data north of Tromsö (see Fig. 3) but are not shown so clearly in Fig. 7. The lack of correspondence of the north-south electric field in a few cases is not unexpected and a time shift of a few minutes will give a good fit (the two measurements are made about 300 km apart and somewhat non-symmetrical patterns such as changes in drift velocity could cause that difference). The correspondence therefore suggests that the east-west current vectors and the north-south electric vectors are physically correlated.

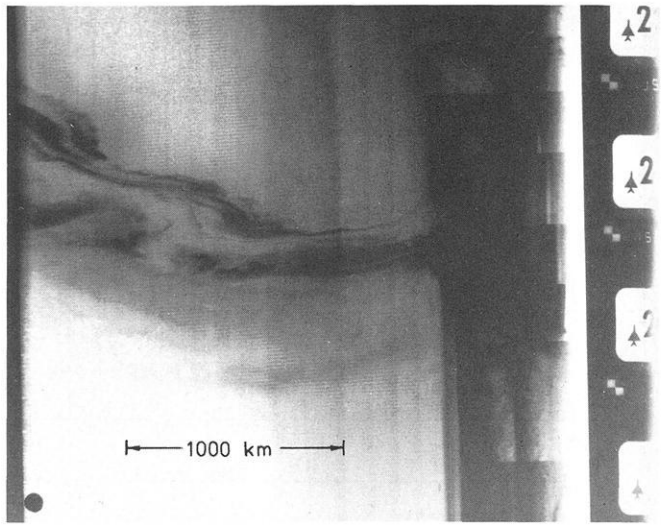

Fig. 8. DMSP picture of the aurora in the southern hemisphere at about 0140 UT

The event discussed here occurred in the middle of the summer and no auroral data could be obtained in Scandinavia. However, the DMSP satellite recorded aurora in the southern hemisphere during the same time interval. Figure 8 shows the auroral image obtained at 0140 UT. Loop structures with a north-south extent of 200–300 km and a separation between the structures of about 900 km were recorded. Similar structures were observed on all the following satellite passes at 0322, 0403 and 0503 UT. The satellite pass at 0545 UT is shown in Fig. 9 where very clear loops can be seen. Comparing this with the magnetic observations in northern Scandinavia it may be concluded that auroral forms were observed in the southern hemisphere auroral zone which could correspond to the eastward travelling magnetic disturbances. A direct comparison cannot be made because the DMSP satellite traversed a region of the auroral oval whose fieldlines are con-

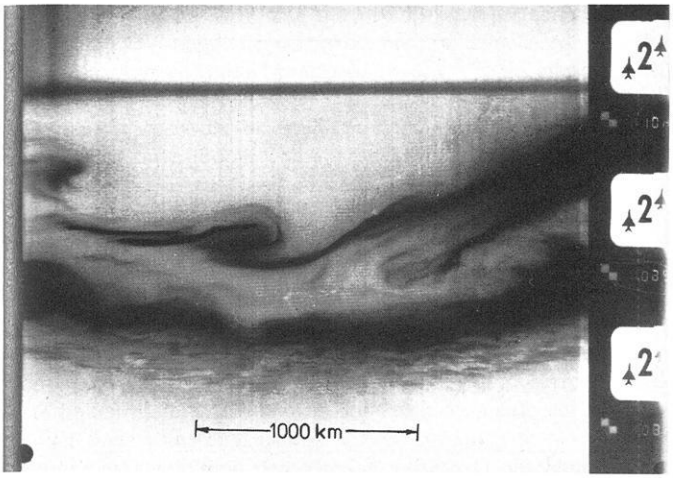

Fig. 9. DMSP picture of the aurora in the southern hemisphere at about 0545 UT

nected in the northern hemisphere to a region several thousand km west of Scandinavia.

Similar temporal variation to that observed by the groundbased and balloon measurements can also be seen in the ATS-6 magnetic field and energetic particle data (ATS-6 was at the time near the Kiruna longitude, personal communications McPherron and McIlwain, respectively). This shows that field aligned currents are observed at the equator along the same field lines. This will be the subject of a later study.

Discussion

The event discussed in this report showed very regular variations in the magnetic field, particularly in the Y and Z components, for several hours. The magnetic variation, with the low frequency component (>30 min) removed has been displayed in Fig. 7 where nine consecutive events with very similar patterns in the equivalent current vectors can be noted. The apparent structure as seen by the magnetometers was a two-cell pattern east and west of a southward current and moving in the eastward direction at a velocity between 1 and 2 km/s, with the higher velocity at the beginning of the disturbance period. The intervals between the patterns were not of exactly equal lengths. The events occurred at 0218, 0234, 0250, 0313, 0325, 0346, 0406, 0425, and 0442 UT which means intervals of 16, 16, 23, 12, 21, 20, 19, and 17 min, respectively, between the events. Using an average velocity of 1.5 km/s this would give a spacing of 1000 to 2000 km between the two-cell structures.

The riometer absorption showed a one to one correlation with the magnetic events. The time when the absorption peak occurred could not be determined very accurately but in general the maximum in the absorption observed over Kiruna occurred close to the center of the eastern counterclockwise current cell and was not coincident with the southward current. This was also supported by the time difference between the electric field and X-ray measurements at the balloon.

The electric field as measured on a balloon a few hundred km west of Kiruna showed variations corresponding to the magnetic variations and the conclusion could be drawn that the orientations of the magnetic and electric field vectors in the east-west direction were coincident, to within the uncertainty of the measurements.

Let us now discuss the three-dimensional current system associated with the observed variations in magnetic and electric fields and riometer absorption. The observed magnetic field pattern could be explained by two possible equivalent current systems. One of these would be similar to a short north-south aligned Boström type 1 system (Boström 1964) and would consist of a pair of field-aligned line currents, about 100 km apart in the region of maximum southward equivalent current, (in Figs. 6 and 7) linked in the ionosphere by a southward directed Cowling current (Baumjohann et al. 1977). The other possible system would be somewhat similar to a Boström type 2 configuration. Here, we again have a pair of field-aligned currents, but now with the upward and downward directed ones located in the eastern and western cells, respectively. If the height-integrated Hall and Pedersen conductivities are homogeneous, the magnetic effects of field-aligned and Pedersen currents will cancel each other and ground-based magnetometers will observe only the clockwise and counter-clockwise Hall current loops around the field-aligned currents (Fukushima 1976; Boström 1977).

The simultaneous observations of electric fields and riometer absorption give some evidence that this second equivalent current system comes closer to the real three-dimensional current system than the first one. Firstly, the maximum riometer absorption, which reflects energetic electron precipitation and hence upward field-aligned current flow (Klumpar et al. 1976; Kamide and Rostoker 1977; Klumpar 1979), tends to be located in the eastern cell and not in the region of maximum southward equivalent current. Secondly, the east-west electric field is parallel to the east-west magnetic field and perpendicular to the north-south equivalent current vectors. This indicated that the magnetic disturbances on the ground are caused solely by Hall-currents, as described in the second model.

In order to support the above discussion and to give some quantitative values, we have constructed a simplified numerical model for the dual equivalent current cell pattern centered on 0313 UT. Following Fukushima (1974) one can calculate the electric field in the ionosphere due to a field-aligned line-current pair by substituting for them a pair of positively and negatively charged fieldlines (the electric charge dissipating as a Pedersen current in the ionosphere from the footprints of those two fieldlines is assumed to be compensated by field-aligned current from the magnetosphere). The radial component of the electric field in the ionosphere is given by (with Q electric charge density per unit height from ionosphere to infinity):

$$E_r(r, \lambda) = \pm Q/4\pi\varepsilon r.$$

By assuming some distribution of height-integrated Hall and Pedersen conductivities, we can compute the ionospheric currents using the ionospheric Ohm's law. Subsequently the field-aligned currents may be determined from the divergence of the horizontal currents.

For numerical modelling we have divided the ionosphere into small cells each 50×50 km and for each cell we have computed electric fields and currents in the manner described above. The height of the ionospheric current layer has been chosen as 100 km above the earth's surface in agreement with the average height of the westward electrojet after Kamide and Brekke (1977). The magnetic fields on the ground caused by the ionospheric-magnetospheric currents and by induced currents in a perfect conductor below 125 km depth (typical depth for periods of the order of 15 min, after Mareschal 1976), have been calculated using the Biot-Savart law.

The model parameters and the resultant equivalent current

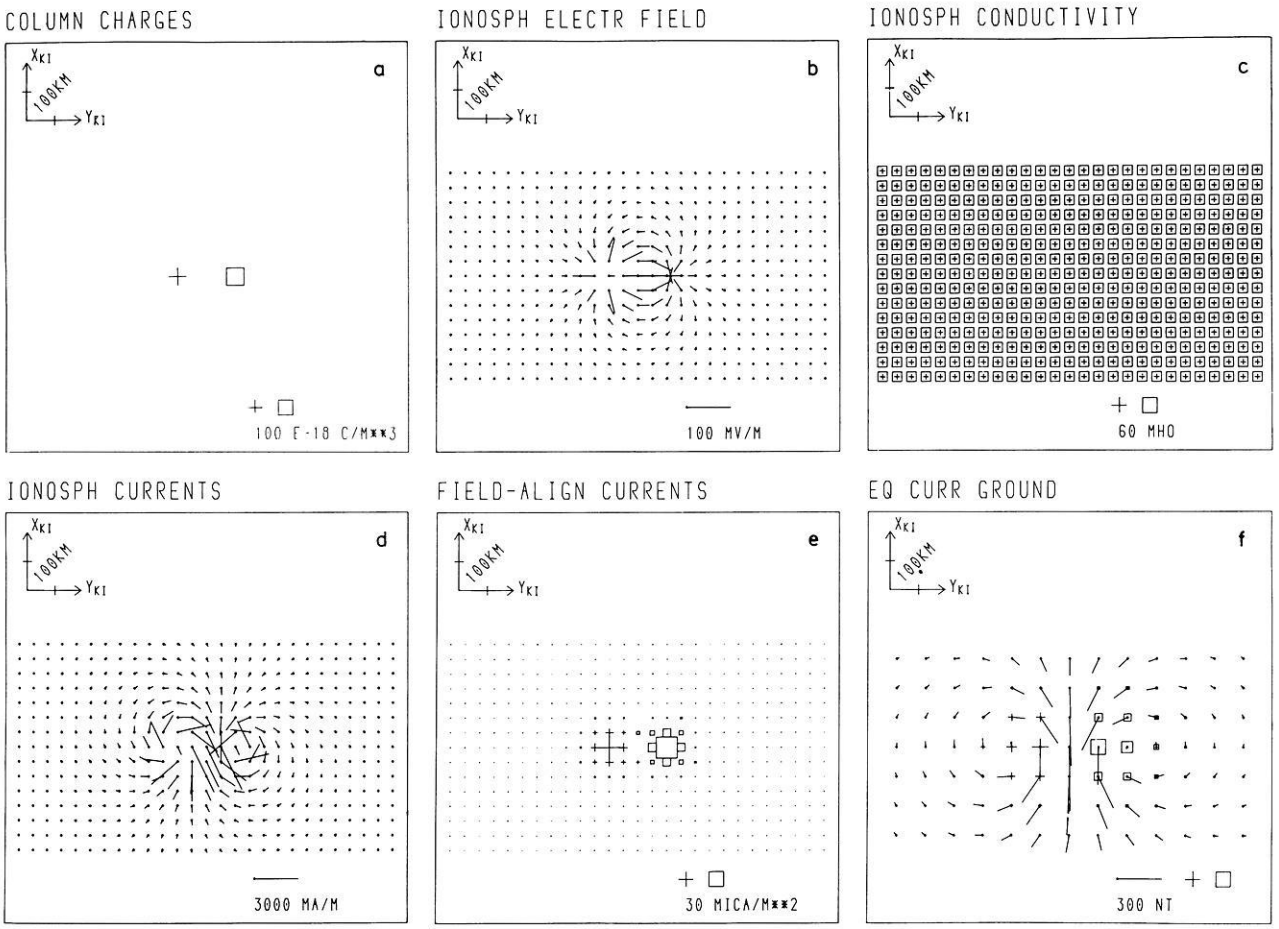

Fig. 10a–f. Parameters of the model current system and resultant equivalent current system on the ground. **a** Location of negatively (*square*) and positively (*cross*) charged fieldlines. **b** Ionospheric electric field vectors attributable to these charges. **c** Ionospheric Hall (*square*) and Pedersen (*cross*) conductivity. **d** Ionospheric currents. **e** Upward (*square*) and downward (*cross*) field aligned currents. **f** Equivalent currents on the ground; *squares* and *crosses* denote negative and positive Z components, respectively

vectors on the ground are displayed in Fig. 10. By assuming a positive and a negative line charge density of $3 \cdot 10^{-7}$ Cm^{-1} and a longitudinal spacing of 200 km (Fig. 10a) we obtained maximum westward electric fields of 70 mVm^{-1} and maximum eastward directed ones of 40 mVm^{-1} (Fig. 10b).

This would be equivalent to peak-to-peak amplitudes of 110 mVm^{-1} and hence in reasonable agreement with the observed values. Furthermore, we have assumed homogeneous Hall and Pedersen conductivities of 40 and 20 Ω^{-1}, respectively, which are in the range of those values given by Horwitz et al. (1978a, b). The assumption of uniform conductivity is probably too simple but good enough for our coarse model. The resultant ionospheric and field-aligned current densities are displayed in Fig. 10d–e and one may note maximum southward height-integrated Hall currents of the order of 2 Am^{-1} and a total up- and downward field-aligned current flow of about $3 \cdot 10^5$ A. The Hall current density of 2 Am^{-1} is very high in comparison to about 500 mAm^{-1} found for the westward electrojet in the morning sector by Sulzbacher et al. (1980) and Baumjohann and Kamide (in press 1981). In addition, the field-aligned current in each of the double cells constitutes 10%–20% of the total field-aligned current flow in the midnight to forenoon sector (Iijima and Potemra 1976, 1978). The equivalent current vectors on the ground, caused by the three-dimensional current system (and the induced currents) are shown in Fig. 10f and we feel that the distribution comes rather close to that observed around 0313 and displayed in Fig. 6. A comparison of horizontal and vertical components of Figs. 6 and 10f. also indicates that a depth of 125 km for the perfect conductor is a good estimate. Otherwise both horizontal and vertical components for the same model could not fit the observed data, since induced currents enhance the horizontal and reduce the vertical components of the external magnetic field. Lastly, we note that our model has been constructed only for one pair of field-aligned currents while the observations show a series of several pairs. However, the pairs are separated by more than 1000 km and since E varies as $1/r$, neighbouring pairs would affect each other's electric field only very slightly and would not change the overall pattern as displayed in Fig. 10.

Several previous studies have been carried out on eastward-travelling features along the morning auroral oval which could be related to the results presented here. Akasofu (1974) and Snyder and Akasofu (1974) reported on eastward drifting Ω-bands. Tsunoda and Fremouw (1976) presented radar auroral signatures with eastward motions in the morning sector. Wescott et al. (1976) found anomalous behaviour of barium streaks in the vicinity of Ω-bands indicating downward acceleration of electrons.

Baumjohann (1979) has shown a case where Ps6 pulsations are actually associated with eastward drifting Ω-bands. He found eastward velocities of 0.8 km s^{-1} and also the equivalent double cell current pattern, consistent with the present results.

Saito (1974) and Saito and Yumoto (1978) investigated several models for Ps6 magnetic perturbations and concluded that the meandering current model proposed by Saito could explain most of the features in the Ps6 data. The model presented in this paper with pairs of east-west oriented, eastward-travelling Hall current loops, when superimposed on a westward electrojet, will produce a current system which is equivalent to the model proposed by Saito. But our model gives the real current configuration while Saito's model is an equivalent one based on magnetic data alone.

Kawasaki and Rostoker (1979) reported eastward-travelling regions of large magnetic perturbations with propagation velocities in the range 0.8–2 km/s, which seem comparable to those found in our event. They modelled the disturbances with a three-dimensional current system where antiparallel Birkeland current sheets were linked by an equatorward flowing ionospheric current. Although their three-dimensional model current system produces the same magnetic field perturbation pattern as our Hall current system, the riometer data, the electric field data and the magnetometer data do not, when taken together, support their model. As mentioned earlier the electron precipitation was located in the eastern cell and not in the region of the maximum equatorward equivalent current and it was also found that the east-west electric field was parallel to the appropriate magnetic field vectors.

Acknowledgements. We are greatly indebted to those past and present members of the magnetometer group at the University of Münster, who were involved in collecting the data. The magnetic observations were performed in cooperation with the Department of Plasma Physics of the Royal Institute of Technology and the Kiruna Geophysical Institute. The magnetometer chain observations and the work of W Baumjohann were supported financially by grants from the Deutsche Forschungsgemeinschaft.

We would like to thank Mrs. H. Ranta, Geophysical Observatory, Sodankylä for the riometer data and Mr. S. Berger, Auroral Observatory, Tromsö for the magnetic data from Tromsö and Ny-Ålesund. The DMSP images were provided by the US Air Force Weather Service.

References

Akasofu, S-I. A study of auroral displays photographed from the DMSP-2 satellite and from the Alaska meridian chain of stations. Space Sci. Rev. **16**, 617–725, 1974

Boström, R. A model of the auroral electrojets. J. Geophys. Res. **69**, 4983–5000, 1964

Boström, R. Current systems in the ionosphere and magnetosphere. In: Radar probing of the auroral plasma, A. Brekke, ed. pp 257–284. Oslo: Universitetsforlaget 1977

Baumjohann, W., Gustafsson, G., Küppers, F. Large-amplitude rapid magnetic variations during a substorm (abstract only). EOS Trans. Am. Geophys. Union **58**, 718, 1977

Baumjohann, W. Spatially inhomogeneous current configurations as seen by the Scandinavian Magnetometer Array. In Proceeding of the International Workshop on Selected Topics of Magnetospheric Physics, Japanese IMS Committee, ed. pp 35–40. Tokyo: 1979

Baumjohann, W., Kamide, Y Joint two-dimensional observations of ground magnetic and ionospheric electric fields associated with auroral zone currents - 2. Three-dimensional current flow in the morning sector during substorm recovery. J. Geomagn. Geoelectr., in press 1981

Fukushima, N. Equivalent current pattern for ground geomagnetic effect when the ionospheric conductivity is discontinuous at the foot of a field-aligned current sheet. Rep. Ionos. Space Res. Jpn. **28**, 147–151, 1974

Fukushima, N. Generalized theorem for no ground magnetic effect of vertical currents connected with Pedersen currents in the uniform-conductivity ionosphere. Rep. Ionos. Space Res. Jpn. **30**, 35–40, 1976

Gustafsson, G. A revised corrected geomagnetic coordinate system. Ark. Geofys. **5**, 595–617, 1970

Horwitz, J.L., Doupnik, J.R., Banks, P.M. Chatanika radar observations of the latitudinal distributions of auroral zone electric fields, conductivities, and currents. J. Geophys. Res. **83**, 1463–1481, 1978a

Horwitz, J.L., Doupnik, J.R., Banks, P.M., Kamide, Y., Akasofu, S-I. The latitudinal distributions of auroral zone electric fields and ground magnetic perturbations and their response to variations in the interplanetary magnetic field. J. Geophys. Res. **83**, 2071–2084, 1978b

Iijima, T., Potemra, T.A. The amplitude distribution of field-aligned currents at northern high latitudes observed by Triad. J. Geophys. Res. **81**, 2165–2174, 1976

Iijima, T., Potemra, T.A. Large-scale characteristics of field-aligned currents associated with substorms. J. Geophys. Res. **83**, 599–615, 1978

Iversen, I.B., Madsen, M.M., Ullaland, S., Brönstad, K., Bjordal, J. Electric field and X-ray measurements with balloons during a magnetic storm. Presented at IAGA Assembly 1977

Kamide, Y., Brekke, A. Altitude of the eastward and westward auroral electrojets. J. Geophys. Res. **82**, 2851–2853, 1977

Kamide, Y., Rostoker, G.. The spatial relationship of field-aligned currents and auroral electrojets to the distribution of nightside auroras. J. Geophys. Res. **82**, 5589–5608, 1977

Kawasaki, K., Rostoker, G. Perturbation magnetic fields and current systems associated with eastward drifting auroral structures. J. Geophys. Res. **84**, 1464–1480, 1979

Kiselev, B.V., Raspopov, O.M. Excitation of Pi3 type pulsations during substorm. In. Proceedings of IAGA meeting on unmanned observatories in Antarctica, T Nagata, ed. pp 88–96. Tokyo: 1976

Klumpar, D.M. Relationship between auroral particle distributions and magnetic field perturbations associated with field-aligned currents. J. Geophys. Res. **84**, 6524–6532, 1979

Klumpar, D.M., Burrows, J.R., Wilson, M.D. Simultaneous observations of field-aligned currents and particle fluxes in the post-midnight sector. Geophys. Res. Lett. **3**, 395–398, 1976

Küppers, F., Untiedt, J., Baumjohann, W., Lange, K., Jones, A.G. A two-dimensional magnetometer array for ground-based observations of auroral zone electric currents during the International Magnetospheric Study (IMS). J. Geophys. **46**, 423–450, 1979

Mareschal, M. On the problem of simulating the earth's induction effects in modelling polar magnetic substorms. Rev. Geophys. Space Phys. **14**, 403–409, 1976

Raspopov, O.M. Sur la diagnostique des changes electriques dans la magnetosphere de la terre. Ann. Geophys. **26**, 751–759, 1970

Saito, T : Some topics for the study of the mechanism of magnetospheric substorm by means of rocket observation in the auroral zone. Antarctic Record **43**, 65–69, 1972

Saito, T Examination of the models for the substorm-associated magnetic pulsation Ps6. Sci. Rep. Tohuku Univ. Ser. 5 Geophys. **22**, 35–59, 1974

Saito, T Long-period irregular magnetic pulsation, Pi3. Space Sci. Rev. **21**, 427–467, 1978

Saito, T., Yumoto, K. Comparison of the two-snake model with the observed polarization of the substorm associated magnetic pulsation Ps6. J. Geomagn. Geoelectr. **30**, 39–45, 1978

Snyder, A.L., Akasofu, S-I. Major auroral substorm features in the dark sector observed by a USAF DMSP satellite. Planet. Space Sci. **22**, 1511–1517, 1974

Sulzbacher, H., Baumjohann, W., Potemra, T.A. Coordinated magnetic observations of morning sector auroral zone currents with Triad and the Scandinavian Magnetometer Array: a case study. J. Geophys. **48**, 7–17, 1980

Tsunoda, R.T., Fremouw, E.J. Radar auroral substorm signatures, 2. East-west motions. J. Geophys. Res. **81**, 6159–6168, 1976.

Wescott, E.M., Stenbaek-Nielsen, H.C., Hallinan, T.J., Davis, T.N., Peek, H.M. The Skylab Barium plasma injection experiments, 2. Evidence for a double layer. J. Geophys. Res. **81**, 4495–4502, 1976

Zaitsev, A.N., Boström, R. On methods of graphical displaying of polar magnetic disturbances. Planet. Space Sci. **19**, 643–649, 1971

Received June 27, 1980; Revised Version October 20, 1980
Accepted October 20, 1980

J Geophys (1981) 49:146–148

Journal of Geophysics

Variability of Solar EUV Fluxes and Exospheric Temperatures

G. Schmidtke, N. Börsken, and G. Sünder
Fraunhofer-Institut für Physikalische Meßtechnik, Heidenhofstrasse 8, D-7800 Freiburg, Federal Republic of Germany

Abstract. The response of exospheric temperature to variations in solar EUV radiation was measured by the AEROS-EUV spectrometer. Correlation of these parameters is strongly impeded by the competing influence of the solar wind and by the changes in EUV heating efficiency. While the comparison of exospheric temperatures with those from the MSIS model gives rather good agreement for geomagnetically quiet conditions, the experimental data are significantly higher than the model data for disturbed conditions.

Key words: Aeronomy – Upper atmosphere – Energy budget

Introduction

Extreme ultra-violet (EUV) flux variations have been measured aboard many rockets and satellites (Hall and Hinteregger 1970; Timothy and Timothy 1970; Schmidtke 1976; Hinteregger 1977; Hinteregger 1979a). Observation of the atmospheric response to these variations, changes in the exospheric temperature for example, is rather difficult. One way to achieve this goal is the application of atmospheric EUV extinction analysis to occultation measurements (Hinteregger and Hall 1969; Schmidtke et al. 1974a; Hinteregger and Chaikin 1977). The purpose of this note is to present results from the AEROS-EUV spectrometer (Schmidtke et al. 1974b), which monitored variations of the solar EUV flux and provided data from which exospheric temperatures could be derived.

Measurements

During the periods December 1972–August 1973 and July 1974–September 1975 aboard the satellites AEROS-A and -B, respectively, solar EUV fluxes in the spectral range 16–106 nm were measured. In addition height profiles of atomic oxygen within the

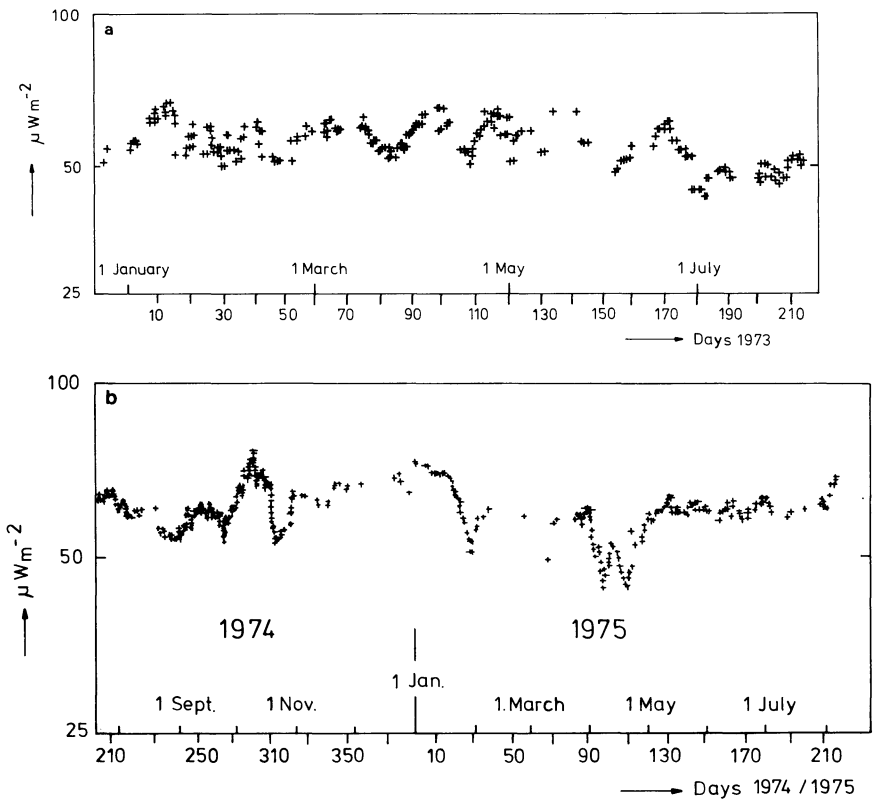

Fig. 1a, b. Temporal variation of the reference emission He 58.4 nm. **a** for AEROS-A, **b** for AEROS-B

0340-062X/81/0049/0146/$01.00

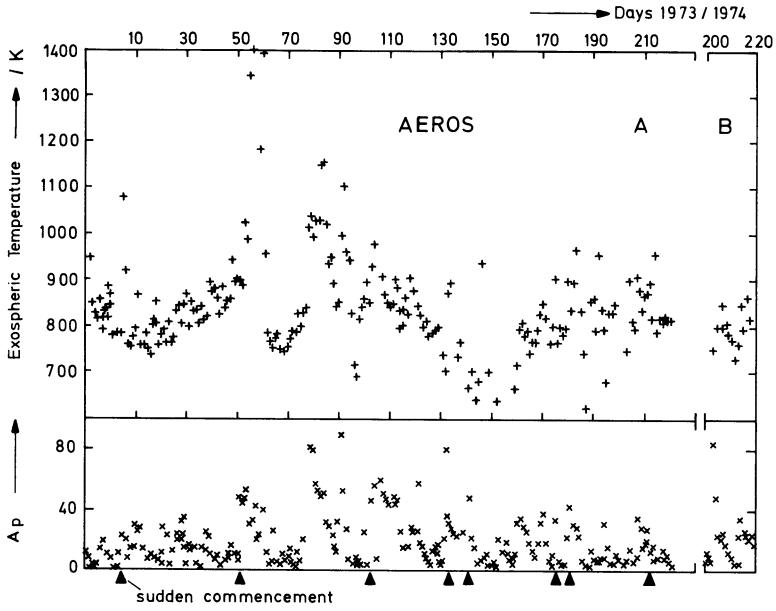

Fig. 2. Exospheric temperatures derived from EUV extinction measurements and A_P Index

height range 200–450 km approximately were derived from occultation measurements at selected solar emissions (Schmidtke et al. 1974a).

For the period of AEROS-A a decrease of the solar EUV flux of about 30% has been reported with the declining Solar Cycle 20 (Schmidtke 1976, Schmidtke 1978). To demonstrate the variability of the solar EUV radiation in more detail, daily averages of the solar emission of helium 58.4 nm radiation are shown in Fig. 1a. Since this line is representative of the chromospheric emissions comprising most of the EUV energy, it is proposed as a 'chromospheric reference' line (Hinteregger, in press 1981). Although the variability of the coronal emissions is much stronger, their contribution to the total EUV flux is relatively small. During the AEROS-B mission no significant long-term flux variation was measured as can be seen in Fig. 1b. A small difference in the flux levels of AEROS-A and B is caused by calibration uncertainties in the absolute values (about $\pm 20\%$ in this case).

The solar 'EUV minimum' first reported by Hinteregger (1977) is seen clearly (Fig. 1b). The agreement of the absolute solar flux numbers from Atmospheric Explorer-C and AEROS-B is also satisfactory for the overlapping periods of both satellite missions, in view of the experimental difficulties.

In Fig. 2 daily average exospheric temperatures are shown in the upper part. The temperatures are derived from scale heights (Schmidtke et al. 1974b) and extrapolated by the Bates formula. This method is also applicable to geomagnetically disturbed conditions, since the optical depth measurement includes the product of the number density times the scale height. For these grazing incidence conditions of the solar radiation in the upper atmosphere the rays traverse a horizontal distance of, for example, about 800 km sensing a height interval of 50 km, which is reasonable for the scale height of atomic oxygen.

The measurements were made at low southern latitudes at the end of 1972 and beginning of 1973, at high latitudes for days 80–220 in 1973, and at mid-latitudes for days 200–220 in 1974.

Comparing Fig. 2 with Fig. 1, it can be seen that the exospheric temperatures reflect neither the solar rotations as seen clearly in the EUV fluxes nor the long-term EUV flux decrease. Geomagnetic activity has a stronger impact on exospheric temperatures than solar EUV activity. The temperature peaks are well correlated with geomagnetic activity such as sudden commencements and increases in A_P index (most pronounced for the events on 3 January, 21 February and 1 March 1973). However, because of operational constraints on the satellite, not all of the geomagnetic events could be traced by this experiment. Intercomparison with similar data from Atmospheric Explorer-C (Hinteregger 1979b) shows this to be consistent.

In addition Hinteregger (1978) reported rather constant temperatures while the EUV radiation increased significantly at the beginning Solar Cycle 21.

In Fig. 3 the AEROS data are compared to the MSIS model, orbit by orbit. Good agreement is found for low A_P values (bearing in mind the uncertainty in the EUV absorption cross section of about 10%–20%), whereas the MSIS model represents too low temperatures for higher A_P's.

Conclusions

The comparison of the relative and absolute solar EUV fluxes, as measured aboard AEROS-B, and of the derived exospheric temperatures, with data from the Atmospheric Explorer-C, show a comfortable agreement. The derived exospheric temperatures are in rather good agreement with the MSIS model for geomagnetic quiet conditions. However, the temperatures of the MSIS model seem to be too low for higher A_P's. More importantly, the decrease in the solar EUV radiation by about 30% from the end of 1972 to August of 1973 seems to be compensated. The decrease of $\Delta Q_{EUV} \approx 0.7\ \mathrm{mWm}^{-2}$ implies, for the whole earth, a decrease of about 10^{11} W (or 10^{18} erg s^{-1}), which is a good order of magnitude for the energy involved in a geomagnetic storm (Akasofu 1979). Joule heating has long been recognized as a major contributor to the energy budget of the upper atmosphere (Cole 1962). Particle dissipation is another energy source. In general, the conversion of the solar wind is probably more important for the upper atmosphere than so far recognized, especially under solar minimum conditions. Changes in the heating efficiency of the solar EUV radiation (Torr et al., in press 1981) might also explain, at least

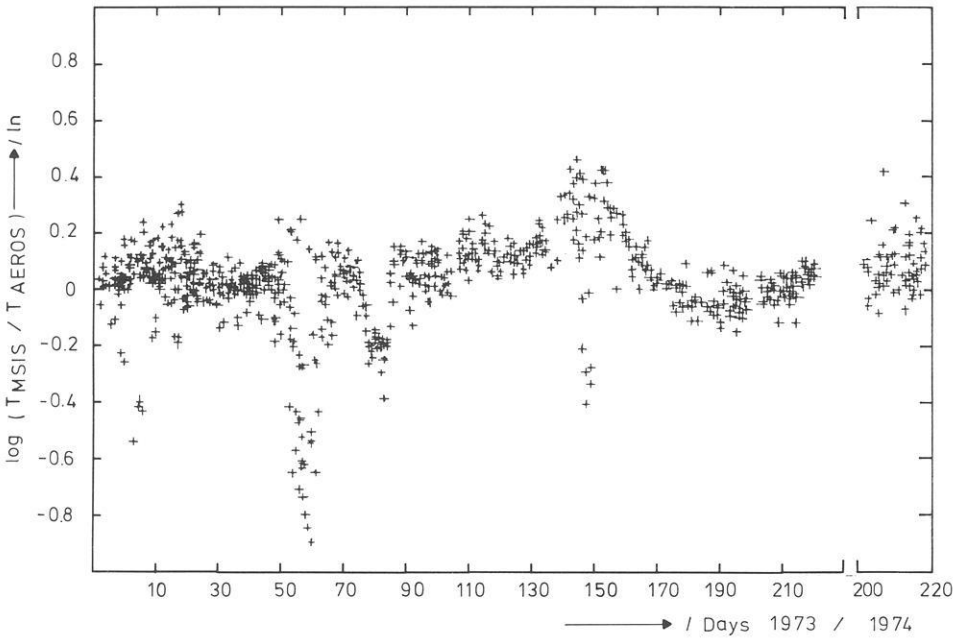

Fig. 3. Comparison of temperatures MSIS/AEROS

in part, the poor correlation of EUV flux and exospheric temperature variations.

Acknowledgements. This work was sponsored by the Bundesministerium für Forschung und Technologie (Grant WRK 274).

References

Akasofu, S.-L.: Interplanetary energy flux associated with magnetospheric substorms. Planet. Space Sci. **27**, 425–431, 1979

Cole, K.D.: Joule heating of the upper atmosphere. Aust. J. Phys. **15**, 223–235, 1962

Hall, L.A., Hinteregger, H.E.: Solar radiation in the extreme ultra-violet and its variation with solar rotation. J. Geophys. Res. **75**, 6959–6965, 1970

Hinteregger, H.E., Hall, L.A.: Thermospheric densities and temperatures from EUV absorption measurements by OSO-III. Space Res. **IX, 519–529, 1969**

Hinteregger, H.E.: EUV flux variation during end of solar cycle 20 and beginning cycle 21, observed from AE-C satellite. Geophys. Res. Lett. **4**, 231–234, 1977

Hinteregger, H.E., Chaikin, L.M.: EUV absorption analysis of thermospheric structure from AE-Satellite observations of 1974–1976. Space Res. **XVII**, 525–532, 1977

Hinteregger, H.E.: Development of solar cycle 21 observed in EUV spectrum and atmospheric absorption. Proc. Solar-Terrestrial Physics Symposium, Innsbruck, 1978

Hinteregger, H.E.: Preliminary results of EUVS experiment on AE-E, presented at NASA/AAS 'Symposium on the study of the solar cycle from space', Wellesley College, Mass., 1979a

Hinteregger, H.E.: private communication, 1979b

Hinteregger, H.E.: Representations of solar EUV fluxes for aeronomical applications. Space Res. **XXI**, in press 1981

Schmidtke, G., Rawer, K., Fischer, Th., Lotze, W.: Atomic Oxygen profiles determined by EUV absorption analysis. Space Res. **XIV**, 169–172, 1974a

Schmidtke, G., Schweizer, W., Knothe, M.: The AEROS-EUV spectrometer. J. Geophys. **40**, 577–584, 1974b

Schmidtke, G.: EUV indices for solar-terrestrial relations. Geophys. Res. Lett. **3**, 573–576, 1976

Schmidtke, G.: Todays knowledge of the solar EUV output and the future needs for more accurate measurements for aeronomy. Planet. Space Sci. **26**, 347–353, 1978

Timothy, A.F., Timothy, J.G.: Long-term intensity variations in the solar helium II Lyman-alpha line. J. Geophys. Res. **75**, 6950–6958, 1970

Torr, M.R., Richards, P.G., Torr, D.G.: Solar EUV energy budget of the thermosphere. Space Res. **XXI**, in press 1981

Received August 8, 1980; Revised Version November 15, 1980
Accepted December 22, 1980

J Geophys (1981) 49:149–152

Journal of Geophysics

Short Communication

Paleomagnetism of Quaternary and Miocene Lavas from North-East and Central Morocco

D. Najid[1], M. Westphal[2], and J. Hernandez[3]

[1] Service de Physique du Globe, Charia Ibn Batouta, B.P. 1014, Rabat, Morocco
[2] Institut de Physique du Globe, 5 rue Descartes, F-67084 Strasbourg Cedex, France
[3] Laboratoire de Pétrologie, Université Pierre et Marie Curie, 4 place Jussieu, F-75230 Paris Cedex, France

Key words: Paleomagnetism – Morocco – Quaternary – Miocene

Introduction

One of the main deficiencies in our knowledge of the behaviour of the earth's ancient magnetic field concerns its magnitude and the long-term stability of its non dipole terms. It has usually been assumed that non dipole terms vanish when field directions are averaged over a sufficient long time. But during the last ten years, several authors (Wilson 1970, 1971; Watkins 1972; Creer et al. 1973) have shown that some non dipole terms seem to persist. Therefore it is necessary to accumulate a large body of paleomagnetic data, for several periods and from widely distributed regions.

We now present new results which complete an initial study made by Hamzeh and Westphal (1973) on rocks from north-eastern Morocco.

Geological Setting

Several volcanic phases are known in Morocco; the most recent being Miocene and Quaternary (Michard 1976).

The Miocene volcanics are restricted to the north-eastern part of the Rif area. All K–Ar date determinations (Bellon 1976) give upper Miocene ages spread between 13 and 5 m.y.

In the Mellila-Nador and Ras Tarf regions, the lavas are mainly calcalkaline (andesites, K-andesites to rhyolites) and are associated with alkaline-trachytic plugs (Hernandez 1975). In addition, a granodiorite batholite of the same age has been recognized in the same area.

The Jebel Guilliz, 100 km south of the area described above, is characterized by alkaline, intermediate and acidic lavas, going from trachyandesites to trachytes.

The last phase, of early to late Quaternary age, is alkaline and basaltic to hawaiitic. It can be found in the above regions

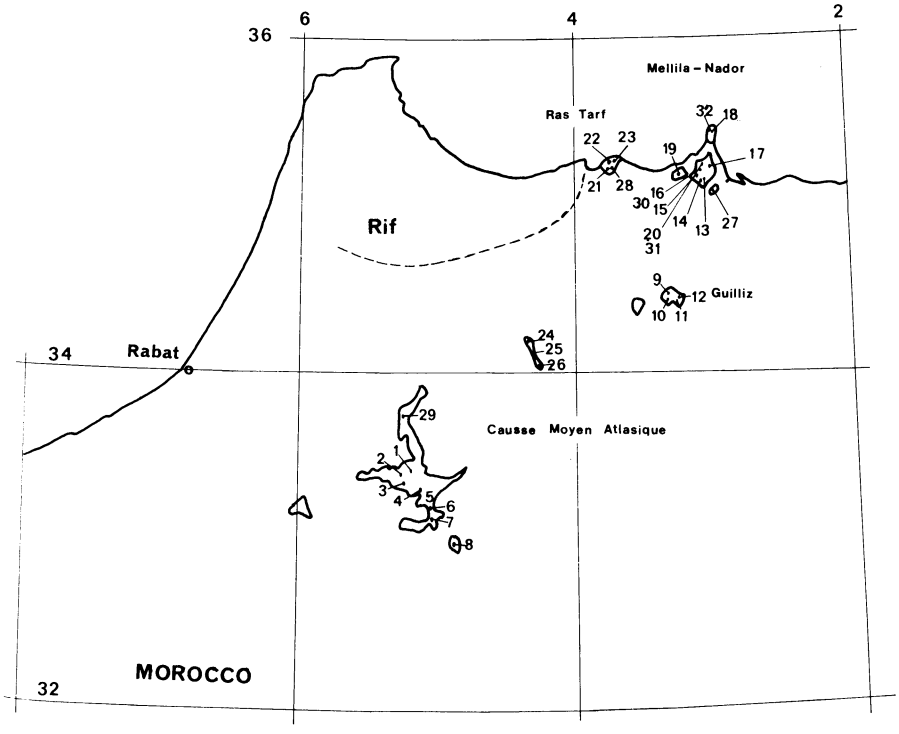

Fig. 1.
Location of sampling regions and site numbers

0340-062X/81/0049/0149/$01.00

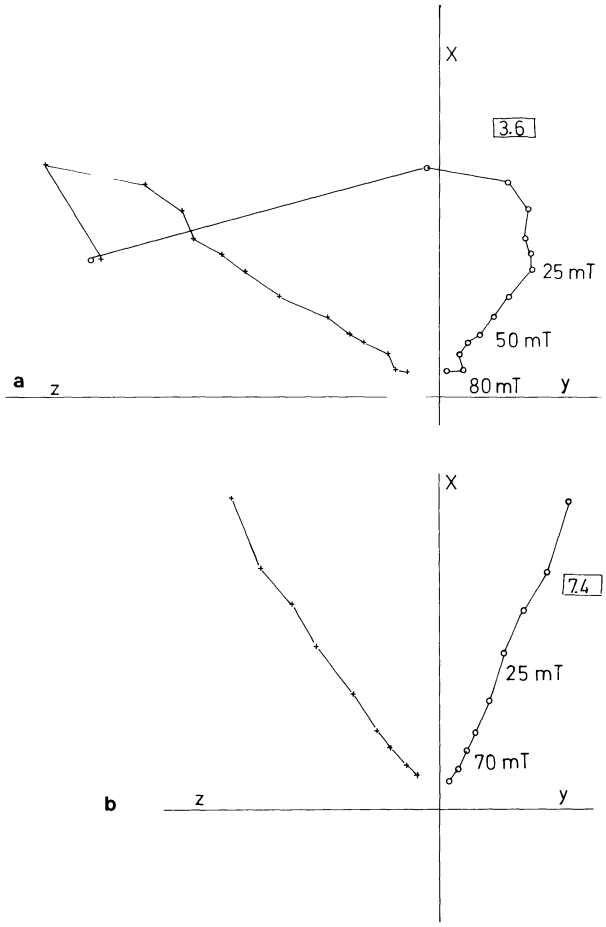

Fig. 2a, b. A.F. demagnetization patterns for two Quaternary rocks samples. *Open circles*: vector end-points in the XY plane, *crosses*: vector end-points in the XZ plane

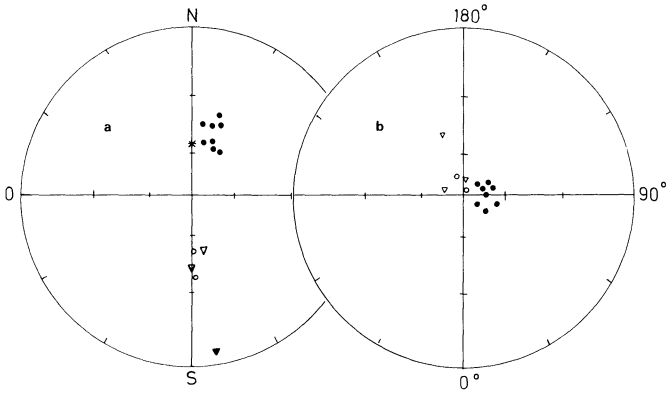

Fig. 3a, b. Quaternary sites. **a** Site mean directions. *Black symbols*. positive inclination, *open symbols*. negative inclination, *circles*. present study, *triangles*: Hamzeh and Westphal 1973, *star* represents axial dipole field. **b** Corresponding virtual geomagnetic poles (northern hemisphere). *Black symbols*. normal directions, *open symbols*. reversed directions

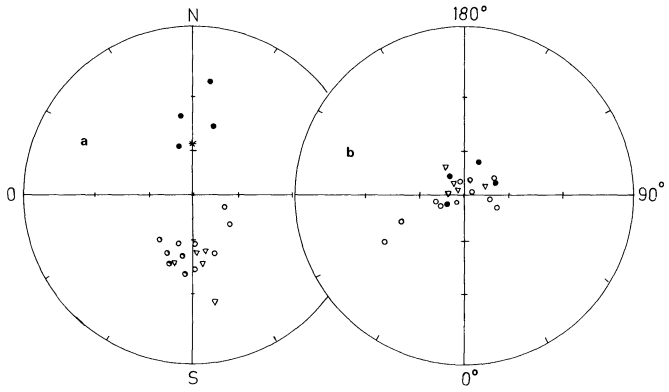

Fig. 4a, b. Miocene sites. **a** Mean site directions, **b** corresponding virtual geomagnetic poles; same conventions as for Fig. 3

and also in the 'Causse moyen Atlas', where it seems to be very recent, sometimes lying in recent wadi terraces which, however, have not yet been accurately dated.

Sampling and Measurements

Five or six hand samples were taken from each outcrop. The orientation was recorded using a magnetic compass and also, if possible, using a sun compass. The samples were then sawn into 50 mm cubes or cored to give standard 25 mm cylinders. The measurements were made with an astatic magnetometer and a Digico spinner.

The presence of a viscous remanent magnetization was checked by two separate measurements as proposed by Thellier and Thellier (1959). Usually the viscous component acquired in a fortnight was less than 5% of the N.R.M.

The samples were then stepwise demagnetized by an alternating field (A.F.) of up to 900 Oe. Some samples, of both Quaternary and Miocene age, possessed a fairly stable single component of magnetization (Fig. 2a), but other samples showed a strong secondary component which could usually be removed by A.F. demagnisation at about 250 Oe (Fig. 2b), revealing a more stable component of magnetization. The within-site scatter was then strongly reduced and a good characteristic magnetization could be defined (Fig. 3).

For a few sites, mainly Quaternary basalts, secondary components were too strong to be removed. The initial magnetization seemed to have been destroyed and replaced by a very strong magnetization which probably originated from lightning strokes. The scatter of directions remained greater than acceptable and these sites were discarded for the calculation of the overall mean (Tables 1 and 2).

Discussion

A.F. demagnetization showed a final, stable, characteristic component of magnetization for most of the samples. Secondary components were either caused by lightning strokes, or for some samples. by sawing or drilling effects, as shown by Burmester (1977) and Lauer (1978). Tests made by acid leaching showed that this secondary magnetization was located near the surface of the sample. A.F. demagnetization seemed to remove this component. The characteristic remanent magnetization has either normal or reversed polarity near to the present field direction, probably parallel to the original magnetization.

Table 1. Mean directions and poles for Quaternary sites

Mean direction.

$N=10$ $D_m=14.5°$ $I_m=50.0°$ $k=51.9$ $\alpha_{95}=6.7°$

With bracketed results.

$N=13$ $D_m=8.8°$ $I_m=45.9°$ $k=22.3$ $\alpha_{95}=8.9°$

Mean pole.

$N=10$ 77.1° N, 95.7° E $k=36.6$ $\alpha_{95}=8.0°$

Site No./Locality	N	D_m (°)	I_m (°)	k	α_{95}	Poles		Polarity
						lat (° N)	long (° E)	
Causse moyen atlasique								
1/Azrou	6	Directions too scattered						
2/Azrou	4	16	45	32	17	74	107	N
3/Azrou	5	29	57	162	6	66	68	N
4/Azrou (J. Hébri)	5	Directions too scattered						
5/Timahdit	5	Directions too scattered						
6/Timahdit	5	Directions too scattered						
7/Oued Guigou	5	19	39	663	3	70	115	N
8/Foum Khneg	4	21	40	230	6	69	109	N
29/Sebâ-âyoun	6	10	45	552	3	78	124	N
24/Sidi Abdallah	6	Directions too scattered						
25/Sidi Abdallah	5	Directions too scattered						
26/Sidi Abdallah	5	14	56	230	5	78	71	N
Ras Tarf region								
21/Ras Tarf	7	21	52	303	4	72	90	N
28/Ras Tarf	3	33	55	156	10	63	76	N
J. Guilliz								
10/J. Guilliz	3	(177)	(−39)	(27)	(24)	(77)	(190)	R
*7/J. Guilliz	5	(168)	(5)	(8)	(30)	(51)	(198)	R
*8/J. Guilliz	4	(180)	(−45)	(19)	(22)	(81)	(177)	R
Mellila – Nador region								
*15/Tiraka (Nador)	5	162	−52	97	8	75	262	R
27/Nador	5	180	−52	276	5	87	178	R

N = number of samples used in the statistic
D_m, I_m = mean declination and inclination
k = Fisher precision parameter
α_{95} = radius of 95% confidence cone
Lat, long = latitude and longitude of corresponding virtual geomagnetic pole

N = normal polarity
R = reversed polarity
Bracketed results = low confidence mean directions
Starred sites = Hamzeh and Westphal (1973) previous results

Results

Quaternary Lavas

Most of the sites are on apparently recent flows from the Causse Moyen Atlasique which all have normal magnetization. The between-site scatter is low and the mean direction is somewhat offset to the east. The few other results are normal or reversed and are nearer to the present north-south direction (Guilliz, Ras Tarf, Mellila). The reversed directions are certainly older than the Matuyama-Brunhes transition. The mean pole positon is significantly different from the present geographic pole.

Miocene Lavas

Both polarities occur. The mean direction is centred in the present north-south direction but the mean inclination is slightly lower than that of the geocentric axial dipole field.

Special mention must be made of the two sites from Cap des Trois Fourches which gave significantly different directions from other sites. The difference may be explained in two ways; either they may represent a true dirction of the field, or the flows have been tilted by about 30° towards the north-east. This tilt cannot be measured but is geologically realistic.

The mean pole position does not exactly coincide with the present geographic pole. The difference is statistically significant for the Quaternary sites but not for the Miocene sites.

Table 2. Mean directions and poles for Miocene sites

Mean directions:

$N=18$ $D_m=182.0°$ $I_m=-49.1°$ $k=35.7$ $\alpha_{95}=5.9°$

Including sites from Cap des Trois Fourches:

$N=20$ $D_m=177.9°$ $I_m=-51.7°$ $k=22.1$ $\alpha_{95}=7.1°$

Mean pole:

$N=18$ 85.8° N, 161.5° E $k=29.6$ $\alpha_{95}=6.4°$

Site No./Locality	N	D_m (°)	I_m (°)	k	α_{95}	Poles		Polarity
						lat (° N)	long (° E)	
J. Guilliz Region								
9/J. Guilliz	5	182	−42	107	8	80	169	R
11/J. Guilliz	5	186	−53	895	3	85	97	R
12/J. Guilliz	5	160	−55	506	3	73	278	R
*1-2-5/J. Guilliz	13	167	−27	3075	2	67	210	R
*3/J. Guilliz	4	167	−56	410	5	80	280	R
*4/J. Guilliz	4	195	−47	259	6	76	108	R
*Guilliz	5	174	−54	627	3	85	264	R
Ras Tarf region								
22/Ras Tarf	4	10	24	784	3	65	152	N
23/Ras Tarf	5	Results too scattered						
Mellila Nador region								
13/Massif du Gourougou	5	194	−59	194	5	78	292	R
14/Segangane	5	196	−46	50	11	74	112	R
15/Oulad Minoun (Gourougou)	5	177	−59	490	3	85	331	R
16/Souk Télat	5	347	58	171	6	79	289	N
17/Atalayoum	6	179	−45	89	7	81	185	R
19/Amjar	4	19	47	114	9	72	106	N
20/Tidienit	8	201	−52	67	7	73	88	R
30/Télat	4	350	39	59	12	74	211	N
31/Tidienit	4	213	−58	1170	3	64	68	R
*Isaroualène (Nador)	5	174	−48	48	11	82	215	R
32/Cap des 3 Fourches	4	123	−60	687	4	45	293	R
18/Cap des 3 Fourches	5	107	−64	97	8	36	302	R

Same conventions as for Table 1.

References

Bellon, H.: Séries magmatiques néogènes et quaternaires du pourtour de la Méditerranée occidentale, comparées dans leur cadre géochronométrique. Implications géodynamiques. Thesis, Paris, 1976

Burmester, R.F.: Origin and stability of drilling induced remanence. Geophys. J.R. Astron. Soc. **48**, 1–4, 1977

Creer, K.M., Georgi, D.T., Lowrie, W.: On the representation of the Quaternary and late Tertiary geomagnetic fields in terms of dipoles and quadrupoles. Geophys. J.R. Astron. Soc. **33**, 323–345, 1973

Hamzeh, R., Westphal, M.: Etude paléomagnétique de formations volcaniques tertiaires et quaternaires du Maroc oriental. Earth Planet. Sci. Lett. **20**, 28–34, 1973

Hernandez, J.: Sur le caractère shoshonitique des andésites du Gourougou, Rif oriental (Maroc). C.R.Acad. Sci. Paris **280**, 233–236, 1975

Lauer, J.P.: Création d'aimantations rémanentes de sciage et de forage au cours de la préparation d'échantillons de roches destinées à une étude paléomagnétique. C.R.Acad. Sci. Paris **287**, Ser D, 1–4, 1978

Michard, A.: Eléments de géologie marocaine. Notes Mém. Serv. Géol. Maroc **252**, 1976

Thellier, E., Thellier, O.: Sur l'intensité du champ magnétique dans le Passé historique et géologique. Ann. Géophys. **15**, 285–376, 1959

Watkins, N.D.: Hemispherical contrasts in support for the offset dipole hypothesis during the Brunhes epoch: the case for a unequal co-axial dipole pair as a possible geomagnetic field source. Geophys. J. R. Astron. Soc. **28**, 193–212, 1972

Wilson, R.L.: Permanent aspects of the Earth's non dipole magnetic field over upper Tertiary times. Geophys. J.R. Astron. Soc. **19**, 417–438, 1970

Wilson, R.L.: Dipole offset – the time-average palaeomagnetic field over the past 25 million years. Geophys. J.R. Astron. Soc. **22**, 491–504, 1971

Received May 9, 1980; Revised Version November 4, 1980
Accepted December 22, 1980

J Geophys (1981) 49:153

Journal of Geophysics

In Memorian

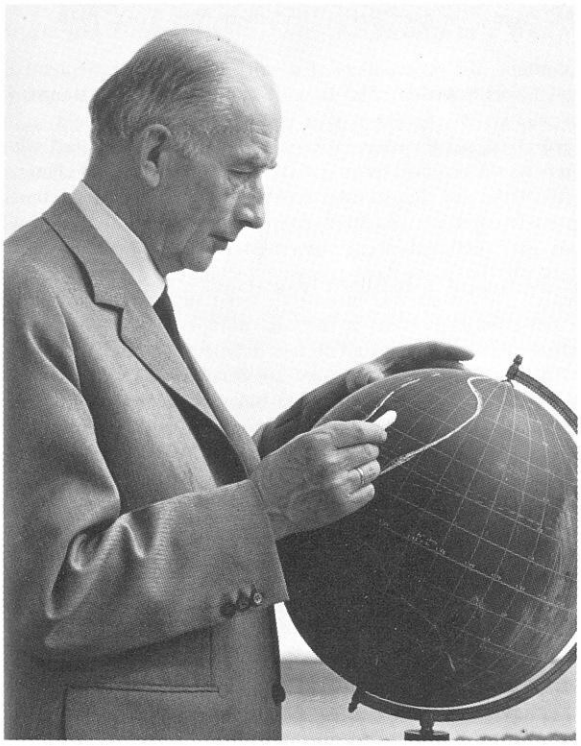

Wilhelm Hiller

***2. Februar 1899 †31. Juli 1980**

Wilhelm Hiller hat in den Jahren 1919 bis 1923 in Stuttgart und Tübingen Naturwissenschaften studiert. Seine Zulassungsarbeit hat er bei E. Regener in Stuttgart angefertigt. Die damals am Stuttgarter Physikalischen Institut sehr aktiv betriebene Erforschung der Atmosphäre bildete für Wilhelm Hiller eine Brücke zu seinem künftigen Arbeitsgebiet. Er trat im Jahre 1923 als wissenschaftlicher Mitarbeiter bei der meteorologisch-geophysikalischen Abteilung des Statistischen Landesamtes in den Dienst des Landes Württemberg. Da die meteorologischen Routineaufgaben ihn nicht sonderlich begeisterten, nahm er im Jahre 1925 die Gelegenheit wahr, innerhalb der gleichen Institution auf das Arbeitsgebiet der Erdbebenforschung überzuwechseln. 1926 hat Wilhelm Hiller in Stuttgart über das Thema „Über die Geschwindigkeit der seismischen Oberflächenwellen bei Weltbeben, insbesondere ihre Abhängigkeit von der geophysikalischen Beschaffenheit des durchlaufenen Weges" zum Dr.-Ing. promoviert. Zu dieser Arbeit war W. Hiller von K. Mack in Hohenheim bei Stuttgart angeregt worden. An dieser Hochschule befand sich die erste Württembergische Erdbebenwarte. Berichterstatter der Arbeit waren P. Ewald und A. Wigand.

Seit Mitte der zwanziger Jahre hat sich W. Hiller vor allem dem Ausbau der Erdbebenbeobachtung in Südwestdeutschland gewidmet. Wichtiger Markstein auf diesem Wege war die Errichtung der Stuttgarter Hauptstation, die im Laufe der Jahrzehnte mit verschiedenen Seismographensystemen – der jeweiligen instrumentellen Entwicklung folgend – ausgerüstet wurde. In Anerkennung dieser Leistung wurde Stuttgart im Jahre 1961 Station des internationalen Beobachtungsnetzes (WWSSN). Der Ausbau des Stationsnetzes für Nahbeben begann 1933 mit der Errichtung der ersten Station im Erdbebengebiet auf der westlichen Schwäbischen Alb in Meßstetten. Neben der Hohenheimer Station existierte bei Hillers Dienstantritt nur noch eine Erdbebenwarte in Ravensburg. Nach dem Kriege wurden die Stationen Meßstetten, Tübingen, Ravensburg, Heidelberg und Feldberg/Schwarzwald neu eingerichtet bzw. ältere Seismographensysteme durch einen Instrumententyp ersetzt, der von H. Berckhemer und W. Hiller gemeinsam entwickelt worden war. Registrierungen der süddeutschen Erdbebenwarten bildeten den Anstoß für eine größere Anzahl von Untersuchungen, die sich mit der Seismizität und Seismotektonik Südwestdeutschlands beschäftigten. Die Ableitung des rezenten tektonischen Spannungszustandes in der Erdkruste aus den Aufzeichnungen des Oberschwaben-Bebens im Jahre 1935 ziert heute viele Lehrbücher der Geophysik.

In der zweiten Lebenshälfte trat für W. Hiller zu den laufenden Aufgaben des Erdbebendienstes noch die Tätigkeit als Hochschullehrer. Er habilitierte sich 1939 in Stuttgart. Nur durch Kriegsdienst und Kriegsgefangenschaft unterbrochen hat er das Fach Geophysik seitdem in Stuttgart und später auch in Tübingen vertreten. 1950 wurde W. Hiller in Stuttgart und 1957 in Tübingen zum Honorarprofessor ernannt. 1962 übernahm er den neu geschaffenen Lehrstuhl für Geophysik in Stuttgart. Bis 1969 hat er das Institut für Geophysik in Stuttgart und die geophysikalische Abteilung des Statistischen Landesamtes Baden-Württemberg geleitet. Unter seiner Obhut sind zahlreiche Diplom-, Zulassungs-, Doktor- und Habilitationsschriften entstanden. Wenn auch die seismologischen Themen vorherrschen, so werden aber auch andere Themen aus dem Fachgebiet der Physik des Erdkörpers behandelt. Insbesondere seien hier die geomagnetischen Arbeiten genannt, für die innerhalb der geophysikalischen Abteilung des Statistischen Landesamtes eine langjährige Tradition bestand. Arbeiten in Gravimetrie, Geoelektrik, Ingenieurseismik und Radiometrie seien nicht vergessen.

In den Jahren nach dem 2. Weltkrieg hat sich W. Hiller mit großer Energie und Ausdauer der nicht immer ganz leichten Aufgabe gewidmet, die Verbindungen zu den Kollegen im Ausland wieder herzustellen. Daß dieses Wirken allgemeine Anerkennung fand, drückt sich in seiner Wahl zum Präsidenten der Europäischen Seismologischen Kommission für die Epoche 1951 bis 1956 aus. Weiter sei an sein Wirken als Nationalvertreter und Mitglied in zahlreichen nationalen und internationalen Gremien und Organisationen der Geophysik erinnert.

1951 bis 1953 war Wilhelm Hiller Vorsitzender der Deutschen Geophysikalischen Gesellschaft.

Götz Schneider, Stuttgart

J Geophys (1981) 49:154

Journal of Geophysics

Book Reviews

Pedlosky, J., Geophysical Fluid Dynamics, 1979. 180 figures, two tables XII, 624 pages. Cloth DM 79.50; US $ 43.80. Springer, Berlin Heidelberg New York, ISBN 3-540-90368-2.

This book is a thorough introduction to the theory of geophysical fluid dynamics with special applications to large-scale flows in the atmosphere and the oceans. It is based on the method of scaling which is consequently applied to the equations of motion. Physical insight and intuition combines with a vigorous mathematical analysis of the problems.

In the first two chapters basic motions of geophysical fluid dynamics are explained with special reference to the essential influence of the Earth's rotation to large-scale flow. Rossby number, vorticity, thermal wind and geostrophic flow and degeneracy as elementary but fundamental topics are discussed at length in order to elucidate the principal ideas on which geophysical fluid dynamics is founded. A first application of the systematic approximation scheme obtained by scaling is given in Chapt. 3 where the dynamics of a thin rotating layer of homogeneous inviscid fluid is studied. The influence of friction, i.e., of turbulent fluctuations on a large-scale homogeneous fluid is examined in Chapt. 4 by conventional use of Reynolds stresses and in Chapt. 5 by their application to the wind-driven circulation of the ocean. In Chapt. 6 stratification and compressibility are introduced and again systematic approximation by scaling leads to the relevant equations for quasigeostrophic motion of a stratified fluid. Physical intuition is trained by preconceiving qualitative aspects of the motion which is necessary for a proper use of scaling arguments. Chapt. 7 is devoted to instability theory as an essential base for the explanation of growing fluctuations of the flow in the atmosphere and the oceans. Finally Chapt. 8 gives a brief account of the theory of ageostrophic motions, for example of frontogenesis. Graduate students of dynamic oceanography and meteorology will sensibly profit from studying the book because it is really an excellently written text introducing to the basic ideas of geophysical fluid dynamics and to their application to problems of current research. This title should also be available in every geophysical library as an important reference book on geophysical fluid dynamics. **Helmut Wilhelm, Karlsruhe**

Roberts, P.H., Soward, A.M.: Rotating Fluids in Geophysics. Academic Press, London, 1978, ISBN 0-12-589650-6

This text evolved from the collected and revised lecture notes of a Summer School for post-graduate students in 1977, held on geophysical problems of rotating fluid dynamics. Applications of the basic concepts of this theory to the atmosphere and the oceans and to the generation of magnetic fields in the stars and planetary cores, but also to laboratory experiments are discussed. In order to give a brief account of the variety of problems incorporated in this volume some topics may be mentioned showing different aspects of rotating fluid dynamics, e.g., waves in homogenous and inhomogeneous fluids, baroclinic instability, frontogenesis, ocean circulation, magnetohydrodynamic waves, kinematic dynamo, convection in the Earth's core, turbulence. These are only a few subjects of a large number described in this book.

The scientist with special interest in geophysical applications of fluid dynamics will find a surprisingly broad spectrum of problems. This book supports the highly valuable effort to create a deeper understanding of the different geophysical applications of rotating fluid dynamics and to stimulate scientists working in this fascinating field. Graduate students interested in fluid dynamics should be able to follow the mathematics leading from basic ideas to current research problems. **Helmut Wilhelm, Karlsruhe**

P. Brosche and J. Sündermann (editors), Tidal Friction and the Earth's Rotation, 242 pages, Springer, Berlin Heidelberg New York, 1978

The book contains the proceedings of a workshop, held in September 1977 at the University of Bielefeld. In addition to a historical summary the twelve chapters of the book give an overview of the field both from the theoretical and the observational point of view. They start with three chapters on the classical techniques to obtain the temporal changes of the length of the day due to tidal deceleration during historic times including pre-telescopic, i.e., essentially eclipse observations, astronomical observations after 1600 and recent observations. These are followed by two chapters on the lunar laser ranging technique and gravimetric measurements. The former has meanwhile been superseded somewhat by more recent published results by the same authors. The latter chapter on gravimetric measurements is much less detailed than the balance of the book. The four following chapters are theoretical in nature with reports on tidal friction in the solid earth but mainly on oceanic tides. The three last chapters deal with changes of the length of the day during geologic time using fossil organism and a final chapter on pertinent geologic and geophysical data in precambrian times. Altogether the book constitutes a fine account of the status of the field which is both interesting for workers in the field but particularly for researchers in neighboring fields, where it may serve as a detailed but sufficiently concise account of recent developments in this very interesting interdisciplinary field of ocean dynamics, geophysics, astronomy, geology, geodesy and palaeontology. **F.M. Neubauer, Braunschweig**

Geothermics and Geothermal Energy. Editors: Ladislaus Rybach and Lajos Stegena. Contributions to Current Research in Geophysics (CCRG) 7, Reprinted from PAGEOPH. Birkhäuser Verlag, Basel Stuttgart, 1979

The rapidly growing interest in geothermal energy for an alternative energy source has raised many basic questions in geothermics, and stimulated much work of earth scientists in this heretofore somewhat neglected field. Especially, the necessity of contributions from many branches of geophysics, geology and mineralogy to the basic understanding of the causes, the development and the distribution of geothermal anomalies, as well as to the various aspects of their tentative utilisation for geothermal resources, has become evident.

For these reasons, a symposium 'Geothermics and Geothermal Energy' was suggested by the International Heat Flow Commission (IHFC) and held in August of 1977 at Durham, England at the occasion of the General Assembly of the International Association of Seismology and Physics of the Earth's Interior (IASPEI) and the International Association of Volcanology and Chemistry of the Earth's Interior (IAVCEI).

The reviewed volume contains most of the papers presented at that symposium, supplemented by several papers intended for presentation but not presented orally there.

It is subdivided into the sections: I. General Geothermics, II. Regional Heat Flow, III. Geothermal Potential, IV. Exploration, Charakterisation and Exploitation of Geothermal Resources, V. Geothermal Effects of Hydrothermal Circulation.

Edited by two well-known specialists in this field and containing contributions by authors from many nations, the volume provides a full view on the international state of the art and is a well-fitting further addition to the established series CCRG.

J.R. Schopper, Clausthal-Zellerfeld

J Geophys (1981) 49:155–162

Journal of Geophysics

Joint Two-Dimensional Observations of Ground Magnetic and Ionospheric Electric Fields Associated with Auroral Zone Currents

3. Auroral Zone Currents During the Passage of a Westward Travelling Surge

B. Inhester[1]*, W. Baumjohann[1], R.A. Greenwald[2]**, and E. Nielsen[2]

[1] Institut für Geophysik der Universität Münster, D-4400 Münster, Federal Republic of Germany
[2] Max-Planck-Institut für Aeronomie, D-3411 Katlenburg-Lindau 3, Federal Republic of Germany

Abstract. Ground magnetic perturbations and ionospheric electric fields have been observed by the Scandinavian Magnetometer Array and the STARE radars, respectively, during the passage of a westward travelling surge in the late evening sector. On the basis of these measurements, the three-dimensional current system in the vicinity of the westward travelling surge is modelled. The results support a current model recently proposed by Rostoker and co-workers on the basis of purely magnetic ground-based measurements. In particular, we can identify an upward field-aligned current of about 5×10^4 A in the head of the surge. Ahead of the surge, we find a south-eastward directed electric field. Additionally, we have some evidence for the existence of a south-westward directed electric field east of the surge. The latter may be explained by the generation of polarisation charges at the northern and southern boundaries of the higher conducting region east of the surge's head.

Key words: Scandinavian Magnetometer Array – STARE radars – Westward travelling surge – Current system modelling

Introduction

In today's understanding of polar ionospheric physics, the *westward travelling surge* (WTS) is regarded as the optical signature of the expansion of magnetospheric substorm energy from the midnight into the evening sector. During the expansive phase of a substorm (Akasofu 1964), energy is released in the form of intensification of auroral arcs and ionospheric electrical currents in the midnight sector. From here, the zone of intensified westward currents spreads into the evening sector along the auroral zone. The propagating head of the enhanced westward electrojet is thought to coincide spatially with the fold of the WTS (Akasofu et al. 1966, 1969).

Kisabeth and Rostoker (1973), Rostoker and Hughes (1979), and Tighe and Rostoker (in press 1981) have studied models for the ionospheric current flow associated with a surge and compared them with ground magnetic perturbations, measured along a chain of magnetometers. They found a localised, positive D deflection in the magnetic variations to be characteristic of the passage of westward travelling surges and explained it by an area of southward ionospheric current travelling together with the auroral form. As a consequence of their model current system, Rostoker and Hughes (1979) predicted an eastward component of the ionospheric electric field at the head of the surge. They assumed a westward electric field behind the surge in agreement with electric field measurements carried out with the Chatanika incoherent scatter radar (Banks et al. 1973; Horwitz et al. 1978).

In the present paper we present data of ground magnetic perturbations and ionospheric electric fields, measured simultaneously in the vicinity of a WTS that crossed northern Scandinavia on 27 March 1977 at approximately 19:00 UT (about 21 MLT). Both magnetic perturbations and electric fields have been measured in a two-dimensional, horizontal plane. In earlier studies of this series (Baumjohann et al. 1980, in press 1981; Baumjohann and Kamide in press 1981) it has already been shown that the simultaneous two-dimensional observations of ground magnetic and ionospheric electric fields have basic advantages over previous observations when studying the three-dimensional current flow associated with auroral electrojets. In this paper we will see that simultaneous two-dimensional measurements help even more when one attempts to understand the highly inhomogeneous and localised current system associated with a westward travelling surge.

In the following we describe the temporal and spatial variations of magnetic and electric fields during the passage of the WTS and, on the basis of those measurements, we model ionospheric and field-aligned currents and height-integrated ionospheric conductivities and discuss the model in the context of previously proposed models.

Instrumentation

The ground magnetic disturbance and ionospheric electric fields have been observed by the two-dimensional *Scandinavian Magnetometer Array* (SMA) and the *Scandinavian Twin Auroral Radar Experiment* (STARE), respectively. In addition, magnetograms from observatories at Ny Ålesund and Bjørnøya were included in this study. Optical recordings of the WTS have been performed by all-sky cameras at Ivalo and in Abisko. A detailed description of the SMA is given by Maurer and Theile (1978) and Küppers

Present addresses:
* Max-Planck-Institut für Aeronomie, D-3411 Katlenburg-Lindau 3, Federal Republic of Germany
** Applied Physics Laboratory, Johns Hopkins University, Laurel, MD 20810, USA

0340-062X/81/0049/0155/$01.60

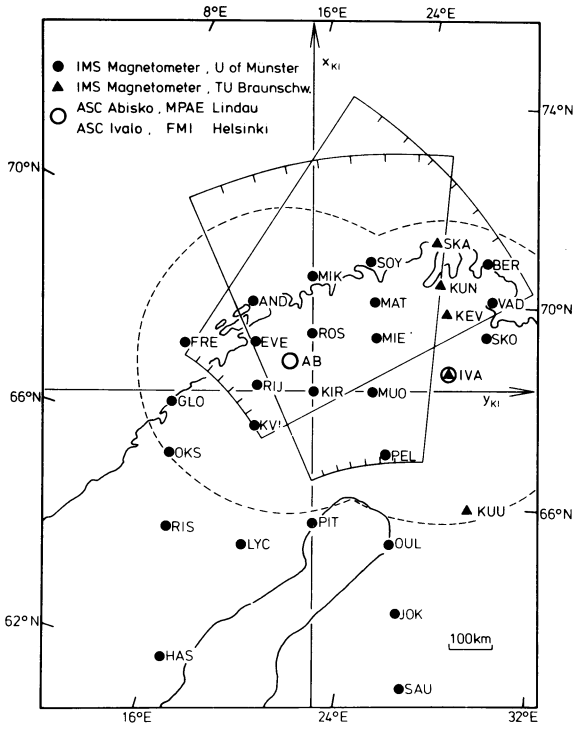

Fig. 1. Locations of the magnetic stations used in this study. The trapezoids define the observation areas of the two STARE radars. The observational coverage of the two all-sky cameras used in this study is indicated by the broken circles (as defined by 70° zenith angle at 110 km height). The axes define the Kiruna system (see text)

et al. (1979). For the STARE-radars, we refer to Greenwald et al. (1978).

The locations of the magnetometers and all-sky cameras, together with the approximate observation area of the latter at 110 km altitude (for a maximum zenith angle of 70 degrees) are shown in Fig. 1. The figure also illustrates the observation area of the two STARE radar antennas, situated at Malvik, near Trondheim, Norway and Hankasalmi, Finland, near the magnetometer station SAU.

The STARE radars measure the Doppler shift of radar signals scattered by plasma waves in the auroral E region (Farley 1963; Rogister and D'Angelo 1970). The combination of the Doppler shifts from both STARE radars give the plasma wave phase velocity perpendicular to the earth's magnetic field with a spatial resolution of roughly 20×40 km^2. There is strong experimental and theoretical evidence that the phase velocity measured coincides with the $\mathbf{E} \times \mathbf{B}$ – drift of E region electrons (Farley 1963; Rogister and D'Angelo 1970; Ecklund et al. 1977; Cahill et al. 1978). Hence the ionospheric electric field perpendicular to the earth's magnetic field can be derived. In order to observe auroral zone electric fields with this type of radar the electric field must exceed a threshold value in order to excite the plasma irregularities. Cahill et al. (1978) found threshold values of 15–20 mV/m for the STARE radars. In regions where appreciable ionospheric currents are due primarily to high conductivities rather than high electric fields, as for example in auroral arcs (Evans et al. 1977), one will not observe radar auroral backscatter if the electric fields are below the threshold.

The coordinate system in Fig. 1 and in all the other maps in this paper is the Kiruna system of Küppers et al. (1979). The x_{KI} axis of this system is chosen perpendicular to the revised corrected geomagnetic latitude circle (Gustafsson 1970) through Kiruna, Sweden, and points approximately 12° west of geographic north. The magnetic disturbance and the irregularity drift vectors have been transformed into the Kiruna system as described by Küppers et al. (1979). The horizontal components of the magnetic disturbance in this system are denoted by A (along x_{KI}, approximately north) and B (along y_{KI}, approximately east). The auroral structures in the all-sky camera pictures have also been mapped into the Kiruna system under the assumption that their lower border is at a mean altitude of 110 km (Boyd et al. 1971).

Observations

On 27 March 1977 a weak substorm commenced in the midnight sector at 19:00 UT. The magnetometer stations at Kharasavey and Tambey on 145° geomagnetic longitude recorded a sharp 100 nT decrease in the H component at that time (A.N. Zaitsev, private communication). About 15 min later, a WTS passed over northern Scandinavia, its head travelling with a speed of roughly 800 ms^{-1}.

Magnetograms from the latitudinal line of magnetometers ranging from station OUL to SOY (see Fig. 1) and BJN (about 500 km north of SOY), are shown in Fig. 2. They are governed by a southward moving eastward electrojet before the onset at 19:00 UT. Afterwards, the eastward electrojet intensifies but the influence of the simultaneously growing westward electrojet keeps the A component of the northernmost stations SOY and MAT from exhibiting large deflections. The passage of the WTS is indicated in the B component by a small peak of 15 nT, embedded in the general substorm variation.

Figure 3 shows the irregularity drift pattern and the ground equivalent current vectors observed during the passage of the WTS for three successive instances of time. A remarkable similarity between the irregularity flow direction and the auroral structures can be seen as soon as the WTS enters the field of view of the STARE antennas. In the immediate vicinity of the auroral luminosity an irregularity drift that is more or less parallel to the auroral form can be found. Hence, the electric field is perpendicular to the auroral structures, as is expected if electrons precipitate strongly into the auroral form. No irregularity drift could be measured in the region east of the surge's fold due, probably, to a subthreshold electric field in this region. As mentioned above, the irregularity drift vectors can be identified with the $\mathbf{E} \times \mathbf{B}$ – drift of ionospheric electrons. Hence, lines of constant electric potential in the plane of the ionosphere coincide with the flow lines of the irregularity drift vector field. Apparently, the auroral form coincides approximately with one of those equipotential lines. If this potential contour were to be extrapolated into the region east of the WTS, where no irregularity drift is detected, a weak southward and westward irregularity flow could be assumed in this region. This assumption is supported by the observation of westward electric fields, or southward electron drifts after the passage of a WTS using the incoherent scatter technique (Horwitz et al. 1978).

The ground equivalent current pattern in the lower part of Fig. 3 is more difficult to relate to the auroral structure, as it is governed by the eastward electrojet flowing south of the surge. Unfortunately, the surge passes along the Scandinavian coastline and the magnetic measurements do not cover the area north of the WTS. Still, an enhancement of the westward component of the equivalent current near the northernmost stations is observable, after the head of the surge has passed, indicating the intrusion

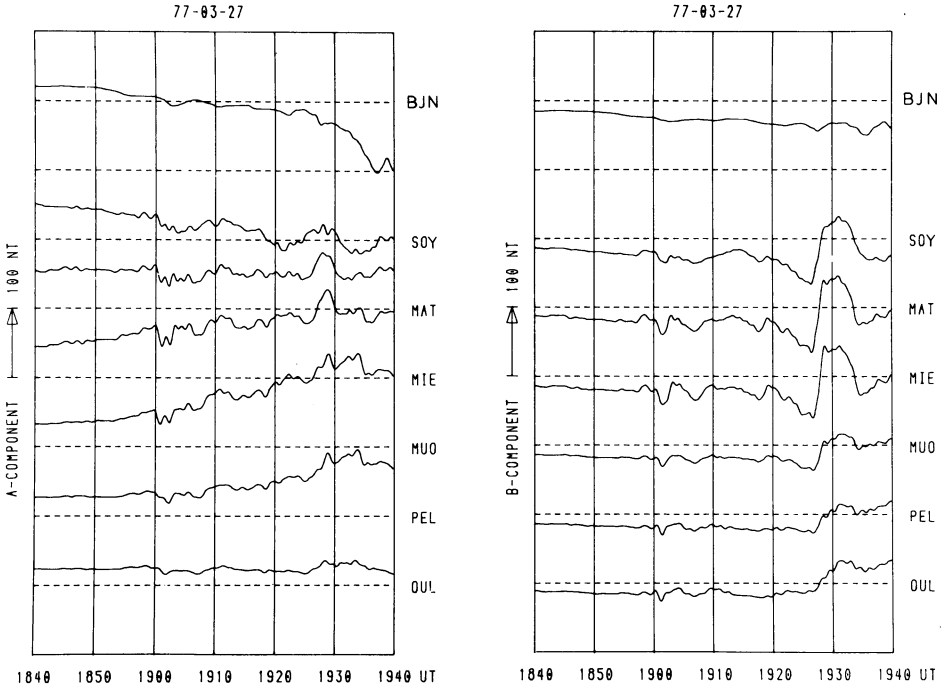

Fig. 2. Magnetograms of A and B components on a latitudinal profile ranging from BJN (Bear Island) to OUL, on 3 March 1977. A and B are horizontal magnetic disturbance components along the x_{KI} and y_{KI} axes, respectively (see Fig. 1)

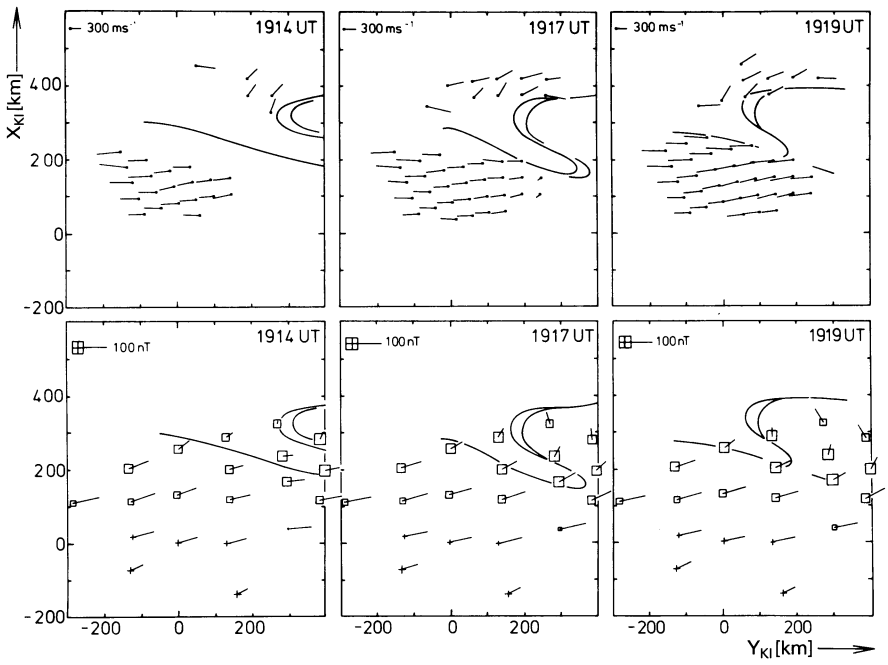

Fig. 3. Spatial distribution of irregularity drift vectors (*upper row*) and equivalent current vectors on the ground (*lower row*; *squares* and *crosses* denote negative and positive Z components, respectively) for three instances of time. Also shown are the digitised lower borders of the surge structure

of the westward electrojet. The pronounced positive D disturbance or southward equivalent current component immediately ahead of a WTS as found by Kisabeth and Rostoker (1973) is not seen in Fig. 3. Instead, there is an overall negative D or northward equivalent current component, that stays stable during the passage of the surge and is probably not related to the WTS.

After 19:20 UT, the auroral structures became barely detectable against the sunlit western horizon. However, as long as the surge can be traced on the all-sky camera pictures, it seems to maintain its shape, except for a slight de-folding, as can be seen in Fig. 3. In addition, the irregularity drift and equivalent current vector fields obviously remain constant relative to the location of the surge. This suggests a stationary pattern for the WTS and the electric and magnetic perturbations related to it which drifts with the WTS. In order to display this behaviour clearly, the auroral luminosity structures and vector fields for the times of Fig. 3, including 19:11 UT, were superimposed on each other in the moving frame of the WTS. The result is shown in Fig. 4, where we have plotted electric fields instead of irregularity drifts and have removed the above mentioned stationary and homogeneous bias of -20 nT in the B components. We did not include in the electric field the Lorentz-force due to the motion of our

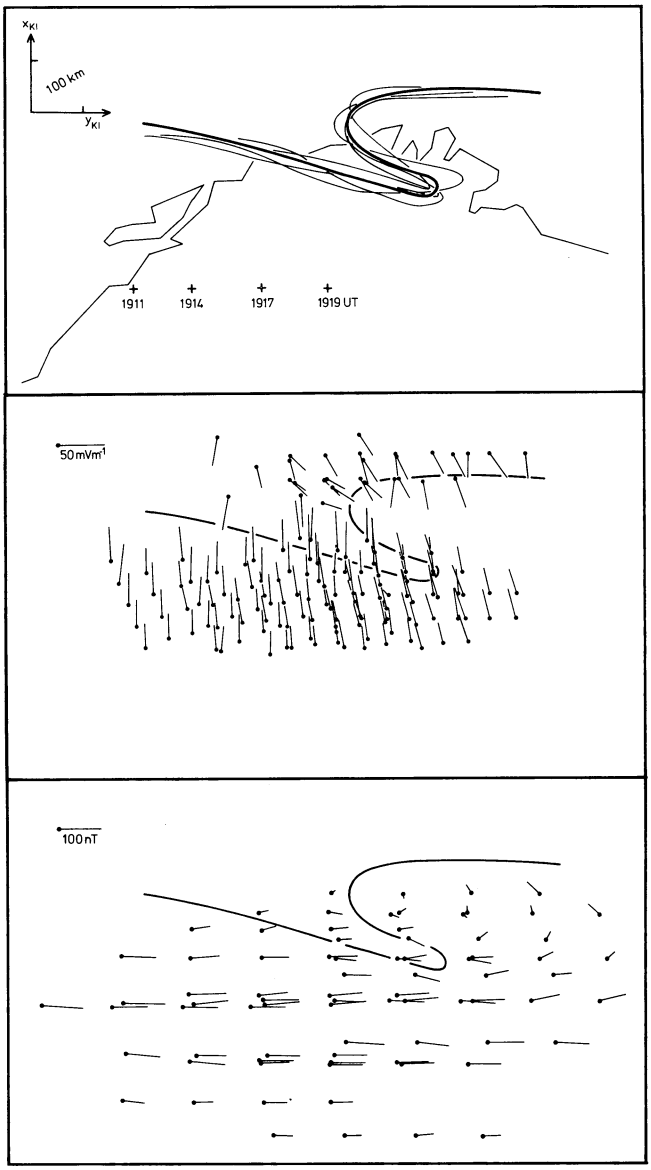

Fig. 4. Spatial distribution of electric field vectors (*middle panel*), equivalent current vectors on the ground (*lower panel*) and auroral luminosity structures (*upper panel*) for the times of Fig. 3 and 19:11 UT plotted one above the other under the assumption of a stationary pattern, drifting with the WTS (relative locations at different times are given by the + signs in the upper panel)

reference frame relative to the earth's magnetic field, because it is not the ionospheric plasma that moves with the surge, but rather the source of its luminosity.

Figure 4 demonstrates the basic results of our observations. The surge basically maintains its shape during the 8 min of its observation. In its vicinity, the electric field is modified to be normal to the auroral structure. The area around the WTS can be divided into three regions: northward directed electric fields south of the WTS, southward directed fields in the north and the west, with an increasing eastward component near the head of the surge. Presumably, a sub-threshold westward directed electric field is located in the fold east of the surge. The observed electric fields are in accord with incoherent scatter measurements (Banks et al. 1973; Horwitz et al. 1978), except that we see an unusually large eastward electric field ahead of the surge as compared to the sub-threshold field behind it. In contrast, Banks et al. (1973) reported westward electric fields of 15 mV m^{-1} after the passage of a surge, while there was no enhancement of the eastward component ahead of the surge. From Fig. 4 it is seen that the area of eastward electric fields ahead of the surge has a longitudinal extent of only 100–200 km. Since the surge propagates with a typical speed of 50 km min^{-1}, a time resolution of better than 3 min would be needed for a radar to detect the eastward field region. Moreover, the radar-beam must be directed into the correct spatial region relative to the shape of the WTS. In the operating mode used by Banks et al. (1973) and Horwitz et al. (1978) the Chatanika incoherent scatter radar required more than 2 min integration time in order to give a reliable electric field value at one point. Thus it is quite probable that they were simply not looking in the right place at the right time in order to observe the eastward electric field ahead of the surge. On the other hand, incoherent scatter radars are not limited to observing electric fields above some threshold value, such as STARE is. So Banks et al. (1973) and Horwitz et al. (1978) were able to observe the region of weaker westward directed electric field behind the surge, which obviously must have had a greater longitudinal extent than the region of the eastward electric field.

The equivalent current in our observations is dominated by the eastward electrojet flowing in the region of northward directed electric field south of the WTS. The influence of the advancing westward electrojet can be seen in the northeast. In the transition region, we find a slight southward current component immediately ahead of the surge, and an increasingly northward component of the ground equivalent current behind it. This behaviour in the north-south current flow is consistent with the observed peak in the B component that is seen in the magnetograms in Fig. 2 at that time, when the surge passes over the magnetometer profile. Kisabeth and Rostoker (1973) found this variation to be typical of a WTS passage, although the magnitude of the peak that we observed is small compared with their observations. On the other hand, above the region of positive B ground magnetic variation, there obviously exists an eastward electric field. This field may drive a southward Hall current giving rise to a strong positive B deflection, according to the model proposed by Rostoker and Hughes (1979). In order to resolve the effects quantitatively, estimates of the distribution of ionospheric conductivities relative to the surge must be included.

Numerical Models

As has already been extensively discussed in the early papers of this series (Baumjohann et al. 1980 in press 1981; Baumjohann and Kamide in press 1981) it is possible to significantly restrict the large number of equivalent current systems that may fit ground magnetic disturbances. This is accomplished by combining two-dimensional measurements of the magnetic variations made by the SMA and ionospheric electric fields observed with STARE. In order to find a probable three-dimensional current system that is consistent with the ground magnetic variation and the ionospheric electric field measurements, we modelled the ionospheric current system numerically.

For the calculations, the ionospheric plane at 110 km height (Kamide and Brekke 1977) was divided into cells of 50×50 km^2 with a constant height-integrated conductivity, electric field and current density. The divergence of the horizontal currents between different cells gives the field-aligned current flow. The ground

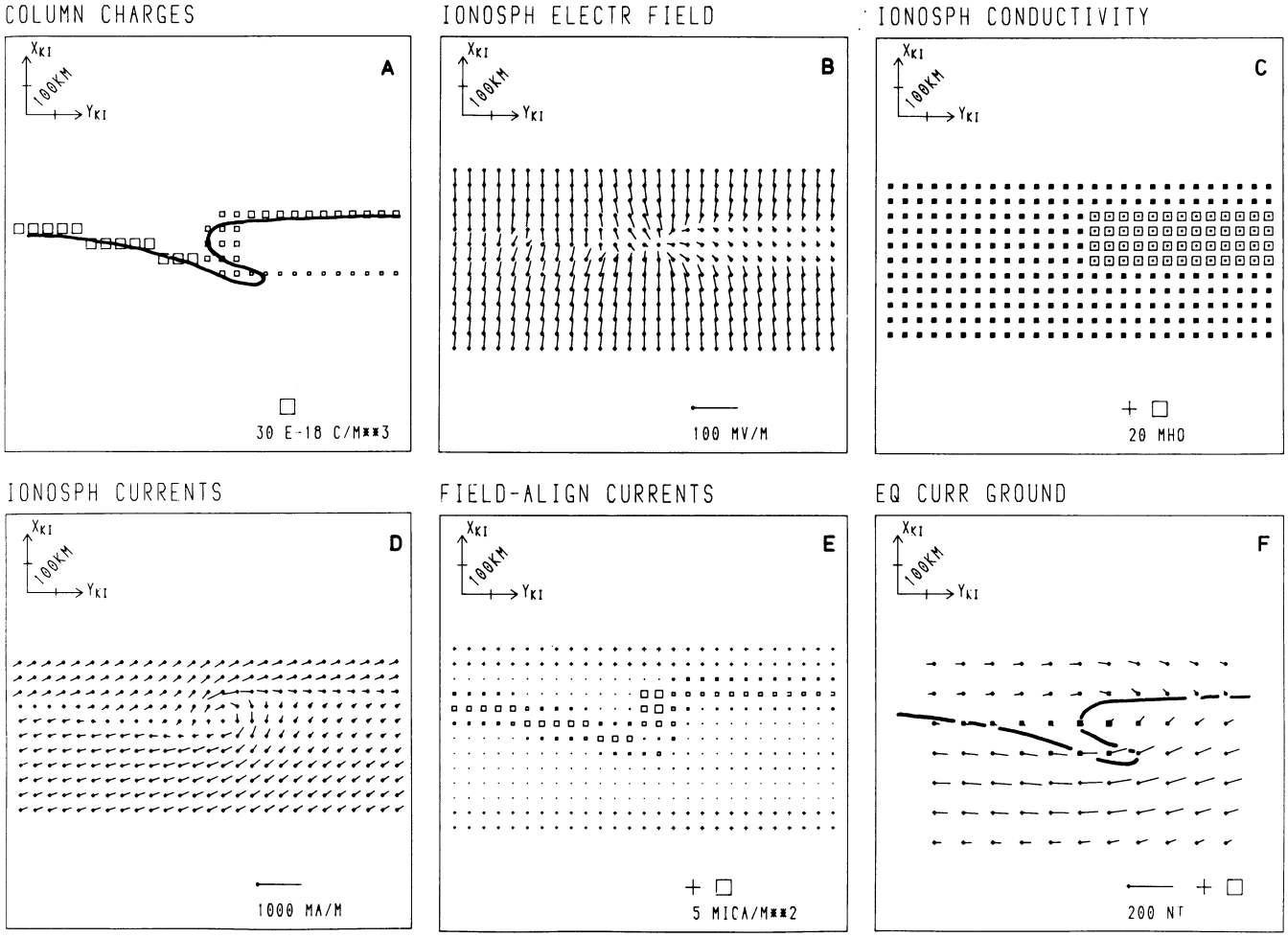

Fig. 5a–f. Parameters of the model current system A and resultant equivalent current vectors on the ground. **a** Distribution of field-aligned columns of negative electrical charges. **b** Ionospheric electric field vectors attributable to these charges. **c** Ionospheric Hall (square) and Pedersen (cross) conductivity. **d** Ionospheric currents. **e** Up- (*square*) and downward (*cross*) field-aligned currents. **f** Equivalent currents on the ground; squares and corosses denote negative and positive Z components, respectively

equivalent current is calculated using a Biot-Savart integration over the horizontal and field-aligned currents of all cells.

We initiate the modelling procedure by assuming a distribution of magnetic field-aligned columns of electrical charges above the ionospheric plane. The distribution of these column charges was to be simply related to the auroral form and consistent with the electric field pattern observed by STARE. Figures 5a and 6a show two different charge distributions that satisfy these criteria. In both cases negative charges are spread along the auroral form of the surge with an accumulation of column charges in the surge's head, this being necessary to create the eastward electric field component ahead of the surge. It was also found necessary to introduce a line of negative column charges along the eastward extension of the surge's hook in the southeast, in order to reduce the electric field magnitude east of the surge's head to sub-threshold values, as seen by STARE. The uncertainty of the electric field in this region gives rise to the two different models displayed in Figs. 5 and 6 (henceforth called models A und B). The two models differ with respect to the relative strength of the column charges north and south of the region of sub-threshold fields, east of the surge's head. Model A has, according to the luminosity distribution of the surge, the stronger column charges in the north and consequently has a north-west directed electric field east of the surge of less than 15 mV/m in magnitude (see Fig. 5b). Model B has the stronger column charges along the southern border of that region, so that the southward electric field from the north can penetrate and gives rise to a sub-threshold, south-west directed electric field (see Fig. 6b). Thus both models give a westward electric field in the region east of the surge, as was to be expected, but differ with respect to the north-south component of the electric field in this region.

The variation of the ionospheric height-integrated conductivity was chosen such that the ionospheric current, following Ohm's law, together with the resultant field-aligned current distribution should reproduce the magnetic disturbances seen on the ground. Additional information is supplied from rocket measurements (Rème and Bosqued 1973; Meng et al. 1978), which have found a strong precipitation of energetic (>5 keV) electrons into the head and the region east of the surge. Restricting ourselves to a simple model, we therefore assumed homogeneously distributed height-integrated conductivities, except for the disturbed region of the surge's head and east of it. In order to find quantitative agreement between the modelled and the measured ground magnetic disturbances, we had to take a value of $5.6\,\Omega^{-1}$ for the un-

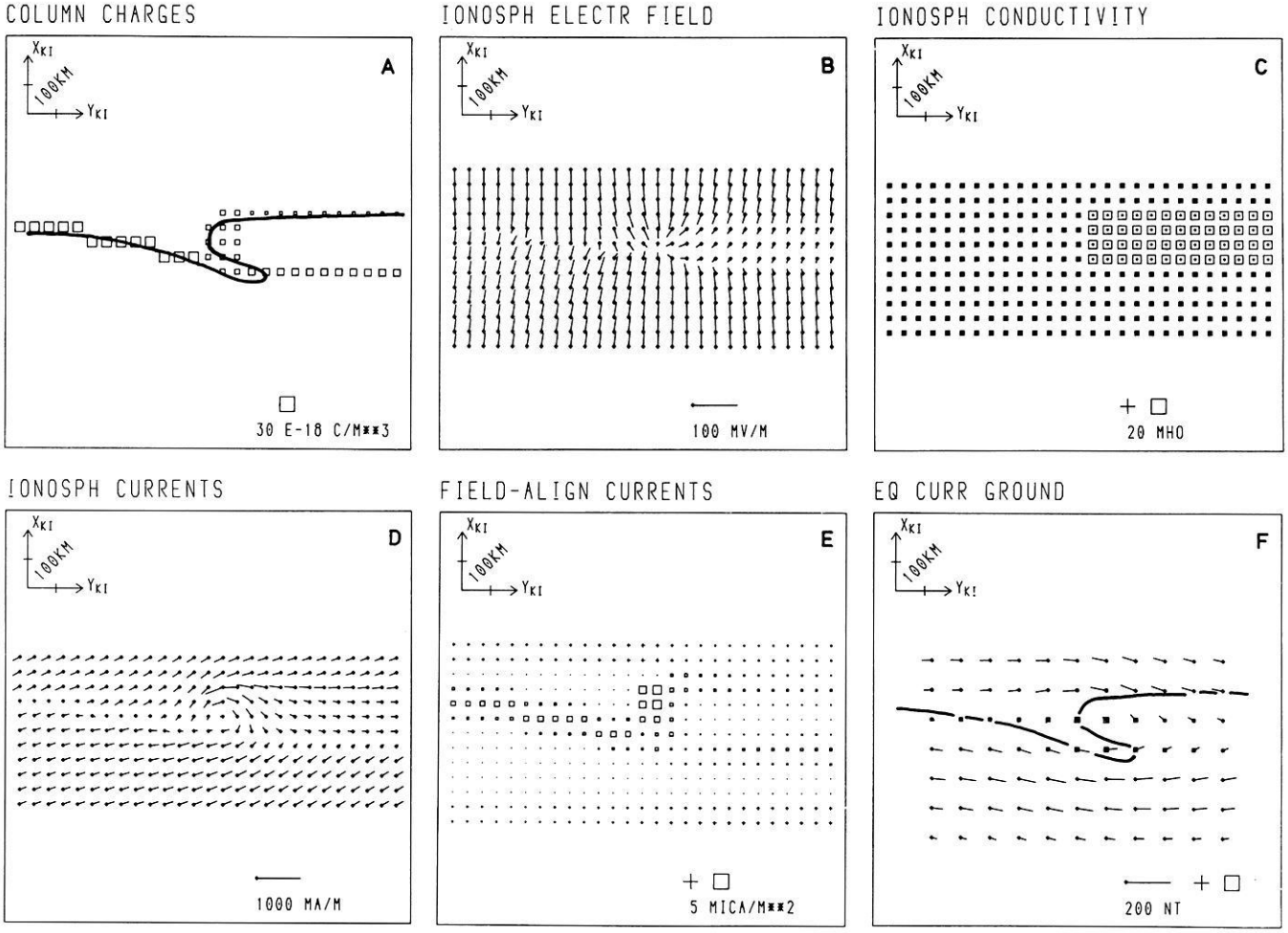

Fig. 6. Parameters of the model current system B and resultant equivalent current vectors on the ground; otherwise same as Fig. 5

disturbed height-integrated Hall conductivity and $2.8\,\Omega^{-1}$ for the Pedersen conductivity. Furthermore, we achieved consistency only if an enhanced Hall conductivity of $11.2\,\Omega^{-1}$ was assumed in the entire region of sub-threshold electric fields inside and east of the surge. For example, a Hall conductivity distribution that gradually decreases to the undisturbed conductivity from the surge's head towards east, does not reproduce the westward equivalent current flow measured behind the surge. The Pedersen conductivity in the disturbed region was set on the undisturbed value of $2.8\,\Omega^{-2}$. As the model ground magnetic disturbances are insensitive to changes of the Pedersen conductivity in this region, this part of the model is somewhat uncertain within a factor of two. The variation of the conductivities used in the model calculation is shown in Figs. 5c and 6c. Basically, the assumed conductivity is in accord with measurements of electron density height-profiles by incoherent scatter radars. These show that in an undisturbed night time auroral ionosphere the height-integrated Hall conductivity varies from $3\text{–}6\,\Omega^{-1}$ and the ratio of Σ_H/Σ_P is about 2 (Banks and Doupnik 1975).

Figures 5d–f and 6d–f show the ionospheric height-integrated current resulting from Ohm's law, the field-aligned current density resulting from the divergence of the ionospheric current and the ground equivalent current calculated from the former by means of a Biot-Savart integration. Both models show eastward and westward current flow in the south and north, respectively, but the models have different currents in the region of enhanced conductivity east of the surge. In model A, the eastward electrojet penetrates into this region and there are almost no field-aligned currents at the southern border of the region of enhanced conductivity. The electrical charges along the southern borderline, (see Fig. 5a) can, for this model, be consistently explained as polarisation charges which result when the north-eastward directed electrical current flow crosses the conductivity gradient. The resultant electric field difference on both sides of this borderline keeps the current flow divergence-free. If this model is correct, a net northward shift of the east-west current system should be observed after the passage of the surge. In model B, there is a westward current system behind the head of the surge, leading to an upward directed field-aligned current totalling 4×10^4 A in the center of the surge. For the westward electrojet we find a total current of 5.5×10^4 A, which is small compared with typical electrojet current strengths. Additionally, there are upward field-aligned currents along the northern and southern border of the region of enhanced conductivity, where we assumed negative electrical column charges. The second model clearly brings about an increase in the westward current flow after the passage of the surge.

A comparison of the model ground equivalent current systems with the measured equivalent currents in Fig. 4 shows clearly that model B is the more realistic one.

Model A does not reproduce the observed change from eastward to westward equivalent current flow, or the positive to negative A variation observed by a magnetometer station under-

neath the surge. Both of these features are observed in the equivalent current system of model B. The observed increase in the northward current flow east of the surge is also consistent with model B. In contrast, some details of the measured equivalent current system are not reproduced very well by model B. One feature is the very homogeneous eastward current south of the surge. We feel, that such details could be reproduced only if our assumed model were made more complex and that the necessary changes in the model would not bring about any basically new feature in the surge's current system.

Discussion

In the preceding sections, we have presented data on the ionospheric electric field and ground equivalent current associated with a westward travelling surge. We have constructed a model for the three-dimensional current system, consistent with our data and previous measurements of the ionospheric electric field (Banks et al. 1973; Horwitz et al. 1978) as well as measurements of electron precipitation (Rème and Bosqued 1973; Meng et al. 1978) near a WTS.

This model (model B of the previous section, shown in Fig. 6) strongly supports the results of Rostoker and Hughes (1979), who identified the WTS with the intrusion of an upward field-aligned current, fed by the westward electrojet and the recent, more refined modelling of Tighe and Rostoker (in press 1981). As their models are based on ground magnetic observations alone, they propose ionospheric electric fields consistent with the current flow. This electric field is directed towards the south-east in a localised region inside and ahead of the WTS. Evidence for the existence of this field is obviously given by our measurements (see Fig. 4). East of the surge, Rostoker and Hughes (1979) assumed a south-west directed electric field, driving a westward current. The existence of this field can be verified only indirectly from our modelling and not directly by STARE, as the field was below the threshold of the STARE radar in this particular example. Incoherent scatter measurements (Banks et al. 1973; Horwitz et al. 1978) have shown that the electric field in this region has a westward component. In our case, a north-west directed electric field (as in model A of the previous section) has had to be discarded, as it does not lead to currents that reproduce our magnetic measurements, whereas a south-west directed electric field gives suitable agreement.

Another model for the surge's ionospheric current system has been proposed by Kisabeth and Rostoker (1973). They explained the ground magnetic variations observed during the passage of a surge as a step-like northward displacement of the westward electrojet. This displacement would be similar to the distortion undergone by a pre-existing auroral arc during the passage of the surge. They include no net field-aligned current in their model current system, and the westward electrojet flows further into the evening sector. Their model resembles somewhat our model A of the previous section with which our magnetic measurements are not in agreement.

An essential feature of the magnetic measurements in Kisabeth and Rostoker (1973) and Rostoker and Hughes (1979) is a positive D deflection under the head of the surge. The fact that we observe it only very weakly is no basic contradiction to Rostoker and Hughes' results. We could easily have produced a larger D deflection in our model, if we had extended the region of enhanced conductivity a little further to the west. In fact, Hughes and Rostoker (1979) assumed that a segment of the south-east directed electric field was located inside the head of the surge, whereas we measure it outside the region of auroral luminosity. The magnitude of the D deflection on the ground is therefore likely to depend critically on the correlation of the ionospheric electric field and the ionospheric conductivity near the head of the surge.

It may be quite interesting to relate the present results (model B of the previous section, shown in Fig. 6) to those reported by Baumjohann et al. (in press 1981) concerning a WTS in the process of being formed, i.e., local auroral breakups. These authors clearly showed that during the auroral breakup a strong southward directed polarisation field, caused by the high electrical conductivity associated with the active aurora, was superimposed on the quiet-time north-westward directed electric field, thus resulting in a total south-westward directed one in the breakup region. This is strikingly similar to what can be concluded from our observations and model calculations, i.e., during the passage of the WTS the previously northward directed electric field south of the auroral arc turned over to a south-westward direction, thus exhibiting the presence of a southward polarisation field in the higher conducting region. The polarisation charges at the boundaries of the higher conducting region (which are created by a northward Hall current driven by the westward electric field behind the surge's head) may be identified in Fig. 6a. Here, the negative charges at the northern boundary within the auroral structure are reduced (if compared to those ahead of the WTS) due to the presence of positive polarisation charges and negative polarisation charges can be seen at the southern boundary of the higher conducting region. Since in our case the conductivity enhancement and therefore the southward polarisation field is minor compared to that reported by Baumjohann et al. (1981), the westward Cowling current behind the surge is also comparatively weaker than the strong jetlike Cowling current observed by those authors.

Acknowledgements. We are greatly indebted to those past and present members of the magnetometer group at the University of Münster, who were involved in collecting the magnetic data. The magnetic observations were performed in cooperation with the Aarhus University, the Royal Institute of Technology at Stockholm, the Finnish Meteorological Institute at Helsinki, the University of Bergen, the Geophysical Observatory at Sodankylä, the Kiruna Geophysical Institute, the University of Oulu, and the University at Tromsö. We thank these institutions for their support. The STARE radars are operated in cooperation with ELAB and the Norwegian Technical University in Trondheim and the Finnish Meteorological Institute in Helsinki. We would like to thank T Barlindhang and T Rinkinen for their efforts in the everyday operation of the stations. Finally, we thank H. Maurer, T.U. Braunschweig, who supplied us with the magnetic data of the Braunschweig chain and R.J. Pellinen, FMI Helsinki, and H. Lauche, MPAE Lindau, who made the all-sky camera data available. The magnetometer array observations and the work of W. Baumjohann were supported financially by grants from the Deutsche Forschungsgemeinschaft. The work of R.A. Greenwald was supported in part by the Division of Atmospheric Sciences, National Science Foundation under grant ATM-8003300. We are grateful to G. Rostoker and another unknown referee for their instructive comments.

References

Akasofu, S.-I.. The development of the auroral substorm. Planet. Space Sci. **12**, 273–282, 1964

Akasofu, S.-I., Meng, C.-I., Kimball, D.S.: Dynamics of the aurora – IV. Polar magnetic substorms and westward travelling surges. J. Atmos. Terr. Phys. **28**, 489–496, 1966

Akasofu, S.-I., Eather, R.H., Bradbury, J.N.: The absence of the hydrogen emission (H_β) in the westward travelling surge. Planet. Space Sci. **17**, 1409–1412, 1969

Banks, P.M., Doupnik, J.R.: A review of auroral zone electrodynamics deduced from incoherent scatter radar observations. J. Atmos. Terr. Phys. **37**, 951–972, 1975

Banks, P.M., Doupnik, J.R., Akasofu, S.-I.: Electric field observations by incoherent scatter radar in the auroral zone. J. Geophys. Res. **78**, 6607–6622, 1973

Baumjohann, W., Kamide, Y.: Joint two-dimensional observations of ground magnetic and ionospheric electric fields associated with auroral zone currents. 2. Three-dimensional current flow in the morning sector during substorm recovery. J. Geomagn. Geoelectr. **33**, in press 1981

Baumjohann, W., Untiedt, J., Greenwald, R.A.: Joint two-dimensional observations of ground magnetic and ionospheric electric fields associated with auroral zone currents. 1. Three-dimensional current flows associated with a substorm-intensified eastward electrojet. J. Geophys. Res. **85**, 1963–1978, 1980

Baumjohann, W., Pellinen, R.J., Opgenoorth, H.J., Nielsen, E.: Joint two-dimensional observations of ground magnetic and ionospheric electric fields associated with auroral zone currents. 4. Current systems associated with local auroral breakups. Planet. Space Sci. **29**, in press 1981

Boyd, J.S., Belon, A.E., Romick, G.J.: Latitude and time variations in precipitated electron energy inferred from measurements of auroral height. J. Geophys. Res. **76**, 7694–7700, 1971

Cahill, L.J. Jr., Greenwald, R.A., Nielsen, E.: Auroral radar and rocket double-probe observations of the electric field across the Harang-discontinuity. Geophys. Res. Lett. **5**, 687–690, 1978

Ecklund, W.L., Balsley, B.B., Carter, D.A.: A preliminary comparison of F region plasma drifts and E region irregularity drifts in the auroral zone. J. Geophys. Res. **82**, 195–197, 1977

Evans, D.S., Maynard, N.C., Trøim, J., Jacobsen, T., Egeland, A.: Auroral vector electric field and particle comparisons. 2. Electrodynamics of an arc. J. Geophys. Res. **82**, 2235–2249, 1977

Farley, D.J.: A plasma instability resulting in field-aligned irregularities in the ionosphere. J. Geophys. Res. **68**, 6083–6097, 1963

Greenwald, R.A., Weiss, W., Nielsen, E., Thomson, N.R.: STARE: a new radar auroral backscatter experiment in northern Scandinavia. Radio Sci. **13**, 1021–1039, 1978

Gustafsson, G.: A revised corrected geomagnetic coordinate system. Ark. Geofys. **5**, 595–617, 1970

Horwitz, J.L., Doupnik, J.R., Banks, P.M.: Chatanika radar observations of the latitudinal distributions of auroral zone electric fields, conductivities, and currents. J. Geophys. Res. **83**, 1463–1481, 1978

Kamide, Y., Brekke, A.: Altitude of the eastward and westward auroral electrojets. J. Geophys. Res. **82**, 2851–2853, 1977

Kisabeth, J.L., Rostoker, G.: Current flow in auroral loops and surges inferred from ground-based magnetic observations. J. Geophys. Res. **78**, 5573–5584, 1973

Küppers, F., Untiedt, J., Baumjohann, W., Lange, K., Jones, A.G.: A two-dimensional magnetometer array for ground-based observations of auroral zone electric currents during the International Magnetospheric Study (IMS). J. Geophys. **46**, 429–450, 1979

Maurer, H., Theile, B.: Parameters of the auroral electrojet from magnetic variations along a meridian. J. Geophys. **44**, 415–426, 1978

Meng, C.-I., Snyder, A.L., Kroehl, H.W.: Observations of auroral westward travelling surges and electron precipitations. J. Geophys. Res. **83**, 575–585, 1978

Rème, H., Bosqued, J.M.: Rocket observations of electron precipitation in a westward travelling surge. J. Geophys. Res. **78**, 5553–5558, 1973

Rogister, A., D'Angelo, N.: Type II irregularities in the equatorial electrojet. J. Geophys. Res. **75**, 3879–3887, 1970

Rostoker, G., Hughes, T.J.: A comprehensive model current system for high-latitude magnetic activity – II. The substorm component. Geophys. J.R. Astron. Soc. **58**, 571–581, 1979

Tighe, W.G., Rostoker, G.: Characteristics of westward travelling surges during magnetospheric substorms. J. Geophys., in press 1981

Received February 18, 1981; Revised Version March 20, 1981
Accepted March 23, 1981

J Geophys (1981) 49:163–168

Journal of Geophysics

Current Flow in Auroral Forms Responsible for Ps 6 Magnetic Disturbances

G. Rostoker and K.S. Apps
Department of Physics and Institute of Earth and Planetary Physics, University of Alberta, Edmonton, Alberta T6G 2J1, Canada

Abstract. In this paper we use magnetometer and riometer data from an east-west station array to evaluate the location of energetic (keV) electron precipitation with respect to the region of equatorward ionospheric current flow responsible, in part, for Ps 6 magnetic disturbances. Using cross-correlation techniques we show that, for clear cut cases, the region of maximum energetic electron precipitation is colocated with the region of equatorward ionospheric current flow responsible for the positive *D*-component perturbation characteristic of the Ps 6 disturbance. This observation is consistent with the model of Kawasaki and Rostoker (1979) for Ps 6 disturbances which attributes the magnetic perturbation to a longitudinally localized three-dimensional current system involving anti-parallel Birkeland current sheets linked by an equatorward ionospheric current.

Key words: Aurora – Ps 6 magnetic disturbance – Auroral electrojet – Three-dimensional current system

Introduction

Ps 6 disturbances are normally seen as quasi-periodic pulses in the auroral zone magnetic field which occur at times of intense auroral electrojet activity. The disturbances have their maximum occurrence frequency at approximately local magnetic dawn (Rostoker and Barichello 1980) and tend to be detectable more often in the summer months than the winter months. Their quasi-periodic nature has caused some researchers to class them as magnetic pulsations (Saito 1978), however a Ps 6 disturbance may occur as an isolated spike so that it may be more correct to regard them as impulsive localized perturbations of the westward auroral electrojet.

Figure 1 shows a typical example of a sequence of Ps 6 disturbances recorded on 27 October 1977 over the Alberta sector. The geomagnetic coordinates and code names of the stations are listed in Table 1. There are three episodes of Ps 6 activity over this day. The first involves an interval from 1100–1215 UT during which severall events occurred in a quasi-periodic fashion. The second

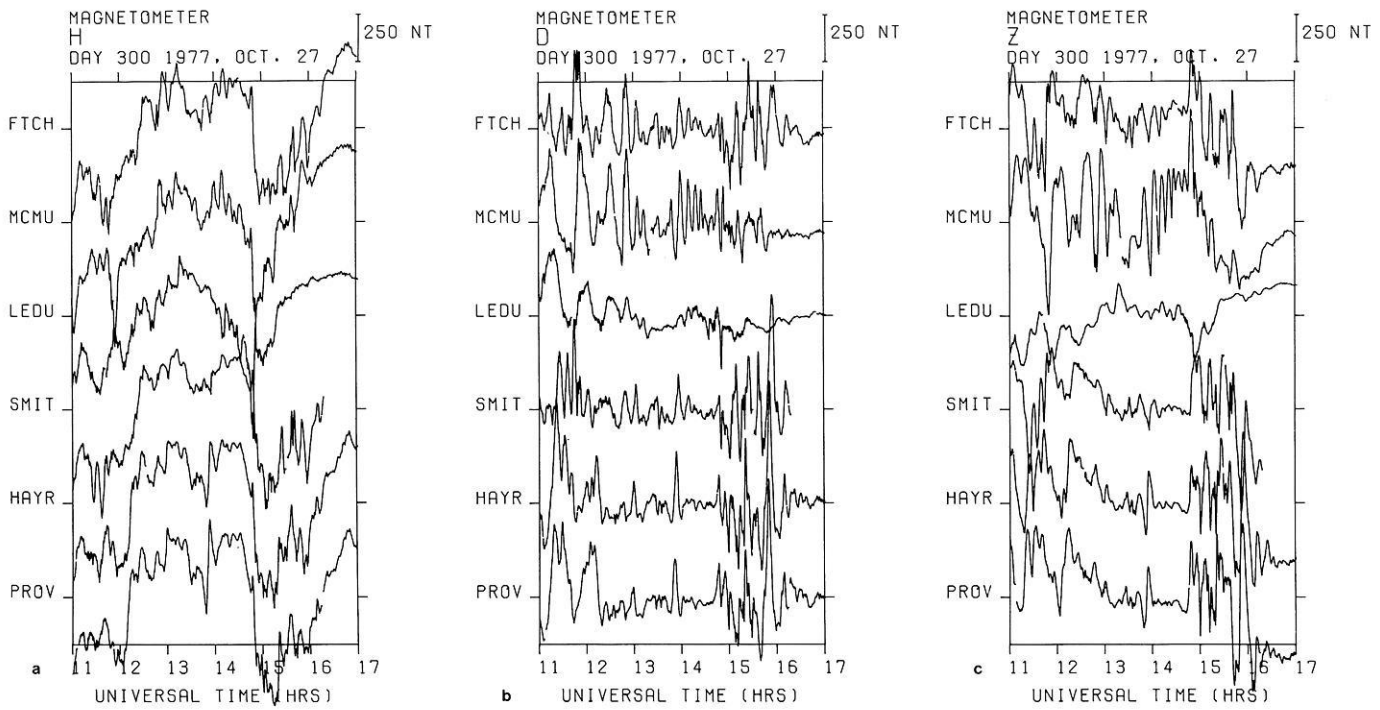

Fig. 1a–c. Magnetograms for 27 October 1977 recorded at stations in the Alberta array. Station coordinates and code names are shown in Table 1. **a** *H*-component; **b** *D*-component; **c** *Z*-component

0340-062X/81/0049/0163/$01.20

Table 1. Geomagnetic coordinates and code names of stations in the Alberta array

Station	Code name	Geomagnetic	
		Latitude (°N)	Longitude (°E)
Fort Providence	PROV	67.5	292.0
Hay River	HAYR	67.3	294.3
Fort Smith	SMIT	67.3	300.0
Uranium City	URAN	67.4	304.3
Fort Chipewyan	FTCH	66.3	302.1
Fort McMurray	MCMU	64.2	303.5
Leduc	LEDU	60.6	302.9

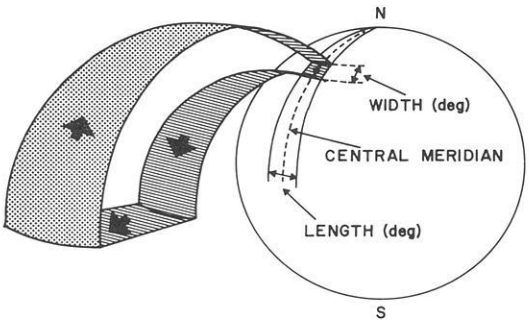

Fig. 2. Three dimensional model current system proposed by Kawasaki and Rostoker (1979) to explain Ps 6 disturbances (after Kisabeth and Rostoker 1977)

episode involves a single isolated Ps 6 event occurring near 1400, while the third episode involves another sequence of quasi-periodic variations from 1440–1620. In keeping with the characteristic behavior of Ps 6 disturbances, most of the perturbation is in the *D*- and *Z*-components with relatively little in the *H*-component. Nonetheless, the negative *H*-perturbation prevailing during the Ps 6 events indicates the presence of significant westward electrojet current flow over the stations of PROV, HAYR and SMIT.

Both Kawasaki and Rostoker (1979) and Baumjohann (1979) have associated Ps 6 disturbances with auroral Ω-bands in which there is a strong equatorward ionospheric current flow. Kawasaki and Rostoker (1979) have estimated the east-west scale size of the current carrying region to be of the order of 5°–10° at 67.5° N, with the location of the equatorward current flow drifting eastward at ~ 0.8–2.0 km s^{-1}. The actual best model of the current system responsible for these perturbations has recently been the topic of some controversy. Kawasaki and Rostoker (1979), based on a limited amount of riometer data, concluded that energetic electron precipitation was maximal in the region of maximal equatorward ionospheric current flow, which led them to a model current system of the type shown in Figure 2. In this model it is suggested that either; (i) A patch of precipitating energetic electrons drifts eastward through a region of southeastward directed electric field under the combined influence of gradient and $\mathbf{E} \times \mathbf{B}$ effects; (ii) The electric field which is normally southward is perturbed toward the southeast over a time scale of a few minutes, after which it returns to its southward configuration. The region in which the perturbation takes place has a high background ionospheric conductivity; (iii) The arrival of a patch of precipitating energetic particles coincides with a southeastward perturbation of the electric field.

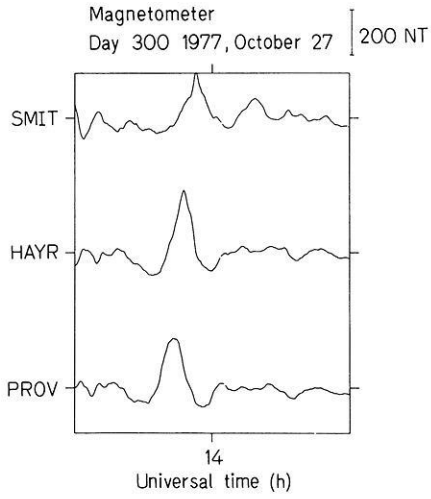

Fig. 3. *D*-component records from the east-west arm of the Alberta array for an expanded time scale of 1 h centered on 1400. The Ps 6 is clearly evident just prior to 1400 with the delay in response from *PROV* to *SMIT* of 4.9 min pointing to an eastward propagation velocity of ~ 1.2 km/s

The key point to which this model addressed itself was the fact that Ps 6 disturbances do not significantly influence the *H*-component of the field. This strongly suggested that the perturbation is due primarily to equatorward current flow.

More recently Gustafsson et al. (1981) have suggested that Ps 6 disturbances are due solely to ionospheric Hall currents, based on the contention that the energetic electron precipitation coincides with a region to the east of the equatorward ionospheric current flow. They claim that the Ps 6 disturbance is caused by the development of an eastward electric field component which drives an equatorward Hall current that closes through the ionosphere in the region of enhanced conductivity due to precipitating electrons. The purpose of this paper is to study, in detail, several Ps 6 disturbances using both ground magnetometer and riometer data to investigate the location of the precipitating energetic electrons with respect to the region of equatorward ionospheric current flow.

Presentation of Data

We shall present data from two separate days which contain four distinct intervals of Ps 6 activity. For each event we shall present detailed plots comparing the positive *D*-component perturbation and the riometer perturbation associated with that event. We shall then present the cross-correlation between the riometer and *D*-component magnetometer, from which quantitative estimates of the displacement of the *D*-component peak and the maximum riometer deflection will be derived.

The first event we shall present is an isolated Ps 6 event which occurred just prior to 1400 UT on 27 October 1977. The normal magnetograms for the Alberta array stations are shown in Fig. 1. The event is clearly visible in the *D*-component at PROV, HAYR, and SMIT. However the degree to which these disturbances can be spatially localized is clearly evident in comparing the perturbation patterns at PROV, HAYR, and SMIT with those at the stations of FTCH and MCMU just to the south. It is interesting to note the extremely large amplitude Pc 5 oscillation at MCMU which is barely detectable along the east-west line (PROV, HAYR,

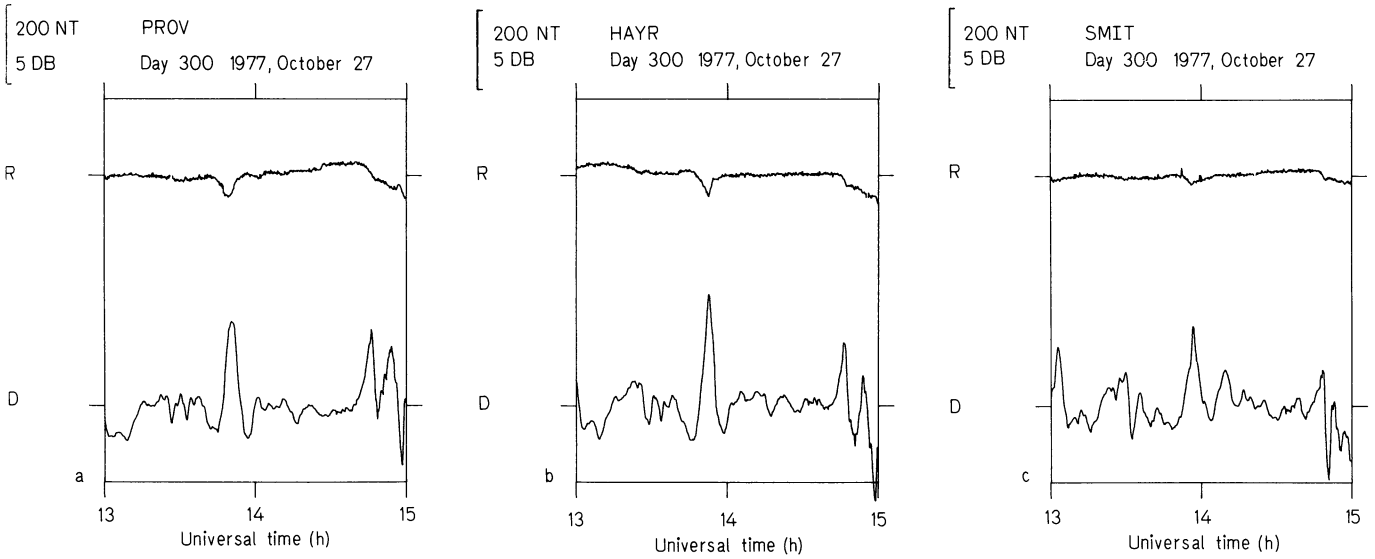

Fig. 4a–c. Riometer and *D*-component perturbations recorded on 27 October 1977. **a** at PROV; **b** at HAYR; **c** at SMIT

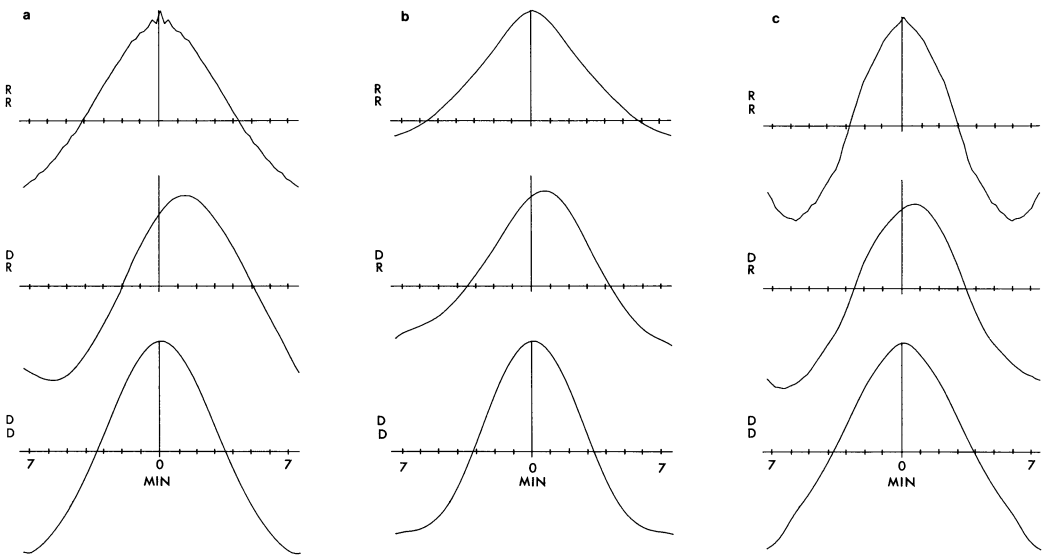

Fig. 5a–c. Cross-correlation function and autocorrelation functions for the riometer and *D*-component disturbances over the interval 1345–1400 on 27 October 1977. The number 35 refers to the number of data points used, the sample interval being 12.8 s. Any ramps in the original data have been removed during the course of the analysis. **a** at PROV; **b** at HAYR; **c** at SMIT and over the interval 1348–1403. The interval is changed slightly to take into account the propagation of the disturbance

SMIT). It is quite possible that the same occurrence which triggered the Ps 6 was responsible for providing the energy for the resonant oscillation near MCMU. Figure 2 shows the east-west line *D*-component data for the hour centered on 1400. The delay times for the appearance of the *D*-component peaks clearly indicate propagation from west to east, in accordance with the results of Kawasaki and Rostoker (1979). Figure 4 shows a detailed comparison between the *D*-component and riometer traces at PROV, HAYR, and SMIT. It is clear that there are well defined riometer responses associated with each *D*-component pulse and that the event maintains its structure over the 8° between PROV and SMIT. Finally we show in Fig. 5 the cross correlations between the *D*-component and riometer time series for PROV, HAYR and SMIT as well as the autocorrelations (which serve to demonstrate the degree of noisiness of the data). It can be seen that, for all three stations, the riometer leads the *D*-component of the magnetometer. This would imply that the precipitation starts slightly in advance of the buildup in equatorward current. However the actual delay times are 1.3 min for PROV, 0.6 min for HAYR and 0.6 min for SMIT. In light of the fact that the *D*-component has positive values above 50% of its maximum achieved value for a period of $\sim 4\ ^1/_2$ min, it is apparent that the delay between the *D*-component peak and riometer maxima is rather small. On the basis of this event, we would suggest that the *D*-component peak (and therefore the region of equatorward flowing ionospheric current) is approximately coincident with the region of energetic electron precipitation.

We now consider a second event which consists of a series

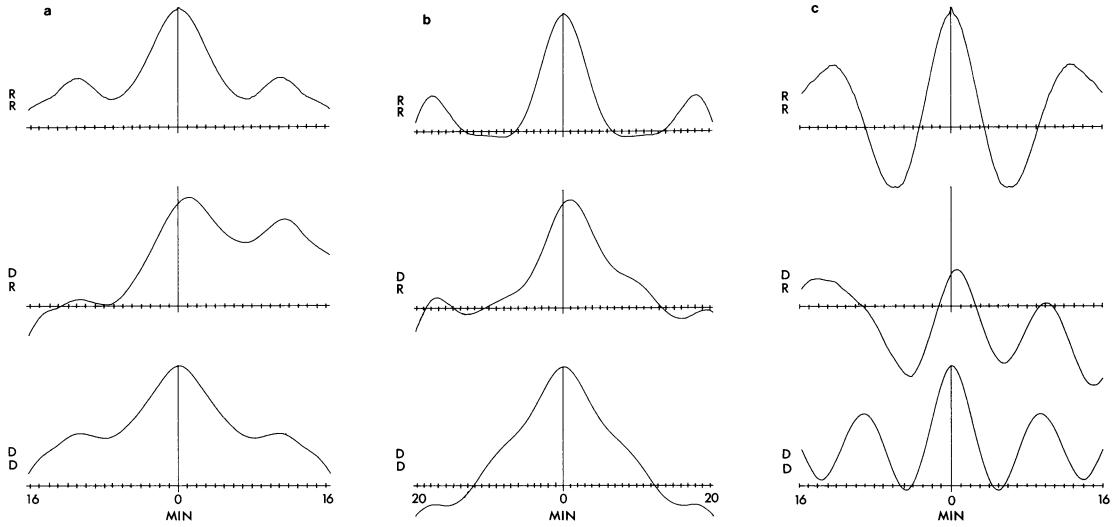

Fig. 6a–c. As Fig. 5 but for different time interval. **a** at PROV, 1109–1142; **b** at HAYR, 1105–1146; **c** at SMIT, 1116–1148

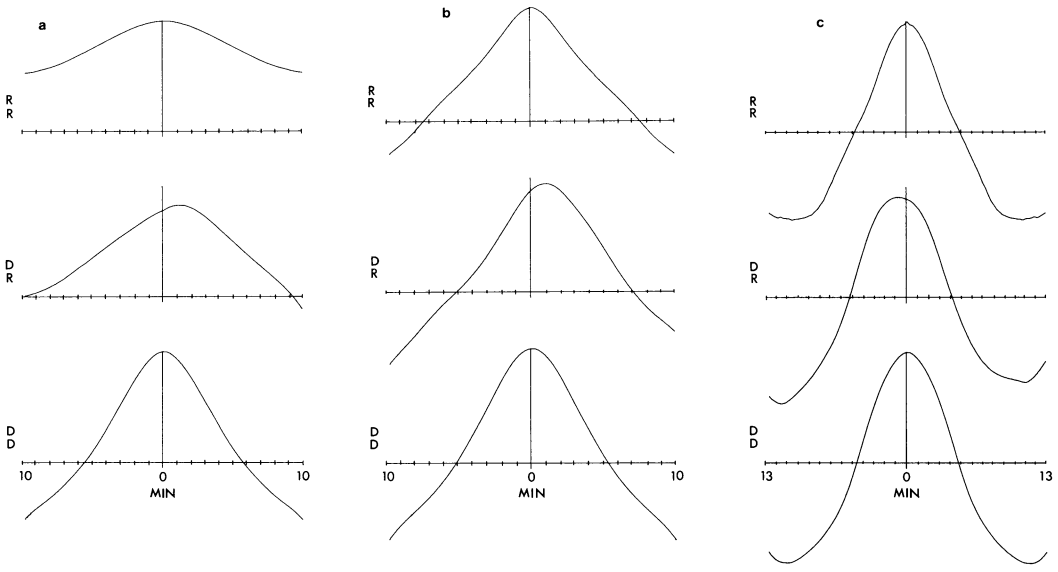

Fig. 7a–c. As Fig. 5 but for different time interval. **a** at PROV, 1540–1600; **b** at HAYR, 1540–1600; **c** at SMIT, 1540–1606

of Ps 6 disturbances which occur over the interval 1100–1215 on 27 October 1977. Figure 6 shows the cross-correlation and autocorrelation functions for the *D*-component and riometer time series for the stations of PROV, HAYR, and SMIT For this case there is more than one peak in the autocorrelation function, indicating that more than one Ps 6 spike occurred in the interval over which the cross-correlation funds are computed. The form of the cross-correlation function changes from station to station in this case, indicative of the fact that the perturbation pattern changes significantly over the east-west extent of the array. However the central peak is well defined in all cases, and indicates that the riometer leads the *D*-component magnetometer trace by 1.1 min at PROV, 0.9 min at HAYR and 0.7 min at SMIT Once again we would contend that the *D*-component positive peak and the riometer maximum are effectively coincident.

Our third event consists of a series of Ps 6 disturbances which occur over the interval 1440–1620 on 22 October 1977. Figure 7 shows the cross-correlation and autocorrelation functions for the *D*-component and riometer time series for the stations of PROV, HAYR, and SMIT The location of the peak in the cross-correlation function varies around the zero-lag marker. The riometer leads the *D*-magnetometer disturbance by 1.1 min at PROV and by 1.1 min at HAYR while it lags the *D*-disturbance by 0.7 min at SMIT Again we would claim that the *D*-component positive peak and the riometer maximum are coincident. We point out that the coincidence between the positive *D*-component peak and the riometer maximum is observed both early in the morning sector ($\sim$1100) as well as later ($\sim$1600).

To conclude this section on the observations, we present data from 30 January 1977 to demonstrate the variability of Ps 6 signatures over an east-west extent of $\sim$12° at auroral zone latitudes ($\sim$67.5° N). Figure 8 shows the magnetograms over the morning hours in the Alberta sector. While we shall analyse the event visible at PROV shortly after 1,400 (and at SMIT and URAN at slightly later times due to the propagation effect), it is useful at least to mention the fact that some disturbances do not maintain their structure across the array. For example, there is a clear sequence of three Ps 6 pulses at URAN between 1345 and 1415

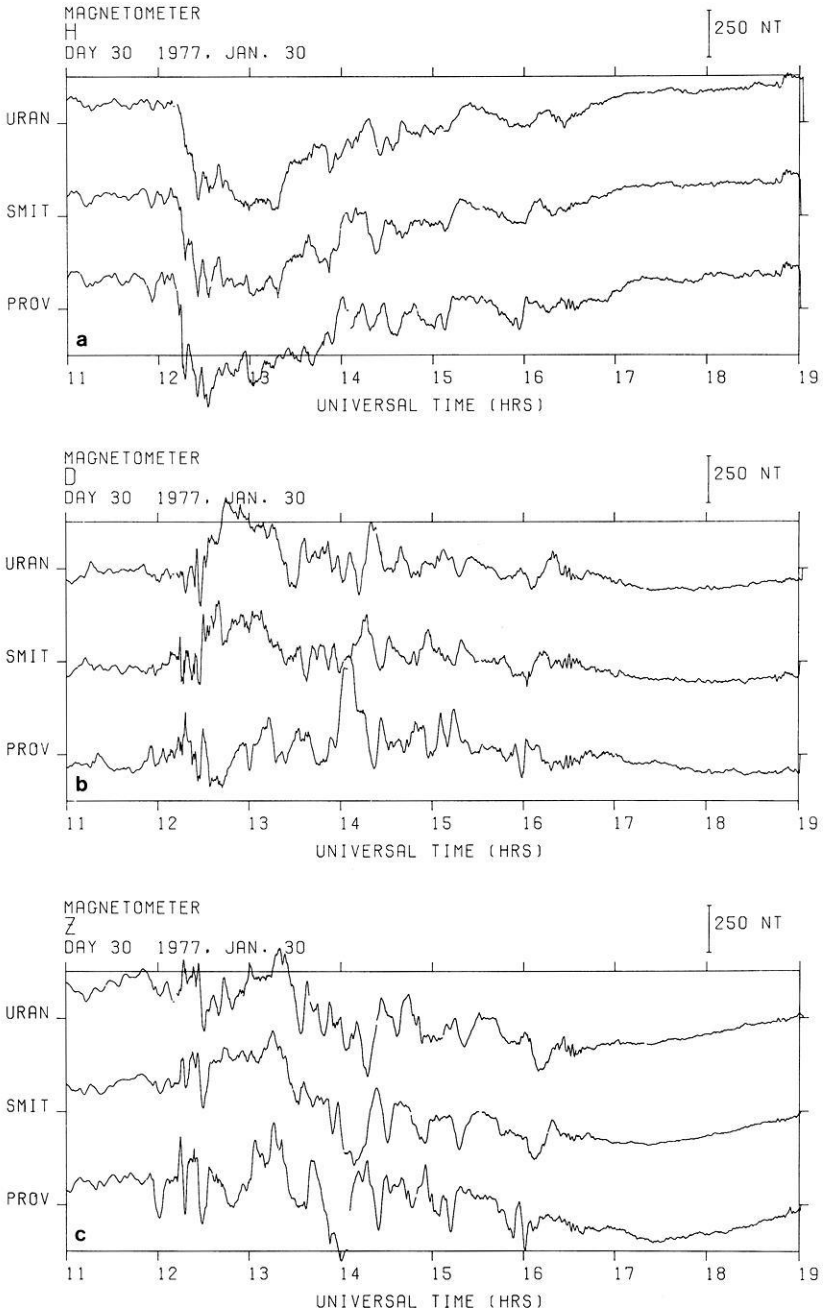

Fig. 8a–c. Magnetograms for 30 January 1977 recorded at stations along the east-west arm of the Alberta array. Station coordinates and code names are given in Table 1. **a** *H-component;* **b** *D*-component; **c** *Z*-component

with a corresponding structure being identifiable at SMIT. However, at PROV at least one of the three pulses is absent. Another example of such longitudinal localization can be seen by examining the two Ps 6 pulses observable at PROV shortly after 1,500. At least one of these pulses has vanished by the time the disturbance reaches SMIT. We can therefore see that the observation of a Ps 6 at a given longitude does not guarantee the continued existence of the structure as little as 5° of longitude away.

Continuing with the analysis of this day, we show in Fig. 9 the *D*-component disturbance and the riometer response on an expanded scale over the two hour interval centered on 1400. Clearly the magnitude of the *D*-component perturbation drops by a factor of ~2 from PROV to SMIT and the clear riometer response at PROV is complemented by a barely visible response at SMIT. The cross-correlation and autocorrelation functions for the *D*-component and riometer time series are shown in Fig. 10. While the PROV cross-correlation function peaks at zero lag (indicating that the peak *D*-component perturbation occurs at the time of maximal riometer response), the response at SMIT is rather different with the riometer appearing to lag the *D*-component by 3.4 min. This indicates that the energetic electron precipitation does not always correspond clearly to the region of maximum equatorward ionospheric current flow. In this particular case we note that the riometer response at SMIT is barely (if at all) identifiable. It is indeed possible that the cross-correlation function is dominated by the general cosmic noise absorption background in this case, rather than by a burst of electron precipitation associated with the Ps 6 disturbance. Nonetheless, this event points to the fact that caution must be exercised in comparing riometer and magnetometer data even when array data are available.

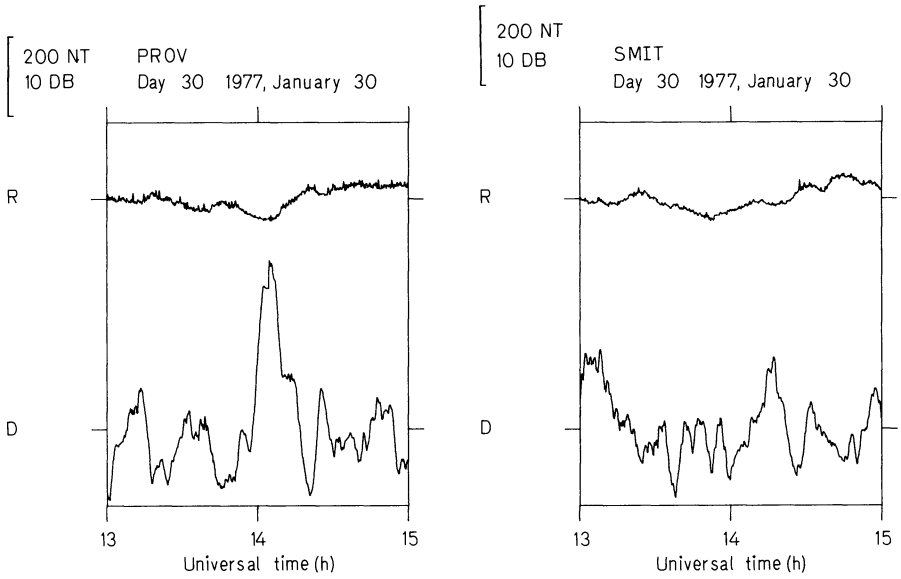

Fig. 9a, b. Riometer and *D*-component perturbations recorded on January 30, 1977. **a** at PROV; **b** at SMIT

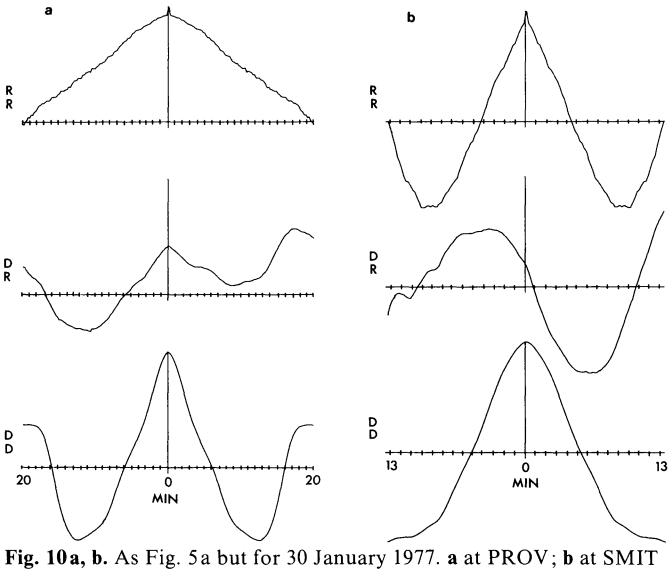

Fig. 10a, b. As Fig. 5a but for 30 January 1977. **a** at PROV; **b** at SMIT

Discussion and Conclusions

In this paper we have shown that the region of maximum equatorward ionospheric current flow in a Ps 6 disturbance occurs, in most cases, in the same region of space where the energetic electron precipitation maximizes. This is not in agreement with the observations of Gustafsson et al. (1981) but is in accord with the earlier contentions of Kawasaki and Rostoker (1979). We should like to note however, that we are still not in a position to distinguish uniquely between the real current systems proposed by Gustafsson et al. and Kawasaki and Rostoker. The results of Gustafsson et al. pointed to maximal electron precipitation in the region adjacent to the region of maximum equatorward current flow, and therefore they concluded that the southward ionopheric current was part of an ionospheric Hall current cell with poleward Hall current flowing both to the east and west of the equatorward current flow. Our results disagree with the observations of Gustafsson et al. but cannot disprove their model. It is possible, for example, that less energetic electron fluxes precipitate to the east and west of the region of equatorward current flow. Large fluxes of electrons having energies of a few keV can strongly influence E-region conductivity while barely penetrating to the D-region (which has the most influence on cosmic noise absorption). In fact, the only difference between the two models in question lies in the behaviour of the ionospheric equatorward current as it approaches the equatorward boundary of the auroral oval. In the model of Kawasaki and Rostoker, the ionospheric current would diverge up the field lines into the magnetosphere while in the model of Gustafsson et al. the current would be deflected to the east and to the west, eventually forming closed Hall current cells in the ionosphere. It is important to note that the model current systems in question produce effectively the same horizontal magnetic perturbation pattern at the earth's surface. Only the vertical component of the perturbation field could distinguish between the models, with the model involving ionospheric closure currents being expected to show weak *Z*-component edge effects associated with the northward Hall currents on either side of the heart of the Ps 6 disturbance region. Such edge effects would be extremely difficult to identify in a disturbed auroral oval, typical of the conditions in which Ps 6 disturbances occur.

Acknowledgements. We are deeply indebted to Environment Canada (Atmospheric Environment Service), to Transport Canada (Telecommunications Branch) and to Mr. and Mrs. Ted Malewski of Fort Providence, N.W.T for their help in operating the stations whose data are used in this study. This research was supported by the Natural Sciences and Engineering Research Council and is part of the International Magnetospheric Study.

References

Baumjohann, W.: Spatially inhomogeneous current configurations as seen by the Scandinavian magnetometer array. In: Proceedings of the International Workshop on Selected Topics of Magnetospheric Physics, pp. 35–40. Tokyo, 1979

Gustafsson, G., Baumjohann, W., Iversen, I.B.. Multi-method observations and modelling of the three-dimensional currents associated with a very strong Ps6 event. J Geophys **49**, 138–145, 1981

Kawasaki, K., Rostoker, G.: Perturbation magnetic fields and current systems associated with eastward drifting auroral structures. J. Geophys. Res. **84**, 1464–1480, 1979

Kisabeth, J.L., Rostoker, G.. Modelling of three-dimensional current systems associated with magnetospheric substorms. Geophys. J.R. Astron. Soc. **49**, 655–683, 1977

Rostoker, G., Barichello, J.C.. Seasonal and diurnal variation of Ps6 magnetic disturbances. J Geophys. Res. **85**, 161–163, 1980

Saito, T.. Long-period irregular micropulsations, Pi 3. Space Sci. Rev **21**, 427–467, 1978

Received November 3, 1980; Revised Version March 31, 1981
Accepted April 9, 1981

J Geophys (1981) 49:169–175

Journal of Geophysics

Correlation of Geomagnetic Activity Indices ap with the Solar Wind Speed and the Southward Interplanetary Magnetic Field

H. Schreiber

Institut für Geophysik der Universität Göttingen, Herzberger Landstraße 180, D-3400 Göttingen, Federal Republic of Germany

Abstract. Correlation studies were carried out wit the geomagnetic activity index ap, the solar wind velocity v and the southward interplanetary magnetic field (IMF) component, using a comprehensive interplanetary data set for the years 1963–1975. The calculations show that ap is best represented by the sum of two terms, one proportional to the second (or higher) power of v and to the first (or higher) power of the IMF southward component. The second term is proportional to v^2 only and contains the main part of the semiannual ap variation. The two terms may be regarded as indicators of two different mechanisms of energy transfer from the solar wind to the magnetosphere.

Key words: Geomagnetic activity – Solar wind velocity – Interplanetary magnetic field – Semiannual wave of geomagnetic activity

Introduction

The three-hourly geomagnetic planetary indices Kp and ap were defined by Bartels (reviewed by Siebert 1971) to be a measure of the solar corpuscular radiation. When in situ observations of the solar wind became available it turned out that these indices were indeed a measure of the influence of the solar wind on the geomagnetic field. Snyder et al. (1963) calculated a correlation coefficient of 0.73 between the daily average solar wind velocity v and the daily sum of Kp. In later years this relation was confirmed with more spacecraft measurements (Wilcox et al. 1967; Olbert 1968; Ballif and Jones 1969). In these studies, however, it was found not only that the solar wind velocity influences geomagnetic activity, and that other parameters of the interplanetary medium such as the interplanetary magnetic field (IMF) and its directions and fluctuations are also related to geomagnetic indices, but also that geomagnetic activity correlates better with some of these parameters than with the solar wind velocity.

The relationship of the IMF fluctuations to geomagnetic activity was studied by Ballif and Jones (1969), among others, indicating high correlations between the standard deviation of the IMF components transverse to the sun-earth line and Kp. On the other hand Garret (1974) emphasized the importance of the variance of the IMF for the magnitude of geomagnetic activity.

In connection with theories of field line reconnection or merging of a southward interplanetary magnetic field with the geomagnetic field, the importance of the IMF north-south component for increasing geomagnetic activity was studied in several papers. Arnoldy (1971) correlated hourly solar wind data with the auroral electrojet index AE and found that the best correlation was between AE and the time-integral of the southward IMF component in solar magnetospheric coordinates. The product of the solar wind velocity v and the southward IMF component B_s, which is important in merging theories, is highly correlated with geomagnetic activity (Russell et al. 1974). Further, the product $B_s \cdot v^2$ was found to be correlated best with the daily activity index Ap (Crooker et al. 1977). The latter authors suggest that variations of long-term averages of geomagnetic activity relate more to variations of v^2 whereas hourly (or three-hourly) activity variations are controlled by variations of B_s.

In this paper a relation is developed for the ap indices using the solar wind velocity and the southward IMF component and taking into account, to a certain degree, the IMF fluctuations by computing an "effective southward IMF component" B_{ZE}, comparable to the quantity Arnoldy (1971) found to be best correlated to the activity indices AE. The calculations show that ap is best represented by the sum of two terms, one proportional to $v^{2.25} \cdot B_{ZE}^{1.25}$ and the other proportional to v^2 (v is in km/s and B_{ZE} in nT throughout this paper). The second term is related to the main part of the semiannual variation of ap.

Effective IMF Southward Component

The interplanetary data used in this study are those prepared and described by King (1977a, b). The data are available on tape at the World Data Center A. From the composite tape containing hourly averages of IMF and interplanetary plasma data of the years 1963–1975, only those time intervals with both IMF and solar wind data have been selected. To correlate the interplanetary data with ap indices, three-hourly averages were computed. Thus, 13,820 three-hour intervals (about 4.7 years) of data are available for our calculations. Though the data were provided by different spacecraft and the temporal coverage varies significantly over the time interval of about one solar cycle, the data are treated as one homogeneous set.

First we correlate ap with the solar wind speed v dividing

0340-062X/81/0049/0169/$01.40

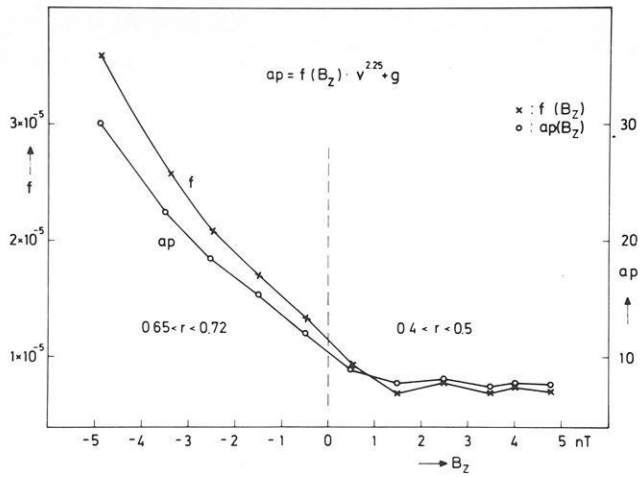

Fig. 1. The coefficient f in the relation $\mathrm{ap}=f(B_Z)\cdot v^{2.25}+g$ as a function of the IMF component B_Z in GSM coordinates. In addition the ap averages for the different B_Z intervals are shown

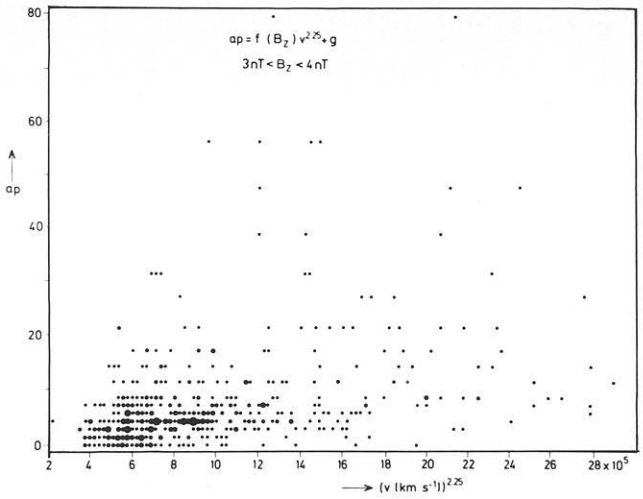

Fig. 3. Scatter plot for the relation $\mathrm{ap}=f(B_Z)\cdot v^{2.25}+g$ for a positive B_Z interval $3\,\mathrm{nT}<B_Z<4\,\mathrm{nT}$

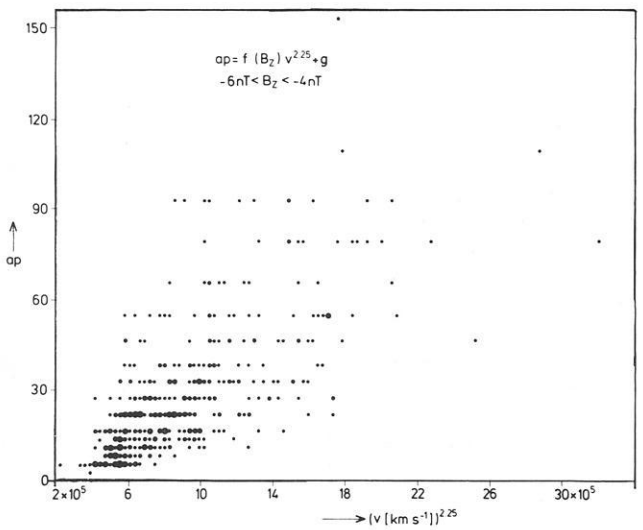

Fig. 2. Scatter plot for the relation $\mathrm{ap}=f(B_Z)\cdot v^{2.25}+g$ for the interval $-6\,\mathrm{nT}<B_Z<-4\,\mathrm{nT}$

the data into groups according to the magnitude of the IMF north-south component B_Z in geocentric solar magnetospheric (GSM) coordinates. Best correlations for all groups were found for a power of 2.25 of v giving

$$\mathrm{ap}=f(B_Z)\cdot v^{2.25}+g(B_Z) \tag{1}$$

where the coefficients $f(B_Z)$ and $g(B_Z)$ may vary with B_Z. The same relation of the am indices (Mayaud 1967) with $v^{2.25}$ was found by Svalgaard (1978). Figure 1 shows the coefficient f as a function of B_Z(B_Z being the average in the corresponding interval). For negative B_Z values f grows nearly linearly with decreasing B_Z; for $B_Z\geqq 1\,\mathrm{nT}$ however, f is nearly constant and small. The correlation is significantly greater for $B_Z<0$ than for $B_Z>0$. Two scatter plots of relation (1) for intervals of negative and positive B_Z are shown in Figures 2 and 3 to demonstrate the different relationship of ap with $v^{2.25}$ for positive and negative B_Z. There is significantly less scatter in Fig. 2 where 438 points in the relatively wide interval $-4\,\mathrm{nT}>B_Z>-6\,\mathrm{nT}$ are plotted (correlation coefficient $r=0.67$) than in Fig. 3 with 506 points in the interval $3\,\mathrm{nT}<B_Z<4\,\mathrm{nT}$ ($r=0.41$). Considering only those points of Figure 3 with ap > 27, no correlation of ap with $v^{2.25}$ is seen. Inspection of the interplanetary data for these three-hourly intervals showed that either (i) at least one hourly averaged B_Z of the corresponding three-hourly interval was negative, or (ii) the three-hourly averages of B_Z are positive but there are strong fluctuations of the IMF in at least one of the hourly intervals, or (iii) in the preceding three-hourly interval there was a negative B_Z value or strong fluctuations of the IMF.

No other remarkable features of the interplanetary data were found. From these examples, remembering that the ap indices are based on the greatest positive and negative geomagnetic disturbances (not an average disturbance) in a three-hourly interval at several observatories, we may conclude that the three-hourly average of B_Z is not the appropriate parameter to correlate with ap. A better parameter to describe the strong influence of the southward IMF component on geomagnetic activity is an "effective southward IMF component" that takes into account at least points *i)* and *ii)* of the foregoing discussion. It is defined as follows:

The individual IMF values, from which the hourly averages of the NSSCD interplanetary data set (King 1977a) are constructed, are assumed to be normally distributed. Thus for the GSM north-south component of the IMF the hourly mean M_{B_Z} may be written

$$M_{B_Z}=\int_{-\infty}^{+\infty} h(B_Z)\cdot B_Z\cdot dB_Z \tag{2}$$

with the frequency distribution

$$h(B_Z)=\frac{1}{\sigma_{B_Z}\cdot\sqrt{2\pi}}\exp\left\{-\frac{(B_Z-M_{B_Z})^2}{2\sigma_{B_Z}}\right\} \tag{3}$$

where σ_{B_Z} is the standard deviation of the B_Z values. The effective southward component B'_{ZE} is defined to be the average of the negative part of the frequency distribution

$$B'_{ZE}=\int_{-\infty}^{0} h(B_Z)\cdot B_Z\cdot dB_Z\simeq\int_{M_{B_Z}-3\sigma_{B_Z}}^{0} h(B_Z)\cdot B_Z\cdot dB_Z \tag{4}$$

From hourly averages M_{B_Z} and standard deviations σ_{B_Z} we may compute B'_{ZE} numerically. Some examples are $M_{B_Z}=-4\,\mathrm{nT}$ and $\sigma_{B_Z}=3\,\mathrm{nT}$ giving $B'_{ZE}=-4.2\,\mathrm{nT}$; $M_{B_Z}=4\,\mathrm{nT}$ and $\sigma_{B_Z}=3\,\mathrm{nT}$ giving $B'_{ZE}=-0.12\,\mathrm{nT}$; $M_{B_Z}=4\,\mathrm{nT}$ and $\sigma_{B_Z}=8\,\mathrm{nT}$ giving $B'_{ZE}=-1.6\,\mathrm{nT}$.

Unfortunately the available IMF data contain σ_{B_Z} values only for a part of the time interval covered by the whole data set. The only consistent measure of IMF fluctuations is the vector standard deviation $(\sigma^2_{Bx}+\sigma^2_{By}+\sigma^2_{Bz})^{1/2}$ (King 1977a). Four our computations of B'_{ZE} we used this quantity as an approximation of σ_{B_Z}.

Significantly better correlations were found by correlating ap with three-hourly averages of B'_{ZE} than by correlating ap with B_Z. A slight enhancement of the correlation coefficients was achieved using the minimum of the three one-hourly B'_{ZE} values instead of the three-hourly means. Therefore, and in order to have positive values for the effective southward IMF component, we redefined

$$B_{ZE}=|\min(B'_{ZE\,1}, B'_{ZE\,2}, B'_{ZE\,3})| \tag{5}$$

where B'_{ZEi} are the three one-hourly values in the respective three-hourly ap interval. The further correlations were carried out using B_{ZE} as defined in Eqs. (4) and (5). It should be added that B_{ZE} is, to a certain degree, comparable with the time-integral of the southward IMF component, which Arnodly (1971) found to be best correlated with AE indices.

Correlation of ap with v and B_{ZE}

The whole data set of 13,820 three-hourly intervals were divided into 10 groups according to the strength of the solar wind velocity. For all groups ap was correlated with B_{ZE}

$$\mathrm{ap}=C(v)\cdot B^q_{ZE}+D(v) \tag{6}$$

where the coefficients $C(v)$ and $D(v)$ may be functions of v. Best correlation was found for a power $q=1.25\pm0.1$; the error was estimated from the slightly varying best power for the different v intervals. In Fig. 4 the two functions $C(v)$ and $D(v)$ of Eq. (6) are shown for $q=1.25$. Both functions may be described by power laws

$$C(v)=c\cdot v^p+d \tag{7}$$

$$D(v)=e\cdot v^{p'}+f \tag{8}$$

Correlating $C(v)$ and $D(v)$ with v, the coefficients c, d, e, f, and the powers p and p' were calculated by maximizing the correlation coefficients. The numerical results were $p=2.25\pm0.10$, $p'=2.0\pm0.3$; $d=0.081\pm0.132$, $f=0.35\pm0.5$; $c=2.77\ 10^{-6}$, $e=2.30\cdot10^{-5}$. Since $c\ v^p\gg d$ and $e\cdot v^{p'}\gg f$, Eqs. (7) and (8) may be simplified with $d=f=0$. Inserting (7) and (8) into (6), one finds

$$\mathrm{ap}=c\ v^{2.25}\cdot B^{1.25}_{ZE}+e\cdot v^2 \tag{9}$$

The same relationship of ap to v and B_{ZE} and equivalent values for the powers and coefficients (in the limits of the error ranges) were obtained by a similar procedure. Dividing the data into groups of different B_{ZE} intensities, the appropriate power of v was calculated by a correlation of the form

$$\mathrm{ap}=A(B_{ZE})\cdot v^p+B(B_{ZE}) \tag{10}$$

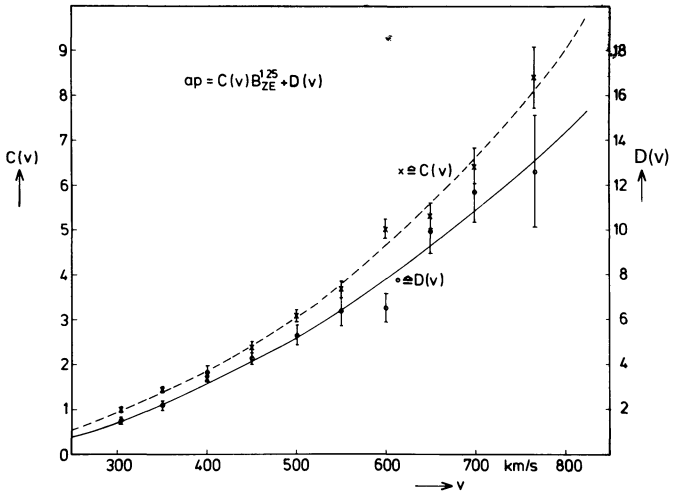

Fig. 4. The functions $C(v)$ and $D(v)$ in the relation $\mathrm{ap}=C(v)\cdot B^{1.25}_{ZE}+D(v)$. The crosses for $C(v)$ and circles for $D(v)$ with error bars were calculated from correlations in the different v intervals. The dashed and solid curves are the best power laws for $C(v)$ and $D(v)$ according to Eqs. (7) and (8)

Thus assuming simple power laws for the relation of ap to v and B_{ZE} the correlation calculations show that at least two terms should be taken into account, one with the second (or higher) power of v and the first (or higher) power of B_{ZE} and the other approximately proportional to v^2.

For a general form of Eq. (9)

$$\mathrm{ap}=h\ v^p\cdot B^q_{ZE}+k\cdot v^{p'}+j \tag{11}$$

with coefficients h, k and j, multiple correlation calculations of ap with v and B_{ZE} were carried out, varying the powers p, q, p'. The best multiple correlation coefficient $r_m=0.82$ was found as expected for $p=2.25$, $q=1.25$, and $p'=2.0$. For these values the coefficients h and k are (within the limits of errors) identical with c and e of Eq. (9) and $j=0.064\pm0.142\simeq0$.

Equations (9) and (11) therefore may be regarded as a reasonable approximation of the activity index ap in terms of solar wind parameters. In a very recent paper extending earlier results of Murayama and Hakamada (1975) and Aoki (1977), Murayama et al. (1980) found a relation similar to Eqs. (9) and (11) of the AL index as a measure of the westward auroral electrojet $\mathrm{AL}=K\cdot(0.5+B_s)v^2$ where B_s was defined and calculated as B_{ZE}; the factor K was found to be a function of the IMF B_y component and of the dipole tilt angle.

Our relations (9) and (11) do not explicitly contain the semiannual variation of ap, which is the most pronounced variation after the 11.5 year solar cycle. To investigate in which term or factor of Eq. (11) the semiannual wave is contained, data for individual months were lumped together and month by month calculation of the multiple correlation coefficients for Eq. (11) was made. Biases which might arise from varying amounts of data for individual months (maximum of 1510 for January and minimum of 840 for October) and uneven distribution for the individual months during the 13 year period were not taken into account.

The results of the calculations are presented in Fig. 5. The upper curve (crosses) shows the monthly averages of ap for the available data. The seminannual variation for these time intervals is not so marked as for longer time interval but is

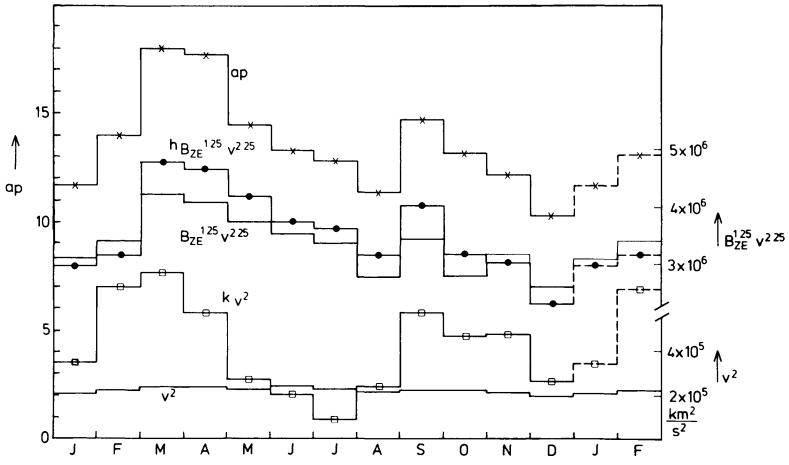

Fig. 5. Monthly averages of observed ap and the different quantities of Eq. (11) computed with multiple correlations for every month

clearly seen, and an annual wave with maximum near the vernal equinox may be superposed. The second curve (full circles) shows the yearly variation of the first term of the right hand side in Eq. (11). A slight semiannual wave is present, again superposed by an annual wave. Harmonic analysis of this curve yields amplitudes of 1.7 and 0.66 ap units for the annual and semiannual waves with maxima near 19 April (annual) and 25 April, 24 October (semiannual). The third curve (thin line) of Fig. 5 shows montly averages of the quantity $B_{ZE}^{1.25}\ v^{2.25}$ on a comparable scale. This curve is nearly parallel to the second curve and the coefficient h of Eq. (11) is seen to be nearly constant for all months. Since $v^{2.25}$ is also nearly constant (see the lower thin curve), the yearly variation of the first right hand term of relation (11) must be attributed to variations in B_{ZE}. These yearly B_{ZE} variations with maximum near spring and minimum near fall should be observed if, in the available interplanetary data, there were more IMF toward than away days, if the average IMF toward fields are stronger than the away fields, or if the IMF southward component is stronger in spring than in fall months. A heliographic latitude dependent variation of the relevant solar wind parameters, which was suggested by Murayama (1974) to cause one part of the semiannual variation of Kp, should also be attributed to the variation of B_{ZE}, since the averages of v^2 and also of $|B|$ (see the corresponding curve in Fig. 6) show no appreciable variation throughout the year. An analysis of the data to investigate the reasons for the B_{ZE} variations has not yet been carried out.

The fourth curve of Fig. 5 (open squares) represents the second right hand term of Eq. (11). This term shows a clear semi annual wave. Harmonic analysis yields an amplitude of 2.7 ap units and maxima at about 22 March and 21 September for this wave. This variation is not seen in v^2 and must be attributed to a semiannual variation in the coefficient k.

Thus it may be concluded that the main part of the semiannual variation of ap is contained in a variation of k in Eq. (11) and not in the variation of the solar wind speed v nor in the variation of the southward IMF component B_{ZE}.

The mechanism proposed by Boller and Stolov (1970, 1973) can account for such a semiannual modulation of the coefficient k in Eq. (11). According to Boller and Stolov the maxima of geomagnetic activity near the equinoxes are caused by an enhanced probability of occurrence of the Kelvin-Helmholtz instability along the flanks of the magnetosphere. The instability criterion they apply is

$$v^2 > \frac{\rho_I + \rho_M}{\mu_0 \cdot \rho_I \cdot \rho_M} (B_I^2 \cos^2 \psi_I + B_M^2 \cos^2 \psi_M) \tag{12}$$

where indices I and M stand for interplanetary and magnetospheric values respectively, ρ are plasma densities, B the magnetic field strengths and ψ the angles between the velocity v and the magnetic fields. The second term on the right hand side of Eq. (12) yields a semi annual variation since at the equinoxes $\psi_M = 90°$ maximizes the instability probability.

For our calculations we simplify the criterion of Eq. (12) by assuming: *(i)* the factor $(\rho_I + \rho_M)/\rho_I \rho_M = 1/\rho$ is constant, *(ii)* the part of the geomagnetic activity indices ap relating to the Kelvin-Helmholtz instability is proportional to the difference between the left and right hand sides of inequality (12), and *(iii)* the two terms $c_0 = B_I^2 \cos^2 \psi_I / \mu_0 \rho v^2$ and $c_2 = B_M^2 / \mu_0 \rho v^2$ are constant. With these simplications we may write

$$\text{ap} = c_1\ v^2 \cdot (1 - c_0 - c_2 \cdot \cos^2 \psi_M) + \ldots \tag{13}$$

where the dots indicate the first term in Eq. (11) and c_0, c_1, and c_2 are constants.

The semiannual variation of ap is described in Eq. (13) only by the variation of $\cos^2 \psi_M$ which is a function of the time of year (Damaske 1977)

$$\cos \psi_M = \sin \delta_0 \cdot \cos \varepsilon_0 \cdot \cos \alpha \tag{14}$$

with the constant angles between the earth's rotation axis and the ecliptic plane $\delta_0 = 23.5°$ and between the rotation axis and the dipole axis $\varepsilon_0 = 11.5°$. The seasonal angle α begins with $\alpha = 0$ on 22 June.

Inserting the constant angles δ_0 and ε_0 and replacing $\cos \psi_M$ in Eq. (13) by $\cos \alpha$, and then comparing Eqs. (13) and (11), we finally have

$$\text{ap} = h\ v^{2.25} \cdot B_{ZE}^{1.25} + c_1 \cdot (1 - c_0 - c_2 \cdot 0.153 \cos^2 \alpha)\ v^2 \tag{15}$$

Multiple correlation calculations of ap with $v^{2.25} \cdot B_{ZE}^{1.25}$ and $(1 - c_0 - c_2 \cdot 0.153 \cos^2 \alpha) \cdot v^2$ were made for different values of the constants c_0 and c_2. The best multiple correlation coefficient is $r_m = 0.84$ for $c_0 = 0.5 \pm 0.25$ and $c_2 = 2.0 \pm 0.5$; for these values $h = (0.276 \pm 0.003) \cdot 10^{-5}$ and $c_1 = (0.591 \pm 0.015) \cdot 10^{-4}$.

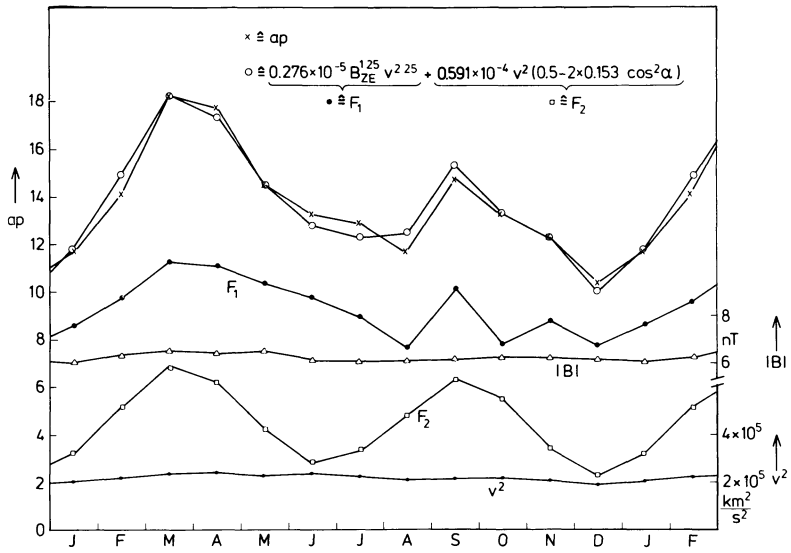

Fig. 6. Monthly averages of observed ap *(crosses)* and reconstructed ap *(circles)* according to Eq. (15), inserted above in explicit form. F_1 and F_2 are monthly averages of the two terms of relation (15), showing different contributions to ap during the year. The monthly averages of v^2 and IMF magnitude $|B|$ show no yearly variation

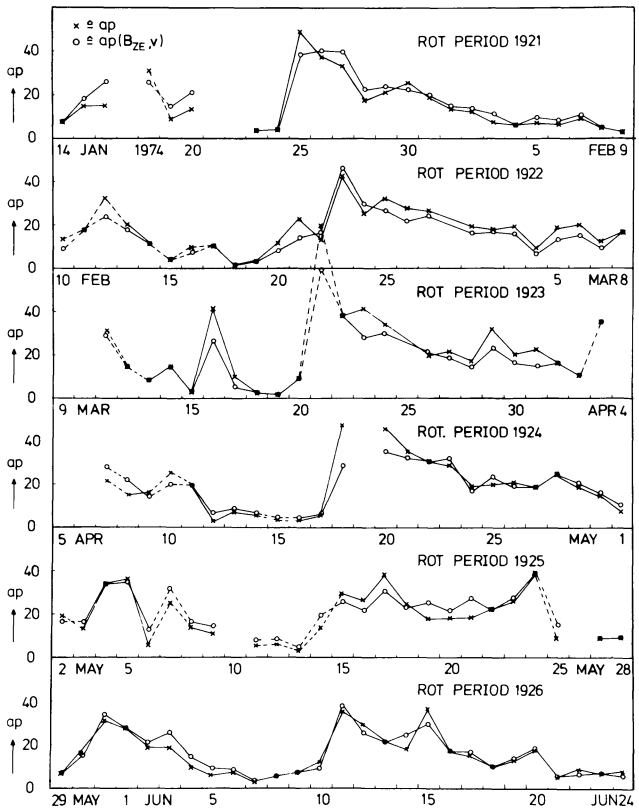

Fig. 7. Daily means of ap *(crosses)* and ap as reconstructed after Eq. (15) *(circles)* for 6 consecutive solar rotation periods in the first half of 1974. Only those days with data available for at least 6 three-hour intervals *(solid)* or 4 three-hour intervals *(dashed)* are shown

Using these numerical values, Eq. (15) is shown in Fig. 6 where monthly averages of different quantities are compared. The two upper curves show monthly averages of the observed ap and the ap values computed from monthly averages of $v^{2.25} \cdot B_{ZE}^{1.25}$ and $v^2 \cdot (0.5 - 2 \cdot 0.153 \cos^2 \alpha)$. The observed and reconstructed annual variations of ap are in good agreement. Comparing the two terms of Eq. (15) it is seen that the first term F_1, containing B_{ZE}, represents on the average about two thirds of ap, but the second term F_2 contains the main part of the semiannual wave. In addition monthly averages of v^2 and the IMF magnitude averages $|B|$ are shown, in comparable scales, indicating no yearly variation. The yearly variation in F_1 is mainly caused by variation of B_{ZE} as was seen in Fig. 5.

As well as the monthly averages, the daily ap means are approximated closely by Eq. (15). An example is shown in Fig. 7, where daily means of observed ap and reconstructed ap are shown for six consecutive solar rotations in 1974. For other periods the same good agreement between the two quantities were found, so Eq. (15) may be regarded as a reasonable representation of daily means of ap in terms of solar wind parameters.

Discussion

Before single three-hourly observed ap indices are compared with the ap values computed with Eq. (15) from solar wind parameters, it should be explained that, in principle, exact agreement between the two quantities is not possible.

The hypothesis proposed by Boller and Stolov (1970) and adopted in this study not only generates semiannual but also daily UT variations of geomagnetic activity. Also any other hypothetical mechanism relating variations of geomagnetic activity to the variations of the angle between the solar wind direction and the geomagnetic dipole axis produces such daily UT variations. This effect is neglected in Eq. (15), since in the procedure for generating ap indices these possible activity variations are eliminated (Siebert 1971). In fact the elimination is imperfect and UT variations remain in ap which are different for the two IMF polarities but are not real activity variations (Schreiber 1978). On the other hand ap is not a continuous measure and only 28 different values between 0 and 400 are possible whereas v and B_{ZE} are continuous.

In spite of these restrictions the observed and reconstructed ap values are compared in Fig. 8 for two solar rotations and give an impression of relatively good agreement, which generally was found for all the data. Although appreciable differences are sometimes evident especially during time intervals of high activity, no systematic behaviour of the differences throughout the solar cycle was discovered.

An improvement of the final relation (15) may be achieved

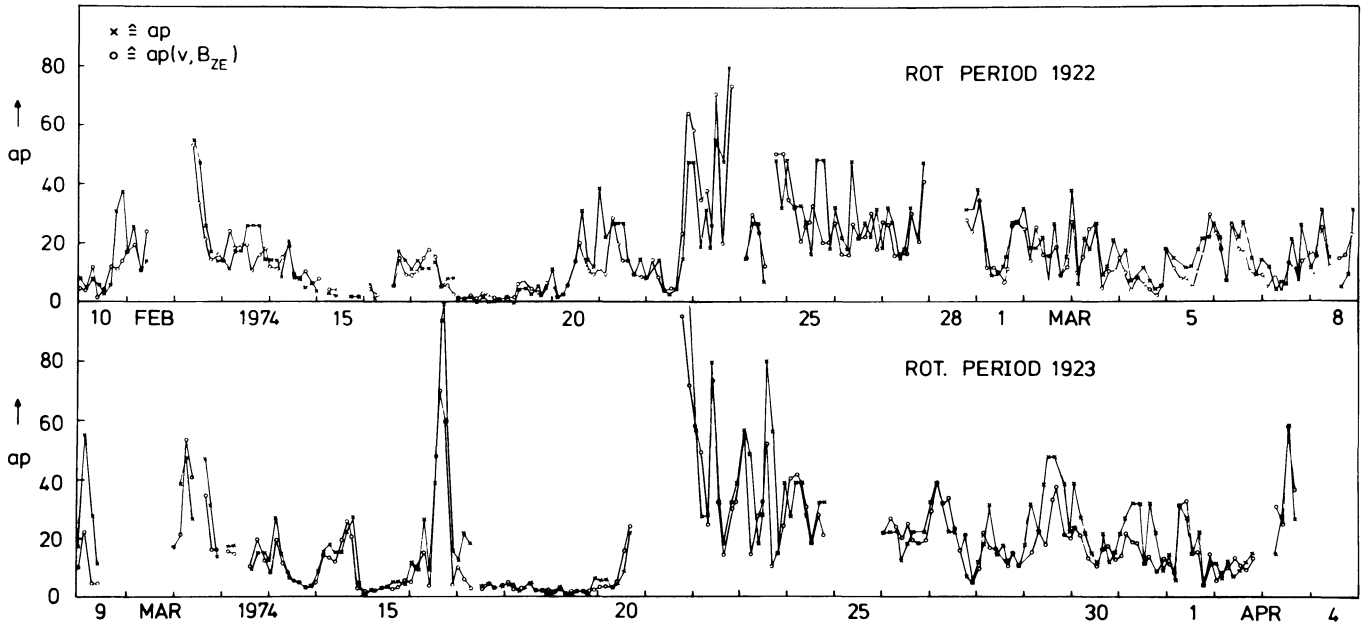

Fig. 8. Comparison of individual ap (observed) and ap (reconstructed) for two solar rotation periods. Gaps indicate missing interplanetary data

by including the above mentioned daily variations. These effects however should be studied using the am indices, introduced by Mayaud (1967), since these indices show the expected daily variations (Mayaud 1977). Taking into account other solar wind parameters, e.g., the plasma density n, for which Svalgaard (1978) observed that am is proportional to $n^{1/3}$ and Murayama et al. (1980) found AL to be proportional to $n^{0.13}$, may also refine the relation.

The main result of the present analysis is the finding of at least two terms of the relation between geomagnetic activity and solar wind parameters, one proportional to the southward IMF component B_{ZE} and the other independent of B_{ZE}. The definition of B_{ZE} includes the assumption that geomagnetic activity is generated, by, for example, a merging process of interplanetary and geomagnetic field lines, only if a southward IMF component is present. This process is sometimes named the half-wave rectifier response of the magnetosphere to the IMF orientation, meaning that energy transfer from the solar wind into the magnetosphere is possible only for a southward oriented IMF component, as first suggested by Arnoldy (1971) (see Crooker 1980, for a discussion of this problem). Russell and McPherron (1973) used this rectifier response in their hypothesis to explain the semiannual wave in geomagnetic activity. The results of the present correlative study (Figs. 5 and 6) indicate a slight semiannual variation due to the B_{ZE} term in Eqs. (11) and (15) in agreement with the Russell-McPherron hypothesis; the main part of the semi annual wave however was found in a second additional term which is essentially independent of a southward IMF component. This second term can be explained with the mechanism proposed by Boller and Stolov (1970) as one possible IMF-independent process of the interaction of the solar wind with the magnetosphere. A similar conclusion was reached by Berthelier (1976) investigating the influence of the IMF polarity on geomagnetic activity.

Thus the two terms of the relation between geomagnetic activity and solar wind parameters may suggest two different mechanisms of energy transfer from the solar wind to the magnetosphere and Eq. (15) and Fig. 6 may be regarded as a rough quantitative separation of the two parts.

Acknowledgements. The interplanetary data used in this study were provided by the World Data Center A; the numerical computations were carried out at the Gesellschaft für wissenschaftliche Datenverarbeitung (GWD), Göttingen. Special thanks to M. Richards for his assistance during the preparation of the manuscript.

References

Aoki, T.: Influence of the dipole tilt angle on the development of auroral electrojets. J. Geomagn. Geoelectr. **29**, 441–453, 1977

Arnoldy, R.L.: Signature of the interplanetary medium for substorms. J. Geophys. Res. **76**, 5189–5201, 1971

Ballif, J.R., Jones, D.E.: Further evidence on the correlation between transverse fluctuations in the interplanetary magnetic field and Kp. J. Geophys. Res. **74**, 2289–2301, 1969

Berthelier, A.: Influence of the polarity of the interplanetary magnetic field on the annual and diurnal variations of geomagnetic activity. J. Geophys. Res. **81**, 4546–4552, 1976

Boller, B.R., Stolov, H.L.: Kelvin-Helmholtz instability and the semiannual variation of geomagnetic activity. J. Geophys. Res. **75**, 6073–6084, 1970

Boller, B.R., Stolov, H.L.: Explorer 18 study of the stability of the magnetopause using Kelvin-Helmholtz instability criterion. J. Geophys. Res. **78**, 8078–8086, 1973

Crooker, N.U., Feynman, J., Gosling, J.T.: On the high correlation between long-term averages of solar wind speed and geomagnetic activity. J. Geophys. Res. **82**, 1933–1937, 1977

Crooker, N.U.: The half-wave rectifier response of the magnetosphere and antiparallel merging. J. Geophys. Res. **85**, 575–578, 1980

Damaske, D.: Magnetospheric modulation of geomagnetic activity I. Harmonic analysis of quasi-logarithmic indices Km, Kn, and Ks. Ann. Géophys. **33**, 461–478, 1977

Garrett, H.B.: The role of fluctuations in the interplanetary magnetic field in determining the magnitude of substorm activity. Planet. Space Sci. **22**, 111–119, 1974

King, J.H.: Interplanetary medium data book. Rep. NSSDC/WDCA-77-04, Goddard Space Flight Center, Greenbelt, Maryland, 1977a

King, J.H.: Interplanetary medium data book. Appendix, Rep. NSSDC/WDC-A 77-04a, Goddard Space Flight Center, Greenbelt, Maryland, 1977b

Mayaud, P.N.: Calcul préliminaire d'indices Km, Kn et Ks ou am an et as, mesure de l'activité magnétique à l'échelle mondiale et dans les hémisphères Nord et Sud. Ann. Géophys. **23**, 585–617, 1967

Mayaud, P.N.: The Boller-Stolov mechanism and the semiannual and daily McIntosh effects in geomagnetic activity. J. Geophys. Res. **82**, 1266–1270, 1977

Murayama, T.: Origin of the semiannual variation of geomagnetic Kp indices. J. Geophys. Res. **79**, 297–300, 1974

Murayama, T., Hakamada, K.: Effects of solar wind parameters on the development of magnetospheric substorms. Planet. Space Sci. **23**, 75–91, 1975

Murayama, T., Aoki, T., Nakai, H., Hakamada, K.: Empirical formula to relate the auroral electrojet intensity with interplanetary parameters. Planet. Space Sci. **28**, 803–813, 1980

Olbert, S.: Summary of experimental results from M.I.T. detector on IMP 1. In: Physics of the Magnetosphere, R.L. Carovillano, J.F. McClay, H.R. Radoski, eds.. pp. 641–659. Dortrecht, Netherlands: D. Reichelt 1968

Russell, C.T., McPherron, R.L.: Semiannual variation of geomagnetic activity. J. Geophys. Res. **78**, 92–108, 1973

Russell, C.T., McPherron, R.L., Burton, R.K.: On the cause of geomagnetic storms. J. Geophys. Res. **79**, 1105–1109, 1974

Schreiber, H.: On the possibility of inferring the interplanetary sector structure from daily variations of geomagnetic ap indices. Planet. Space Sci. **26**, 767–775, 1978

Siebert, M.: Maßzahlen der erdmagnetischen Aktivität, In: Handbuch der Physik, 49 (3), S. Flügge, ed.: pp. 206–270. New York: Springer 1971

Snyder, C.W., Neugebauer, M., Rao, U.R.: The solar wind velocity and its correlation with cosmic-ray variation and with solar and geomagnetic activity. J. Geophys. Res. **68**, 6361–6370, 1963

Svalgaard, L.: Geomagnetic activity dependence on solar wind parameters. In: Skylab Workshop Monograph on Coronal Holes, Chap. IX, J. Zirker, ed. Col. Univ. Press 1978

Wilcox, J.M., Schatten, K.H., Ness, N.F.: Influence of interplanetary magnetic field and plasma on geomagnetic activity during the quiet-Sun conditions. J. Geophys. Res. **72**, 19–26, 1967

Received December 2, 1980; Revised Version March 3, 1981
Accepted April 9, 1981

J Geophys (1981) 49:176–185

Journal of Geophysics

High Time-Resolution Correlation Between the Magnetic Field Behaviour at 37 R_E Distance in the Magnetotail Plasma Sheet and Ground Phenomena During Substorm Expansive Phase

V.A. Sergeev
Physical Institute of Leningrad, State University, Leningrad 198904, USSR

Abstract. The changes of the magnetic field, detected by the IMP-8 satellite during six successive well-defined substorms on 3 March 1976, are studied in relation to the typical expansive phase microstructure (microsubstorm sequence or multi-step substorm) derived from the extensive complex of ground observations, and also in relation to the thin structure of separate microsubstorms (the formation of new arcs at the poleward front of the expanding auroral bulge with simultaneous abrupt changes in the Pi2 pulsation regime of mid-latitudes). Both the successive Pi2 onsets and the moments of abrupt changes in their regime, along with the corresponding auroral phenomena, are simultaneous (usually within the 0.5 min resolution of the data) with the impulsive magnetic field variations in the plasma sheet, whose pattern at 37 R_E was found to change typically in a sequence of microsubstorms, constituting the whole expansive phase; each of them is also related to the fast particle energization.

Key words: Auroral substorm – Magnetospheric substorm – Expansive phase – Substorm microstructure

Introduction

Changes of the magnetic field and plasma properties in the magnetotail during substorms have been investigated in many papers, but it is mainly the large-scale features, having the time scale of the expansion phase duration (0.5–1 h) which have been determined unambiguously (Fairfield and Ness 1970; Hones et al. 1973; Russell and McPherron 1973; Nishida and Nagayama 1973; Hones 1979). At the same time a number of experimental results obtained recently demand a more detailed description of the magnetospheric phenomena, this being necessary for understanding and modelling of the explosive energy dissipation process operating in the magnetotail during the substorm expansion phase. The time scale of the explosive energy dissipation is often only 0.1–1 min, as suggested by the direct observation of strong impulsive electric fields (Aggson and Heppner 1977; Pedersen and Grard 1978) and particle bursts up to MeV energy (Krimigis and Sarris 1979). A study of the magnetic field and plasma particles also displays brief periods of intense variations, repeated a few times during the expansion phase (Pytte et al. 1976b, 1978; Sergeev 1977). The observation of high-energy particle bursts (Krimigis and Sarris 1979) and studies of magnetic and plasma variations (Rostoker and Camidge 1971; Sergeev 1977; Pytte et al. 1976b; Lui et al. 1977a, b) also suggest the spatial localization of the active region. In particular, its longitudinal range, is less than the magnetotail width.

Thus the process of the explosive energy transformation is apparently short-lived and localized and occurs sporadically at different regions of the magnetotail during the substorm expansive phase.

This paper is devoted to a detailed study of the magnetic field response at 37 R_E distance in the vicinity of the magnetotail plasma sheet to the discrete time structure of the substorm expansive phase. The results, combined with similar ones obtained for the 10–20 R_E distances (Pytte et al. 1976b, 1978; Sergeev 1977) are used to infer the pattern of magnetic field variations and its changes during the successive events in the whole expansion phase.

Such studies demand the independent determination of the times of explosive energy dissipation events (microsubstorms). These can be found by means of ground signatures. There have been several previous studies, where the onsets of separate microsubstorms (a series of which is also named a multi-step, multi-staged or multi-onset substorm) are defined by one or a complex of signatures: auroral expansion, rapid intensification of westward auroral electrojet, onset or abrupt changes of the mid-latitude magnetic bays, or Pi2 train onset (Clauer and McPherron 1974; Vorobjev and Rezenov 1973; Sergeev 1974, 1977; Wiens and Rostoker 1975; Pytte et al. 1976a, b; Sergeev and Yahnin 1979a, Saito et al. 1976; Untiedt et al. 1978). The summary by Sergeev and Tsyganenko (1980) shows that in practically all events under investigation the discrete structure (series of microsubstorms) is evident, if the station network used is appropriate for such studies. The microsubstorms have a duration of expansion of about 5 min with 5–20 min intervals between them, the active region can displace (or widen) both to the east and/or to the west in successive microsubstorms and new activity can arise in the region outside the previous one. The microsubstorm onsets, defined by these signatures, are synchronous with the abrupt changes of magnetic field and plasma properties in the magnetotail (Sergeev 1977; Pytte et al. 1976b, 1978).

Recent investigations have also revealed the thin structure of separate microsubstorms: the rapid auroral expansion usually proceeds through the formation of new arcs at the poleward edge of the expanding auroral bulge in 1–3 min (Sergeev and Yahnin 1978, 1979b), the times of arc formation are marked by strong impulses of the bremsstrahlung X-ray emission and by separate Pi1B bursts under the bulge and also by simultaneous changes in the characteristics (amplitude, phase, polarization) of the Pi2

0340-062X/81/0049/0176/$02.00

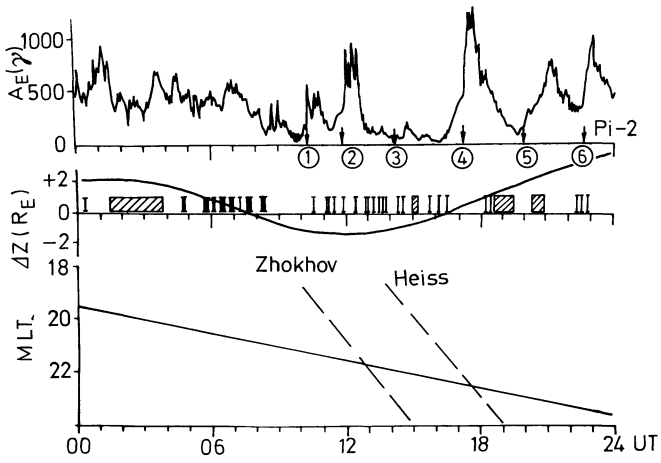

Fig. 1. *Top*. AE (γ) index (from Allen et al. 1977) for 3 March 1976, *arrows* mark the onsets of first Pi2 trains, in sequence, during each substorm event. *Center bos*: the distance of IMP-8 satellite from calculated neutral sheet position (Vette 1975), *vertical bars* indicate the times of neutral sheet crossings and hatched boxes, the gaps in the data. *Bottom*: the MLT meridian of IMP-8 projection into the ionosphere (from Tsyganenko (1979) model) and MLT positions of two all-sky cameras (coordinates in Table 1), whose data we use for detailed ground-satellite correlations

train at mid-latitudes (Sergeev et al. 1978). An attempt to correlate the magnetic variations in the magnetotail with this thin structure of the expansion phase is also undertaken in our paper.

Data

The magnetic field data in the magnetotail are the IMP-8 satellite measurements; 15.36 s averages of field components in (GSM) coordinate systems along with the standard deviation of separate 1.28 s points in 12 point sequence (SD) are used in this study. We select for the analysis the period 10–23 hours UT on 3 March 1976. Five successive substorms (events 1–2, 4–6 in Fig. 1) during this interval are rather intense and well-defined both in auroral zone and low-latitude magnetic variations and have a duration $\leqslant 2$ h. The event 3 in contrast appears only in Pi2 pulsation data, and thus provides on opportunity to compare its magnetospheric signatures with the ones during intense substorm events.

During all this period the IMP-8 satellite was in a favourable location within 2 R_E from the calculated position of the neutral sheet (Vette 1975). Its data display the multiple crossings of the neutral sheet. The magnetic local time (MLT) meridian of IMP-8 projection into the ionosphere is shown also at the bottom of Fig. 1, a semi-empirical magnetospheric model of Tsyganenko (1979) being used.

For the determination of the microsubstorm onsets we used an extensive complex of ground data, including the normal magnetometer data of auroral zone stations and of the dense mid-latitude net of Soviet stations; rapid-run magnetometer (sensitivity 0.1–0.3 γ/mm at 0.2–0.02 Hz, chart speed 15 mm/min), induction magnetometer, and all-sky camera data are also used (Table 1). The most complete reconstruction of the expansive phase microstructure is possible for event 4 in Figs. 1 and 2, when the station network was optimal for the range 19-03 MLT and four all-sky cameras were operated. This substorm is also an extremely favourable event in view of its large intensity ($\gtrsim 1{,}500\ \gamma$ in AE index and $\gtrsim 50\ \gamma$ at mid-latitudes) and the isolation of its onset. The IMP-8 satellite was located within 1 R_E of the estimated neutral sheet, slightly towards the evening of the magnetotail center ($Y_{SM} \sim +5\ R_E$). Therefore we start the data presentation from this ideal event.

Experimental Data

Space-Time Microstructure of the Expansion Phase of the Ideal (Isolated, Intense) Substorm Event on 3 March 1976 (17·16 UT)

All four above-mentioned ground signatures showed consistently the onset of an explosive phase at 17:16.0–17:16.5 UT Prior to this time the smooth development of the twin-vortex current system with the pronounced westward and eastward electrojets was noted. After 16:20 the quiet auroral arcs drifted equatorwards and the magnetic field magnitude at the IMP-8 location increased smoothly.

First of all let us consider the data from the all-sky cameras (their positions are indicated in Table 1), supplemented by the information on the appearance periods of short-lived discrete ra-

Table 1. List of stations from which data have been used in this study

Station	Symbol	Type of[a] instrument	CG Latitude[b] and Longitude		Station	Symbol	Type of[a] instrument	CG Latitude[b] and Longitude	
Leirvogour	LEI	NM, RM	65.6	69	Hermanus	HER	NM	−42	81
Bear Is.	BJO	NM	71.0	110	Kaliningrad	KAL	P	50	98
Ny Alesund	NYA	NM	75.6	114	Lvov	LVO	NM	45	99
Loparskaya	LOP	ASC, NM	64.4	115	Tbilisi	TBI	NM, P	37	117
Heiss Is.	HEI	ASC	74.6	144	Ashkhabad	ASH	NM	33	130
Dixon	DIX	NM	67.7	156	Sverdlovsk	SVE	NM,RM	52	134
Norilsk	NOR	NM	63.4	161	Alma-Ata	AA	NM	38	149
Cape Cheluskin	CHE	NM	71.1	175	Novosybirsk	NOV	NM	49	159
Tixie Bay	TIX	NM	65.2	196	Irkutsk	IRK	NM	47	176
Zhokhov Is.	ZHO	ASC	70.0	210	Yakutsk	YAK	RM, P	55	200
Barrow	BAR	NM	69.5	248	Magadan	MAG	NM	53	218
College	COL	RM	65.0	261	Petropavlovsk	PET	NM, P	45	225
					Guam	GU	RM	4	212

[a] NM and RM – normal and rapid-run magnetometers, P = induction magnetometer, ASC = all-sky camera
[b] Corrected Geomagnetic Coordinates for 1980,0 epoch (Tsyganenko 1979)

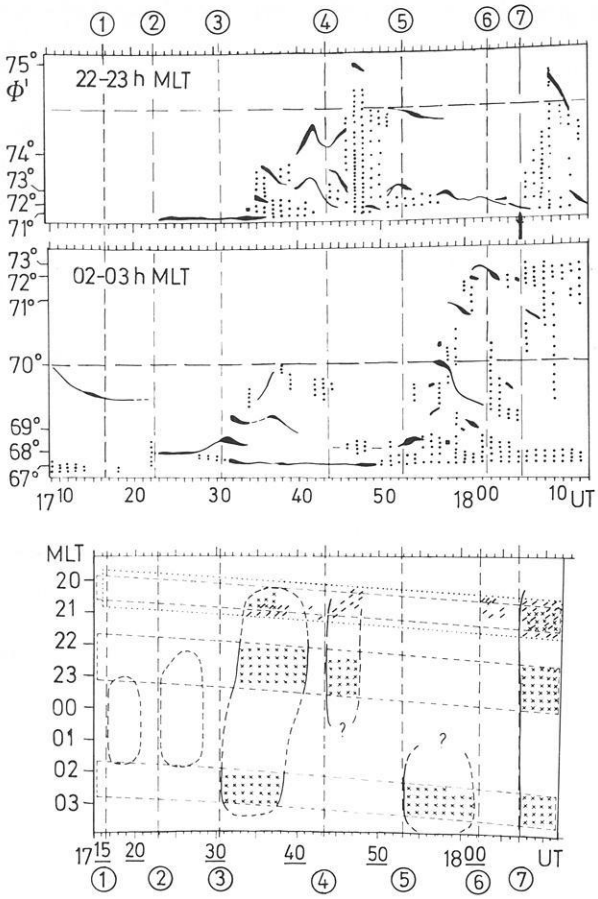

Fig. 2. *Top*: profiles of aurora position over Heiss Is. (22–23 h MLT) and Zhokhov Is (02–03 h MLT) meridians in supposition of 110-km auroral form height. *The lines and points* indicate the discrete and diffuse (and irregular) auroras, *the line thickness and density of points* show qualitatively their brightness. *Bottom:* UT-MLT diagram showing the fields of view of all-sky cameras (*broken lines*) and auroral radar at Essoila (*pinted lines*); the periods of auroral expansions and appearance of short-lived discrete radio-auroral signal (from Timofeev and Yahnin 1980) are hatched to see claerly the onsets of different activizations and their longitudinal ranges

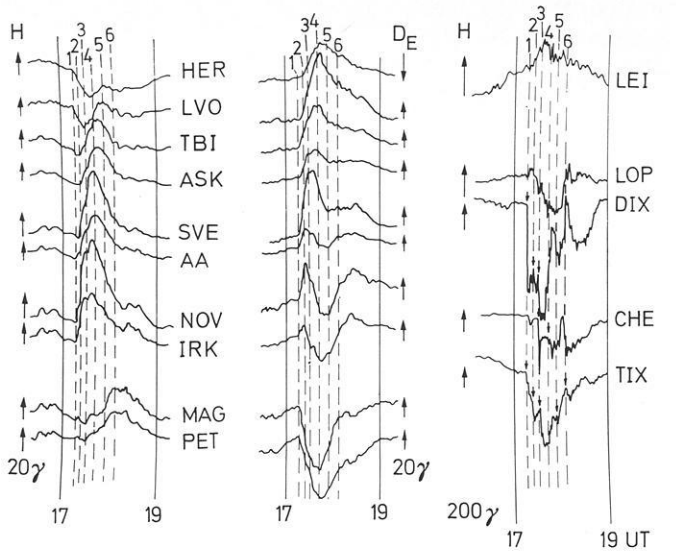

Fig. 3. Magnetograms of mid-latitude and auroral zone stations, *the vertical broken lines* indicate the onsets of separate microsubstorms

dio-auroral reflections at 95 MHz frequency, seen in the sector 20–21 h MLT in the auroral zone. The latter were presented by Timofeev and Yahnin (1981), where the close relationship of these signals to auroral expansions was well-documented. The more useful information on the dynamics of the poleward part of the auroral bulge during this event follows from the data from the most poleward stations, Heiss and Zhokhov Islands, whose data are displayed in the form of the meridional profile of auroras at the top of Fig. 2. The bottom part of this figure shows the approximate MLT location of the auroral expansion region in the form of an UT-MLT diagram.

The onset of auroral expansion is marked by the strong auroral brightening and auroral break-up at 17:16 UT (1 on Fig. 2) over the northern sky of Norilsk. At 17:23 UT (2) the brightening is evident over Zhokhov Island, and the NW portion of the auroral bulge appears at the SE horizon of Heiss Island. Until to it fades near 17:29 the westward travelling surge is situated in the sector 130–140° longitude. At 17:31 (3) the brightness of northern arcs suddenly increases over Loparskaya and Zhokhov Island, then the strong auroral expansion is evident in the data from Heiss and Zhokhov Islands (Fig. 2), and the westward edge of the auroral bulge appears over Scandinavia, coinciding with the appearance of discrete radio-auroras in this sector. The time structure of this intense expansion will be considered in more detail in the following section. The following event is less evident: at 17:42 (4) the brightening of the edge of the auroral bulge can be inferred from the data of Heiss Island and Loparskaya, followed by a small expansion after 17:44 UT. At 17:53 (5) strong brightening was detected over Zhokhov Island, followed by significant expansion; some brightening was observed at the northern bulge edge over Heiss Island, but, in contrast to the morning sector, there was no observable expansion (see Fig. 2). The definition of the next event (6) at 18:03 UT is more subjective, as it is based only on the appearance of the discrete radio-auroras in the evening sector (the auroral bulge in this sector is located polewards of the field of view at Loparskaya at this time), but the following event (7) at 18.07 UT results in fast auroral expansion, simultaneously observed in all of the sector 20-03 h MLT (Fig. 2).

The auroral zone magnetograms, displayed in Fig. 3, support the above definition of the expansion events, showing the pronounced intensifications of the westward auroral electrojet in those sectors where the auroral expansions take place. The last expansion (7) results in the sharp negative bay at Barrow (05 hours MLT), thus the MLT range of this event is very wide compared to the previous expansions.

The low-latitude bay-like disturbances (Fig. 3) also display pronounced sharp changes at the times marked. The changes of their longitudinal pattern are consistent with the evolution of MLT sectors of separate auroral expansions, shown in Fig. 2. At the onset of expansion phase (1) the positive bays in the H component started in the sector between NOV and YAK. Event (2) resulted in westward expansion ($+\Delta H$ appeared at AA, ASK, TBI, ΔD changes its sign from positive to negative at IRK). The next intense event (3) displayed the onset of $+\Delta H$ at both western and eastern stations (LVO, TBI, MAG, PET). The following events (4) and (5) are evident as $+\Delta H$ excursions only at the most western (LVO, HER) and eastern (MAG, PET) stations respectively. Very weak perturbations are associated with the fast expansion (7).

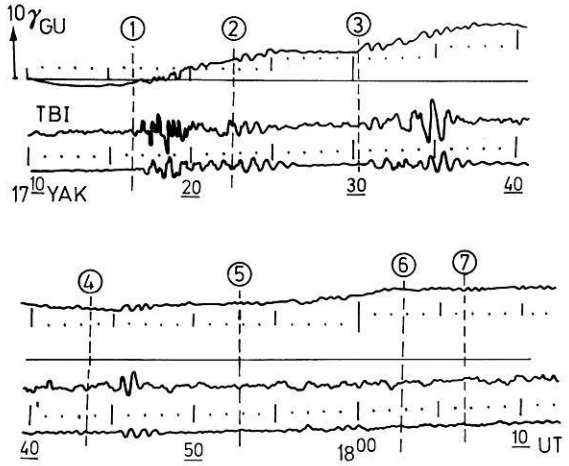

Fig. 4. Induction magnetograms from Tbilisi and Yakutsk along with the rapid-run magnetogram from Guam

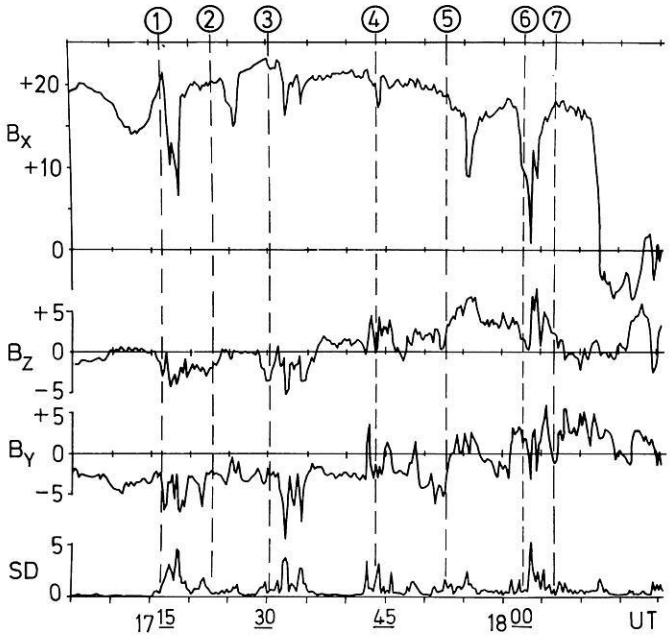

Fig. 5. 15.36 s resolution data of magnetic field components in SM coordinate system at IMP-8 satellite for event 4, *broken lines* mark the onsets of separate microsubstorms inferred from the ground data

The first Pi2 train, starting at 17:16.5 UT (Fig. 4), was characterized by the predominance of the short-period component, the intensification of pulsations without this component is evident near 17:23. At 17:30.5 the onset of a new well-defined train is apparent. These three times are in a good agreement with the onsets of auroral expansions. One more intense Pi2 train is observed after 17:45.5 UT which is two minutes after the beginning of expansion over Heiss Island, but in coincidence with the marked auroral intensifications (see auroral profile in Fig. 2). Some intensifications of pulsations can be found after the times (5) and (7) which are correlated with obvious auroral expansions, however they are not so well-defined as the trains associated with expansions (1)–(3).

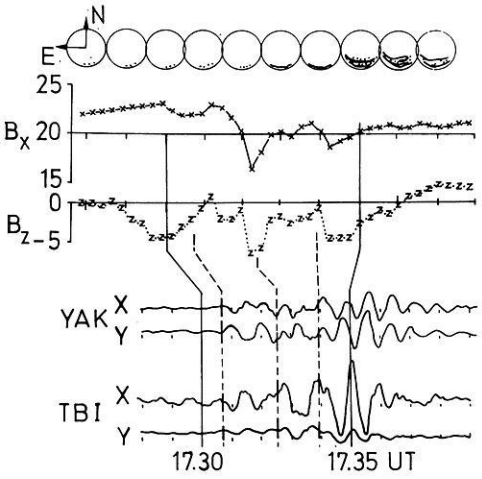

Fig. 6. Drawings of Heiss Is. ascafilms (20 s exposure frames centered at the onset of each minute), 15.36 s data points of B_z and B_x components at IMP-8 and the pulsation records from Tbilisi and Yakutsk for the most intense microsubstorm of event 4 (see text for explanation). The *lines* and *dots* on drawings corresponds to the discrete and diffuse auroras

The IMP-8 satellite was situated at this time near the northern boundary of plasma sheet, as suggested by the large value of the B_x component ($\geq 15\,\gamma$) throughout most of the event and by the significant flux of electrons with energy ≥ 85 KeV (T.P. Armstrong, private communication). Looking at the satellite magnetic field data (Fig. 5), we find impulsive magnetic field variations closely associated with times (1)–(7). The typical response of the B_x component is an impulsive decrease (1)–(6), while the B_z component decreases impulsively in a few early micro-substorms (1)–(3) and increases in the later ones (4)–(6). The impulsive variations of the B_y component and low-frequency magnetic noise (SD) intensifications are also features of microsubstorms. The last widespread expansion (7) results in a new B_z decrease and also in full expansion of the plasma sheet, following 4 min later.

Thus during the expansion phase of this ideal event we can recognize 7 activizations (microsubstorms), most of them (1), (3), (5), (7) are well documented by a complex of ground and satellite signatures and timed to within the 0.5 min resolution of the data.

Thin Structure of the Single Expansion (Microsubstorm)

The Heiss Island all-sky data are displayed in Fig. 6 for the period of the most intense microsubstorm, event (3), along with the induction magnetograms of low-latitude stations Yakutsk and Tbilisi. The latter show the onset of Pi2 trains at 17:30.6 UT, a change of phase is evident at 17:32.5 (more clearly in B_Y components at both locations) and significant amplification of the $T > 50$ s component starts at 17:34.0. These three features are clearly evident at other stations (see for example the Guam rapid-run magnetogram in Fig. 4). The first feature coincides with the auroral intensification in the post-midnight sector (Zhokhov Island, Fig. 2). Coinciding with the second feature (17:32:30), bright auroras appeared in the southern sky at Heiss Island at 17:33 and, at just this time, the formation of the westward part of the auroral bulge is evident in the all-sky data from Loparskaya, situated 30° westwards of the Heiss Island meridian. The structure which appeared at 17:33, is evident in the following frames, but at 17:35 the new bright auroral band formed polewards of the pre-existing one. Thus, in this case, the auroral expansion over the Heiss

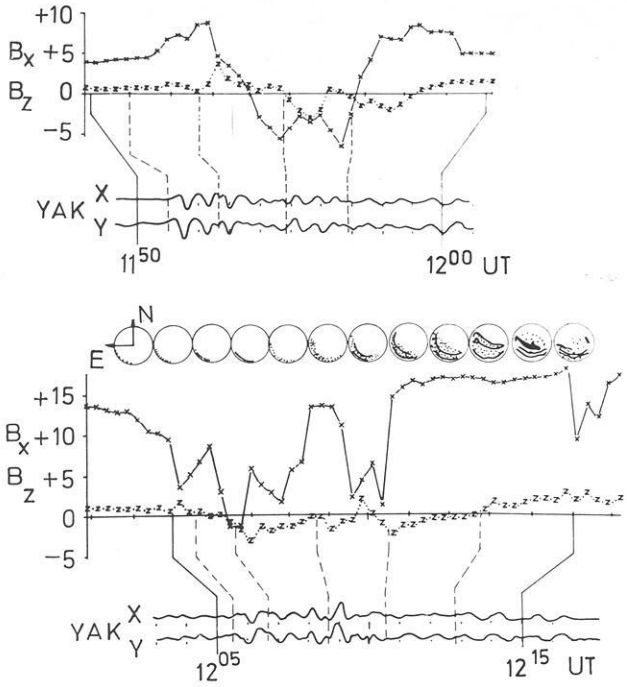

Fig. 7. The same as in Fig. 6 for 11:50–12:15 UT interval, but for Zhokhov Is. all-sky data

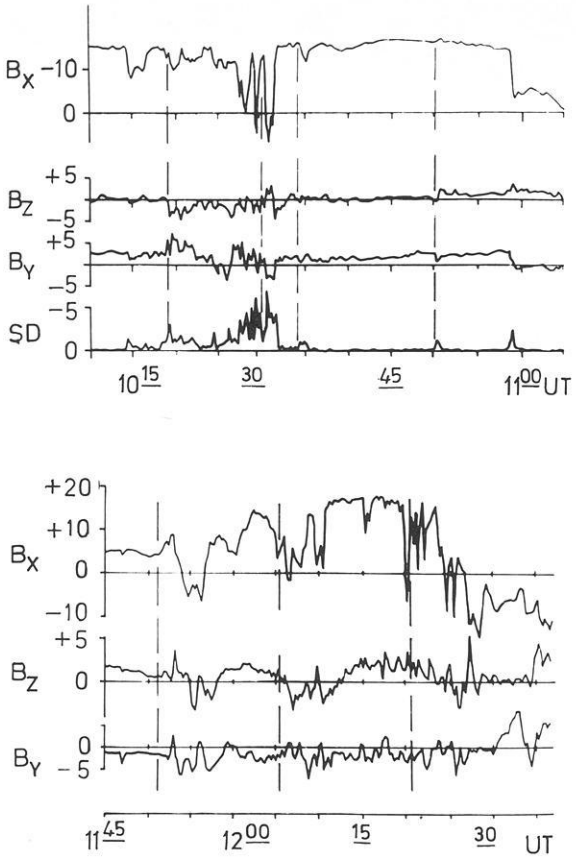

Fig. 8. IMP-8 magnetic field data for the substorm events 1 and 2 (see text for explanation)

meridian proceeds through two stages at 17:33 and 17:35, these times of appearance of new poleward structures being correlated to the times of the two Pi2 regime changes (17:32.5 and 17:34.0), and synchronous at widely spaced (more than a thousand km) stations. At just these times (within 0.5 min accuracy) the impulsive decreases of both B_x and B_z components at the IMP-8 location are observed (Fig. 6) with similar structure in the B_y and SD components (Fig. 5). The pulsation onset at 17:30.5 is evident as a small decrease in the B_x component, but the relatively smooth decrease of the B_z component had started one minute earlier and this feature is not so evident in the B_y and SD components.

The second example concerns the substorm event (2), for which we use the all-sky data from Zhokhov station, situated this time near the MLT sector of satellite projection, as in the previous case (Fig. 1). This event started at 11:51 UT, as evidenced by the Pi2 onset (Fig. 7) and abrupt bay onset at the College rapid-run magnetogram. This first microsubstorm did not occupy the MLT sector of Zhokhov station, where the regular evening arcs were observed. The times of the abrupt changes of the Pi2 regime (phase, period, polarization) are related to the simultaneous appearance of impulsive B_z variations inside the plasma sheet, the two last times strictly coinciding with negative B_z excursions.

The second microsubstorm began at 12:05.5 as new amplification of pulsations and auroral brightening in the southern sky at Zhokhov Island, started at 12:06 and reached its maximum at 12:07. It coincides well with a new negative excursion of the B_z component in the neighbourhood of the neutral sheet. At 12:08.7 we detect a new change of Pi2 phase and a corresponding intensification. After the auroral fading at 12:08 we observe the next intensification at 12:09–12:10, when the auroras expand polewards and two bright auroral bands are seen clearly. Two more negative B_z excursions are evident this time. Between 12:12 and 12:13 the new (third) auroral form appears near the station zenith and an obvious change of Pi2 polarization (appearance of the pulsations in B_x component) is observed. At the same time the B_z component becomes positive.

These examples give clear evidence that the features of expansion thin structure (new arc formations at the leading edge of the bulge, with simultaneous abrupt changes of Pi2 regime and other corresponding phenomena (Sergeev and Yahnin 1978, 1979b; Sergeev et al. 1978), are intimately related to impulsive changes of the magnetic field in the plasma sheet.

Other Examples of Magnetic Field Response to Substorm Microstructure

We now present briefly the other substorm events during the interval 10–24 h UT on 3 March 1976. Accurate derivation of the full discrete structure of these events is more difficult since we do not have such a good net work of all-sky stations and rapid-run magnetometers as in the previous case. Therefore we will base our presentations on the Pi2 pulsation data, marking by broken lines the instants of their onsets and also the instants of their abrupt regime changes, which are synchronous at widely spaced mid-latitude stations. The possibilities of this method are however limited, and we can reconstruct only a part of all the microsubstorm events in the sequence (see discussion in next section).

Event 1. The expansive phase starts at 10:19, as evidenced by the onset of Pi2, low-latitude magnetic bays and electrojet intensification over College. Two more microsubstorms are seen in the Pi2 data (10:30 and 10:34). The all-sky camera at Zhokhov Island

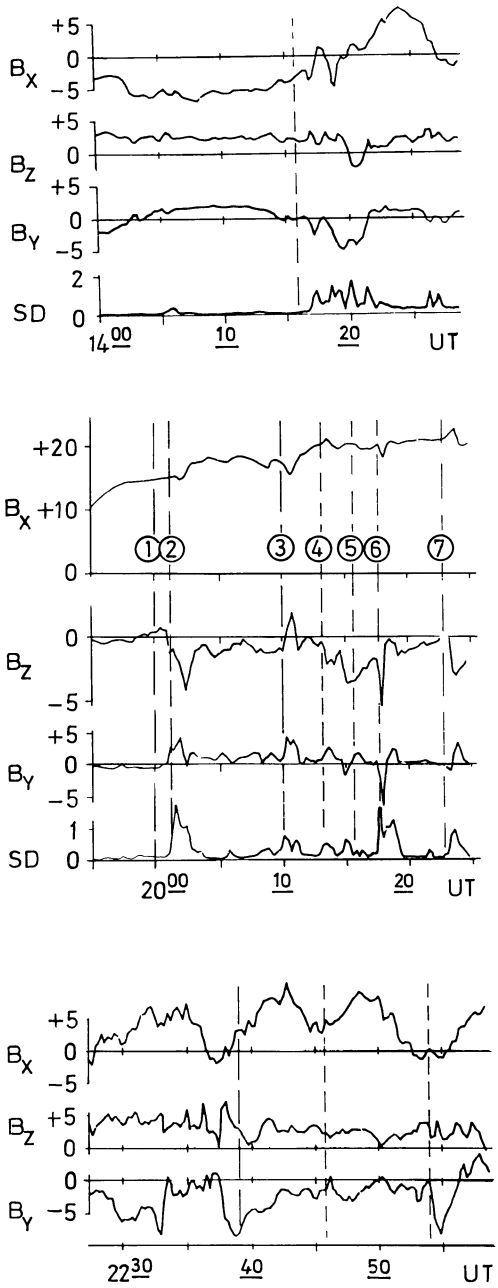

Fig. 9. IMP-8 magnetic field data for the events 3, 4, and 5

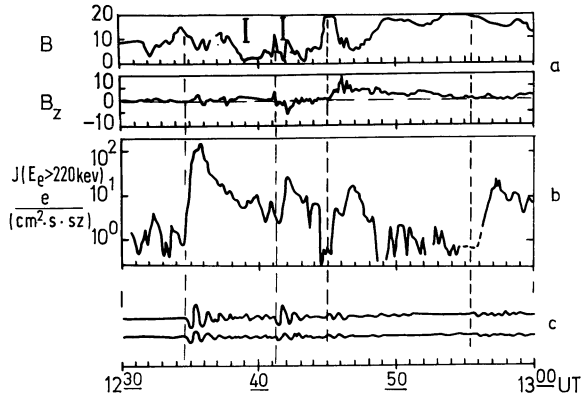

Fig. 10. IMP-8 magnetic field (*a*) and high-energy electron (*b*) data for 26, November 1973 substorm event (from Kirsch et al. 1977) combined with the induction magnetogram from Kanoya. *Vertical bars* in (*a*) denotes the times of neutral sheet crossings

was turned on at 10:35 and registrated the regular evening arcs and also the westward edge of the bulge in the eastern sky until 10:51, when the fast poleward expansion started and proceeded through the new arc formation process.

At the expansion onset we detect, at the IMP-8 position (Fig. 8), a southward turn in the magnetic field and its magnitude decreases, followed by sharp variations in all parameters, related to satellite movement with respect to the plasma sheet boundary. One of these coincides with the Pi2 onset (10:30), then the satellite exit from the plasma sheet and detects the impulsive B_x decrease during the next Pi2 onset. After the onset of auroral expansion at the 20 hours MLT meridian (10:51 UT), the smooth decrease of B_x and impulsive positive change of B_z are seen. Complete plasma sheet recovery takes place 8 min later, towards the end of auroral expansion over Zhokhov Island.

Event 2 (11 51 UT). The first two microsubstorms of this event were discussed in the previous section (Fig. 7). The satellite was located during this period inside the plasma sheet until 12:10. A new auroral expansion developed after 12:21, when brightening and subsequent poleward motion of the bulge was observed in the northern sky over Zhokhov Island until 12:27. During this time interval the satellite moved back into the expanded plasma sheet (Fig. 8) and detected the smooth decrease of magnetic field B_z component, its impulsive negative excursion at 12:26 correlating with the abrupt brightening and break-up of the northern arc. After 12:34 the stable positive B_z regime was observed at the IMP-8 location, the auroras over Zhokhov Island having already completely lost any distinct structure.

Event 3. Only one very intense Pi2 pulsation train was detected at 14:15.5 without any evident bay-like disturbances at either the auroral zone or mid-latitude stations available for this study. No drastic changes in the auroral structure and brightness were observed over Zhokhov Island (23 h MLT). At the same time, in contrast to the preceding time interval there is an obvious magnetic disturbance at the IMP-8 position (Fig. 9), which was located in the proximity of the neutral sheet ($B_z \geqq B_x$). The data from the high energy particle experiment on IMP-8 (courtesy of T.P. Armstrong) also displayed the intense burst of energetic electrons (up to 1 MeV), whose intensity increased near 14:15 by more than an order of magnitude. The absence of ground signatures of this event can be understood if it was very localized in space (see the examples of this type in Sergeev and Yahnin 1979a).

Event 5. Three intense and distinct Pi2 trains displayed clear thin structure and were detected from the expansion onset at 20:00 until the gap in the satellite data (20:25). Coinciding with the times 2, 3, 4, 6, and 7 we see impulsive changes of magnetic field, mostly decreases in both B_x and B_z components and magnetic noise (SD) spikes (Fig. 9). The pulsations at the onset (20:00) were very weak. The satellite was near the plasma sheet boundary throughout this event, as evidenced by the large B_x magnitude and the high level of electron flux at energies $\geqq 85$ KeV.

Event 6. From the rapid-run magnetogram of Leirvogour we define the expansion onset at 22:39. The H component negative excursion reached $-500\ \gamma$ near 22:50 and the first Z component excursion was positive, showing electrojet intensification southwards of the

position of Leirvogour (66° latitude). Three distinct Pi2 trains were detected up to 23:00 UT, coinciding with electrojet intensifications and poleward expansions. The satellite in this period was situated deep inside the plasma sheet ($B_x \leqq 10\,\gamma$, a few neutral sheet crossings, Fig. 9). In the presence of the continuous complex variations of magnetic field in this region it is difficult to recognize unambiguously the response to the three microsubstorms indicated. However we want to emphasize the essentially positive sign of the B_z component inside the plasma sheet near the magnetotail center during the first 20 min of very intense substorm activity, initiated at a latitude $\leqq 65°$ in the midnight auroral zone sector. The ground data available for this event are unsufficient to distinguish the microsubstorms following after 23:00 UT

High-Energy Particle Bursts as Signatures of Explosive Energy Dissipation Process During Separate Microsubstorms

The intense spikes of energetic (0.1–1 MeV) particles were detected by the JHU experiment on board the IMP-8 satellite during the events under examination. From the 5 min resolution data we have, by courtesy of T.P. Armstrong, the onsets of the substorm-related particle events are defined to be at approximately 10.18, 11:51, 14:15, 17:18, 20:00 and 22:40 UT, in good accordance with our determination of the expansion phase onset from the ground signatures.

To show the energetic particle response to the microsubstorm sequence in more detail we have used data on both the magnetic field and energetic electron flux at IMP-8 during the event on 26 November 1973, published by Kirsch et al. (1977), supplemented in Fig. 10 by the Kanoya induction magnetogram. We again see the impulsive B_z component variation at the onsets of separate Pi2 trains (microsubstorms). The remarkable coincidence of separate particle bursts and microsubstorm onsets is also obvious from Fig. 10.

Results and Discussions

Reconstruction of Discrete Microstructure of Substorms From Ground Data

In all of five successive, intense and well-defined substorms on 3 March 1976 we found the complex multistage temporal structure of the expansive phase, which thus represents a typical feature of substorms in good accordance with the other detailed studied, which are mentioned in the Introduction. A clear example of the sporadic activizations of auroral expansions and of the complex changes in their latitudinal and longitudinal ranges is provided by the data on the intense and isolated event 4.

The timing of microsubstorms represents one of the most important and difficult problems for future detailed studies of explosive energy dissipation events. The defects of the magnetic variation data obtained in the auroral zone and at mid-latitudes (inadequate net work, low time-resolution of normal magnetograms, difficulties in distinguishing the nature of distinct peaks at auroral zone stations, low level of signal/noise ratio at mid-latitudes) are well known, and in many papers most attention has been paid to the registration of mid-latitude Pi2 pulsations in view of the high time-resolution of this method and the global character of these pulsations (Pytte et al. 1976a, b; Saito et al. 1976; Sakurai and Saito 1976). Our data demonstrate, however (see Fig. 4 for example), that these pulsations are intense and well-defined only during the few first microsubstorms, whereas in the later ones their presence cannot be defined unambiguously. Thus this method is very useful but is not sufficient to indicate every microsubstorm in the sequence.

The accuracy of this method is also sometimes limited even in the cases of intense and well-defined Pi2 trains. So, in the microsubstorms 4 and 5 of event 4 the onsets of these trains were evidently delayed for a few minutes, relative to the microsubstorm signatures in auroral and magnetospheric data. Similar delays of Pi2 onset (0–2 min), when compared to the auroral brightening, were obtained by statistical analysis by Sakurai and Saito (1976). A cause of these delays, as suggested by the results of Sergeev et al. (1978), can be related to the thin structure of the separate expansion event (previons section). If the regime changes in the Pi2 train are caused by superimposed trains, originating from separate impulses (as suggested by their correlations with the abrupt changes in auroral structure and impulsive magnetic field variations in the magnetotail), the onsets of low-intensity trains might be missed in the analysis. So Sergeev et al. (1978) presented examples, where an initial brightening of the aurora resulted only in a simultaneous low intensity Pi2 pulsation, not detected at low-latitudes, but the successive formation of new arcs at the front of the expanding bulge superimposed intense Pi2 at low-latitudes. Data for the microsubstorm 5 in event 4 are similar · the intensification of Pi2 pulsations at Yakutsk (Fig. 4) is evident at 17:56.5 simultaneously with the new arc formations over Zhokhov Island (Fig. 2), but there were no observable pulsations during the very strong auroral brightening at 17:53.

Thus only the observation of auroral dynamics and intensity over the whole sector 65°–75° latitude and 20–04 h MLT provides a reliable means for the reconstruction of the full space-time history of a substorm. Unfortunately such study is possible only in extremely rare cases.

Magnetic Field Variations During Separate and Sequantial Microsubstorms with the Satellite Near the Plasma Sheet Boundary

Preliminary inspection of the data has shown that when impulsive magnetic variations accompany the onsets of microsubstorms, their character displays many individual features. A major part of these differences seems to arise from both the variety of space-time history in substorms and differences in location of the satellite relative to the regions of fast energy dissipation. We try below to infer typical patterns of microsubstorm-associated variations and their sequence in the substorm. The results, of course, are preliminary, as they are based on a limited number of events; still we feel that they are representative. The latter conclusion can be supported by reference to the large number of events analysed by Pytte et al. (1976b, 1978) and Sergeev (1977), as the features which have been pointed out can invariably be found in their data. The above-mentioned data corresponds mainly to the 10–20 R_E distance in the magnetotail.

Types of Variation. Based on the behaviour of the B_x (or $|B|$) and B_z components of the magnetic field at the microsubstorm onset, we can distinguish the four following types of variations

A. Decrease of both $|B|$ and B_z component by a few γ in magnitude.

B. Decrease in $|B|$ and increase in B_z by the same amounts.

C. A large decrease of $|B|$ of more than 5–10 γ, when the satellite is embedded into the expanded plasma sheet.

D. A short-lived large $|B|$ decrease during the transient plasma sheet expansion.

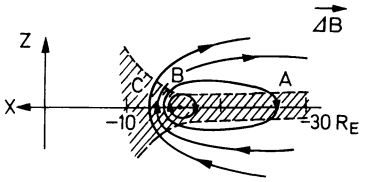

Fig. 11. The magnetic field disturbance pattern in the XOZ plane, used for explanation of magnetic field response at IMP-8 to the sequence of separate microsubstorms

All four types of magnetic field behaviour are evident in data for event 4, and partly in events 1,5. All these patterns are present in the data for the substorms which started at 09.38 UT and 14.36 UT on 4 September 1968 and at 07.52 UT on 19 August 1969, when the OGO-5 satellite was situated 20 R_E from the Earth within 3 R_E from the calculated neutral sheet position (Pytte et al. 1978). Only *B* and *C* types are evident in the data for other events in papers of Pytte et al. (1976b, 1978), when the satellite was located closer to the Earth.

Occurrence of Different Types: The changes of *A* and *B* type are typically synchronous (within one minute) with the microsubstorm onsets, determined from the ground data (see also Pytte et al. 1976b, 1978). The transient expansion type (*D*) is often superimposed on these variations, with the sign of B_z variation being preserved, but is sometimes delayed with respect to the *A* and *B* types (see, for example, microsubstorm 5 in event 4 and also Pytte et al. 1978).

The transient expansion-contraction of the plasma sheet can be found in papers where plasma data were analyzed. A striking example of the expansion-contraction sequence with repeated changes in the plasma flow direction was described by Hones et al. (1976), the auroral data also displaying the sequence of auroral bulge expansions (the appearance of new WTS) with similar intervals of time between them (5–20 min).

Sequences of Variation Types. During the expansion phase the magnetic field responses usually change through the sequence of microsubstorms as $A \rightarrow B \rightarrow C$ at 35 R_E distances (see also the similar example in Sergeev 1977). A similar succession is evident in the above-mentioned events in Pytte et al. 1978, and the succession $B \rightarrow C$ in other events studied in the papers by Pytte et al. (1976b, 1978). Each response type may be repeated a few times. This pattern of a change in magnetic field response through the sequence of separate microsubstorms can be easily interpreted if the pattern of magnetic field change at the substorm onset (first microsubstorm) is taken into account. In the enormous number of events observed, magnetic field signatures at the substorm onset display a B_x magnitude decrease everywhere outside the plasma sheet, a B_z decrease at or tailwards of 20 R_E distance (type *A*), a B_z increase earthwards of *15–20* R_E distance (type *B*) and the pronounced plasma sheet expansion (type *C*) at <15 R_E from the Earth (Nishida and Nagayama 1973; Russell and McPherron 1973; Hones 1979; Pytte et al. 1976b, 1978). Thus all these types *A, B, C* are observed simultaneously and differ only spatially (Fig. 11) the separation line between regimes *A* and *B* in the equatorial plane being identified as the *X*-type neutral line position (see next section). Therefore the trend $A \rightarrow B \rightarrow C$ can be explained as the sudden appearances of a neutral line at more tailward distances in the magnetotail

Underlying Trends in $|B|$. After the changes of *A* and *B* type, synchronous with the microsubstorm onset, the magnetic field usually recovered before the onset of the subsequent microsubstorm if it was sufficiently separated in time from the previous microsubstorm. In our cases 1, 4, 5 as well as in the above-mentioned events in Pytte et al. (1978), the following trend can be recognized: during the successive microsubstorms, resulting in an *A(B)* magnetic variation pattern, the restored values of $|B|$ increase (decrease) in a sequence of responses of similar type. Since the Pytte et al. (1978) paper included the plasma data, showing the absence of plasma sheet particles during the periods under consideration, we infer that the intensity of the plasma sheet current tailwards of the *X*-type neutral line region, where the *A* type response is observed, according to our interpretation, *continues to increase* during the current disruption process in the near-Earth region. The relative contribution of these two parts of the current sheet (disrupted or increasing in intensity) to the observed magnetic variation apparently depends on the satellite position. The contribution of the slowly varying tailward part can dominate only when the satellite is situated near the current sheet (at $|Z| \leq 6$ R_E as follows from the statistical data of Iijima (1972), for definition of Z see Fig. 11).

Discussion. Unfortunately the data gaps in some events and difficulties in diagnosting the last microsubstorm in a sequence prevent the detailed study of magnetic field variations after complete plasma sheet recovery (*C*-type response). In the two cases (events 1 and 4) when such recovery was observed, it was detected a few minutes after the onset of a microsubstorm, characterized by fast expansion in the widest longitudinal sector. Pytte et al. (1978) and Hones (1979) suggested that the phase of the plasma sheet recovery tailwards of 15 R_E distance (leap, in their definition) is physically different from the preceding activizations (microsubstorms). However they base this mainly on the absence of the Pi2 pulsations at mid-latitudes and the appearance of the bulge at latitudes of 74° In the case of event 4, however, the auroral expansion reached 74° latitude at microsubstorm 3, but four later microsubstorms are evident in our data (Figs. 2–4), being qualitatively similar to event 3. The absence of clear Pi2 pulsations also can not be used to distinguish the physical nature of the microsubstorm phenomena Thus we feel that the conclusion about the existence of two different expansion modes during the expansion phase is not yet well founded.

Magnetic Field Changes Inside of the Plasma Sheet and Magnetotail Topology During the Substorm Expansion Phase

Cases when the satellite stays inside the plasma sheet at and after the substorm onset are extremely rare at distances tailwards of 15 R_E, but events 2, 3, and 6 in our study do fall into this category.

B_z Variations. During the first twenty minutes of the expansion phase of event 6 the satellite was evidently in the plasma sheet near the magnetotail center ($Y_{SM} \sim +1$ R_E). Three microsubstorms occured this time. However, only positive B_z values were detected at IMP-8. Whereas the intense ($\Delta H \sim -500$ γ) westward electrojet intensification took place at latitudes $\leq 65°$ at midnight, the probability of the formation of the *X*-type neutral line at distances >40 R_E in the magnetotail during this period seems to be very small.

During event 2 the B_z component of the magnetic field displayed two brief decreases into the negative range during the first two microsubstorms, but in the 8 min interval between them

B_z was continuously positive ($+2.5\,\gamma$) inside the plasma sheet ($|B_x| < 10\,\gamma$). There is another similar example in Fig. 10.

These facts are compatible with the results of Lui et al. (1977a, b), showing the predominance of positive B_z values in the neutral sheet regions at tailward distances of about 30 and 60 R_E during the substorm expansion phase. Thus the region of negative B_z (if it exists) must occupy only a localized part of the magnetotail equatorial region, and the resultant magnetotail topology must be similar to that with a pair (or a few pairs) of X- and O-type neutral lines (Vasiliunas 1976).

B_s Variations. The impulsive character of B_s in the plasma sheet may be caused by both the brief appearance of neutral lines, and also by their continuous existence in the case where the dimensions of the B_s region contract between the microsubstorms. We are not in a position to distinguish between these possibilities from the data of one satellite. These properties, however, are in conflict with the schemes of Vasiliunas (1976) and Hones (1979), in which the dimension of the B_s region increases continuously during the expansion phase.

B_y Variations. The existence of the intense variation in the B_y component during microsubstorms both inside and outside the plasma sheet along with the strong B_y component in the neutral sheet ($|B_x| \approx 0$, events 3, 6), pointed out earlier by Akasofu et al. (1978), suggest the complex and essentially three-dimensional character of the magnetic disturbance, which demands a more careful investigation.

Thin Structure of Separate Microsubstorms as Possible Indicator of Tearing-Like Instability of the Magnetotail Current Sheet

Only two microsubstorm events, when auroral expansion occured in the field of view of an all-sky camera and the satellite projection into the ionosphere was situated in the same MLT sector, were suitable for detailed comparisons of all-sky and satellite data. Both these events (see above) have given distinct examples of synchronization of the southward B_z spikes at the satellite position with the formation of new auroral arcs at the leading auroral bulge, accompanied by simultaneous changes in the regime of Pi2 pulsations.

Two other examples, when the data on auroral expansion were absent, also display the distinct coincidence of magnetic field spikes and changes in the regime of Pi2 pulsations (see upper and central parts of Figs. 7 and 9 respectively). Since the successive formation of new arcs was found to be the usual feature of auroral expansion during a microsubstorm (Sergeev and Yahnin 1978, 1979b; Sergeev et al. 1978), it is important to understand the possible physical significance of the correlation obtained.

To do this we must bear in mind two consequences of the impulsive appearance of the southward B_z component in the plasma sheet. On the one hand it is evidence of the existence of the X-type neutral line (lines) at least during the period of expansion. On the other hand fast magnetic field variations may be naturally related to the strong impulsive electric field, whose brief appearance during the expansive phase of substorms has already been observed (Kirsch et al. 1977; Aggson and Heppner 1977; Pedersen and Grard 1978). As follows from the numerical simulation of Tsyganenko and Zaitzeva (1979), the intense arc-like structure of electron precipitation will appear in the ionospheric projection of the X-type neutral line when the strong dawn-dusk directed electric field is applied to this region.

The close association of the impulsive electric field with the formation of auroral arcs during expansion seems to be in line with observations of energetic particles. So, as shown by Sergeev et al. (1978), the precipitation of energetic electrons under the expanding auroral bulge appears as a sequence of short impulses, occuring synchronously with the generation of new auroral arcs and concurrent changes in the regime of irregular pulsations. On the other hand, as follows from observations of spikes of energetic particles (Krimigis and Sarris 1979) and simulations of the particle acceleration (Pellinen and Heikkila 1978), the intense inductive electric fields are very probably the source for the particle acceleration up to MeV energy. In this connection we must mention also the results of Pedersen and Grard (1978). As the typical feature of the expansion phase, they have distinguished the sequence of strong impulses of the electric field, whose repetition interval (1–2 min) is the same as that of new arc formations and the simultaneons impulses of energetic electron precipitation.

In view of this evidence we have some physical grounds for considering the process of generation of new auroral arcs at the poleward front of expanding auroral bulge as the consequence of impulsive formation of a few X-type neutral lines during microsubstorms. This process corresponds well to the picture of the explosive growth of the tearing-mode instability (Galeev et al. 1978; Schindler 1979). If our conclusion appears to be valid, some very important features of tearing-mode operation may be deduced from auroral data.

The Substorm Sequence, and Concluding Remarks

As shown in this and similar studies (see Introduction), the space-time history of substorms appears to be complex and variable. However it seems possible to distinguish a definite hierarchy in the construction of the substorm sequence, depending on space and time scales.

The second in this hierarchy is the microsubstorm phenomenon, operating on a time scale 5–10 min in a localized part of the magnetotail and its conjugate auroral ionosphere (see Fig. 2 for illustration). Its main physical characteristics consist in the fast (explosive-like) energy dissipation, as evidenced, for example, by the data on high-energy particles (see Fig. 10 and the statistical data of Murayama (1970), who first found the remarkable correlation of Pi2 and relativistic electron spikes). The main features of microsubstorms can be explained both consistently and quantitatively by a Birkeland loop (current disruption) model Akasofu 1977; Sergeev and Tsyganenko 1980).

The substorm as a whole apparently represents the top level of this hierarchy. It is related to the way in which the whole tail dissipates surplus magnetic energy through the sequence of localized microsubstorms.

On a more detailed level, processes important for the explosive energy transformation in a substorm, seem to be represented by what we called "thin structure" Data on the magnetospheric features of this phenomenon are very scarce at present.

To support this view of the hierarchical structure of substorms we must mention the possibility of relative independence of phenomena at different levels of hierarchy. So, for example, a single microsubstorm can occur during quiet conditions, as in the case of our event 4.

As regards the behaviour of the magnetic field in the magnetotail, we feel that the data presented in this study give clear examples of the changes, related to the microsubstorms and their thin structure. Although some preliminary results have been discussed in

this paper, much more effort must be made to describe consistently the three-dimensional patterns of the related disturbances.

Acknowledgements. Magnetic field data from the IMP-8 satellite (N.F. Ness and R.P. Lepping are the principal investigators) were made accessible through WDC-A (Rockets and Satellites) and it is a pleasure to thank Dr. R.P. Lepping for additional data and information. I am also indebted to Dr. T.P. Armstrong from the Applied Physics Laboratory of John Hopkins University, who kindly provided the data from their energetic particle experiment. The auroral and ground magnetic data were obtained through WDC-B.

It is a pleasure to thank Drs. Y.A. Nadubovich, A.G. Yahnin, E.E. Timofeev, I.E. Ievenko, G.V. Starkov, L.A. Natzvalyan, Y.M. Gogatishvili for their kind assistance in receiving the different observational data and L.L. Nemtzeva and M.V. Holeva for their assistance during the preparation of paper.

References

Aggson, T.L., Heppner, J.P.: Observations of large transient magnetospheric electric fields. J. Geophys. Res. **82**, 5155–5154, 1977

Allen, J.H., Abston, C.C., Morris, L.D.: Geomagnetic data for March 1976. WDC-A report UAG-63, 1977

Akasofu, S.-I.: Physics of magnetospheric substorms. Dordrecht: D. Reidel Publ. Comp. 1977

Akasofu, S.-I., Lui, A.T.Y., Meng, C.-I., Haurowitz M.: Needs for a three-dimensional analysis of magnetic fields in the magnetotail during substorms. Geophys. Res. Lett. **5**, 283–286, 1978

Clauer, C.R., McPherron, R.L.: Mapping the local time – universal time development of magnetospheric substorms using mid-latitude magnetic observations. J. Geophys. Res. **79**, 2811–2819, 1974

Fairfield, D.H., Ness, N.F.: Configuration of the geomagnetic tail during substorms. J. Geophys. Res. **75**, 7032–7042, 1970

Galeev, A.A., Coroniti, F.V., Ashour-Abdalla, M.: Explosive tearing mode reconnection in the magnetospheric tail. Geophys. Res. Lett. **5**, 707–712, 1978

Hones, E.W., Asbridge, J.R., Bame, S.J., Singer, S.: Substorm variations in the magnetotail plasma sheet from $X=-6$ R_E to -60 R_E. J. Geophys. Res. **78**, 109–122, 1973

Hones, E.W., Akasofu, S.-I., Perreault, P.: Associations of IMF polarity, plasma sheet thinning and substorm occurrence on March 6, 1970. J. Geophys. Res. **81**, 6029–6041, 1976

Hones, E.W.: Plasma flow in the magnetotail and its implications for substorm theories. Space Sci. Rev. **23**, 393, 1979

Iijima, T.: Relationship of magnetospheric substorms on the ground and in the distant magnetotail. Rep. Ionos. Space Res. Jp **26**, 149–157, 1972

Kirsch, E., Krimigis, S.M., Sarris, E.T., Lepping, R.P., Armstrong, T.P.: Possible evidence for large, transient electric fields in the magnetotail from oppositely directed anisotropies of energetic protons and electrons. Geophys. Res. Lett **4**, 137–141, 1977

Krimigis, S.M., Sarris, E.T.: Energetic particle bursts in the Earth magnetotail. In: Dynamics of the Magnetosphere, S.-I. Akasofu, ed: pp. 590–360. Dordrech: D. Reidel Publ. Comp 1979

Lui, A.T.Y., Meng, C.-I., Akasofu, S.-I.: Search for the magnetic neutral line in the near-earth plasma sheet: 2. Systematic study of IMP-6 magnetic field observations. J. Geophys. Res. **82**, 1547–1556, 1977a

Lui, A.T.Y., Meng, C.-I., Akasofu, S.-I.: Search for the magnetic neutral line in the near-earth plasma sheet: 3. An extensive study of magnetic field observations at the lunar distance. J. Geophys Res. **82**, 3603–3612, 1977b

Murayama, T.: Correlated occurence of energetic electron bursts in the magnetotail and geomagnetic impulsive micropulsation. Rep. Ionos. Space Res. Jp **24**, 135–147, 1970

Nishida, A., Nagayama, N.: Synoptic survey for the neutral line in the magnetotail during the substorm expansion phase. J. Geophys. Res. **78**, 3782–3796, 1973

Pedersen, A., Grard, R.: Quasistatic electric field measurements on the GEOS-1 and GEOS-2 satellites. Preprint ESLAB N81, October 1978

Pellinen, R., Heikkila, W.J.: Energization of charged particles to high energies by an induced substorm electric field within the magnetotail. J. Geophys. Res. **83**, 1544–1550, 1978

Pytte, T., McPherron, R.L., Kokubun, S.: The ground signatures of the expansion phase during multiple onset substorms. Planet. Space Sci. **24**, 1115–1132, 1976a

Pytte, T., McPherron, R.L., Kivelson, M.G., West, H.I., Hones, E.W.: Multiple-satellite studies of magnetospheric substorm: Radial dynamics of the plasma sheet. J. Geophys. Res. **81**, 5921–5933, 1976b

Pytte, T., McPherron, R.L., Kivelson, M.G., Hones, E.W., West, H.I.: Multiple-satellite studies of magnetospheric substorms: Plasma sheet recovery and the poleward leap of auroral zone activity. J. Geophys. Res. **83**, 663–678, 1978

Rostoker, G., Camidge, F.P.: Localized character of magnetotail magnetic fluctuations during polar magnetic substorm. J. Geophys. Res. **76**, 6944–6949, 1971

Russell, C.T., McPherron, R.L.: The magnetotail and substorms. Space Sci. Rev. **15**, 205–263, 1973

Saito, T., Sakurai, T., Koyama, Y.: Mechanism of association between Pi2 pulsation and magnetospheric substorm. J. Atmos. Terr. Phys. **38**, 1265–1269, 1976

Sakurai, T., Saito, T.: Magnetic pulsations Pi2 and substorm onset, Planet. Space Sci **24**, 573–575, 1976

Schindler, K.: Macroinstabilities of the magnetotail. In: Dynamics of the magnetosphere, S.-I. Akasofu, ed.: pp. 311–326. Dordrecht: D. Reidel Publ. Comp. 1979

Sergeev, V.A.: On the longitudinal localization of the substorm active region and its changes during the substorm. Planet. Space Sci. **22**, 1341–1343, 1974

Sergeev, V.A.: On the microstructure of the magnetospheric substorm. Geomagn. Res. (In Russian) **21**, 5–15, 1977

Sergeev, V.A., Yahnin, A.G.: The features of auroral expansion during the substorm explosive phase and the model of microsubstorms in the magnetosphere. Phys. Solariterr., Potsdam **7**, 23–46, 1978

Sergeev, V.A., Yahnin, A.G.: A correspondence of the substorm expansive phase signatures. Geomagn. Res (In Russian) **24**, 78–89, 1979a

Sergeev, V.A., Yahnin, A.G.: The features of auroral bulge expansion. Planet. Space Sci. **27**, 1429–1444, 1979b

Sergeev, V.A., Yahnin, A.G., Raspopov, O.M.: On the spatial-temporal structure of the expansive phase of microsubstorm. In: Dynamical processes and structure of auroral magnetosphere (SAMBO experiment) (In Russian), O.M. Raspopov, L.L. Lazutin, eds. pp. 42–54. Apatity: Kola Branch Acad. Sci. USSR 1978

Sergeev, V.A., Tsyganenko, N.A.: The Earth's magnetosphere. Moscow: Science Publ. House 1980

Timofeev, E.E., Yahnin, A.G.: On the distribution of types of the radioaurora relative to the auroral bulge. 'Polar aurora' (In Russian) **28**, in press, 1981

Tsyganenko, N.A.: The subroutines and tables for the calculation of geomagnetic field. WDC-B report 1979

Tsyganenko, N.A., Zaitzeva, S.A.: On the mechanism for the formation of quiet auroral arcs. Geomagn Res. (In Russian) **24**, 61–70, 1979

Untiedt, J., Pellinen, R., Küppers, F., Opgenoorth, H.J., Pelster, W.D., Baumjohann, W., Ranta, H., Kangas, J., Czechowsky, P., Heikkila, W.J.: Observations of the initial development of an auroral and magnetic substorm at magnetic midnight. J. Geophys. Res. **45**, 41–65, 1978

Vasiliunas, V.M.: An overview of magnetospheric dynamics. In: Magnetospheric Particles and Fields, B.M. McCormac, ed.: pp. 99–105. Dordrecht: D. Reidel Publ. Comp 1976

Vette, J. (ed.): Special IMS periods for 1976, IMS/SSC rept. N6, 1975

Vorobjev, V.G., Rezenov, B.V.: Progressive westward displacements of the region of the auroral substorm localization in conjunction with impulsive variations of the magnetic field. Inst. Ass. Geomagn. Aeron. Bull. **34**, 441–449, 1973

Wiens, R.G., Rostoker, G.: Characteristics of the development of the westward electrojet during the expansive phase of the magnetospheric substorms. J. Geophys. Res. **80**, 2109–2128, 1975

Received December 5, 1979; Revised Version October 7, 1980
Accepted January 16, 1981

J Geophys (1981) 49:186–191

Journal of Geophysics

Simultaneous Observations of Energetic Protons Close to the Bow Shock and Far Upstream*

M. Scholer[1], F.M. Ipavich[2], G. Gloeckler[2], and D. Hovestadt[1]

[1] Max-Planck-Institut für Physik und Astrophysik, Institut für extraterrestrische Physik, D-8046 Garching, Federal Republic of Germany

[2] Department of Physics and Astronomy, University of Maryland, College Park, Maryland 20742, USA

Abstract. We have investigated four energetic proton events (30 keV–75 keV) upstream of the earth's bow shock with two identical experiments of the Max-Planck-Institut/University of Maryland on satellites ISEE-1 and ISEE-3. Close to the bow shock the particle distribution is more or less isotropic and indicates relatively strong scattering of these particles in the upstream wave field. At ISEE-3 between 100 and 200 R_E upstream from the earth's bow shock, the particles move essentially scatter-free from the general bow shock direction. The proton differential intensity at ISEE-3 is a factor of about 4–15 less than at ISEE-1 at 30 keV. The spectra at ISEE-1 are steeper than the spectra at ISEE-3. Flux ratios and spectra are discussed in terms of a first order Fermi acceleration model with a diffusion coefficient increasing approximately linearly with energy and a free escape boundary at some distance upstream.

Key words: Earth's bow shock – Upstream particles – Shock acceleration

Introduction

Early observations of energetic particles upstream of the earth's bow shock have been reported by Asbridge et al. (1968) and Lin et al. (1974). The ISEE-1 and -2 satellites with their highly eccentric orbits and the ISEE-3 satellite in a halo orbit around the libration point have opened a new era in the study of bow shock associated particle and wave phenomena. The ions upstream of the bow shock exist in two distinctly different components (Gosling et al. 1978), the socalled reflected and diffuse components. The reflected component is essentially a beam directed outward from the shock along interplanetary field lines, whereas the diffuse ions are characterized by relatively flat energy spectra and broad angular distributions. The reflected ion beam typically has energies of several keV and can be explained by an acceleration of solar wind ions in terms of a displacement along the interplanetary electric field during particle reflection at the bow shock (Paschmann et al. 1980). One rare occasions ion beams up to energies of ~65 keV have been observed (Scholer et al. in press 1981). Diffuse upstream ion events usually last up to several hours and can extend in energy up to least 100 keV (Ipavich et al. 1979; Scholer et al. 1979). Ipavich et al. (1981) have shown that the spectra of protons and alpha particles in these events are generally well described as exponentials in energy per charge and that the ratio of the fluxes of the two species is constant as a function of energy. In a statistical analysis Scholer et al. (1980a) have shown that the rate of occurrence of upstream diffuse events increases with decreasing angle between magnetic field and radial direction (i.e., sun-earth direction). They concluded that the field line connection time with the bow shock is the determining factor for the occurrence of diffuse upstream ions, and they suggested that these ions are accelerated by a first order Fermi mechanism at the shock. Such an acceleration process has been discussed in detail by Fisk (1971), Scholer and Morfill (1975), Axford et al. (1977), Bell (1978a, b), and Blandford and Ostriker (1978).

Simultaneous measurements at ISEE-1 close to the bow shock and at ISEE-3 far upstream have shown that, whereas the particle distribution close to the shock is more or less isotropic, the particles far upstream are moving essentially scatter free (Scholer et al. 1980b). Thus, the turbulent magnetic waves responsible for particle scattering have to be limited to some region close to the bow shock. Beyond some distance L particle transport becomes scatter free and the particles can escape freely into the far upstream medium. Sanderson et al. (in press 1981) and Anderson (in press 1981) have studied detailed pitch angle distributions at ISEE-3. They reported, in addition to the sunward streaming along the interplanetary magnetic field, pitch angle asymmetries due to density gradients and due to the electric field induced by the motion of the interplanetary magnetic field.

In this paper we study in detail four upstream particle events which were simultaneously observed by ISEE-1 and ISEE-3. In particular, we make a comparison between the absolute flux values $\sim 200 R_E$ (earth radii) from the bow shock and flux values several R_E in front of the bow shock at two different energies and interpret the results in terms of a model invoking a first order Fermi mechanism at the shock and a free escape boundary somewhere upstream.

The observations were obtained with two identical instruments, the *Ultra-Low-Energy-Charge-Analyzer* (ULECA) of the Max-Planck-Institut/University of Maryland sensor system on ISEE-1 and ISEE-3. A detailed description of the instrument may be found in Hovestadt et al. (1978).

Observations

In the following, we discuss four upstream particle events for which we have simultaneous measurements at ISEE-1 and -3. The positions of the two spacecraft during these events are shown in Fig. 1 in a projection onto the solar-ecliptic plane. Figure 2

* Paper presented at the Workshop on Acceleration of Particles by Shock Waves, October 7–9, 1980, Max-Planck-Institut für Aeronomie, Lindau, FRG

0340-062X/81/0049/0186/$01.20

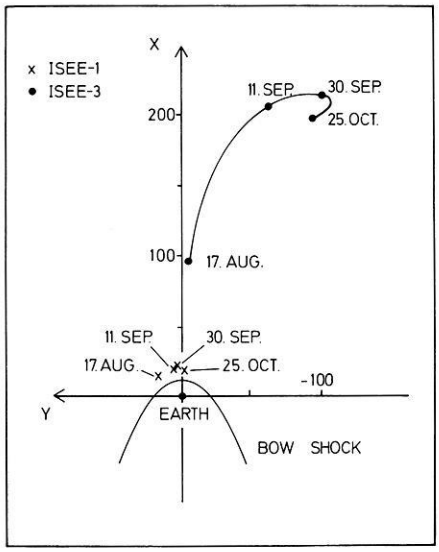

Fig. 1. The spatial location of the ISEE-1 and -3 spacecraft at times of the upstream particle events discussed in the paper, in the solar ecliptic plane

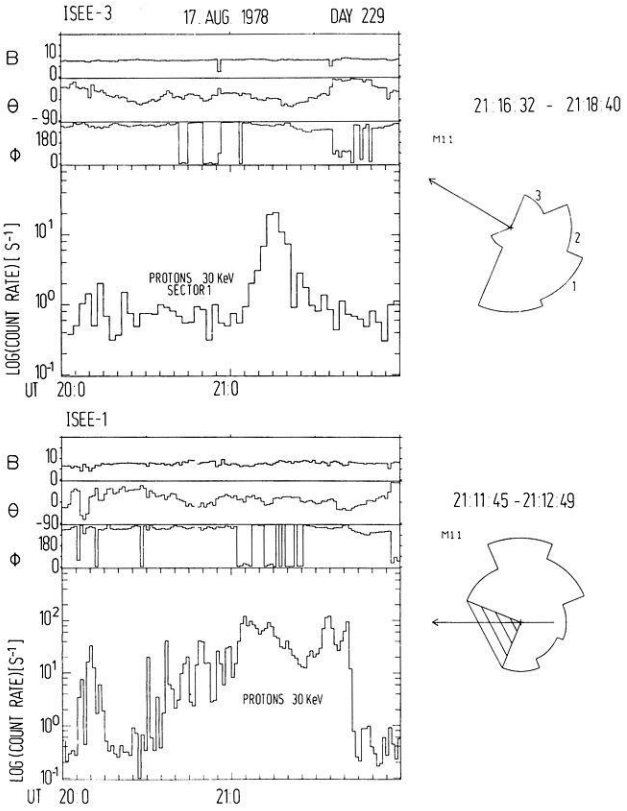

Fig. 2. Magnetic field and particle data during the 17 August 1978 event. *Top left:* magnetic field in gammas, θ and Φ component in solar-ecliptic coordinates (*upper three panels*) and intensity-time profile of energetic particles at ISEE-3; *top right*: typical anisotropy measurement during the upstream particle burst. *Lower left:* magnetic field and particle data at ISEE-1 during same time period; *lower right:* typical anisotropy measurement observed at ISEE-1. The sun is to the left, the *arrow* indicates the projection of the magnetic field onto the ecliptic

shows, on the left side, a 2 h interval of particle and magnetic field data on 17 August 1978. The upper left part of Fig. 2 shows, in the upper three panels, the magnetic field magnitude (in gammas) and the θ and Φ components in solarecliptic coordinates as measured on ISEE-3. The next panel shows the 30 keV proton count rate. The lower left part of Fig. 2 shows the same data for ISEE-1. To the upper and lower right side of Fig. 2 we show typical examples of anisotropy measurements during this time period at the two satellites; shown is the counting rate (on a linear scale) in 8 sectors which are scanning in the ecliptic plane (the sun is to the left of the figure). Due to the fan-like aperture the fluxes are integrated over an angular range of $\pm 30°$ out of the ecliptic. The time-intensity profile at ISEE-3 is the intensity in sector 1 (for sector numbering see the anisotropy samples). For ISEE-1 we show the spin averaged count rate.

Since several rate channels of the ULECA sensor on ISEE-1 are sensitive to sunlight, depending on the orientation of the spin axis with respect to the spacecraft-sun line, the sun sector (and sometimes the following sector) has to be eliminated as indicated by the shaded portion. Also shown is the magnetic field direction in the ecliptic plane. At ISEE-3 particles arrive anti-parallel to the field from the bow shock direction with pitch angles down to 90°, while at ISEE-1 the distribution is more or less isotropic. This has already been observed during other events by Scholer et al. (1980b) and by Sanderson et al. (in press 1981) and Anderson (in press 1981).

In comparing absolute fluxes and spectra at the two spacecraft we have to consider an important point. Charged particles moving upstream are subject to the electric field induced by the motion of the interplanetary magnetic field. The resulting drift perpendicular to the magnetic field leads for each particle velocity parallel to the magnetic field, $v_{\parallel}$, to a foreshock boundary; upstream of this boundary no particles with velocity $v_{\parallel}$ can be observed. Close to the field line tangent to the bow shock particles are therefore arranged in the form of sheets according to their parallel velocity (Anderson, in press 1981). However, assuming that acceleration takes place everywhere at the bow shock and not only close to the point of tangency as assumed by Anderson (in press 1981) we will have, at any point not too close to the line of tangency, a superposition of particles with different velocities $v_{\parallel}$. (Actually, as shown by Scholer et al. (1980a) diffuse ions are not accelerated close to the point of tangency of a field line with the bow shock, but reach their steady state after a relatively long ($\sim$60 min) field line connection time).

Spectra taken well within an event and not at the event onset are therfore most likely to be representative of the spectra at the distance from the bow shock where the particles escape freely into the upstream medium. At the event onset, on the other hand, one might observe high energy particles first and low energy particles later, as the sunward side of the ion sheets moves over the spacecraft. There is also an earthward spatial limitation of the particle distribution; as this boundary sweeps over the spacecraft one will observe anisotropies of the particle distribution perpendicular to the magnetic field due to the effect of a density gradient perpendicular to the magnetic field.

Sanderson et al. (in press 1981) report gradient anisotropies at the onset as well as at the end of an upstream particle event observed at ISEE-3. Note, however, that these authors present data from ISEE-3 only. Observations of particle bursts far upstream from the bow shock cannot alone reveal whether these particles are bow shock associated or of magnetospheric origin.

Figure 3 shows differential spectra during the 17 August 1978 event at both spacecraft. We have taken, at both spacecraft, the

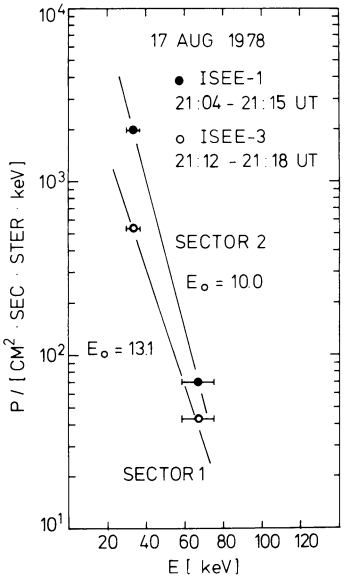

Fig. 3. Two-point spectra (of the flux in the sector containing the magnetic field) during the 17 August 1978 event as observed on ISEE-1 and ISEE-3. The flux is plotted linearly vs energy (in cm^2 s.sr.keV)$^{-1}$; E_0 the e-folding energy assuming a representation as an exponential in energy

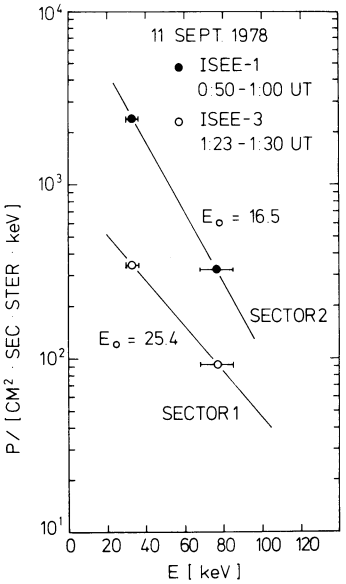

Fig. 5. Spectra during the 11 September 1978 event

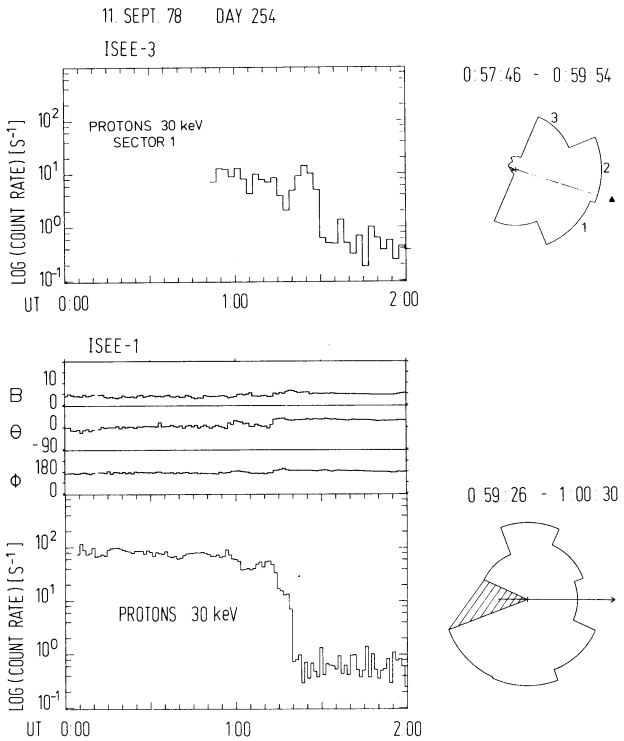

Fig. 4. Magnetic field (ISEE-1 only) and particle data for the 11 September 1978 upstream event

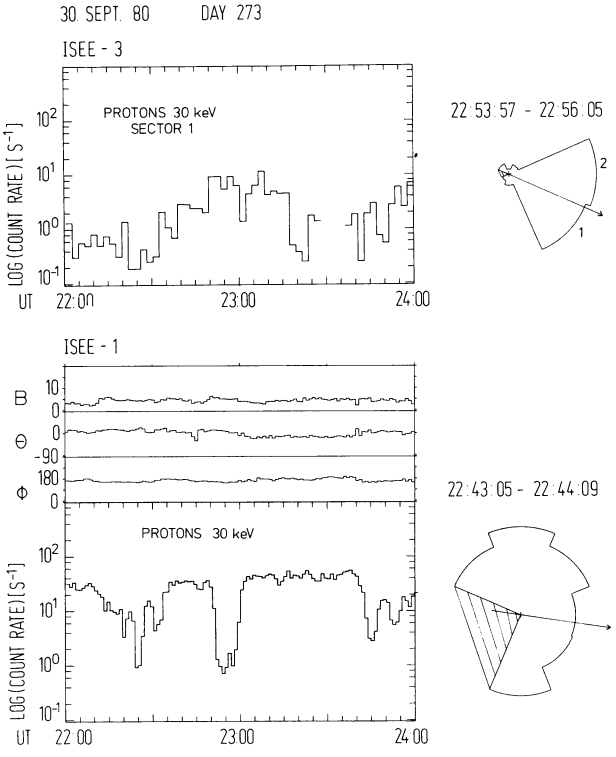

Fig. 6. Magnetic field (ISEE-1 only) and particle data for the 30 September 1978 upstream event

intensity in the sector containing the magnetic field direction (flux of particles streaming away from the bow shock along the interplanetary magnetic field). The spectra are plotted linearly against energy. It has been shown by Ipavich et al. (in press 1981) in a statistical analysis of upstream events measured at ISEE-1 that the spectra can be represented reasonably well by exponentials in energy over the energy range 30–160 keV. Therefore we have fitted exponentials in energy through the two point spectra obtained in this analysis (the fluxes at higher energies, i.e., at 120–160 keV, at ISEE-3 for these events are always at background level and cannot be used in the spectral representation). Also given in Fig. 3 is the e-folding energy E_0 of the two point spectra. As can be seen from Fig. 3 the spectrum at ISEE-1 is steeper ($E_0 = 10$) than the ISEE-3 spectrum ($E_0 = 13.1$). Flux ratios between

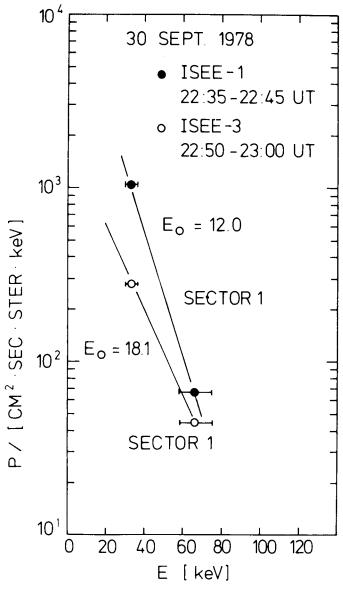

Fig. 7. Spectra during the 30 September 1978 event

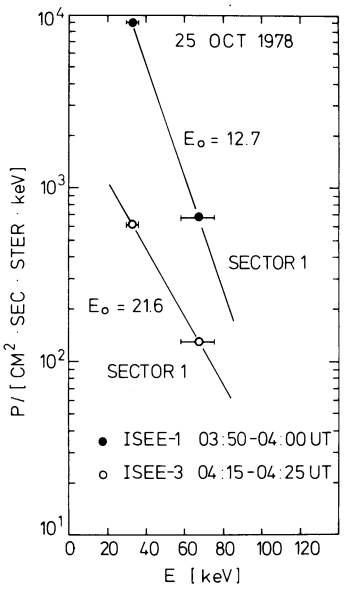

Fig. 9. Spectra during the 25 October 1978 event

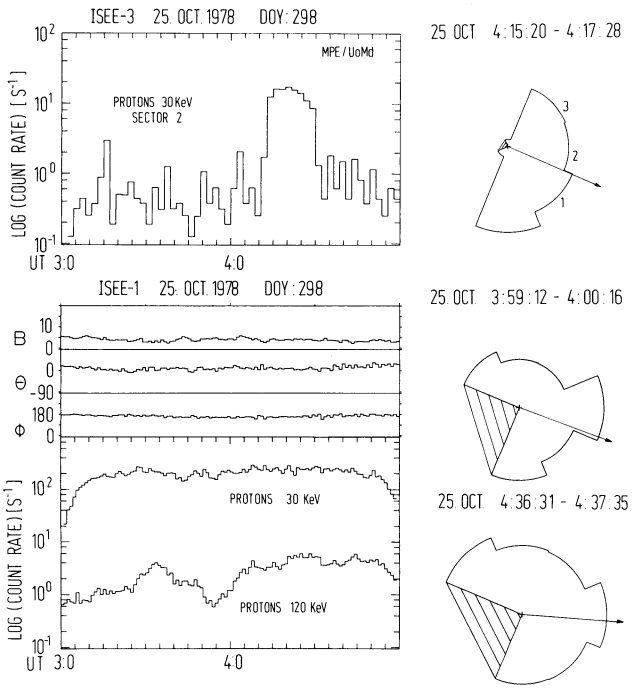

Fig. 8. Magnetic field (ISEE-1 only) and particle data for the 25 October 1978 upstream event

ISEE-1 and ISEE-3 are 3.7 at ~30 keV and 1.6 at ~65 keV, respectively. When comparing spectra between ISEE-1 and ISEE-3 it should be noted that the intensities at both satellites are time variable and that intensities are different in different sectors. Thus a comparison as made here has, of course, to be considered with caution.

Figure 4 shows magnetic field (ISEE-1 only) and particle data during an upstream event on 11 September 1978 in the same representation as in Fig. 2. Figure 5 shows corresponding spectra. The spectra are somewhat harder (E_o = 16.5 and 25.4, respectively), the flux ratios are 7.0 and 3.5 at ~30 keV and ~65 kev, respectively.

Figure 6 shows an event on 30 September 1978 and Fig. 7 shows the corresponding spectra. We have always taken the spectra 10–20 min earlier at ISEE-1 than at ISEE-3, allowing for a propagation time of protons parallel to the field between the region close to the shock and ISEE-3 at ~200 R_E. The flux ratios of upstream moving particles during the 30 September event are 3.8 and 1.5 at ~30 keV and ~65 keV, respectively. Finally, Fig. 8 shows magnetic field and particle data for the 25 October 1978 event, which has been previously published in Scholer et al. (1980c). The spectra in Fig. 9 show that there are large flux changes between the two satellites, flux ratios being 14.8 and 5.2 at ~30 keV and ~65 keV, repectively.

At ISEE-1 there is a flux decrease at higher energies (~120 keV) from ~3:50–4:00 UT. If we had chosen the time interval from 4:05–4:15 UT for the spectral representation at ISEE-1 the flux ratios would have been ~14.5 and ~10 at ~30 keV and ~65 keV, respectively; the *e*-folding energy during this time interval is ~16.8 keV.

Discussion and Interpretation

We have presented simultaneous observations of upstream energetic protons close to the bow shock at ISEE-1 and far upstream at ISEE-3 during four different events. The results of this investigation are:

1. The proton angular distributions are more or less isotropic at ISEE-1 whereas at ISEE-3 no particles are seen to return from upstream to the spacecraft. Scattering of particles at ISEE-3 is therefore weak and particles move essentially scatter free.

2. Comparison of absolute flux values shows that there is a flux decrease between ISEE-1 and ISEE-3 by a factor which varies between ~4 and ~15 at ~30 keV.

3. Spectra close to the bow shock are always steeper than spectra far upstream. At ~65 keV the flux is reduced only by ~1.6 to ~5.

4. It seems that the flux decrease is larger if the spectra close to the bow shock are harder (11 September event) and less if the spectra close to the shock are steeper (e.g., 17 August event). This is clearly based on only a few events and is not conclusive.

In Scholer et al. (1980a) we have argued that diffuse upstream

particles at energies $\gtrsim 30$ keV can probably be explained in terms of a first order Fermi mechanism at the bow shock. In an infinite medium such an acceleration mechanism predicts a power law spectrum close to the shock, whereas the observations show that the spectrum is very close to an exponential in energy. We have therefore suggested that the spatial limitation of the scattering region upstream of the shock together with a mean free path increasing with energy leads to a spectral form similar to an exponential in energy. From intensity-time profiles at different energies Scholer et al. (1980a) have indeed derived a diffusion coefficient, κ, proportional to energy, more specifically to energy per charge, $\kappa \propto E/Q$.

Recently, Lee et al. (in press 1981) have solved the stationary equations for first order Fermi acceleration at a plane shock under the boundary condition that, at some distance L upstream, the omnidirectional distribution function, f, is zero. They find that in the limit $V_S L/\kappa \ll 1$ (V_S=upstream plasma velocity relative to the shock) and under the assumption $\kappa \propto E$ the energy dependence of f is given by an exponential in energy. Assuming f to be zero at some distance $x=L$ is not critical for calculating spectra close to the shock, but in the frame work of such a model we can, of course, not compare spectra close to the shock and at or beyond the distance L. If we want to compare spectra close to the shock and far upstream we have to invoke a two-component model for the particle populations moving in the $+x$ and $-x$ directions, respectively, as proposed by Terasawa (in press 1981). With U^+ and U^- as the corresponding differential number densities, the diffusion-convection equations in the rest frame of the shock read:

$$(\bar{v}-V_S)\frac{\partial}{\partial x}U^+ = \frac{1}{\tau}(U^- - U^+)$$
$$(\bar{v}+V_S)\frac{\partial}{\partial x}U^- = \frac{1}{\tau}(U^+ - U^-) \qquad (1)$$

where τ is the characteristic scattering time, $\bar{v}$ is the pitch angle averaged velocity in the rest frame of the plasma: $\bar{v}\approx v/2$; $\kappa \approx \frac{1}{2}\tau\bar{v}^2$. Assuming at $x=L$ the boundary condition $U^-(x=L)=0$ the solution to (1) is (Terasawa, in press 1981):

$$U^+ = g(\bar{v})\left[\exp(-V_S x/\kappa) - \frac{\bar{v}-V_S}{\bar{v}+V_S}\exp(-V_S L/\kappa)\right]$$
$$U^- = g(\bar{v})\frac{\bar{v}-V_S}{\bar{v}+V_S}\left[\exp(-V_S x/\kappa) - \exp(-V_S L/\kappa)\right] \qquad (2)$$

where $g(\bar{v})$ is a function of velocity only and has to be determined by the boundary condition at the shock, $x=0$.

Figure 10 shows the ratio $\chi = U^+(x=L)/U^+(x=0)$, as obtained from (2) for two different energies and a solar wind velocity of 400 km/s vs the parameter $V_S L/\kappa$. Assuming $\kappa \propto E$ the value of $V_S L/\kappa$ is, at 60 keV only half the value of $V_S L/\kappa$ at 30 keV and this results, according to Fig. 10, in a larger value χ (60 keV). This predicts a flattening of the spectrum between ISEE-1 and ISEE-3, which is indeed observed during all four events investigated. Variability in the flux ratios between ISEE-1 and ISEE-3 from one event to the next is, according to this model, due to changes in the parameter $V_S L/\kappa$. From the measured flux decreases we obtain values of $V_S L/\kappa$ at 30 keV between ~ 1 and ~ 2. This is, of course, only true if there is no further loss between the region of free escape and the point of observation far upstream.

The measured difference in the flux ratio between ISEE-1 and ISEE-3 at the two different energies, ~ 30 keV and ~ 60 keV,

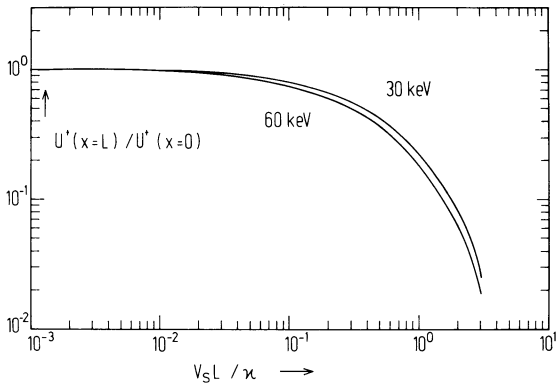

Fig. 10. Ratio of flux of particles flowing upstream at the free escape boundary ($x=L$) to flux of particles flowing upstream at the shock ($x=0$) vs $V_S L/\kappa$

can only be explained if the diffusion coefficient increases with energy at least according to $\kappa \propto E$ (assuming L to be independent of energy). Note, that this results is independent of the knowledge of the spectral shape, i.e., the function $g(\bar{v})$, and is based only on ratios near the shock and beyond L at different energies. This is consistent with our earlier result in Scholer et al. (1980a), where we derived a linear dependence of κ on E from the intensity-time profiles. However, the data are also not inconsistent with an energy dependence of κ such as $\kappa \propto E^{1.5}$ as required by Terasawa (in press 1981) in his acceleration model, where the shock is considered to be a partial reflector of particles.

As mentioned earlier, Lee et al. (in press 1981) have derived the spectrum of the accelerated particles by assuming that, at the shock, the product of particle differential streaming with the cross sectional area of a flux tube across the shock is conserved. In the limit $V_S L/\kappa << 1$ and assuming $\kappa \propto v^2$ the distribution function, f, at the shock is an exponential in velocity squared. From the absolute flux comparison we have seen that $V_S L/\kappa$ is of the order of 1. It can, however, be shown that even for values $V_S L/\kappa \sim 1$ the distribution function can still be fitted very well over a limited energy range, say from 30–160 keV, by an exponential in energy and that values of $V_S L/\kappa_{30}$ between 1 and 2 ($\kappa_{30}=\kappa$ at 30 keV) will result in e-folding energies, E_o, between ~ 10 and 20. The e-folding energy increases with $V_S L/\kappa_{30}$, larger values of $V_S L/\kappa_{30}$ lead, according to Fig. 10, to larger flux differences between $x=0$ and $x=L$ which is consistent with the observations of e-folding energies close to the shock, as presented in this paper.

In summary, we have studied four upstream particle events where simultaneous data exist close to the bow shock from ISEE-1 and far upstream from ISEE-3. The flux (in the sector containing the magnetic field) far upstream is lower by a factor which ranges from 4 to 15 at 30 keV for the four events. The spectra far upstream are harder than the spectra close to the shock. The spectra and flux differences can be understood in a model where particles are accelerated by a first order Fermi mechanism at the shock. The scattering has to be limited to some region close to the shock, the distance from the shock is of the order of κ/V_S with κ as the diffusion coefficient at ~ 30 keV and V_S as the solar wind velocity. The diffusion coefficient used in this model has to increase approximately linearly with energy.

Acknowledgements. The authors are grateful to the many individuals at the Max-Planck-Institut and the University of Maryland who have contributed to the success of the ISEE mission. In particular we thank P. Laeverenz, E. Künneth, E. Tums, and J. Cain for designing and

preparing the experiment for launch. We thank C.T Russell for use of ISEE-1 magnetic field data and E.J. Smith for use of ISEE-3 magnetic field data. We are very grateful for discussions with L.A. Fisk. This work has been supported by NASA under contract number NAS5-20062 and by the Bundesministerium für Forschung und Technologie, FRG, under contract number RC14-B8/74.

References

Anderson, K.A.: Measurements of bow shock particles far upstream from the earth. J. Geophys. Res. in press 1981

Asbridge, J.R., Bame, S.J., Strong, I.B.: Outward flow of protons from the earth's bow shock. J. Geophys. Res. **73**, 5777–5782, 1968

Axford, W.I., Leer, E., Skadron, G. The acceleration of cosmic rays by shock waves. Proc. 15th Int. Cosmic Ray Conf. **11**, 132–137, 1977

Bell, A.R.. The acceleration of cosmic rays in shock fronts – I. Monthly Notices R. Astron. Soc. **182**, 147–156, 1978a

Bell, A.R.. The acceleration of cosmic rays in shock fronts – II. Monthly Notices R. Astron. Soc. **182**, 443–455, 1978b

Blandford, R.D., Ostriker, J.P.: Particle acceleration by astrophysical shocks. Astrophys. J. **221**, L29–L32, 1978

Fisk, L.A.. Increases in the low energy cosmic ray intensity at the front of propagating interplanetary shock waves. J. Geophys. Res. **76**, 1662–1672, 1971

Gosling, J.T., Asbridge, J.R., Bame, S.J., Paschmann, G., Sckopke N., Observations of two distinct populations of bow shock ions in the supstream solar wind. Geophys. Res. Lett. **5**, 957–960, 1978

Hovestadt, D., Gloeckler, G., Fan, C.Y., Fisk, LA., Ipavich, F.M., Klecker, B., O'Gallagher, J.J., Scholer, M., Arbinger, H., Cain, J., Höfner, H., Künneth, E., Laeverenz, P., Tums, E.: The nuclear and ionic charge distribution particle experiments on the ISEE-1 and ISEE-C spacecraft, IEEE. Trans. Geosci. Electron. **GE16**, 166–175, 1978

Ipavich, F.M., Gloeckler, G., Fan, C.Y., Fisk, L.A., Hovestadt, D., Klecker, B., O'Gallagher, J.J., Scholer, M.. Initial observations of low energy charged particle near the earth's bow shock on ISEE-1. Space Sci. Rev. **23**, 93–101, 1979

Ipavich, F.M., Galvin, A.B., Gloeckler, G., Scholer, M., Hovestadt, D.. A statistical survey of ions observed upstream of the earth's bow shock: energy spectra, composition, and spatial variation. J. Geophys. Res. in press 1981

Lee, M.A., Skadron, G., Fisk, L.A.. Acceleration of energetic ions at the Earth's bow shock. Geophys. Res. Lett. in press 1981

Lin, R.P., Meng, C.I., Anderson, K.A.. 30 to 100 keV protons upstream from the earth's bow shock. J Geophys. Res. **79**, 489–498, 1974

Paschmann, G., Sckopke, N., Asbridge, J.R., Bame, S.J., Gosling, J.T · Energization of solar wind ions by reflection from the earth's bow shock. J. Geophys. Res. **85**, 4689–4693, 1980

Sanderson, T.R., Reinhard, R., Wenzel, K.P. The propagation of upstream protons between the earth's bow shock and ISEE-3. J. Geophys. Res. in press 1981

Scholer, M., Morfill, G.. Simulation of solar flare particle interaction with interplanetary shock waves. Solar Phys. **45**, 227–240, 1975

Scholer, M., Gloeckler, G., Ipavich, F.M., Hovestadt, D., Klecker, B.: Pitch angle distributions of energetic protons near the earth's bow shock. Geophys. Res Lett. **6**, 707–710, 1979

Scholer, M., Ipavich, F.M., Gloeckler, G., Hovestadt, D.: Conditions for acceleration of energetic ions $\gtrsim 30$ keV associated with the earth's bow shock. J. Geophys. Res. **85**, 4602–4606, 1980a

Scholer, M., Ipavich, F.M., Gloeckler, G., Hovestadt, D., Klecker, B. Upstream particle events close to the bow shock and 200 R_E upstream: ISEE-1 and ISEE-3 observations. Geophys. Res. Lett. **7**, 73–76, 1980b

Scholer, M., Ipavich, F.M., Gloeckler, G.: Beams of protons and alpha particles $\gtrsim 30$ keV/charge from the earth's bow shock. J. Geophys. Res. in press 1981

Terasawa, T.. Energy spectrum of ions accelerated through Fermi process at the terrestrial bow shock. J. Geophys. Res. in press 1981

Received January 22, 1981; Revised Version March 9, 1981
Accepted March 23, 1981

J Geophys (1981) 49:192–197

Journal of Geophysics

Non-Adiabatic Expansion of Low-Temperature Solar Wind Radial Temperature Gradients

A. Geranios*

Nuclear Physics Laboratory, Cosmic Ray Group, University of Athens, Solonos str. 104, Athens 144, Greece

Abstract. The occasional observation of very low temperatures in the solar wind at 1 AU are of great interest temperatures in the solar plasma dropping on average, to one third and one tenth of the value for the ambient solar wind, for electrons and protons, respectively. In explanation of this phenomenon, a hypothetical magnetically closed structure in the solar wind is tested assuming two different sets of conditions. The first considers the structure, hereafter called "blob", expanding radially outwards from the sun but not adiabatically. The second involves a rapid pressure equalization across the boundary of the moving blob. To test these models, we used a set of semi-empirical specific heats, different for protons and electrons, and applied semi-empirical temperature gradients in the ambient solar wind, different for fast and slow flow.

Contrary to an older model, which assumed a pure adiabatic expansion and used the Hartle-Barnes theoretical temperature gradients, the result, after this test, showed that the modified blob model could reasonably support the observations, suggesting additionally a possible blob-origin at a distance of the order of ten solar radii.

Key words: Solar wind temperature – Radial temperature gradients

Introduction

Theoretical treatment of the hydrodynamic conditions in the solar wind, its heat conduction and especially the prediction of its temperature (Parker 1963; Whang and Chang 1965; Hartle and Sturrock 1968; Hartle and Barnes 1970; Yeh 1971; Hundhausen 1972; Hollweg 1976) is supported by experiments in space but these also reveal new aspects of solar wind properties (Montgomery et al. 1968; Burlaga and Ogilvie 1970; Gosling et al. 1972; Feldman et al. 1975).

One surprising phenomenon, the detection of "very cold" solar wind plasma, has attracted a systematic analysis (Gosling et al. 1973; Montgomery et al. 1974; Gosling and Roelof 1974; Geranios 1978). These observations, made by Vela 5, 6 and IMP 6 satellites, after the passage of an interplanetary shock front or solar wind stream, last on the average 10–40 h, or even longer. During this period both the electron and proton temperatures are anomalously low. It is generally believed (above mentioned authors) that this effect could possibly originate from regions in the solar wind which are surrounded by closed or nearly closed interplanetary magnetic field lines. Therefore, these regions are thermally isolated from the relatively hot corona and are cooling down in relation to the plasma embedded in open field lines, as they expand away from the sun.

Theoretical models, proposed by Whang and Chang 1965; Hartle and Sturrock 1968; Hartle and Barnes 1970, express the parameters of the solar wind analytically assuming good thermal contact between the solar plasma and the solar corona along the interplanetary magnetic field lines. Consequently, observations of cold plasma suggest an interruption of this thermal conduction.

Due to the expansion and convection of such regions, "blobs", by the solar wind, at an average speed of 400 km/s, by 1 AU they grow to a large size, of about 0.1–0.4 AU. (Originally, the expression "blob" was used by Barouch and Burlaga (1975), for a region in which the interplanetary magnetic field strength is high.) It is assumed that blobs started expanding somewhere between the sun and the earth. By assumming that they have followed a certain law during their expansion, for example an adiabatic expansion, we could estimate the place of their origin.

A method shown in principle in Fig. 1, described elsewhere (Geranios 1978), is based on the fact that at the origin the temperature inside the blob should be equal with that outside. The inner temperature falls progressively down to the measured value at 1 AU, 5.5×10^4 °K and 1.5×10^4 °K for electrons and protons respectively.

Using the Hartle and Barnes temperature gradients for electrons and protons in the ambient solar wind provided by the two-fluid model (Harthe and Barnes 1970) and the above observed low temperatures, we calculated independently for each main plasma component the radial distance from the sun of the apparent origin of the blobs. At this distance, the particles under consideration should be thermally decoupled from the corona. For the calculations we used two different models of the type of expansion:

(a) pure adiabatic expansion in radially streaming solar wind, and

(b) rapid pressure equalization across the boundary,

hereafter called model I and model II. The blob-formation distances thus calculated showed large discrepancies between electrons and protons, a fact which is inconsistent with what we might expect: that in the cold, expanding region, part of the solar wind, both electrons and protons should stay together (charge neutrality) (Geranios 1978). Therefore, under these conditions the closed magnetic loop or blob model is unlikely to

* *Present address.* Max Planck Institut für Aeronomie, D-3411 Katlenburg, Lindau 3, FRG

0340-062X/81/0049/0192/$01.20

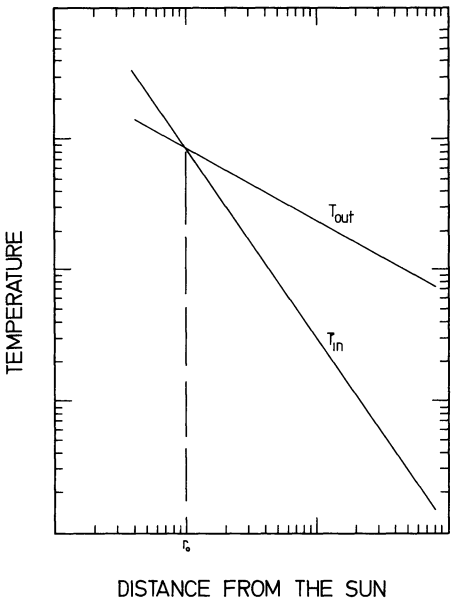

Fig. 1. The temperature variation of the solar wind plasma outside the blob, T_{out}, and inside, T_{in}, as this structure expands, moving radially outward from the sun towards the earth ($T_{out} > T_{in}$). The formation distance of the blob (r_o) is determined by the intersection of T_{out} and T_{in}, straight lines on a log-log scale

be the major cause of the electron and proton temperature depressions.

In this paper we attempt a new explanation of the anomalous solar wind temperature effect with the calculation of empirical specific heat coefficients, different for electrons and protons. In addition, we give empirical electron and proton temperature gradients, discriminating fast from slow solar wind (Helios-1, Rosenbauer et al. 1977).

Calculation of Semi-Empirical Specific Heats for the Low-Temperature Regions

Inside the blob we assume a radial, spherically symmetric temperature variation within the plasma and time independent expansion

$$T_i/T_o = (r/r_o)^{-2(\gamma_1 - 1)} \tag{1a}$$

T_i, T_o are the temperatures of the plasma at radial distances r and r_o, respectively, and γ is the ratio of the specific heat at constant pressure to that at constant volume. For an adiabatic expansion $\gamma = 5/3$, as in a fully ionized gas with three degrees of freedom (Spitzer 1962). To apply Eq. (1a) with $\gamma = 5/3$ to the electron and proton temperatures, the region under study should be completely thermally isolated from the neighbouring plasma. But this is an ideal condition. For a more realistic case we assume that

(1) the expansion is not purely adiabatic, so γ should be lower than 5/3, and

(2) γ is different for electrons and protons.

With these restrictions we calculate the new values (γ_1^e) for electrons and (γ_1^p) for protons, using

(a) the boundary conditions of the Hartle-Barnes model, and

(b) the experimentally measured temperatures at 1 AU (Geranios 1978):

at $r_o = 2R_o$, $T_o = 1.2 \times 10^6$ °K for protons
$T_o = 1.5 \times 10^6$ °K for electrons,

and

at $r = 1$ AU, $T_i = 1.5 \times 10^4$ °K for protons,

and

$T_i = 0.5 \times 10^5$ °K for electrons.

R_o, being the radius of the sun.

Equation (1a) gives

$$\gamma_1 = (2 - A)/2$$

where $A = \ln(T_i/T_o) : \ln(r/r_o)$ and with substitution of the above boundary values we have

$\gamma_1^p = 1.53$ for protons, where $A_p = -0.94$

and

$\gamma_1^e = 1.37$ for electrons, where $A_e = -0.73$

yielding $\gamma_1^e < \gamma_1^p < \gamma_{ad}$.

Subscripts 1, 2 refer to models I, II. For model II we also use the same boundary conditions and as the electrons of the solar wind are much hotter than the protons, the total pressure of the ambient solar wind is represented by the electron pressure. The corresponding equation for this model is:

$$T_i/T_o = (r/r_o)^{-(\gamma_2 - 1)(\varepsilon + 2)/\gamma_2} \tag{1b}$$

(Geranios 1978) $\varepsilon = 0.316$, being the electron temperature gradient (Hartle and Barnes 1970), according to which we obtain

$$\gamma_2 = (\varepsilon + 2)/(\varepsilon + 2 + A)$$

and we have

$\gamma_2^p = 1.68$ for protons, and
$\gamma_2^e = 1.46$ for electrons.

Models Using an Empirical Model for the Ambient Solar Wind

Measurements of solar wind electron and proton temperatures at different distances from the sun (0.3–1.0) AU, performed by Helios-1, revealed radial gradients not only different from those theoretically predicted, but also different for slow and fast solar wind speed (Rosenbauer et al. 1977). The data for the electron and proton temperature gradients are obtained from temperature and solar wind speed measurements for the period 14 December 1974–15 April 1975, during which Helios-1 approached the sun up to a radial distance of 0.309 AU, after its launch on 10 December 1974. The caluclated gradients take into account that the solar wind is distinguished into slow and fast, $V_s < 550$ km/s, $V_f > 550$ km/s. An example of temperature gradients is given below (all are unitless exponents)

Electrons $\varepsilon_f = 0.8$ for fast,
Electrons $\varepsilon_s = 0.5$ for slow solar wind.
Protons $b_f = 0.35$ for fast,
Protons $b_s = 0.62$ for slow solar wind.

Generally, for fast solar wind, ε_s tends to the value of 0.5, while for slow solar wind, ε_f tends to 1 (Philipp 1978). Figure 2

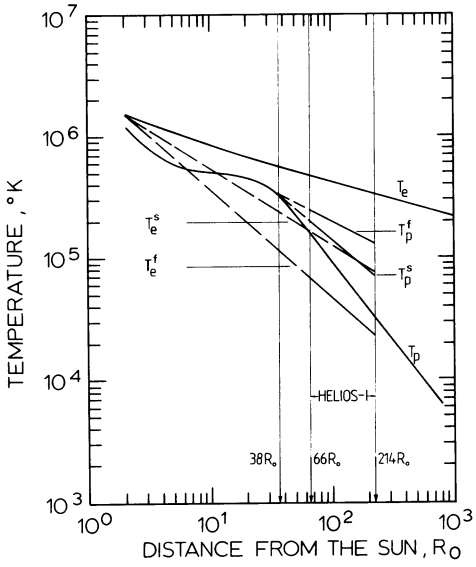

Fig. 2. Comparison between theoretically calculated H-B temperature gradients and those experimentally derived. T_e, T_p refer to the Hartle-Barnes two-fluid model. T_e^f, T_e^s, T_p^f, T_p^s are the calculated gradients for electrons and protons respectively for fast and slow solar wind. $38\,R_o$ is the distance at which the H-B model predicts a break-down of the gradient T_p. $66\,R_o$-$214\,R_o$ is the distance explored by Helios-1

compares the theoretical gradients with the empirical ones used. Applying these four temperature gradients and assuming that they are constant over the range 2-$214R_o$, having similar values for the period August 1969-May 1974 (the period during which the low temperature regions are detected), we test the two models I and II. We used the same value suggested by Hartle and Barnes (1970) for the proton temperature gradients for $2R_o$-$38R_o$. For the calculated proton temperature gradients we used 16000 approximately hourly temperature-speed data covering a period of three years (December 1974-December 1977), measured by Helios-1.

For each of the 30 very low temperatures analysed (Geranios 1978), detected by the IMP and VELA satellites at 1 AU (Feldman et al. 1975), we measure the temperature before and after the low temperature period (two values of T_a), and the minimum temperature (T_i). These values are shown in Table 1.

We classify the 30 events observed (Table 1) into two categories,

(1) fast solar wind, and

(2) slow solar wind.

(The cases related to fast solar wind are marked in Table 1 with *f*.) All coefficients involved in the calculations are shown in Table 2.

Model I

For protons we have

$$T_a/T_o=(38/r_o)^{-a}(r/38)^{-b_{f,s}} \quad \text{for } 38R_o\leqq r\leqq 214R_o \tag{2}$$

and

$$T_a/T_o=(r/r_o)^{-a} \quad \text{for } 2R_o\leqq r<38R_o \tag{3}$$

both

$$\text{for } 2R\leqq r_0<38R_o.$$

Table 1. Temperatures before (T_1) and after (T_2) very low temperature observations, minimum temperature T_m, recorded by IMP and VELA satellites. Subscript *e* refers to electrons, *p* to protons. Letter *f* denotes fast solar wind

No.	T_m^e	T_1^e	T_2^e	T_m^p	T_1^p	T_2^p	V
	$\times 10^4$ °K						(km/s)
1	–	–	–	0.8	19	15	490
2	5.0	11.8	12.0	2.5	7.5	14	375
3	4.2	17.0	26.7	3.5	15	50	700 *f*
4	7.5	14.2	10.0	2.0	29	16	415
5	6.8	9.5	10.0	0.8	7	3	370
6	4.5	22.0	12.0	4.0	30	10	500
7	6.5	15.5	12.2	1.2	10	7.5	365
8	7.5	21.5	14.5	–	–	–	710 *f*
9	4.5	11.5	8.0	1.8	18	7	455
10	3.3	9.5	15.1	3.7	25	14	620 *f*
11	5.0	13.0	16.5	3.0	18	8	495
12	6.0	15.0	17.0	2.0	16	24	370
13	–	–	–	0.3	16	10	430
14	5.0	8.0	13.0	1.5	17	13	400
15	5.0	10.0	18.0	2.0	14	18	380
16	5.0	10.8	7.6	1.8	12	16	440
17	4.5	15.6	10.3	1.0	18	12	430
18	8.3	25.5	20.8	0.8	42	11	525
19	6.6	30.0	14.5	1.0	4.7	3.7	350
20	5.0	19.0	15.1	0.8	10.7	16	455
21	6.1	13.6	23.9	1.6	9	33	–
22	5.8	20.6	15.1	1.3	20	16	635 *f*
23	5.6	13.5	10.6	0.8	4.7	3	370
24	5.6	10.6	15.1	0.8	3	16	300
25	5.3	27.5	13.1	0.8	44	13.5	600 *f*
26	1.4	7.3	7.0	3.1	20.5	10.2	–
27	4.4	13.8	25.0	1.3	22	12	420
28	6.6	16.0	24.0	1.3	6	36	–
29	5.0	20.0	24.0	2.5	51	41	565 *f*
30	6.3	15.6	14.4	1.7	18	13.6	600 *f*
31	4.6	13.3	13.5	1.6	7.8	16.7	400
32	–	–	–	2.1	19	16	600 *f*

Table 2. Polytropic indices (γ) and electron and proton temperature gradients (ε and b) for fast (f) and slow (s) solar winds

	Electrons	Protons
Model I	$\gamma_1^e=1.37$	$\gamma_1^p=1.53$
Model II	$\gamma_2^e=1.46$	$\gamma_2^p=1.68$
Fast	$\varepsilon_f=0.8$	$b_f=0.35$
Slow	$\varepsilon_s=0.5$	$b_s=0.62$
Theoret.	$\gamma_{ad}=1.67$	$a=0.349$
	$\varepsilon=0.316$	$b=1.272$

(From here, r denotes distance from the sun, variable, and r_o denotes location of the blob-origin, indices f, s apply to fast, slow solar wind cases, Table 1.)

$a=0.349$ (Hartle and Barnes 1970)

T_a is the temperature outside the blob at the sistance r. Using Eq. (1 a) we have, for fast and slow solar wind, respectively.

$$r_o=(T_i/T_a)^{1/(CP-a)}38^{(a-b_{f,s})(a-CP)}r^{(b_{f,s}-CP)/(a-CP)} \tag{4}$$

for

$38R_o \leqq r \leqq 214R_o$, and $2R_o \leqq r_0 < 38R_o$

$C^{p,e} = 2(\gamma_1^{p,e} - 1)$.

For each of the two categories we obtain

$$r_o = r(T_i/T_a)^{1/(C^p - a)} \quad \text{for } 2R_o \leqq r < 38R_o, 2R_o \leqq r_o < 38R_o. \tag{5}$$

A third case, which does not apply here is

$$r_o = r(T_i/T_a)^{1/(C^{p-b_{f,s}})} \quad \text{for } 38R_o \leqq r \leqq 214R_o, 38R_o \leqq r_o \leqq 214R_o.$$

For electrons, the corresponding equations are

$$T_a/T_o = (r/r_o)^{-\varepsilon_{f,s}} \tag{6}$$

and using Eq. (1a) we have

$$r_o = r(T_i/T_a)^{1/(C^e - \varepsilon_{f,s})} \quad \text{for fast and slow speeds.} \tag{7}$$

Model II

For protons we use Eq. (1b)

$$T_i/T_o = (r/r_o)^{-d_{f,s}}$$

and with

$$T_a/T_o = (38/r_o)^{-a}(r/38)^{-b_{f,s}}$$

gives for

$38R_o \leqq r \leqq 214R_o$, $2R_o \leqq r_o < 38R_o$

$$r_o = (T_i/T_a)^{1/(d^p_{f,s} - a)} 38^{-(a - b_{f,s})/(d^p_{f,s} - a)} r^{(b_{f,s} - d^p_{f,s})/(a - d^p_{f,s})} \tag{8}$$

for fast and slow solar wind, respectively.

$$d^{p,e}_{f,s} = (\gamma_2^{p,e} - 1)(\varepsilon_{f,s} + 2)/\gamma_2^{p,e}$$

p applies to protons and e to electrons.

In the range 2–38R_o for fast *or* slow solar wind we have

$$r_o = r(T_i/T_a)^{1/(d^p - a)} \quad \text{for } 2R_o \leqq r_o < 38R_o. \tag{9}$$

Similarly, for electrons we obtain, for $2R_o \leqq r \leqq 214R_o$

$$r_o = r(T_i/T_a)^{1/(d^e_{f,s} - \varepsilon_{f,s})}$$

for fast and slow solar wind.

for $2R_o \leqq r_o < 38R_o$.

Substitution of r by 214 (the distance of the observation) and of the measured temperatures T_i and the two T_1, T_2, which are the outside temperatures T_a (Table 1), into the above equations gives the possible ranges inside which the blobs might originate (Table 3). These ranges correspond to T_1–T_2 in Table 1. For the cases in Table 1 related to fast solar wind the possible ranges for electrons are at much larger distances than 1 AU for model I, while for model 2 they are at much shorter distances than one solar radius. This result is due to the apparently very large radial gradient used (0.8).

The frequency distributions of these distances are shown in Fig. 3. Here, the whole of the electron and proton distributions are overlapped, suggesting a mean distance of the origin of the blobs of protons and electrons around 10R_o for both models. The large width of the frequency distributions is due mainly to the large uncertainties in the temperature measurements and to the logarithmic scale used in the ordinates.

Results

Blob models which have previously been considered as possible candidates for the explanation of the phenomenon of very low

Table 3. Distance ranges where blob apparantly originated, calculated for the two models, separately for electrons and protons

No.	Model I		Model II	
	Range of r_o^e (R_o)	Range of r_o^p (R_o)	Range of r_o^e (R_o)	Range of r_o^p (R_o)
1	–	1.3 – 1.8	–	0.9 – 1.3
2	5.6 – 6.0	9.8 – 23.6	10.2 – 10.8	7.9 – 20.1
3	$\gg 214R_o$	5.1 – 27.6	$\ll 1R_o$	7.2 – 33.4
4	15.2 – 64.5	2.6 – 5.9	23.3 – 78.7	1.9 – 4.6
5	42.9 – 53.1	5.2 – 17.3	56.0 – 67.0	4.0 – 14.4
6	0.3 – 3.6	6.5 – 30.5	0.7 – 7.1	5.1 – 26.5
7	5.7 – 15.1	5.6 – 8.4	10.4 – 24.0	4.3 – 6.7
8	$\gg 214R_o$	–	$\ll 1R_o$	–
9	4.3 – 19.5	4.3 – 16.4	8.2 – 29.0	3.3 – 13.6
10	$\gg 214R_o$	14.5 – 32.8	$\ll 1R_o$	18.7 – 39.1
11	1.5 – 4.0	8.9 – 27.9	3.4 – 7.7	7.1 – 24.0
12	2.8 – 4.7	3.4 – 5.9	5.7 – 8.9	2.5 – 4.6
13	–	0.4 – 0.8	–	0.3 – 0.5
14	4.0 – 30.2	3.6 – 5.3	7.7 – 41.8	2.7 – 4.1
15	1.0 – 11.9	5.0 – 7.2	2.5 – 19.2	3.8 – 5.6
16	8.6 – 37.4	5.1 – 7.7	14.7 – 49.9	3.9 – 6.0
17	1.2 – 6.8	1.9 – 3.4	2.8 – 12.0	1.4 – 2.5
18	2.0 – 4.7	0.4 – 2.8	4.3 – 8.8	0.3 – 2.0
19	0.4 – 8.0	12.6 – 17.6	1.1 – 13.9	10.2 – 14.7
20	0.8 – 2.1	1.6 – 2.9	2.1 – 4.6	1.2 – 2.1
21	–	–	–	–
22	$\gg 214R_o$	4.6 – 6.3	$\ll 1R_o$	6.5 – 8.7
23	5.5 – 15.0	9.2 – 17.3	10.0 – 23.3	7.3 – 14.4
24	3.4 – 15.0	1.6 – 17.3	6.8 – 23.3	1.2 – 14.4
25	$\gg 214R_o$	0.8 – 4.0	$\ll 1R_o$	1.3 – 5.8
26	–	–	–	–
27	0.2 – 1.8	2.1 – 4.9	0.5 – 4.0	1.5 – 3.7
28	–	–	–	–
29	$\gg 214R_o$	3.1 – 4.2	$\ll 1R_o$	4.6 – 6.0
30	$\gg 214R_o$	7.7 – 11.5	$\ll 1R_o$	10.5 – 15.1
31	2.4 – 2.6	4.1 – 11.9	5.1 – 5.3	3.1 – 9.7
32	$\gg 214R_o$	9.6 – 12.3	$\ll 1R_o$	12.9 – 16.0

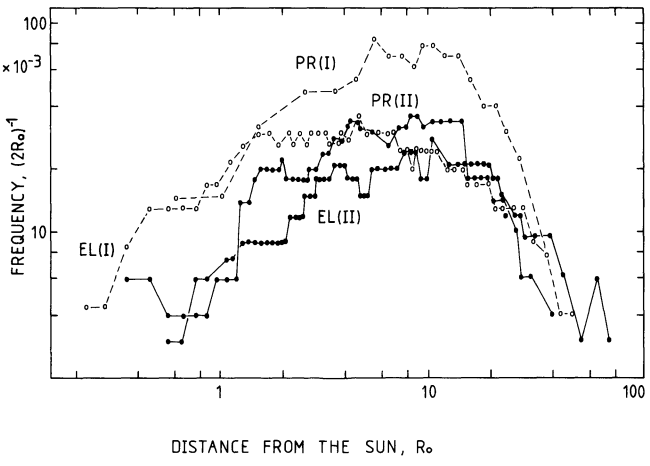

Fig. 3. The frequency of occurence of blob formation distances r_o versus R_o with the same calculated γ's as in Fig. 2 and the experimentally estimated temperature gradients for protons and electrons according to models I and II. The distinction between fast and slow solar wind is also taken into account

temperatures in the solar wind plasma under conditions of adiabatic expansion could not explain the temperature depressions (Geranios 1978).

In the paragraph here concerning specific heat calculations, which are different for protons and electrons, we have changed the condition of diabatic expansion, which the models tested previously were based on. Due to the fact that up to distance of at least 2/3 of 1 AU the temperature of protons and electrons in the solar wind have been measured by the heliocentric satellite Helios-1, we can calculate the radial temperature gradients.

The new test of the blob model is based on the assumption that the mean temperature gradient during the observed low temperature periods (August 1969–May 1974) is the same as the gradient during the period of Helios measurements, and is valid from 2–214 R_o. For protons, we assume a validity in the range 38–214 R_o, and for the distance 2–38 R_o we apply the same gradients as suggested by the Hartle-Barnes model.

The new information, that, the variation of temperature with distance is not unique but different for slow and fast solar wind (Rosenbauer et al. 1977) suggested two acceleration mechanisms for the solar plasma and led us to calculate two different values of radial temperature gradients for each component. Comparison with the theoretically derived values generally shows lower values for protons but higher for electrons

Protons $b_f = 0.3\, b_{HB}$
Protons $b_s = 0.5\, b_{HB}$
Electrons $\varepsilon_f = 2.5\, b_{HB}$
Electrons $\varepsilon_s = 1.5\, b_{HB}$

The calculated values of the proton radial temperature gradient are generally in agreement with the suggestions of Eyni and Steinitz (1978). According to their analysis, the slow solar wind ($V < 500$ km/s) shows a gradient of -0.8, while for the fast ($V > 500$ km/s) solar wind, there is no evidence for cooling of protons because the gradient is less steep. The discrepancy between our calculated gradient (-0.62) and that calculated by Eyni and Steinitz (-0.8) may be due to the

(1) different periods of analysis (possible temporal effects)

(2) restricted distance range used by Eyni and Steinitz (0.707–1.01 AU), and

(3) strong dependence of temparature on speed, which we have taken into account.

The result after treating the blob model with experimental temperature gradients which are different for low and high solar wind speed, while the adiabatic expansion of the blob is not retained, suggests that the blob might provide an explanation for the depressed temperature regions as shown in Fig. 3. According to this Figure, the suggested formation distance for these regions (blobs), for both models, fluctuates around 10 R_o.

Due to the fact that nearly all calculated polytropic indices γ_1^e, γ_1^p, γ_2^e, and γ_2^p are close to the value 5/3 which characterizes an adiabatic expansion, an independent adiabatic model as the explanation of the very "cold" solar wind would also work.

Discussion

The result shown in Fig. 3 suggests that it is not unreasonable that blobs are formed at heliocentric distances of 10 R_o. Following the recognition of bidirectional anisotropies in solar wind protons and electrons, observed by Explorer 34, 41 and Vela 5B, 6A and 6B, aligned with the interplanetary magnetic field lines, Palmer et al. (1978) suggested the existence of large-scale magnetic bottles behind interplanetary shocks. The mean duration of the bidirectional anisotropies was nine hours, representing a spatial extension of the region characterized by these anisotropies of about 0.13 AU. During these periods, a decrease of high-energy cosmic ray flux takes place, as in our case, when an interplanetary shock wave is identified simoultaneously with a very low temperature plasma (Geranios 1978). The main difference is that in their model the magnetically closed region is attached to the sun, while in our case it is detached from the sun. In addition, during the 4th International Solar Wind Conference, it was reported (Pilipp et al. 1978) that low temperatures coinside with interplanetary magnetic sector boundaries, where the field configuration shows closed features. Possible observations of very low plasma temperatures in the solar wind, not only at 1 AU but also nearer to the sun, performed succesively by Helios-1 and Helios-2, could eliminate temporal effects, and therefore could offer better observations for a further analysis of this phenomenon.

Acknowledgements. The author would like to express his gratitude to Drs. K. Mühlhäuser (Max-Planck-Institut für Extraterrestrische Physik, Garching), H. Rosenbauer, and R. Schwenn (Max-Planck-Institut für Aeronomie, Lindau) for making available the Helios plasma data, and Dr. W. Pilipp (Max-Planck-Institut für Extraterrestrische Physik, Garching) for the useful discussions and for permission to use preliminary electron temperature data from Helios-1.

References

Barouch, E., Burlaga, L.: Causes of Forbush Decreases and other cosmic-ray variations. J. Geophys. Res. **80**, 449–456, 1975

Bulaga, L., Ogilvie, K.: Heating of the solar wind. Astrophys. J. **159**, 659–670, 1970

Eyni, M., Steinitz, R.: The cooling of the solar wind protons from Mariner 2 data. J. Geophys. Res. **83**, 215–216, 1978

Feldman, W., Asbridge, J., Bame, S., Montgomery, M., Gary, S.: Solar wind electrons. J. Geophys. Res. **80**, 4181–4196, 1975

Geranios, A.: A search for the origin of very low electron temperatures. Planet. Space Sci. **26**, 571–579, 1978

Gosling, J., Hundhausen, A., Pizzo, V.: Compressions and rarefactions in the solar wind: Vela 3. J. Geophys. Res. **77**, 5442–5454, 1972

Gosling, J., Pizzo, V., Bame, S.: Anomalously low proton temperatures in the solar wind following interplanetary shock waves – Evidence for magnetic bottles? J. Geophys. Res. **78**, 2001–2009, 1973

Gosling, J., Roelof, E.: A comment on the detection of closed magnetic structures in the solar wind. Solar Phys. **39**, 405–408, 1974

Hartle, R., Sturrock, P.: Two-fluid model of the solar wind. Astrophys. J. **151**, 1155–1170, 1968

Hartle, R., Barnes, A.: Nonthermal heating in the two-fluid solar wind model. J. Geophys. Res. **75**, 6915–6931, 1970

Hollweg, J.: Collisionless electron heat conduction in the solar wind. J. Geophys. Res. **81**, 1649–1658, 1976

Hundhausen, A.: Coronal expansion and solar wind. Berlin, Heidelberg, New York: Springer 1972

Montgomery, M., Bame, S., Hundhausen, A.: Solar wind electrons: Vela 4 measurements. J. Geophys. Res. **73**, 4999–5003, 1968

Montgomery, M., Asbridge, J., Bame, S., Feldman, W.: Solar wind electron temperature depressions following some interplanetary shock waves: Evidence for magnetic merging? J. Geophys. Res. **79**, 3103–3110, 1974

Palmer, I., Allum, F., Singer, S.: Bidirectional anisotropies in solar cosmic ray events: evidence for magnetic bottles. J. Geophys. Res. **83**, 75–90, 1978

Parker, E.: Interplanetary dynamical processes. New York: Interscience 1963
Pilipp, W.: Private communication, Max-Planck-Institut für Extraterrestrische Physik, 8046 Garching, FRG, 1978
Pilipp, W., Schwenn, R., March, E., Mühlhäuser, K., Rosenbauer, H.: Electron characteristics in the solar wind between 1 AU and 0.3 AU as deduced from Helios observations. Paper presented at the 4th Solar Wind Conference, Burghausen, FRG, 1978
Rosenbauer, H., Schwenn, R., Marsch, E., Meyer, B., Miggenrieder, H., Montgomery, M., Mühlhäuser, K., Pilipp, W., Voges, W., Zink, S.: A survey on initial results of the Helios plasma experiment. J. Geophys. **42**, 561–580, 1977
Spitzer, L.: Physics of fully ionized gases. New York: Interscience 1962
Whang, Y., Chang, C.: An invisci model of the solar wind. J. Geophys. Res. **70**, 4175–4180, 1965
Yeh, T.: Temperature profile of solar winds. J. Geophys. Res. **76**, 7508–7515, 1971

Received June 18, 1979; Revised Version January 21, 1981
Accepted February 4, 1981

J Geophys (1981) 49:198–206

Journal of Geophysics

Correlation Between Seismic Microactivity, Temperature and Subsidence of Water Level at Reservoirs

G. Merkler*, G. Bock**, and K. Fuchs
Geophysikalisches Institut der Universität Karlsruhe, Hertzstr. 16, D-7500 Karlsruhe 21, Federal Republic of Germany

Abstract. Large reservoirs in the Alps and Romanian Carpathians have been monitored by high gain seismic stations over a period of six years. Microearthquakes with local magnitudes less than zero showed a clear correlation with variations of the water level. A model is presented which explains the time-distribution of this weak seismic activity as caused by the freezing of water in near-surface cracks exposed to freezing temperatures when the water level falls. This model is supported by an analysis of the correlation between the seismic micro-activity, average daily temperature distribution and rate of water-level-decrease. Precise locations of the events and estimates of energy corroborate the proposed model for the generation of this type of seismic micro-activity at reservoirs in high mountain regions.

Key words: Ice induced seismicity – Daily variation of microtremors – Microtremors at reservoirs – Freezing water in near-surface cracks

Introduction

In 1971 a seismic monitoring program was started at two reservoirs in the Austrian and Swiss Alps. In addition, three reservoirs in the Romanian Carpathians have been monitored seismically since 1974. At the five reservoir sites compatible high gain short period seismic stations have been operated.

The longest duration of seismic recording was at the Schlegeis reservoir, Austria. Recording commenced in May 1971 and is still continuing. Results of the seismic observations at Schlegeis have been reported earlier (Blum and Fuchs 1974; Blum et al. 1977; Bock 1978 b).

Numerous weak tremors with local magnitudes less than zero occurred here, predominantly during periods when the water level was being lowered and while it was at a minimum. This result was not expected because at other reservoirs with reported induced seismic activity, the activity usually starts during periods of rising water level. An example is the Vajont reservoir, Italy (Caloi 1966; Bozović 1974). Many other similar examples have been reported by Gupta and Rastogi (1976). But the characteristic feature of the temporal distribution of the seismic events at Schlegeis was not an isolated case. Similar seismic activity was also observed at other reservoirs such as Emosson (Switzerland), Bicaz, Lotru and Arges (Romania), where the seismic surveillance started later than at the Schlegeis. This paper summarizes the common features of the local seismic activity observed at the five reservoirs and presents a model which explains the observations.

Seismic Observations

At each reservoir at least one short-period vertical component seismic station was installed. The amplification of the total recording system was up to 10^6 at 10 Hz. Details of the reservoir and the seismic surveillance are given in Table 1, together with the dimensions of the reservoirs.

The seismometers are placed within the dam at Schlegeis, Emosson and Bicaz, and at the other reservoirs, within a distance of a few hundred metres from the dam. The seismic station in the Emosson dam is operated by the Schweizerischer Erdbebendienst, Zürich. Recordings are made on an ink recorder with continuous paper loop at a speed of 300 mm/min at Schlegeis (Blum and Fuchs 1974) and 240 mm/min at the seismic stations in the Romanian Carpathians (Merkler et al. 1975). The time-reading precision is 0.05 s. At Emosson a film recorder was installed providing a time-reading precision of 0.1 s.

Seismogram examples from local events are shown in Fig. 1. They are characterized by high frequency oscillations between 10–15 Hz with a duration of about 1 s. *S-P* travel times, as read in the case of some of the stronger tremors, are less than 0.2 s.

Local magnitudes of these local tremors have been estimated roughly from their signal duration (Tsumara 1967; Lee et al. 1972) to be $M_L < 0$. No local tremors with magnitudes greater than 0 have been observed. The radiated seismic energy ranges between 10^7–10^{12} erg, from application of the empirical relation between seismic energy and local magnitudes derived by Gutenberg and Richter (1956).

The time distribution of local events observed at the five reservoirs is depicted in Fig. 2. A striking feature in Fig. 2a–c is that the times when the water level was rising are characterized by decreasing seismic activity or even its absence. The maximum of local seismic activity is predominantly observed during periods of decreasing and minimum water level.

This is clearly seen for the time distribution of local events at the reservoirs Schlegeis, Emosson and Bicaz in Fig. 2a–c. At Lotru (Fig. 2d) a periodic occurrence of seismic events is also observed. But the variation of the lake level is too small to establish a coincidence of increasing activity and subsiding water level. However, there is a seasonal variation, the local events at Lotru also occurring predominantly in winter and spring. At Arges

* *Present address*. Geologisches Institut der Universität Karlsruhe, D-7500 Karlsruhe 1, Federal Republic of Germany
** *Present address*. Research School of Earth Sciences, Australian National University, P.O. Box 4, Canberra ACT 2600, Australia
Contribution No. 231 of the Geophysical Institute of Karlsruhe University, Sonderforschungsbereich 77, Felsmechanik of Karlsruhe University

0340-062X/81/0049/0198/$01.80

Table 1. Reservoirs under seismic surveillance

	Dam			Volume (10^6 m^3)	Year of completetion	Beginning of seismic observation	Amplification of ground displacement at 1 Hz
	Height (m)	Type	Basement rock				
Schlegeis, Austria	130	Arch. butress	Gneiss	129	1971	May 1971	16500 till April 1972; later 33000
Emosson, Switzerland	180	Arch	Granite	225	1974	Sept. 1973	10000 till Sept. 1974 later on 20000
Bicaz, Romania	127	Gravity	Flysch	1230	1961	Nov. 1974	30000 during the day 100000 during the night[a]
Lotru, Romania	118	Rockfill	Gneiss	340	1975	Nov. 1974	35000 during the day 70000 during the night[a]
Arges, Romania	166	Arch	Gneiss	465	1965	April 1965	30000 during the day 100000 during the night[a]

[a] Night amplification from 8 p.m. to 6 a.m. local time

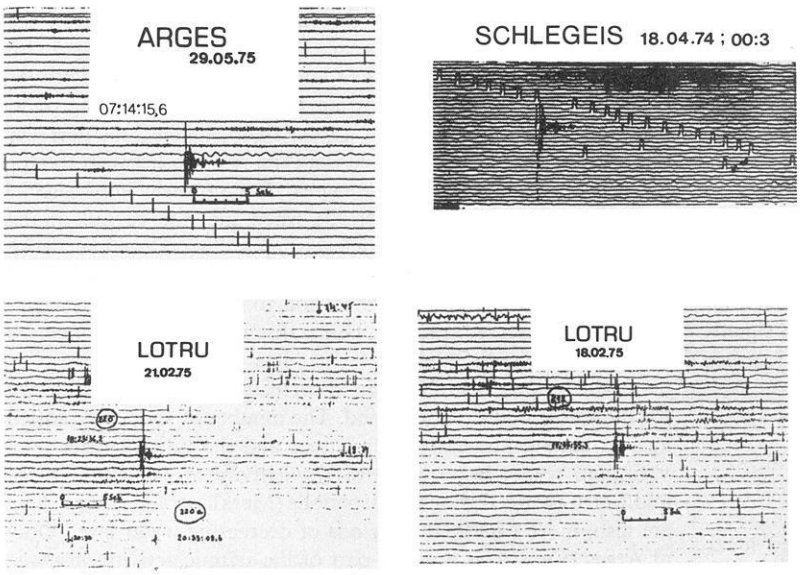

Fig. 1. Examples of seismograms

Table 2. Number of seismic events observed at the Romanian reservoirs Bicaz, Lotru, and Arges

Location	Total number	Number of events with S-P times between					Period of analysis
	(S-$P \leqq 5$ s)	(0–1 s)	(1–2 s)	(2–3 s)	(3–4 s)	(4–5 s)	
Bicaz	943	857	10	3	69	4	Nov. 4, 1974; June 1, 1978
Lotru	1777	1144	94	78	366	95	Nov. 7, 1974; June 1, 1978
Arges	651	75	314	155	79	28	April 4, 1975; June 1, 1978

(Fig. 2e) seismic activity increases during times of low water level. However, this area is characterized by a comparatively high level of seismicity, most likely of tectonic origin, throughout the year. For the Schlegeis reservoir (Fig. 2a), all local shocks have S-P times less than 0.2 s. For the Emosson reservoir (Fig. 2b) events with S-P times less than 0.2 s are plotted in the upper part of the temporal distribution. Most of the shocks with S-P times greater than 0.2 s are of natural tectonic origin (Bock 1978b).

The observed data from the seismic stations at the Romanian reservoirs are shown in Fig. 2c–e and all seismic events with S-P times up to 5 s are considered. However, at Bicaz and Lotru most of them have S-P times less than 1 s. At Arges, the maximum number of seismic events falls into the S-P time range between 1 and 2 s (i.e., 8–16 km). The proportion of local events with S-P times less than 1 s (i.e., <8 km) at Arges is not as conspicuous as at the other two reservoirs in the Carpathians (see Table 2).

In the plot of the time distribution observed at the Romanian reservoir stations, earthquakes are also included which are part of the increased seismic activity in the Carpathians after the strong Vrancea-earthquake of 4 March 1977.

It has been pointed out by Fuchs et al. (1979) that seismic activity migrated after this date not only to the foredeep in the

Vrancea region but also into the Carpathian mountains up to distances of more than 100 km. At Bicaz (Fig. 2c) the peaks in seismic activity in March and April 1977 are part of this migration phenomenon. At Lotru the number of earthquakes also increased drastically in March and April 1977 (ISPH-IGK 1977) as can be seen in Fig. 2d. At Arges seismic activity doubled after the Vrancea-earthquake (Fuchs et al. 1979).

As reported by the Romanian-German seismological working group (Bock 1978a) epicenters of earthquakes from these series (March–April 1977) were located 20 km away from the Bicaz and Lotru stations. Therefore, seismic events connected with the migration phenomenon are eliminated from further analysis in this paper. They clearly fall outside the range of local events situated close to the reservoir stations which are characterized by *S-P* times of less than 0.2 s and 1 s, respectively.

Locations of some of the seismic events have been obtained for the Schlegeis reservoir (Blum et al. 1977). All located shocks are shallow and not deeper than 300 m. Due to lack of spatial resolution a more accurate determination of focal depths within the range $0 \leqq z \leqq 300$ m could not be given.

The epicenters are concentrated on the waterside of the dam. Only a few events appeared in the region of greatest water depth (Blum 1975; Blum et al. 1977). Bock (1978b) argues, on the basis of detailed numerical experiments, that in the case of Schlegeis reservoir the stress induced by loading and unloading and changes in effective water pressure at depth do not reach critical values for rock fracture.

In October 1977, two additional seismic stations were brought into operation at the Schlegeis reservoir, situated about 2 and 3 km south of the dam at the waterside (Fig. 3a). Local events were also recorded by these stations. An example is given in Fig. 3b. On the records of the dam stations no seismic signals were observed from these events. That means that their foci are located further away from the dam site.

Correlation Between Number of Events, Temperature, and Water Level Variations

The key to understanding the mechanism of the observed local shocks is in their seasonal variation **and** daily time distribution which is depicted in Fig. 4. With the exception of Arges, a clear maximum of seismic activity appears between 0 and 10 a.m. local time. The minimum activity occurs at noon.

At Bicaz and Lotru the stations had to be run during the day with $^1/_2$ or $^1/_3$ of the nightly gain, respectively, due to industrial noise (Table 1). The number of events likely to be unobserved by these stations during the day due to the reduced gain is negligible compared to the actually observed decrease in the number of detected events during the day (Bicaz about 250, Lotru about 230). Similar daily distributions of seismic events have been observed at the Kurobe dam (Hagiwara and Ohtake 1972), and the Kamafusa dam (Suzuki 1975), both in Japan, and also in Italy (Caloi 1972). They concluded that variations of physical parameters with a daily period should be part of the mechanism. From these parameters, the variations of atmospheric pressure and earth tides can be ruled out, because the seasonal variation of seismic activity could not be thus explained. Therefore, it seems to be more promising to consider seasonal and daily temperature variations as a possible mechanism. The correlations between the number of shocks on the one hand and the temperature and the change of lake level on the other hand are now discussed in detail.

In the Fig. 5a–d the occurrence of local tremors is analysed with respect to the average daily temperature and with respect to changes of the water level. For one interval typical of the whole observation period the measured air temperature and the number of events are plotted in the upper parts of Fig. 5a–d. At Schlegeis as well as at Bicaz and Lotru, seismic acitivity increases as soon as the temperature falls below the freezing point of water. The relation between tremor frequency and the decrease of water level is less pronounced than the relation between tremor frequency and freezing temperatures. For instance local shocks were also observed during periods when the rate of fall of the water level was low (e.g., at Schlegeis in October–December 1974, see Fig. 5a). In spite of this the subsidence of the water level must also be taken into consideration to understand the mechanism of the observed tremors. This is discussed later in connection with the proposed model.

In the lower parts of Fig. 5a–d correlation diagrams are shown for the whole observation period. The number of shocks is plotted against the average daily temperature and the rate of water level variation, respectively. Most of the activity at Schlegeis, Bicaz and Lotru occurs during frosty periods (Merkler et al. 1980). These are also, more or less, the periods of decreasing water level. Only at Arges (Fig. 5d) is a major part of the seismic activity observed at periods when the average daily temperatures are positive. In Table 3 the corresponding values are given for the correlation diagrams. The observations are summarized as follows:

(a) the ratio between the number of frosty days with observed seismic activity and without activity is between 0.29 and 0.55.

Table 3

		Schlegeis 05.71–01.77	Lotru 06.74–03.77	Bicaz 11.74–02.77	Arges 04.75–06.78
Frosty days	With seismic activity ($n^- B$)	170	77	74	85
	Without seismic activity ($n^- 0$)	583	222	212	154
	$n^- B/n^- 0$	0.29	0.35	0.35	0.55
Frosty days with Subsidence of water level	With seismic activity ($n^{- -} B$)	140	58	56	59
	Without seismic activity ($n^{- -} 0$)	449	120	208	114
	$n^{- -} B/n^{- -} 0$	0.31	0.48	0.27	0.52
Frost-free days	With seismic activity ($n^+ B$)	73	35	38	263
	Without seismic activity ($n^+ 0$)	1277	304	540	654
	$n^+ B/n^+ 0$	0.06	0.12	0.07	0.40
	$n^+ B/n^- B$	0.43	0.45	0.51	3.09
	$n^+ B/n^{- -} B$	0.52	0.60	0.68	4.46

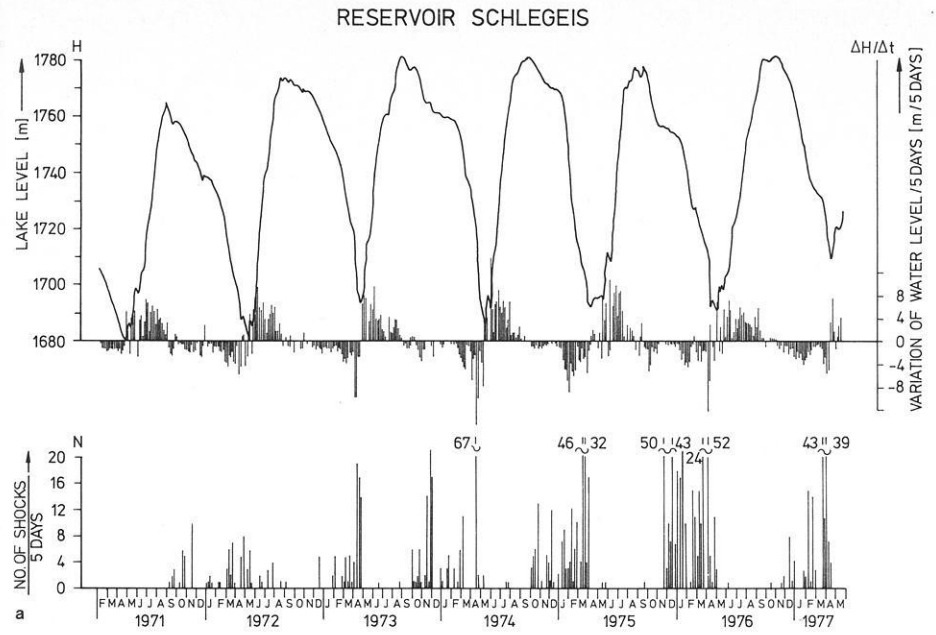
RESERVOIR SCHLEGEIS
H
ΔH/Δt
LAKE LEVEL [m]
1780
1760
1740
1720
1700
1680
VARIATION OF WATER LEVEL/5 DAYS [m/5 DAYS]
8
4
0
-4
-8
N
NO. OF SHOCKS 5 DAYS
20
16
12
8
4
0
67
46
32
50
43
24
52
43
39
F M A M J J A S O N D J F M A M J J A S O N D J F M A M J J A S O N D J F M A M J J A S O N D J F M A M J J A S O N D J F M A M J J A S O N D J F M A M
1971
1972
1973
1974
1975
1976
1977
a

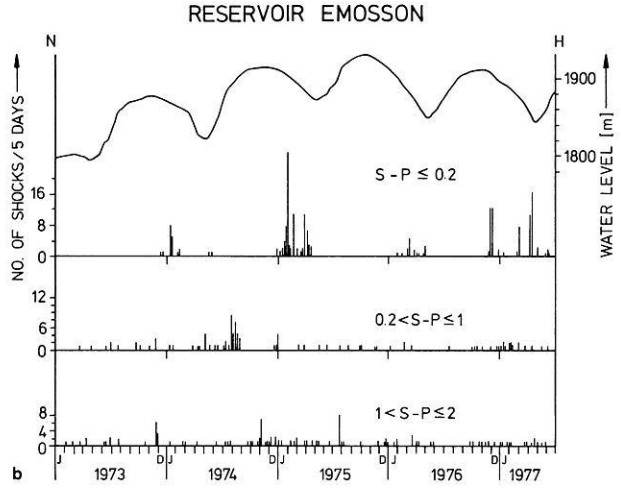
RESERVOIR EMOSSON
N
H
NO. OF SHOCKS/5 DAYS
WATER LEVEL [m]
1900
1800
S - P ≤ 0.2
16
8
0
0.2<S-P≤1
12
6
0
1<S-P≤2
8
4
0
J
D J
1973
1974
1975
1976
1977
b

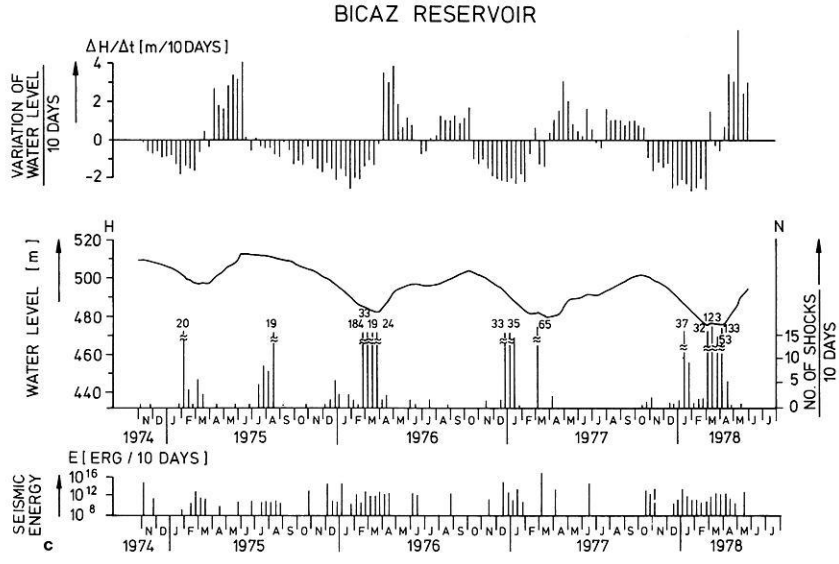
BICAZ RESERVOIR
ΔH/Δt [m/10 DAYS]
VARIATION OF WATER LEVEL 10 DAYS
4
2
0
-2
H
N
WATER LEVEL [m]
520
500
480
460
440
NO. OF SHOCKS 10 DAYS
15
10
5
0
20
19
33
184 19 24
33 35
65
37
32
123
133
53
N D J F M A M J J A S O N D J F M A M J J A S O N D J F M A M J J A S O N D J F M A M J J
1974
1975
1976
1977
1978
E [ERG / 10 DAYS]
SEISMIC ENERGY
10^16
10^12
10^8
c

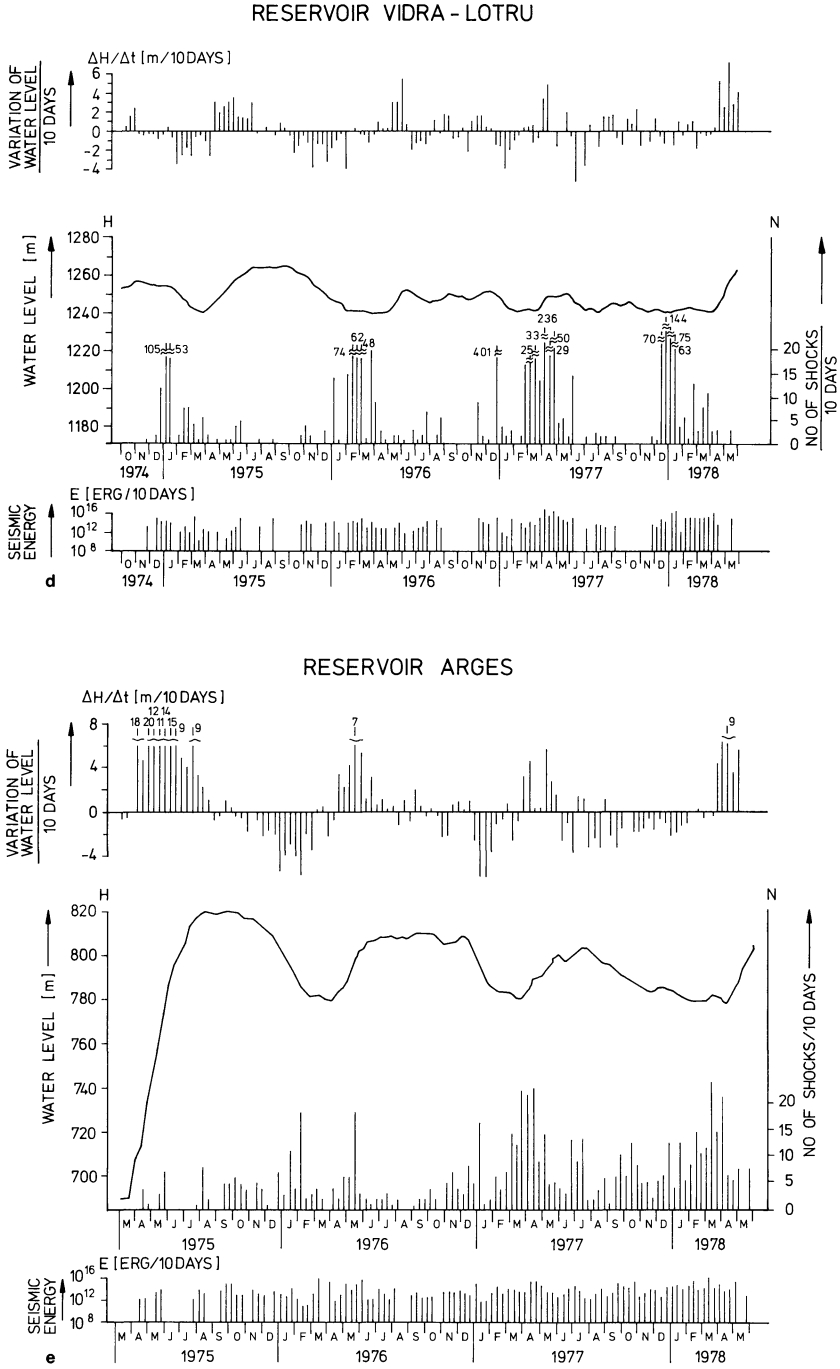

Fig. 2a–e. Lake level, rate of variation of lake level and number of shocks at **a** Schlegeis reservoir; **b** Emosson reservoir; **c** Bicaz Reservoir; **d** Lotru reservoir; **e** Arges reservoir

(b) a similar ratio is observed for the number of days on which frosty temperatures **and** decrease of the water level occurred at the same time and day. It is between 0.27 and 0.52. This indicates that most of the tremors on frosty days occur during subsidence of the water level.

(c) the ratio between the number of frost-free days with and without seismic activity observed at Schlegeis, Lotru and Bicaz is a factor between 3 and 5 smaller than the corresponding ratio for frosty days under (a). In contrast, the ratios under (a) and (b) observed at Arges are of the same order.

(d) the ratio between the number of frost-free days and frosty days with seismic activity is, at Schlegeis, Lotru and Bicaz, between 0.43 and 0.51. That means that about two thirds of the seismic activity shows up during frosty periods. On the other hand, at Arges this ratio is 3.09, that is more tremors occur on frost-free days. The ratio of the number of frost-free days with observed seismic activity to the number of frosty days with subsidence of water level at the same time is between 0.52 and 0.68 (lowest row of Table 3). At Arges, this ratio is also greater than 1 (Merkler et al. 1978).

Correlation coefficients have been computed between the number of shocks and the temperature or the rate of subsidence of the lake level, respectively. They have been calculated allowing for a time delay λ between the two corresponding time series

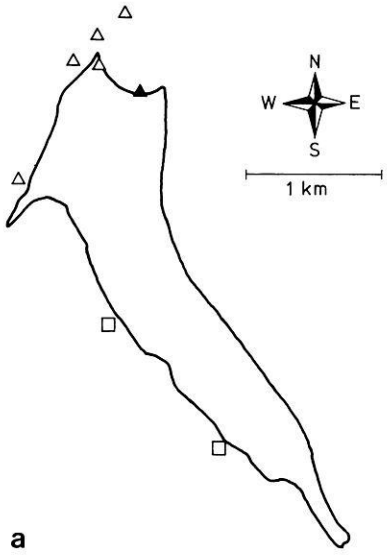

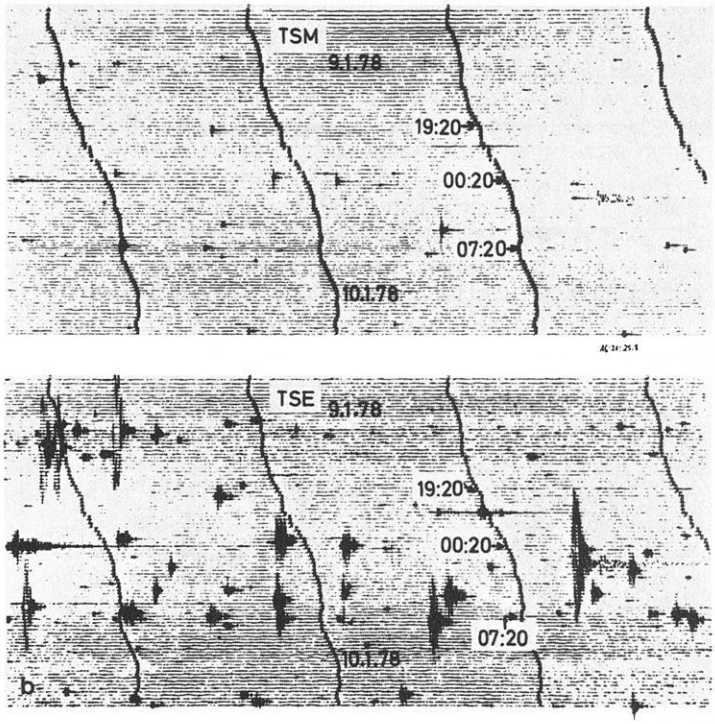

Fig. 3. a Location map of Schlegeis reservoir, Austria. Position of seismic stations marked as: ▲, Permanent seismic station (SCE); △, Temporary network 1974; □, Temporary telemetric stations 1977–1979. **b** Seismogram example from the seismic telemetric stations at Schlegeis reservoir

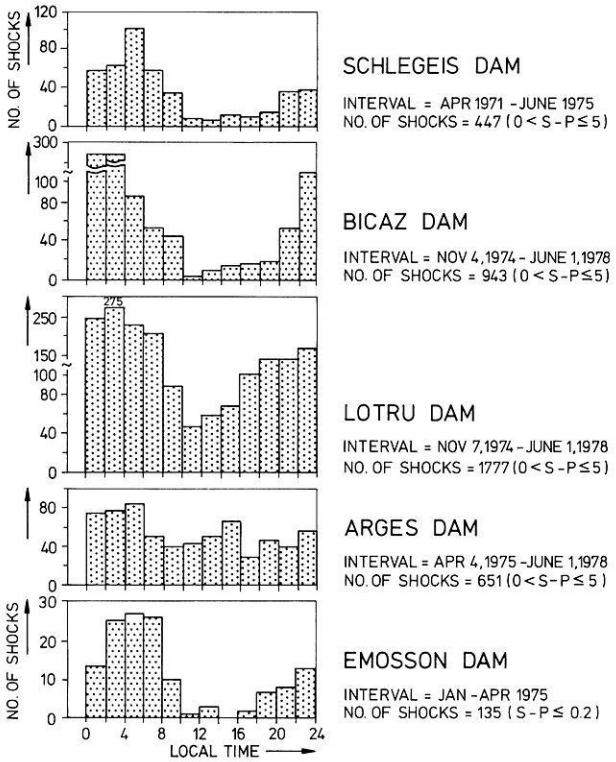

Fig. 4. Daily distribution of tremors

according to Taubenheim (1969):

$$\rho(\lambda)=\frac{\sum_{r=1}^{n}(X_{r+\lambda}-\bar{X})\cdot(Y_r-\bar{Y})}{\sqrt{\sum_{r=1}^{n}(X_{r+\lambda}-\bar{X})^2}\cdot\sqrt{\sum_{r=1}^{n}(Y_r-\bar{Y})^2}}$$

with $X_{r+\lambda}=0$ if $r+\lambda<0$ or $r+\lambda>n$. $(X_{r+\lambda}-\bar{X})$ and $(Y_r-\bar{Y})$ are the deviations of the values of two time series from their mean value. The expressions in the denominator are proportional to the standard deviations of the time series. The summation is carried out over n points. The X-series corresponds to the average daily temperatures and to the daily rate of subsidence of the lake level, respectively, the Y-series to the number of shocks per day. The 99.9 % significance level is given by $3.291/(N-\lambda-1)^{1/2}$ (Taubenheim 1969).

The absolute value of ρ (λ) for the Schlegeis reservoir reaches a maximum of 0.25 for the correlation of number of events and rate of level subsidence with a delay of 1 day compared to the rate of water subsidence (Blum 1975). There is a prompt seismic reaction following a temperature decrease (Fig. 6).

Discussion of Mechanism

The seismic observations at Schlegeis, Bicaz and Lotru indicate a certain correlation between the occurrence of local seismic events and negative temperatures. It is assumed that part of the local seismic activity observed at Lake Emosson is also caused by the same mechanism. This suggestion is mainly based on the characteristic daily time distributions of the local seismic events. Average daily temperatures which could confirm this suggestion were not available for the Emosson area at the time of this study. A model which does explain most of the observations is proposed in the following:

In the model proposed cracks are assumed which extend to the surface (Fig. 7). During periods of increasing and maximum water level the cracks are water-filled by the reservoir. In the period of subsiding water level, i.e., in winter and spring, the thermal insulation provided by the reservoir water is removed. The water level falls below the openings of the cracks. However, the cracks remain water-filled because the water cannot drain off quickly enough due to the low permeability of the surrounding rock. At temperatures below zero the water in the cracks freezes

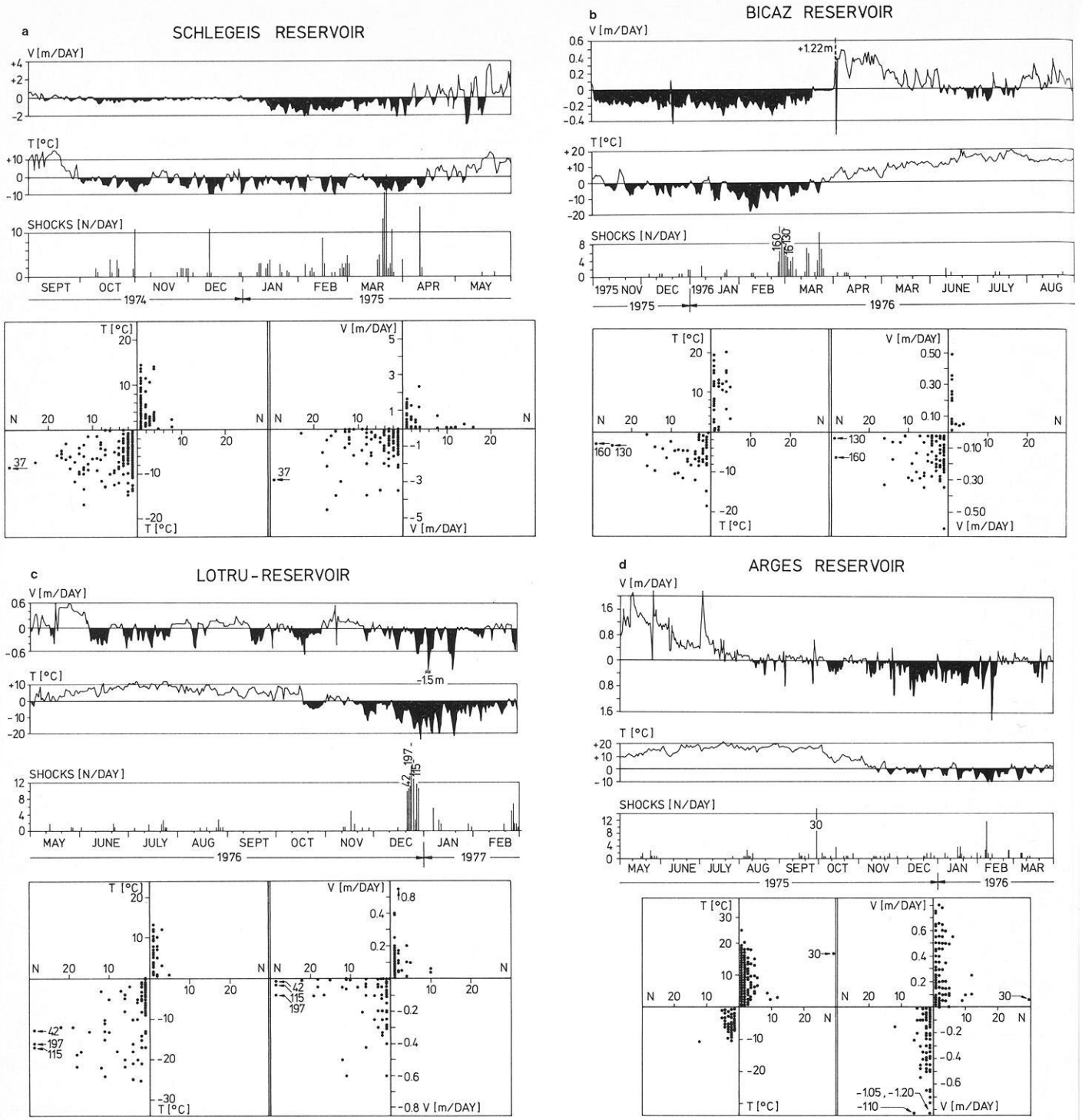

Fig. 5a–d. Correlation diagram between number of shocks and rate of lake level and temperature respectively **a** at Schlegeis reservoir; **b** at Bicaz reservoir; **c** at Lotru reservoir; **d** at Arges reservoir

leading to an increase in volume by 9% and to an extension of the crack width. The extension V of the crack with a length $2c$ can be estimated under plane stress conditions to (Jaeger and Cook 1971, p. 312):

$$V = 2\,pc/E \qquad (1)$$

with the inner pressure in the crack p, and the Young modulus E of the surrounding rock. An example illustrates the order of magnitude of p. A crack of width 0.1 cm is extended by 0.009 cm by the volume increase of the freezing water. If we put $c = 5$ cm and $E = 200000$ bar, an inner pressure of 180 bar is obtained. Assuming that all the water in the crack freezes, the induced stresses near the tip of the cracks can be estimated using the relations in Jaeger and Cook (1971, p. 262). The maximum tensional stress at a distance $r = c/2$ from the crack tip amounts to $^1/_3\,p$, the maximum shear stress at $r = c/2$ is $0.5\,p$. According to Müller

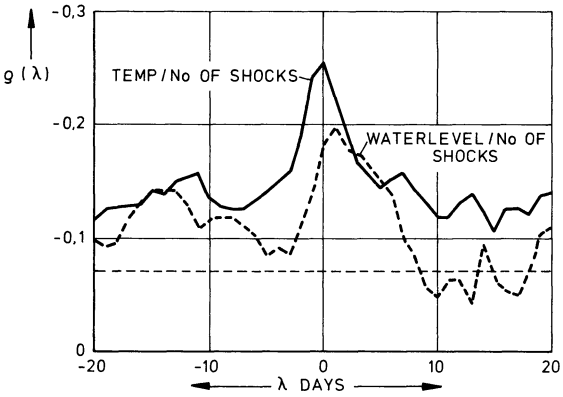

Fig. 6. Computed correlation coefficient between the number of shocks, temperature and rate of subsidence of lake level at Schlegeis reservoir (----- significance level)

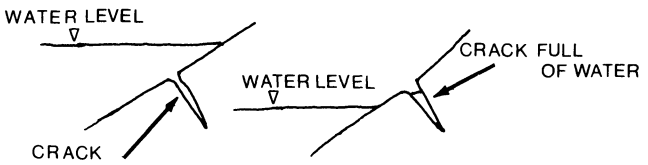

Fig. 7. Model of water-filled crack

(1963) it is difficult to give values for the tensional strength of a rock unit. They may be of the order of several bars to tenths of bars. The shear strength of Schlegeis basement rock is, according to Widmann (1973), in the range between 6 bar parallel and 350 bar perpendicular to the foliation plane. Therefore, it is reasonable to assume that the induced stresses near the end of cracks can be high enough to exceed the rock strength.

The model of triggering of local seismic events by freezing of water in cracks involves very shallow focal depths (10 m at most) since temperature variations can only affect the uppermost layer of the outcrop.

Focal depth determination for some of the shocks observed at the Schlegeis reservoir are not accurate enough to confirm or to reject the model. However, from the epicenter determination it is obvious that most of the epicenters are situated outside the area of the lake covered by water at the time of occurrence, which is compatible with the proposed model. For comparison the reader is referred to the paper by Blum et al. (1977).

A further observation which can be explained by the model is the low seismic energy radiated from foci, which is between 10^7 and 10^{12} ergs. Stronger local tremors have never been observed. In a plane of stress the potential strain energy W of a crack in disk of thickness t is given by (Jaeger and Cook 1971, p. 313):

$$W=\pi \cdot p^2 \cdot c^2 \cdot t/E.$$

Eliminating p by Eq. (1) leads to

$$W=0.25 \cdot \pi \cdot V^2 \cdot t \cdot E.$$

In this very rough approximation the strain energy W does not depend on the length $2c$ of the crack. For a numerial estimate we assume $V=0.009$ cm; $E=200000$ bar; $t=1$ cm and 100 cm. Then the strain erergy is 1.3×10^7 erg for $t=1$ cm and 1.3×10^9 erg for $t=100$ cm. These values are within the range of the estimated seismic energy.

Conclusions

Over the past 6 years microearthquake activity correlating with changes in reservoir level has occurred at the 5 reservoirs investigated. The activity is characterized by a concentration of near-reservoir microearthquakes when the water level is lowered and its minimum is reached during the months October to April. These microearthquakes were previously taken as being associated with a buildup of tectonic stresses during filling and their subsequent sudden release during rapid emptying of the reservoir. However, this hypothesis now appears less plausible, because most earthquakes tend to occur late at night, and there is a clear correlation between the onset of activity and sub-zero air temperatures during fast reservoir unloading. This correlation is now explained by a model in which cracks are exposed to freezing temperatures by the falling water table, causing the water remaining in the cracks to turn to ice. The estimated energy release of this process of in the same order of magnitude as that observed in the microearthquakes. The implication of these "ice-quakes" for the safety and stability of the dam walls warrants further investigation. Based on the experience of the present survey it would be relatively simple to monitor the weak zones of the slopes of reservoirs by locating the "ice-quakes" with a high resolution seismic network.

Acknowledgements. This investigation was carried out within the Sonderforschungsbereich 77 "Felsmechanik" of the Deutsche Forschungsgemeinschaft at Karlsruhe University in cooperation with the respective reservoir authorities in Austria, Switzerland and Romania. The work in Romania is a joint research effort of the Institute of Hydroelectrical Studies and Design, Bucharest and the Geophysical Institute, University of Karlsruhe under the auspices of the German-Romanian Government agreement. The authors thank all colleagues for stimulating discussions, Mrs. S. Di Pillo and Mrs. Kunz for typing the manuscript.

References

Blum, R.: Seismische Überwachung der Schlegeis-Talsperre und die Ursachen induzierter Seismizität. Diss. Universität Karlsruhe, 1975

Blum, R., Fuchs, K.: Observation of low-magnitude seismicity at a reservoir in the Eastern Alps. Eng. Geol. **8**, 99–106, 1974

Blum, R., Bock, G., Fuchs, K., Merkler, G., Widman, R.: Correlation between micro-activity and variation of water level at the Schlegeis-Reservoir. J. Geophys. **43**, 561–567, 1977

Bock, G.: Seismische Beobachtungen an Stauseen in den Karpaten und die Migration seismischer Aktivität nach dem Vrancea-Beben vom 4.3.1977 – Rumänisch-deutsche Seismologische Arbeitsgruppe. Jahrestagung der Deutschen Geophysikalischen Gesellschaft, Münster, März 1978a

Bock, G.: Induzierte Seismizität: Modelle und Beobachtungen am Schlegeis- und Emosson-Stausee. Diss. Universität Karlsruhe, 1978b

Bozović, A.: Review and appraisal of case histories related to seismic effects of reservoir impounding. Engl. Geol. **8**, 9–27, 1974

Caloi, P.: L'evento del Vajont nei suoi aspetti geodinamici. Ann. Geofis. **19**, 1–74, 1966

Caloi, P., Migani, M., Spadea, M.C.: Comportamento di una grande diga sotto il gelo. Ann. Geofis. **25**, 505–525, 1972

Fuchs, K., Bonjer, K.-P., Bock, G., Cornea, I., Radu, C., Enescu, D., Tianu, D., Nourescu, A., Merkler, G., Moldoveanu, T., Tudorache, G.. The Romanian earthquake at March 4, 1977. II. Aftershocks and migration of seismic activity. Tectonophysics **53**, 225–247, 1979

Gupta, H.K., Rastogi, B.K.: Dams and Earthquakes. Amsterdam: Elsevier 1976

Gutenberg, B., Richter, C.F.: Earthquake magnitude, intensity, energy and acceleration. Bull. Seismol. Soc. Am. **46**, 105–145, 1956

Hagiwara, T., Ohtake, M.: Seismic activity associated with the filling of the reservoir behind the Kurobe dam, Japan. Tectonophysics **15**, 241–254, 1972

ISPH-IGK: Bericht über die seismische Überwachung des Bicaz-, Lotru- and Arges-Dammes in Rumänien nach dem Vrancea-Beben vom 4. 3. 1977. Geophysikalisches Institut Karlsruhe, ISPH Bukarest, Sept. 1977

Jaeger, J.C., Cook, N.G.W.: Fundamentals of rock mechanics. London: Chapman and Hall 1971

Lee, W.H.K., Bennett, R.E., Meagher, K.L. A method of estimating magnitude of local earthquakes from signal duration. U.S. Geol. Surv. Open File Rep. 1972

Merkler, G., Blum, R., Bock, G., Bonjer, K.-P., Fuchs, K., Budeanu, C., Cosma, A., Moldoveanu, T., Privighetorita, C.: Seismic surveillance of reservoirs in the Carpathian Mountains of Romania. First Int. Symp. on Induced Seismicity, Banff, Canada, Sept. 1975

Merkler, G., Bock, G., Fuchs, K.: Ice induced seismic microactivity at reservoirs. Sixteenth European Seismological Commission – General assembly, Strasbourg, Sept. 1978

Merkler, G., Fuchs, K., Bock, G.: Untersuchungen seismischer Aktivität in den Alpen und in den rumänischen Karpaten, SFB 77 – Felsmechanik, Jahresbericht 1978, Universität Karlsruhe, 1980

Müller, L.: Der Felsbau, Band 1. Stuttgart: Ferdinand Enke Verlag 1963

Suzuki, Z.: Induced seismicity at the Kamafusa Dam. Japan, Paper presented at First Int. Symp. on Induced Seismicity, Banff, Canada, Sept. 1975

Taubenheim, J.: Statistische Auswertung geophysikalischer und meteorologischer Daten. Leipzig: Akad. Verlagsgesellschaft Geest & Portig KG 1969

Tsumara, K.: Determination of earthquake magnitude from total duration of oscillation. Bull. Earthquake Res. Inst. Tokyo Univ. **45**, 17–18, 1967

Widmann, R.: Bogengewichtsmauer Schlegeis. Das Verhalten des Felsuntergrundes während der ersten beiden Teilstauperioden. Rock Mech. **2**, 181–192, 1973

Received September 18, 1980; Revised Version April 10, 1981
Accepted May 14, 1981

J Geophys (1981) 49:207–211

Journal of Geophysics

$^{40}Ar/^{39}Ar$ Dating of Himalayan Rocks from the Mount Everest Region

Ichiro Kaneoka and Masaru Kono
Geophysical Institute, Faculty of Science, University of Tokyo, Bunkyo-ku, Tokyo 113, Japan

Abstract. $^{40}Ar/^{39}Ar$ dating results for one granitic and four metamorphic rocks from the Everest region suggest that the initiation of the major uplift of Everest occurred about 17 m.y. ago. The surrounding area has been involved in subsequent orogenic events in this region.

On the basis of present results and other geochronological data for this region, the Himalayan orogeny is suggested to have occurred a few tens of m.y. after the collision of the Indian plate with the Asian plate.

Key words: $^{40}Ar/^{39}Ar$ age – Everest – Himalaya – Orogeny – Granite – Metamorphic rocks – Plate-collision – Uplift – Excess Ar

Introduction

The Himalayas are regarded as one of the typical examples of mountain building due to the collision between two continents (Dewey and Bird 1970). Although the collision of the Indian plate with the Asian plate is estimated to have occurred about 45 m.y. ago, the uplift of the Himalayas seem to have been initiated later (Powell and Canaghan 1973). To clarify the mechanism of mountain building due to the continental collision, it is necessary to know the time relationship between the various stages (e.g., the time of collision and that of mountain building).

So far, Himalayan rocks have been dated by the K–Ar, Rb–Sr and fission track methods, with ages ranging from a few m.y. to more than 1000 m.y. (e.g., Hamet and Allègre 1976; Krummenacher 1961, 1971; Mehta 1977; Virk and Koul 1977). However, most samples show ages less than 75 m.y. Further, we cannot eliminate the possibility that some of the samples dated might have been affected by secondary disturbances or by the occurrence of excess Ar or of Ar loss. In order to examine these cases and to investigate the age of mountain building of the Himalayas, the $^{40}Ar/^{39}Ar$ method has been applied to one granitic and four metamorphic rocks, which were collected from the Everest region. We expected that the application of the $^{40}Ar/^{39}Ar$ method to these rocks would clarify the fine structure of the tectonic events in this region.

Samples

More than 100 samples were collected by one of us (M.K.) from the eastern part of Nepal during the Japanese Mount Everest Expedition 1970. The samples include granitic, metamorphic and sedimentary rocks. Among them, five samples from the Everest region were selected for the present analysis, three of which (JE 121, 126 and 131) were collected directly from Everest itself.

Sample JE 131 is a greenschist, collected at an altitude of about 8200 m on the southwest ridge of Everest and is considered to be typical of samples forming the upper part of the mountain. Samples JE 121 (granite) and JE 126 (schist) were collected at an altitude of 5350 m at the northern flank wall of Khumbu glacier, below the Lho-la pass where the Makalu granite is in intrusive contact with the overlying schist (Bordet 1961). The Makalu granite is named after Makalu, a peak located about 20 km southeast of Everest, but it is also abundant in the Everest massif (Bordet 1961).

Sample JE 117 is a gneiss collected on the southwestern flank of Nuptse bordering the Khumbu glacier, at an altitude of 5120 m. Sample JE 065 is also a gneiss, but was collected at Pakie, about 50 km to the southwest of Everest. This sample is located farthest away from Everest among the samples dated in this study. The sampling localities are shown in Fig. 1 and their latitudes and the longitudes given in Table 1.

As shown in Table 1, these rocks contain K-rich minerals such as biotite, muscovite and K-feldspars. The K-contents of the total rocks range from 3% to 5% as determined by X-ray fluorescence analysis. Some samples contain plagioclase, but in small amounts compared with other minerals. Hence, their Ca content is generally low, less than 1%, except for the sample JE 126 whose Ca content is estimated to be about 1.7% by X-ray fluorescence analysis.

Experimental Procedures

Total rock samples of grain size 35 to 60 meshes were wrapped in Al foil and stacked in air in quartz ampoules ($10\phi \times 70$ mm) with standard samples at both ends. They received a total fast neutron flux of about 2×10^{18} n/cm^2 in the core of the Japan Material Test Reactor, Tohoku University. USGS standard LP–6 (biotite) was used as the age monitor, which has the K–Ar age of 128 m.y. (Engels and Ingamells 1973).

Ar gas was extracted and purified by conventional procedures and analysed on a Reynolds type mass spectrometer. Details of the experimental procedure have been described before (Kaneoka and Aoki 1978).

Since the samples were analysed 3 years after neutron irradiation, ^{37}Ar, a measure for the Ca-concentration, had already decayed below the detection limit. As a consequence, Ca-derived contributions to ^{36}Ar and ^{39}Ar could not be corrected for. However, as shown in Table 2, the samples have relatively high K-contents (3–5%) and high K/Ca ratios (2.9–10.4). Therefore, the effect

0340-062X/81/0049/0207/$01.00

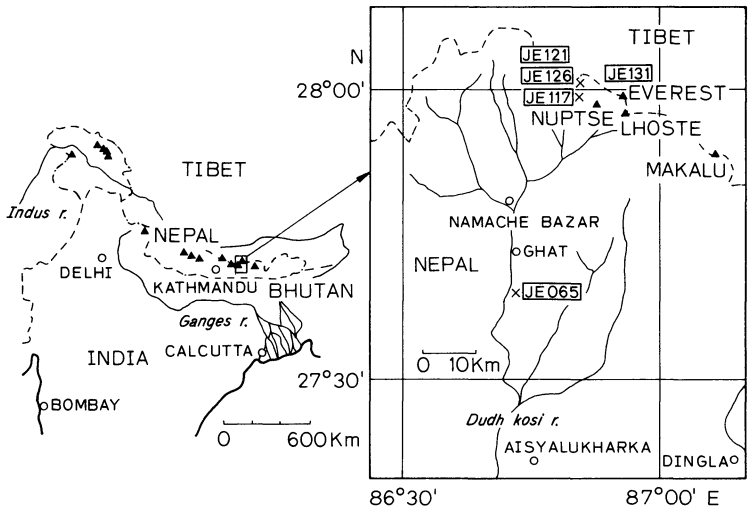

Fig. 1. Schematic map of sampling localities

Table 1. Samples used for $^{40}Ar/^{39}Ar$ analyses

Sample No.	Sampling locality				Rock type	Forming minerals[a]
	Location	Latitude	Longitude	Altitude		
JE 131	Southwest ridge above the South Col	27° 58.9′ N	86° 55.9′ E	8200m	Green schist	Bi, Mu, Qz, Pl, To, Zi, Ch
JE 126	Beneath the Lho-la Peak	28° 00.6′	86° 50.9′	5350	Schist	Bi, Mu, K-feld, Qz, Pl, Zi
JE 121	Beneath the Lho-la Peak	28° 00.6′	86° 50.9′	5350	Granite	Bi, Mu, K-feld, Qz, Pl, Zi, Ap
JE 117	Nuptse, beneath the 5325 m Peak	27° 59.0′	86° 50.8′	5120	Gneiss	Si, Bi, K-feld, Mu, Pl, Qz, Ap, Zi
JE 065	Pakie	27° 38.9′	86° 43.5′	2550	Gneiss	Bi, Mu, K-feld, Qz, Pl, Ga, Zi, Ap, Il

[a] Bi = biotite, Mu = muscovite, Qz = quartz, Pl = plagioclase, To = tourmaline, Zi = zircon, Ch = chlorite, K-feld = K-feldspar, Ap = apatite, Si = sillimanite, Ga = garnet, Il = ilmenite

Table 2. Summary of $^{40}Ar-^{39}Ar$ ages of samples from Himalaya

Sample (Weight)	K (%)[a]	K/Ca[a]	$^{40}Ar-^{39}Ar$ ages (m.y.)				
			Total	Minimum	Maximum	Plateau	Plateau range
JE 131 (1.465 g)	4.34	10.4	15.3	3.3 ± 0.1	19.0 ± 0.6	16.7 ± 0.5	1,100°–1,300° C (50.4% of ^{39}Ar released)
JE 126 (0.559 g)	4.88	2.87	21.1	16.7 ± 0.5	72.3 ± 6.3	16.9 ± 0.4	900°–1,100° C (40.0% of ^{39}Ar released)
JE 121 (1.465 g)	4.13	9.90	23.2	15.1 ± 0.5	185 ± 3	16.8 ± 0.3	900°–1,150° C (62.6% of ^{39}Ar released)
JE 117 (1.053 g)	3.15	3.00	56.8	11.8 ± 0.2	360 ± 4		
JE 065 (1.006 g)	3.87	5.45	25.3	5.2 ± 0.1	751 ± 41		

[a] K content and K/Ca ratio of samples were determined by the X-ray fluorescence method with the precision of about 5%

° Error Figures: 1σ (standard deviation)

° $\lambda_e = 0.581 \times 10^{-10}\ yr^{-1}$; $\lambda = 5.543 \times 10^{-10}\ yr^{-1}$ (Steiger and Jäger 1977)

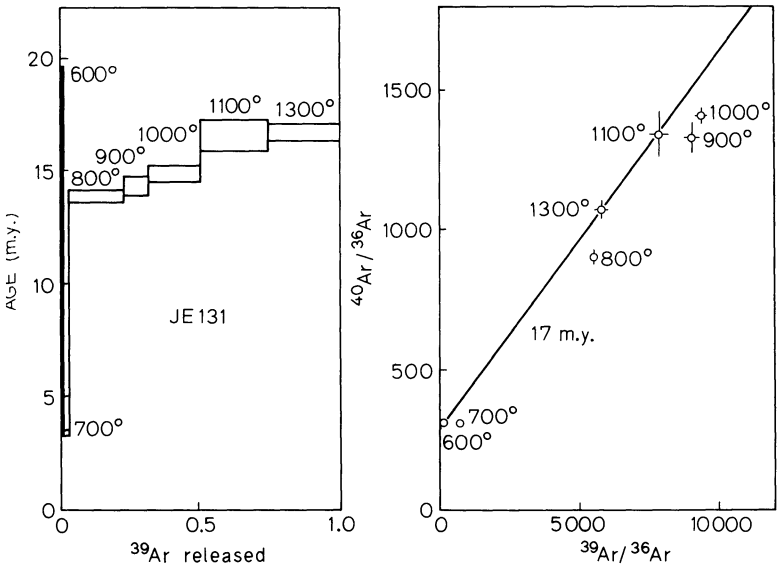

Fig. 2. Sample JE 131. $^{40}Ar/^{39}Ar$ age spectra as a function of ^{39}Ar released *(left)* and $^{40}Ar/^{36}Ar$ vs. $^{39}Ar/^{36}Ar$ isochron diagram *(right)*. The band in the $^{40}Ar/^{39}Ar$ spectra diagram indicates the $\pm 1\sigma$ (standard deviation) envelope about the calculated age of each temperature fraction. In the isochron diagram, a reference isochron of 17 m.y. is drawn which goes through the atmospheric $^{40}Ar/^{36}Ar$ value. All temperatures are given in degrees Celsius

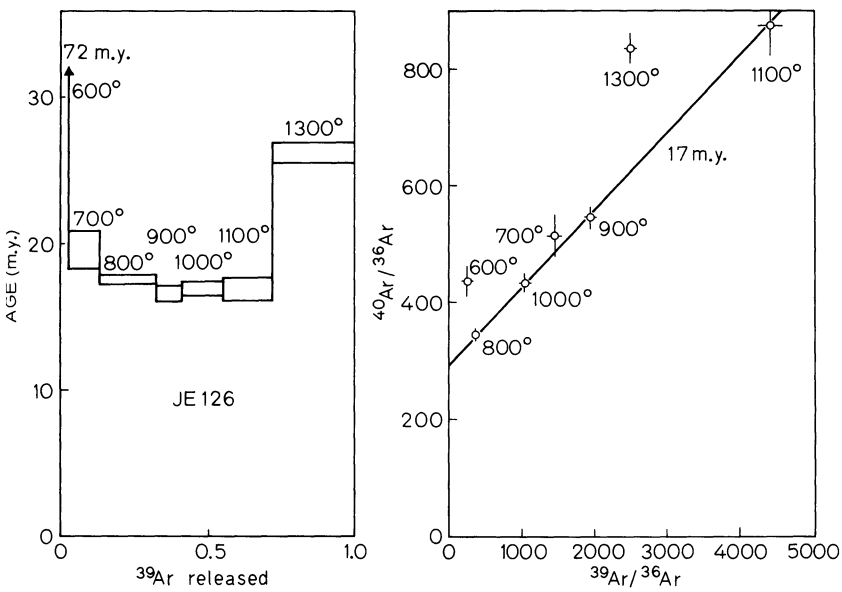

Fig. 3. Sample JE 126. In the age spectra diagram, the 900°–1,100° C fractions show almost similar ages of about 17 m.y. In the isochron diagram, a reference isochron of 17 m.y. is drawn assuming the atmospheric ratio for the $(^{40}Ar/^{36}Ar)_i$ ratio

of Ca-derived Ar isotopes on the age is estimated to be relatively small, less than 1 m.y. at the maximum.

Results and Discussion

The results are shown in Figs. 2–6 and summarized in Table 2. Sample JE 131 shows a typical stair-case pattern with higher $^{40}Ar/^{39}Ar$ ages at higher temperatures (Fig. 2). The apparent low $^{40}Ar/^{39}Ar$ ages at lower temperatures suggest partial radiogenic ^{40}Ar loss from this sample. On the other hand, the 1100° and 1300° C fractions indicate almost the same ages of 16.7 ± 0.5 m.y. and cover about 50% of total ^{39}Ar released. Although only two fractions are included in this case, this age may be regarded as a plateau age, considering the results of JE 126 and JE 121.

As shown in Figs. 3 and 4, samples JE 126 and JE 121 indicate saddle-shaped age spectra, which are typically observed in deep-seated samples with excess Ar (Kaneoka 1974; Lanphere and Dalrymple 1976). In such cases, the apparent lower $^{40}Ar/^{39}Ar$ age at the intermediate temperatures may represent the maximum estimated age for the thermal event affecting the sample and is sometimes very close to the age of the event (Kaneoka 1974; Lanphere and Dalrymple 1976). For the present samples, such an event is considered to have been some orogenic processes and the samples were affected at some depth. Hence, the occurrence of excess and/or inherited ^{40}Ar in these samples is quite likely. It is noteworthy that both samples have intermediate plateau ages of about 17 m.y. This age agrees well with the plateau age of sample JE 131 at higher temperatures. Since three samples from different sites and of different rock type show almost the same age, 17 m.y. seems to have geochronological significance. Since the Makalu granite has a relatively wide distribution in this region, it may be conjectured that the age represents the time of granite intrusion. As shown in Fig. 4, however, sample JE 121 (granite) shows $^{40}Ar/^{39}Ar$ ages above 17 m.y. in the lowest and highest temperature fractions with a total $^{40}Ar/^{39}Ar$ age of about 23 m.y. Hence, it is less likely that the age of 17 m.y. corresponds to that of the granite intrusion. Sample JE 126 (schist) also indicates a slight-

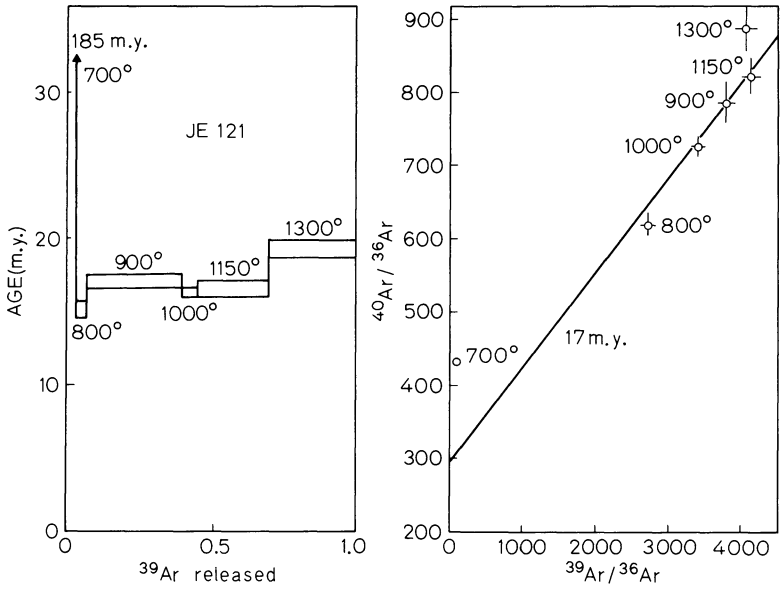

Fig. 4. Sample JE 121. The 900°–1,150° C fractions show almost similar ages of about 17 m.y. in the age spectra diagram. In the isochron diagram, an isochron of 17 m.y. is drawn as a reference which goes through the atmospheric $^{40}Ar/^{36}Ar$ ratio

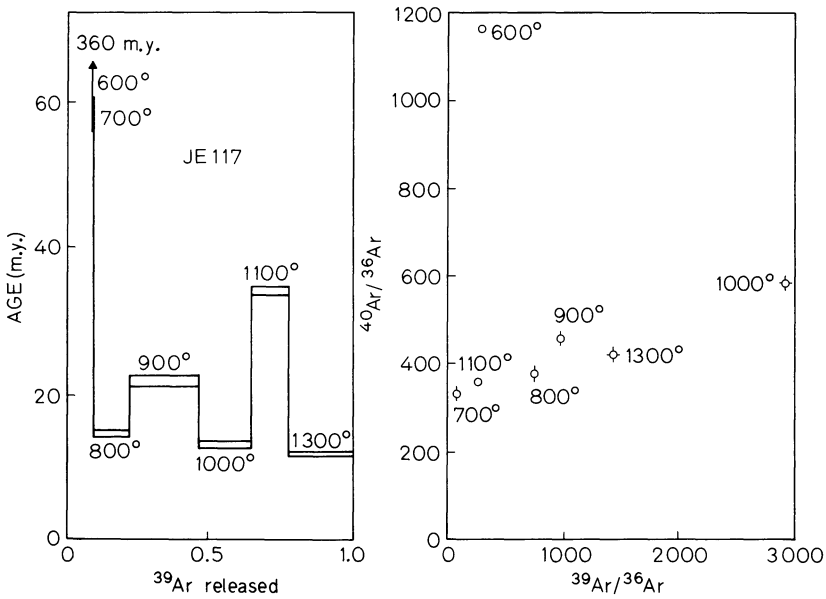

Fig. 5. Sample JE 117. The age spectra show disturbed pattern for this sample

ly older total $^{40}Ar/^{30}Ar$ age of about 21 m.y. These situations suggest that the age would probably correspond to a time when these samples began to keep a closed system with respect to Ar systematics after having been involved in an earlier orogenic process, or processes, in this region. Since these three sample belong to the main body of Everest itself and the elevated part would have cooled more rapidly than the lower part, these results might imply that the major uplift of Everest began about 17 m.y. ago.

If this is the case, then the lower part might have been further involved in the later orogenic processes in this region. In effect, sample JE 117 and JE 065 apparently show the evidence of such later event(s) in their age spectra. In the case of sample JE 117 (Fig. 5), the age spectrum is highly disturbed, but the 800°, 1000° and 1300° C fractions indicate $^{40}Ar/^{39}Ar$ ages of 12–15 m.y. The other four fractions show much higher $^{40}Ar/^{39}Ar$ ages with the total $^{40}Ar/^{39}Ar$ age of about 57 m.y., probably reflecting the presence of inherited and/or excess ^{40}Ar.

Sample JE 065 also shows a saddle-shaped age spectrum (Fig. 6), but the minimum $^{40}Ar/^{39}Ar$ age observed in the 900° C fraction indicates an age of only 5 m.y. Since the 700° C fraction in this sample shows an apparent $^{40}Ar/^{39}Ar$ age of about 750 m.y. and the 1300° C fraction an age of about 46 m.y., this sample was clearly disturbed by later event(s). The age of the event(s) was probably less than 5 m.y. and is considered to have been an orogenic process, or processes, in this region. Although no mineral separates were analysed in this study, the consistent results on ages of the present samples will be regarded as geochronologically significant.

Krummenacher (1961) reported a K–Ar age of 18.2 ± 0.6 m.y. (recalculated after new decay constants (Steiger and Jäger 1977)) for a schist from an altitude of 8400 m on Everest. If we take into account the experimental uncertainty, there is no difference between the K–Ar age reported by Krummenacher (1961) and the present results. His data further suggest that K–Ar ages of

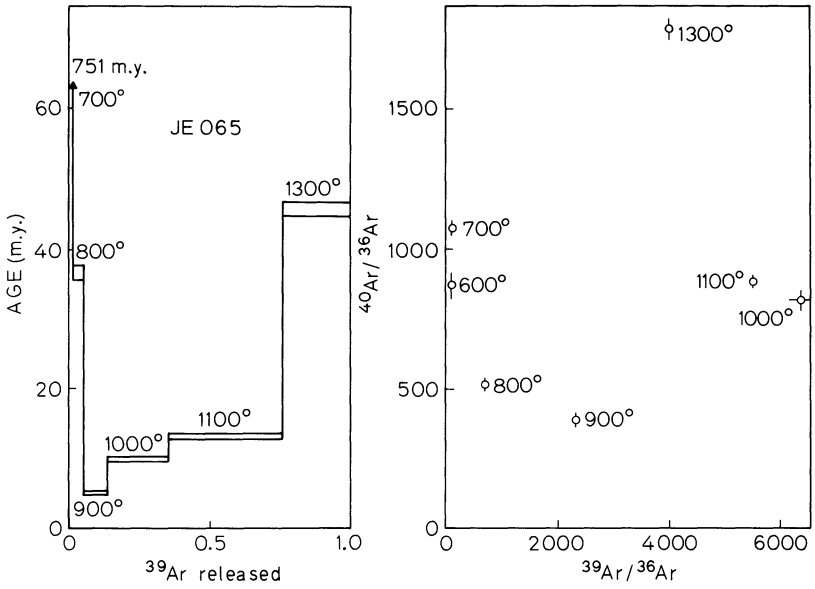

Fig. 6. Sample 065. The age spectra suggest some secondary effect on this sample about no more than 5 m.y. ago

biotites from rocks from the Nepal Himalayas range from about 10–18 m.y. On the other hand, fission track ages of Himalayan muscovites in Nepal range from about 3–23 m.y. (Virk and Koul 1977). The younger age probably reflects the relatively recent and less intense orogenic processes in this region and may correspond to the youngest result observed in sample JE 065. Hamet and Allègre (1976) reported a whole rock Rb-Sr age of about 29 m.y. for granites from central Nepal. Such differences in the apparent ages probably reflect the different sensitivity of each isotopic system to thermal events.

Since the collision of the Indian plate with the Asian plate is estimated to have occurred about 45 m.y. ago (Powell and Canaghan 1973), these geochronological results suggest that the major uplift of the Himalayas occurred a few tens of m.y. after the collision of both plates. Such a delay in the process of the uplift may be attributed to the possibility that the later deformation of continental lithosphere required some time. The present results imply that the Makalu granite might have intruded more than 20 m.y. ago. Although the major elevation of the Everest region occurred about 17 m.y. ago, the surrounding region has been involved in subsequent orogenic processes.

The analyses of gravity data in this region suggest that the Himalayas are not in isostatic equilibrium and are currently under the influence of large scale tectonic forces, probably due to the collision of the Indian plate with the Asian plate (Kono 1974; Molnar and Tapponier 1975). Thus, the younger orogenic processes reflected in the geochronological data probably correspond to the uplift of the Himalayas which is still in progress.

Acknowledgements. We are grateful to Dr. N. Shimizu for his microscopic observations of present samples. This work was carried out as a part of the scientific program of the Japanese Mount Everest Expedition 1970.

References

Bordet, P.: Recherches géologiques dans l'Himalaya du Népal région du Makalu, Paris: Édition CNRS 1961

Dewey, J.F., Bird, J.M.: Mountain belts and the new global tectonics. J. Geophys. Res. **75**, 2625–2647, 1970

Engels, J.C., Ingamells, C.O.: Geochemical standard biotite LP–6 Bio 40–60 #. Information Sheets 1–8, Menlo Park, Calif., U.S. Geol. Surv. 1973

Hamet, J., Allègre, C.J.: Rb–Sr systematics in granite from central Nepal (Manaslu): Significance of the Oligocene age and high $^{87}Sr/^{86}Sr$ ratio in Himalayan orogeny. Geology **4**, 470–472, 1976

Kaneoka, I.: Investigation of excess argon in ultramafic rocks from the Kola Penisula by the $^{40}Ar/^{39}Ar$ method. Earth Planet. Sci. Lett. **22**, 145–156, 1974

Kaneoka, I., Aoki, K.. $^{40}Ar/^{39}Ar$ analyses of phlogopite nodules and phlogopite-bearing peridotites in South African kimberlites. Earth Planet. Sci. Lett. **40**, 119–129, 1978

Kono, M.: Gravity anomalies in East Nepal and their implications to the crustal structure of the Himalayas. Geophys. J.R. Astron. Soc. **39**, 283–299, 1974

Krummenacher, D.: Détarminations d'âge isotopique faites sur quelques roches de l'Himalaya du Népal par la méthode potassium argon. Schweiz. Mineral. Petrogr. Mitt. **41**, 273–283, 1961

Krummenacher, D.: Géochronométrie des roches de l'Himalaya. In: Recherches géologiques dans l'Himalaya du Népal, région de la Takkhola, P. Bordet et al., ed.: pp. 187–202. Paris: CNRS 1971

Lanphere, M.A., Dalrymple, G.B.. Identification of excess ^{40}Ar by the $^{40}Ar/^{39}Ar$ age spectrum technique. Earth Planet. Sci. Lett. **32**, 141–148, 1976

Mehta, P.K.: Rb–Sr geochronology of the Kulu-Maudi Belt: Its implications for the Himalayan tectogenesis. Geol. Rundsch. **66**, 156–175, 1977

Molnar, P., Tapponier, P.: Cenozoic tectonics of Asia: Effects of a continental collision. Science **189**, 419–426, 1975

Powell, C. McA., Canaghan, P.J.: Plate tectonics and the Himalayas. Earth Planet. Sci. Lett. **20**, 1–12, 1973

Steiger, R.H., Jäger, E.. Subcommision on geochronology: Convention on the use of decay constants in geo- and cosmochronology. Earth Planet. Sci. Lett. **36**, 359–362, 1977

Virk, H.S., Koul, S.L.: Fission track ages and uranium estimation of Himalayan muscovites (Kathmandu Valley, Nepal). J. Phys. Earth **25**, 177–186, 1977

Received October 9, 1980
Accepted March 18, 1981

J Geophys (1981) 49:212–216

Journal of Geophysics

A Comparison of the Thermal and Mechanical Structure of the Lithosphere Beneath the Bohemian Massif and the Pannonian Basin

K.M. Onuoha

Institut für Geophysik, TU Clausthal, Postfach 230, D-3392 Clausthal-Zellerfeld, Federal Republic of Germany*

Abstract. Temperature-depth profiles for the Bohemian Massif and the Pannonian Basin have been determined on the basis of: the known surface heat flow values in both regions, a vertical crustal radiogenic heat production that is estimated from seismic velocity (v_P) profiles, and a thermal conductivity that varies with depth. From these profiles, effective viscosity and stress-depth curves have been determined to a depth of 250 km assuming both linear and non-linear mantle rheology. There is a relative dominance of Newtonian Nabarro-Herring creep in the asthenosphere beneath the Pannonian Basin. Stress values are also significantly lower here than in the lithosphere beneath the Bohemian Massif. The transition from lithosphere to asthenosphere appears to occur at depths of 48–60 km under the Pannonian Basin. The absence of a viscosity minimum under the Bohemian Massif renders an estimate of the depth of this transition difficult, but stress curves appear to level off around depths of 180–200 km, and may thus provide estimates of the depth to the asthenosphere under the Bohemian Massif. Models of the lithosphere beneath these two tectonically different regions are also presented.

Key words: Stress – Effective viscosity – Brittle lithosphere – Ductile lithosphere – Temperature regime

Introduction

The Bohemian Massif of Czechoslovakia is a platform-type cratonic block, consolidated during the Variscan orogeny. Approximately rhombic in shape and bordered by deep SW–NE, NW–SE trending faults, the western margin of the Massif is in the Federal Republic of Germany while the southern margin is in Austria. It is bordered towards the north and north-east by the North-German-Polish lowland. The core of the Bohemian Massif is the Moldanubicum, a metamorphosed Precambrian unit interspersed with Hercynian granites (Máska et al. 1960). The Pannonian Basin on the other hand is a Late Miocene-Pliocene feature whose formation is believed to have been genetically connected with the Late Oligocene-Early Miocene subduction in the Carpathian realm (Stegena et al. 1975; Horváth et al. 1977).

Both the Pannonian Basin and the Bohemian Massif have been relatively well studied geologically and geophysically. In this paper the temperature regimes of the lithosphere in both regions are compared, and the effects of the differences on such rheological parameters as effective viscosity and stress are discussed. The depths to the zone of transition between brittle and creep dominated behaviour in the lithosphere beneath both regions are examined, and their bearing on seismicity and faulting is discussed. The Moldanubicum which forms the core and the best consolidated part of the Bohemian Massif is the actual area referred to in the discussions because the temperature-depth distribution for this unit can be regarded as characteristic for most of the Bohemian Massif (Cermák 1975). The temperature-depth distribution for the Karcag-Debrecen region of Eastern Hungary is taken as representative for most of the Pannonian Basin. These specific locations have been chosen for the determination of the profiles because in each area reliable data exist for heat flow and crustal structure. Moreover the calculated temperature, stress and viscosity profiles help to illustrate the differences in lithospheric structure between two characteristically different regions of the earth's crust: the Pannonian Basin representing a young intermontane basin and the Bohemian Massif representing a consolidated Variscan platform.

Temperature-Depth Profiles

Results of heat flow and geothermal studies in the Bohemian Massif and the surrounding regions have been reported by Cermák (1975, 1977). Important results of heat flow studies in the Pannonian Basin were reported by Stegena (1976), Stegena et al. (1975) and Horváth et al. (1979).

Temperature-depth profiles have been calculated for both regions using a computational model of steady-state conduction of heat in a layered medium. The surface heat flow Q is assumed to be in equilibrium with the heat flowing into a slab of the earth at its base, plus the heat generated by sources within it. Neglecting the earth's curvature and assuming that the temperature T depends only on depth z, we have the one-dimensional heat conduction equation:

$$\frac{d}{dz}\left[k(z)\frac{dT}{dz}\right] = -A(z) \tag{1}$$

where k is the coefficient of thermal conductivity, and A is the heat generation.

If $T(z_0)$ is the temperature at the top of the first layer (with conductivity $k_1 = \text{const.}$ and heat generation $A_1 = \text{const.}$) and $Q(z_0)$ the heat flow through the upper boundary of the first layer, the temperature in the first layer is

* *Present address:* Department of Geology, University of Nigeria, Nsukka, Nigeria

0340-062X/81/0049/0212/$01.00

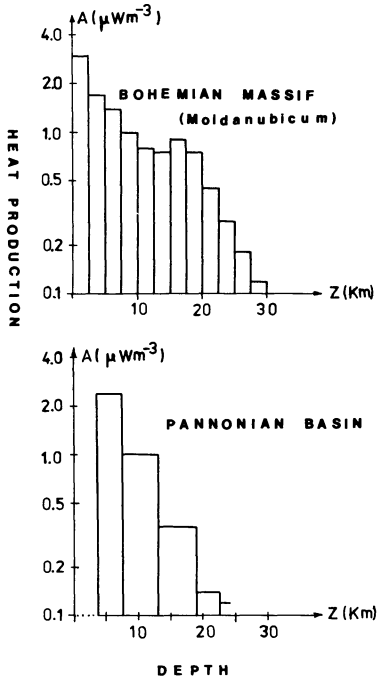

Fig. 1. Heat production-depth relationships for the Moldanubicum (Bohemian Massif) and the Pannonian Basin, based on v_P-depth profiles of Beránek (1971), Mituch and Posgay (1972), Ádám et al. (1979)

$$T(z)=T(z_0)+\frac{Q(z_0)}{k_1}z-\frac{A_1}{2k_1}z^2. \quad (2)$$

$(z_0 \leqq z \leqq z_1)$

Pollack (1965) has shown that for any arbitrarily layered model (with homogeneous individual layers) the temperature at the base of the n-th layer is:

$$T(z)=T(z_0)+\sum_{i=1}^{n}\left\{\frac{z_i-z_{i-1}}{k_i}\left[Q(z_0-\sum_{j=1}^{i-1}A_j(z_j-z_{j-1})\right]-A_i\frac{(z_i-z_{i-1})^2}{2k_i}\right\}. \quad (3)$$

In the present paper the vertical profile of crustal heat generation A has been determined from the seismic velocity (v_P) profiles, making use of the implicit relationship between A and v_P as described by Rybach (1973) and Buntebarth (1976). Following closely the same assumptions as those of Pollack and Chapman (1977) the value of k was taken as $2.5\,\mathrm{Wm^{-1}K^{-1}}$ for $T \leq 500\,^\circ\mathrm{C}$, while for higher temperatures, the values of k were obtained using the results of Schatz and Simmons (1972). The heat generation-depth relations are shown in Fig. 1, while the temperature-depth profiles are displayed in Fig. 2. The sedimentary cover in the Karcag-Debrecen area of the Pannonian Basin is between 2 and 3.5 km thick in many places. The $A-v_P$ relation is not strictly valid for such sedimentary series, and this explains why the $A-z$ relation for the Pannonian Basin is given only from the depth $z=4$ km in Fig. 1. The heat production in this uppermost layer has no appreciable effect on the overall shape of profile 2 in Fig. 2. It should also be noted that, in this figure, profiles 1 and 2 are mean curves of a family of profiles

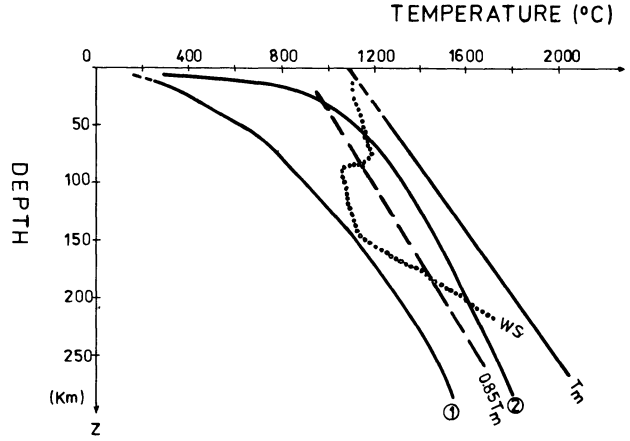

Fig. 2. Temperature-depth profiles: *1* = Bohemian Massif; *2* = Pannonian Basin; T_m = dry pyrolite sodius; WS = solidus for pyrolite containing 0.1 % water [T_m and WS are after Ringwood (1975)]

corresponding to the range of surface heat flow data available for each of the two regions under consideration.

Continuation of the geotherms further downwards into the asthenosphere would necessitate a departure from the purely conductive model of heat transfer which is assumed in the calculations. It should be noted that the solidus temperature in an anhydrous mantle would increase with depth. The actual level at which the solidus is reached in the mantle remains debatable, but it is now agreed that this depends on the role of volatiles in depressing the solidus temperature. The Pannonian geotherm intersects the solidus for pyrolite containing 0.1 % water at a depth of less than 60 km. It is thus likely that a partial melt zone should characterise the upper mantle in this region at this shallow depth. Beneath the Bohemian Massif such an intercept does not occur within the depth range investigated.

Stress-Depth and Viscosity-Depth Profiles

Following Weertman and Weertman (1975) or Meissner and Vetter (1976), we take the following general creep equation to be valid for the creep properties of rocks at high temperatures:

$$\dot{\varepsilon}=C_i\sigma^n\exp\left[-(Q^*+PV^*)/RT\right] \quad (4)$$

$$\dot{\varepsilon}\approx C_i\sigma^n\exp(-g^*T_m/T) \quad (5)$$

where

g^*	= constant	P	= pressure
$\dot{\varepsilon}$	= strain rate	V^*	= activation volume
C_i	= quasi constant	R	= gas constant
σ	= shear stress	T	= absolute temperature
n	= creep exponent	T_m	= absolute melting temperature
Q^*	= activation energy		

For Nabarro-Herring or diffusion (Newtonian) creep $n=1$, and

$$\dot{\varepsilon}_{NH}=C_1\sigma\exp(-g^*T_m/T) \quad (6)$$

with

$$C_1=\alpha_1\Omega D_0/d^2kT \quad (7)$$

and

α_1 = constant
k = Boltzmann's constant
D_0 = diffusion constant.
d = grain size
Ω = atomic volume

For dislocation glide (or power law) creep $n=3$ and

$$\dot{\varepsilon}_{PL} = C_3 \sigma^3 \exp(-g^* T_m/T) \tag{8}$$

with

$$C_3 = \alpha_3 \Omega D_0/\mu^2 kT$$

and

α_3 = constant,
μ = shear modulus.

Introducing the effective viscosity η

$$\eta \approx \sigma/\dot{\varepsilon} \tag{9}$$

From these equations the viscosities for both creep laws can be expressed explicitly:

$$\eta_{NH} = (1/C_1) \exp(g^* T_m/T) \tag{10}$$

$$\eta_{PL} = (1/C_3)(1/\sigma^2) \exp(g^* T_m/T). \tag{11}$$

These relations have been discussed in detail by Meissner and Vetter (1976).

The stress-depth curves (Figs. 3 and 4) and the Newtonian creep viscosity profiles (Fig. 5) have been calculated on the basis of Eqs. (5)–(9) assuming a grain size of 5 mm for the material of mantle rock, and with T/T_m values obtained from Fig. 2. The dry solidus was used for the calculations, not the hypothetical 0.1 % H_2O curve. The values of the constants C_1, C_3 and g^* were taken from Vetter and Meissner (1977, 1979). The non-linear stress-strain relation with $n=3$ has been shown to be more appropriate for much of the lithosphere (Neugebauer and Breitmayer 1975; Mercier et al. 1977).

Discussion

It is obvious from the above figures that the upper mantle regions beneath the Pannonian Basin and the Bohemian Massif differ significantly from each other not only in their temperature regimes, but probably also in composition, at least within the depth range considered here. The temperature-depth curves for the two regions do not intersect even at depths of about 250 km. There is however no information on whether these differences might exist up to and possibly beyond a depth of 400 km. In the sense of Oxburgh and Turcotte (1976) the lithosphere can be divided into an upper elastic layer characterised by brittle response to stresses, and a lower ductile or plastic layer where elastic stresses are relaxed by creep processes.

The temperature at which the transition from elastic to creep-dominated behaviour occurs in the lithosphere depends on the rheological properties of the material of the lithosphere. These are in turn dependent on the homologous temperature (T/T_m), and on the variation of T_m with depth. A value of 0.62 for T/T_m has been assumed in the present paper to define this transition. Other authors (e.g., Vetter and Meissner 1979) have also assumed T/T_m values close to this.

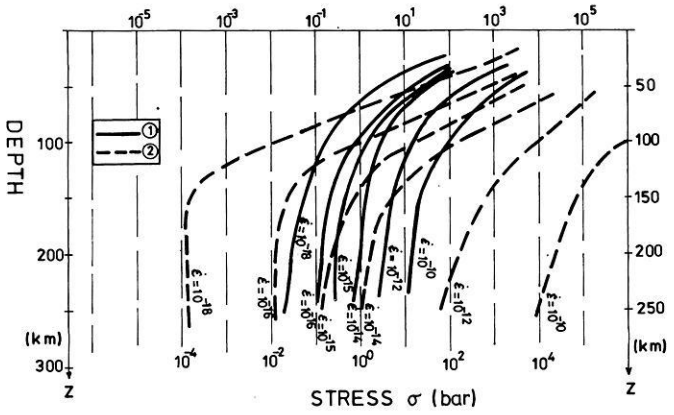

Fig. 3. Stress-depth curves for the Bohemian Massif: *1* = dislocation (power law creep), *2* = Newtonian diffusion creep, with strain rate values (in s^{-1}) as parameter

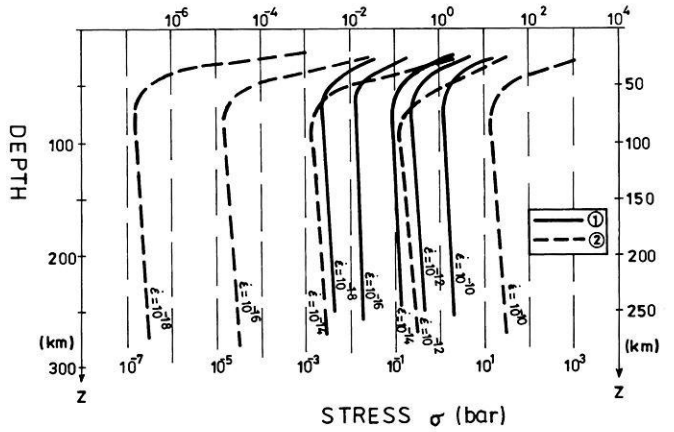

Fig. 4. Stress-depth curves for the Pannonian Basin: key as for Fig. 3

Under the Pannonian Basin the elastic lithosphere according to the above definition is only 10–12 km thick while under the Bohemian Massif its thickness lies between 58 and 65 km (see Fig. 5). The occurrence of exceptionally deep faults and grabens in the Bohemian Massif and their conspicuous absence within the Pannonian Basin can now be understood considering the fact that the maximum depth of faults in a region seems to depend on the thickness of the brittle layer. The Central Bohemian suture, the Pribyslav fault zone and the Ohře graben are examples of deep faults of great length found in the Bohemian Massif. Their extents, laterally and in depth, have been investigated by Beránek and Dudek (1972).

The deformation diagrams (Figs. 3 and 4) show that beneath the Bohemian Massif, power-law creep dominates for strain rates higher than $10^{-15}\,s^{-1}$. For lower strain rates (and at depths greater than 185 km for $\dot{\varepsilon}=10^{-15}\,s^{-1}$) Newtonian creep appears to dominate. The transition between the two creep laws is at about 0.6 bar. This corresponds to the stress level at which the two mechanisms contribute equally to the strain rate. It is however known that the actual value of this transition depends mainly on the assumed grain size in Eqs. (7) and (10) (Stocker and Ashby 1973).

Beneath the Pannonian Basin stresses are very much lower because of the higher temperature regime. Consequently diffusion (Nabarro-Herring) creep dominates even for strain rates as high as $10^{-12}\,s^{-1}$. For $\dot{\varepsilon}<10^{-12}\,s^{-1}$ and for depths greater than

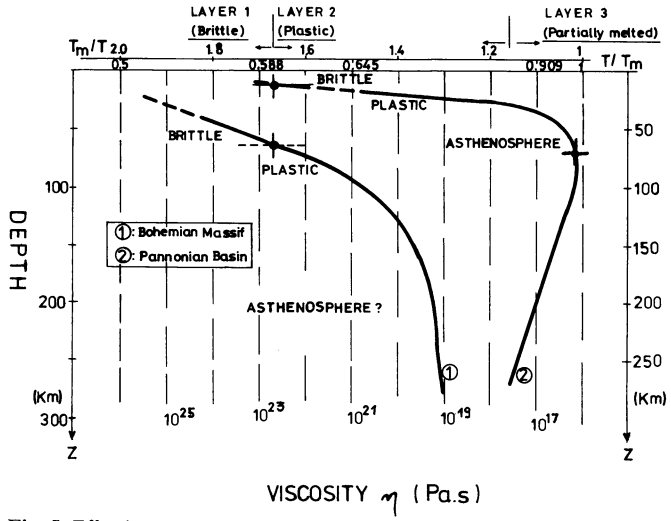

Fig. 5. Effective viscosity-depth profiles

60 km diffusion creep governs all creep processes in the Pannonian upper mantle. Comparing these results with those of Vetter and Meissner (1977), the Pannonian upper mantle can be seen to show mechanical properties reminiscent of the oceanic upper mantle. The transition from lithosphere to asthenosphere appears to occur at depths of 48–60 km under the Pannonian Basin. These results are in good agreement with geoelectric induction and magnetotelluric results which have located the intermediate conductive layer (ICL) at depths of 60 km below the Pannonian Basin (Ádám 1976). Figure 4 also shows that stresses under the Pannonian Basin appear to level off for all curves with constant strain rate at the depth of about 50—60 km. The depth at which this levelling off of stress occurs is usually identified as marking the top of the asthenosphere (Mercier et al. 1977).

Very often there have been speculations about the possible absence of the asthenosphere under shields and stable platforms. In the case of the Bohemian Massif where the absence of a viscosity minimum (see Fig. 5) renders an estimate of the depth of transition from lithosphere to asthenosphere difficult, this view might appear to be substantiated. However, if there is no viscous layer undergoing shear in the upper mantle under stable platforms and shields, it is then difficult to imagine how such parts of the lithospheric plate could take part in the world-wide plate motions. Deep geoelectric soundings (Pecová et al. 1976) located some conductive layers at shallower levels of 60–70 and 100 km, but it appears likely that the conductive zone located near 200 km under the Bohemian Massif might correspond to the base of the lithosphere. The stress curves (Fig. 3) show signs of levelling off only at depths of about 170–200 km. It is thus likely that this zone may really mark the top of the asthenosphere beneath the Bohemian Massif. Figure 6 shows the preferred models of the Pannonian and Bohemian lithospheres.

In the Pannonian Basin dispersed earthquakes occur with shallow focal depths (5–14 km). With the exception of the Dunaharaszti earthquake (12 January 1956; $M = 5.5$–6.0) which was apparently related to sinistral faulting along the Balaton line (Csomor 1967), the seismic activity in the Pannonian Basin shows no correlation with tectonic lines. It is thus likely that this activity is due to the relaxation of thermoelastic stresses in the brittle upper part of the Pannonian lithosphere which is only 10–12 km thick. The Bohemian Massif shows very little seismic activity except along the deeply faulted margins. However, it has long been known that seismic energy originating from earthquakes in the Eastern and Southern Alps was transmitted with little or no absorption through the Bohemian Massif, while seismic energy propagating towards the Western Carpathians and the Pannonian Basin became strongly damped (Kárnik 1967). Zátopek (1957) sought to explain this damping by suggesting the existence, in the contact zone between the two tectonic regions, of deep-seated barriers which reflect the energy further downwards. The difference in the observed teleseismic delay-time residuals between the two regions under consideration is of the order of $+2s$. The stations in the Pannonian Basin are far "slower" (i.e., they record far higher positive residuals), than those in the Bohemian Massif. It is easy to see using simple model calculations that the differences in the range of P_n anomalies or teleseismic delay-time residuals cannot be explained in terms of differences in crustal structure alone, between the Bohemian Massif and the Pannonian Basin. The differences rather reflect the variations in the physical state of the upper mantle under these regions. This in turn means that differences in the sub-Moho temperature regime and rheology are the obvious causes of the variations in P_n anomalies.

Gravity anomalies in the Bohemian Massif seem to be very

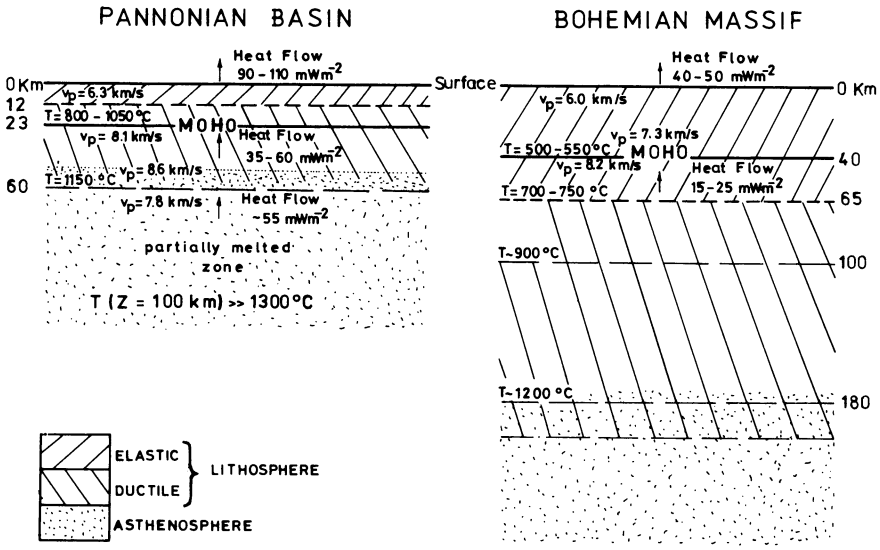

Fig. 6. Preferred lithospheric models: surface heat flow data from Cermák (1975), Horváth et al. (1979); v_P values from Benárek (1971), Ádám et al. (1979), temperature values from this study

well accounted for by granitic intrusions and other near-surface density inhomogenities (Tomek, personal communication). The Pannonian Basin on the other hand is characterized by average Bouguer anomalies between +10 and +15 mgal. Taking into consideration the anomalously thin crust and the elevation of the high-density upper mantle material, these anomalies are strikingly low. Deep seismic soundings have revealed that beneath the Pannonian *M*-discontinuity, *P*-wave velocities are in the range 8.0–8.1 km/s (see Fig. 6). These velocity values indicate the range of probable density values under the Moho. It then becomes apparent that a discrepancy exists in the observed gravity anomalies. The mass which compensates the missing positive anomalies probably exists deeper down in the asthenosphere and is likely to be of thermal origin.

Concluding Remarks

It should again be pointed out that the profiles calculated in this study are models and refer to dry conditions in the lithosphere. The presence of water-bearing minerals (e.g., phlogopite and amphibole) in some xenoliths from the upper mantle beneath many continental regions does indicate that the upper mantle probably contains reasonable quantities of H_2O. The depth of the lithosphere/asthenosphere transition estimated from deformation diagrams (Figs. 3 and 4) or viscosity profiles (Fig. 5) may not necessarily agree with that obtained from purely thermal models (Pollack and Chapman 1977) or with the depth to the low-velocity zone (LVZ). The strong differences in the stress-depth and viscosity-depth profiles in both regions are enough to explain the seismological, teleseismic and other geological differences such as the occurrence and depth of faults. These differences between the two tectonic regions are all thermally controlled and remain valid even if other models are assumed for the melting conditions in the mantle.

Acknowledgement. The author would like to thank Dr. F. Horváth and Professor L. Stegena (both of Eötvös University, Budapest) for instructive discussions. Dr. G. Buntebarth and Professor H.J. Neugebauer suggested improvements to the manuscript. This work was carried out at the Techn. Univ. Clausthal during the tenure of a fellowship from Deutscher Akademischer Austauschdienst (DAAD).

References

Adám, A.: Results of deep electromagnetic investigations in the Pannonian Basin. In: Geoelectric and geothermal studies, A. Adám, ed.: pp. 547–561. Budapest: Akadémiai Kiadó 1976

Adám, A., Bisztricsány, E., Wallner, A., Horváth, F., Meskó, A., Stegena, L., Tarcsai, Gy., Posgay, K.: Hungarian IASPEI report for the general assembly of IUGG, Canberra, Australia, 1979

Beránek, B.: Study of velocity conditions in the earth's crust in the regions of the Bohemian Massif and the Carpathian system. Stud. Geophs Geod. **15**, 316–330, 1971

Beránek, B., Dudek, A.: The results of deep seismic sounding in Czechoslovakia. J. Geophys. **38**, 415–427, 1972

Buntebarth, G.: Methoden zur Abschätzung der Wärmeflußdichte aus dem Oberen Mantel. Geol. Rundsch. **65**, 809–919, 1976

Cermák, V.: Temperature-depth profiles in Czechoslovakia and some adjacent areas derived from heat flow measurements, deep seismic sounding and other geophysical data. Tectonophysics **26**, 103–119, 1975

Cermák, V.: Heat flow map of the Bohemian Massif. J. Geophys. **42**, 455–458, 1977

Csomor, D.: Focal mechanism solution of the Hungarian earthquake 12:1:1956 (in Russian). Ann. Univ. Sci. Budap., Rolando Eotvos Nominatae Sect. Geol. **10**, 3–8, 1967

Horváth, F., Vörös, A., Onuoha, K.M.: Plate tectonics of the western Carpatho-Pannonian region: a working hypothesis. Acta Geol. Acad. Sci. Hung. **21**, 207–221, 1977

Horváth, F., Bodri, L., Ottlik, P.: Geothermics of Hungary and the tectonophysics of the Pannonian Basin "red spot" In: Terrestrial heat flow in Europe, V. Cermák, L. Rybach, eds.: pp. 206–217. Berlin, Heidelberg, New York: Springer 1979

Kárnik, V.: Crustal and upper mantle seismic activity in the European Area. Stud. Geophs. Geod. **11**, 324–334, 1967

Máska, M., Matejka, A., Zoubek, V.: Tectonic development of Czechoslovakia (Collected papers and the tectonic map 1:1,000,000), pp. 224. Praha: Nakl. CSAV 1960

Meissner, R.O., Vetter, U.R.: Isostatic and dynamic processes and their relation to viscosity. Tectonophysics **35**, 137–148, 1976

Mercier, J.C., Anderson, D.A., Carter, N.L.: Stress in the lithosphere: Inferences from the steady state flow of rocks. Pure Appl. Geophys. **115**, 199–226, 1977

Mituch, E., Posgay, K.: Results of DSS measurements in Hungary. In: The crustal structure of Central and Southeastern Europe based on the results of explosion seismology. Geophysical Transactions, Gy. Szénás, ed.: pp. 118–129. Budapest: ELGI 1972

Neugebauer, H.-J., Breitmayer, G.: Dominant creep mechanism and the descending lithosphere. Geophys. J. R. Abstron. Soc. **43**, 873–895. 1975

Oxburgh, E.R., Turcotte, D.L.: The physico-chemical behaviour of the descending lithosphere. Tectonophysics **32**, 107–128, 1976

Pecová, J., Petr, V., Praus, O.: Depth distribution of the electric conductivity in Czechoslovakia from electromagnetic studies. In: A. Adám (editor), Geoelectric and geothermal studies, A. Adám, ed.: pp. 517–537. Budapest: Akadémiai Kiadó 1976

Pollack, H.N.: Steady heat conduction in layered mediums: the half-space and sphere. J. Geophys. Res. **70**, 5645–5648, 1965

Pollack, H.N., Chapman, D.S.: On the regional variation of heat flow, geotherms, and lithospheric thickness. Tectonophysics **38**, 279–296, 1977

Ringwood, A.E.: Composition and petrology of the earth's mantle. Int. Ser. Earth Planet. Sci. New York: McGraw-Hill, 1975

Rybach, L.: Wärmeproduktionsbestimmungen an Gesteinen der Schweizer Alpen. Beitr. Geol. Schweiz., Geotech. Ser., Lief. **51**, Bern, 1973

Schatz, J.F., Simmons, G.: Thermal conductivity of earth materials at high temperatures. J. Geophys. Res. **77**, 6966–6983, 1972

Stegena, L.: The variation of temperature with depth in the Pannonian Basin. In: Geoelectric and geothermal studies, A. Adám, ed.: pp. 425–438. Budapest: Akadémiai Kiadó 1976

Stegena, L., Géczy, B., Horváth, F.: Late Cenozoic evolution of the Pannonian Basin. Tectonophysics **26**, 71–90, 1975

Stocker, R.L., Ashby, M.F.: On the rheology of the upper mantle. Rev. Geophys. Space Phys. **11**, 391–426, 1973

Vetter, U.R., Meissner, R.O.: Creep in geodynamic processes. Tectonophysics **42**, 37–54, 1977

Vetter, U.R., Meissner, R.O.: Rheologic properties of the lithosphere and applications to passive continental margins. Tectonophysics **59**, 367–380, 1979

Weertman, H., Weertman, J.R.: High temperature creep of rock and mantle viscosity. Annu. Rev. Earth Planet. Sci. **3**, 293–315, 1975

Zátopek, A.: Zu einigen Problemen der Krustendynamik im Karpatengebiet. Geofiz. Kozl. **8**, 196–110, Budapest, 1957

Received July 4, 1980; Revised Version September 11, 1980
Accepted November 6, 1980

J Geophys (1981) 49:217–225

Journal of Geophysics

Extremal Models for Electromagnetic Induction in Two-Dimensional Perfect Conductors

P. Weidelt

Bundesanstalt für Geowissenschaften und Rohstoffe, Stilleweg 2, D-3000 Hannover 51, Federal Republic of Germany

Abstract. The simple problem of electromagnetic induction in two-dimensional perfect conductors is considered. Extremal models are constructed maximizing the depth to the top of the conductor for magnetic field data at $N=1$ or 2 observation points. It is assumed that the inducing magnetic field is quasi-uniform and that the electromagnetic field is excluded from a depth greater than $z=A$, where A is prescribed. Then the extremal models consist of two levels: a conducting plane at a depth $z=A$ and either N conducting strips or N gaps in a conducting plane at a depth $z=z_0$, which is the maximum possible depth as calculated from the data. The problem is solved by conformal mapping and illustrated by data from the North German conductivity anomaly.

Key words: Electromagnetic induction – Maximum depth rule – Conformal mapping – North German conductivity anomaly

1 Introduction

Now that techniques have been developed for estimating by various kinds of generalized matrix inversion the degree of non-uniqueness of a given imperfect data set, interest has arisen in the problem of how to obtain geophysically relevant properties common to all models, which both fit the data and satisfy certain a priori assumptions (i.e., the feasible models). The research of Parker on ideal bodies is a typical example of this approach (Parker 1972, 1974, 1975). Work along similar lines has been carried out by Sabatier (1977a–c), Safon et al. (1977), Rietsch (1978), Huestis (1979), and Barcilon (1979). The investigation of the upper bound of a minimum value (or the lower bound of a maximum value) of a special model parameter has been of particular importance in this development. For instance, if a data set is to be interpreted in terms of a buried structure, then any feasible model has a minimum depth of burial (the depth to the top of the structure). If we could find the model with the greatest minimum depth of burial, then the minimum depth of burial of all feasible models cannot be greater than this upper bound. The search for the maximum depth of the top of a buried structure leads to maximum depth rules. For potential field data many rules of this nature have been established (Bott and Smith 1958; Smith 1959, 1960).

In this paper maximum depth rules are derived for the simplest problem in electromagnetic induction, where the model is two-dimensional and consists only of perfect conductors and insulators, thus admitting a treatment by conformal mapping. In this limit the surface of the conductor coincides with a field line, since the magnetic field component normal to the conductor vanishes. The following problem is considered: Assume cartesian coordinates y, z (z positive downwards, surface at $z=0$) and a quasi-uniform inducing field in y-direction. Further, assume that the perfect conductor extends with horizontal tangents to infinity and that it excludes the electromagnetic field from a depth greater than $z=A$, where A is known or can be estimated. The magnetic field components $H_y(p)$ and $H_z(p)$, normalized by H_n, the horizontal magnetic surface field for $y\to\pm\infty$, are given at a surface point p

$$h_y=H_y(p)/H_n, \qquad h_z=H_z(p)/H_n \tag{1.1}$$

The problem is to determine the conductor with the deepest top complying with h_y, h_z and A.

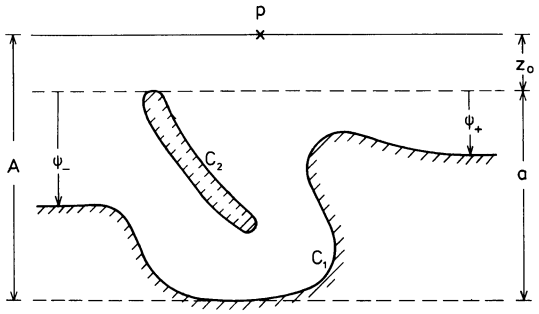

Fig. 1. The model under consideration. C_1 and C_2 are the surfaces of perfect conductors. The other symbols are explained in the text

A section across the most general model under consideration is shown in Fig. 1. It consists of a perfect conductor with undulating interface C_1 extending to infinity and a second isolated conductor with boundary C_2. It turns out that a doubly connected conductor is necessary to construct extremal models for all possible values of h_y and h_z. Fig. 1 introduces z_0 as the depth to the top of the conductor and $a=A-z_0$ as the depth range of irregular distribution of conducting material. The horizontal asymptotes of C_1 lie at depths $\psi_\pm$ below z_0.

The above problem is solved for a single observation point p in Sect. 2, and partial results for two observation points are presented in Sect. 3. Finally, in Sect. 4, the findings are applied to real data.

0340-062X/81/0049/0217/$01.80

2 Single-Point Extremal Models

2.1 Simply Connected Conductors

For ease of presentation we first search for extremal models within the class of simply connected conductors, restricting attention to the undulating interface C_1. Let

$$p=y-i(z-z_0) \quad \text{and} \quad w=u+iv \tag{2.1}$$

be two complex variables and let $p(w)$ map the line $v=0$ conformally into the interface C_1 and the half-plane $v>0$ into the insulator above C_1. Let this mapping be normalized by

$$p'(w)\to 1 \quad \text{for} \quad w\to\infty,\ v>0 \tag{2.2}$$

The parameter representation of C_1 is

$$p(w)=y(u)-i\psi(u) \quad \text{for} \quad -\infty<u<+\infty,\ v=0 \tag{2.3}$$

where $\psi=z-z_0$ is subject to $0\leqq\psi(u)\leqq a$ with $a=A-z_0$ (Fig. 1). The function $\psi(u)$ with $\psi=z-z_0$ and $a=A-z_0$ (Fig. 1). The function $\psi(u)$ with the limiting values $\psi_\pm$ for $u\to\pm\infty$ is the boundary value of the negative imaginary part of $p(w)$. The function $p(w)$ is analytic in $v>0$ and satisfies Eq. (2.2). Hence,

$$p(w)=w+\frac{1}{\pi}(\psi_+-\psi_-)\log w-\frac{1}{\pi}\int_{-\infty}^{+\infty}\frac{\tilde{\psi}(t)\,dt}{t-w} \tag{2.4}$$

where

$$\tilde{\psi}(u)=\begin{cases}\psi(u)+\psi_+-\psi, & u<0\\ \psi(u), & u>0\end{cases}$$

The subtraction term in $\tilde{\psi}$ and its subsequent reconsideration in the log term is necessary to ensure the convergence of Eq. (2.4) if $\psi_+\neq\psi_-$. Using the identity

$$\operatorname{Im}\left\{\lim_{v\to+0}\frac{1}{\pi}\int_{-\infty}^{+\infty}\frac{\tilde{\psi}(t)\,dt}{t-w}\right\}=\tilde{\psi}(u)$$

it is easily verified that Eq. (2.4) meets all requirements. The normalized magnetic field in the p-plane,

$$h=h_y+ih_z=(H_y+iH_z)/H_n \tag{2.5}$$

is derived from a normalized complex potential $f(p)$ by $h(p)=f'(p)$ where, by virtue of the Cauchy-Riemann differential equations, the lines $\operatorname{Re}f=\text{const.}$ are the equipotential lines and the lines $\operatorname{Im}f=\text{const.}$ the field lines. By the conformal mapping $w(p)$ this field is mapped into a magnetic field in the w-plane, which is derived from the complex potential $g(w)=f(p)$. In view of the quasi-uniform inducing field the magnetic field in the upper w-halfplane is also uniform and can be derived from the normalized complex potential $g(w)=w$, where Eq. (2.2) has been used. Hence the magnetic field in the p-plane is simply

$$h(p)=f'(p)=g'(w)\,w'(p)=1/p'(w) \tag{2.6}$$

or expressing h by means of Eq. (2.4) in terms of ψ,

$$\frac{1}{h}=1-\frac{1}{\pi}\int_{-\infty}^{+\infty}\frac{\psi(t)\,dt}{(t-w)^2} \tag{2.7}$$

For computational ease it is temporarily assumed that instead of A the quantity a is prescribed. We are then faced with the following problem:

The normalized complex magnetic field h and the depth range a are given. Determine the complex point w and the real function $\psi(u)$ with $0\leqq\psi\leqq a$, which maximizes $z_0=\operatorname{Im}p(w)$ subject to Eq. (2.7). Moreover, for $v\geqq 0$ $p(w)$ has to be a univalent (or one-to-one) mapping.

This problem of constrained maximization is best solved by the use of Lagrangian multipliers (Luenberger 1969, p. 249), yielding, for the minimization of $-z_0$ (to retain the canonical form), the Lagrange function

$$L=\operatorname{Im}\{-p(w)+\lambda[p'(w)-1/h]\}-\int_{-\infty}^{+\infty}\mu^-(t)\,\psi(t)\,dt+\int_{-\infty}^{+\infty}\mu^+(t)(\psi(t)-a)\,dt \tag{2.8}$$

The complex multiplier $\lambda=\lambda_y+i\lambda_z$, where λ_y and λ_z are unrestricted in sign, is associated with the equality constraint Eq. (2.7). On the other hand, the functions $\mu^-(t)$ and $\mu^+(t)$ associated with the inequalities $-\psi(t)\leqq 0$ and $\psi(t)-a\leqq 0$, respectively, are *positive* where the inequalities are binding (i.e., satisfied with the equality sign), and zero elsewhere. The existence of an extremum requires that the first variation of L with respect to ψ vanishes. Hence,

$$\operatorname{Im}\left\{\frac{1}{\pi(t-w)}-\frac{\lambda}{\pi(t-w)^2}\right\}-\mu^-(t)+\mu^+(t)=0 \tag{2.9}$$

Since L is linear in ψ, this function does not occur in Eq. (2.5). From the fact that $\mu^-=0$ for $\psi>0$ and $\mu^+=0$ for $\psi<a$ it is immediately deduced that the only points t where $\psi(t)$ attains neither its lower nor its upper bound, are the roots of

$$\operatorname{Im}\left\{\frac{1}{t-w}-\frac{\lambda}{(t-w)^2}\right\}=0 \tag{2.10}$$

which has at most two real roots. This is assumed here and verified in a later stage. The origin on the real axis of the w-plane is now fixed by placing the two roots at $t=\pm c$, $c>0$. Hence, either

$$\text{a)}\quad \psi(t)=\begin{cases}a, & |t|<c\\ 0, & |t|>c\end{cases} \tag{2.11a}$$

or

$$\text{b)}\quad \psi(t)=\begin{cases}0, & |t|<c\\ a, & |t|>c\end{cases} \tag{2.11b}$$

These two cases will be discussed below. The model parameters w and c are determined from the fact that at an extremum the three partial derivatives of

$$L=\operatorname{Im}\{-p(w)+\lambda[p'(w)-1/h]\}$$

with respect to u, v and c have to vanish. This latter form of L differs from Eq. (2.8) by the inequality terms, which vanish for a choice of $p(w)$ according to Eq. (2.11a, b). An analytic function $f(w)$ satisfies

$$\partial_u\operatorname{Im}f(w)=\operatorname{Im}f'(w), \qquad \partial_v\operatorname{Im}f(w)=\operatorname{Re}f'(w)$$

where $\partial_u=\partial/\partial_u$, etc. Hence, the first two conditions are equivalent to

$$-p'+\lambda p''=0 \quad \text{or} \quad \lambda=p'/p'' \tag{2.12}$$

which combined with $\partial_c L=0$ yields the extremal condition

$$\operatorname{Im}\{-\partial_c p+(p'/p'')\,\partial_c p'\}=0 \tag{2.13}$$

Case a:

From Eqs. (2.4) and (2.11a) it follows that

$$p(w)=w+\frac{a}{\pi}\log\left(\frac{-c-w}{+c-w}\right)$$

reducing Eq. (2.13) to

$$\pi(|w|^2-c^2)-2ac=0 \tag{2.14}$$

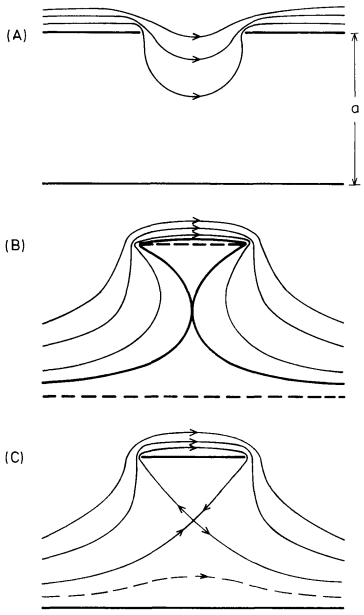

Fig. 2A–C. Types of extremal models for a single observation point showing upper and lower conducting sheets and magnetic field lines: (**A**) for $h_y<1$, (**B**) approximate model for $h_y>1$, (**C**) exact model for $h_y>1$ (see text for full explanation)

Equation (2.14) supplements the complex equation $p'(w)=1/h$. This set of three real equations is solved by

$$u=\frac{a}{\pi}\frac{h_z}{h_y-1}\tan\beta, \quad v=\frac{a}{\pi}\tan\beta, \quad c=\frac{a}{\pi}\frac{2h_y-1}{1-h_y} \tag{2.15a-c}$$

where

$$\tan^2\beta=\frac{2h_y-1}{(h_y-1)^2+h_z^2} \tag{2.16}$$

implying

$$z_0=\operatorname{Im} p(w)=\frac{a}{\pi}(-\beta+\tan\beta)=A\left(1-\frac{\pi}{\pi-\beta+\tan\beta}\right) \tag{2.17}$$

For consistency, insertion of Eq. (2.15a-c) and of λ from Eq. (2.12) will verify that $t=\pm c$ are the two real roots of Eq. (2.10). Equations (2.17) and (2.16) provide a partial answer to the problem under consideration. The answer is incomplete because c, assumed to be positive, becomes negative for $h_y>1$. The second change of sign of c at $h_y=0.5$ is not serious, since the horizontal magnetic field of internal origin, $h_y-0.5$, is always non-negative. (The normal magnetic field H_n consists of the external inducing field and the internal normally induced field in equal parts.)

The type of the extreme model and a few field lines are shown in Fig. 2, part A. It consists of two horizontal halfplanes at $z=z_0$ and a horizontal plane at $z=A$. The width of the gap between the halfplanes (i.e., the distance between the two points where $p'(w)=0$) is

$$d=\frac{2a}{\pi}\left\{\frac{2\varepsilon}{1-\varepsilon^2}+\log\frac{1+\varepsilon}{1-\varepsilon}\right\}, \quad \varepsilon=\sqrt{2h_y-1}$$

For $h_y\to 1-0$ and $h_z>0$ (say), the right halfplane is displaced to infinity, yielding an infinite width.

Case b:

Combining Eqs. (2.4) and (2.11b) we obtain

$$p(w)=w+\frac{a}{\pi}\log\left(\frac{c-w}{c+w}\right) \tag{2.18}$$

and the extremal condition

$$\pi(|w|^2-c^2)+2ac=0$$

The resulting parameters u, v, and z_0 are identical with those given in Eqs. (2.15a, b) and (2.17), whereas

$$c=\frac{a}{\pi}\frac{2h_y-1}{h_y-1}$$

suggests that case b covers the range $h_y>1$. However, an inspection of Eq. (2.18) reveals that $p(w)$ is not univalent for all $v>0$. Only for sufficiently large v are the lines $v=$const., which are field lines for a quasi-uniform inducing field, mapped into the corresponding field lines in the p-plane (Fig. 2, part B). The value of v can decrease until a limiting field line is reached where two different parts of the field line touch at the axis of symmetry. For smaller v, the image of the line $v=$const. has two points of intersection on the axis of symmetry, implying that for $-a\leqq\operatorname{Im} p(w)\leqq 0$ two different points of the w-plane are mapped into the same point of the p-plane. The deepest physically real conductor is traced by the limiting field line, whereas contrary to our assumption the line $v=0$ does not map the interface of a physically real conductor.

Since the search for an extremum model within the restricted class of simply connected conductors failed for $h_y>1$, the broader class of doubly connected conductors will now be considered.

2.2 Doubly Connected Conductors

An account of the theory of conformal mapping of doubly connected domains, which is intimately related to the theory of doubly periodic functions, is given by Koppenfels and Stallmann (1959).

We assume the conductor configuration of Fig. 1: A conductor C_1 with undulating interface extending at both sides, with horizontal tangents, to infinity and an isolated conductor C_2 of finite extent. A very special case of this class is shown at the top of Fig. 3. A branch cut from any point of C_2 to infinity creates a simply connected domain. As in Sect. 2.1 we introduce two complex variables

$$p=y-i(z-z_0), \quad w=u+iv \tag{2.19}$$

where w will now be dimensionless. Using the univalent conformal mapping $w(p)$, the simply connected domain is mapped into a rectangle of length π and heigth $\frac{1}{2}\alpha$ in the w-plane, such that C_1 is mapped into $v=0$ and C_2 into $v=\frac{1}{2}\alpha$, $0\leqq u\leqq\pi$ (top and centre of Fig. 3, for illustration). The aspect ratio of the rectangle depends on the conductor system C_1, C_2. Broadly speaking, α is large if the minimum distance between C_1 and C_2 is large compared with the dimension of C_2, and vice versa. To each physical contour around C_2, which must cross the branch cut, corresponds a *different* rectangle in the w-plane, displaced by a distance π to the right (left) if C_2 was lying to the left (right) of the contour. Hence, $w(p)$ is multi-valued and $p(w)$ periodic, satisfying $p(w+k\pi)=p(w)$ for any integer k.

Let $p=\infty$ be mapped into $w=0$. Then the asymptotic behaviour

$$w(p)=-b/p \quad \text{for } p\to\infty,\ \operatorname{Im} p>0 \tag{2.20}$$

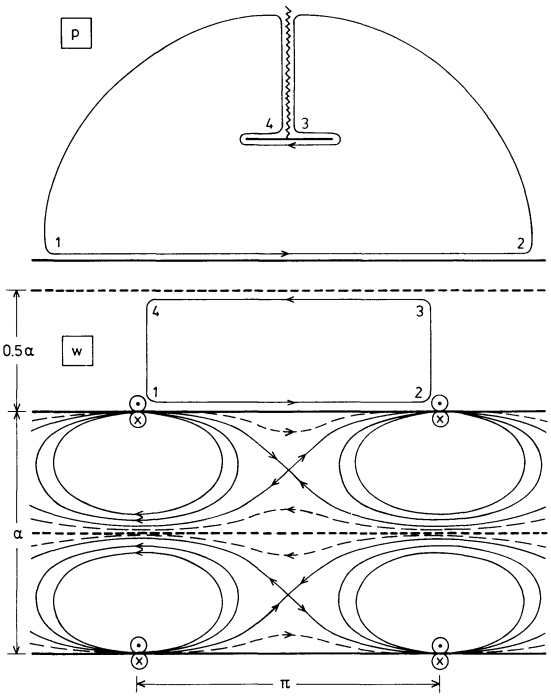

Fig. 3. Example of the mapping of a doubly connected domain in the p-plane (*upper diagram*) onto half a period rectangle in the w-plane (*lower diagram*). The period rectangle is completed by the mirror image at $v=\alpha/2$ and periodically reproduced with periods π and $i\alpha$. The *bottom* shows magnetic field lines for a doubly periodic dipole and a uniform magnetic field in the w-plane. As a consequence of Eq. (2.23) the uniform field is adjusted to yield a vanishing net flux across a line from any point at $v=0$ (except source points) to any point at $v=\alpha/2$. The magnetic field in the w-plane corresponds to a quasi-uniform inducing field in the p-plane

establishes a conformal one-to-one mapping of a neighbourhood of $p=\infty$ onto a neighbourhood of $w=0$, where the scaling length $b>0$ has to be determined. The minus sign ensures that $\mathrm{Im}\, w>0$ if $\mathrm{Im}\, p>0$.

For a quasi-uniform inducing field let

$$H(p)/H_n=h(p)=f'(p), \tag{2.21}$$

where $f(p)$ with $f(p)=p$ for $p\to\infty$ is the normalized complex potential. Then the corresponding normalized potential $g(w)=f(p)$ behaves according to Eq. (2.20) as

$$g(w)=-b/w \quad \text{for } w\to 0, \tag{2.22}$$

which can be interpreted as the potential of a horizontal magnetic dipole or current doublet at $w=0$, corresponding to the fact that the normal magnetic field in the p-plane can be conceived as the limit of a distant line current and its mirror image at C_1.

In virtue of the Cauchy-Riemann differential equations the real part of the complex potential can be interpreted as the ordinary scalar magnetic potential and the imaginary part as the only component of the vector potential. At boundaries to perfect conductors this component vanishes since it is proportional to the time derivative of the electric field, vanishing at conductors. Hence, g satisfies the boundary condition

$$\mathrm{Im}\, g(w)=0 \quad \text{for } v=0 \text{ and } v=\alpha/2 \tag{2.23}$$

The complete potential $g(w)$ can be considered as the superposition of the potentials of the infinite sequence of dipoles a distance π apart along the horizontal axis, plus the potentials of the infinite number of images of this sequence at $v=\alpha$, $-\alpha$, 2α, -2α, ... which ensures that $\mathrm{Im}\, g$ is constant at the conductors at $v=0$ and $v=\alpha/2$, plus the potential of a still unspecified uniform horizontal field which adjusts $\mathrm{Im}\, g$ at both conductors to zero. Hence,

$$g(w)=-b\{\varphi(w,\alpha)+c_1 w+c_2\} \tag{2.24}$$

where

$$\varphi(w,\alpha)=\lim_{M\to\infty}\sum_{m=-M}^{+M}\sum_{k=-\infty}^{+\infty}\frac{1}{w-k\pi-im\alpha}$$

$$=\lim_{M\to\infty}\sum_{m=-M}^{+M}\cot(w-im\alpha) \tag{2.25}$$

$$=\cot w+2\sum_{m=1}^{\infty}\frac{\sin 2w}{\cosh 2m\alpha-\cos 2w} \tag{2.26}$$

$$=\sum_{m=-\infty}^{+\infty}\frac{\sin 2w}{\cosh 2m\alpha-\cos 2w}$$

$$=\vartheta_1'(w)/\vartheta_1(w) \tag{2.27}$$

with

$$\vartheta_1(w)=2\sum_{n=0}^{\infty}(-1)^n e^{-\alpha(n+\frac{1}{2})^2}\sin(2n+1)w \tag{2.28}$$

The above derivations are based on the identities 4.3.91, 4.3.39 and 4.3.31 of Abramowitz and Stegun (1965) and Example 15, Chap. 21 of Whittaker and Watson (1927). In Eq. (2.27) $\vartheta_1(w)$ is the first Theta function for the period ratio $\tau=i\alpha/\pi$ in the notation of Whittaker and Watson. The series (2.26) is rapidly convergent for $\alpha\geqq\pi$. For $\alpha<\pi$ the application of Jacobi's imaginary transformation (Whittaker and Watson 1927, p. 474) to ϑ_1 also yields a rapidly convergent representation:

$$\varphi(w,\alpha)=-\frac{2w}{\alpha}+\frac{\pi}{i\alpha}\varphi\left(\frac{\pi w}{i\alpha},\frac{\pi^2}{\alpha}\right) \tag{2.29}$$

The constants c_1 and c_2 in Eq. (2.24) are determined from the observation that

$$\mathrm{Im}\,\varphi(w,\alpha)=\begin{cases}0, & v=0 \quad \text{(except source points)}\\ -1, & v=\alpha/2\end{cases}$$

The latter result is obtained by rearranging the terms of Eq. (2.25), yielding only a contribution for $m=-M$. Hence, satisfying Eq. (2.23) by $c_1=2/\alpha$, $c_2=0$, we end up with

$$g(w)=-b\{\varphi(w,\alpha)+2w/\alpha\} \tag{2.30}$$

The bottom of Fig. 3 shows a few magnetic field lines, $\mathrm{Im}\, g=\text{const.}$, within a complete period rectangle of length π and height α. A particular feature of the field in any doubly connected domain is the existence of a neutral point ($g'=0$).

The presence of a linear term in the complex potential reflects the fact that the scalar magnetic potential and hence the complex potential is a multi-valued function, increasing after any closed clockwise contour by the amount of current encircled, reckoned positive if flowing in x-direction (into the sheet). Hence, the total current I flowing in the conductor C_2 is

$$I=\frac{2\pi b}{\alpha}H_n \tag{2.31}$$

After having determined $g(w)$, the normalized magnetic field in the p-plane is given by

$$h(p)=f'(p)=g'(w)\cdot w'(p)=g'(w)/p'(w) \tag{2.32}$$

Let $\psi_1(u)$ and $\psi_2(u)$ be the boundary values of the negative imaginary part of $p(w)$ at $v=0$ and $v=\alpha/2$. With the formula of Villat (Koppenfels and Stallmann 1959, p. 107) the mapping function $p(w)$ - analytic in $0<v<\alpha/2$ - is, apart from a real additive constant, given by

$$p(w)=-\frac{1}{\pi}\int_0^\pi \{\psi_1(t)\,\varphi(t-w)-\psi_2(t)\,\chi(t-w)\}\,dt + \frac{2w}{\alpha\pi}\int_0^\pi \{\psi_1(t)-\psi_2(t)\}\,dt \tag{2.33}$$

where

$$\chi(w)=\varphi(w+\tfrac{1}{2}i\alpha)+i=\vartheta_4'(w)/\vartheta_4(w) = \sum_{m=1}^{\infty}\frac{2\sin 2w}{\cosh(2m-1)\,\alpha-\cos 2w} \tag{2.34}$$

using a set of identities given in Chap. 21 of Whittaker and Watson (1927).

Unlike the complex potential $g(w)$, the mapping $p(w)$ is periodic $p(w+\pi)=p(w)$, requiring that the second term of Eq. (2.33) vanishes, i.e.,

$$\int_0^\pi \{\psi_1(t)-\psi_2(t)\}\,dt=0 \tag{2.35}$$

provided that the domain is strictly doubly connected ($\alpha<\infty$).

Because of Eq. (2.20), $p=-b/w$ for $w\to 0$, and

$$\lim_{v\to+0}\frac{1}{\pi}\frac{v}{u^2+v^2}=\delta(u)$$

it is reasonable to split ψ_1 into a bounded part $\tilde{\psi}_1$ and an unbounded part,

$$\psi_1(u)=\tilde{\psi}_1(u)-b\pi\,\delta(u) \tag{2.36}$$

implying that the proper range of integration in Eqs. (2.33) and (2.35) is from -0 to $\pi-0$. For $0\leqq u\leqq\pi$ the functions $\tilde{\psi}_1$ and ψ_2 are bounded by

$$0\leqq\tilde{\psi}_1(u)\leqq a,\qquad 0\leqq\psi_2(u)\leqq a \tag{2.37}$$

where again $a=A-z_0$ (Fig. 1). Hence we are faced with the following problem: The complex number $h=g'(w)/p'(w)$ and the depth range a are given. Determine the two real functions $\tilde{\psi}_1$ and ψ_2, subject to Eq. (2.37), the complex point w and the scale length b such that $z_0=\operatorname{Im} p(w)$ is a maximum.

As in Sect. 2.1, the problem is solved by means of a Lagrange function L, which now reads

$$L=\operatorname{Im}\{-p(w)+\lambda[p'(w)/g'(w)-1/h]\} + \int_0^\pi \{-\mu_1^-\,\tilde{\psi}_1+\mu_1^+(\tilde{\psi}_1-a)-\mu_2^-\,\psi_2+\mu_2^+(\psi_2-a)\}\,dt + \lambda_0\left\{\int_0^\pi(\tilde{\psi}_1-\psi_2)\,dt-\pi b\right\} \tag{2.38}$$

The difference from Eq. (2.8) is only that two functions have to be determined, constrained by Eq. (2.35). Since L is linear in $\tilde{\psi}_1$ and ψ_2, the same arguments as in Sect. 2.1 lead to the result that in an extremal model $\tilde{\psi}_1$ and ψ_2 can attain only the values 0 and a. Since C_2 contours a conductor which does not extend to infinity, ψ_2 must be continuous. The only possible choice is $\psi_2=0$. (In the case $\psi_2=a$ the doubly connected domain degenerates into a simply connected domain, and the results of Sect. 2 can be recovered.) The function $\tilde{\psi}_1(t)$ may have either none or two points of discontinuity, the latter being the roots of

$$\operatorname{Im}\{\varphi(t-w)+\lambda\varphi'(t-w)/g'(w)\}+\pi\lambda_0=0 \tag{2.39}$$

which are mapped into $p=\infty$. First it is assumed that Eq. (2.39) has no roots. Then we have to choose $\tilde{\psi}_1=a$, which implies according to Eqs. (2.35), (2.36) and (2.33) that $b=a$ and

$$p(w)=-a\{\varphi(w)+i\} \tag{2.40}$$

In Eq. (2.33) we have used

$$\int_0^\pi \varphi(t-w)\,dt=\log\vartheta_1(t-w)|_0^\pi=i\pi,\qquad v>0$$

The mapping of Eq. (2.40) maps the line $v=\frac{1}{2}\alpha$ into a horizontal strip at $z=z_0$ and the line $v=0$ into a plane at $z=z_0+a=A$. The model is illustrated in Fig. 2, part C. Inserting Eq. (2.40), the Lagrange function, Eq. (2.38) reduces to

$$L=\operatorname{Im}\{a(\varphi+i)+\lambda[\varphi'/(\varphi'+2/\alpha)-1/h]\}$$

At an extremum, the three partial derivatives with respect to u, v and α vanish. As in Sect. 2.1, the first two admit the elimination of λ, and the third then provides the extremal condition

$$\operatorname{Im}\{\alpha\partial_\alpha\varphi-(\varphi'/\varphi'')\cdot\partial_\alpha(\alpha\varphi')\}=0 \tag{2.41}$$

which supplements the constraint

$$h=1+2/(\alpha\varphi') \tag{2.42}$$

The nonlinear system, Eqs. (2.41) and (2.42) is solved easily by numerical means. Some insight, however, is obtained by an approximate solution. For h_y slightly greater than unity the extremal model must be close to that for $h_y\leqq 1$, i.e., the strip at $z=z_0$ is wide and α is small. In this limit, Eqs. (2.29) and (2.26) yield the approximation

$$\varphi(w,\alpha)=-\frac{2w}{\alpha}+\frac{\pi}{i\alpha}\cot\left(\frac{\pi w}{i\alpha}\right),\qquad \alpha\ll\pi$$

reducing the extremal condition Eq. (2.41) to

$$\cosh\left(\frac{2\pi u}{\alpha}\right)+\left(\frac{\pi^2}{\alpha}-1\right)\cos\left(\frac{2\pi v}{\alpha}\right)=0$$

After solving for u, v, and α, the relationship Eq. (2.17) is reproduced *exactly*. Hence, Eq. (2.17) gives reliable results for $h_y>1$ also if

$$\alpha/\pi^2=(h_y-1)/(2h_y-1)$$

is small. The applicability of Eq. (2.17) for $h_y>1$ is revealed from Fig. 2, parts B and C. The field lines, which become identical at infinity, show a remarkable similarity, except for the different field line topology in the region of weak magnetic fields. The approximation of Eq. (2.17) is worst if both h_y and $|h_z|$ are large, i.e., for points near the edge of the strip. However, the results of Table 1 indicate that for all cases of geophysical interest, Eq. (2.17) provides a completely satisfactory approximation. The figures of Table 1 underline that the search in the extended class of doubly connected conductors consistently yields a slightly greater z_0/A-value than the search in the class of simply connected conductors.

At $h_y=1$ the transition between the extremum models of Fig. 2, parts A and C is continuous: Assuming $h_z>0$, the right edge of the gap (A) tends to $y=+\infty$ for $h_y=1-0$ and the left edge of the strip (C) tends to $y=-\infty$ for $h_y=1+0$.

Table 1. Comparison of approximate and exact z_0/A values

h_y	$\lvert h_z\rvert$	z_0/A (approx.)	z_0/A (exact)
2.0	1.0	0.0973	0.1027
2.0	0.5	0.1494	0.1534
2.0	0.0	0.1790	0.1822
1.5	1.0	0.1036	0.1057
1.5	0.5	0.2213	0.2225
1.5	0.0	0.3371	0.3376

Iso-lines of z_0/A which are circular arcs for $h_y \leqq 1$, are shown in Fig. 4. If only h_y or h_z is given, z_0 is the greatest value attained if the unknown parameter varies freely. If h_y is given, z_0 reaches its maximum for $h_z=0$; if h_z is given the maximum of z_0 occurs on the light dashed line, which in the approximation of Eq. (2.17) is given by $h_z^2=h_y(h_y-1)$.

3 Two-Point Extremum Models

Now we assume that the complex magnetic fields h_1 and h_2 are given at the two surface points p_1 and p_2 with $p_2-p_1=d$, and that the electromagnetic field does not penetrate deeper than a given depth A. From these data we want to obtain the upper bound z_0 of the depth to the top of the anomalous conductivity. For this two-point problem the answer will remain incomplete since for certain combinations of the data triply connected conductors will be required, which cannot be handled with the present tools.

We are going to determine the mapping function $p(w)$, Eq. (2.33), depending on ψ_1 and ψ_2 with $p(w_k)=p_k$, $k=1,2$. The complete Lagrange function is (cf. Eq. (2.38))

$$\begin{aligned} L=\operatorname{Im}\Big\{ & -p_1+\lambda_d(p_2-p_1-d)+\lambda_A(p_1+ia-iA) \\ & +\sum_{k=1}^{2}\lambda_k(p_k'/g_k'-1/h_k)\Big\} \\ & +\int_0^\pi\{-\mu_1^-\tilde{\psi}_1+\mu_1^+(\tilde{\psi}_1-a)-\mu_2^-\psi_2+\mu_2^+(\psi_2-a)\}\,dt \\ & +\lambda_0\Big\{\int_0^\pi(\tilde{\psi}_1-\psi_2)\,dt-\pi b\Big\} \end{aligned} \tag{3.1}$$

The multiplieers λ_1, λ_2, and λ_d are complex, since each accounts for two constraints, whereas λ_A and λ_0 are real. The length $a=A-z_0$ is now explicitly treated as variable. Again, the linearity of L in $\tilde{\psi}_1$ and ψ_2 implies that these functions attain only the values 0 and a. In particular $\psi_2=0$, since ψ_2 has to be continuous. On the other hand, $\tilde{\psi}_1$ may have (at most) two jumps between 0 and a, occurring at the roots of the first variation of L with respect to $\tilde{\psi}_1$,

$$\begin{aligned} \operatorname{Im}\Big\{ & (1+\lambda_d-\lambda_A)\cdot\varphi(t-w_1)-\lambda_d\varphi(t-w_2) \\ & +\sum_{k=1}^{2}\lambda_k\varphi'(t-w_k)/g_k'\Big\}+\pi\lambda_0=0 \end{aligned} \tag{3.2}$$

Let these roots be γ_1 and γ_2 with $0\leqq\gamma_1\leqq\gamma_2\leqq\pi$, i.e.,

$$\tilde{\psi}_1(t)=\begin{cases} 0, & 0\leqq t\leqq\gamma_1 \\ a, & \gamma_1\leqq t\leqq\gamma_2 \\ 0, & \gamma_2\leqq t\leqq\pi \end{cases} \tag{3.3}$$

Then Eq. (2.35) yields $b=(\gamma_2-\gamma_1)a/\pi$ and the mapping according to Eq. (2.33) using Eq. (2.27) is

$$p(w)=\frac{a}{\pi}\left\{-(\gamma_2-\gamma_1)\varphi(w)+\log\frac{\vartheta_1(\gamma_1-w)}{\vartheta_1(\gamma_2-w)}\right\} \tag{3.4}$$

The model consists of two halfplanes at $z=z_0$ with a horizontal strip in the gap and a plane at $z=A$. It includes as limiting cases the extreme models (A) and (C) of Fig. 2, which correspond to $\alpha=\infty$ and $\gamma_1=0$, $\gamma_2=\pi$, respectively. To determine the model parameters for a given data set h_1, h_2, d, and A, the slightly modified Lagrange function

$$\begin{aligned} L=\operatorname{Im}\Big\{ & -p_1+\lambda_d(p_2-p_1-d)+\lambda_A(p_1+ia-iA) \\ & +\sum_{k=1}^{2}\tilde{\lambda}_k(g_k'/p_k'-h_k)\Big\} \end{aligned} \tag{3.5}$$

is used, differing from Eq. (3.1) in that, instead of the data kernels for $1/h_k$, the kernels for h_k are considered. The reason for this is that the associated $\tilde{\lambda}_k$ has an immediate interpretation, since the Lagrangian multipliers measure the sensitivity of the objective function z_0 to small changes in the data (Luenberger 1969, p. 221).

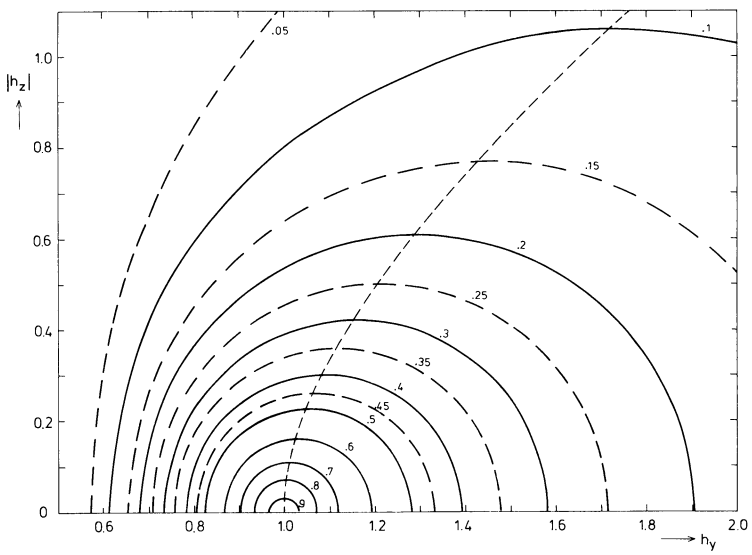

Fig. 4. Iso-lines for z_0/A (curve parameter) and the curve joining the maxima of the iso-lines. The latter curve is used if only h_z is given

In particular

$$\tilde{\lambda}_k=\frac{\partial z_0}{\partial h_{zk}}+i\,\frac{\partial z_0}{\partial h_{yk}},\qquad \mathrm{Im}\,\lambda_d=\partial_d z_0,\ \lambda_A=\partial_A z_0 \tag{3.6}$$

At an extremum, the partial derivatives of L with respect to real and imaginary part (if present) of the variables $\tilde{\lambda}_1$, $\tilde{\lambda}_2$, λ_d, λ_A, w_1, w_2, γ_1, γ_2, a and α have to vanish, yielding a system of fifteen equations (linear in the Lagrangian multipliers) for fifteen real unknowns. Also, Eq. (3.2) has to be satisfied for $t=\gamma_1, \gamma_2$, introducing λ_0 as an additional variable. It is easily verified that the two latter conditions and the conditions on the partial derivatives of L with respect to γ_1 and γ_2 provide only three independent equations, implying that Eq. (3.2) can be ignored (since λ_0 is of no interest).

As an example, for $h_1=(1.0,\ -0.5)$, $h_2=(1.5,\ 0.0)$ and $d/A=0.25$ we obtain

$$\tilde{\lambda}_1=(0.2113, 0.2672)\,A,\quad \tilde{\lambda}_2=(-0.1018,\ -0.0538)\,A$$
$$\lambda_d=(-0.3550, 0.3528),\quad \lambda_A=0.0694$$
$$w_1=(0.3387, 0.9118),\quad w_2=(2.9917, 1.1482)$$
$$\gamma_1=0.2389,\quad \gamma_2=2.3056,\quad a=0.8424\,A,\quad \alpha=3.8923$$

Hence, $z_0=0.1576\,A$. The abscissae of observation points and of halfplane and strip edges are, respectively, $-0.2241\,A$, $+0.0259\,A$; $-3.5008\,A$, $+1.1141\,A$; $-0.0623\,A$, $+0.0619\,A$. In a single-point extremum model h_1 and h_2 would yield $z_0/A=0.2213$ and 0.3376. This demonstrates that consideration of the field gradient can significantly improve the depth estimate. For different data, one might try to find the corresponding parameters by solving a sequence of problems, which gradually transform the above data into that required.

The doubly connected model breaks down if the solution of the system demands $\gamma_1<0$ or $\gamma_2>\pi$. In this case a triply connected model is required, where for $\gamma_1<0$ ($\gamma_2>\pi$) the two halfplanes at $z=z_0$ merge into a second strip to the right (left) of the first. It has not been possible to formulate the conditions under which a switch to triply connected conductors becomes necessary, in terms of the data. However, from

$$\partial_{\gamma_1} L=0\quad\text{or}\quad \partial_{\gamma_2} L=0$$

it is inferred that limiting models satisfy

$$\mathrm{Im}\,(\tilde{\lambda}_1 h_1+\tilde{\lambda}_2 h_2)=0 \tag{3.7}$$

Defining the vector

$$\mathbf{h}=(h_{y1}, h_{z1}, h_{y2}, h_{z2})\quad\text{and}\quad D=\mathbf{h}\cdot\nabla z_0(\mathbf{h})$$

Equations (3.7) and (3.6) imply that for limiting models $D=0$, i.e., at the corresponding magnetic field values the hyperplanes through the origin are tangential to the surface $z_0=\text{const}$. An analogue of condition (3.7) also holds for single-point problems, where it means that the switch from simply to doubly connected conductors occurs, where in Fig. 4 the lines through $(h_y, h_z)=0$ are tangential to the z_0-isolines, i.e., at $h_y=1$.

The two-point problem becomes particularly simple if A (and a) tends to infinity. In this case, the image of the plane $z=A$ reduces to a point, i.e., $\gamma_1\to\gamma_2(=\gamma)$ such that $b=(\gamma_2-\gamma_1)a/\pi$ remains finite. Expanding Eq. (3.4) at $\gamma=\gamma_1$ using Eq. (2.27),

$$p(w)=-b\{\varphi(w)+\varphi(\gamma-w)\} \tag{3.8}$$

The edges of the halfplanes ($v=0$) and of the strip ($v=\alpha/2$), defined by $p'(w)=0$, occur at $u=\gamma/2$ and $u=(\pi+\gamma)/2$. Knowing the type of the model, the extremal parameters for the data set h_1, h_2 and d can be inferred as follows:

The current flows in the same direction in halfplanes and the strip. This is obvious for physical reasons and can be deduced from

$$h_y(y, z_0)\,dy=g'(w)\,du>0\quad\text{for}\quad v=0\quad\text{and}\quad v=\alpha/2$$

(Eqs. (2.32), (2.30), (2.29)), implying that h_y is different in sign immediately above and below the conductors. Let $j(y)\geqq 0$ be the induced sheet-current density at $z=z_0$, normalized by H_n. Then the normalized magnetic field of internal origin at a surface point $p=y+iz_0$ is given by ($p_0=y_0$)

$$h(p)-\frac{1}{2}=\frac{i}{2\pi}\int_{-\infty}^{+\infty}\frac{j(y_0)\,dy_0}{p-p_0}$$

whence using Schwarz's inequality

$$\begin{aligned}|h_1-h_2|^2&=\frac{d^2}{4\pi^2}\left|\int_{-\infty}^{+\infty}\frac{j(y_0)\,dy_0}{(p_1-p_0)(p_2-p_0)}\right|^2\\&\leqq\frac{d^2}{4\pi^2}\int_{-\infty}^{+\infty}\frac{j(y_0)\,dy_0}{|p_1-p_0|^2}\cdot\int_{-\infty}^{+\infty}\frac{j(y_0)\,dy_0}{|p_2-p_0|^2}\\&=\frac{d^2}{4z_0^2}\,(2h_{y1}-1)(2h_{y2}-1)\end{aligned}$$

or

$$z_0\leqq\frac{\sqrt{(2h_{y1}-1)(2h_{y2}-1)}}{2|h_1-h_2|}\,d \tag{3.9}$$

Equation (3.9) provides an upper bound for z_0, where the equality sign holds for a line current. The upper bound is also attained if a uniform vertical magnetic field is added to the line current field. This field can be conceived as the magnetic field of induced currents in remote halfplanes at such a distance from the surface observation points that a uniform vertical field is observed.

The currents in the strip degenerate into a line current if $\alpha\to\infty$. In this limit Eq. (3.8) reduces to

$$p(w)=-b\{\cot w+\cot(\gamma-w)\} \tag{3.10}$$

The condition that the edges of the two halfplanes ($u=\gamma/2$ and $u=(\pi+\gamma)/2$), lying at

$$y=-2b\cot(\gamma/2)\quad\text{and}\quad y=+2b\tan(\gamma/2) \tag{3.11}$$

tend to $y=\pm\infty$ requires that $b\to\infty$, however in such a way that b/α is finite, ensuring according to Eq. (2.31) a finite total current in the strip. The latter limit implies, in view of Eq. (3.10), that at a point p (not at infinity) $v\to\infty$, leaving be^{-2v} finite. Hence, using Eq. (2.32) and taking all limits into account,

$$h(p)=\tfrac{1}{2}(1-i\cot\gamma)+\frac{ib}{\alpha p} \tag{3.12}$$

The first term is the inducing field, the second term the uniform vertical field from the induced currents in the remote halfplanes, and the third term the field of an induced line current at the origin of strength I, given by Eq. (2.31). A simple relationship between γ and the ratio of the distances to the edges of the halfplanes can be established by Eq. (3.11). By means of Eq. (3.12) for $p=p_1$ and $p=p_2$ the five parameters z_0, γ, b/α, y_1, and y_2 are easily adjusted to the five data h_1, h_2, and d. In particular, as expected,

$$z_0=\frac{\sqrt{(2h_{y1}-1)(2h_{y2}-1)}}{2|h_1-h_2|}\,d \tag{3.13}$$

Equation (3.13) assigns a depth z_0 to any data set, even if inconsistent (e.g., $h_{y1}=0.5$, $h_{y2}>0.5$) or pathologic ($h_{y1}=h_{y2}$, $h_{z1}>h_{z2}$, where $y_1\to\pm\infty$ for $h_{y2}=h_{y1}\mp 0$).

Although it is appealing that Eq. (3.13) depends on measurable data only, the absence of a priori assumptions renders it inefficient.

Finally, a comment on the triply connected domain with two horizontal strips at $z=z_0$, which is necessary for $\gamma_1<0$ or $\gamma_2>\pi$. Although the mapping is no longer univalent in this case, the value obtained for z_0 will still be very reliable, as in the single-point problem. As an alternative we may try to adjust the parameters of the model (of known type) by direct model calculations. For a sheet-current density $j(y)$ at $z=z_0$ the magnetic field is

$$h(p)=1+\frac{i}{2\pi}\int_{-\infty}^{+\infty}\left\{\frac{1}{p-y_0}-\frac{1}{p-(y_0-2ia)}\right\}j(y_0)\,dy_0 \tag{3.14}$$

The second term in the integral is the mirror image of j at $\mathrm{Im}\,p=-a$, where the imaginary part of the complex potential $f(p)$ has to vanish. Hence,

$$f(p)=p+ia+\frac{i}{2\pi}\int_{-\infty}^{+\infty}\log\left\{\frac{p-y_0}{p-y_0+2ia}\right\}j(y_0)\,dy_0$$

The condition $\mathrm{Im}\,f(p)=0$ for $y\in C$, where C is the union of conductors at the level $z=z_0$, then leads to the integral equation

$$a+\frac{1}{4\pi}\int_{-\infty}^{+\infty}\log\left\{\frac{(y-y_0)^2}{(y-y_0)^2+4a^2}\right\}j(y_0)\,dy_0=0,\qquad y\in C \tag{3.15}$$

which is easily solved, particularly if the edge singularities of j in a strip from y_1 to y_2 are isolated by assuming

$$j(y)=\tilde{j}(y)/\sqrt{(y_2-y)(y-y_1)},\qquad y\in(y_1,y_2)$$

4 An Application

In cooperation with U. Schmucker, parts of his magnetic field data collected during the IGY along north-south profiles across the North German conductivity anomaly (Schmucker 1959) have been reanalyzed with particular emphasis on the construction of a reasonable magnetic reference field (Weidelt 1978). Figure 5 presents the transfer functions h_y and h_z for a period of $T=1800$ s on the eastern profile. Of course, the out-of-phase component has to be ignored in the simple perfect conductor model.

The depth to the top of the anomalous conductivity causing this pronounced anomaly is most restricted by the magnetic fields at the three sites

GT (Göttingen): $h(\mathrm{GT})=(0.69,\,-0.20)$
FAL (Fallersleben): $h(\mathrm{FAL})=(1.06,\,-0.78)$
EBS (Ebstorf): $h(\mathrm{EBS})=(1.24,\,+0.07)$

at profile distances 99 km and 68 km apart.

First the two-point formula, Eq. (3.13) for $A=\infty$ is applied. The depth z_0 can be obtained for any two points of the profile. However, only the *smallest* value obtained is of geophysical interest. The pair FAL-EBS yields $z_0=50$ km and the pair GT-FAL $z_0=47$ km.

For more useful estimates we have to fix the depth A, which in the real geophysical situation can be approximately identified with a regional average of

$$\mathrm{Re}\,\{E_x(\omega)/(i\omega\mu_0 H_y(\omega))\}$$

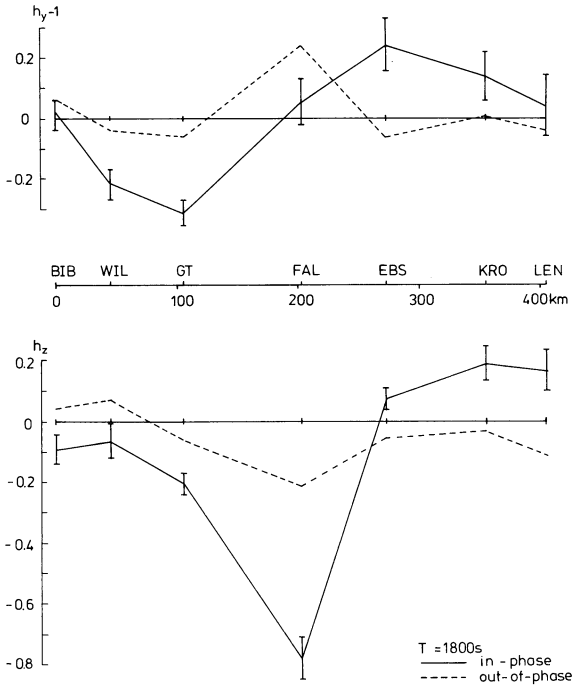

Fig. 5. Transfer functions and their standard variations on the eastern profile across the North German conductivity anomaly

for the frequency $\omega=2\pi/T$ (Schmucker 1970), where E_x is the horizontal electric field perpendicular to H_y. Taking $A=200$ km, the site FAL is the most restricting for the single-point problem, yielding according to Fig. 4 $z_0=24$ km. To a minor extent, the depth is also restricted by the low h_y(GT)-value ($z_0=34$ km).

Proceeding to two-point problems with finite A, the stations FAL-EBS reduce z_0 to 22 km, and the sites GT-FAL reduce it even further to 17.7 km. In the latter case the extremal model consists at the level z_0 of a conducting strip between 18 km and 133 km north of FAL and two remote halfplanes with edges 431 km south and 719 km north of FAL and of a conducting plane at the level A. The Lagrange multiplier $\lambda_A=0.05$ indicates that an increase of the poorly known depth A by 50 km (say) would increase z_0 by about 2.5 km.

It should be emphasized that the actual extremal model, which fits only a few data, is not of great interest. The only relevant information is the number $z_0=17.7$ km, meaning that any two-dimensional perfect conductor model with $A=200$ km explaining the data will show a conductor shallower than z_0. The data errors introduce into z_0 an uncertainty of at most ± 5.6 km, as can be deduced from $\tilde{\lambda}_1$ and $\tilde{\lambda}_2$.

5 Conclusions

The extremal models, which have been constructed for $N=1$ or 2 observation points, consist of a conducting plane at a given depth $z=A$ and either N gaps or N conducting strips at the level $z=z_0$. Apart from transition models, strips and gaps are of finite lateral extent. Including z_0, the coordinates of the edges with respect to the observation points are specified by $2N+1$ real constants. $2N$ equations are furnished by the data and the last by an extremal condition (not given explicitly for $N=2$).

The above results can be generalized to arbitrary N, yielding an M-connected conductor ($M=N$ or $N+1$). The exterior of the conductors is mapped by a univalent mapping onto the exterior of M parallel slits with pre-assigned inclination to the real axis (Goluzin 1969, pp. 210, 275). Although some insight into the general structure of the problem is obtained by considering arbitrary N, the problem is not open to simple numerical treatment. However, knowing the structure of the extremal model, the problem may be handled by Eqs. (3.14) and (3.15): Pre-assigning a small value of z_0, we try to infer the $2N$ edge coordinates from the $2N$ data, which is a nonlinear problem. If a set of coordinates can be found, z_0 is gradually increased until a solution is no longer obtained. The limiting value of z_0 will be considered as the best possible estimate.

A more urgent need than the generalization to arbitrary N is the generalization to conductors of finite conductivity, incorporating the out-of-phase component of the transfer functions into rating the out-of-phase component of the transfer functions into the data. These models will certainly considerably improve the depth estimate. Although the above results may serve as guidelines, the method of solution must be quite different from that presented here. Perhaps the method of analytic continuation of electromagnetic fields, as developed by Zdhanov (1980), may turn out to be quite useful.

Acknowledgements. I would like to thank the two referees for their helpful criticism.

References

Abramowitz, M., Stegun, I.A.: Handbook of mathematical functions. New York: Dover Publications 1965

Barcilon, V.: Ideal solution of an inverse normal mode problem with finite spectral data. Geophys. J.R. Astron. Soc. **56**, 399–408, 1979

Bott, M.H.P., Smith, R.A.: The estimation of the limiting depth of gravitating bodies. Geophys. Prospect **6**, 1–10, 1958

Goluzin, G.M.: Geometric theory of functions of a complex variable. Transl. Math. Monographs, Vol. 26. Providence: Amer. Math. Soc. 1969

Huestis, S.P.: Extremal temperature bounds from surface gradient measurements. Geophys. J.R. Astron. Soc. **58**, 249–260, 1979

Koppenfels, W.v., Stallmann, F.: Praxis der konformen Abbildung. Grundlehren Math. Wiss., Vol. 100. Berlin: Springer 1959

Luenberger, D.G.: Optimization by vector space methods. New York: Wiley 1969

Parker, R.L.: Inverse theory with grossly inadequate data. Geophys. J.R. Astron. Soc. **29**, 123–138, 1972

Parker, R.L.: Best bounds on density and depth from gravity data. Geophysics **29**, 123–138, 1974

Parker, R.L.: The theory of ideal bodies for gravity interpretation. Geophys. J.R. Astron. Soc. **42**, 315–334, 1975

Rietsch, E.: Extreme models from the maximum entropy formulation of inverse problems. J. Geophys. **44**, 273–275, 1978

Sabatier, P.C.: Positivity constraints in linear inverse problems, parts I and II. Geophys. J.R. Astron. Soc. **48**, 415–469, 1977a, b

Sabatier, P.C.: On geophysical inverse problems and constraints J. Geophys. **43**, 115–137, 1977c

Safon, C., Vasseur, G., Cuer, M.: Some applications of linear programming to the inverse gravity problem. Geophysics **42**, 1215–1229, 1977

Schmucker, U.: Erdmagnetische Tiefensondierung in Deutschland 1957/59: Magnetogramme und erste Auswertung. Abh. Akad. Wiss. Göttingen, Math.-Phys. Kl. Beitr. z. IGJ, Heft 5, 1959

Schmucker, U.: Anomalies of geomagnetic variations in the southwestern United States. Bull. Scripps Inst. Oceanogr. **13**, 1–165, 1970

Smith, R.A.: Some depth formulae for local magnetic and gravity anomalies. Geophys. Prospect **7**, 55–63, 1959

Smith, R.A.: Some formulae for interpreting local gravity anomalies. Geophys. Prospect **8**, 607–613, 1960

Weidelt, P.: Entwicklung und Erprobung eines Verfahrens zur Inversion zweidimensionaler Leitfähigkeitsstrukturen in E-Polarisation. Habilitationsschrift, Math.-Nat. Fak. Univ. Göttingen 1978

Whittaker, E.T., Watson, G.N.: A course of modern analysis, 4th edn. London: Cambridge University Press 1927

Zdhanov, M.S.: Cauchy integral analogues for the separation and continuation of electromagnetic fields within conducting matter. Geophys. Surv. **4**, 115–136, 1980

Received October 23, 1980; Revised Version January 27, 1981
Accepted January 27, 1981

J Geophys (1981) 49:226–233

Journal of Geophysics

On a Type Classification of Lower Crustal Layers Under Precambrian Regions

A.G. Jones
Institut für Geophysik der Westfälischen Wilhelms-Universität, Gievenbecker Weg 61, D-4400 Münster, Federal Republic of Germany

Abstract. Various parameters pertinent to the lower crustal layer under Precambrian regions are listed for locations where seismic, and geomagnetic or geoelectric, studies have been undertaken. The parameters define three distinct types of lower crustal layer with certain dominant characteristics: Type I – "Normal" – typical continental seismic parameters and a high electrical resistivity (10^3–10^4 Ωm); Type II – "Intermediate" – high compressional wave velocity (either fixed $V_p = 7.0$ km s^{-1} or transitional $V_p = 6.7 \rightarrow 7.3$ km s^{-1}) and a moderate resistivity (100–300 Ωm); Type III – "Low" – a low shear wave velocity layer (LV_sL), high Poisson's ratio (> 0.30) and low electrical resistivity (10–50 Ωm). Possible conditions and rock types, existing at the P–T environment of the lower crust and which could account for the observations, are suggested. The zoning of Canada into types implies that Type II layers are shield "edge" effects, and that inability to observe what is regarded as the final stage of development of a shield region under certain shields may be due to their being too small.

Key words: Precambrian regions – Crustal structure – Electromagnetic induction studies – Seismic studies

Introduction

Various seismic and electrical studies over Precambrian regions of the world have been able in the past to detail some of the parameters of the lower crustal layers, e.g., compressional wave velocity (V_p), shear wave velocity (V_s), density (ρ), Poisson's ratio (σ) from multi-method seismic studies, and electrical resistivity (R – the normal symbol for electrical resistivity ρ is not used to avoid confusion with density) from geoelectric and geomagnetic methods. However, confusion is often apparent in the literature as to why certain features are found in some parts of the world, but not in others. This confusion is perhaps highlighted by Kovtun (1976) who states, with reference to geomagnetic studies, that "at present, we have almost no results on which a study of the 'normal' distribution of conductivity vs depth in Precambrian shields could be based"

It is with these points in mind, that the author has attempted a broad classification of lower crustal Precambrian layers into three types. In the following section, each of these types will be described in turn and examples of their locations will be specified. The locations and their corresponding data sets, both seismic and geoelectric, were chosen for the following reasons:

(i) all come from stable regions of low seismicity and heat flow,
(ii) the data sets have all been thoroughly scrutinized by the groups involved, and
(iii) the information is readily available.

Finally, possible candidates for the rocks at lower crustal depths causing the various observed responses are suggested.

Classification

Type I – "Normal"

The prime example of a Type I lower crustal layer is that observed in the centre of the Canadian shield. Seismic models presented by Wickens and Buchbinder (1980), based on surface waves (Wickens 1971) and refraction information (Mereu and Hunter 1969), Hall and Hajnal (1973), and Green et al. (1980), representative of middle and northern Manitoba, are illustrated in Fig. 1a, and their estimated parameters for the lower crustal layer are detailed in Table 1. The model of Wickens and Buchbinder (1980) was shown by them to be consistent with the S-wave residuals observed in the central shield region.

A transient electromagnetic sounding investigation undertaken by Jacobson (1969; reported in Keller 1971) in Manitoba inferred that there must exist a layer of uniform resistivity, of $R \simeq 2{,}000$ Ωm, to depths greater than 20 km, whilst magnetotelluric (MT) investigations by three groups in Alberta (Srivastava and Jacobs 1964; Vozoff and Ellis 1966; Reddy and Rankin 1971) all infer resistivities for this layer of 10^3–10^4 Ωm.

It appears that the Ukrainian shield also falls into this Type I category. Models P2 and P3 of Jentsch (1979) display a lower crustal layer with $V_p = 6.2$–6.4 km s^{-1} (the very thin transitional layer between 32.5–33.4 km depth, of velocity increase from 6.8 to 7.6 km s^{-1} can be ignored for this comparison), and the data from the majority of magnetotelluric stations recorded by Tkachev (1973; reported in Kovtun 1976) display apparent resistivities of greater than 10^3 Ωm over the period range 1–10^3 s. Such values require a highly resistive crust, i.e., resistivity greater than about 4,000 Ωm.

The heat flow observed on the Canadian shield is, on average, 39 mW m^{-2} (Rao and Jessop 1975), i.e., 0.93 HFU, whilst on the Ukranian shield values of 25–35 mW m^{-2} (Kutas et al. 1979), i.e., 0.60–0.84 HFU, are reported.

Type II – "Intermediate"

The three main examples of a Type II lower crust are to be found in northern Scotland, eastern Canada, and northern Sweden. No heat flow estimates are available for northern Scotland (Bloomer

0340-062X/81/0049/0226/$01.60

Table 1. Lower crustal parameters as inferred by the investigations reported in the text

Type	Code	Area	Parameters					Reference
			V_p (km s ^{1})	V_s (km s^{-1})	ρ (g cm^{-3})	σ	R (Ωm)	
I	W	Central Canadian shield	6.6	3.8		0.252[a]		Wickens and Buchbinder (1980)
	G		6.55					Green et al. (1980)
	HA		6.85	4.0		0.241[a]		Hall and Hajnal (1973)
	JA	Manitoba					2,000	Jacobson (1969)
	SR	Alberta					940	Srivastava and Jacobs (1964)
	R	Alberta					3,500	Reddy and Rankin (1971)
	VO	Alberta					10,000	Vozoff and Ellis (1966)
	JE	Ukrainian shield	6.4					Jentsch (1979)
	T						>4,000	Tkachev (1973)
II	BA	Northern Scotland	7.0					Bamford et al. (1978)
	A			4.04[a]		0.249		Assumpção and Bamford (1978)
	H						100–300	Hutton et al. (1980, 1981)
	O	Southern Superior Province	7.0–7.2					O'Brien (1968)
	ST						50–1,500	Sternberg (1979)
	B1	Eastern Superior Province	6.7→7.1					Berry and Fuchs (1973)
	HA	Southwestern Superior Province	7.1 ± 0.04					Hall and Hajnal (1973)
	G	Southern Churchill Province	7.1, 7.2					Green et al. (1980)
	B2	Northern Grenville Province	6.7→7.5					Berry and Fuchs (1973)
	KU	Grenville Province					200	Kurtz and Garland (1976)
	D	Superior Province					270	Duncan et al. (1980)
	JO	Southeastern Grenville Province	7.14	4.11	3.11	0.25		Jordan and Frazer (1975)
	J	Northern Sweden	6.75→7.15					Hirschleber et al. (1975)
			~7					Lund (1970)
							140–450	Jones (1981)
		Southern Norway	7.17					Massé and Alexander (1974)
III	BL	Southeastern Africa	6.8	3.75–3.85	2.95	0.28[a]		Block et al. (1969)
	V						10–50	van Zijl (1977)
	B						50	Blohm et al. (1977)
	JO	Southeastern Grenville Province	>6.8	3.4	3.11	>0.30		Jordan and Frazer (1975)
	C						10–30	Connerney et al. (1980), Connerney and Kuckes (1980)

[a] denotes a calculated value assuming perfect elasticity on the rock

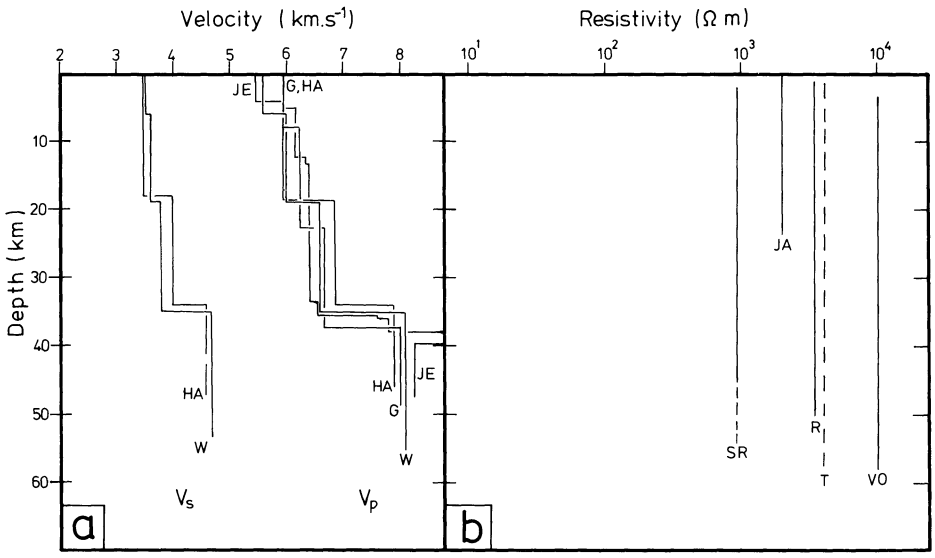

Fig. 1. a Seismic profiles as determined by several investigations over Type I lower crustal layers (for key see Table 1). **b** Resistivity profiles for the same locations as in **a**, dashed lines denote minimum values

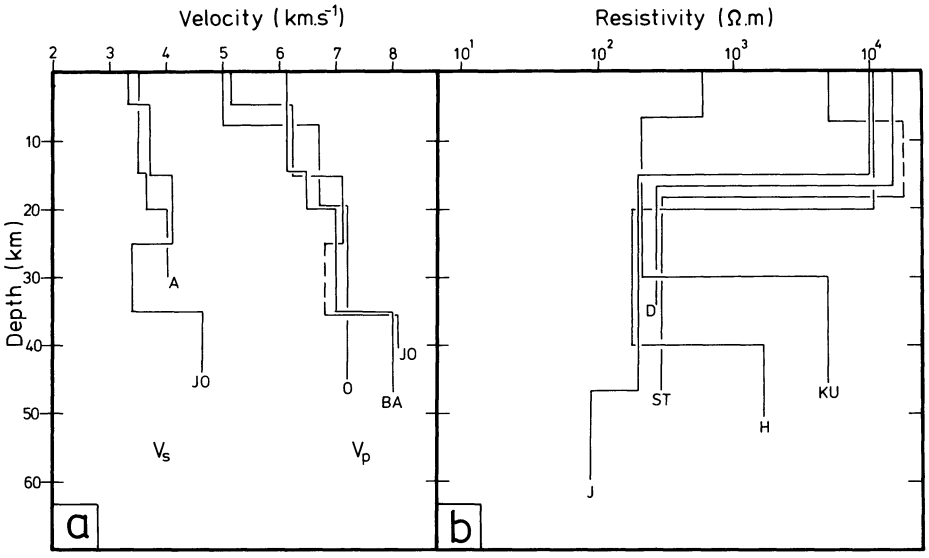

Fig. 2. a, b as Fig. 1 but for investigations over Type II lower crustal layers

et al. 1979), but in eastern Canada values of 40–50 mW m^{-2} (1.0–1.25 HFU) are most commonly observed (Lachenbruch and Sass 1977), and in northern Sweden 38–47 mW m^{-2} (0.91–1.12 HFU) are reported (Eriksson and Malmquist 1979).

In northern Scotland there exists between the Highland Boundary Fault and the Great Glen Fault a lower crustal layer with $V_p = 7.0$ km s^{-1} (Bamford et al. 1978) and $\sigma = 0.249$ (Assumpção and Bamford 1978), giving a calculated $V_s = 4.04$ km s^{-1}, which corresponds with a layer of electrical resistivity $R = 100$–300 Ωm (Hutton et al. 1980, 1981). The original seismic interpretation of this layer was of a velocity gradient layer from 6.7 to 7.3 km s^{-1} (Bamford et al. 1976), but such a layer was later found not to be consistent with ray-tracing and a uniform layer of 7.0 km s^{-1} was found to be most effective (Bamford et al. 1978).

In eastern Canada, various seismic and geomagnetic studies have been carried out. In southern Superior Province, O'Brien (1968) reported a zone with $V_p = 7.0$–7.2 km s^{-1} at a depth of 19.5 km for stations on the north eastern side of Lake Superior, whilst Berry and Fuchs (1973; reproduced in Berry and Mair 1977) interpret their data as inferring a velocity gradient layer with $V_p = 6.7 \rightarrow 7.5$ km s^{-1} between 27–40 km depth. This layer correlates with a geoelectric layer of 270 Ωm, the top of which deepens from 19 km in the south-west to 29 km in the north-east, defined by Duncan et al. (1980) for the region around Timmins, and with a layer of $R = 50$–$1{,}500$ Ωm for Wisconsin found by Sternberg (1979).

In Grenville Province, Berry and Fuchs (1973) find another velocity gradient layer with $V_p = 6.7 \rightarrow 7.1$ km s^{-1} between 22–40 km, whilst Jordan and Frazer (1975) report a layer between 15–25 km with $V_p = 7.14$ km s^{-1} and $V_s = 4.11$ km s^{-1}. The 2-dimensional geoelectric model for eastern Canada presented by Kurtz and Garland (1976) has a uniform crust under Grenville Province of $R = 200$ Ωm.

In northern Sweden, the best fitting gradient model to the "Blue Road" seismic data includes a layer with V_p increasing from 6.5 km s^{-1} at 20 km depth to $V_p = 7.15$ km s^{-1} at 42 km depth (Hirschleber et al. 1975). Values of around 7 km s^{-1} for the bottom crustal layer were confirmed in a more sophisticated analysis of the data by Lund (1979). Monte-Carlo inversion (Jones and Hutton 1979) of the geomagnetic response function observed at Kiruna (Jones 1980), with the constraints that i) the top layer have a resistance of 10^4 Ωm (Westerlund 1972) and ii) that the second interface be at 46 km, to correspond with the latest values of Moho depth (Bungum et al. 1980), yielded a lower crustal layer of $R = 140$–450 Ωm (Jones 1981).

Type III – "Low"

The two examples for a Type III lower crustal layer are from the Adirondacks, New York State, and the southeastern African shield region.

In the Adirondacks, a joint controlled-source and horizontal spatial gradient (HSG) investigation by Connerney et al. (1980) and Connerney and Kuckes (1980) determined a zone of low electrical resistivity (L*R*L – low resistivity layer) of $R = 10$–30 Ωm at a depth of 25–34 km. This is exactly the depth at which Jordan and Frazer (1975) interpret a shear wave low velocity layer (LV_sL) from S_p phases for stations mostly situated close to Ottawa. The studies of Jordan and Frazer inferred that the layer must have a *minimum* Poisson's ratio of $\sigma = 0.30$, hence the value of the compressional wave velocity for the layer $V_p = 6.80$ km s^{-1} is to be regarded as a minimum. Thus, the existence of a compresssional wave low velocity layer (LV_pL) is not proven, but the existence of an LV_sL has been confirmed by Wickens and Buchbinder (1980).

Two geoelectric studies on southern African cratons inferred L*R*Ls. These were on the Kaapvaal craton (van Zijl 1977) and the Zimbabwe (formerly Rhodesian) craton (Blohm et al. 1977). Data from the Limpopo mobile belt also were explained in terms of an L*R*L, but heat flow estimates on mobile belts have been observed to be anomalously high when compared with cratonic terrains (Carte and van Rooyen 1969) hence the model is not included here. Bloch et al. (1969), in an analysis of surface waves observed by an array of seismometers centered on Johannesburg, infer from their data the existence of two LV_sLs, one at 12 km and the other at 24 km (Fig. 3a). The depth of the deeper LV_sL corresponds exactly to the depth of the L*R*L as interpreted by Blohm et al. (1977), and the L*R*L under the Limpopo mobile belt (van Zijl 1977). It may be significant that the model of Bloch et al. (1969) does not display an LV_pL.

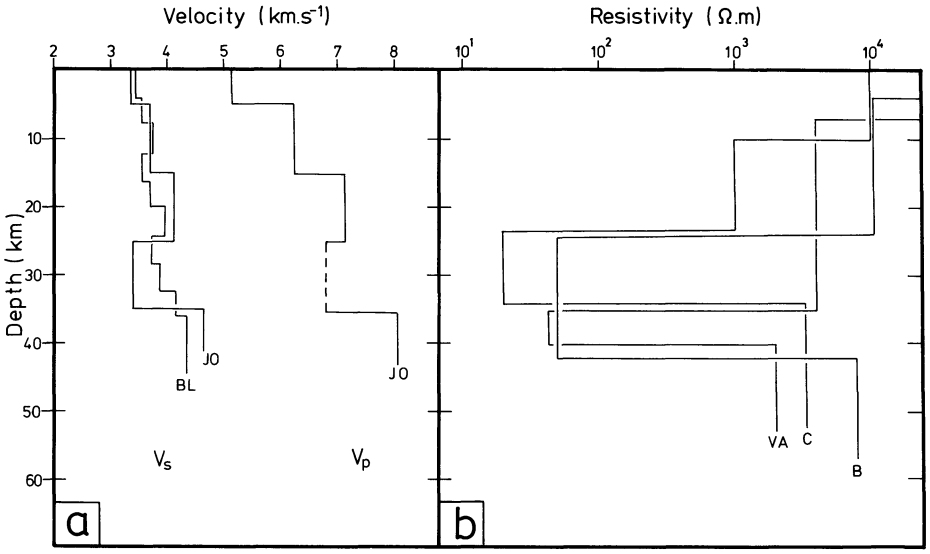

Fig. 3. a, b as Fig. 1 but for investigations over Type III lower crustal layers

Discussion

The notable characteristics of the three types classified are:

a) Type I – Normal

- typical continental V_p, V_s and σ values
- highly resistive, i.e., greater than 10^3 Ωm.

b) Type II – Intermediate

- V_p of around 7.0 km s^{-1}, either fixed (northern Scotland) or transitional from 6.7 → 7.2 km s^{-1} (eastern Canada, northern Sweden)
- typical σ values of around 0.25
- moderately resistive, R=100–300 Ωm.

c) Type III – Low

- low shear wave velocity layer (LV_sL), possibly without a corresponding low compressional wave velocity (no LV_pL)
- high Poisson's ratio, of $\sigma > 0.30$
- highly conductive, with R=10–50 Ωm.

The association of LV_pL layers with LRL layers in more tectonic regions has been known since the early 1970's (see, for example, Landisman et al. 1971), even though the existence of both was initially in question (Healy 1971; Porath 1971). Many theories have been proposed to explain these layers, the two most often mentioned being the rôle of water of dehydration escaping into pore spaces (Hyndman and Hyndman 1968), or of hydrated rocks under typical P–T conditions in the lower crust (Landisman et al. 1971; Jordan and Frazer 1975). For Precambrian regions, the former of these is however considered untenable (see later).

At Moho depths under the centre of the Canadian shield (~ 35 km, Wickens and Buchbinder 1980), the temperature is believed to be in the range 400°–500° C (Rao and Jessop 1975), preferably towards the upper end of this limit (475° C as given by Eq. (5) of Hall 1977), with a pressure of around 10 kbar (9.5 kbar, Eq. (7), Hall 1977). At such P–T and anhydrous conditions, eclogite is the stable mineral assemblage for basalt of quartz tholeiite composition, rather than garnet granulite (Ringwood 1975, p. 25, Figs. 1–6). However, the inferred compressional wave velocities for eclogite under these P–T conditions, of V_p=7.8–8.6 km s^{-1} (Press 1966, Table 9–2; Manghnani et al. 1974; Christensen 1979), require the presence of large amounts of minerals of relatively low V_p, e.g., quartz and alkali feldspars (Ringwood 1975, p. 39). This implies a dioritic rock in the granulite-eclogite facies as a suitable candidate, e.g., quartz diorite, V_p=6.71 km s^{-1}, V_s=3.8 km s^{-1} (Press 1966, Tables 9–2 and 9–3), ρ=2.68–2.96 g cm^{-3} (Daly et al. 1966, Table 4.1). Measurements of electrical conductivity on alkali basalts at 500° C indicate values in the range $R=10^3$–10^4 Ωm (Bondarenko and Galdin 1972; reported in Haak 1980) whilst Volarovich and Parkhomenko (1976) specify a range of $R=10^4$–10^5 Ωm for granodiorites, quartz diorites and diorites at this temperature.

The compressional wave velocity for the Type II layer, V_p= 6.8 → 7.2 km s^{-1}, can be explained by either a garnet granulite in an anhydrous crust, as suggested by Manghnani et al. (1974) and Ringwood (1975, p. 39), or by amphibolites in a hydrous crust (Ringwood 1975, p. 41). Measurements of Poisson's ratio at 10 kbar by Manghnani et al. (1974) on their garnet granulite samples give a mean of $\bar{\sigma}=0.282\pm0.017$ (one standard deviation), which is too large compared with field observations (northern Scotland, $\sigma=0.249\pm0.020$, Assumpção and Bamford 1978; eastern Canada, $\sigma=0.25$, Jordan and Frazer 1975). Also, the electrical resistivity of the majority of dry rocks expected to be found at lower-crustal depths under Precambrian regions is never below 10^3 Ωm for temperatures less than 500° C (Brace 1971, Fig. 3; Haak 1980), with the notable exception of a Wisconsin gabbro with R=650 Ωm at T=500° C (Housley and Oliver 1977). The effects of increasing the pressure to 10 kbar at this temperature were shown by Volarovich and Parkhomenko (1976) to have little effect on the electrical conductivity, i.e., less than one third an order of magnitude. However, Ringwood (1975, pp. 35–47) believes that gabbro is not stable at the P–T conditions of the lower crust. Seismic evidence appears to confirm this suggestion because although gabbros display compressional wave velocities of the correct order when at 10 kbar (V_p ~ 7.2 km s^{-1}, Press 1966, Table 9–2), the effects of temperature will reduce this to V_p ~ 6.8 km s^{-1} (Press 1966, Fig. 9–7; Christensen 1979). Also, gabbros do not show sufficiently large shear wave velocities, e.g., V_s= 3.84 km s^{-1} (Press 1966, Table 9–4). Thus, having apparently disqualified all suitable rocks that might exist in an anhydrous lower crust, it is necessary to conclude that hydrous conditions prevail

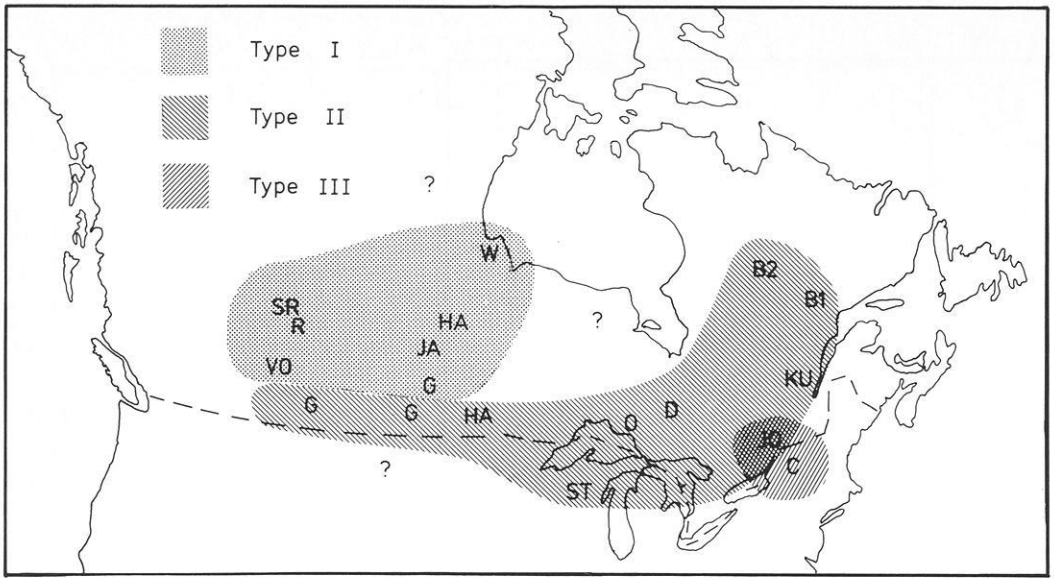

Fig. 4. Sketch map of Canada illustrating the zones of lower crustal layers, letters refer to investigations as reported in the text (see Table 1)

in Type II lower crustal layers. Amphibolites, as suggested by Ringwood (1975, p. 41) as the probable rock at the P–T conditions of a hydrous lower crust, display the correct order of seismic velocities (V_p=7.18–7.22 km s^{-1}, Christensen 1965; V_s= 4.03 km s^{-1}, Christensen 1966) but it is probably necessary to infer a slightly seismically faster epidote amphibolite (V_p=7.67–7.75 km s^{-1}, Christensen 1965) due to the reduction in velocities at temperatures of around 400–500° C (Christensen 1979). Unfortunately, not many measurements of the electrical resistivity of amphibolites at these P–T conditions have been made, but the data of Volarovich and Parkhomenko (1976) illustrate that certain amphibolites display the required resistivity of a few hundreds of Ωm at 500° C.

For the Type III lower crustal layer, Jordan and Frazer (1975), van Zijl (1977), and Connerney et al. (1980) all independently suggested the effects of serpentinisation to explain their data. Jordan and Frazer (1975) observe that a serpentinised peridotite has the high Poisson's ratio required, and van Zijl (1977) and Connerney et al. (1980) both remark that serpentinised rocks display the appropriately low resistivities, of 10–50 Ωm, provided that the water of hydration does not escape (Zablocki 1964; see van Zijl 1977).

An interpretation of the high conductivities observed in Type III crusts in terms of electrolytic conduction is considered untenable by Connerney et al. (1980) because investigations by Richter and Simmons (1977) on Precambrian igneous rocks showed that the majority of the original cracks were healed or sealed by secondary minerals. However, the somewhat speculative models presented by Dewey (1969a) and Ringwood (1975, p. 298–304) for the development of a Benioff zone require, as a passive initial state, a thick accumulation of sediments, the prime example of which is the non-volcanic margin of the spreading Atlantic Ocean (Drake et al. 1959). Assuming that the east coast of North America represents such an initial state, and considering that there is much support in the Appalachians for a progressive migration of deformation and metamorphism towards the stable continental foreland (Dewey 1969b), it is not inconceivable that the lower foreland crust be fractured and fissured. If so, then electrolytic conduction effects would become significant, which would explain the results of Connerney et al. (1980) for the Adirondacks, and also those of Edwards and Greenhouse (1975), of a highly conducting lower crustal layer, R=2 Ωm, underlying the southern Appalachians.

An eigenparameter investigation by Edwards et al. (1980) of the model presented by Blohm et al. (1977) revealed that the resistivity and depth of the lower crustal conducting layer are not independently estimated when geoelectric sounding data are inverted. The resolvable eigenparameter pertinent to this layer is the layer's depth-integrated conductivity, i.e., thickness-conductivity product. Hence it may be possible that the data of van Zijl (1977) and Blohm et al. (1977) are also consistent with a slightly less conducting but thicker zone of Type II class. A similar possibility cannot be suggested for the conducting zone delineated by Connerney and Kuckes (1980) and Connerney et al. (1980) as their controlled-source electromagnetic induction experiment inferred a resistivity in the range R=12.5–25 Ωm for this layer. The conductance of this layer was defined by Horizontal Spatial Gradient (HSG) data as being approximately 400 S (Connerney and Kuckes 1980), hence inferring a thickness of 5–10 km. This estimate is fully consistent with the 10 km thick LV_sL delineated by Jordan and Frazer (1975).

There is evidence from Jordan and Frazer (1975) that a Type III crustal layer underlies a Type II layer. The data from Berry and Fuchs (1972) and Kurtz and Garland (1976) imply that the Type III layer pinches out to the north, leaving solely a Type II layer, and the work of Connerney et al. (1980) suggests the opposite is true on going further southeast, i.e., that the Type II layer pinches out and a Type III layer exists alone. For the Canadian shield, a sketch map is shown in Fig. 4 illustrating the lower crustal layers as classified in this paper. The illustration includes the recent results of Green et al. (1980) with a layer of V_p=7.1–7.2 km s^{-1} underlying southeastern Churchill Province at a depth of 36–45 km and those of Hall and Hajnal (1973) of a layer with V_p=7.1±0.04 km s^{-1}, observed south of Lake Winnipeg.

It is apparent from Fig. 4 that a Type II lower crustal layer is an "edge" phenomenon of the Canadian shield, where "edge" means not the actual physical boundary of the shield, but a wide zone encompassing the central core of the shield. This may be evidence of a general feature of shield regions in that their centres

Table 2. Classification system with values of the parameters inferred for the lower crustal layer and conditions and possible candidates for the rock responsible

Classification	Parameters					Conditions and possible rock types
	V_p (km s^{-1})	V_s (km s^{-1})	ρ (g cm^{-3})	σ	R (Ωm)	
Type I "Normal"	6.6	3.8		0.25	10^3–10^4	Anhydrous: Quartz Diorite
Type II "Intermediate"	6.8→7.3	4.1	3.11	0.25	100–300	Hydrous: Amphibolite
Type III "Low"	6.8	3.4–3.7	3.11	>0.30	10–50	Hydrous: Serpentinite

have evolved into what is regarded as the final stage of development of a continental plate (see, for example, Hyndman and Hyndman 1968) whilst their edges develop much more slowly due to their tectonic juxtaposition to other environments. This is in agreement with the classification that the "edge" of the Fennoscandian shield, as inferred not only in northern Sweden (see above) but also by Massé and Alexander's (1974) reinterpretation of Sellevoll and Warrick's (1971) data revealing a lower crustal layer of between 21.8–42.2 km depth with $V_p = 7.17 \pm 0.05$ km s^{-1} for southern Norway, displays a Type II lower crustal layer. Such an interpretation of the information described by Fig. 4 leads naturally to the suggestion that there may be a size criterion involved, in that if a shield is below a certain size, it may never evolve into the final stage, hence explaining the southeast African data.

It is possible that a different explanation is required for the existence of the Type II lower crustal layer observed in northern Scotland, as the temperature at the depth of the transition from high to intermediate resistivities could be of the order of 500° C (Hutton et al. 1980), leading to a hotter Moho boundary than herein discussed. However, the tectonic equivalence of northern Scotland and the Grenville Province of eastern Canada, i.e., both zones belonged to the same continent before the closure of the Early Paleozoic Iapetus Ocean, has been noted by many authors (see, for example, Phillips et al. 1976; Jones and Hutton 1979; Keen and Hyndman 1979; Williams 1979) and hence it is not too surprising that they should display the same type of lower crustal layer.

Conclusions

From this comparison of seismic and electric investigations over various Precambrian regions of the world, it appears that the data may be classified into three distinct groupings with regard to their information content concerning the lower crustal layer. The descriptive parameters of each of these three types are listed in Table 2, together with possible conditions and rock types that display the required characteristics in the P–T environments involved.

The zoning of the Canadian shield region implies that the Type I layer should be expected in the centre of large shields, surrounded by a Type II layer. This suggests that there may be some size criterion, in that if a shield is too small it does not fully develop to a Type I crust, which may be regarded as the end stage of a development process (Hyndman and Hyndman 1968).

The Type III lower crustal layer requires a more complete explanation, especially in terms of the high values of conductivity associated with it. The two observations reported here may be local effects, in that both have radically differing explanations (possible fracturing due to the passive initial state of Benioff zone development in eastern North America?), or may be global effects, e.g., that the layer is another edge effect of a shield region.

It must be remarked that it is not expected that all Precambrian lower crustal layers fall into one of the three general categories detailed in Table 2. One seemingly notable exception to this classification is the East European Platform. Seismic models of this platform include a lower crustal layer with $V_p = 6.8$–7.2 km s^{-1} (Bozhko and Starovoit 1969; Kosminskaya and Pavlenkova 1979; Pavlenkova 1979; Patton 1980), hence defining it as Type II. However, magnetotelluric data (Kovtun and Chicherina 1969), particularly the "generalised curve" for the region (Vanyan et al. 1977), imply a highly resistive crust, i.e., a Type I lower crustal layer. This latter result is, in the opinion of the author, not totally conclusive as it is based solely on apparent resistivity information, whereas the magnetotelluric phase is far more discriminating between Types I, II, and III.

Finally, this study has shown the decided advantages of undertaking cooperative seismic and geomagnetic or geoelectric measurements in the same area. Independent interpretations of the data recorded may differ wildly, hence either, or both, may be wildly wrong. This may be particularly true for seismic data from shield regions because, as noted by Pavlenkova (1979), compressional wave velocities of between 6.6–7.7 km s^{-1} are not usually observed in the first arrivals, hence implying that seismically Type II layers are difficult to delineate. A good example of this is Massé and Alexander's (1974) reinterpretation of Sellevoll and Warrick's (1971) data from southern Norway. The initial model had a lower crustal layer of $V_p = 6.51$ km s^{-1} (Sellevoll and Warrick 1971), whereas a more sophisticated analysis gave a value of $V_p = 7.17$ km s^{-1} (Massé and Alexander 1974). Joint interpretation of dual data sets, in the manner described in this work, is likely to reduce drastically the number of possible likely candidates for the lower crustal layer.

Acknowledgements. The author wishes to express his gratitude to Drs. Haak, Prodehl, and Wright for critical comments on an earlier version of this manuscript. The Deutsche Forschungsgemeinschaft is thanked for financial support.

References

Assumpção, M., Bamford, D.: LISPB – V. Studies of crustal shear waves. Geophys. J.R. Astron. Soc. **54**, 61–74, 1978

Bamford, D., Faber, S., Jacob, B., Kaminski, W., Nunn, K., Prodehl, C., Fuchs, K., King, R., Willmore, P.: A lithospheric profile in Britain – I. Preliminary results. Geophys. J.R. Astron. Soc. **44**, 145–160, 1976

Bamford, D., Nunn, K., Prodehl, C., Jacob, B.: LISPB – IV. Crustal structure of Northern Britain. Geophys. J.R. Astron. Soc. **54**, 43–60, 1978

Berry, M.J., Fuchs, K.: Crustal structure of the Superior and Grenville provinces of the northeastern Canadian shield. Bull. Seismol. Soc. Am. **63**, 1393–1432, 1973

Berry, M.J., Mair, J.A.: The nature of the Earth's crust in Canada. In: The Earth's Crust: Its nature and physical properties, Geophys.

Monogr. Ser. Vol. 20, J.G. Heacock, ed.: pp. 319–348. Washington DC: Am. Geophys. Union 1977

Bloch, S., Hales, A.L., Landisman, M.: Velocities in the crust and upper mantle of southern Africa from multi-mode surface wave dispersion. Bull. Seismol. Soc. Am. **59**, 1599–1629, 1969

Blohm, E.K., Worzyk, P., Scriba, H.: Geoelectrical Deep Soundings in southern Africa using the Cabora Bassa power line. J. Geophys. **43**, 665–679, 1977

Bloomer, J.R., Richardson, S.W., Oxburgh, E.R.: Heat flow in Britain: an assessment of the values and their reliability. In: Terrestrial Heat Flow in Europe, Inter-Union Comm. Geodyn. Sci. Rep. No. 58, V. Cermák and L. Rybach, eds.: pp. 293–300. Berlin: Springer 1979

Bondarenko, A.T., Galdin, N.Y.: On the physiomechanical and electrical properties of basalts at high pressures and temperatures. Izv. Akad. Nauk. SSSR, Earth Physics **5**, 28–40, 1972

Bozhko, G.N., Starovoit, O.E.: Phase velocities of Rayleigh waves on the Russian platform. In: Proceedings of the Eight Assembly of the European Seismological Commission, E. Bisztricsany, ed.: pp. 339–343. Budapest, Hungary: Akad. Kiadó 1969

Brace, W.F.: Resistivity of Saturated Crustal Rocks to 40 km based on laboratory studies. In: The Structure and Physical Properties of the Earth's Crust, Geophys. Monogr. Ser. Vol. 14, J.G. Heacock, ed.: pp. 243–255. Washington, D.C.: Am. Geophys. Union 1971

Bungum, H., Pirhonen, S.E., Husebye, E.S.: Crustal thickness in Fennoscandia. Geophys. J.R. Astron. Soc. **63**, 759–774, 1980

Carte, A.E., Rooyen, A.I.M. van: Further measurements of heat flow in South Africa. Upper Mantle Project. Geol. Soc. S. Afr. Spec. Publ. **2**, 445–448, 1969

Christensen, N.I.: Compressional wave velocities in metamorphic rocks at pressures to 10 kilobars. J. Geophys. Res. **70**, 6147–6154, 1965

Christensen, N.I.: Shear wave velocities in metamorphic rocks at pressures to 10 kilobars. J. Geophys. Res. **71**, 3549–3556, 1966

Christensen, N.I.: Compressional wave velocities in rocks at high temperatures and pressures, critical thermal gradients and crustal low-velocity zones. J. Geophys. Res. **84**, 6849–6857, 1979

Connerney, J.E.P., Kuckes, A.F.: Gradient analysis of geomagnetic fluctuations in the Adirondacks. J. Geophys. Res. **85**, 2615–2624, 1980

Connerney, J.E.P., Nekut, A., Kuckes, A.F.: Deep crustal electrical conductivity in the Adirondacks. J. Geophys. Res. **85**, 2603–2614, 1980

Daly, R.A., Manger, G.E., Clark, S.P.: Density of rocks. In: Handbook of Physical Constants, S.P. Clark, ed.: pp. 19–26. New York: Geol. Soc. Am. Inc. 1966

Dewey, J.F.: Continental margins: a model for conversion of Atlantic type to Andean type. Earth Planet. Sci. Lett. 189–197, 1969a

Dewey, J.F.: Evolution of the Appalachian/Caledonian orogen. Nature **222**, 124–219, 1969b

Drake, C.L., Ewing, M., Sutton, G.H.: Continental margins and geosynclines: The east coast of North America, north of Cape Hatteras. In: Physics and Chemistry of the Earth, Vol. 2, L.H. Ahrens, F.Press, K. Rankama and S.K. Runcorn, eds.: pp. 110–198. London: Pergamon Press 1959

Duncan, P.M., Hwang, A., Edwards, R.N., Bailey, R.C., Garland, G.D.: The development and applications of a wide band electromagnetic sounding system using a pseudo-noise source. Geophysics **45**, 1276–1296, 1980

Edwards, R.N., Bailey, R.C., Garland, G.D.: Crustal and upper mantle electrical conductivity studies with natural and artificial sources. In: The Continental Crust and Its Mineral Deposits, Spec. Pap. No. 20, D.W. Strangway, ed.: pp. 255–271. Geol. Assoc. Can. 1980

Edwards, R.N., Greenhouse, J.P.: Geomagnetic variations in the eastern United States: evidence for a highly conducting lower crust. Science **188**, 726–728, 1975

Eriksson, K.G., Malmquist, D.: A review of the Past and Present Investigations of Heat Flow in Sweden. In: Terrestrial Heat Flow in Europe, Inter-Union Comm. Geodyn. Sci. Rep No. 58, V. Cermák and L. Rybach, eds.: pp. 267–277. Berlin: Springer 1979

Green, A.G., Stephenson, O.G., Mann, G.D., Kanasewich, E.R., Cumming, G.L., Hajnal, Z., Mair, J.A., West, G.F.: Cooperative surveys across the Superior-Churchill boundary zone in southern Canada. Can. J. Earth Sci. **17**, 617–632, 1980

Haak, V.: Relations between electrical conductivity and the petrological parameters of the crust and upper mantle. Geophys. Surveys **4**, 57–69, 1980

Hall, D.H.: Partial melting and mineral-stability boundaries and their bearing on the seismic exploration of the lithosphere in Canada. Can. J. Earth Sci. **14**, 2638–2650, 1977

Hall, D.H., Hajnal, Z.: Deep seismic crustal studies in Manitoba. Bull. Seismol. Soc. Am. **63**, 885–910, 1973

Healy, J.H.: A comment on the evidence for a worldwide zone of low seismic velocity at shallow depths in the Earth's crust. In: The Structure and Physical Properties of the Earth's Crust, Geophys. Monogr. Ser. Vol. 14, J.G. Heacock, ed.: pp. 35–40. Washington, D.C.: Am. Geophys. Union 1971

Hirschleber, H.B., Lund, C.-E., Meissner, R., Vogel, A., Weinrebe, W.: Seismic investigations along the Scandinavian "Blue Road" traverse. J. Geophys. **41**, 135–148, 1975

Housley, R.M., Oliver, J.R.: Electrical characteristics of igneous Precambrian basement rocks of central North America. In: The Earth's Crust, Geophys. Monogr. Ser. Vol. 20, J.G. Heacock, ed.: pp. 181–195. Washington, D.C.: Am. Geophys. Union 1977

Hutton, V.R.S., Dawes, G., Ingham, M., Kirkwood, S., Mbipom, E.W., Sik, J.: Recent studies of time variations of natural electromagnetic fields in Scotland. Phys. Earth Planet. Inter. **24**, 66–87, 1981

Hutton, V.R.S., Ingham, M.R., Mbipom, E.W.: An electrical model of the crust and upper mantle in Scotland. Nature **287**, 30–33, 1980

Hyndman, R.D., Hyndman, D.W.: Water saturation and high electrical conductivity in the lower continental crust. Earth Planet. Sci. Lett. **4**, 427–432, 1968

Jacobson, J.J.: Deep electromagnetic sounding technique. D.Sc. Thesis T-1252. Golden, Colorado: Colorado School of Mines 1969

Jentsch, M.: Reinterpretation of a deep-seismic-sounding profile on the Ukrainian shield. J. Geophys. **45**, 355–372, 1979

Jones, A.G.: Geomagnetic induction studies in Scandinavia – I. Determination of the inductive response function from the magnetometer array data. J. Geophys. **48**, 181–194, 1980

Jones, A.G.: On the electrical crust-upper mantle structure in Fennoscandia: No Moho, and the Asthenosphere revealed? Geophys. J.R. Astron. Soc., in press 1981

Jones, A.G., Hutton, R.: A multi-station magnetotelluric study in southern Scotland – II. Monte-Carlo inversion of the data and its geophysical and tectonic implications. Geophys. J.R. Astron. Soc. **56**, 351–368, 1979

Jordan, T.H., Frazer, L.N.: Crustal and upper mantle structure from S_p phases. J. Geophys. Res. **80**, 1504–1518, 1975

Keen, C.E., Hyndman, R.D.: Geophysical review of the continental margins of eastern and western Canada. Can. J. Earth Sci. **16**, 712–747, 1979

Keller, G.V.: Electrical studies of the Crust and Upper Mantle. In: The Structure and Physical Properties of the Earth's Crust, Geophys. Monogr. Ser. Vol. 14, J.G. Heacock, ed.: pp. 107–125. Washington D.C.: Am. Geophys. Union 1971

Kosminskaya, I.P., Pavlenkova, N.I.: Seismic models of inner parts of the Euro-Asian continent and its margins. Tectonophysics **59**, 307–320, 1979

Kovtun, A.A.: Induction studies in stable shield and platform areas. Acta Geod. Geophys. Montan. Acad. Sci. Hung. **11**, 333–346, 1976 (paper originally presented as a Review at the Third IAGA Workshop on Electromagnetic Induction in the Earth, Sopron, Hungary, 4–10 July 1976)

Kovtun, A.A., Chicherina, N.D.: Results of magnetotelluric investigations in the central Russian depression. In: Magnetotelluric methods for studying the structure of the Earth's Crust and Upper Mantle (in Russian). Moscow: Nauka 1969

Kurtz, R.D., Garland, G.D.: Magnetotelluric measurements in eastern Canada. Geophys. J.R. Astron. Soc. **45**, 321–347, 1976

Kutas, RI., Lubimova, E.A., Smirnov, Ya.B.: Heat flow studies in the European part of the Soviet Union. In: Terrestrial Heat Flow in Europe, Inter-Union Comm. Geodyn. Sci. Rep. No. 58, V. Cermák and L. Rybach, eds.: pp. 301–308. Berlin: Springer 1979

Lachenbruch, A.H., Sass, J.H.: Heat flow in the United States and

the Thermal Regime of the crust. In: The Earth's Crust: Its nature and physical properties, Geophys. Monogr. Ser. Vol. 20, J.G. Heacock, ed.: pp. 626–675. Washington D.C.: Am. Geophys. Union 1977

Landisman, M., Mueller, S., Mitchell, B.J.: Review of evidence for velocity inversions in the continental crust. In: The Structure and Physical Properties of the Earth's Crust, Geophys. Monogr. Ser. Vol. 14, J.G. Heacock, ed.: pp. 11–34. Washington D.C.: Am. Geophys. Union 1971

Lund, C.-E.: Crustal structure along the Blue Road Profile in northern Scandinavia. Geol. Fören. Stockholm Förh. **101**, 191–204, 1979

Manghnani, M.H., Ramananantoandro, R., Clark, S.P.: Compressional and shear wave velocities in Granulite Facies rocks and Eclogites to 10 kbar. J. Geophys. Res. **79**, 5427–5446, 1974

Massé, R.P., Alexander, S.S.: Compressional velocity distribution beneath Scandinavia and western Russia. Geophys. J. **39**, 587–602, 1974

Mereu, R.F., Hunter, J.A.: Crustal and upper mantle structure under the Canadian shield from project early rise data. Bull. Seismol. Soc. Am. **59**, 147–165, 1969

O'Brien, P.N.S.: Lake Superior Crustal Structure – A Reinterpretation of the 1963 Seismic Experiment. J. Geophys. Res. **73**, 2669–2689, 1968

Patton, H.: Crust and Upper Mantle Structure of the Eurasian Continent from the Phase Velocity and Q of Surface Waves. Rev. Geophys. Space Phys. **18**, 605–625, 1980

Pavlenkova, N.L.: Generalised geophysical model and dynamic properties of the continental crust. Tectonophysics **59**, 381–390, 1979

Phillips, W.E.A., Stillman, C.J., Murphy, T.: A Caledonian plate tectonic model. J. Geol. Soc. Lond. **132**, 576–609, 1976

Porath, H.: A review of the evidence on low-resistivity layers in the Earth's crust. In: The Structure and Physical Properties of the Earth's Crust, Geophys. Monogr. Ser. Vol. 14, J.G. Heacock, ed.: pp. 127–144. Washington D.C.: Am. Geophys. Union 1971

Press, F.: Seismic velocities. In: Handbook of Physical Constants, S.P. Clark, ed.: pp. 195–218. New York: Geol. Soc. Am. Inc. 1966

Rao, R.U.M., Jessop, A.M.: A comparison of the thermal characteristics of shields. Can. J. Earth Sci. **12**, 347–360, 1975

Reddy, I.K., Rankin, D.: Magnetotelluric measurements in central Alberta. Geophysics **36**, 739–753, 1971

Richter, D., Simmons, G.: Microcracks in crustal igneous rocks. In: The Earth's Crust, Geophys. Monogr. Ser. Vol. 20, J.G. Heacock, ed.: pp. 149–181. Washington D.C.: Am. Geophys. Union 1966

Ringwood, A.E.: Composition and Petrology of the Earth's Mantle. New York: McGraw-Hill 1975

Sellevoll, M.A., Warrick, R.E.: A refraction study of the crustal structure in southern Norway. Bull. Seismol. Soc. Am. **61**, 457–471, 1971

Srivastava, S.P., Jacobs, J.A.: Determination of the electrical resistivity at Meanook, Alberta, Canada, by the Magnetotelluric method. J. Geomagn. Geoelectr. **15**, 280–288, 1964

Sternberg, B.K.: Electrical resistivity structure of the Crust in the southern extension of the Canadian Shield – layered Earth models. J. Geophys. Res. **84**, 212–228, 1979

Tkachev, G.N.: Experiment of abyssal magnetotelluric soundings on the Ukrainian shield (in Russian). Geofiz. Sb. **52**, 62–65, 1973

Vanyan, L.L., Berdichewski, M.N., Fainberg, E.B., Fiskina, M.V.: The study of the asthenosphere of the East European platform by electromagnetic methods. Phys. Earth Planet. Inter. **14**, P1–P2, 1977

Volarovich, M.P., Parkhomenko, E.I.: Electrical Properties of Rocks at High Temperatures and Pressures. In: Geolectric and Geothermal Studies (East-Central Europe, Soviet Asia), KAPG Geophys. Monogr., A. Ádám, ed.: pp. 319–369. Budapest: Akadémiai Kiadó 1976

Vozoff, K., Ellis, R.M.: Magnetotelluric measurements in southern Alberta. Geophysics **31**, 1153–1157, 1966

Westerlund S.: Magnetotelluric experiments in the frequency range 0.01 Hz to 10 kHz. KGO Report No. 72:10, Kiruna Geophysical Observatory, Nov. 1972

Wickens, A.J.: Variations in lithospheric thickness in Canada. Can. J. Earth Sci. **8**, 1154–1162, 1971

Wickens, A.J., Buchbinder, G.G.R.: S-wave residuals in Canada. Bull. Seismol. Soc. Am. **70**, 809–822, 1980

Williams, H.: Appalachian orogen in Canada. Can. J. Earth Sci. **16**, 792–807, 1979

Zablocki, C.J.: Electrical properties of serpentinite from Mayaguez, Puerto Rico. In: A Study of Serpentinite of the Amsoc Core Hole Near Mayaguez, p. 1188. Washington D.C.: National Academy of Sciences, National Research Centre 1964

Received February 11, 1981; Revised April 9, 1981
Accepted April 30, 1981

J Geophys (1981) 49:234–242

Journal of Geophysics

Spherical-Earth Gravity and Magnetic Anomaly Modeling by Gauss-Legendre Quadrature Integration

R.R.B. von Frese[1], W.J. Hinze[1], L.W. Braile[1], and A.J. Luca[2]

[1] Department of Geosciences, Purdue University, West Lafayette, Indiana 47907, USA
[2] Chevron Geophysical Co., 400 5th Ave. SW, Calgary, Alberta TPOL7, Canada

Abstract. The usefulness of long-wavelength potential field anomalies in lithospheric interpretation is greatly increased with spherical earth modeling techniques. Gauss-Legendre quadrature integration is used to calculate the anomalous potential of gravity and magnetic fields and their spatial derivatives on a spherical earth for an arbitrary body represented by an equivalent point source distribution of gravity poles or magnetic dipoles. The distribution of equivalent point sources is determined directly from the coordinate limits of the source volume. Variable integration limits for an arbitrarily shaped body are derived from interpolation of points which approximate the body's surface envelope. The versatility of the method is enhanced by the ability to treat physical property variations within the source volume and to consider variable magnetic fields over the source and observation surface. A number of examples verify and illustrate the capabilities of the technique, including preliminary modeling of potential field signatures for Mississippi embayment crustal structure at satellite elevations.

Key words: Spherical coordinate gravity modeling – Spherical coordinate magnetic modeling – Equivalent sources – Gauss-Legendre quadrature integration – Satellite potential fields – Mississippi embayment

Introduction

Computation of theoretical anomalous gravity and magnetic fields from geologic models is an important element in interpreting potential field data and designing surveys. For regional gravity and magnetic surveys measured in degrees of latitude and longitude, procedures are desired which model directly, in spherical coordinates, potential field anomalies due to large-scale, arbitrarily shaped sources of variable density or magnetization characteristics.

In a review of computer modeling techniques Bhattacharyya (1978) presents methods that in principle are suitable for spherical earth modeling of regional features. These procedures are generally based on approximations of the anomalous source as a group of prisms or polygonal laminae, the effects of which are evaluated and summed at each observation point to yield the total anomaly. However, for typical spherical earth modeling applications, the book-keeping problem involved with subdividing the large-scale source into simple forms to reflect arbitrary characteristics of geometry and physical properties is commonly formidable.

A simple and more efficient procedure is to represent quadratures of the source volume by equivalent point sources according to the well known technique of Gaussian quadrature integration. In principle, the appropriate geometric distribution of equivalent point sources can be determined directly from the coordinate limits of the source volume, so that an accurate estimate of the source-affiliated anomaly is obtained by evaluating and summing at each observation point the anomaly values due to each point source of the equivalent source distribution.

Gaussian quadrature is a time-honored technique for numerical integration and has been well studied in the literature of numerical methods (Carnahan et al. 1969). Potential field modeling by Gauss-Legendre quadrature was used by Ku (1977) to evaluate gravity and magnetic anomalies in Cartesian coordinates due to bodies of arbitrary shape and magnetic polarization. In this discussion, the method is extended to spherical coordinates and the general problem of sources with arbitrary shape and variable density and magnetization properties.

Description of Method

As illustrated in Fig. 1, it is convenient for gravity and magnetic modeling problems to consider the anomalous body as being composed of a source volume distribution of gravity point poles or magnetic point dipoles, respectively. Hence, to estimate the anomalous gravity or magnetic field at some observation point, it is necessary to evaluate and sum the anomaly values due to each of these point sources at the observation point.

In particular, the radial anomaly, Δg, due to a gravity point pole referred to a geocentric coordinate system as shown in Fig. 1 is given by

$$\Delta g = \left\{ -G \frac{\partial}{\partial R} \left(\frac{1}{R} \right) \frac{\partial R}{\partial r} \right\} \Delta m \tag{1}$$

where

G = universal gravitational constant ($=6.67 \times 10^{-8}$ cm^3/(g sec^2)),
R = distance from observation point (r, θ, ϕ) to source point (r', θ', ϕ'),
r, r' = radial distances from earth's center to the observation point and source point, repectively,
θ, θ' = co-latitude coordinates of observation and source points, respectively,

0340-062X/81/0049/0234/$01.80

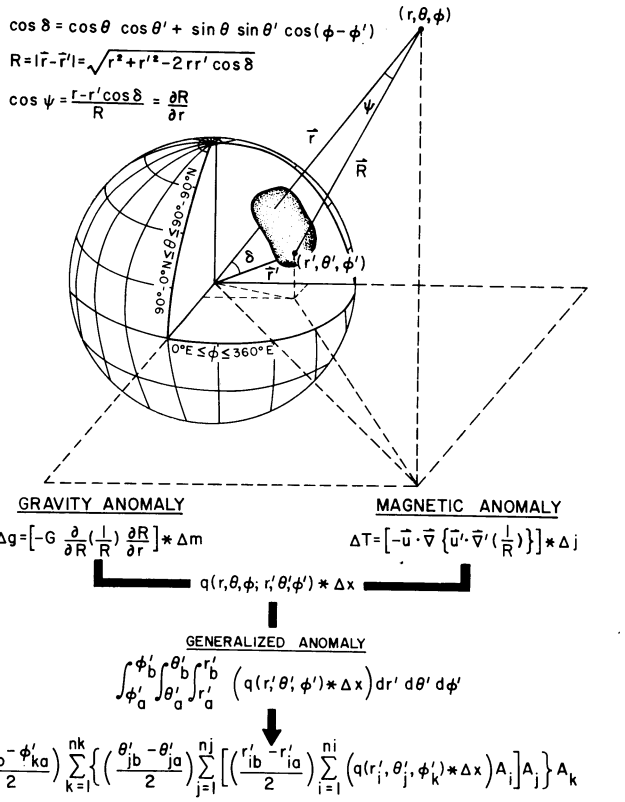

Fig. 1. Gravity and magnetic anomaly modeling in spherical coordinates of a geologic body with arbitrary shape and physical properties by Gauss-Legendre quadrature integration (see text for details)

ϕ, ϕ' = longitude coordinates of observation and source points, respectively, and
Δm = mass contrast of the point pole.

For a magnetic point dipole, on the other hand, the total magnetic intensity anomaly, ΔT, is given by

$$\Delta T=\left\{-\mathbf{u}\cdot\nabla\left(\mathbf{u}'\cdot\nabla'\left(\frac{1}{R}\right)\right)\right\}\Delta j \tag{2}$$

where

∇, ∇' = gradient operators in observation point and source point coordinates, respectively,
Δj = magnetization contrast of the point dipole, and
$\mathbf{u}, \mathbf{u}'$ = unit geomagnetic field vectors at the observation point and source point, respectively.

Conventionally, the unit vectors $\mathbf{u}$ and $\mathbf{u}'$ are expressed in terms of geomagnetic field inclination (I, I') and declination (D, D'). Also, when the point dipole polarization is by induction

$$\Delta j=\Delta k\, F' \tag{3}$$

where

Δk = magnetic susceptibility contrast of the point dipole, and
F' = scalar geomagnetic field intensity at the source point.

Hence, in regional-scale applications of Eq. (2) geomagnetic field models such as the IGRF-1965 (Cain et al. 1967) are normally used to obtain pertinent values of (I', D', F') at the source point and (I, D) at the observation point.

Consideration of Eqs. (1) and (2) shows that the incremental gravity and magnetic anomaly values due to a point source located a distance R from the observation point can be generalized according to the relation

$$q(R)\,\Delta x \tag{4}$$

where

$q(R)$ = the geometrical point source function which describes the inverse distance between the observation point and source point, and
Δx = the appropriate physical property contrast of the point source.

Hence, to determine the total potential field anomaly it is necessary to evaluate at each observation point (r, θ, ϕ) the volume integral given by

$$\int_{\phi'_a}^{\phi'_b}\int_{\theta'_a}^{\theta'_b}\int_{r'_a}^{r'_b}(q(r,\theta,\phi;r',\theta',\phi')\,\Delta x)\,dr'\,d\theta'\,d\phi' \tag{5}$$

where the primed variables refer to the coordinates of the anomalous body such that

ϕ'_a, ϕ'_b = lower and upper longitude limits of the source volume,
θ'_a, θ'_b = lower and upper co-latitude limits of the source volume, and
r'_a, r'_b = lower and upper radial limits of the source volume.

Consider, now, the numerical evaluation of the innermost integral in Eq. (5). Most numerical integration techniques involve the use of interpolation polynomials to approximate the integrand according to a summation formula of the general type given by

$$\int_{r'_a}^{r'_b}(q(r')\,\Delta x)\,dr'\simeq\sum_{i=1}^{ni}A_i q(r'_i)\,\Delta x \tag{6}$$

where the ni values A_i are the weights to be given to the ni functional values $(q(r'_i)\,\Delta x)$ evaluated at the interpolation coordinates, r'_i. Conventional integration formulae such as Simpson's rule or the trapezoidal rule assume equal spacing of the arguments r'_i which is generally appropriate when dealing with an integrand that is not well known analytically. However, as shown in Eqs. (1) and (2) the integrand being considered here involves a familar analytic function which may be computed for any argument to great precision. In such instances, Gaussian quadrature formulae can be developed to yield selected values of interpolation r'_i and coefficients A_i so that the sum in Eq. (6) gives the integral exactly when $(q(r')\,\Delta x)$ is a polynomial of degree $2ni$ or less (Carnahan et al. 1969).

In general, it may be shown that the Gaussian coefficients A_i can be obtained from a polynomial of order ni which is orthogonal over the interval of integration such that the ni points of interpolation r'_i are the zeros of the polynomial. Families of orthogonal polynomials which are commonly used to develop Gaussian quadrature formulae include Legendre, Laguerre, Chebyshev and Hermite polynomials. However, in this discussion, only the prototype of the Gaussian method involving Legendre polynomials is considered.

Legendre polynomials $P_{ni}(\bar{r})$ of order ni which are orthogonal over the interval $-1\le\bar{r}\le1$ are given by

$$P_{ni}(\bar{r})=\left(\frac{1}{2^{ni}ni!}\right)\left(\frac{d^{ni}}{d\bar{r}'^{ni}}(\bar{r}'^2-1)^{ni}\right),\quad\text{where } P_0(\bar{r})=1 \tag{7}$$

Accordingly, the standard Gauss-Legendre quadrature over the interval $(-1, 1)$ is given by

$$\int_{-1}^{1} (q(\bar{r}')\,\Delta x)\,d\bar{r}' \simeq \sum_{i=1}^{ni} A_i q(\bar{r}'_i)\,\Delta x \tag{8}$$

where the interpolation points $\bar{r}'_i$ at which the integrand is evaluated are the zeros of Eq. (7) and the Gaussian coefficients are

$$A_i = \frac{2(1-\bar{r}'^2_i)}{ni^2\{P_{ni-1}(\bar{r}'_i)\}^2} \tag{9}$$

Now for arbitrary limits of integration such as indicated in Eq. (6) it is necessary to map the standard interval $-1 \leqq \bar{r}'_i \leqq 1$ into the interval of integration $r'_a \leqq r'_i \leqq r'_b$ according to the transformation

$$r'_i = \frac{\bar{r}'_i(r'_b - r'_a) + (r'_b + r'_a)}{2} \tag{10}$$

Accordingly, the integral in Eq. (6) can be approximated as

$$\int_{r'_a}^{r'_b} (q(r')\,\Delta x)\,dr' = \frac{(r'_b - r'_a)}{2} \int_{-1}^{1} \left(q\left\{ \frac{\bar{r}'_i(r'_b - r'_a) + (r'_b + r'_a)}{2} \right\} \Delta x \right) dr'$$

$$\simeq \frac{(r'_b - r'_a)}{2} \sum_{i=1}^{ni} A_i q(r'_i)\,\Delta x \tag{11}$$

Extending this procedure to volume integrals is straightforward. Thus, the Gauss-Legendre formula for the general evaluation of Eq. (5) is given by

$$\int_{\phi'_a}^{\phi'_b} \int_{\theta'_a}^{\theta'_b} \int_{r'_a}^{r'_b} (q(r', \theta', \phi')\,\Delta x)\,dr'\,d\theta'\,d\phi' \simeq \left(\frac{\phi'_{kb} - \phi'_{ka}}{2}\right) \sum_{k=1}^{nk} \left\{ \left(\frac{\theta'_{jb} - \theta'_{ja}}{2}\right) \times \sum_{j=1}^{nj} \left\{ \left(\frac{r'_{ib} - r'_{ia}}{2}\right) \sum_{i=1}^{ni} (q(r'_i, \theta'_j, \phi'_k)\,\Delta x)\,A_i \right\} A_j \right\} A_k \tag{12}$$

where

$$r'_i = 0.5\,\{\bar{r}'_i(r'_{ib} - r'^a_{ia}) + r'_{ib} + r'_{ia}\}$$
$$\theta'_j = 0.5\{\bar{\theta}'_j(\theta'_{jb} - \theta'_{ja}) + \theta'_{jb} + \theta'_{ja}\}$$
$$\phi'_k = 0.5\,\{\bar{\phi}'_k(\phi'_{kb} - \phi'_{ka}) + \phi'_{kb} + \phi'_{ka}\}$$

$\bar{r}'_i, \bar{\theta}'_j, \bar{\phi}'_k$ = coordinates of the subdivision in the limits of integration from -1 to 1 which correspond to zero nodes of Eq. (7),

A_i, A_j, A_k = Gauss-Legendre quadrature coefficients given by Eq. (9),

ϕ'_{ka}, ϕ'_{kb} = lower and upper longitude limits of the body for the k-th longitude component of the equivalent point source coordinates,

$\theta'_{ja}, \theta'_{jb}$ = lower and upper co-latitude limits of the body for the j-th co-latitude component of the equivalent point source coordinates, and

r'_{ia}, r'_{ib} = lower and upper radial limits of the body for the i-th radial component of the equivalent point source coordinates.

The quadrature formula given in Eq. (12) shows that gravity and magnetic anomalies can be computed accurately by summing at each observation point the anomalous effect of $nk \times nj \times ni$ equivalent point sources located at source point coordinates $(r'_i, \theta'_j, \phi'_k)$, where each of the differential point source anomalies is appropriately weighted by Gauss-Legendre quadrature coefficients and the volume coordinate limits of the anomalous body being modeled. This result is well suited to machine computation where the input consists principally of values of the integrand for selected source points $(r'_i, \theta'_j, \phi'_k)$, affiliated subdivision coordinates $(\bar{r}'_i, \bar{\theta}'_j, \bar{\phi}'_k)$, and coefficients (A_i, A_j, A_k), and the volume coordinate limits of the body for each dimension of every source point coordinate $(r'_i, \theta'_j, \phi'_k)$.

The selected values of the integrand for gravity or magnetic modeling purposes are readily obtained from Eqs. (1) or (2), respectively. Also, the Legendre subdivision coordinates of the interval $(-1, 1)$ and associated Gaussian coefficients may be computed directly from Eqs. (7) and (9), respectively. However, it is generally found to be more machine efficient to input these values from tables using an algorithm such as described by Carnahan et al. (1969). Values which are applicable for such algorithms are tabulated to 30 digit precision for orders $n = 2$–512 by Stroud and Secrest (1966). However, for most regional lithospheric modeling applications experience suggests that subdivision coordinates and associated coefficients to 10 digit precision for orders up to $n = 16$ are normally sufficient.

For a uniformly dimensioned body such as a prism, the integration limits for the evaluation of Eq. (12) are easy to specify. In this case, for example, $(\phi'_{ka}, \phi'_{kb}) = (\phi'_a, \phi'_b)$, $(\theta'_{ja}, \theta'_{jb}) = (\theta'_a, \theta'_b)$ and $(r'_{ia}, r'_{ib}) = (r'_a, r'_b)$. However, for the more general case of a body with arbitrary shape the integration limits are known in one dimension only, so that the problem of determining the integration limits in the remaining two dimensions for each equivalent point source coordinate must be considered.

Procedures can be developed to handle this problem efficiently, such as the method described by Ku (1977) where a modified cubic spline function is used to interpolate the desired integration limits from a set of body point coordinates which provide a rough approximation of the surface envelope of the body. Typically, the procedure is to specify, for example, the longitudinal limits of integration of the body to obtain the nk Gauss-Legendre nodes ϕ'_k as described above. Interpolations of the body point coordinates are performed next to determine the maximum and minimum latitude coordinates of the body for each longitude coordinate ϕ'_k. These values of course provide the latitude limits of integration for evaluating the nj nodes θ'_j. Similarly, the radial coordinates of the body points are interpolated at each horizontal coordinate (ϕ'_k, θ'_j) to yield appropriate radial limits of integration from which the ni nodes r'_i can be determined. Procedures such as this are readily adapted for efficient machine processing so that the integration limits of arbitrarily shaped bodies can be determined accurately for evaluation of the quadrature formula given in Eq. (12).

The quadrature formula in general has considerable versatility in modeling applications because anomalous gravity and magnetic potentials and their respective spatial derivatives of any order are all linearly related. Hence, to model the radial derivative of the potential field anomaly due to an arbitrary source, for example, it is necessary simply to exchange $q(R)$ for $\partial q(R)/\partial r$ in Eq. (12). Additional geophysically interesting quantities which can be modeled from simple linear transformations of the integrand of Eq. (12) include the anomalous potential, vector anomaly components and the spatial derivatives of any order. Relative geoidal anomalies can also be modeled by computing the anomalous gravitational potential of the body at the surface of the earth and dividing it by normal gravity according to Brun's formula (Heiskanen and Moritz 1967).

Bodies with variable physical property contrast are also accommodated readily by the quadrature solution. To emphas-

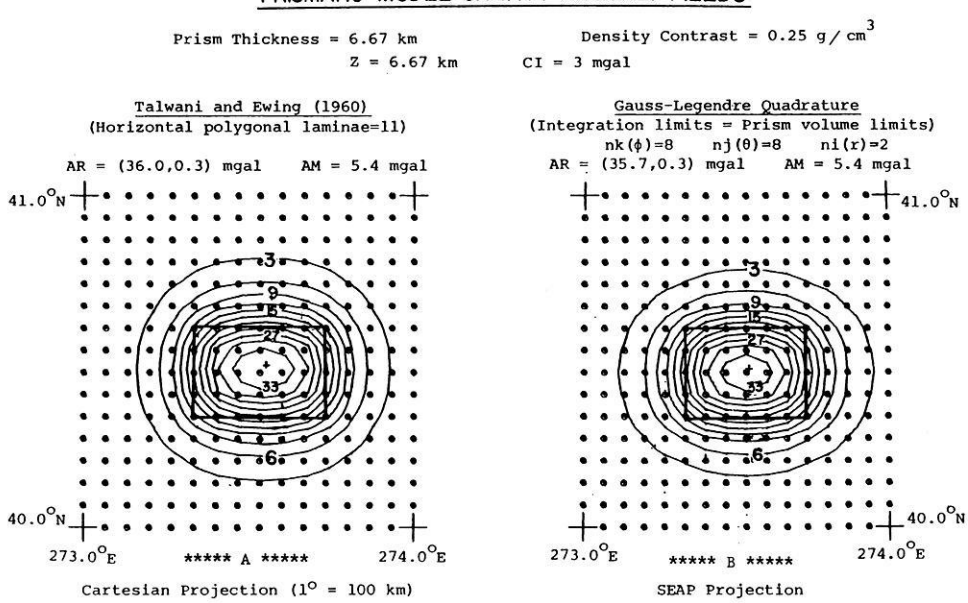

Fig. 2. Gravity anomaly comparisons for a spherical prism

ize the fact that Δx can be expressed as a function of source position (i.e., $\Delta x = \Delta x(r', \theta', \phi')$) when necessary, the generalized point source anomaly $(q(R)\,\Delta x)$ has been carried intact throughout the foregoing developments. Conventional modeling procedures normally assume bodies with uniform physical properties so that each property variation must be modeled as a separate body. To model the total intensity magnetic anomaly due to a regional source subject to regional variations of geomagnetic field induction by the well known method of Talwani (1965), for example, requires that the source be subdivided into blocks wherein the geomagnetic field polarization is uniform. Each block in turn must be subdivided into a group of approximating polygonal laminae to ensure accuracy of the numerical integration which evaluates the anomaly. By contrast, the Gauss-Legendre quadrature approach is simply to polarize each point dipole in the quadrature formula according to the polarization characteristics of an acceptable numerical model of the geomagnetic field (e.g., the IGRF-1965 by Cain et al. 1967). This example also illustrates the technique for modeling bodies with remanent magnetization by quadrature formulation. Here, the magnetization of the point dipoles is achieved using a polarization field that represents the vector sum of induced and remanent magnetic polarizations.

Finally, considerable computational flexibility is available for the practical implementation of the quadrature formulation. Ku (1977) noted the trade-offs which occur in applications of the method between efficient computation and the accuracy of the solution. A large number of Gauss-Legendre nodes ensures a very accurate quadrature solution, although the same degree of accuracy can often be achieved by a substantially smaller number of equivalent point sources. In fact, the accuracy of the solution remains essentially unchanged for different numbers of nodes as long as the node spacing is smaller than the distance to the observation point. Hence, the minimum number of nodes specified in a given application should be such that the distance to the observation point is greater than the node spacing. In general, then, the accuracy of the quadrature formulation can be readily controlled by adjusting the number of Gauss-Legendre nodes relative to the elevation of the observation point.

Illustration of Method

A computer program is described in von Frese et al. (1980) which was developed for regional lithospheric gravity and magnetic modeling applications by Gauss-Legendre quadrature. The program was used to construct examples that illustrate some of the capabilities of the method.

To demonstrate and verify the method for regional-scale modeling applications, gravity and magnetic anomalies due to a three-dimensional spherical prism were modeled on a spatial scale small enough that the results could be compared readily with conventional modeling techniques in Cartesian coordinates. In Fig. 2, for example, a comparison is made between the two coordinate systems for calculations of gravity anomalies due to a 6.67 km thick prism with density contrast 0.25 g/cm^3. The observation grid consists of (16,16) stations uniformly spanning the region (273–274) °E, (40–41) °N at an elevation (Z) of 6.67 km above the top of the prism.

The well known method of Talwani and Ewing (1960) was used to calculate the gravity effect of the prismatic model as shown in Fig. 2A. The gravity anomaly was determined by evaluating and summing at each observation point the gravity anomalies due to 11 horizontal polygonal laminae used to approximate the prism. As shown in Fig. 2A, the resultant anomaly has an amplitude range (AR) between 36.0 mgal and 0.3 mgal and an amplitude mean (AM) of 5.4 mgal. The anomaly was computed and contoured in Cartesian coordinates assuming $1° = 100$ km. This assumption distorts slightly the true geometry of a spherical prism in this $1° \times 1°$ region in northwestern Indiana where 1° in longitude or latitude is more nearly equal to 88 km or 112 km, respectively.

In Fig. 2B the gravity anomaly of the spherical prism computed by Gauss-Legendre quadrature integration is contoured on a stereographic equal-area polar (SEAP) projection. In this case, the gravity anomaly was calculated in spherical coordinates by evaluating at each observation point an $nk \times nj \times ni = 8 \times 8 \times 2 = 128$ point quadrature formula where the integration limits were specified directly from the spherical coordinate limits of the prism volume. The results shown in Fig. 2 indicate that the two methods agree very well with respect to

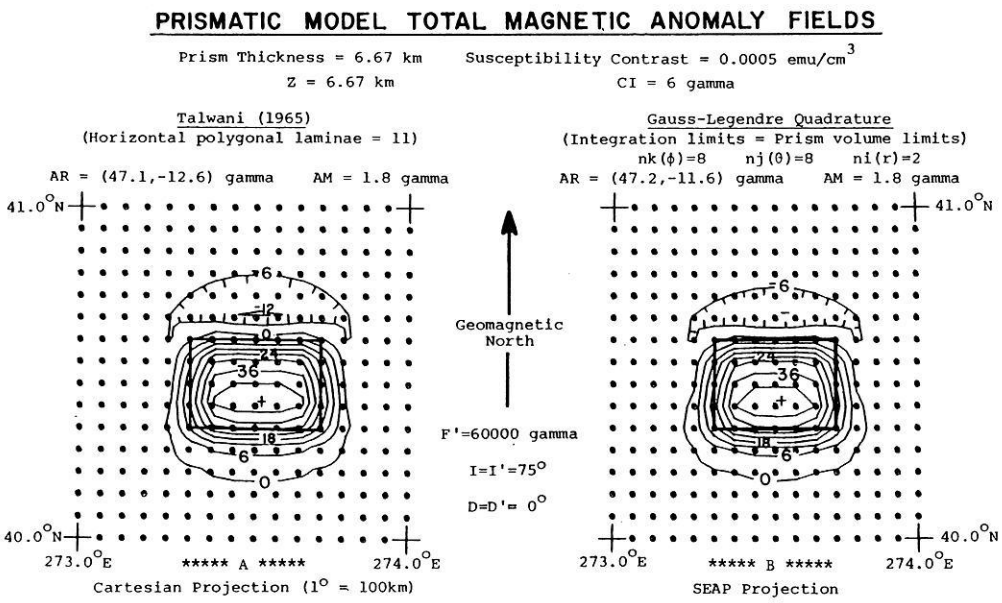

Fig. 3. Magnetic anomaly comparisons for a spherical prism

the relatively small spatial scale under consideration. The slight disparity between the results is probably due to geometric distortion introduced by the use of Cartesian coordinates for calculation of the spherical prism anomaly.

A comparison of magnetic anomaly fields is illustrated in Fig. 3 for the prism model with volume magnetic susceptibility contrast equal to 0.0005 emu/cm^3 ($4\pi \times 0.0005$ in SI units) and uniform polarizing intensity $F' = 60{,}000$ gamma (60,000 nT), inclination $I' = 75°$ and declination $D' = 0°$. Over the observation grid, uniform geomagnetic field attitude characteristics of inclination $I = 75°$ and declination $D = 0°$ are also assumed. The total intensity magnetic anomaly of the spherical prism calculated in Cartesian coordinates according to the method of Talwani (1965) is shown in Fig. 3A. The resultant anomaly corresponds well with the magnetic anomaly calculated in spherical coordinates by Gauss-Legendre quadrature in Fig. 3B.

As a more regional-scale example, consider the application of Gauss-Legendre quadrature integration for modeling gravity and magnetic anomaly signatures, at the satellite elevation of 450 km, due to the crustal thickness anomaly which is gridded in Fig. 4A. This zone of enhanced crustal thickness, extending from the Texas panhandle northeastward into Kansas, is portrayed by seismic evidence (Warren and Healy 1973) as roughly 10 km of lighter crustal material displacing denser (mantle) material to a depth of 50 km. To illustrate the gravity modeling procedure, a density contrast of -0.3 g/cm^3 was assumed for this feature.

Magnetic considerations, on the other hand, suggest that the crustal thickness anomaly may represent a zone of positive magnetization contrast due to downward deflection of the Curie isotherm in the region of thick, cooler crustal material or thicker magnetic crust extending into non-magnetic mantle material. For the purposes of this example, a volume susceptibility contrast of 10^{-2} emu/cm^3 was assumed for the zone of enhanced crustal thickness which is representative of the general magnetization reported for the lower crust (Hall 1974; Shuey et al. 1973).

To determine the variable limits of integration for the evaluation of the quadrature formula, the crustal thickness anomaly was referred to the body point grid shown in Fig. 4A. For each Gauss-Legendre node in the ϕ'-longitude coordinates of the body, the θ'-latitude limits of the body were interpolated from the 6 points describing the body's boundary. The radial limits, in turn, were interpolated from the 6 boundary points and 3 interior points of the body for each Gauss-Legendre node with horizontal (ϕ', θ')-coordinates. For the particular model considered here, of course, the radial coordinates of the 9 body points used to approximate the subsurface configuration of the body were specified to represent a uniform thickness of 10 km.

The resultant gravity anomaly at 450 km elevation due to this feature is illustrated in Fig. 4B. The gravity effect was calculated by evaluating an $nk \times nj \times ni = 16 \times 16 \times 2 = 512$ point Gauss-Legendre quadrature formula over the (41, 41) grid of observations. The magnetic effect of the crustal thickness anomaly was also computed in this manner at 450 km elevation. The resultant total intensity magnetic anomaly in the 1GRF-1965 updated to 1968 is demonstrated in Fig. 5A. To remove anomaly distortion due to regional variability of the reference field, the magnetic effect was next computed, assuming a uniform polarizing field intensity of 60,000 gamma and radial geomagnetic field inclination at both source and observation points. Accordingly, Fig. 5B illustrates the resultant magnetic anomaly field reduced to radial polarization at 450 km elevation for the crustal thickness model.

Finally, for accurate implementation of the method the distance between the equivalent source points and the observation point must be greater than the equivalent source point spacing within the body. This limitation can be minimized in practice by either subdividing the body into an appropriate number of smaller bodies, or increasing the number of equivalent point sources, or increasing the distance between the observation point and the body. The latter consideration suggests that the Gauss-Legendre quadrature formulation is especially well suited for modeling satellite-level gravity and magnetic anomalies because of the large elevations involved with these measurements. The gravity and magnetic anomaly signatures of the crustal thickness model, for example, can be computed using an $nk \times nj \times ni = 4 \times 4 \times 2 = 32$ point quadrature formula to nearly the same precision as developed by the 512 point formula in Fig. 4B and 5, respectively.

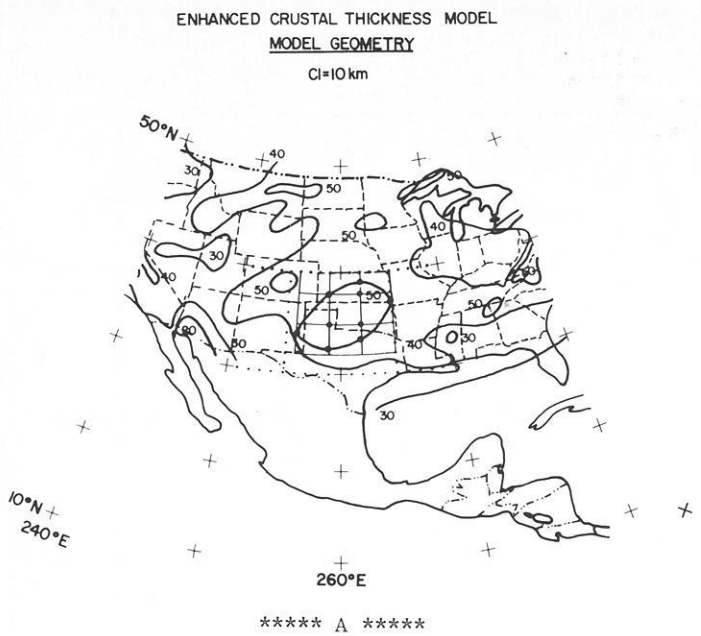

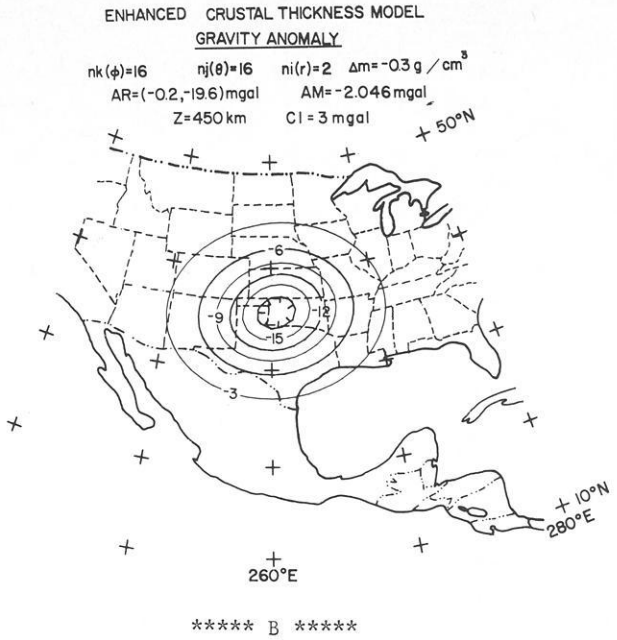

Fig. 4. A SEAP projection of crustal thickness anomaly model geometry adapted from Warren and Healy (1973). The model is referred to a body point grid which gives latitude, longitude, and top and bottom radial coordinates for the 9 points of the model's surface envelope used to interpolate the variable volume limits of integration. The shape of the thickened crust (10 km) is indicated by the 50 km depth contour on which the grid is superimposed. **B** SEAP projection of the gravity anomaly for the crustal thickness model calculated at 450 km elevation by Gauss-Legendre quadrature integration

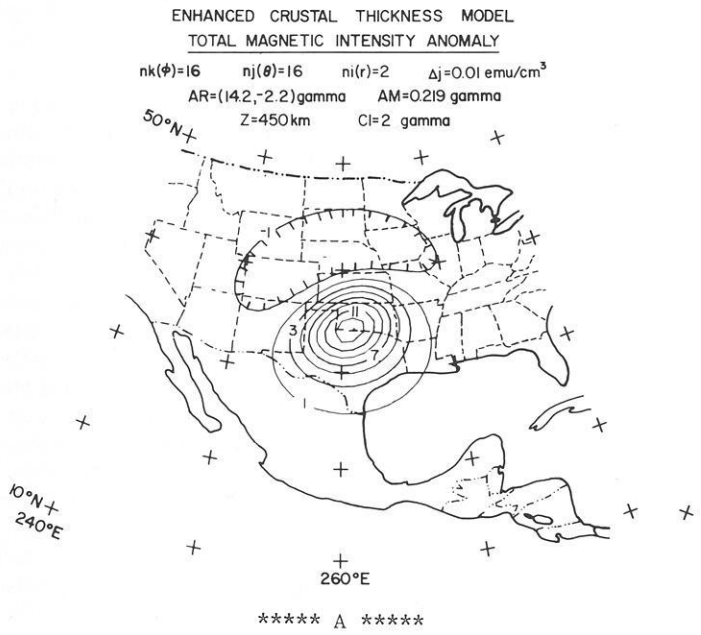

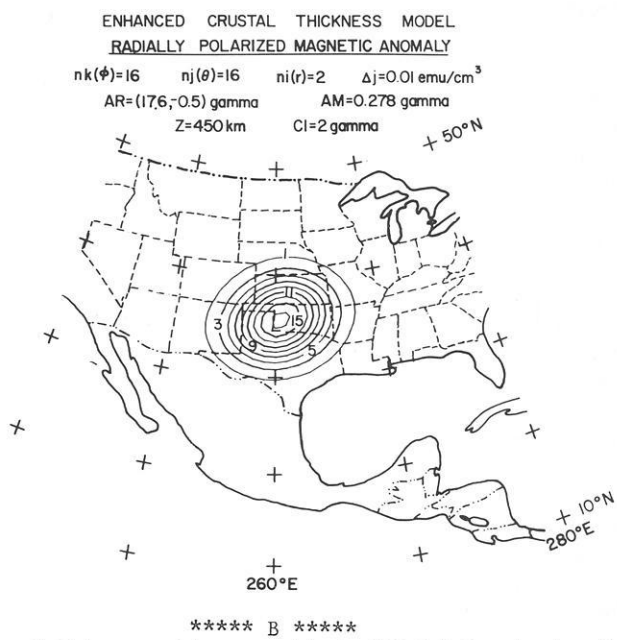

Fig. 5. A SEAP projection of total magnetic intensity anomaly for the crustal thickness model computed in the IGRF-1965 updated to 1968 by Gauss-Legendre quadrature integration. **B** SEAP projection of reduced-to-the-pole magnetic anomaly for the crustal thickness model by Gauss-Legendre quadrature integration using a normalized polarizing amplitude of 60,000 gamma

Application of Method

The spherical earth modeling procedure was used to obtain a preliminary view of the gravity and magnetic anomaly characteristics for the Mississippi embayment at 450 km elevation. This information is pertinent to evaluating, for example, the feasibility of using satellite gravity and magnetic surveys for detecting anomaly signatures due to failed rifts.

The Mississippi embayment represents a broad, spoon-shaped re-entrant of Mesozoic and Cenozoic sedimentary rocks which extends into the Paleozoic terrain of the North American craton from the south as outlined by the shaded contour of Fig. 6D. The axis of this feature roughly parallels the Mississippi River tapering northward into the tectonically active region of the New Madrid seismic zone. An integrated analysis of gravity, seismic, stratigraphic and petrologic data by Ervin

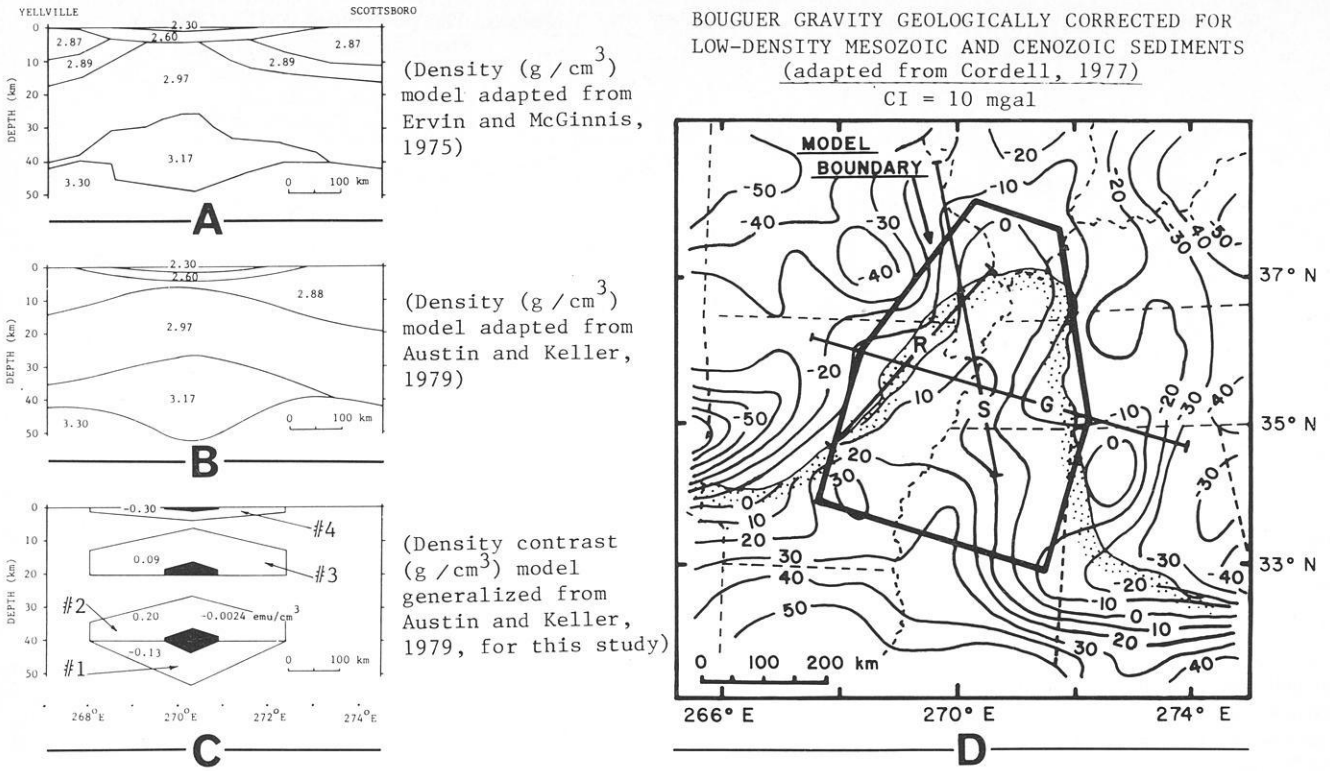

Fig. 6A–D. Development of Mississippi embayment density and magnetization models. Also shown in (**D**) is an index map of the embayment (*shaded contour*) where *G* is the gravity profile studied by Ervin and McGinnis (1975), *R* is the seismic refraction line studied by McCamy and Meyer (1965), and *S* is the surface wave propagation path studied by Austin and Keller (1979)

and McGinnis (1975) suggests the embayment is a late Precambrian aulacogen which was reactivated most recently in the late Cretaceous by tensional forces initiated during the formation of the present Atlantic ocean basin by subsidence of the Gulf coastal plain.

Figure 6A is a cross-section of the density structure of the Mississippi embayment given by Ervin and McGinnis (1975) along a profile between Yellville, Arkansas and Scottsboro, Alabama (hereafter called $Y-S$ profile). This density model was synthesized from regional gravity data derived from the U.S. Bouguer gravity anomaly map of Woollard and Joesting (1964) and the results of a reversed seismic refraction profile between Little Rock, Arkansas and Cape Girardeau, Missouri as described by McCamy and Meyer (1966). Austin and Keller (1979) integrated the work of McCamy and Meyer (1966) with an analysis of Rayleigh wave dispersion along a propagation path between Oxford, Mississippi and Florissant, Missouri to obtain a similar density model for the $Y-S$ profile which is illustrated in Fig. 6B. An index map for locating these various studies is given in Fig. 6D. In general, the crustal cross-sections shown in Fig. 6A, B support the failed-rift model for the origin of the Mississippi embayment.

The agreement of surface wave, seismic refraction, and gravity data in the region of the embayment suggests that the crustal cross-section given in Fig. 6B can be useful for developing a reasonably valid three-dimensional model of the embayment. Accordingly, the crustal cross-section that was generalized from Fig. 6B for the purposes of this study is given as the four-body model shown in Fig. 6C. The gravity analysis due to Cordell (1977) was used to project the characteristics of this generalized crustal cross-section north and south of the $Y-S$ profile.

Cordell (1977) corrected the smoothed positive Bouguer anomaly of the embayment for the low-density sediments and observed the long continuous positive anomaly with an amplitude of 15–45 mgal increasing southward illustrated in Fig. 6D. The axis of this anomaly closely follows the Mississippi River northward beyond its confluence with the Ohio River into southern Illinois. The anomaly exhibits relatively uniform behavior south of the $Y-S$ profile until about 33° N where it increases sharply, thus suggesting that the crustal cross-section may be uniformly projected southward along the Mississippi River to approximately 33° N. To the north, decreasing gravity anomaly values in conjunction with the northward tapering surface configuration of the embayment suggest a commensurate northward tapering projection of the crustal cross-section along the Mississippi River into southern Illinois. Hence, to obtain the first-order, three-dimensional generalization of the crustal structure of the embayment used in this investigation, the crustal cross-section of Fig. 6C was projected uniformly south of the $Y-S$ profile and tapered uniformly northward as outlined in Fig. 6D. The northern ends of the four bodies of this generalized model as projected onto the cross-section along the $Y-S$ profile are given by the shaded regions of Fig. 6C.

To compute the potential field anomalies at 450 km elevation, each of the four bodies of this generalized model was represented by a Gauss-Legendre quadrature formula consisting of 128 equivalent point sources. The latitude and longitude limits of each body were represented by 8 point sources and the radial limits by 2 point sources. Pertinent body volume limits were interpolated from a set of body points that sampled the coordinates of the surface envelope for each body. The quadrature formulae were next evaluated and summed over a (21, 13) observation grid spanning the region (260–280) °E, (33–

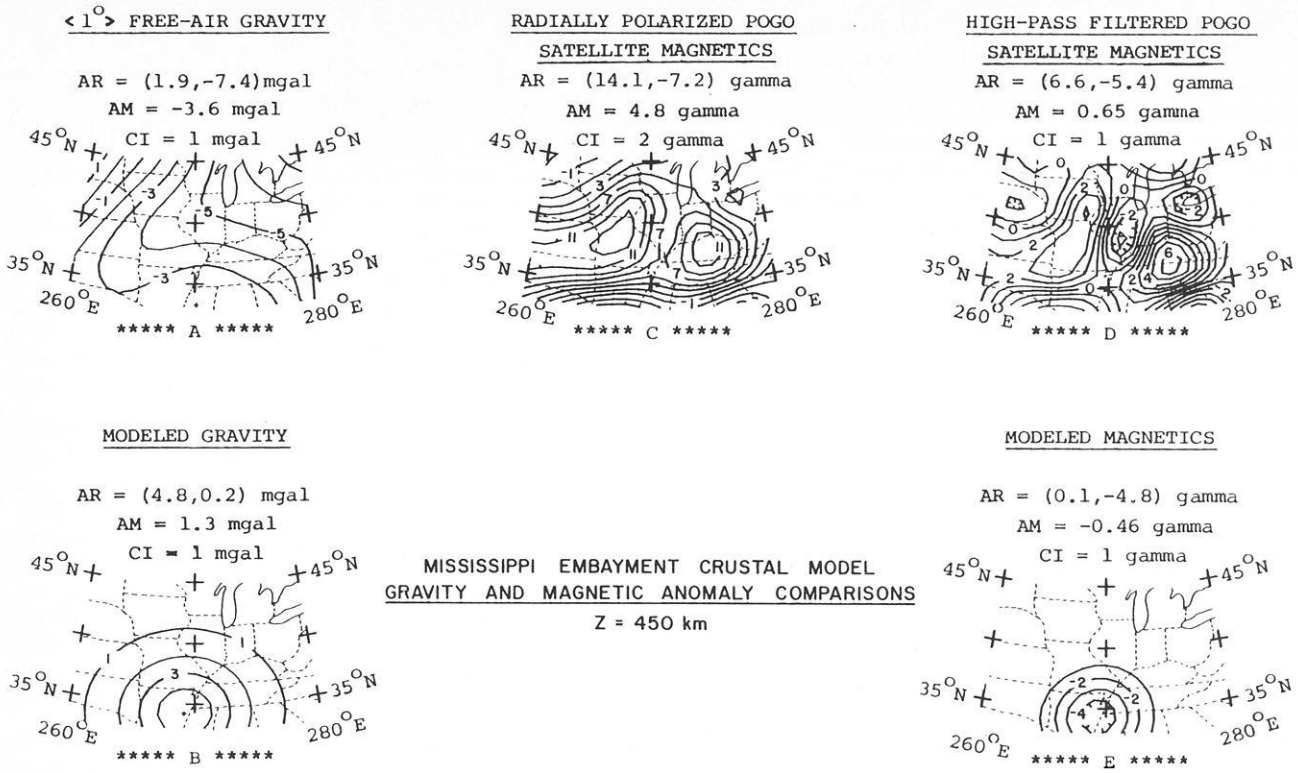

Fig. 7A–E. Mississippi embayment satellite-level comparisons between Gauss-Legendre quadrature modeled gravity and magnetic anomalies and upward continued 1°-averaged free-air gravity and reduced-to-the-pole POGO satellite magnetic anomaly data. Each anomaly field is plotted on a stereographic equal-area polar projection

45) °N and compared to observed gravity and magnetic anomaly data at 450 km elevation.

Upward continuation of free-air gravity anomaly values from the surface of the earth to an elevation of 450 km by equivalent point source inversion for the study area leads to the results shown in Fig. 7A. These data exhibit a pronounced relative positive anomaly with slightly greater than 3 mgal of relative amplitude in the region of the embayment. The gravity effect of the generalized four-body model described above is shown in Fig. 7B as roughly a 4 mgal anomaly. The general agreement between the modeled and observed data over the embayment suggests that the observed gravity anomaly can be reasonably well accounted for at 450 km elevation by the generalized four-body model.

Polar Orbiting Geophysical Observatory (POGO) satellite magnetometer observations reduced to radial polarization using a normalization amplitude of 60,000 gamma by equivalent point source inversion are given for the study area in Fig. 7C. These data show a prominent east-west magnetic high that is breached in the vicinity of the embayment by a magnetic low. To give better resolution of the characteristics of the magnetic anomaly for the embayment region, the radially polarized data were high-pass filtered for anomaly wavelengths smaller than about 10°. The high-pass filtered data are illustrated in Fig. 7D and show a negative anomaly of roughly −3 gamma over the embayment.

Wasilewski et al. (1979) found that most analyses of medium to long-wavelength magnetic anomalies suggest that sources are probably contained in the lower crust which, in general, may be substantially more magnetic than the upper crust. The conditions for coherent regional magnetization are enhanced as crustal depth increases. Remanence and thermal overprints are diminished, and viscous magnetization and initial susceptibility are enhanced with increasing temperature especially within 100°–150° C of the Curie point. The thickness of the crust within this thermal regime may be 5–20 km depending on the steepness of the geothermal gradient. Accordingly, they suggest that deep crustal magnetic sources are probably related to lateral variations of petrologic factors or Curie isotherm topography.

Accordingly, an obvious deep crustal source for the observed magnetic anomaly is body #2 (Fig. 6C) which also represents the major gravity source of the embayment model. Austin and Keller (1979) propose that the combination of bodies #1 and #2 was formed as a manifestation of a mantle upwarp beneath the embayment comprising of a mixture of crust and upper mantle material which subsequently cooled to form a block of high density material. Magnetic hypotheses which are consistent with this view include body #2 as a zone of negative magnetization contrast with respect to the lower crust due to depletion of magnetic minerals. Negative magnetization for body #2 also can result from temperatures which exceed the Curie point, although present heat flow data (Sass et al. 1976) do not appear to warrant this hypothesis for the embayment.

Body #3 may represent an additional magnetic source for the embayment assuming crustal magnetization increases with depth. However, the positive magnetic contribution of body #3 will be relatively weak if the Curie isotherm depth is about 40 km or more. Arguments for including bodies #1 and #4 in a magnetic model of the embayment appear to be lacking, so that body #2 probably represents the primary source for the observed magnetic anomaly data if the Curie isotherm is at about 40 km of depth in the region of the embayment.

Hence, the magnetic anomaly due to body #2 was calculated in Fig. 7E using a magnetization contrast of -2.4×10^{-3} emu/cm^3. These results show that the anomaly amplitude observed for the region of the embayment at 450 km elevation can be matched well by a source such as body #2 located near the base of the crust with magnetic properties which correspond with the magnetization characteristics anticipated for the lower crust. Substantial disparity is apparent, however, when the spatial characteristics of the observed and modeled magnetic anomalies are compared. Further refinements of the magnetic model are necessary and will be particularly warrented when data are available from the current Magsat program (Langel 1979) to verify and further upgrade the POGO satellite magnetic anomalies for lithospheric applications. Accordingly, body #2 as determined by gravity modeling considerations represents only a preliminary magnetic model for the embayment.

Conclusions

Regional gravity and magnetic anomaly modeling for arbitrarily shaped lithospheric sources with variable physical properties can be achieved accurately and efficiently in spherical coordinates using Gauss-Legendre quadrature integration. The procedure involves representation of the anomalous source as a distribution of equivalent point gravity poles or point magnetic dipoles which contribute incremental anomaly values evaluated and summed at each observation point to obtain the total anomaly. The distribution of equivalent point sources is determined directly from the volume limits of the anomalous body. For an arbitrarily shaped body, the variable limits of integration can be obtained from interpolations performed on a set of body points which approximate the surface envelope of the anomalous source.

A chief practical advantage of the method is its considerable versatility. The physical properties of the equivalent point sources, for example, can be individually varied to reflect physical property variations of the body being modeled. The method can also be readily extended to model the geoidal anomaly, vector components, and spatial derivatives to any order of the body's anomalous gravitational and magnetic potentials. Finally, the accuracy of the method can be controlled by adjusting the number of equivalent point sources or the distance between the source and observation point. In this regard, the method is particularly well suited for satellite gravity and magnetic anomaly modeling because the efficiency and accuracy of the application increases with increasing distance between source and observation points.

In consideration of the foregoing results, it is concluded that Gauss-Legendre quadrature integration facilitates a powerful and efficient approach to spherical earth modeling of regional-scale lithospheric gravity and magnetic anomaly sources. Accordingly, the method has widespread application in the analysis and design of regional-scale gravity and magnetic surveys for lithospheric investigation.

Acknowledgements. Financial support for this investigation was provided by the Goddard Space Flight Center under NASA Contract NAS5-25030.

References

Austin, C.B., Keller, G.R.: A crustal structure study of the Mississippi Embayment. In: An integrated geophysical and geological study of the tectonic framework of the 38th parallel lineament in the vicinity of its intersection with the extension of the New Madrid fault zone, U.S. Nuclear Regulatory Commission Rept. NUREG/CR-1014, Braile, L.W., Hinze, W.J., Sexton, J.L., Keller, G.R., Lidiak, E.G., eds: 101–133, 1979

Bhattacharyya, B.K.: Computer modeling in gravity and magnetic interpretation. Geophysics **43**, 912–929, 1978

Cain, J.C., Hendricks, S.J., Langel, R.A., Hudson, W.V.: A proposed model for the International Geomagnetic Reference Field, 1965. J. Geomagn. Geoelectr. **19**, 335–355, 1967

Carnahan, B., Luther, H.A., Wilkes, J.O.: Applied Numerical Methods. New York: J. Wiley and Sons, Inc. 1969

Cordell, L.: Regional positive gravity anomaly over the Mississippi Embayment. Geophys. Res. Lett. **4**, 285–287, 1977

Ervin, C.P., McGinnis, L.D.: Reelfoot rift: Reactivated precursor to the Mississippi Embayment. Geol. Soc. Am. Bull. **86**, 1287–1295, 1975

Frese, R.R.B. von, Hinze, W.J., Braile, L.W., Luca, A.J.: Spherical earth gravity and magnetic anomaly modeling by Gauss-Legendre quadrature integration. NASA Rept NAS5-25030, 1980

Hall, D.H.: Long-wavelength aeromagnetic anomalies and deep crustal magnetization in Manitoba and Northwestern Ontario, Canada. Pageoph. **40**, 403–430, 1974

Heiskanen, W.A., Mortiz, H.: Physical Geodesy. San Francisco: W.H. Freeman and Co. 1967

Ku, C.C.: A direct computation of gravity and magnetic anomalies caused by 2- and 3-dimensional bodies of arbitrary shape and arbitrary magnetic polarization by equivalent point method and a simplified cubic spline. Geophysics **42**, 610–622, 1977

Langel, R.A.: Near-earth satellite magnetic field measurements: A prelude to Magsat. EOS (Trans. Am. Geophys. Union) **60**, 667–668, 1979

McCamy, K., Meyer, R.P.: Crustal results of fixed multiple shots in the Mississippi Embayment; In: The Earth Beneath the Continents, Steinhart, J.S., Smith, T.J., eds: Am. Geophys. Union Geophys. Monogr. **19**, 370–381, 1966

Sass, J.H., Diment, W.H., Lachenbruch, A.H., Marshall, B.V., Munroe, R.J., Moses, T.H., Jr., Urban, T.C.: A new heat-flow contour map of the conterminous United States. U.S.G.S. Open-file Rept. 76–756, 1976

Shuey, R.T., Schellinger, D.K., Johnson, E.H., Alley, L.B.: Aeromagnetics and the transition between the Colorado Plateau and the Basin and Range Provinces. Geology **1**, 107–110, 1973

Stroud, A.H., Secrest, D.: Gaussian Quadrature Formulas. New Jersey: Prentice-Hall 1966

Talwani, M., Ewing, M.: Rapid computation of gravitational attraction of three-dimensional bodies of arbitrary shape. Geophysics **25**, 203–225, 1960

Talwani, M.: Computation with the help of a digital computer of magnetic anomalies caused by bodies of arbitrary shape. Geophysics **30**, 797–817, 1965

Warren, D.H., Healy, J.H.: Structure of the crust in the conterminous United States. Tectonophysics **20**, 203–213, 1973

Wasilewski, P.J., Thomas, H.H., Mayhew, M.A.: The Moho as a magnetic boundary, NASA Rept. NASA-GSFC TM80245, 1979

Woollard, G.P., Joesting, H.R.: Bouguer gravity anomaly map of the United States. Am. Geophys. Union and U.S. Geological Survey, scale 1:2,500,000, 1964

Received July 29, 1980
Accepted January 15, 1981

J Geophys (1981) 49:243–244

Journal of Geophysics

Short Communication

Detection Probabilities for Earthquakes in Sweden

A. Shapira, O. Kulhánek, and R. Wahlström
Seismological Department, Box 12019, S-750 12 Uppsala, Sweden

Key words: Detection probability – Earthquakes in Sweden – Swedish Seismograph Station Network – Threshold magnitude – Weak regional seismic events

In recent years, the need for improved seismic risk evaluations in Sweden has led to accurate estimates of detection probabilities with respect to weak Swedish earthquakes. Generally, these rather low-magnitude events ($M_L < 4$) are recorded only by means of the *Swedish Seismograph Station Network* (SSSN), currently consisting of six permanent stations. Only occasionally do neighbouring Finnish and/or Norwegian stations also contribute with arrival-time readings. Hence, for weak regional events, we lack the usual reference system of organisations like ISC, NEIS or EMSC when estimating the detection performance of the SSSN-stations. The problem has recently been studied and a solution suggested by Shapira et al. (1979a), to be referred to as Paper I. In short, their method, which is based upon a modification of the approach of Ringdal (1975), enables the estimation of threshold magnitudes for weak events monitored exclusively by regional networks.

The main objective of the present short communication is to indicate the ability of the SSSN to detect earthquakes in Sweden and the relative detection contributions from individual network stations. The data used comprise 121 earthquakes located within Sweden and adjacent waters (Wahlström 1978). The statistical model used and other theoretical aspects of the modified approach are discussed in greater detail in Paper I and are not repeated here.

When applying the modified approach, the detectability is related to the epicentral distance rather than to a certain seismic region. To introduce the distance dependence, all available earthquakes are relocated to a common epicentral distance. It is assumed that recorded amplitudes and periods are not influenced by performing the distance and corresponding magnitude conversion. Employment of the distance transformation enables calculations of magnitudes for fictitious events located at a number of chosen epicentral distances. For more details, the reader is referred to Paper I and to Shapira et al. (1979b).

The decision "detected" or "not detected" is based upon the conserved amplitude and period values linked with the *Sg*-phase. Thus, when the actual earthquake is detected by station *A*, then it is assumed that all relocated events associated with this actual earthquake, are also detected. The percentage of detections, for each magnitude, is fitted to the detection curve $P(M_R)$ which yields estimates of biased threshold magnitudes $b \pm s$. Corrected threshold magnitudes $\hat{b} = b + C_A$ and their variance $\hat{s}^2 = s^2 - \rho_A^2$ are to be used when comparing the detecting power of stations within the network. C_A is station magnitude bias and ρ_A^2 is magnitude variance.

The modified approach has been applied to each of the six SSSN-stations. Events were relocated to a common epicentral distance of 500 km. A fit to the detection curve and estimates of b and s, associated with 50% probability, are presented in Fig. 1 Numerical values of $\hat{b}$ and $\hat{s}$, corresponding to 50% probabilities, are also given in Fig. 1. Considering 90% detection levels, station UDD contributes to the detecting power more than any other station of the SSSN. The second best station is SKA, although its operational magnification is the lowest among the six stations.

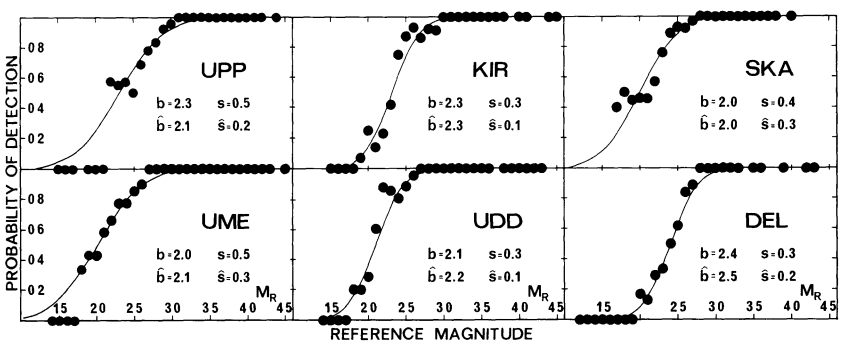

Fig. 1. Matched detection curves, $P(M_R)$ (*solid lines*), and observed detection probabilities (*solid circles*) for the six stations considered (*UPP* = Uppsala, *KIR* = Kiruna, *SKA* = Skalstugan, *UME* = Umeå, *UDD* = Uddeholm, *DEL* = Delary) and for epicentral distance of 500 km. Biased and corrected threshold magnitudes and corresponding variances, associated with 50% probabilities, are given for each station

0340-062X/81/0049/0243/$01.00

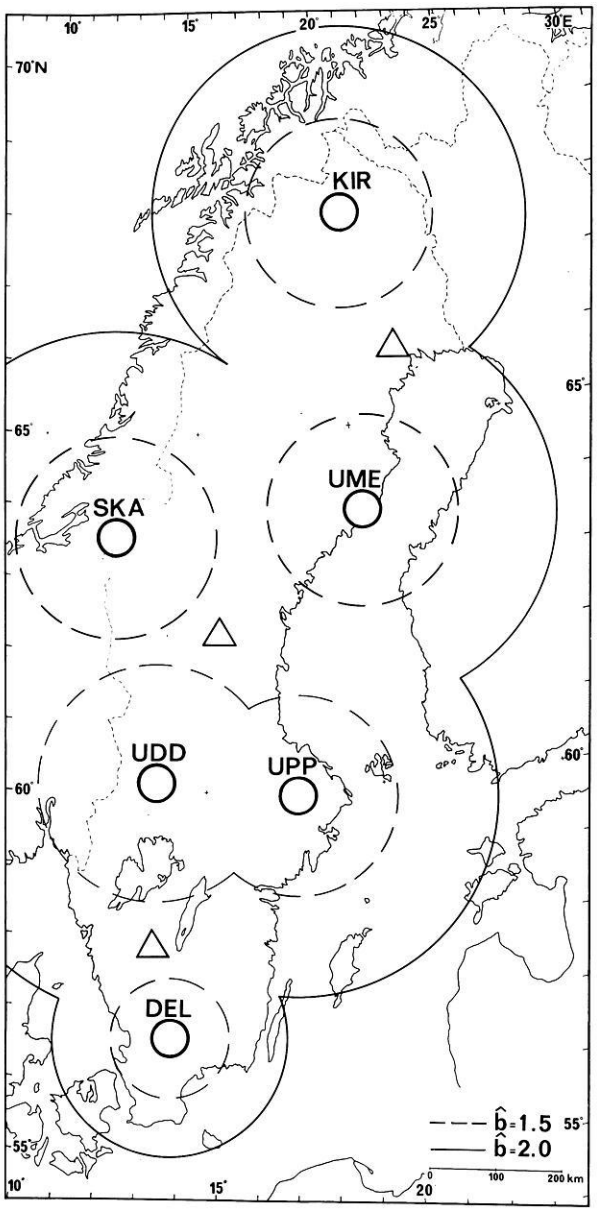

Fig. 2. Locations of the six permanent seismograph stations of the current SSSN (*open circles*). Loci of constant threshold magnitudes $\hat{b}=1.5$ and $\hat{b}=2.0$ (*thin circles*) with respect to the SSSN and 90% detection level. *Open triangles* show three suggested new recording sites

In Fig. 2, 90% probability contours corresponding to $\hat{b}=1.5$ and $\hat{b}=2.0$ are displayed. It follows from the figure, that Swedish earthquakes of magnitude 2.0 or larger will be detected by at least one station of the current SSSN. To increase the detection capability, say, to a threshold magnitude of 1.5, we may suggest three additional stations, as shown in Fig. 2. The three new recording sites are suggested with regard to the known seismicity of Sweden.

Our main conclusions may be summarized as follows: (1) The applicability of the well-known direct estimation method has been extended to weak earthquakes recorded solely by regional seismograph networks. (2) Swedish earthquakes of magnitude $M_L=2.0$ or larger are detected with 90% probability by at least one station of the current SSSN.

Acknowledgement. This work was carried out at the Seismological Dept Uppsala University, Sweden. One of the authors (A.S.) received a research grant from the Swedish Institute for Cultural Relations with Foreign Countries.

References

Ringdal, F.: On the estimation of seismic detection thresholds. Bull. Seismol. Soc. Am. **65**, 1631–1642, 1975

Shapira, A., Kulhánek, O., Wahlström, R.: Detection probabilities for weak regional seismic events. J. Geophys. **46**, 123–133, 1979a

Shapira, A., Kulhánek, O., Wahlström, R.: Detectability of regional events by means of the Swedish Seismograph Station Network. Seismol. Inst., Uppsala, Report 7–79, 17 pp. 1979b

Wahlström, R.: Magnitude-scaling of earthquakes in Fennoscandia. Seismol. Inst., Uppsala, Report 3–78, 47 pp, 1978

Received September 8, 1980; Revised Version February 23, 1981
Accepted March 23, 1981

J Geophys (1981) 49:245–246

Journal of Geophysics

Short Communication

The Geocyclotron Revisited: Potentialities of Modulated Wave Injection

Armando L. Brinca*
Max-Planck-Institut für Aeronomie, D-3411 Katlenburg-Lindau 3, Federal Republic of Germany

Key words: Modulated wave injection – Continuous cyclotron resonance – Whistler-electron interaction

Introduction

Controlled VLF-wave injection into the magnetosphere has been used in the Siple experiment (Antarctica, $L=4$) since 1973 (Helliwell 1977); similar capability also exists in the high-latitude ionospheric heating experiments ($L\sim 6$) run by the Murmansk Polar Geophysical Institute and the Max-Planck-Institut für Aeronomie, through modulation of the polar electrojet (Stubbe and Kopka 1977), and might possibly be implemented in an early space shuttle mission or on a satellite. We here draw attention to the potentialities offered by an adequate variation of the frequency and amplitude of the coherent, injected radio signal. They include selective modifications of the energetic electron distribution along a given magnetic field line, testing of nonlinear (wave-particle) interaction theories and enhancement, at lower power levels, of magnetospheric phenomena associated with wave injection. The modulation of the injected frequency extends the cyclotron resonance interval in the inhomogeneous magnetosphere, whereas the eventual need for amplitude modulation is suggested by a stability analysis of the trapped electron motion in the whistler field.

Modification of the energy of radiation-belt electrons through their gyro-resonance with artificial whistlers of modulated frequency was suggested twenty years ago as an alternative to high-altitude (e.g., Argus) nuclear detonations (Helliwell and Bell 1960). The idea was then to vary the frequency of the circularly polarized whistler in order to compensate for the change of mass experienced by relativistic cyclotron resonant electrons. This 'geocyclotron' was, however, not implemented; the feasibility study concluded that the information required to make a reliable prediction was not available at the time (Bell 1964).

Stability of Interaction

In contrast to the original geocyclotron mechanism whereby the electrons stayed in the vicinity of the equatorial plane and the change in the wave frequency compensated for the relativistic effects, we now propose to program the wave frequency so that energetic electrons moving towards the transmitter experience continuous cyclotron resonance with the wave in a way which maximizes the modification of the electrons energy and pitch angle.

The interaction between ducted CW parallel whistler mode waves and counter-streaming cyclotron resonant electrons ($v_\perp$, $v_\parallel$) might induce phase trapping (Dysthe 1971; Gendrin 1975). The evolution for the angle $\psi=\mathrm{ang}(-B_w, v_\perp)$, with $\mathrm{sgn}\,\psi = \mathrm{sgn}(E_w, v_\perp)$, is identical to the pendulum equation having a steady forcing term resulting from the inhomogeneity of the medium. This forcing term, which causes the equilibrium position ψ_0 of a trapped particle to be non-zero, increases as the particle moves away from the equator and detrapping eventually occurs. It should be stressed that a non-zero ψ_0 implies that even a deeply trapped (weakly oscillating) particle has a non-zero electrical force acting on it. Thus the energy, E, and the equatorial pitch angle, α_e, increase (decrease) when $\sin\psi_0$ is negative (positive). Although the inhomogeneity limits the effective interaction time, resonances involving CW whistlers are responsible for a wide variety of magnetospheric phenomena; extension of the interaction time would be expected to enhance these effects.

Variation of the whistler frequency ω originates a new forcing term in the pendulum equation proportional to $\dot{\omega}$. Adequate choice of the wave frequency can then lead to a constant equilibrium angle, ψ_0, and hence to a steady unidirectional transfer of energy between the particle and the wave. We have found, for a given ψ_0, the appropriate ω to be

$$\dot{\omega}=\left\{\left[\frac{k v_\perp^2}{2\omega_c}+\left(1+\frac{v_\parallel}{2V_G}\right)v_\parallel\right]\frac{d\omega_c}{dz}-\frac{k v_\parallel^2}{\omega_p}\frac{d\omega_p}{dz}-\omega_{NL}^2\sin\psi_0\right\}\Bigg/\left(1+\frac{v_\parallel}{2V_G}\frac{\omega_c}{\omega}\right), \tag{1}$$

where V_G is the cyclotron resonant parallel velocity, $\omega_c/2\pi$ the gyrofrequency defined by the geomagnetic field aligned with the z-axis, $\omega_p/2\pi$ the plasma frequency, and $\omega_{NL}/2\pi$ the bounce frequency of deeply trapped electrons in the CW, homogeneous medium case.

Clearly, particle trapping has to be stable if the expected interaction enhancement is to occur. In this respect, we first note that direct analysis of the pendulum equation shows small deviations from ψ_0 to be unstable when $\cos\psi_0<0$; elsewhere, in the stable domain $|\psi_0|<\pi/2$, deeply trapped electrons have harmonic motion with angular frequency $\omega_{NL}\,(\cos\psi_0)^{1/2}$. The long term stability of the trapped orbits can be assessed by following the evolution of a generalized trapping parameter. In the CW homogeneous case, the trapping parameter $\xi=\eta^2$ characterizes the resonant trajectories (Dysthe 1971): the separatrix ($\xi=1$) divides the phase plane into trapped ($0<\xi<1$) and untrapped ($\xi>1$) domains. For the general interaction, noting that our oscillating system is Hamiltonian with slowly (on the scale of $1/\omega_{NL}$) varying parameters, and adopting the generalized trapping parameter used by Dysthe and Gudmestad

* *Present address:* Centro de Electrodinâmica, Instituto Superior Técnico, P-1096 Lisboa Codex, Portugal

0340-062X/81/0049/0245/$01.00

(1977) in the study of trapping by Langmuir waves, we can establish that $\xi\,\omega_{NL}$ is an invariant of the interaction. Since ω_{NL}^2 is proportional to the whistler amplitude, trapping stability (non-increasing ξ) can prevail, even for particles initially not very deeply trapped, by appropriate amplitude modulation of the injected wave, thus preventing too large a decrease of ω_{NL} and a corresponding increase of ξ above unity.

Results and Discussion

Figures 1 and 2 show typical results obtained from the simultaneous solution of the average (deeply trapped, $\psi \sim \psi_0$) electron motion equations and Eq. (1). The electrons initiate the interaction at the equator, or at 10° N latitude, with $v_{\|*} = V_G$, as defined by the initial wave frequency ω_*, and $v_{\perp *} = v_{\|*} \tan \alpha_*$. Having computed the locally required whistler frequency $\omega(z,t)$, the desirable format of the ground transmitter spectrogram is determined by the propagation times of the various wavepackets from (z,t) to the emitter site. Occurrence of mirroring ($v_\| \sim 0$), entrance into the loss cone ($\alpha_e < 5.5°$), or un-ducting ($\omega/\omega_c > 0.5$) halted the computation. We adopted a diffuse equilibrium model for the thermal magnetospheric plasma, with the parameters used by Bernhardt (1979). Frequency modulated wavetrains of 10 mγ (duct) amplitude, propagating from south to north along $L=4$, with (transmitter) durations ranging from $\sim$400 ms to $\sim$800 ms are able, either to more than triple initial equatorial pitch angles of $\alpha_{e*}=10°$ (interactions with $\psi_0 < 0$), or to push into the loss cone resonant electrons with $\alpha_{e*}=20°$ (interactions with $\psi_0 > 0$); except for the deeply trapped particles, interactions with $\psi_0 > 0$ would require a stabilizing wave amplitude modulation. Although the occurrence of $\Delta\alpha_e \neq 0$ implies $\Delta E \neq 0$, the change of the electron energy ($E \sim 2$ keV) in these examples is well below 20%; the slope of the variation of the average α_e with position,

$$\frac{d\alpha_e}{dz} = -a\frac{v_\|}{v^3}\left(v^2 + \frac{\omega}{k}v_\|\right)\sin\psi_0\left(\frac{\omega_c}{\omega_{c_e}} - \frac{v_\perp^2}{v^2}\right)^{-1/2}, \qquad v^2 = v_\perp^2 + v_\|^2$$

is almost constant here, and the interaction might induce a sizable alteration in the pitch angle distribution (and hence, in the whistler stability through the 'temperature' anisotropy). The sharpness of the cyclotron resonance (roughly $\pm 2\omega_{NL}/k$ in $v_\|$) imposes stringent limits on the accuracy of the magnetospheric parameters used in the calculation of the appropriate frequency variation, curtailing the generalized implementation of the proposed mechanism. However, analysis of resonances occurring under favorable conditions (small interaction regions near the equatorial plane with large $|d\alpha_e/dz|$) suggests that use of data from whistler ground stations and in situ satellite measurements might overcome this difficulty in the plasmasphere.

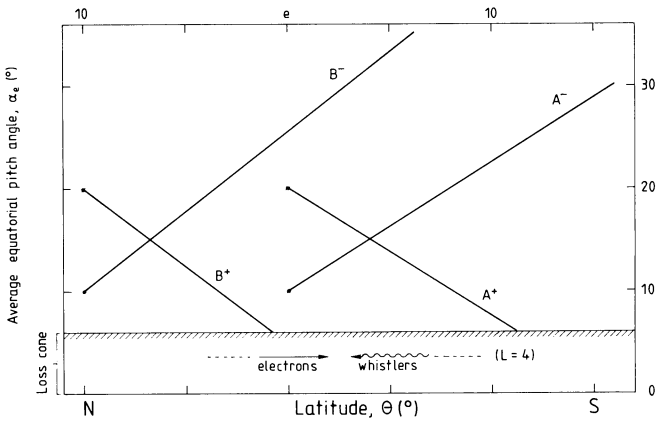

Fig. 1. Evolution of the average equatorial pitch angle of resonant electrons along a field line $L=4$ when appropriate (Fig. 2) whistler frequency modulation is used (* identifiers the conditions at the start, $t=0$, of the interaction). $\omega_*/\omega_{c_e} = 0.366$ (A), 0.5 (B); $\alpha_{e*} = 20°(+)$, $10°(-)$; $\psi_0 = 30°(+)$, $-30°(-)$

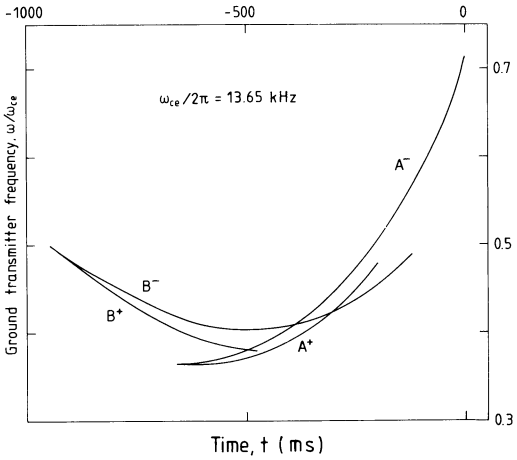

Fig. 2. Formats of the ground transmitter spectrogram required to achieve continuous cyclotron resonance for the cases contemplated in Fig. 1

An appropriate choice of the transmitter spectrogram format (possibly utilizing sequences of variable frequency pulses) permits selection within generous bounds of the location of the interaction region, and the type of selective modifications to be introduced in a given domain of the energetic electron distribution. This flexibility is welcome in the research of waves and wave-particle interactions in the magnetosphere (Gendrin 1975), and is a recommendation for the use of the technique in the near future since, in contrast to the situation faced twenty years ago, the expensive components of the required experimental setups are now (or will soon become) installed.

Acknowledgments. I thank Professor J.A. Fejer for helpful comments. This research was carried out as a Research Fellow of the Alexander von Humboldt Foundation.

References

Bell, T.F.: Wave particle gyroresonance interactions in the earth's outer ionosphere. Ph. D. Thesis, Stanford University, 1964

Bernhardt, P.A.: Theory and analysis of the 'super-whistler'. J. Geophys. Res. **84**, 5131-5142, 1979

Dysthe, K.B.: Some studies of triggered whistler emissions. J. Geophys. Res. **76**, 6915-6931, 1971

Dysthe, K.B., Gudmestad, O.J.: Acceleration of trapped particles by a Langmuir wave in an inhomogeneous plasma. J. Plasma Phys. **18**, 509-523, 1977

Gendrin, R.: Waves and wave-particle interactions in the magnetosphere: a review. Space Sci. Rev. **18**, 145-200, 1975

Helliwell, R.A.: Active VLF experiments on the magnetosphere from Siple Station, Antarctica. Philos. Trans. R. Soc. London Ser B: **279**, 213-224, 1977

Helliwell, R.A., Bell, T.F.: A new mechanism for accelerating electrons in the outer ionosphere. J. Geophys. Res. **65**, 1839-1842, 1960

Stubbe, P., Kopka, H.: Modulation of the polar electrojet by powerful HF waves. J. Geophys. Res. **82**, 2319-2325, 1977

Received April 9, 1980; Revised Version February 25, 1981
Accepted March 5, 1981

J Geophys (1981) 49:247–248

Journal of Geophysics

Short Communication

Eine kleine Historie zur Namengebung der Fachdisziplin Geophysik

G. Buntebarth
Institut für Geophysik der TU Clausthal, Postfach 230, D-3392 Clausthal-Zellerfeld, Federal Republic of Germany

A Short History on the Naming of the Discipline Geophysics

Abstract. During the first half of the 19th century the established geography was represented by Carl Ritter. The geography was treated in a manner which evoked Fröbel's sharp criticism. He called for a pure geography treating the earth as an indivisible whole, not subdivided into countless parts, the countries of which each was considered as an individuum by Carl Ritter. Julius Fröbel (1834) planned a theoretical geography and he called its physical part "Geophysik". During the following four decades the name "Geophysik" was used scarcely. After the seventieth of the last century, however, the name "Geophysik" became more popular.

Key words: History of geophysics – Julius Fröbel

Der Anreiz zu abenteuerlichen Seefahrten in unbekannte Gewässer ging etwa Mitte des 17. Jahrhunderts mehr und mehr verloren. Fast alle Küsten der Kontinente waren den seefahrenden Nationen bekannt. Spektakuläre Neuentdeckungen von Ländern konnten nicht mehr erwartet werden. Die Zeit war reif für eine Umorientierung in der Zielsetzung von Entdeckungsfahrten. Politische Aspekte wurden zugunsten wissenschaftlicher Aufgabenstellungen hintenan gestellt, und den wissenschaftlichen Entdeckungsreisen wurde der Weg geebnet. Dies war aber nur möglich, weil in der Zwischenzeit die Stiftungen gelehrter Körperschaften die Basis sowohl in organisatorischer wie auch in finanzieller Hinsicht dafür schufen. 1645 wurde die Royal Society in London gegründet, 1652 die Kaiserliche Leopoldinisch-Carolinische Akademie, 1666 die französische, um nur einige der ersten Stiftungen zu nennen. Vielleicht 200 Jahre lang währte die Zeit der großen wissenschaftlichen Entdeckungsreisen in alle Gegenden der Welt.

Bis Anfang des 19. Jahrhunderts hatte sich reichlich Beobachtungsmaterial auch auf dem Gebiete der Geographie angesammelt, und die Gelehrten machten sich nun daran, darüber nachzudenken, wie man die Einzeldarstellungen zusammenfasse und ordne. Die Geographie wurde im wesentlichen historisch-politisch betrachtet, so daß eine Erdbeschreibung bei dieser Betrachtungsweise nur recht kurze Zeit Gültigkeit haben konnte. Die häufigen Grenzverschiebungen zwangen eine „neueste Erdbeschreibung" nach der anderen zu verfassen, die bestimmt in manchen Fällen schon bei ihrer Erscheinung veraltet war.

Es war nun ein Verdienst Carl Ritters, daß er alle geographischen Tatsachen unter die leitende Idee der Kultur im weitesten Sinne stellte. Diese anthropozentrische Behandlung der geographischen Elemente war von der damals vorherrschenden romantischen Naturphilosophie vorgezeichnet. Jedoch gaben Carl Ritters Antipathie gegen klare Definition von Begriffen und seine unklare Trennung wissenschaftlicher Aufgaben Julius Fröbel (1831) Anlaß genug, eine scharfe Kritik zu formulieren. Julius Fröbel, der 1805 in Griesheim/Thüringen geboren wurde, studierte in jener Zeit in Jena, und mit Vorliebe beschäftigte er sich mit methodologischen Fragen der Geographie. Nach Fröbels Ansicht wurde die Geographie völlig unwissenschaftlich dargestellt wegen der Zergliederung der Erdoberfläche in individualistische Teile, den einzelnen Ländern. Fröbel wollte die Erde als Ganzes betrachtet wissen, als ein Individuum im Raume. Sichtlich beeinflußt von Kant, gab Fröbel seiner Geographie die leitende Idee, alle Elemente der reinen Erdkunde auf das Erdganze zu beziehen, sowohl für einen beschreibenden Teil wie auch für einen theoretischen. Die so geschaffene theoretische Erdkunde soll das Zusammenwirken aller tellurischen Erscheinungen zum Gesamtorganismus der Erde erklären. Diese umfassende theoretische Lehre von der Erde nennt Fröbel (1834) auch Geophysik. Die Geophysik ist Teil einer allgemeinen Theorie der Erde, die nach Fröbel die Aufgabe hat, erstens die allgemeinen physikalischen und chemischen Prozesse daraufhin zu erforschen, wie sie im Gesamtleben der Erde zusammenwirken und zweitens die Gesetze des tellurischen Ineinandergreifens aufzuklären.

Obwohl die Ziele unserer heutigen allgemeinen Geophysik schon vor nahezu 150 Jahren im wesentlichen vorgezeichnet wurden, konnte sich zu jener Zeit die Geophysik nicht als Fachdisziplin konstituieren, jedoch der Name blieb gegeben. Ein wesentlicher Grund war sicherlich, daß Fröbel gar kein Geophysiker war. Er war Professor für Mineralogie an der Universität Zürich und Lehrer für Geographie an der Oberen Industrieschule in Zürich. Seine methodologischen Arbeiten zur Geographie beendete er noch in den dreißiger Jahren des vorigen Jahrhunderts, und seinem zunehmenden Interesse am öffentlichen Leben zufolge wurde er schließlich als Publizist und Politiker bekannt. Er verbrachte nach einem wechselvollen Leben seine letzten Jahre bis zu seinem Tode 1893 in Zürich.

Die Diskussion um die Methodik der Erdkunde hat trotzdem Früchte getragen. Obwohl der Name Geophysik in der Folgezeit nur selten im Schrifttum auftaucht (Kertz 1979), z.B., in Meyer's Großem Conversationslexikon, Band 12 (1848) und bei Mühry (1858, 1863), gerät er nicht gänzlich in Vergessenheit, sondern wird von den siebziger Jahren des vorigen Jahrhunderts an allmählich zu Allgemeingut (z.B. v. Richthofen 1877; Wagner 1878; Zöppritz 1881; Günther 1884).

0340-062X/81/0049/0247/$01.00

Daß die geographische Methodik Carl Ritters seit Fröbels Kritik immer wieder Gegenstand von Diskussionen war, lag, wie Fröbel aufzeigte, in der Schwäche des Systems; daß aber keine Änderung möglich war, lag an der Stärke von Carl Ritters Autorität. Erst etwa 35 Jahre nach Fröbels Angriff kritisierte Oscar Peschel erneut die Rittersche Geographie (in: Wagner, 1878). Die Kritik Peschels zeigt deutlich kompromißbereite Züge. Peschel fordert nicht wie Fröbel die rigorose Beseitigung aller teleologischen Aspekte, und im Gegensatz zu Fröbel wendet Peschel sein System auch an. Dem Fröbelschen System konnten Ritter und seine Anhänger noch triumphierend entgegnen (Ritter 1831), daß diese „Theorie der Konstruktion, die ohne Anwendung ein Luftgebilde bleibt, nur zu leicht wieder in Vergessenheit versinkt", was auch geschah.

Die Vermehrung geophysikalischer Erkenntnisse in jener Zeit, hauptsächlich auf den Gebieten der Schwerkraft und Figur der Erde, ihrer Dichte, des Erdmagnetismus und der Geothermie, führten zu ihrer Abspaltung von der mathematischen und physikalischen Geographie. Die Geographen selbst beschäftigten sich kaum oder gar nicht mit diesen Fachgebieten, sondern benutzten die von Astronomen, Mathematikern und Physikern erarbeiteten Ergebnisse schon längst als einführende Grundlagen in ihre Disziplin.

Eine so allumfassende Fachdisziplin, die alle tellurischen Erscheinungen in sich vereinigt, eine so allgemeine Geographie wie Fröbel sie plante, war gar nicht realisierbar. Der Stoff war schon damals viel zu umfangreich, und die Betrachtungsweisen waren viel zu unterschiedlich. Es gingen schon bald aus der physikalischen Geographie beispielsweise folgende Fachdisziplinen hervor: die Geologie, die die festen Teile der Erdoberfläche beschreibt, die Hydrographie, die die Verteilung des Wassers beschreibt, die Meteorologie, die die Lufthülle der Erde beschreibt, und auch die Geophysik, der physikalische Teil einer naturwissenschaftlichen Erdkunde, wie Fröbel sie plante.

Literatur

Fröbel, J.: Einige Blicke auf den jetzigen formellen Zustand der Erdkunde. Ann. Erd-, Völker- u. Staatenkunde **4**, 493–506, Berlin 1831

Fröbel, J.: Entwurf eines Systemes der geographischen Wissenschaften I. Mitteil. aus dem Gebiete d. Theoret. Erdkunde, **1**, 1–35, Zürich 1834

Günther, S.: Lehrbuch der Geophysik und Physikalischen Geographie, Bd. 1. Stuttgart: F. Enke 1884

Kertz, W.: Die Entwicklung der Geophysik zur eigenständigen Wissenschaft. Mitt. Gauss-Gesellschaft E.V. Göttingen **16**, 41–54, Göttingen 1979

Meyer's Großes Conversationslexikon, Bd. 12, Artikel: Geophysik, 530–534, Hildburghausen: Bibliogr. Inst. 1848

Mühry, A.: Klimatologische Untersuchungen oder Grundzüge der Klimatologie in ihrer Beziehung auf die Gesundheits-Verhältnisse der Bevölkerungen. Leipzig u. Heidelberg: C.F. Winter 1858

Mühry, A.: Beiträge zur Geo-Physik und Klimatographie. Leipzig, Heidelberg: C.F. Winter 1863

Richthofen, F. Freiherr von: China, Ergebnisse eigener Reisen und darauf gegründeter Studien, Bd. 1. Berlin: D. Reimer 1877

Ritter, C.: Schreiben an H. Berghaus in Beziehung auf den vorstehenden Aufsatz des Herrn Julius Fröbel. Ann. Erd-, Völker- u. Staatenkunde **4**, 506–520, Berlin 1831

Wagner, H.: Der gegenwärtige Standpunkt der Methodik der Erdkunde. Geograph. Jahrbuch **7**, 550–636, Gotha 1878

Zöppritz, K.: Der gegenwärtige Standpunkt der Geophysik. Geograph. Jahrbuch **8** (1880), 1–76, Gotha 1881

Received May 6, 1981
Accepted June 10, 1981

J Geophys (1981) 49:249

Journal of Geophysics

Correction

J Geophys (1980) 48:158–160

High Precision Measurement of the Frequency of Mode $_oS_o$

W. Zürn,[1] L. Knopoff,[2] and P.A. Rydelek[2]

[1] Geowissenschaftliches Gemeinschaftsobservatorium, Universitäten Karlsruhe/Stuttgart, Heubach 206, D-7620 Wolfach, Federal Republic of Germany
[2] Institute of Geophysics and Planetary Physics, University of California at Los Angeles, Los Angeles, California 90024, USA

We are very grateful to Dr. Michael Shimshoni for pointing out a small numerical error (< 1 s.d.) in the paper by Zürn et al. (1980). The corrected frequency of mode $_oS_o$ is:

$f(_oS_o) = 2.932827$ cph ± 11 ppm.

The new value is in agreement at the 1 s.d. level with the frequency reported by Riedesel et al. (1980).

References

Riedesel, M.A., Agnew, D., Berger, J., Gilbert, F.: Stacking for the frequencies and Qs of $_oS_o$ and $_1S_o$. Geophys. J.R. Astron. Soc. **62**, 457–471, 1980

Zürn, W., Knopoff, L., Rydelek, P.A.: High precision measurement of the frequency of mode $_oS_o$. J. Geophys. **48**, 158–160, 1980

Received April 6, 1981